

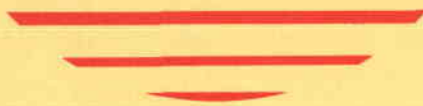
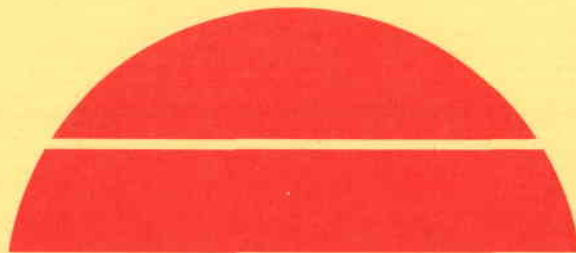
SOLAR PILOT PLANT, PHASE 1
PRELIMINARY DESIGN REPORT

Volume 3. Collector Subsystem (CDRL Item 2)

May 1, 1977

Work Performed Under Contract No. EY-76-C-03-1109

Honeywell, Incorporated
Energy Resources Center
Minneapolis, Minnesota



U.S. Department of Energy



Solar Energy

NOTICE

This report was prepared as an account of work sponsored by the United States Government. Neither the United States nor the United States Department of Energy, nor any of their employees, nor any of their contractors, subcontractors, or their employees, makes any warranty, express or implied, or assumes any legal liability or responsibility for the accuracy, completeness or usefulness of any information, apparatus, product or process disclosed, or represents that its use would not infringe privately owned rights.

This report has been reproduced directly from the best available copy.

Available from the National Technical Information Service, U. S. Department of Commerce, Springfield, Virginia 22161.

**Price: Paper Copy \$16.25
Microfiche \$3.00**

Honeywell

ERDA Contract No. E(04-3)-1109

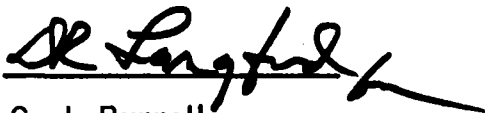
1 MAY 1977

SOLAR PILOT PLANT
PHASE I

PRELIMINARY DESIGN REPORT

VOLUME III
COLLECTOR SUBSYSTEM

CDRL Item 2



C. J. Bunnell
Contract Administrator



J. C. Powell
Program Manager

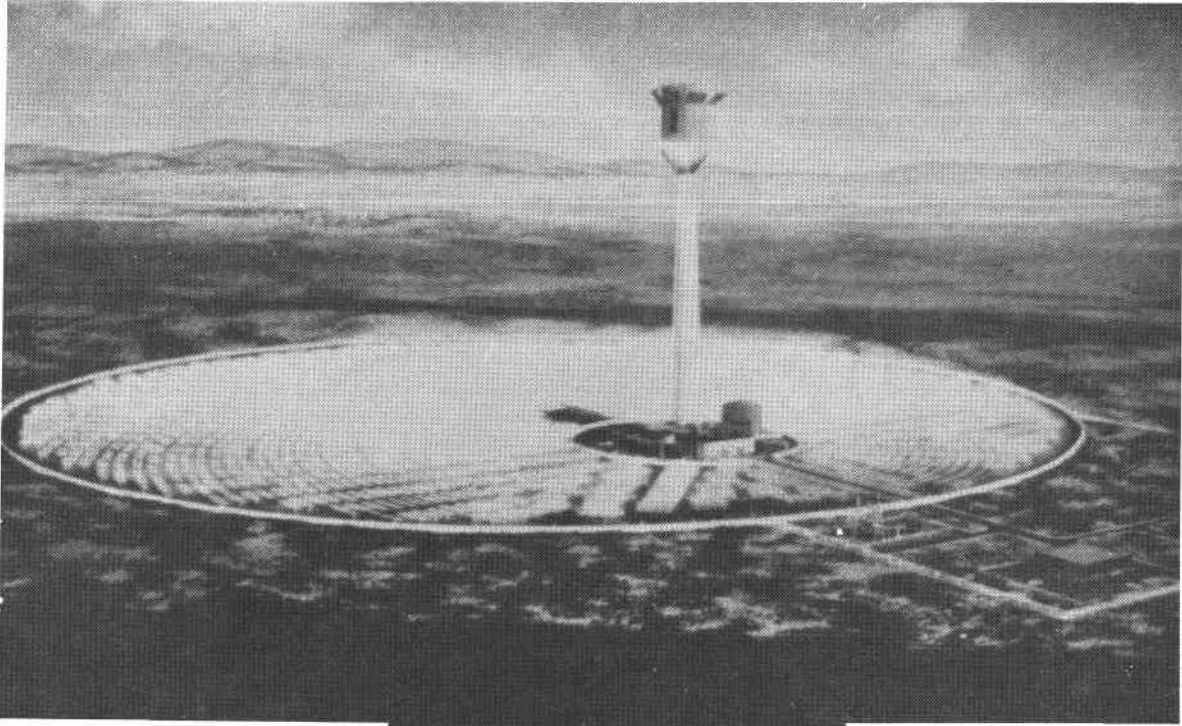
Energy Resources Center
2600 RIDGWAY PARKWAY,
MINNEAPOLIS, MINNESOTA 55413

FOREWORD

This is the initial submittal of the Solar Pilot Plant Preliminary Design Report per Contract Data Requirement List Item 2 of ERDA Contract E(04-3)-1109. The report is submitted for review and approval by ERDA. This is Volume III of seven volumes.

ABSTRACT

The Honeywell collector subsystem features a low-profile, multifaceted heliostat designed to provide high reflectivity and accurate angular and spatial positioning of the redirected solar energy under all conditions of wind load and mirror attitude within the design operational envelope. The heliostats are arranged in a circular field around a cavity receiver on a tower halfway south of the field center. A calibration array mounted on the receiver tower provides capability to measure individual heliostat beam location and energy periodically. This information and weather data from the collector field are transmitted to a computerized control subsystem that addresses the individual heliostat to correct pointing errors and determine when the mirrors need cleaning. This volume contains a detailed subsystem design description, a presentation of the design process, and the results of the SRE heliostat test program.



10 MEGAWATT SOLAR PILOT PLANT
ENERGY RESEARCH AND DEVELOPMENT ADMINISTRATION

TABLE OF CONTENTS

	<u>Page</u>
Foreword	ii
Abstract	iii
10 Megawatt Solar Pilot Plant	v
List of Illustrations	xv
List of Tables	xxv
 <u>Section</u>	
1 INTRODUCTION	1-1
Background	1-1
Phase I Program Scope	1-1
Organization of the Preliminary Design Report	1-3
2 SUMMARY COLLECTOR SUBSYSTEM DESCRIPTION	2-1
General Overview	2-2
Heliostat Overview	2-2
Field Overview	2-4
Command Computer Overview	2-6
Calibration Array and Instrumentation Overview	2-7
Overview Conclusion	2-8
Requirements and Specification Summary	2-8
System Operation Summary	2-8
Analysis Summary Description	2-11
SRE Test Results Summary	2-13
Comparison Between the SRE and Pilot Plant Collector Subsystem	2-14
Commercial Plant	2-19
Conclusion	2-19
3 DETAIL SUBSYSTEM DESCRIPTION SUMMARY	3-1
Introduction	3-1
Documentation Tree	3-4
Collector Subsystem Schematic	3-4
Heliostat Detail Mechanical Description	3-11
Heliostat Foundation and Post	3-11
Frame	3-15
Mirror Modules	3-17
Heliostat Inner Axis Drive	3-20
Heliostat Outer Axis Drive	3-25

TABLE OF CONTENTS (Continued)

<u>Section</u>	<u>Page</u>
3	DETAIL SUBSYSTEM DESCRIPTION SUMMARY (Continued)
Initialization Switches	3-29
Heliostat Weight	3-32
Parts Count	3-32
Heliostat Electronics, Detailed Operation	3-35
Heliostat Electronics, Overall Operation	3-35
Tracking Mode	3-35
Initialization Mode	3-37
Other Functions	3-37
Heliostat Electronics Communications	
Interface Details	3-37
Up/Down Counter and Counter Control	
Circuitry	3-38
Control Computer Updates	3-39
Incremental Encoder Updates	3-39
Digital to Analog Converter	3-39
Servo Output Amplifier	3-41
Incremental Encoder	3-43
Initialization	3-45
Outer Axis Two Motor Synchronizer	3-47
Timing Generator	3-48
SRE Heliostat Power Supply AC Power	3-51
DC Power	3-51
SRE Manual Operation	3-52
SRE Special Test Equipment	3-52
Electronics Packaging	3-54
Comparison of Electronics for SRE and Pilot Plant	3-57
Address Decoder	3-57
Uninterruptable Power	3-57
Other Fail-Safe Feature Additions	3-57
Power Sequencing to the Heliostat	
Electronics	3-57
Summary of Differences Between Electronics	
for SRE and Pilot Plant	3-59
Future Plans for the Heliostat Electronics	3-59
All Digital Gimbal Control Servos	3-59
Elimination of the ± 15 Volt Power Supply	3-60
Substitution of a Third Control Loop for	
the Two Motor Synchronizer	3-60
Long Term Improvements	3-62
Summary of Electronic Improvements	3-62

TABLE OF CONTENTS (Continued)

<u>Section</u>		<u>Page</u>
3	DETAIL SUBSYSTEM DESCRIPTION SUMMARY (Continued)	
	Power Analysis and Discussion	3-63
	Collector Field Arrangement	3-64
	Power Wiring	3-64
	Control Signal Wiring	3-66
	Field Instrumentation and Calibration	
	Array Wiring	3-66
	Overall Operation	3-70
	Command Control Arrangement	3-71
	Computer System Overview	3-73
	Computer Architecture	3-81
	Timing	3-81
	Software	3-82
	Operational Program	3-82
	Executive Modules	3-86
	Test Data Reduction Programs	3-89
	Conclusion	3-90
4	PERFORMANCE ANALYSIS AND TRADE STUDIES	4-1
	Analysis Summary	4-1
	Structural States and Dynamic Analysis	4-3
	Aerodynamic Analysis	4-11
	Collector Subsystem Pointing Accuracy Analysis	4-11
	Thermal Considerations of Heliostat Design	4-19
	Drive System Analyses	4-21
	Mass Properties Analysis	4-29
	Inner Axis Balance Analysis	4-29
	Solar Research Experiment Image Analysis	4-33
	Coordinate Transformations Analysis	4-38
	Motor Sizing Analysis	4-44
	Control Loop Stability Analysis	4-48
	Servo Analysis and Simulation	4-52
	Heliostat Servo Output AMP Small Signal	
	Simulation and Analysis	4-54
	Analysis of Heliostat Response to Environmental	
	Effects	4-56
	Analysis and Prognosis for Commercial Plant	
	Changes	4-63
	Calibration Array Analysis	4-65
	Heliostat Location Analysis	4-68
	Trade Off Studies	4-71

TABLE OF CONTENTS (Continued)

<u>Section</u>	<u>Page</u>
4	PERFORMANCE ANALYSIS AND TRADE STUDIES (Continued)
	Parametric Trade Study 4-71
	Foam Versus Honeycomb Mirror Modules 4-78
	Linear Actuator Trade Offs and Selection (Ball Screw Versus Machine Screw) 4-79
	Pulse Operation 4-81
	Compressive Spring Rate 4-82
	Column Buckling Stress 4-82
	Gear Ratio 4-82
	Self-Locking 4-82
	Side Loads 4-82
	Dynamic Range 4-83
	Power Distribution Trade-Off 4-83
	Calorimetry Versus Calibration Array Measurements 4-86
	Sensible Heat Absorption Calorimeter 4-86
	Thermo-Electric Calorimeter 4-87
	Optical Calorimeter 4-88
	Calibration Array Grid Spacing 4-89
	Command Computer Choice 4-93
	Interrupt Structure 4-94
	Bus Bandwidth 4-94
	Number of Buses in Basic System 4-95
	Bus Memory Address Range 4-97
	Number of Controller/Device Addresses 4-98
	Conclusion 4-99
5	OPERATION, INSTRUMENTATION AND CONTROL 5-1
	Introduction 5-1
	Operation and Control Arrangement 5-1
	Operation Instrumentation and Control 5-16
	Operation Instructions 5-16
	Instrumentation 5-18
	Calibration Array and Electronics 5-19
	Cal Array Mechanical 5-22
	Photodetector Operation 5-25
	Multiplexer Operation 5-29
	Two Year Special Tests 5-33
	Special Long Term Tests 5-33
	Special One-Time Tests

TABLE OF CONTENTS (Continued)

<u>Section</u>	<u>Page</u>
5	OPERATION, INSTRUMENTATION AND CONTROL (Continued)
	Maintenance and Logistic Support 5-34
	Availability 5-35
	Logistical Support of Level 6 Computer System 5-37
	Mean Time to Repairs (MTTR) 5-39
	Unit MTTR Goal - 1 Hour 5-39
	Preplanned Diagnosis - 30 Minutes 5-39
	Maximum, 90 Percent Effective 5-39
	Replacement of ORU - 15 Minutes Maximum 5-40
	Conclusion 5-40
6	SUPPORTING DATA 6-1
	Field Assembly Process 6-1
	Heliostat Focusing and Alignment Procedure 6-10
	Assembly and Alignment Procedure 6-10
	Alignment Procedure Rationale 6-12
	Mirror Cleaning Method 6-22
	Degradation Rates 6-22
	Contour Change 6-24
	Permanent Reflectivity Degradation 6-24
	Temporary Degradation 6-25
	Infant Mortality Avoidance 6-26
	Method of Safe Control of Reflected Light 6-31
	Fail Safe Features 6-32
	Heliostat Battery 6-33
	Power Loss Detector 6-33
	Communications Loss Detector 6-33
	Motor Overtemp Detector 6-33
	Manual Control 6-33
	Non-Reversing Gears 6-34
	Redundant High Voltage Power Feed 6-34
	Summary of Fail Safe Features 6-34
	Make or Buy Analysis Potential 6-34
	Procurement Plans 6-35
	Reference Documentation 6-38
	TCL List 6-40
	Conclusion 6-49

TABLE OF CONTENTS (Continued)

<u>Section</u>	<u>Page</u>	
7	SRE TEST RESULTS	7-1
	SRE System Description	7-1
	Honeywell DDP516 Computer with 32K Memory and Peripherals	7-1
	Two 7-Track Magnetic Tape Units	7-2
	One ASR-35	7-2
	Special RS232C Interface Box	7-7
	Software	7-8
	Heliostats	7-9
	Engineering Model	7-9
	Experimental Model	7-9
	Test Support Hardware	7-12
	Calibration Array	7-12
	Weather Data	
	Test Approach	7-17
	Component and Subassembly Level Testing	7-21
	Mirror Modules	7-21
	Plywood Mirror Module (MM1)	7-23
	Variable Focus Mirror Module (MM2)	7-31
	Foam Filled Mirror Modules (MM3B)	7-31
	Aluminum Honeycomb Mirror Modules	7-45
	Tapered Cross Section Honeycomb Mirror Module	7-45
	Rectangular Cross Section Mirror Module	7-48
	Test Method	7-51
	Data Discussion	7-51
	Mirror Adhesive Bond	7-61
	Mirror Module Reflectance	7-61
	Motor Characterization	7-66
	Thermal Gradient Test	7-73
	Heliostat Actuators and Outer Gimbal Drive Characteristics	7-79
	Machine Screw Actuators	7-79
	Ball Screw Actuator - Comparison with Machine Screw	7-82
	Ball Screw Actuator Scale Factors	7-88
	Outer Frame Lash	7-97
	Outer Frame Assembly and Balance	7-97
	Inner Drive	7-101
	Inner Drive Lash and Torsion Characteristics	7-101
	Inner Drive Power and Slew Rate Performance	7-108
	Electronics Performance	7-112
	Heliostat Electronics	7-112
	Test Equipment Electronics	7-113
	Power Frequency Variation	7-115

TABLE OF CONTENTS (Continued)

<u>Section</u>		<u>Page</u>
7	Electronic Breadboard Test Data	7-115
	System Level Testing	7-117
	Foundation and Post Stability	7-117
	Movement During Gimbal Travel	7-117
	Long Term Foundation Stability	7-118
	System Level Tracking	7-120
	Engineering Model Heliostat	7-120
	South Site Experimental Model Heliostat	7-123
	North Site Experimental Model	7-137
	East Site Experimental Model	7-140
	Toe-In Strategy	7-142
	Initialization	7-146
	Calibration of Heliostat Parameters	7-148
	Initial Calibration	7-148
	Periodic Calibrations	7-149
	Operational Slew Rates	7-149
	Control Software Update	7-150
	Environmental Testing	7-153
	Wind	7-153
	Background Discussion	7-153
	Results to Date	7-154
	Redirected Energy Measurement	7-156
	Background	7-156
	Insolation Recording	7-176
	Lightning	7-176
	Cold Weather Testing	7-177
	Error Budget Comparison	7-177
 <u>Appendix</u>		
A	REFERENCE LOCATIONS OF DATA LISTS	A-1
B	OPERATING CHARACTERISTICS	B-1
C	DESIGN DISCUSSION	C-1
D	HELIOSTAT POWER CONSUMPTION ANALYSIS	D-1
E	PROGRAM LISTING HELIOSTAT CONTROL PROGRAM	E-1
F	MATERIALS ENGINEERING LABORATORY TEST REPORT ON MATERIALS AND PROCESS DESIGN FOR MIRROR MODULE ADHESIVE	F-1

LIST OF ILLUSTRATIONS

<u>Figure</u>	<u>Title</u>	<u>Page</u>
1-1	Honeywell Team for Phase I Solar Pilot Plant Program	1-2
1-2	Chronology of Phase I Solar Pilot Plant Program	1-2
2-1	Honeywell Solar Energy Heliostat	2-1
2-2	Collector Subsystem Overview	2-3
2-3	Pilot Plant Heliostat	2-5
2-4	Array Data Flow	2-12
2-5	Simulated 13.4 M/S Wind Load	2-15
3-1	Collector Subsystem Tower 1/2 South Field Layout	3-2
3-2	Pilot Plant Collector Subsystem Block Diagram	3-3
3-3	Top Level Collector Subsystem Documentation Tree	3-5
3-4	Drawing Trees of the Collector Subsystem	3-6
3-5	Drawing Trees of the Collector Subsystem	3-7
3-6	Collector Subsystem Control Subsystem	3-8
3-7	Calibration Arrays and Their Associated Electronics	3-9
3-8	Collector Subsystem Interconnection One Line Diagram (Pilot Plant)	3-10
3-9	Collector Subsystem Interconnection One Line Diagram (Commercial Plant)	3-12
3-10	Heliostat	3-13
3-11	Heliostat Foundations	3-14
3-12	Installing Posts to Foundations	3-14
3-13	Heliostat Frame (Pilot Plant Preliminary Design)	3-16
3-14	Heliostat Frame (Latest Concept)	3-18
3-15	Aluminum Honeycomb 120 by 120 Inch Mirror Module (14 Procured)	3-19
3-16	Mirror Module Assembly Details	3-21
3-17	Heliostat Inner Axis Drive (Spur Gear Cover Removed for Clarity)	3-22
3-18	Inner Drive Gear Box	3-22
3-19	Inner Drive Cover and Seals	3-23
3-20	Taper Lock Interface	3-24
3-21	Heliostat Outer Axis Drive	3-26
3-22	Heliostat Actuator	3-26

LIST OF ILLUSTRATIONS (Continued)

<u>Figure</u>	<u>Title</u>	<u>Page</u>
3-23	Ball Screw Actuator	3-27
3-24	Initialization Switch SRE Units	3-30
3-25	Initialization Pilot Plant Units	3-31
3-26	Heliostat Weight Estimates	3-33
3-27	Heliostat Electronics Block Diagram	3-36
3-28	Heliostat Communications Interface Schematic Diagram	3-38
3-29	Heliostat Counter Control/Up-Down Counter	3-40
3-30	Heliostat Servo Output Amplifier	3-42
3-31	Heliostat Incremental Encoder	3-44
3-32	Initialization Electronics	3-46
3-33	Schematic Diagram Outer Axis Two Motor Synchronizer	3-49
3-34	Timing Generator Heliostat Electronics	3-50
3-35	SRE Heliostat Power Circuits	3-52
3-36	Schematic Diagram Manual Mode Operation	3-53
3-37	Solar Test Box Schematic Diagram	3-54
3-38	Heliostat Electronics Package	3-55
3-39	Power Sequencing Mechanization	3-58
3-40	Replacement Circuitry	3-61
3-41	Field Layout Showing Low Voltage Feed On Left Side and High Voltage Feed on Right	3-65
3-42	Heliostat Communications Signal Interconnect Diagram and Communications Wiring Summation	3-68
3-43	Location and Interconnect Diagram Pilot Plant Collector Subsystem Field Instrumentation	3-69
3-44	Calibration Array and Electronics	3-72
3-45	Communication Interface	3-74
3-46	Collector Subsystem Operators Console	3-75
3-47	Megabus	3-76
3-48	Rack Mounted Computer and Peripherals	3-77
3-49	Floor Space Plan	3-78
3-50	Software Overview	3-87
3-51	Program Development Sequence	3-87
3-52	Interrelationships of the Executive Modules With the Heliostat Control Computer Tasks	3-88

LIST OF ILLUSTRATIONS (Continued)

<u>Figure</u>	<u>Title</u>	<u>Page</u>
4-1	Summary Heliostat Deflections and Stresses Heliostat in Horizontal Position 1G Static Load	4-6
4-2	Summary Heliostat Deflections and Stresses, Heliostat at 75 Degrees Outer Axis Rotation	4-7
4-3	Modal Shape Heliostat in Stowed Position	4-8
4-4	Deformed Plot - Heliostat Horizontal - First Mode - Mirror Modules Displacement Case 1	4-9
4-5	Wind Forces and Moment on Mirror-Torsion Tube Assembly	4-12
4-6	Heliostat Rotation Frames	4-18
4-7	Circular Mirror Images	4-34
4-8	Site Images - $10M^2$ Square Facet	4-34
4-9	Sun's Spectral Distribution at Sea Level	4-36
4-10	Sun's Cumulative Distance 100% = $850 W/M^2$ at Sea Level	4-36
4-11	Reflectance of 0.25 Inch Float Glass, Second Surface Silver	4-36
4-12	Reflectance Times Sun's IR Radiance/0.1	4-36
4-13	Cumulative Specular Reflectance	4-36
4-14	Heliostat Pointing Error Flow Diagram	4-40
4-15	Computational Frames	4-42
4-16	Circle Diagram	4-42
4-17	Functional Block Diagram	4-49
4-17a	Simulation Results Showing High Gain Loop Response to Step 834#-FT Wind Torque and 6 MR Step Command Inputs	4-49
4-18	Gimbal Control Loop Model Used in Simulation	4-53
4-19	Small Signal Model	4-55
4-20	Heliostat Servo Bode Plot	4-55
4-21	Percent Energy Losses Versus Line-of-Sight Distances for Humidity 55 Percent	4-62
4-22	Ray Blocking During Heliostat Calibration	4-66
4-23	Array Analysis Model	4-67
4-24	Calibration Array Frame	4-69
4-25	Heliostat Evaluation Process	4-72
4-26	Gimbal Configuration	4-73
4-27	Parametric Analysis Flow Diagram	4-74

LIST OF ILLUSTRATION (Continued)

<u>Figure</u>	<u>Title</u>	<u>Page</u>
4-28	Flow Chart for Tilt-Tilt Heliostat Computer Program	4-75
4-29	Sensitivity to Area	4-76
4-30	Sensitivity to Pointing Accuracy	4-76
4-31	Effective Cost Versus Heliostat Wind Speed Capability	4-77
4-32	Sensitivity to Mirror Module Spacing	4-77
4-33	Ball Screw Actuator	4-80
4-34	Machine Screw Actuator	4-80
4-35	AC/DC Power Distribution	4-84
4-36	Block Diagram for Sensible Heat Absorption Calorimeter	4-87
4-37	Block Diagram for Optical Calorimeter	4-88
4-38	Concentrated Image Using Coefficients	4-91
4-39	Flat Distribution Using Coefficients	4-92
5-1	Standby Position	5-2
5-2	Standby Pattern	5-4
5-3	Single Facet Curved Mirror	5-8
5-4	Four Facet Mirror	5-11
5-5	Zone of Concern	5-12
5-6	Flux Versus Distance	5-13
5-7	Barrier Concept	5-15
5-8	Location and Interconnect Diagram Pilot Plant Collector Sybsystem Field Instrumentation	5-20
5-9	Field Instrumentation Data Processor and Transmitter	5-21
5-10	Calibration Array and Electronics	5-23
5-11	Receiver and Calibration Array	5-24
5-12	Photodetector Circuit	5-26
5-13	Cal Array Electronics and Multiplexer Switching Diagrams	5-30
5-14	A Three Tiered Multiplexer with 756 Channel Capacity	5-32
6-1	Concept of Double Gantry for Assembly of Frames to Posts	6-4
6-2	(T1) Frame Pivot Axis Leveling and Azimuth Measuring Tool	6-15
6-3	(T2) Actuator Pivot Bracket Alignment Tool	6-16
6-4	(T3) Actuator Pivot Axis Alignment Tool	6-17
6-5	(T4) Fixed Length Trammel Tool	6-18

LIST OF ILLUSTRATIONS (Continued)

<u>Figure</u>	<u>Title</u>	<u>Page</u>
6-6	(T5) Mirror Module Clamping Tool	6-19
6-7	(T6) Precision Beam Level	6-20
6-8	(T7) Tooling Pin	6-21
6-9	Semiautomatic Mirror Cleaning Concept	6-23
6-10	AQL Levels on Functionality Versus Board Rework Rates	6-28
6-11	Relative Failure Rate Versus Time	6-28
6-12	Collector Subsystem Vendors	6-36
7-1	Research Experiment Collector Subsection Functional Diagram	7-3
7-2	Aerial Photograph, Honeywell Complex	7-5
7-3	SRE Computer Facility	7-6
7-4	ASR Output	7-7
7-5	Engineering Model Heliostat Assembly and Alignment	7-10
7-6	Engineering Model in Stowed Position	7-11
7-7	Engineering Model Tracking	7-11
7-8	Experimental Model Heliostat Assembly	7-13
7-9	East Experimental Model During Operation 12/17/76, 1930 GMT	7-14
7-10	Calibration Array Facing North, 9/27/76, Engineering Model Image	7-15
7-11	Backview of Calibration Array	7-16
7-12	Weather Tower at Experimental Model Heliostat	7-18
7-13	Data Collection System	7-19
7-14	Plywood Mirror Module Construction	7-24
7-15	Contour Data Plywood Data	7-25
7-16	Contour Data Plywood MM	7-26
7-17	Contour Data Plywood MM	7-27
7-18	Contour Measurements Via Theodolite With Mirror Module Under Solar Loading	7-28
7-19	Plywood Mirror Module Focused on North Side of Building E-2	7-29
7-20	Scattered Image from Plywood Mirror Module	7-29
7-21	Drawing of Cracks Developed in Plywood MM as of 5/4/76	7-30
7-22	Variable Focus Mirror Module Under Test	7-32
7-23	MM2 Contour Data	7-33

LIST OF ILLUSTRATIONS (Continued)

<u>Figure</u>	<u>Title</u>	<u>Page</u>
7-24	MM2 Beam on Photodetector Array Range: Approximately 500 Ft. Date: 4/28/76	7-34
7-25	Mirror Module MM3B End View	7-35
7-26	Foam Blocks Being Carved	7-35
7-27	Engineering Model Heliostat Showing Effect of Foam Mirror Module	7-37
7-28	Contour Data (Replot)	7-38
7-29	Contour Data (Replot)	7-39
7-30	Contour Data	7-40
7-31	Contour Data	7-41
7-32A	Edge Load Mirror Module Torsional Test Set-Up	7-43
7-32B	Crank Arm Torsional Test Set-Up	7-43
7-33	Deflection Measurement Due to Edge Load	7-44
7-34A	Aluminum Honeycomb 125 by 125 Inch Mirror Module (2 Procured)	7-46
7-34B	Aluminum Honeycomb 120 by 120 Inch Mirror Module (14 Procured)	7-46
7-35	Contour Data - Parson's Mirror Modules (Tapered Cross Section)	7-47
7-36	Contour Measurements with Piano Wire	7-52
7-37A	Contour Deviations Parsons Mirror Module, SN 005, Loaded and Unloaded	7-53
7-37B	Contour Deviations Parsons Mirror Module, SN 005, Loaded and Unloaded	7-53
7-38A	Contour Deviations Parsons Mirror Module, SN 005, Unloaded	7-54
7-39B	Contour Deviations Parsons Mirror Module, SN 005, Unloaded	7-54
7-39A	Contour Deviations Parsons Mirror Module, SN 001, Unloaded	7-55
7-39B	Contour Deviations Parsons Mirror Module, SN 001, Unloaded	7-55
7-40A	Contour Error Mirror Surface Down	7-56
7-40B	Contour Error Solar Load	7-56
7-41	Mirror Contour Data	7-57
7-42	Mirror Contour Data	7-58
7-43	Edge Load Deflection Test Set-Up	7-59
7-44	Crank Arm Torsion Test Set-Up	7-60

LIST OF ILLUSTRATIONS (Continued)

<u>Figure</u>	<u>Title</u>	<u>Page</u>
7-45A	Typical Reflectance Measurement on Dirty Mirror Module Facet-Mirror Module SN P001	7-63
7-45B	Typical Reflectance Measurement on Clean Mirror Module Facet	7-64
7-46	SN 001 Dirty Mirror Module	7-65
7-47	Water Droplets 26 Minutes After Light Rain	7-65
7-48	100 In-Oz Motor Characterization	7-67
7-49	Stall Torque - Inland Motor T1806-H (No. 1) - As a Function of Time	7-68
7-50 (A-I)	200 In-Oz Inland Motor (P/N T1811-B) Characterization Data Taken at 1, 2, 3, 6 Ampere in CCW and CW Direction	7-69
7-51	Motor Thermal Response Characteristics	7-72
7-52	Engineering Model Heliostat Temperature Monitor Points	7-74
7-53A	Typical Thermal Time History for Selected Heliostat Points	7-76
7-53B	Typical Thermal Time History for Selected Heliostat Points	7-77
7-53C	Typical Thermal Time History for Selected Heliostat Points	7-78
7-54	Engineering Model Heliostat Machine Screw Actuator No. 1	7-80
7-55	Engineering Model Heliostat Machine Screw Actuator No. 2	7-81
7-56	Engineering Model Heliostat Front (Tung End) Frame Drive Motor $R_{DC} = 6.66$ Ohms	7-83
7-57	Engineering Model Heliostat Rear Frame Drive Motor $R_{DC} = 8.06$ Ohms	7-84
7-58	Engineering Model Heliostat Front (Tung End) Frame Drive Motor	7-85
7-59	Engineering Model Heliostat Rear Frame Drive Motor	7-86
7-60	Engineering Model Heliostat Ball Screw Linear Actuators	7-87
7-61A	Outer Axis Slew Rate	7-93
7-61B	Outer Axis Slew Rate	7-94
7-62A	Ball Screw Linear Actuator Power Response During OA Slew (+25° to -70°)	7-95
7-62B	Machine Screw Linear Actuator Power Response During OA Slew (+30° to -70°)	

LIST OF ILLUSTRATIONS (Continued)

<u>Figure</u>	<u>Title</u>	<u>Page</u>
7-63	Outer Frame Mounting Shaft	7-98
7-64	Cracked Frame Pivot Pillot Block Engineering Model Heliostat	7-99
7-65	Engineering Model Heliostat Imbalance About Frame Axle (Linear Actuators Not Connected)	7-100
7-66	Engineering Model Heliostat Gear Driven MM	7-102
7-67	Experimental Model Inner Drive Gear Box Lash/ Spring Rate Test Set-Up	7-104
7-68	Mirror Module Rotation Versus Moment Loads	7-107
7-69	Engineering Model Heliostat Mirror Module Drive Motor	7-109
7-69A	Experimental Model Inner Drive Results	7-110
7-69B	Experimental Model Inner Drive Results	7-111
7-70	Foundation Movement Orientation	7-117
7-71	Top of Post Rotation Due to Outer Axis Frame Position	7-119
7-72A	Engineering Model Open Loop Tracking Results	7-124
7-72B	Engineering Model Open Loop Tracking Results	7-125
7-72C	Engineering Model Open Loop Tracking Results	7-126
7-72D	Engineering Model Open Loop Tracking Results	7-127
7-72E	Engineering Model Open Loop Tracking Results	7-128
7-72F	Engineering Model Open Loop Tracking Results	7-129
7-72G	Engineering Model Open Loop Tracking Results	7-130
7-72H	Engineering Model Open Loop Tracking Results	7-131
7-72I	Engineering Model Open Loop Tracking Results	7-132
7-72J	Engineering Model Open Loop Tracking Results	7-133
7-72K	Engineering Model Open Loop Tracking Results	7-134
7-72L	Engineering Model Open Loop Tracking Results	7-135
7-73	Calibration Array Image	7-136
7-74	Image Horizontal Centroid Track, South Site, Second Day of Operation	7-138
7-75	Image Vertical Centroid Track, South Site, Second Day of Operation	7-139
7-76	Mirror Module Toe-In Angle Representation	7-144
7-77	Image Centroid Variation Least Squares Fit East Site	7-155
7-78	Sensor Bandwidth Versus Cost	7-157
7-79	Photodetector Directional Sensitivity Measurements	7-158

LIST OF ILLUSTRATIONS (Continued)

<u>Figure</u>	<u>Title</u>	<u>Page</u>
7-80	Photosensor Directional Sensitivity	7-159
7-81	One Sun (DNI) Flux (Before Repairs)	7-161
7-82	Tracking Pyrheliometer and Silicon Photocell	7-163
7-83	Typical Level of Residual Calibration Array Readout with no Redirected Insolation	7-165
7-84	Energy Losses	7-167
7-85	Energy Losses	7-168
7-86	Energy Losses	7-169
7-87	Energy Losses	7-170
7-88	Energy Losses	7-171
7-89	Percent Energy Losses Versus Line of Sight Distances for Humidity 55 Percent	7-172
7-90	North Site - March 1977 Flux Map	7-173
7-91	Flux Map, North Site December 17, 1976	7-174
7-92	Flux Map - Single Mirror Module, North Site	7-175

LIST OF TABLES

<u>Table</u>	<u>Title</u>	<u>Page</u>
2-1	Satisfaction of Specification	2-9
2-2	SRE Versus Pilot Plant	2-16
3-1	Comparison of Mirror Modules	3-19
3-2	Heliostat D/A Converter Operation	3-41
3-3	Comparison of Measured and Predicted Values of Power Supply Current Drains	3-63
3-4	Gimbal Update Power Requirements	3-64
3-5	Heliostat Low Voltage Power Wiring	3-67
3-6	Solar Computer Complex for Pilot Plant or One Commercial Plant Module	3-79
3-7	Priority Levels	3-80
3-8	Nominal Level 6/43 Execution Times	3-83
3-9	Performance of Scientific Instructions (Normal Memory)	3-84
4-1	LG8016B Heliostat Assembly Survivability Stress	4-11
4-2	Torsional Stiffness Parameters	4-13
4-3	Mirror/Heliostat Response to Static Wind Loads and Wind Turbulence	4-14
4-4	Error Budget Comparison	4-15
4-5	Independent Error Sources	4-16
4-6	Inner Drive Backlash Summary	4-17
4-7	Stress Margin Versus Inner Axis Moment Loading	4-60
4-8	Calibration Array Parameters	4-68
4-9	Indoor Build	4-85
4-10	Outdoor Build	4-86
4-11	Centroid Computation	4-93
5-1	Focal Area	5-10
5-2	Flux Versus Slant Range Four Facets	5-14
5-3	Command Initiation	5-17
5-4	Solar Pilot Plant Preliminary MTTR and MTBR Predictions	5-36
6-1	"Enhanced-Quality" Vendor Process Programs	6-29
7-1	Engineering Model Mirror Module Test Data Summary	7-22
7-2	Mirror Module Static Stiffness Due to MM3P SNP01 Taper Locks Torqued to 150 Ft-Lbs	7-49

LIST OF TABLES (Continued)

<u>Table</u>	<u>Title</u>	<u>Page</u>
7-3	Mirror Module Static Stiffness MM3P SNP01 Taper Locks Torqued to 200 Ft-Lbs	7-50
7-4	Edge Load Deflection	7-59
7-5	Deflection Due to Crank Arm Load	7-60
7-6	Reflectances at Various Wave-Lengths for Parsons Mirror Samples	7-61
7-7	Thermal Gradient Data	7-75
7-8A	North Site, 28 October 1976, 200 In-Oz Motor, SN No. 3 Using Machine Screw Actuator No. 1	7-89
7-8B	North Site, 28 October 1976, 200 In-Oz Motor, SN No. 4 Using Machine Screw Actuator No. 2	7-90
7-9A	North Site, 3 November 1976, 200 In-Oz Motor, SN No. 3 Using Ball Screw Actuator	7-91
7-9B	North Site, 3 November 1976, 200 In-Oz Motor, SN No. 4 Using Ball Screw Actuator 241847	7-92
7-10	Backlash Components at ± 870 In-Lbs	7-106
7-11	Spring Rate Contributions	7-106
7-12	Post and Foundation Movement During Gimbal Travel of 0 Degree to -70 Degrees	7-118
7-13	Comparison of Buffered Refraction Correction Algorithm	7-121
7-14	23 November 1976 Close Loop Track Data	7-141
7-15	24 November 1976 Close Loop Track Data	7-143
7-16	TIL99 Phototransistor Gain Calibration	7-160
7-17	Typical Time History of Photocell/Pyrheliometer Comparison	7-162
7-18	Energy Balance Comparison	7-172
7-19	Error Budget/Result Comparison	7-178

Section 1 INTRODUCTION

BACKGROUND

Supplies of most conventional fuels are being depleted rapidly. Consequently, it is necessary to identify alternate sources of energy and to develop the most promising to ensure availability when needed.

An alternative with great potential is the conversion of sunlight to energy. One aspect of this usage is generating electricity through solar energy. A goal of the national energy program is to demonstrate the technical and economic feasibility of a central receiver solar power plant for generating electricity. Pursuant to that goal, the Energy Research and Development Administration (ERDA), on 1 July 1975, awarded Honeywell Inc a two-year contract for Phase I of such a program.

The initial program phase, which is the subject of this report, consisted of developing a preliminary design for a 10 mw(e) proof-of-concept solar pilot plant. The second phase will consist of building and operating the pilot plant and projecting the information gained to larger scale plants. This phase is scheduled to be completed in the early 1980s. The third phase will consist of designing, building, and operating two 50-100 mw(e) demonstration plants. The final phase, will consist of building and operating plants in the 100-300 mw(e) range.

PHASE I PROGRAM SCOPE

The Phase I program consisted of developing a pilot plant preliminary design by first developing a preliminary baseline design to meet specified and assumed performance requirements. The baseline was then refined through analysis and experimentation, and evaluated by testing key subsystems, i.e., collector, steam generator, and thermal energy storage.

The complexity of the undertaking dictated a team approach to provide the technical and managerial skills required. The Honeywell team is identified in Figure 1-1.

A unique feature of the test plan was the use of selected facilities of an operating power plant, Northern States Power's Riverside Plant in Minneapolis, Minnesota to test the steam generator and thermal energy storage subsystems. An ERDA-directed change from latent heat (phase change) storage to sensible heat cancelled the storage portion of the test plan. The steam generator was tested using a solar array to simulate the insolation required to generator steam. The collector subsystem hardware, one mobile and three stationary full scale 4-mirror units, was field tested for performance and reaction to operation environments at Honeywell's Avionics Division facility in St. Petersburg, Florida.

The information obtained from the subsystems tests was used to complete the pilot plant preliminary design, and to project performance and cost of a 100 mw(e) plant to facility long range planning.

The chronology of the work done in Phase I is summarized in Figure 1-2.

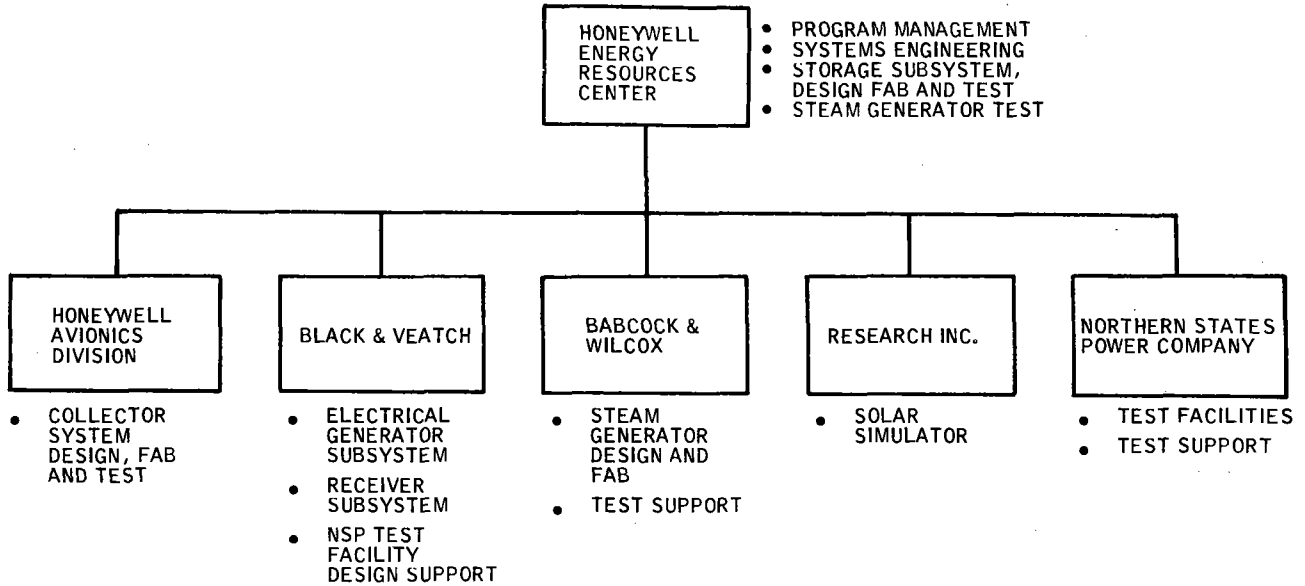


Figure 1-1. Honeywell Team for Phase I Solar Pilot Plant Program

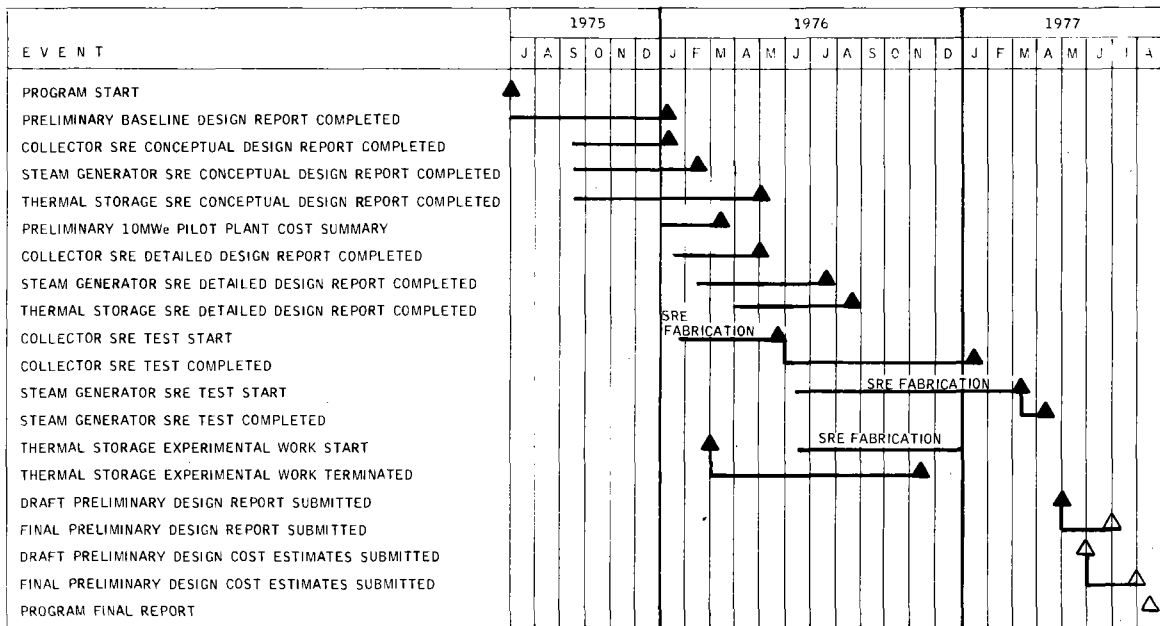


Figure 1-2. Chronology of Phase I Solar Pilot Plant Program

ORGANIZATION OF THE PRELIMINARY DESIGN REPORT

The preliminary design and supportive data resulting from the Phase I work are presented in seven volumes:

- I - Executive Overview
- II - System Description and System Analysis (3 books)*
- III - Collector Subsystem
- IV - Receiver Subsystem
- V - Thermal Storage Subsystem
- VI - Electrical Power Generation/Master Control Subsystems and Balance of Plant
- VII - Pilot Plant Cost/Commercial Plant Cost and Performance

Abstracts of volumes other than the one in hand and Volumes I and VII are on the following pages.

* Book 2 is Central Receiver Optical Model Users Manual
Book 3 is Dynamic Simulation Model and Computer Program Descriptions

Section 2
SUMMARY COLLECTOR SUBSYSTEM DESCRIPTION

The objective of this report is to present in a clear logical fashion the preliminary design of collector subsystems for both the pilot plant and a commercial scale plant. Basis for most design decisions was work performed on the SRE contract. Manifold references to the results from the SRE will reveal the reasons why we have confidence that our design will perform successfully.

It is useful to keep in mind that this is a preliminary design which is to be followed by a detailed design phase. Our emphasis has been on the heliostat because of the sensitivity of the power plants to cost and performance of this most critical element of the collector subsystem. Our heliostat built and tested during the SRE is shown in Figure 2-1. Other elements of the collector subsystem are less well defined than the heliostat but all have been adequately demonstrated during SRE tests.

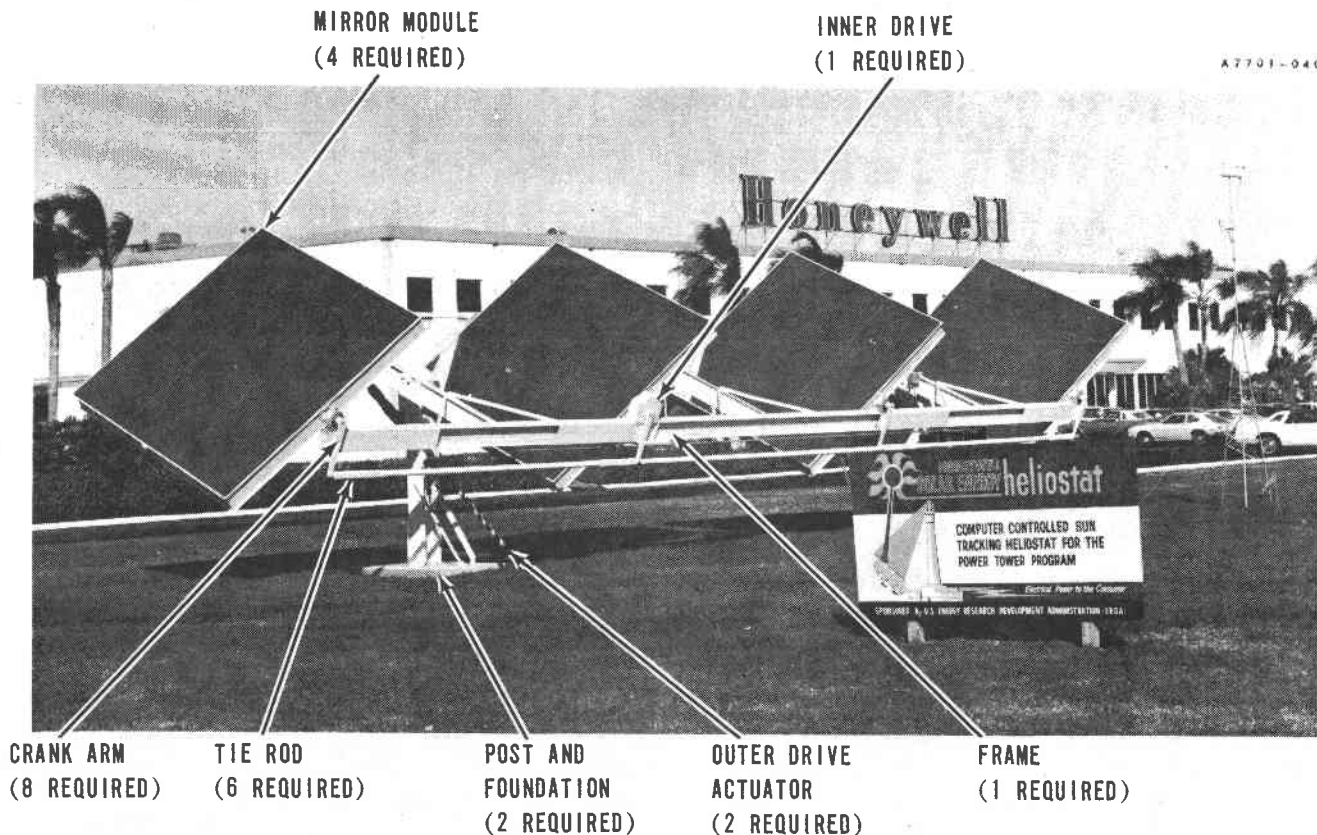


Figure 2-1. Honeywell Solar Energy Heliostat

GENERAL OVERVIEW

The Honeywell Collector Subsystem consists of (1) the heliostats, (2) the collector field, (3) computer command controls, and (4) instrumentation and wiring equipment. Each of these items is shown in Figure 2-2 and will be discussed in summary below.

Heliostat Overview

The heliostat is the heart of the collector subsystem and must provide high reflectivity and accurate angular and spatial positioning of the reflected energy under all conditions of wind load and attitude of the mirrors. The four facet, tilt-tilt, low profile, open loop, fixed focus, second surface glass mirrored heliostat developed by Honeywell during the SRE satisfies these requirements and others in several unique ways. The first of these unique ways is the low profile aspect of the heliostat combined with the placement of all moving parts three feet above the floor of the desert on which the heliostats will be placed. These features and the face down stowability assures a maximum cleanliness of both mirrors and working moving parts while at the same time reducing the area of the heliostat exposed to high wind environments. Another unique way the Honeywell heliostat satisfies the requirements is in its ability to resist overturning moments through the use of more than one foundation support assembly. The Honeywell design stands on two posts with the center of gravity of the heliostat midway between them. Other designs for heliostats have a cantilever arrangement rather than two support foundations, thus the overturning moment requires much larger foundations and much more additional support than does the Honeywell design. The last unique solution to satisfying the collector subsystem requirement is that the Honeywell second surface glass mirrors have actually no load imposed upon them except the weight of the silvered glass as affected by gravity in several attitudes. This is achieved by virtue of a substrate structure which is lightweight and yet very stiff. This structure is an aluminum honeycomb sandwich panel with steel faces and two hubs. Contour is achieved by machining an auxiliary surface bonded to the face of the sandwich panel. The sandwich panel, which weighs 600 pounds, also has requirements that it shall not deflect more than 1 milliradian under worst case wind loads.

Another singular feature of the Honeywell heliostat is the use of dc motors and a battery which reduces peak load on the electrical distribution system to the heliostat field. These motors, while simple in construction and high in reliability, provide a minimum number of piece parts and a torque level inversely proportional to speeds from stall (maximum torque) to maximum speed (minimum torque). Similar motors are now employed widely in electric drills and other portable battery powered hand tools. Battery power, in addition to peak load shaving, provides auxiliary power in the event that station power fails for any reason. Thus, a degree of reliability, not possible to obtain through other means, is afforded in a very redundant fashion such that no failure of a central component can remove power from all heliostats simultaneously. This choice also places the heliostat in a position to employ more advanced batteries as they become available from ERDA efforts to improve storage hardware.

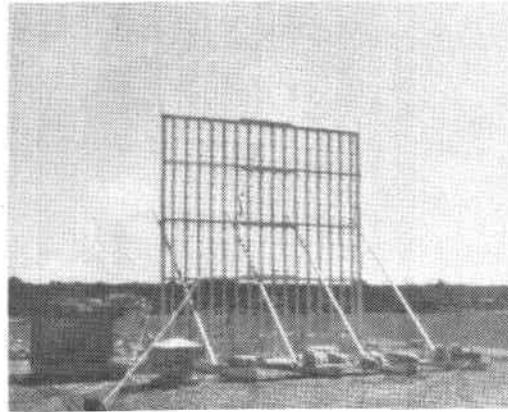
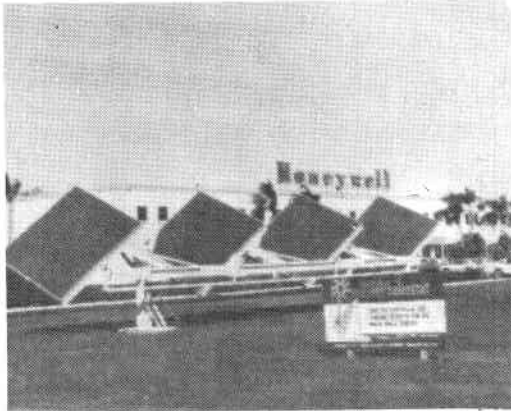
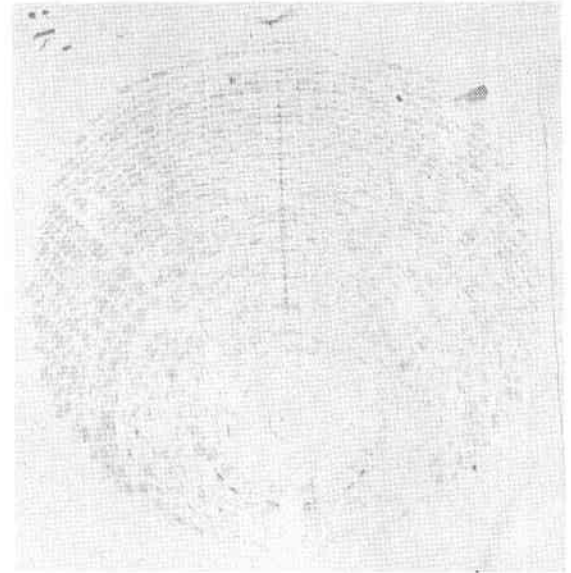
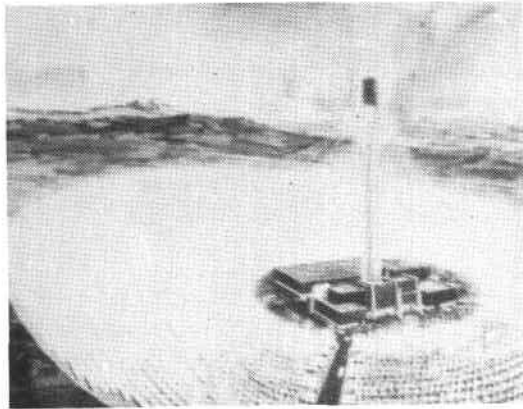


Figure 2-2. Collector Subsystem Overview

Field Overview

The field of 1598 heliostats is distinguished by the following features:

- Collectors surround the tower located halfway south of center.
- Heliostats are oriented in a polar fashion (i.e., longest axis normal to a radial line from the tower).
- Non-uniform spacing between rows of heliostats (higher density near tower).

Each of these items is briefly discussed to indicate some of the important advantages resulting from this unique arrangement:

- Collectors surrounding the tower provides the benefits of using a symmetrical steam generator thus averaging "hot spots" is effected. The tower situated in the south half of the field permits taking advantage of the more efficient north field heliostats without losing steam generator advantages of averaging and symmetry.
- Polar heliostat orientation generally simplifies the axis control laws. With this arrangement mirror module (MM) axis rotation moves the beam across the tower. Ball screw travel moves the beam up and down the tower.
- Non-uniform spacing is established to eliminate interference of one heliostat with another heliostat in the form of shading and blocking the suns rays to or from the mirrors, respectively.

Thus it can clearly be seen that the collector field is disturbed only by a single access road south from the tower. The otherwise unbroken array of the mirror field provides high performance as described elsewhere by ray trace analysis. More data on the field layout and its wiring and orientation may be found in Section 3.

The pilot plant heliostats reflect the research experiment experience and test results. The pilot plant heliostat is a tilt-tilt gimbal configuration with 40 square meters of mirror surface. The unit has four mirror assemblies 3.05m x 3.28m spaced five meters on centers. Heliostat weight at outer axis bearings is estimated at 3,454 kg (7,600 pounds). See Figure 2-3.

Each mirror module assembly supports a 3mm second surface float glass mirror with a built-in focal length of 418 meters which is the longest line of sight in the pilot plant heliostat field (1,372 feet). The support structures are aluminum coated steel skinned sandwich panels using aluminum honeycomb core. Stub shafts at each end interface bearings and drive components. Tooling points are included in the mirror modules.

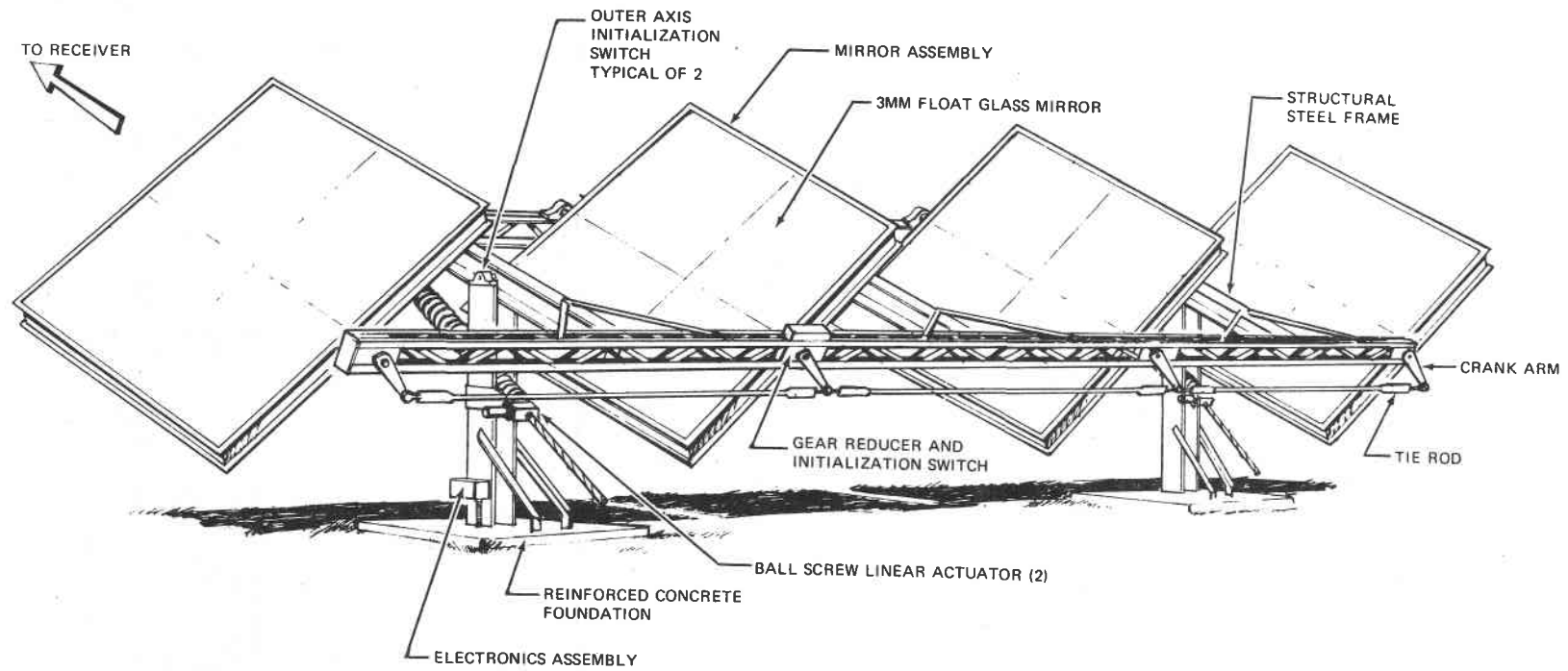


Figure 2-3. Pilot Plant Heliostat

The second mirror module from one end is supported and driven by an assembly which includes a dc motor, 2-stage gear reducer, 16 inch pitch diameter spur gear, initialization switch and support bearing. This assembly is sealed against dust and dirt. The reducer is self-contained, sealed and lubed adequate for the proposed 30 year life.

The other three mirror modules are slaved with rigid tie-rods and crank arms which provide full circle range and face down stowage.

The reinforced I-beam frame has pivot pins located at the center of gravity of the rotating mass. Angle sections provide the stiffness required under one "g" loading at high (75 degree) gimbals angles.

Two synchronized ball screw linear actuators control frame tilt and provide 105 degrees of rotation freedom allowing use of common actuators in any field location.

Reinforced concrete footings control rocking modes as well as support the heliostat weight.

This heliostat with its reinforced I-beam frame and its strategically spaced mirror modules standing on two posts with ball screw drive for the frame resulted from a comprehensive and thorough trade study to develop the stiffest components per unit cost using a specially developed computer trade-off analysis tool. This trade study between the azimuth elevation versus tilt-tilt heliostat concepts was used to assure the stiffest structure (under wind and g' loads which vary with attitude) for each dollar spent. Though quite expensive in the performance of the Solar Research Experiment contract, this trade study resulted in a design which has been thoroughly analyzed and evaluated and has proven worthwhile through the detailed design build and test phases of the SRE contract. More data about this trade study and other design rationale may be found in Section 4. Thus, after evolutionary changes, exhaustive trade studies, and careful consideration of all requirements, Honeywell has developed a unique heliostat design which satisfies those requirements while at the same time providing opportunity for very low cost. More information can be found on the heliostat and collector field in Page 3-7.

Command Computer Overview

The computer command control scheme which Honeywell has configured for the pilot plant and commercial plant preliminary design consists of a Honeywell Level 6/43 computer providing commands to all heliostats in the given field. These computers have the capability to address more than 25,000 heliostats simultaneously. At the same time they perform numerous calculations of sun position and pointing direction as well as compensation for fixed known errors. Part of a system known as distributed processing, the computer design provides a fail-safe design when supplied with uninterruptable power. This reliable and safe design approach results from the use of several modular elements (CPUs) which can check one another and which use only the best calculated data available from all elements. Capable of much more than fulfilling the pilot and commercial plant requirements, the Level 6/43 is

enjoying wide success in industry today and is shown in Figure 2-2(c). More data on the command control design may be found in Pages 3-73 and 3-74 as well as Section 5.

Calibration Array and Instrumentation Overview

Along with the heliostat and the command control computer is a list of miscellaneous equipment needed to insure proper operation of the collector subsystem. Included in this list are (1) a calibration array, (2) an instrumentation set and (3) an operator's console shown in Figure 3-46.

Calibration Array. The calibration array (cal array) provides a unique means of testing heliostats. It is an array of sensors mounted to a gridwork support structure. This array of sensors mounted to a centroid of the "spot" which is defined to be the center of the beam of reflected light. The device was designed and built during the SRE and has performed well. This design was chosen over laser beams or mechanical means of measurement as the calibration array measures heliostat performance more like the actual performance. Lasers or other means of performance measurement must be scanned across the facets of the heliostat rather than taking a "snapshot" of the image. This calibration array approach has provided capability to accurately measure both beam location and amount of energy in the beam. In the pilot and commercial plant designs, the calibration arrays will be mounted at the top of the towers and will be used to correct minor pointing errors as well as to determine when mirrors need washing. The SRE calibration array is shown in Figure 7-10. More information about the calibration array is contained in Section 5.

Instrumentation Set. Operation of the pilot and commercial plants requires some knowledge of the weather and solar radiation. To provide this data Honeywell plans to provide a number of remote weather stations located in the collector field. These stations will transmit data back to the computer and control room. The data will be used to decide when to stow the heliostats as well as to determine effects of insolation passing through the atmosphere (that is refraction, attenuation, and scattering). Cloud data will also permit control of the plant in the presence of clouds blocking certain sections of the field causing changes in the heliostats to become necessary. More information about the instrumentation may be found on Page 5-21.

Operator Console. The Honeywell preliminary design provides an operator's console which permits the operator to control the collector subsystem. The console contains miscellaneous switches and a CRT display which is used to display data and performance information from the computer. The console also provides alarms like audible buzzers and flashing lights to cue operator action. More information on the operator's console is contained on Page 5-17.

The miscellaneous equipment described above provides an extraordinary degree of flexibility to accommodate different design changes yet it keeps costs down and provides for man-in-the-loop control and supervision of the collector subsystem.

Overview Conclusion

The heliostat and its associated control equipment have been sufficiently evaluated in the SRE through analysis and test that technical risk to the pilot plant is minimum. The pilot plant requirements have been satisfied in several unique fashions which contribute to an effective pilot plant design of the collector subsystem.

REQUIREMENTS AND SPECIFICATION SUMMARY

The collector subsystem is constrained by numerous requirements/specifications which generally fall into four categories:

1. Maximizing energy into receiver for minimum life cycle cost
2. Operating in or surviving environments
3. Interfacing other subsystems
4. Safety

Table 2-1 provides an overview of the major requirements by category along with the approach Honeywell has selected to satisfy them.

The collector subsystem has three major components; collector field, computer control complex and calibration array, each with areas of major cost sensitivity to the above requirements.

The collector field cost driver is the heliostat. Heliostat cost is driven by the need to point the reflected rays accurately by not deflecting in the presence of specified wind. However, recent changes to the survival wind requirement (40 m/s at 10 degrees of attack) will cause some items to be sized by stress considerations which were previously sized by deflection requirements.

The computer command control system is most affected by wiring costs, the need to command large numbers of heliostats and the various modes it must operate in to satisfy the interface requirements with the receiver and the master plant controller.

The calibration array frames must withstand high winds and acceleration forces due to tower amplification of seismic inputs. The photodetector assembly design is driven by 10 - sun flux levels (approximately 10 kw/m²) expected from a single heliostat.

SYSTEM OPERATION SUMMARY

The heliostat and its control system, called the collector subsystem, is made up of three operating blocks. They are the Control Computer, the Heliostat and the Calibration Array. A normally operating system functions as follows.

The Control Computer is the heart of the control system. Using WWV as a timing reference, the computer calculates the time dependent sun position at 1 second intervals from which gimbal angle tracking information is computed for all of the field heliostats. As required

Table 2-1. Satisfaction of Specification

<u>category</u>	<u>Spec Requirement</u>	<u>How Satisfied</u>
1	Reflectivity 90 percent min	Low iron 2nd surface float glass mirror
1	Clear reflective surface w/o degradation	Sealed mirror edges and periodic cleaning
1	95 percent of redirected energy into aperture	Focused panels (f = 418m) MM spacing - 1.6 x panel width Variable ground cover ratio Toe-in strategy: March 21 noon sun position Frame axis perpendicular to radial from tower
1,2	Pointing accuracy 2 mr 1σ	Budgeting of deterministic and stochastic errors Periodic calibration with photodetector arrays
1,2	Optical accuracy 1 mr 1σ	Machined contour (836m spherical radius) mirror module; Sandwich panel construction
1	Interchangeable heliostats for all field positions	Common design
3	Easily maintained	Modular design
2	30 year life	Scheduled maintenance
2	Operating Wind: 13.5 m/sec at 10m height	Design components to budgeted spring rates
2	Survival Wind: 40 m/sec at 10m height	Design components to allow stress; stow mirrors face down, horizontal
2	Operating Temperature: -20°F to 120°F	Match expansion coefficients in critical areas Structural compliance in noncritical areas Shaded electronics (all elements) have high reflectance paint
2	Seismic: NRC 1.60 spectrum	Design for acceleration induced stress
2	Lightning: No effect due to transient	Zeners, gas discharge tubes Grounding and shielding
2	Moisture	Sealed bearings, drives, electronics

Table 2-1. Satisfaction of Specification (Continued)

<u>Category</u>	<u>Spec Requirements</u>	<u>How Satisfied</u>
3	Operating Modes	
	Initialization	Electro-optical switches on gimbals
	Offset Track (Standby near receiver)	Software/Electronics
	Startup Sequence	Master Control Interface
	Track Receiver	Software/Electronics (incremental digital) Aim strategy
	Calibrate at photodector array	Software/Electronics (incremental digital)
	Emergency Defocus	2 axis high rate, batteries
	Shutdown Sequence	Master control interface
	Stow	Electro-optical switches, batteries
	Limit Control	Mech stops (OA only); motor thermostats
	Manual Control	Manual control box and portable aux motors
4	Safety	Enclosed gearing, shield on 110V
		Software Beam Control
		Opaque Fences
		Redundant Computers
		Comm Loss Detectors
		Power Loss Detectors
		Uninterruptible Power Supply
		Battery Powered Heliostats

to maintain track, updates, in the form of incremental gimbal angle step commands, are sent from the computer to the field heliostats. Data is transmitted in serial digital fashion over 18 buried twisted shielded lines.

At the heliostat the information from the computer is received by the heliostat electronics which decodes the data and executes the required gimbal incremental commands. Gimbal updates are 1 or 15 step increments. A step is a gimbal drive motor shaft revolution which corresponds to ≈ 81 arc-seconds of gimbal travel. One step commands are used for fine tracking while 15 step commands are used for controlled speed slewing. All the information for a complete 2 axis update is contained in a single 8 bit command word. In the tracking mode, the computer commands the redirected beam to track the receiver aperture, or secondary targets which can simply be points in space.

In addition to the tracking mode just described, the computer also commands the heliostat to initialize. Initialization provides the means to drive the two heliostat gimbals to known reference positions. It is used to reestablish known gimbal positions (mirrors level glass down) in the computer should they for some reason become lost. All the hardware to accomplish initialization is contained at the heliostat. Initialization is commanded by the setting of a single bit in the command word. The heliostat also contains communications and power line monitors which will automatically initiate a stow (mirrors level glass down) maneuver should interruptions occur for a sufficiently long time period.

The calibration array is used to make periodic measurements on the redirected beam. By commanding the redirected beam to the calibration array and reading out the array's photodetectors, the computer can determine differences between the predicted and measured positions of the beam and make appropriate corrections. This information can also be accumulated to help identify possible variations in long term effects such as foundation drift and can also be used to help predict when washing may be required. Array data is multiplexed to the computer over a twisted shielded pair. See Figure 2-4.

Operating details of the heliostat and its control system are contained in the ensuing paragraphs of this report.

ANALYSIS SUMMARY DESCRIPTION

Analyses of various types and to different degrees have been conducted during the pilot plant collector subsystem preliminary design. The results are covered in detail in the appropriate sections of this report. The data presented here summarizes some of the more significant results.

Power and Thermal Analysis. The power required for operation of a solar research experiment heliostat was 35W with 23.4W in the electronics package. The air within the electronics package was calculated

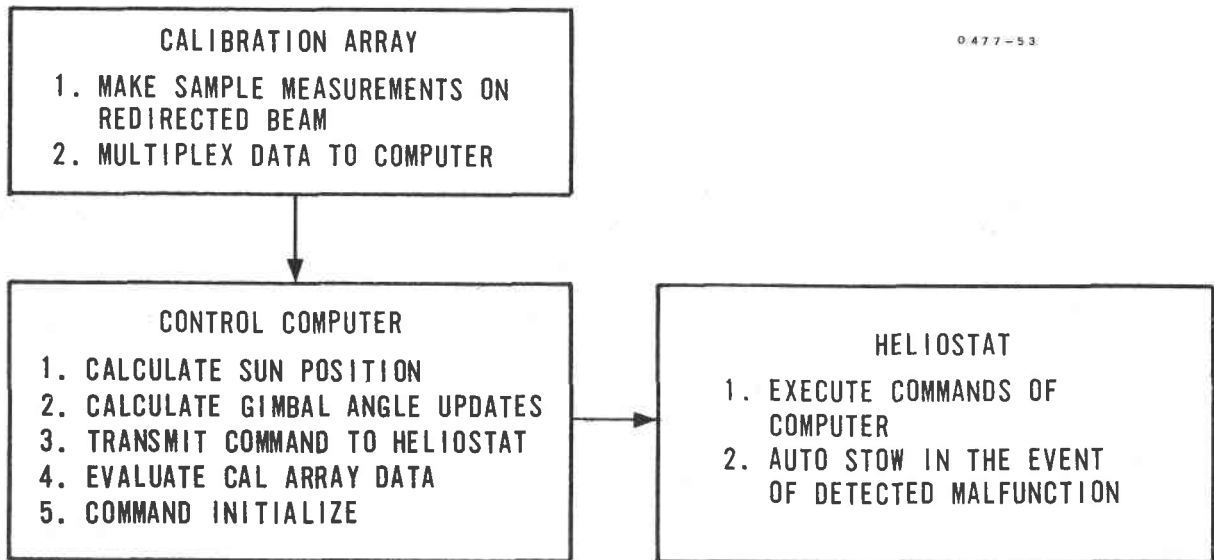


Figure 2-4. Array Data Flow

to be a maximum of 59°C (138°F) for ambient temperature of 49°C (120°). The power required for operation of a pilot plant heliostat will be 47W with 38W in the electronic package. The air within the electronics package was calculated to reach a maximum temperature of 64°C (148°F) with ambient temperature of 64°C (148°F). This data shows satisfactory thermal environment of less than 70°C (148°F), the temperature allowable for components. The analysis showed that the electronics would overheat if exposed to direct solar radiation. An awning is proposed to provide shade for the package to prevent direct solar radiation.

Motors selected were Inland Motors model T1806H with 0.077 kg-m (0.56 ft-lbs) torque, 1241 rpm and model T1804 with 0.144 kg-m (1.04 ft-lbs) torque, 812 rpm. Thermal analysis and testing were conducted to prove motor maximum temperature of 122°C (252°F) compared to limit of 155°C (311°F).

Parametric Analysis. A major parameter trade study was conducted to optimize the type of heliostat, its physical properties and design requirements to arrive at the most cost effective design. The purpose of this study was to minimize the cost of energy at the input to the receiver (\$/MWH). The study results gave the following heliostat parameters:

Tilt-Tilt Heliostat Configuration

4 Mirror Modules per Heliostat

40m² of Mirror Surface per Heliostat

2 m Pointing Accuracy (1σ)

Mirror to Mirror Spacing Ratio of 1.6

13.5 m/sec Wind Velocity

Mirror Module Aspect Ratio of 1.0

Structural Analysis. In depth static and dynamic structural analyses of mirror modules and heliostat assemblies were conducted. In all but very special cases, such as the crank arm in survivability environment, the complete heliostat design was deflection limited. The following results were obtained:

Mirror Modules

Margin of safety at maximum stress point - 2.8

Linear deflection at operating winds - insignificant

Torsional deflection - 0.7 mr at maximum torque.

Heliostat

Static

Horizontal - Stress margins of safety - 2.47

75 degrees - Stress margins of safety - 1.0

Dynamic

Lowest natural frequency - 2.7 Hz

Stress margin of safety - 0.3 (crank arm)

Error Analysis. Analyses of over 30 collector subsystem errors have been made and budgets for various sources established. Deterministic error sources such as wind, temperature, and the effect of gravity, along with independent error sources such as build and assembly tolerances and control errors have been considered. Page 4-15 of this report presents details of the error budget analysis. The significant results were as follows:

	<u>3σ</u>	<u>1σ</u>
Solar Research Experiment Heliostats	1.8 mr	1.15 mr
Pilot Plant Heliostats	1.82 mr	1.22 mr

These results show total error within the 2 mr, 1 σ requirement.

These and other analyses have shown that the heliostat is suitable for the pilot plant, will meet necessary pointing accuracy requirements, and is compatible with the utility company practices.

SRE TEST RESULTS SUMMARY

SRE tests were made to assure the components and system was ready for detail design. Test results show the heliostat performance is superior to requirements. Both correlation of subsystem level test results with the detail design review error budget (Page 7-179) and end

to end system level testing show that a 2 mr operational tracking accuracy can be maintained under open loop tracking with the present heliostat configuration and control software.

The structural rigidity of the mirror modules under all simulated environmental loads surpassed the contour control requirements. Under operational wind loading the outer axis (vertical image movement) combined deflections did not exceed ± 0.6 mr. Inner axis deflections under gusts have exhibited instantaneous extremes of 2.9 mr but a more nominal average of ± 1.3 mr centroid deflections can be expected across a field average.

A two part calibration scheme was devised where measured heliostat unique parameters will consist of site geodetic constants, outer drive scale factors, and initial initialization offset constants. The periodic calibrations via the calibration array will remove trending errors. The SRE test program demonstrated a weekly or longer interval requirement for periodic calibrations during which offset constants will be updated.

Different mirror module build techniques were evaluated. Both aluminum honeycomb backed structures-- a tapered cross-section and a 9-inch thick rectangular cross-section-- met all contour control and torsional deflection strength requirements under a simulated 13.4 M/S wind load as shown in Figure 2-5. Uniform, solar, and 'g' loading showed no significant contour changes.

Results and indicated problems from the test program gave direction to many suggested hardware modifications such as initialization mechanization, mirror module shaft interface to the inner drive, actuator types, motor sizing and housing, production and assembly improvements, etc. These results are reflected in this pilot plant collector subsystem preliminary design, including subsystem control techniques and impact of environmental influences. A technique was developed and implemented for directly determining the redirected energy via continuously calibrating the calibration array outputs with respect to absolute insolation levels (pyrheliometer).

Additional and more detailed test results may be found in Section 7.

COMPARISON BETWEEN THE SRE AND PILOT PLANT COLLECTOR SUBSYSTEM
Table 2-2 titled "SRE Versus Pilot Plant" describes some of the important differences between the SRE and the Pilot Plant Collector Subsystem elements. The differences between the heliostats begins with the mirror modules which are slightly different in form factor and size between the three experimental models and the pilot plant units. The difference in dimensions results from the fact that the vendor has a press for bonding sandwich panels which has a 120 inch limit in one dimension. Thus, in order to keep the same area we have increased the other dimension to 120 inches resulting in a 10 square meter mirror module area for each unit but with a 10 foot by 11 foot

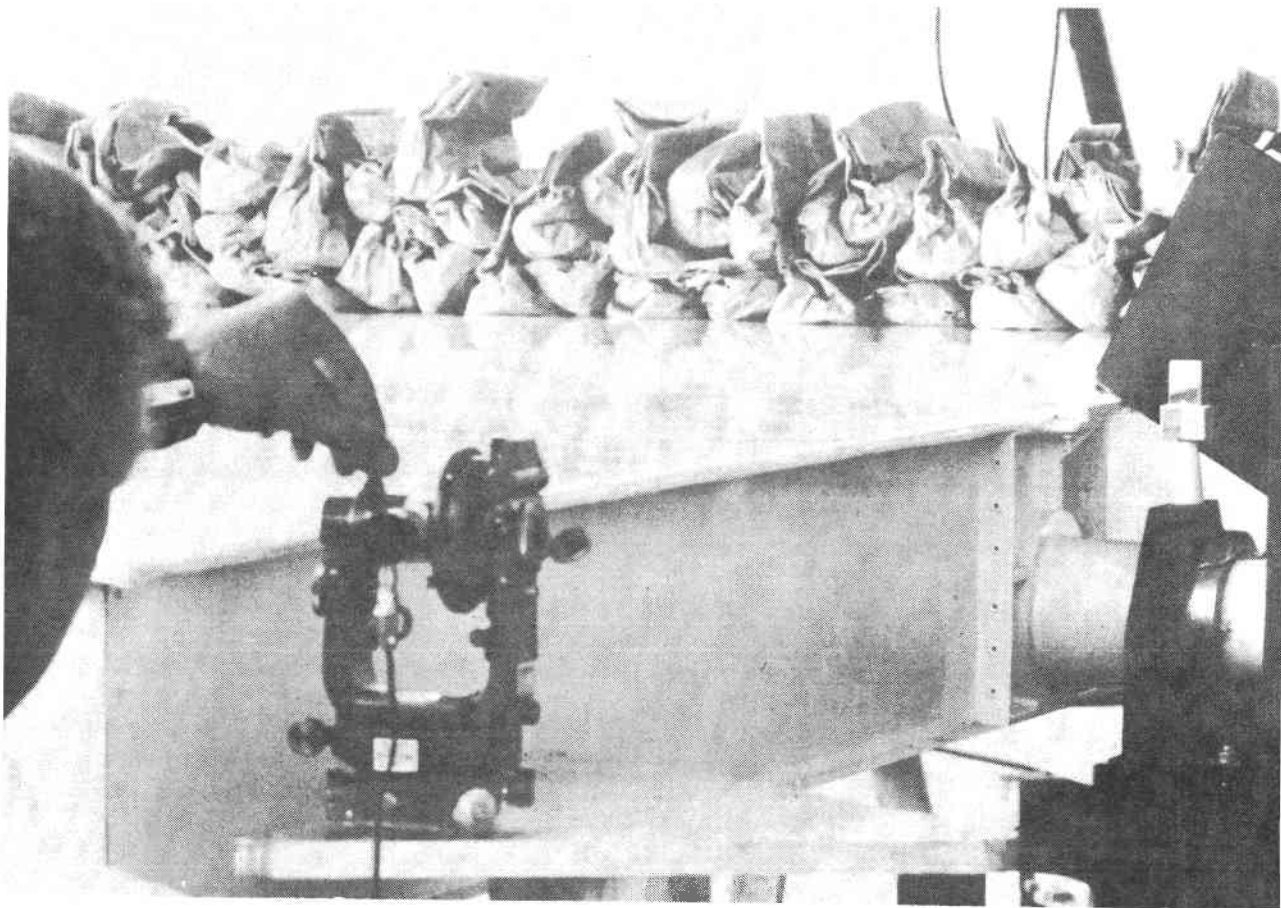


Figure 2-5. Simulated 13.4 M/S Wind Load

dimension on the mirror module. Additionally, the units built to date have had 9 facets of glass on each mirror module whereas for the pilot plant we anticipate using two facets of very large pieces of glass. Another difference between mirror modules consists of the hub material. In the SRE cast aluminum was used and was found to be unsatisfactory from the standpoint of galling and shearing under the loads imposed by the taper locks. Thus we plan to use steel hubs for the pilot plant to avoid this problem. An added benefit is the increased stiffness of the steel to resist torsional loads on the hubs.

Presently we plan no differences between the pilot plant and the SRE frame. The inner drive for the pilot plant is the same as the inner drive used on the SRE although some changes are planned to improve the waterproof and dustproof characteristics of the drive. Outer drive ball screws are sealed and have a standard iron tube to cover the back end of the ball screw. This iron tube, which is heavy, and expensive, will be replaced by a lightweight tube which will be lower cost. The motors will be weather tight while on the pilot plant even though this is a difference from non-weather type motors used on the SRE. The electronics differences are all minor and are planned to

Table 2-2. SRE versus Pilot Plant

<u>Item</u>	<u>SRE</u>	<u>Pilot Plant</u>
Mirror Modules (MM)	Engineering Model 10m ² 3.18 x 3.18m - 2 units (125 x 125 inches)	All units - 10m ² 3.04m x 3.3m (120 x 130 inches)
	Experimental Models 9.3m ² 3.04m x 3.04x - 14 units (120 x 120 inches)	
	Radius of Curvature 670m (2200 feet)	Radius of Curvature 836m (2742 feet)
	9 facets second surface 2.36mm* (0.093 inch) glass	2 facets second surface 2.36mm* (0.093 inch) glass Low iron content
	Factory mounted glass	Field mounted glass
	Hubs cast aluminum	Cast steel
	25.3cm (10 inch) WF I-Beam	25.3cm (10 inch) WF I-Beam
	Inside I-Beam	Inside I-Beam
	Under hub of MM	Under hub of MM
	Not weather tight	Weather tight seals
Outer Drive (Ball Screws)	Bellows sealed	Bellows sealed - improved
	Iron tube - heavy	Lightweight tube
	Motor not weather tight	Weather proof motor
Electronics	3 electronics cards Hand wired	4 electronics cards Printed circuits
	Unscreened parts	Screened parts
	Commercial 115vac power supply	24 vdc commercial power supply
	Dedicated communication lines	Address decode
	No sun roof	Sun roof
	No fail-safe circuits	Motor over temp, power and communication loss detector

*This is nominal 3mm glass but experience shows actual numbers are these.

Table 2-2. SRE versus Pilot Plant (Continued)

<u>Item</u>	<u>SRE</u>	<u>Pilot Plant</u>
Electronics (Continued)	2 gray boxes, weathertight	1 white box, weathertight
	Commercial auto batteries (unsealed)	Industrial stationary battery (sealed)
	Separate mounting	Post mounted
	Commercial charger (Universal)	Commercial trickle charger (Special)
Wiring	Indoor conduit - TSP	Outdoor conduit - TSP
Computer	DDP-516 - Honeywell	L6/43 - Honeywell baseline or equivalent
Data Link/Rate	TSP/4800 bps - 1 tap (H/S)	TSP/4800 bps/average 90 taps (H/S)
Wire Length (max)	314m (1,031 feet) Underground Conduit	2,087m (6,850 feet) Underground Direct Burial
Initialization	Add on bracket optopair supports	Redesigned optopair bracket support
	Inadequate adjustment provisions	New micrometer tool adjustment provisions
Foundation	0.914m (3 ft) x 1.524m (5 ft) x 3.05m (1 ft) Fla. sand No seismic consideration	1.83m (6 ft) x 3.05m (10 ft) x 0.305m (1 ft) With seismic consideration
Heliostat Area	37m ²	40m ²
Heliostat Quantity	4	1598
Longest Line of Sight and Focal Length	335m	418m
Number of Heliostats per Command Line	1	90
Heliostat Instrumentation	None	18 units with shaft encoders

improve the producibility of the electronic assemblies. The screened parts provide a better life and lower infant mortalities. Printed circuits are substituted for hand made wire wrap interconnections. The 24 volt dc commercial power supply is to operate off of the battery whereas the SRE could not function totally on the battery due to the fact that some voltages were derived from 115 volt ac power supplies. Thermal characteristics in the desert indicate that a sun roof to cast a shadow on the electronics box will be necessary. Although no sun roof was used on the SRE, a sun roof is planned for the pilot plant to cast a shadow during the peak parts of the day; thus reducing the temperature of the electronics inside the weather tight box.

Additionally, the electronics differ in that the watchdog timer, motor overtemp, power and communication loss detector circuits will be included in the pilot plant but these were not required for the SRE.

Another difference between the SRE and the pilot plant is the wiring on the heliostat. On the SRE units indoor conduit with twisted shielded pairs inside was used whereas on the pilot plant an outdoor harness with twisted shielded pairs is planned.

The DDP-516 computer used in the SRE is being replaced by the Level 6/43 Honeywell computer as a baseline. This is not the only computer which can be used so any equivalent machine which is capable of distributed processing can be used. However, we have baselined this machine as being most suitable and as being a lowest cost machine available to use. The data link and data rates are the same for the SRE and for the pilot plant with the exception that the data link for the SRE has only one tap while the pilot plant will have an average of 90 taps on each twisted shielded pair.

The wire length for the SRE was established at an early time at 314 meters which is the one way distance maximum to a heliostat in an earlier tower centered configuration. For the pilot plant current plans are to have a maximum signal wire run of over 2,000 meters which includes the distance from the computer out through the heliostat field and then back to the computer so that an entire loop is formed which will allow checking at the end of the line of all signals which are put on the start of the line. This is another approach and a lower cost approach to reliability of the command control scheme.

The initialization hardware is different since the brackets which supported the opto-pair for the SRE had merely slotted holes and these were found to be a very coarse adjustment such that actually bending the bracket was necessary to provide the accuracy necessary. For the pilot plant this bracket and adjustment provision is completely redesigned so as to allow a tool similar to an inside micrometer to be used in adjusting the location of the opto-pair which indicates the stow or initialization positions.

The foundation for the SRE was roughly 3 feet by 5 feet by 1 foot thick in the Florida sand and considered no seismic loads. After some analysis, it was determined that the pilot plant foundation will need to

be twice as big in order to carry the seismic loads as well as to comply with the lower modulus soil at Barstow, California.

Generally speaking the differences between the SRE and the pilot plant are of a minor nature and no problems are anticipated during detail design in completing these design changes on a short schedule and within reasonable costs. There is no technical risk that is foreseen in any of these changes in terms of performance. There is obviously some technical risk from the standpoint of impact on cost. Most cost impacts will be in the nonrecurring rather than the recurring areas.

COMMERCIAL PLANT

The commercial plant is merely a scale up of the pilot plant (PP) using four fields (modules) larger than the PP. Thus, each of the four modules for the commercial plant will have its own heliostat field, computer command control scheme and other associated equipment. Thus, there are 4 towers, 4 calibration arrays, 4 computers, and 4 heliostat fields for the commercial plant. The heliostats, the computers, and the calibration arrays are merely scale-ups or identical to the pilot plant, heliostats being identical and calibration arrays being scaled up. The computer is identical with the software being revised in order to address the larger number of heliostats in the one commercial plant module size facility.

Conclusion

Honeywell's work on the collector subsystem for the solar thermal electric power system can best be categorized as immature but progressing. Many aspects of the design and performance have been checked, evaluated and proven during the preliminary design contract. However, many worthwhile areas of the design were given cursory treatment by necessity of cost and schedule considerations. The foregoing summary should show some of the areas which need minor additional work, as well as those which may need substantial effort in the design phase. That the Honeywell collector subsystem is ready for detail design should be readily apparent from the balance of this report.

Section 3 DETAIL SUBSYSTEM DESCRIPTION SUMMARY

The detail description of a system as large and complex as the collector can be tedious in the extreme. This section introduces the subject through several overall tools including a system schematic and drawing trees. Description of the mechanical hardware is undertaken next and is followed by the electronics hardware and field wiring. The final descriptive section is the command computer and its software. A conclusion paragraph closes the section.

INTRODUCTION

The pilot plant collector subsystem field consists of 1598 tilt-tilt configuration heliostats with $40M^2$ reflective surface area per heliostat. The field is a circular layout with the receiver located $1/2$ of the radius south of the center as shown in Figure 3-1. Eight zones are defined. Field power, instrumentation, grounding and communication wiring schemes are laid out in these zones and explained in more detail on pages 3-64 through 3-70.

Figure 3-1 is drawn from a computer tabulation which spaces the heliostats both radially and tangentially to minimize shadowing and blocking. As can be seen some radial lanes were maintained to expedite cable routing and vehicle field access. The area cover ratio of mirror surface area to field area is 0.29.

Diameter of the field is 535m (1756 feet) with a radial distance of 50.3m (165 feet) from the tower center line to the nearest heliostat for a LOS distance of 140.4m to the target.

The northern most heliostat is 401m (1315 feet) from the tower center line for a LOS distance of 418m to the target.

A perimeter fence circles the field to provide plant security, re-directed beam safing, and help minimize the adverse influence of direct winds upon the outer heliostats. Barriers within the field are erected as required to prevent hazard to personnel and equipment due to redirected beam travel.

The eight calibration arrays will be fixed atop the receiver tower for pilot plant applications. The control facility (computers, displays, etc.) will be housed within buildings near the base of the receiver.

Figure 3-2 is a functional block diagram of the pilot plant collector subsystem. The main intent of this diagram is to show the functional interfaces that are associated with the control and heliostat portions of the collector subsystem. The control arrangement is further described on pages 3-71 and 3-72 while the individual

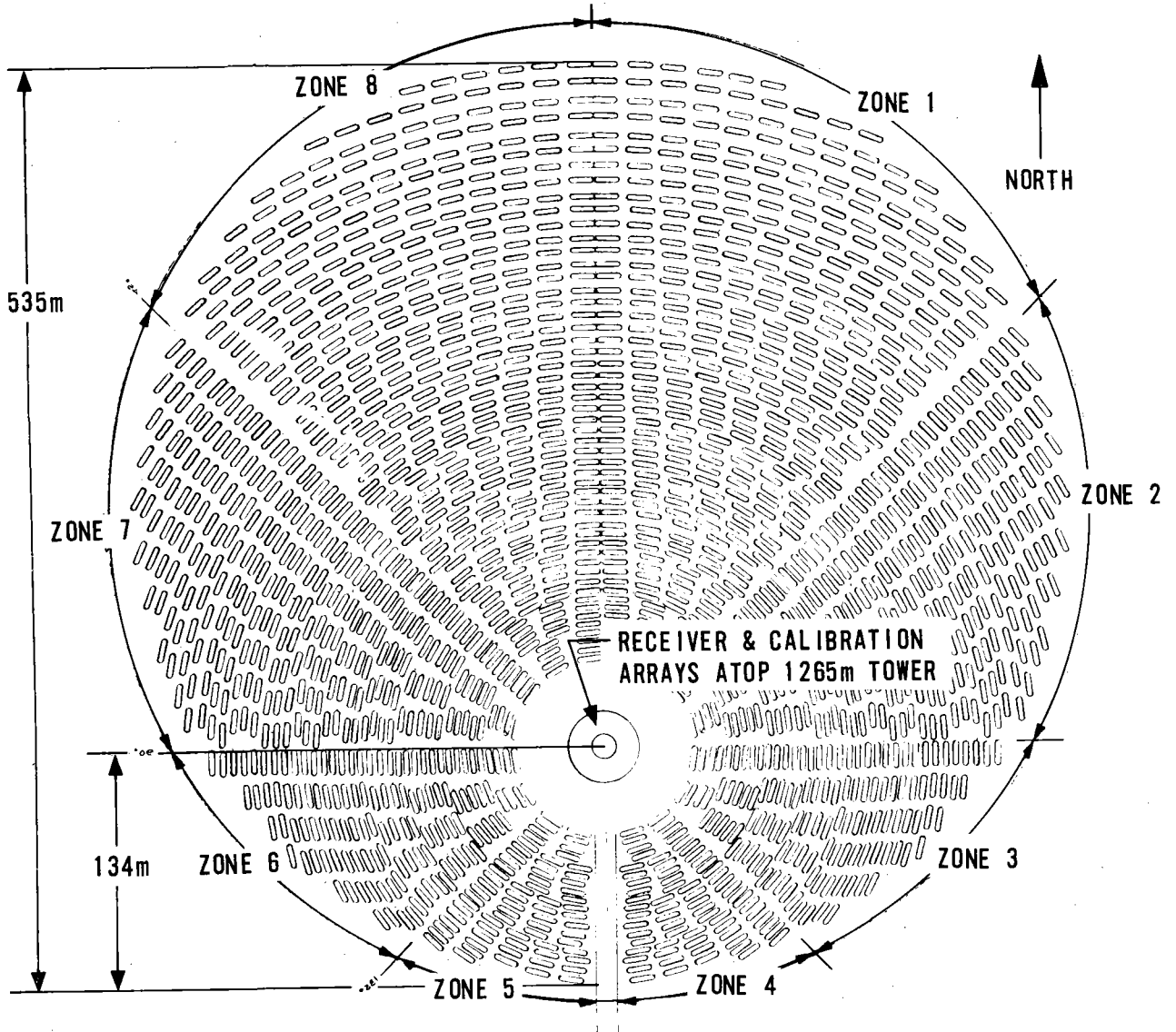


Figure 3-1. Collector Subsystem Tower
1/2 South Field Layout

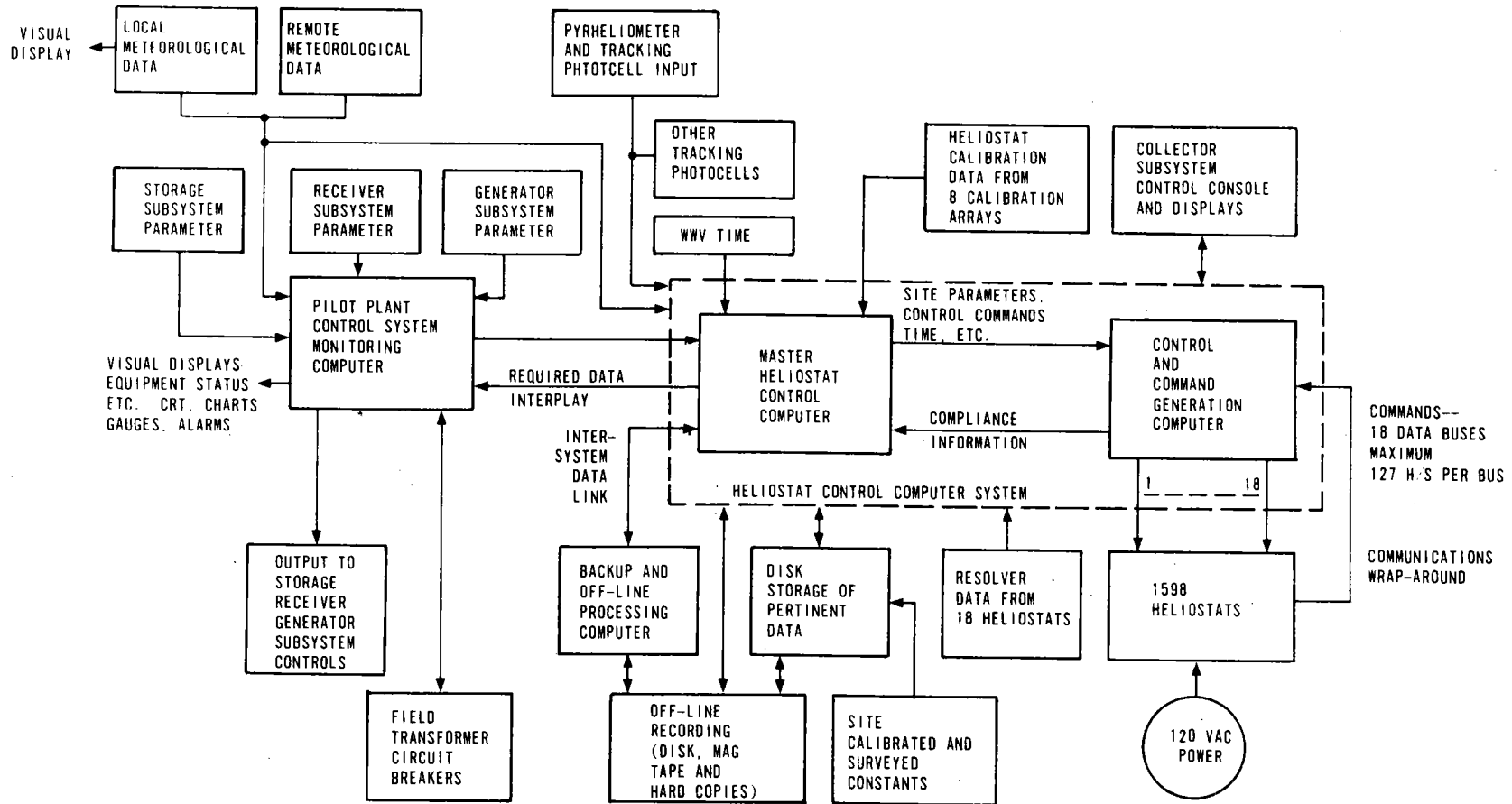


Figure 3-2. Pilot Plant Collector Subsystem Block Diagram

heliostat site electronics control is defined on page 3-35. The collector subsystem is further divided into three additional major subsystems:

- HG8652A1 Collector Field
- BG8251B1 Control Subsystem
- LG8015B1 Calibration Subsystem

DOCUMENTATION TREE

The pilot plant documentation tree is shown in Figure 3-3. Each major element of the collector subsystem is further broken down in the drawing trees shown by Figure 3-4.

The collector field (Figure 3-4) is broken into five major subelements:

- Heliostat assemblies
- Field instrumentation for control and performance monitoring purposes
- Heliostat assembly and calibration procedures
- Field wiring (power and communications)
- Logistical support elements

The LG8016C1 tilt-tilt gimballed heliostat assembly itself is further broken down into its main parts in Figure 3-5. Eighteen pilot plant heliostats (LG8016C2) are instrumented to provide precise inner and outer axis orientation information back to the collector subsystem control computer networks for comparison with commanded position. One heliostat per data bus will be instrumented to detect any improper motion.

Figure 3-6 shows a top level breakdown of the control subsystem, which consists primarily of three level 6/43 CPUs, control software, post-test and performance monitoring programs, control console, storage and display peripherals, and logistical support elements. Two processors with 96K of memory will be used on line while one level 6 processor with 64K of memory will remain ready as backup and be used primarily for post-test data reduction and analysis.

The eight calibration arrays and their associated electronics are depicted under the LG8015B1 calibration subsystem (Figure 3-7). They will be mounted at the top of the receiver housing and measure approximately 8.5m wide by 7.3m high (28 feet by 24 feet).

COLLECTOR SUBSYSTEM SCHEMATIC

Figure 3-8 shows the pilot plant flow of information from the computer counterclockwise out to the heliostats which then "feed back" position data from shaft encoders and solar energy to the calibration array or boiler. This results in different information being input to the computer such that comparisons with commands can be made as a special

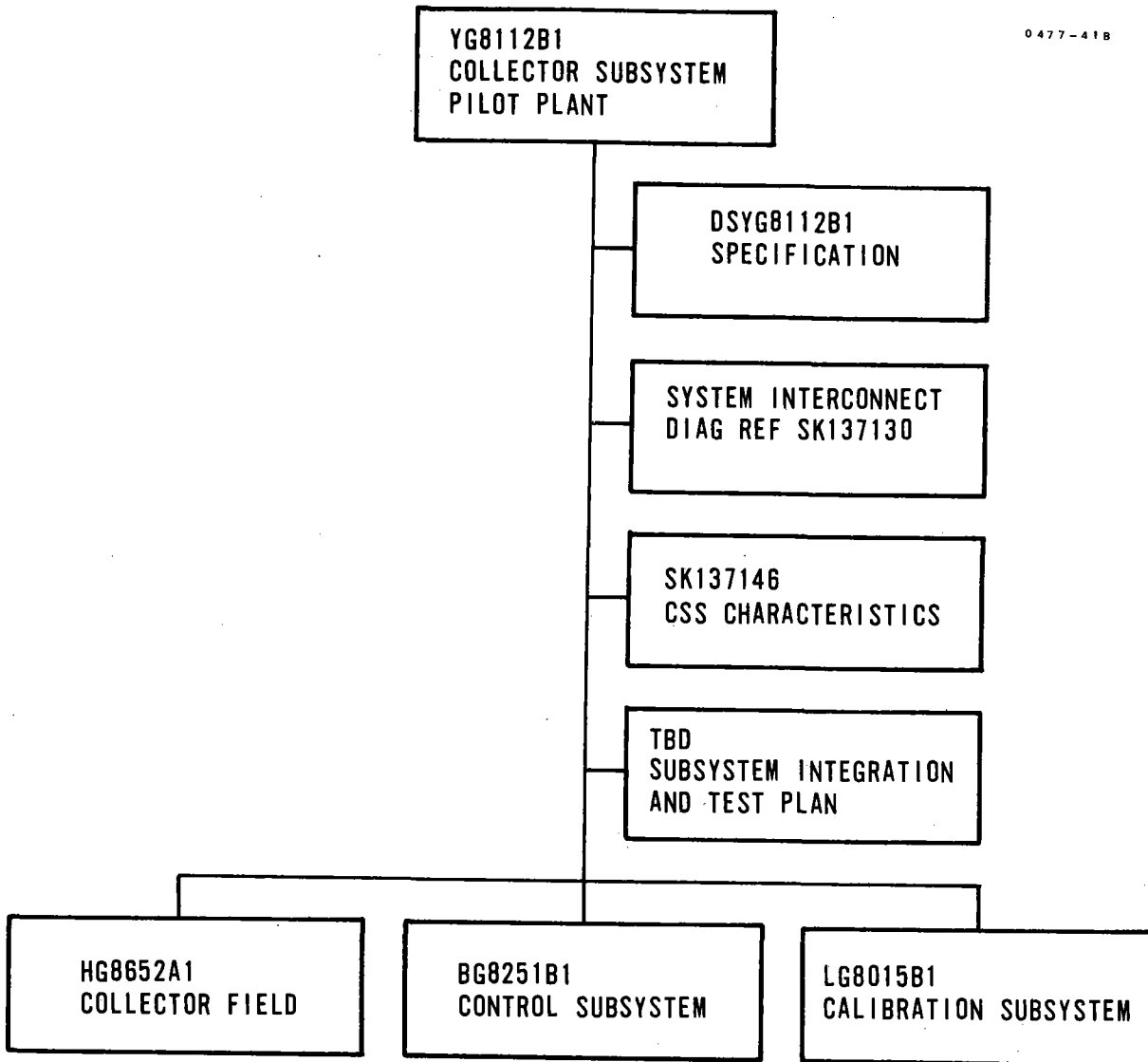


Figure 3-3. Top Level Collector Subsystem Documentation Tree

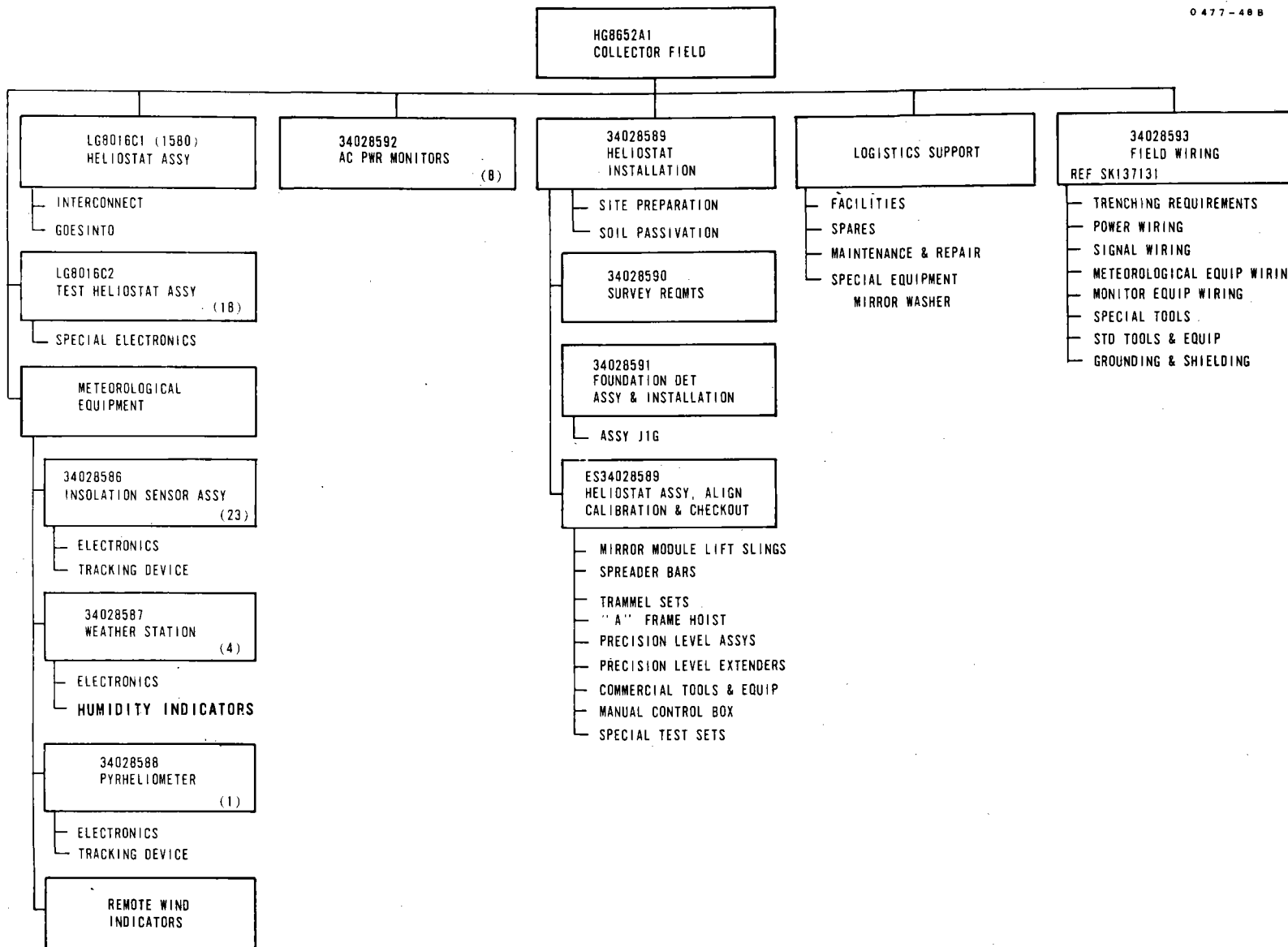
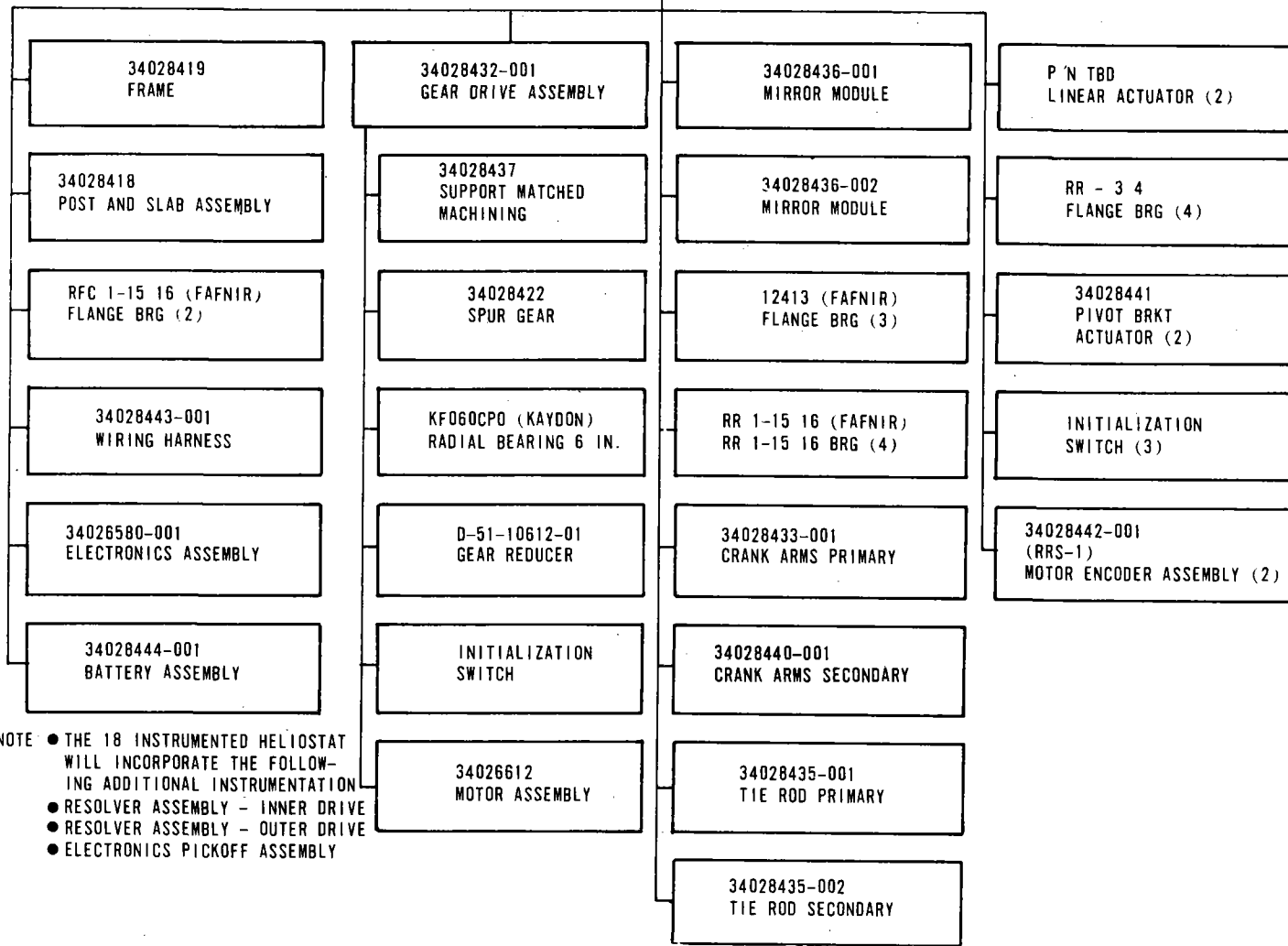


Figure 3-4. Drawing Trees of the Collector Subsystem

LG8016C1
HELIOSTAT ASSEMBLY

0477-30B



NOTE ● THE 18 INSTRUMENTED HELIOSTAT WILL INCORPORATE THE FOLLOWING ADDITIONAL INSTRUMENTATION

- RESOLVER ASSEMBLY - INNER DRIVE
- RESOLVER ASSEMBLY - OUTER DRIVE
- ELECTRONICS PICKOFF ASSEMBLY

Figure 3-5. Drawing Trees of the Collector Subsystem

BGB251B1
CONTROL SUBSYSTEM

0477-159C

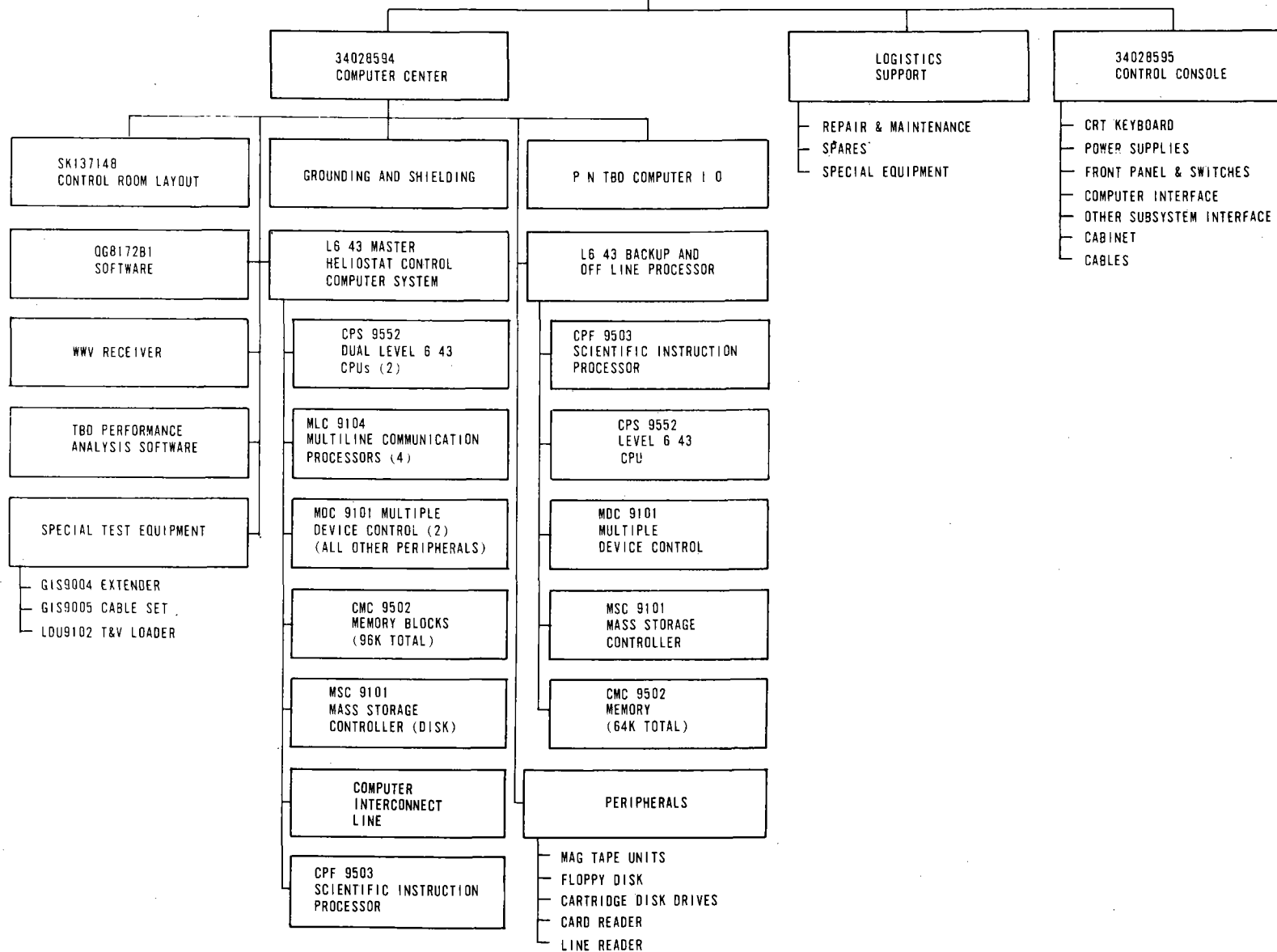


Figure 3-6. Collector Subsystem Control Subsystem

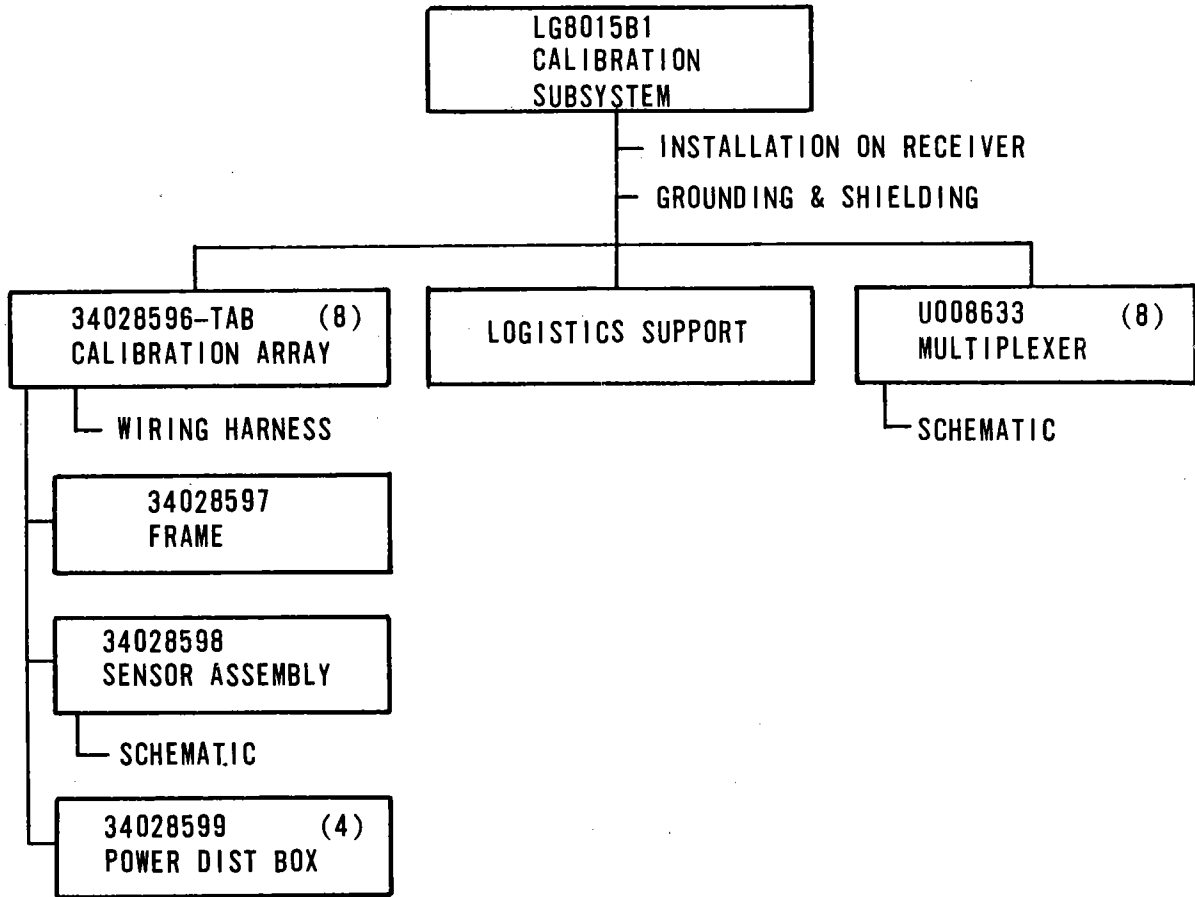


Figure 3-7. Calibration Arrays and Their Associated Electronics

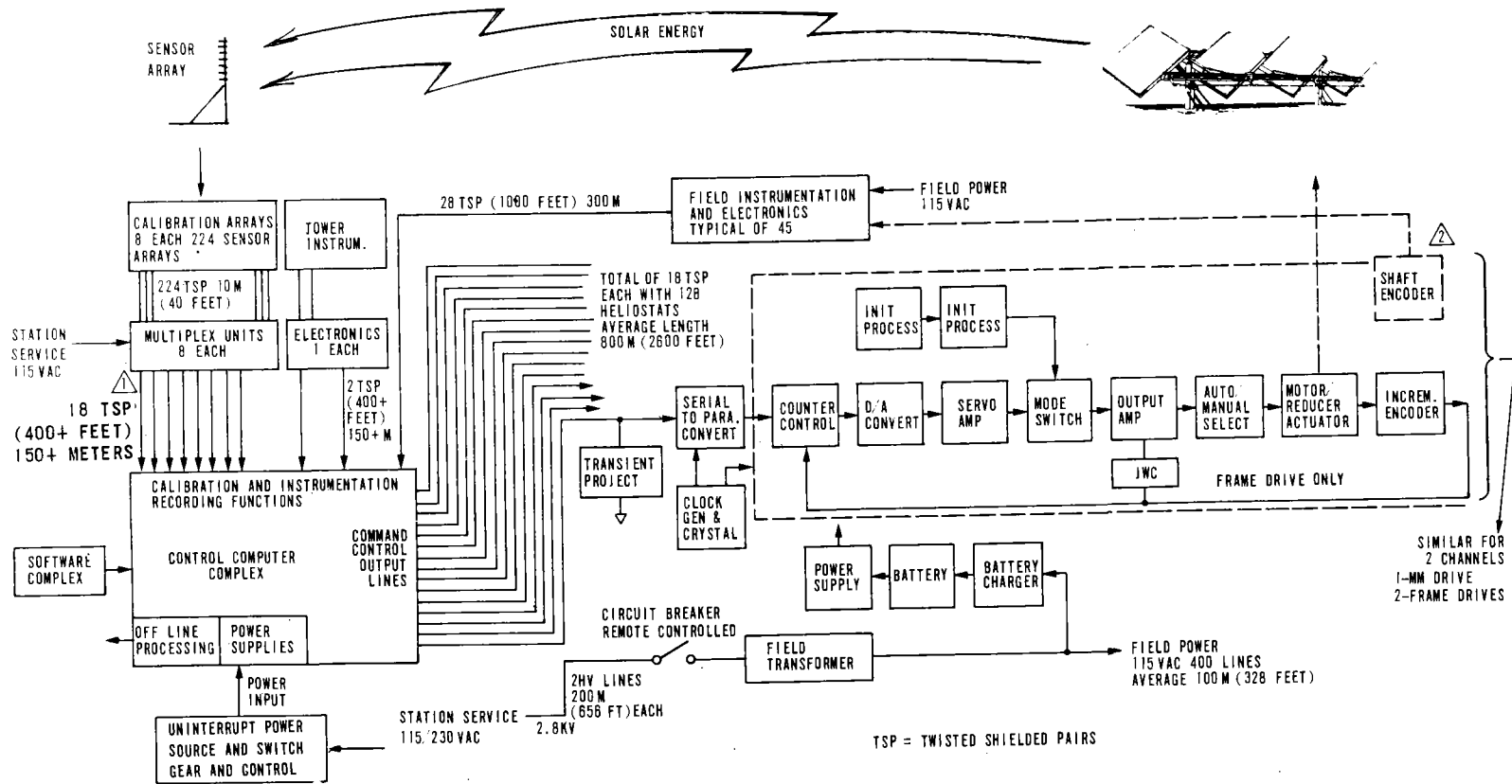


Figure 3-8. Collector Subsystem Interconnection One Line Diagram (Pilot Plant)

check for pilot plant only. Figure 3-9 shows the commercial plant flow which does not have special instrumentation used on the pilot plant. It is intended in the collector subsystem design to maintain as much commonality as possible between pilot plant and commercial plant. This simplifies the commercial plant definition task as well as eliminates risk.

HELIOSTAT DETAIL MECHANICAL DESCRIPTION

The Honeywell heliostat concept (LG8016) was determined by a parametric cost trade study. The results of this study indicated the Pilot Plant Tilt-Tilt gimbal arrangement is superior. The resulting low profile heliostat contains four mirror modules each with 10m² of surface mounted in a 15.65m long frame. The heliostats are positioned on a series of arcs of constant radius about the tower. Each heliostat has its long axis perpendicular to a radius from the tower. This long axis or frame axis is also known as the outer axis and is mounted on bearings at the top of the two posts allowing frame rotation (or Tilt) of up to 75 degrees toward the tower and 30 degrees away from the tower. Two ball screw actuators, one at each post, are used to position this outer gimbal (frame). They point toward the tower. The inner gimbal is formed by each of the four mirror modules rotating (or tilting) about an axis perpendicular to the outer axis and in the plane of the frame. This is also known as the inner axis. The four mirror modules operate from a single gear drive through a series of crank arms and tie rods. A photograph of a heliostat with major components identified is presented in Figure 3-10. In the following paragraphs the major components of the heliostat will be discussed in detail.

Heliostat Foundation and Post

The wide stance, two-post and slab configuration is key to the stability of the Honeywell Heliostat. Figures 3-11 and 3-12 show the two-stage construction process.

The stub posts are 25.4 cm x 3.8 cm channels extending 0.5 meter above the surface of the concrete. They are welded into a two-level mat of 13 mm steel reinforcement bar. These weldments are lowered into prepared rectangular holes 0.2 meter deep and held with I-beams and cribbing during concrete pour. The two foundations are 10.16m (33 feet, 4 inches) on centers. Reinforcement bars are covered with the minimum thicknesses of concrete recommended by the American Concrete Institute for corrosion protection. The size of pilot plant foundations are 1.83m (6 feet) x 3.05m (10 feet) based on seismic loads and properties data supplied for the Barstow site. The slabs are designed to limit soil bearing pressure under combined horizontal and vertical accelerations specified plus dead weight.

Other slab design criteria such as rocking spring rate and overturning moments under wind load are lesser requirements.

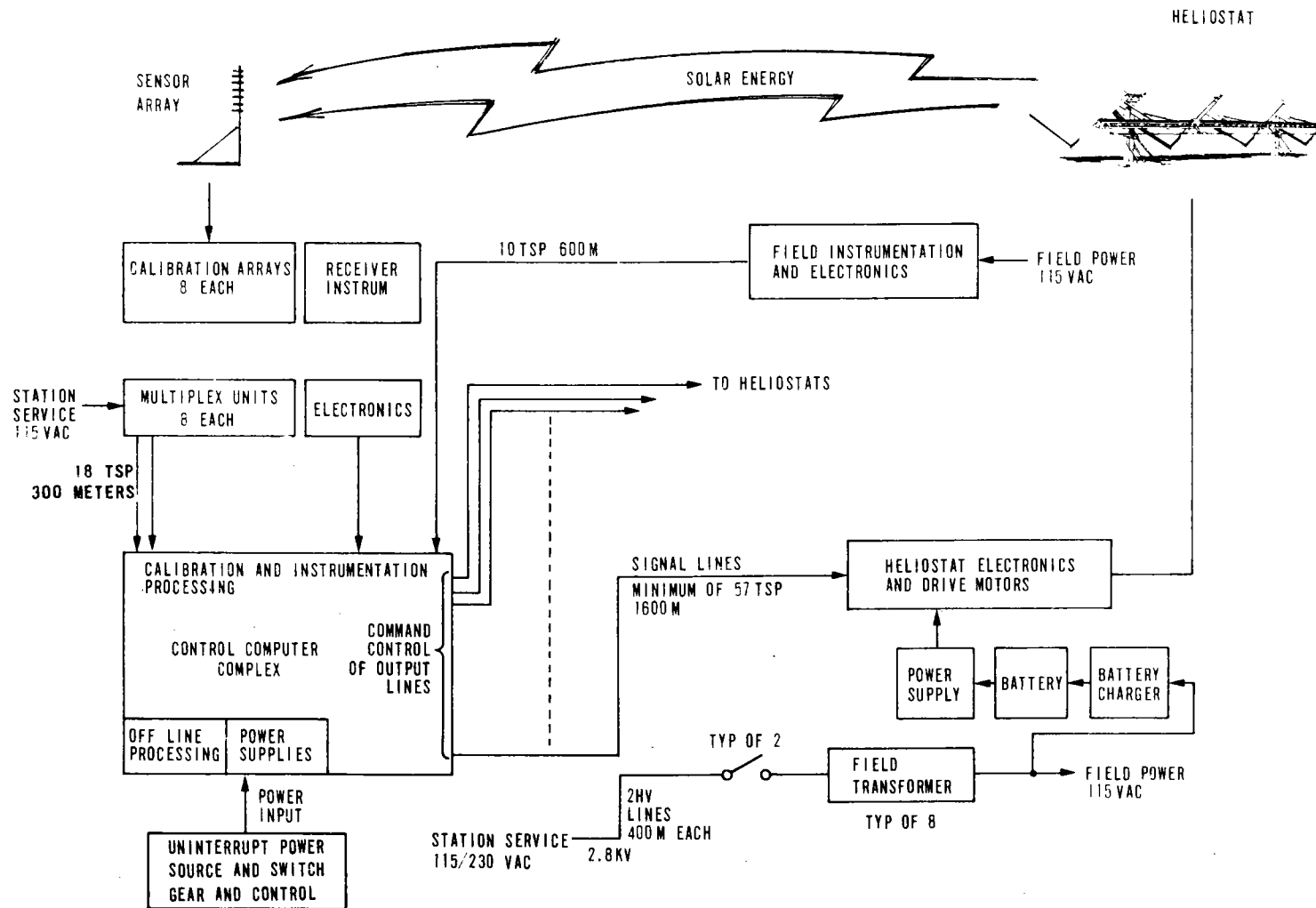


Figure 3-9. Collector Subsystem Interconnection One Line Diagram (Commercial Plant)

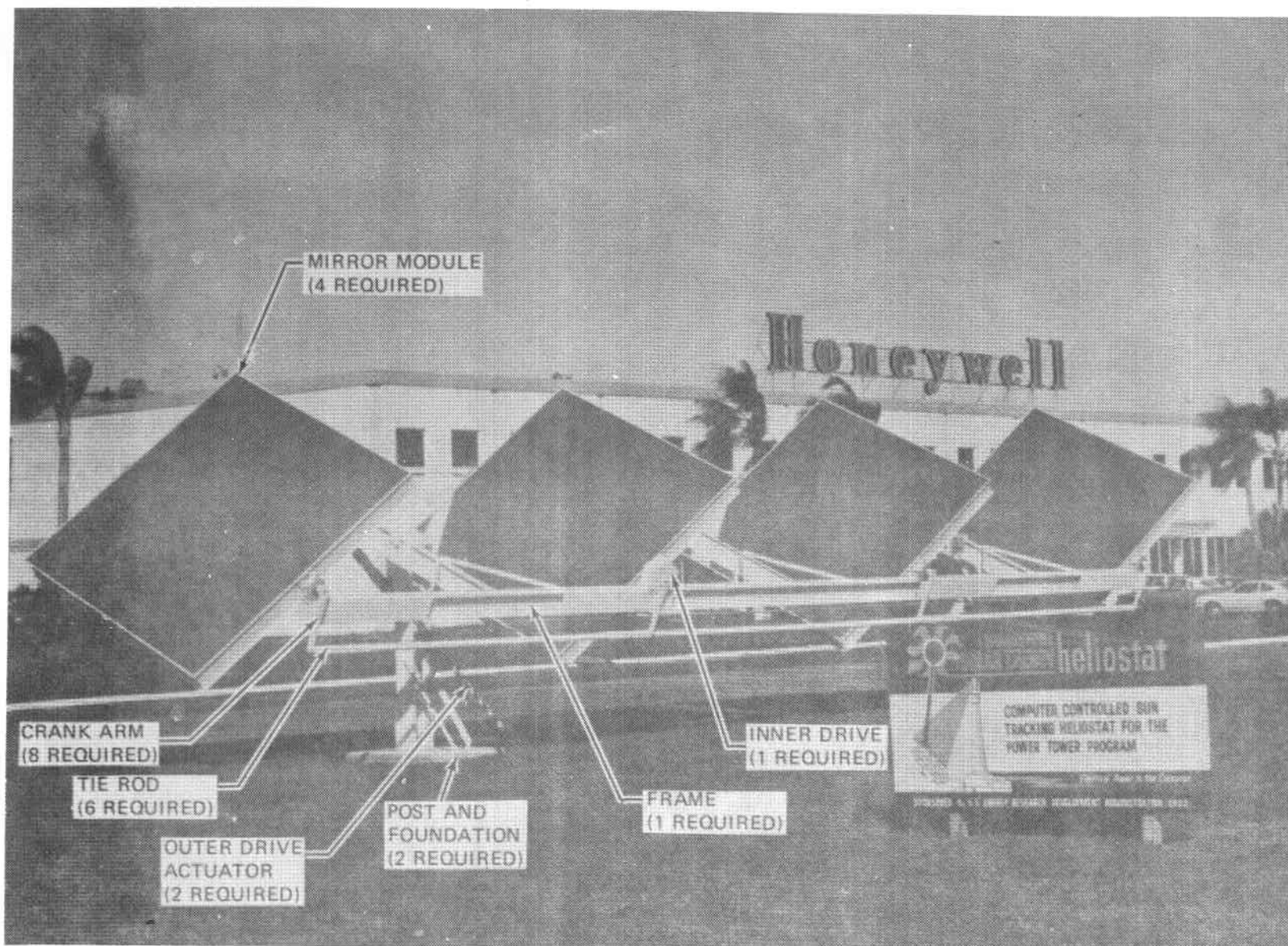


Figure 3-10. Heliostat

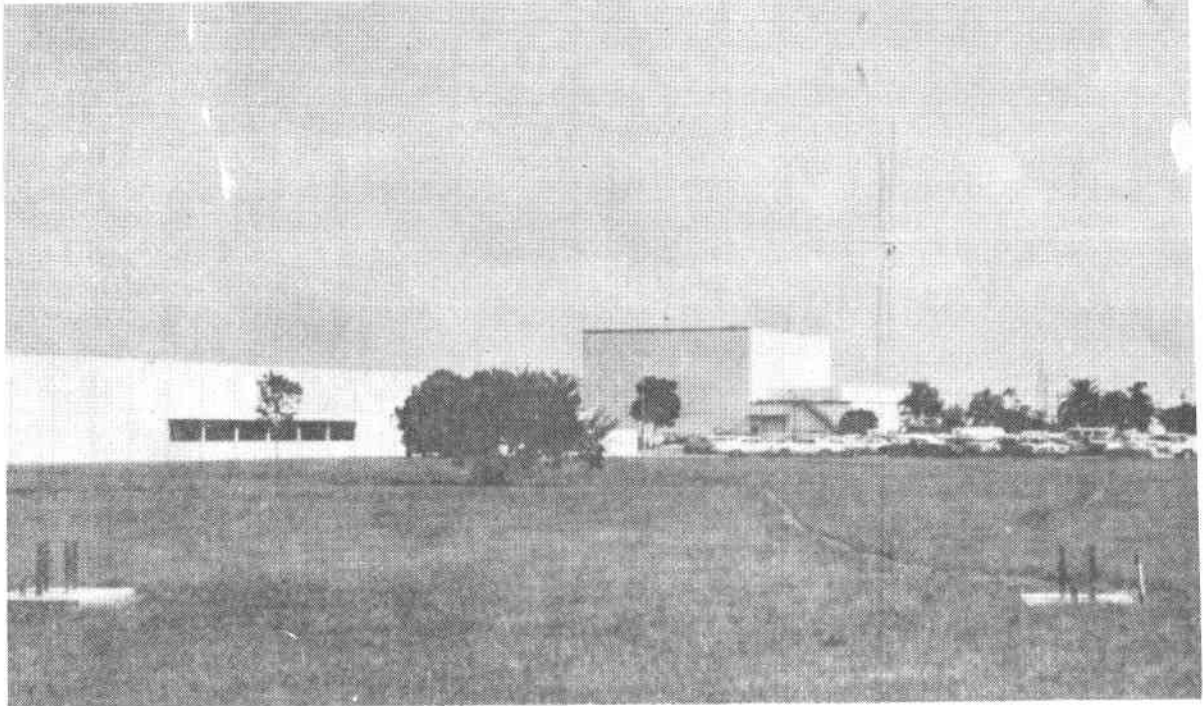


Figure 3-11. Heliostat Foundations

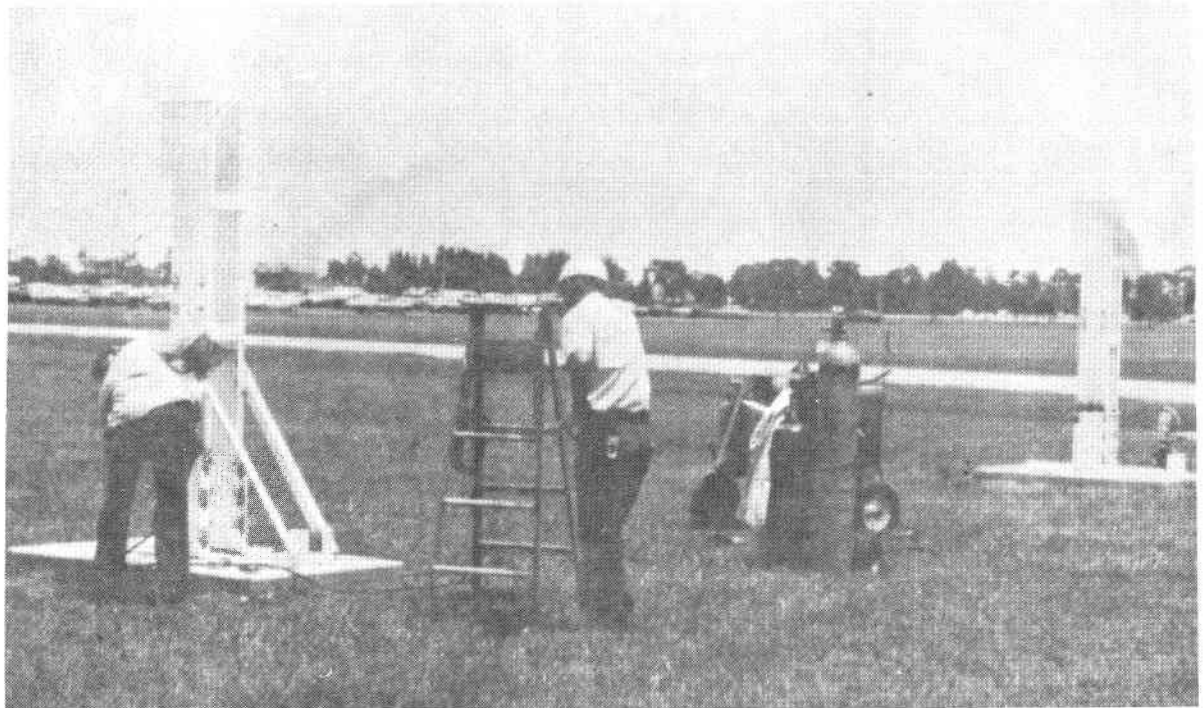


Figure 3-12. Installing Posts to Foundations

The post weldments are assembled to the foundations after a one week minimum cure time. Slotted holes are provided for vertical adjustment to assure the tops of the two posts are level. The up-rights are fabricated from the same channel sections with stiffeners as required. Two diagonal braces are used to control pointing errors under wind loads.

Post height is determined by the clearance required for full mirror rotation under all frame orientations. Each post weldment supports 1643 kg and has been analyzed to assure adequate stress margin for column loading.

The "split post" design was selected because of its symmetrical support of both the actuator and the frame cross rail. This design also facilitates the 75 degree frame rotation required by some heliostats to track for a full day.

Frame

Although gimbal structures are critical in precision pointing devices, the heliostat frame has been designed to be compatible with the capabilities of steel fabricators. Use of special (but simple) tools and techniques during field assembly minimizes the need for close dimensional control during frame fabrication.

The frame design driver is the bending stiffness required to limit mirror rotations under wind induced moments. A secondary driver is the stress induced by the weight of the mirror modules when the frame is rotated 75 degrees from level.

The dual actuator drive system eliminates the need for torsional rigidity over the 15 meter length of the frame allowing significant economies.

The Honeywell frame minimizes the dependence on cantilever type structures inherent in competitive designs by supporting both ends of each mirror module. The symmetry of the frame about its axis facilitates gimbal balancing and minimizes its sensitivity to varying "g" loads at different angles.

The frame length (15.5m) has been sized by an optimization study to obtain maximum optical efficiency at minimum cost. As the mirror module axes are moved closer together they block both incident and reflected rays from each other. If they are spread beyond the optimum, dispersion losses increase. The design driver in this case is optical efficiency; frame costs were found to vary only slightly over the range of interest.

The frame baselined for the preliminary design is shown in Figure 3-13. It is fabricated entirely from standard structural shapes. I-beams of various weights are used for the main members. Angles and plates relieve stresses in critical areas.

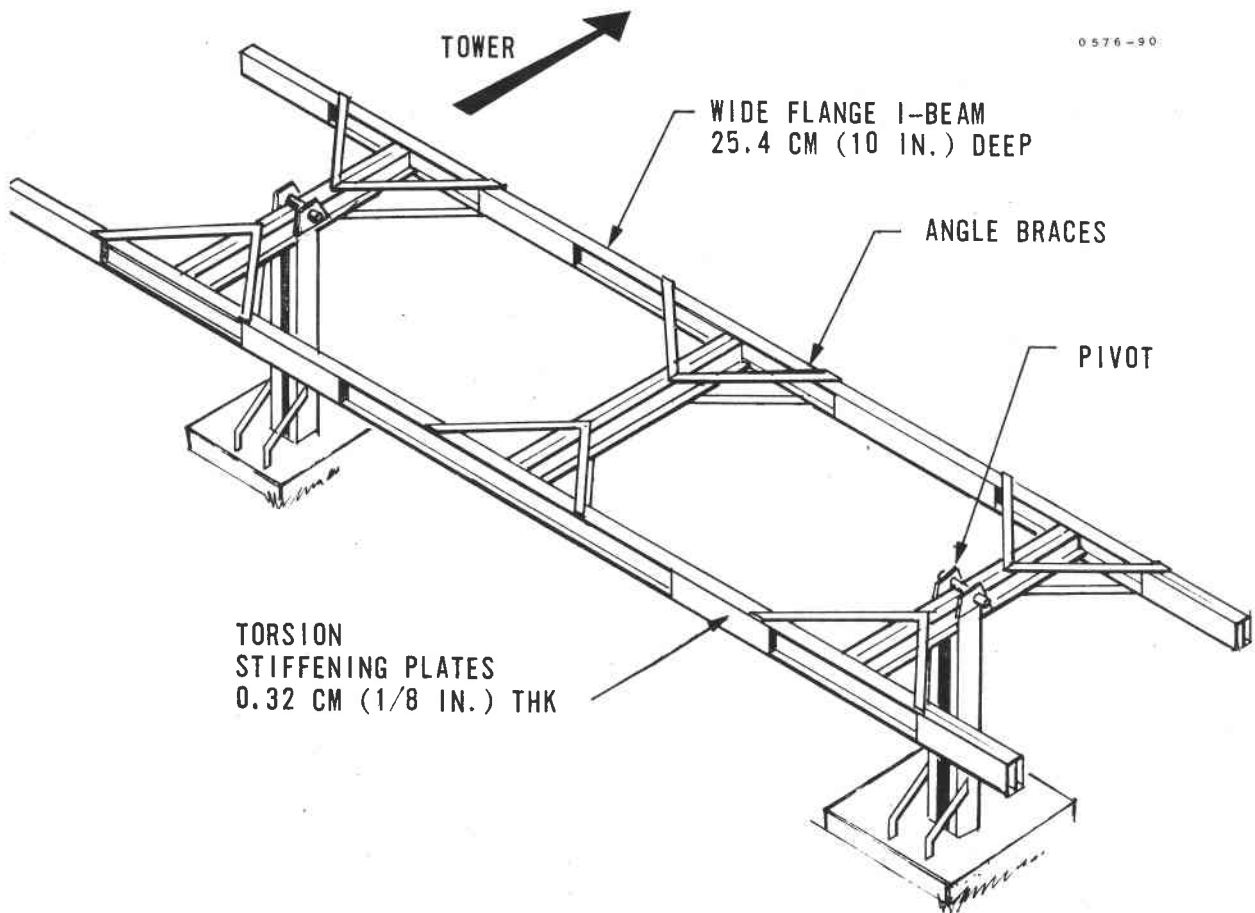


Figure 3-13. Heliostat Frame
(Pilot Plant Preliminary Design)

Recent optical studies using Honeywell's ray trace software have provided a key to frame simplification. They have shown that the mirror module axes can be lowered down to the center of the frame side rails without significant loss of reflected energy due to frame shading and blocking. Figure 3-14 shows a new frame concept with centered MM axes. The new frame is also expected to provide significant reductions in cost and weight.

Thermal effects are controlled by passive design techniques. White paint is used to minimize temperature rise above ambient. This also controls differential temperatures which otherwise would induce pointing errors. Absolute expansion of the frame over its length due to the ambient temperature range is of concern only with respect to the soil. The post is designed with compliance in this direction to control stresses induced on the foundation/soil.

Mirror Modules

The mirror modules are square sandwich type structures with 3mm float glass second surface mirrors providing the reflective surface (see Figure 3-15). The top surface of the mirror module for the Engineering Model and Solar Research experiment were contoured to 677.9m (2224 feet) spherical radius before bonding the glass mirrors. The pilot plant heliostat design is contoured to 836m (2744 feet) spherical radius to match dimensions of the field. This technique provides a focused image of the sun from the heliostat at the maximum distance (line of sight) from the receiver. The change to mirror contour will be made by a simple tooling change. The design and production concepts have already been proven. Ray trace studies have shown that mirror module efficiency is not significantly effected by using a focal length for all units of the maximum line of sight distance. These analyses have also been confirmed by test results. Mirror modules used at line of sight distances less than their focal length do not produce images significantly larger than optimum.

A total of 18 mirror modules have been fabricated for engineering development and the solar research experiment programs. Two of these mirror modules were designed and fabricated by Brunswick Corporation using urethane foam as the core material. The performance of these units was not satisfactory. The results of tests are presented in other portions of this report. The remaining 16 mirror modules were designed and fabricated by Parsons Corporation. Two engineering development modules were fabricated to the original design. A second similar design with some cost saving features was used for 12 units on the solar research experiment plus two units to replace the foam core units on the Engineering Model. The Parsons designs both exhibited superior performance; however, this discussion will limit itself to the design developed for the solar research experiment.

Complete requirements for mirror modules are contained in Honeywell Drawing 34026575. A summary of these for the Engineering Model and Solar Research Experiment are given in Table 3-1. The requirements for the engineering model mirror modules and for the solar research experiment mirror modules differed only in that the area of the solar

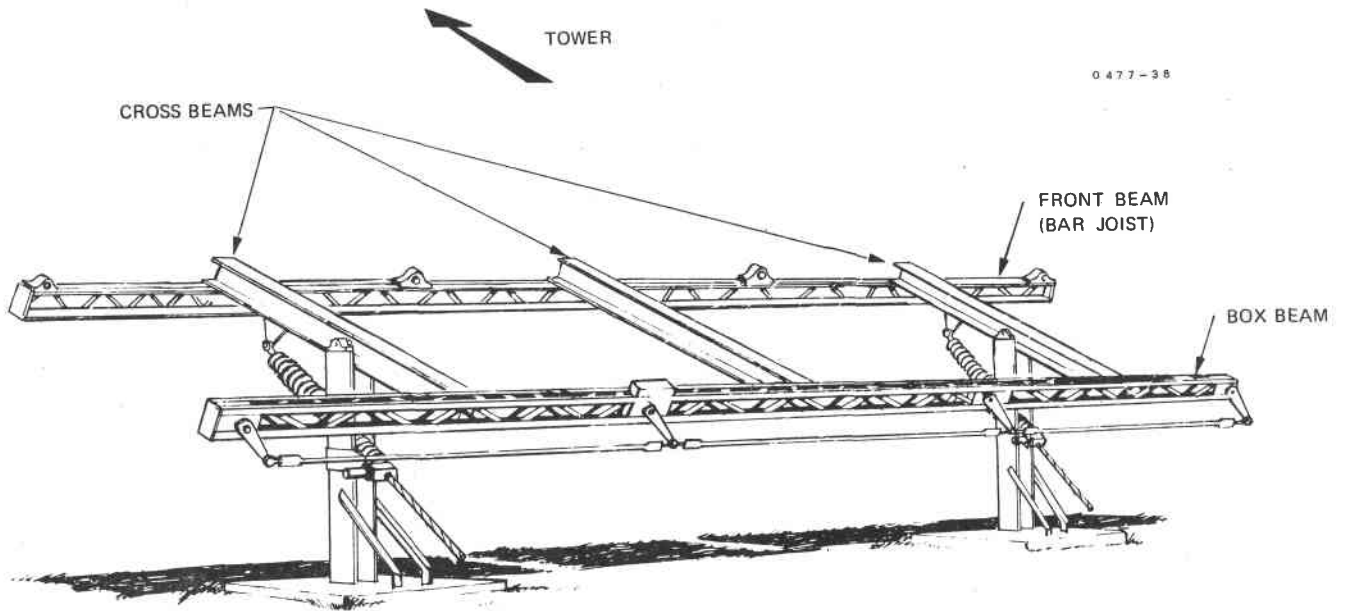


Figure 3-14. Heliostat Frame (Latest Concept)

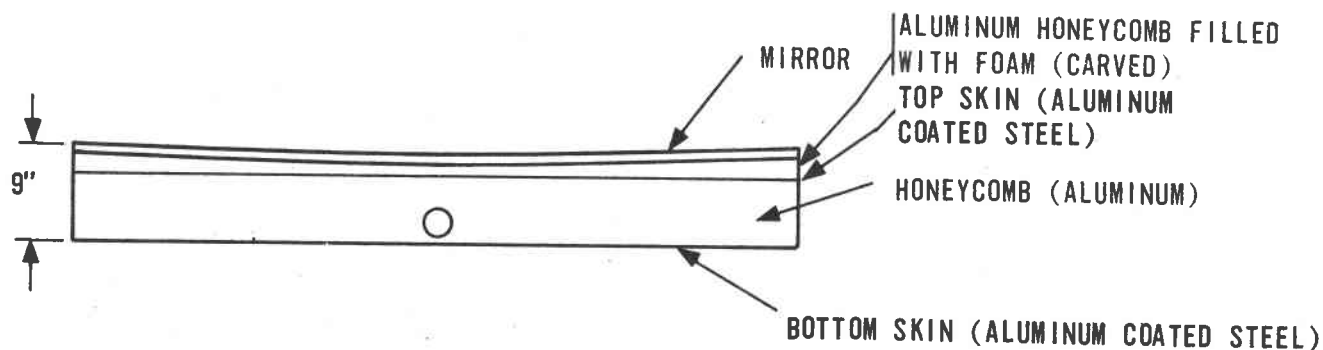


Figure 3-15. Aluminum Honeycomb 120 by 120 Inch Mirror Module
(14 Procured)

Table 3-1. Comparison of Mirror Modules

	Units	Engineering Model (4)*	Experimental Model (14)*	Pilot Plant	Commercial Plant
Area	m ²	10	9.3	10	10
Dimensions	m	3.17 x 3.17	3.05 x 3.05	3.05 x 3.30	3.05 x 3.30
	in	125 x 125	120 x 120	120 x 130	120 x 130
Mirror Surface Contour					
Spherical Radius	m	677.9	677.9	836.0	1,496
	ft	2,224	2,224	2,744	4,908
Allowable Tolerance					
Static Load	mr	1.0	1.0	1.0	1.0
Dynamic Loads	mr	1.0	1.0	1.0	1.0
Maximum Torsional Deflection (79 rg torque)					
Design Load	kg/m ²	9.77	9.77	9.77	9.77
	lbs/ft ²	2.0	2.0	2.0	2.0

research experiment mirror modules was slightly smaller to permit better utilization of existing facilities. An exploded view of the solar research experiment mirror module is shown in Figure 3-16. The same construction technique will be used for pilot plant mirror modules.

Heliostat Inner Axis Drive

Angular positioning of the four mirror modules is accomplished by two separate systems. The first consists of a dc motor and gear train which drive one mirror module. The second is a linkage assembly which gangs or slaves the remaining three mirrors to the driven mirror.

The gear train (shown in Figures 3-17 and 3-18) is driven by a 100 ounce-inch dc motor/encoder assembly. The motor drives a two-stage 1600:1 reductor designed by Spiroid Division of Illinois Tool Works. The final stage is a 10.1:1 spur gear pass which allows preloading (235 pounds) for backlash control with a small (3 percent) reduction in drive efficiency. The spur gear (16 inch pitch diameter) is secured to the stub shaft of one mirror module.

The gearbox has a two stage helical gear set which is self-locking; that is, cannot be driven by mirror torques when the motor power is off. This assures that pointing reference is not lost during storage or between computer updates during tracking.

The final gear ratio is 16158:1 from which one motor revolution (that is, one computer command) rotates the mirror modules 80.2 arc-seconds.

The motor/gear box assembly is a sealed, field replaceable module. It is mounted to the frame with a spherical sleeve bearing to allow the spur gear and reductor output pinion to self-align. This assures uniform stress across the width of the teeth. A standard die spring and bolt set the anti-backlash preload.

The two-piece cover assembly shown in Figure 3-19 will protect the spur gear mesh from sand and dust. The width and hardness of the spur teeth are specified to provide 30 year life under expected loads and speeds.

The linkage assembly is similar to that of a steam locomotive with cranks set 90 degrees apart to avoid lock-up. This system was selected because of its inherent stiffness, repeatability and continuous rotation capability.

The eight crank arms are secured to the ends of the 4 inch diameter stub shafts using the taper lock shown in Figure 3-20. This approach allows quick assembly and removal of crank arms as well as adjustment of mirror module toe-in. The 24 inch crank arm length was selected to keep errors resulting from rod end clearances within acceptable limits. The crank arm section is designed to control bending in three axes as well as twist.

0477-66B

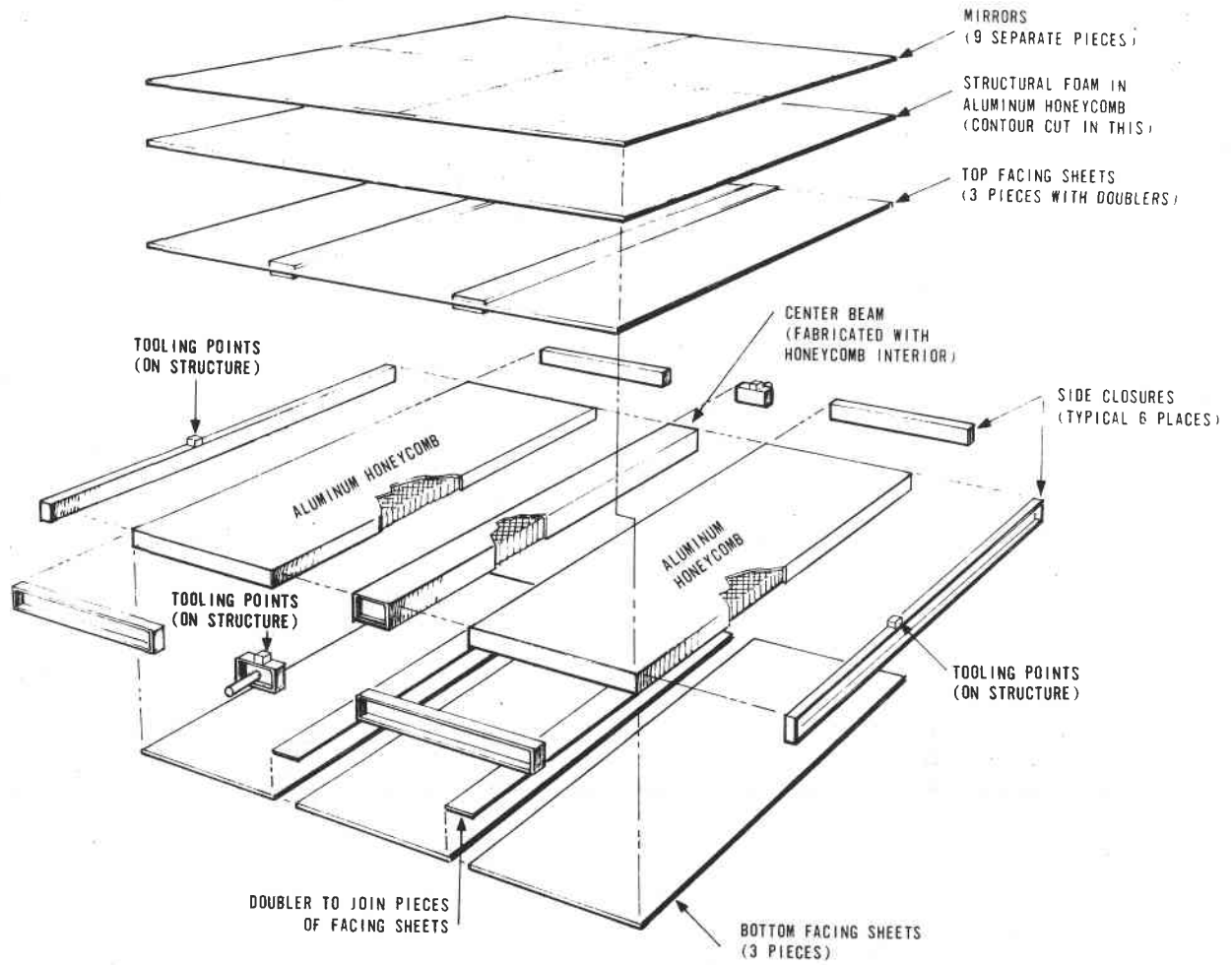


Figure 3-16. Mirror Module Assembly Details

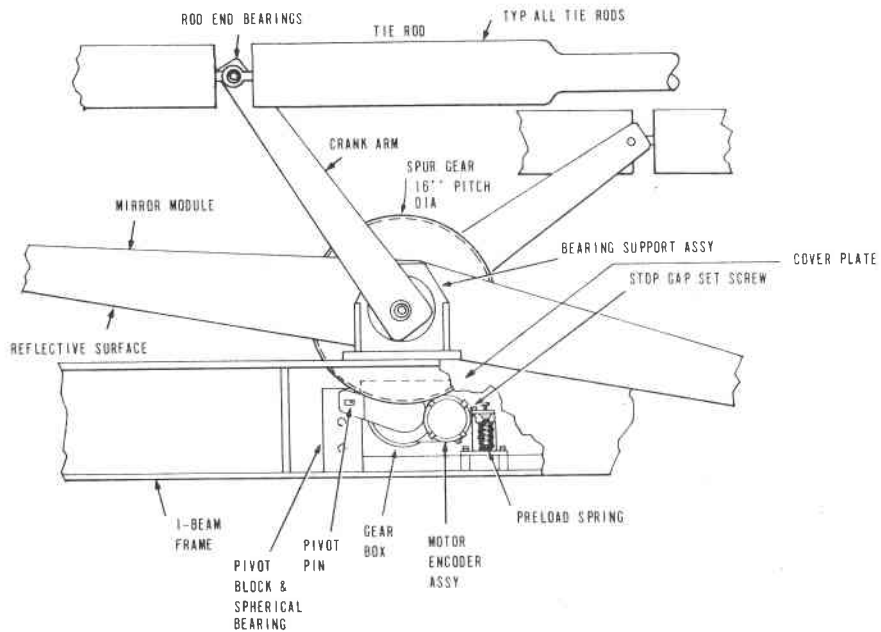


Figure 3-17. Heliostat Inner Axis Drive (Spur Gear Cover Removed for Clarity)

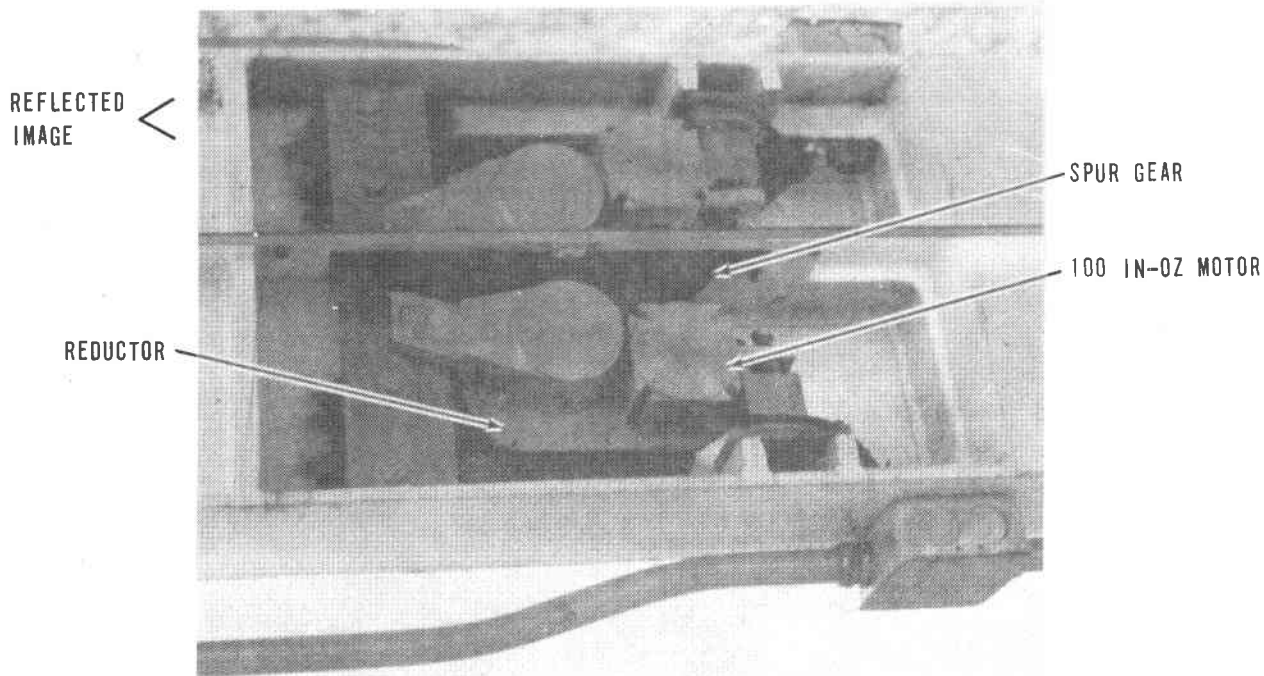


Figure 3-18. Inner Drive Gear Box

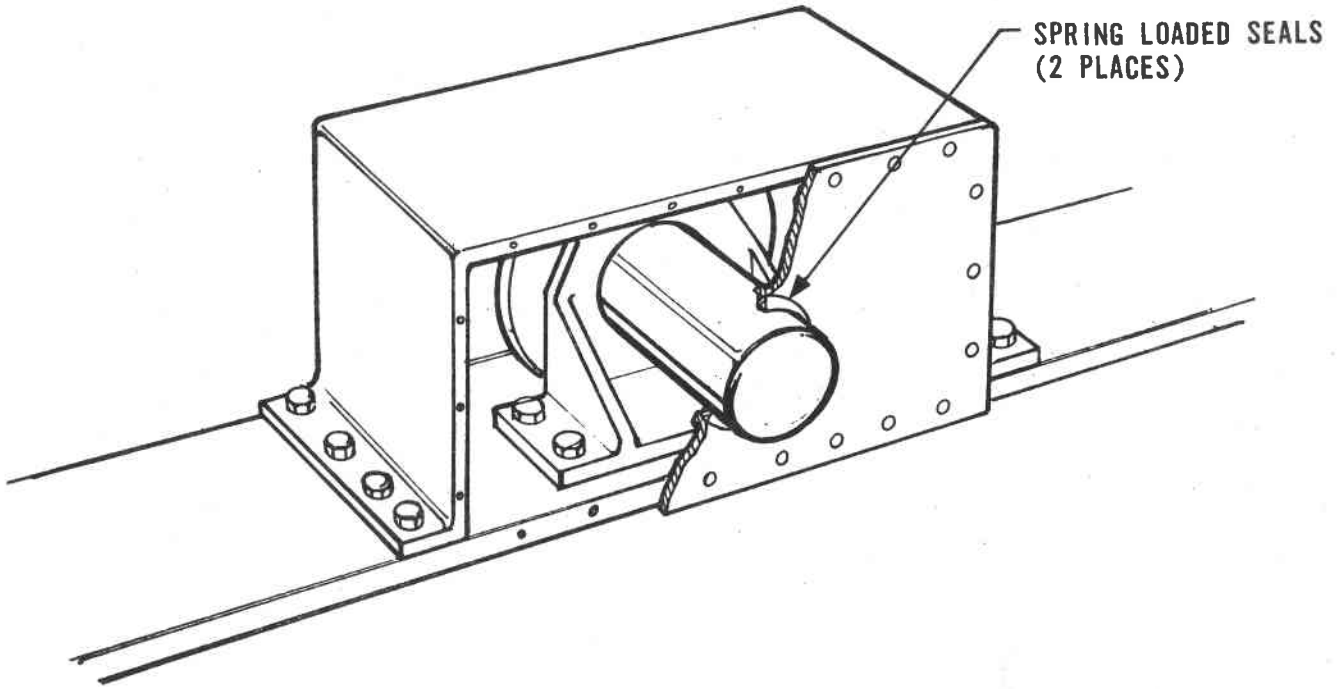


Figure 3-19. Inner Drive Cover and Seals

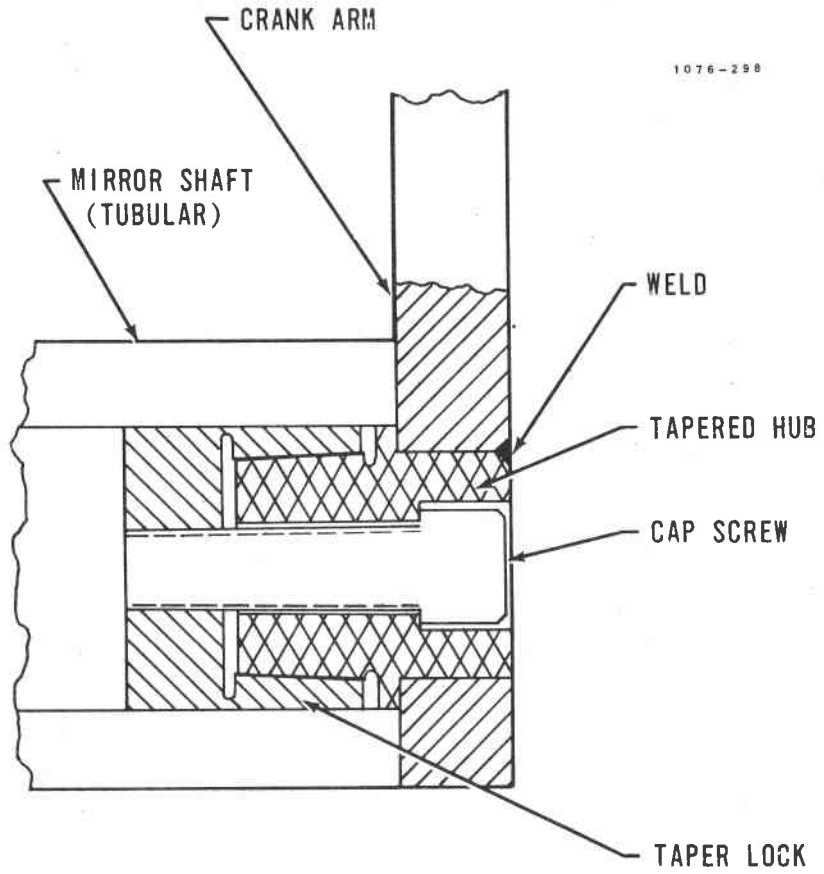


Figure 3-20. Taper Lock Interface

The junction between crank arms and tie rods is provided by rod end ball joints. The spherical bearing surface of these units is a glass-filled, injection-molded nylon with molybdenum disulfide for lubricity. The 1/2 inch units selected have a radial load capacity of 7000 pounds.

Tie rods are made from rolled, welded seam tubing and weigh approximately 45 pounds with rod ends. The cross section area is sized for simple compressive spring rate. The diameter is sized to limit lateral deflection under combinations of lg and end loading. The tubular design also makes them insensitive to outer gimbal elevation angle. The rod ends are used to adjust tie rod lengths at the top-dead-center position of the crank arms.

Lock-up at top-dead-center (crank arm horizontal) is not possible due to the high mechanical advantage of the crank arm and the compliance of the tie rod.

Heliostat Outer Axis Drive

The outer axis drive consists of two linear actuators, each driven by a 200 ounce-inch motor/encoder assembly. The dc motor drives a worm gear set which in turn drives a bearing supported nut. Rotation of this nut causes the screw to translate in or out depending on the motor direction for a distance of nominally ± 0.0118 inch per motor revolution.

The actuator, frame, and post form a nonright triangle which the computer solves to obtain the desired screw length as a function of gimbal angle (see Figures 3-21 and 3-22).

Linear ball screw actuators provide a rigid, repeatable drive system with adequate backlash control. Actuator mounting geometry is common for all heliostats in the field as shown in Figure 3-23.

The heliostat outer axis drive consists of two linear actuators as shown in Figure 3-22 developed for use on the pilot plant heliostat. Two screws are used to provide torsional rigidity over the frame's 51 foot length. The selected attachment geometry for the actuators is based on the following considerations:

- Operating range of 105 degrees makes one geometry suitable for any field location.
- Screw length of 72 inches allows maximum use of 144 inch standard length.
- Standard backlash values for screw/nut and fittings are within error budget allotment.
- Easy access to gear box and motor assemblies for initial alignment and maintenance.
- Field replaceable unit.

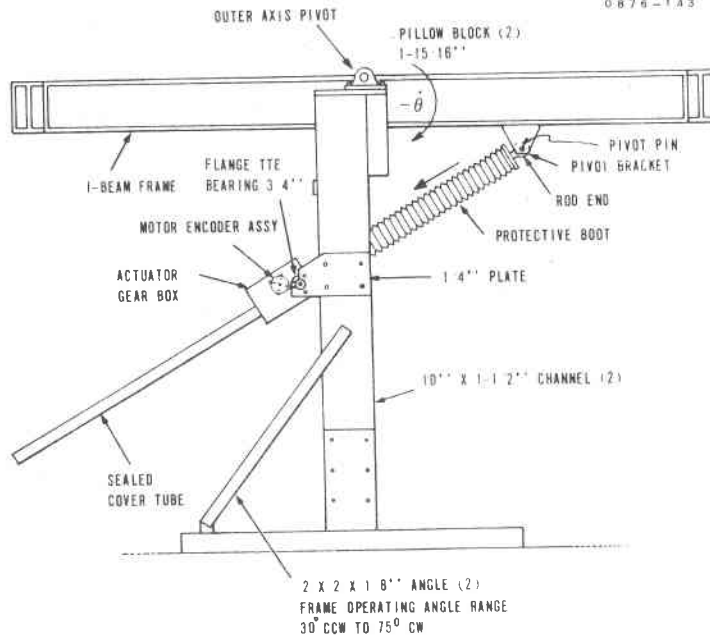


Figure 3-21. Heliostat Outer Axis Drive

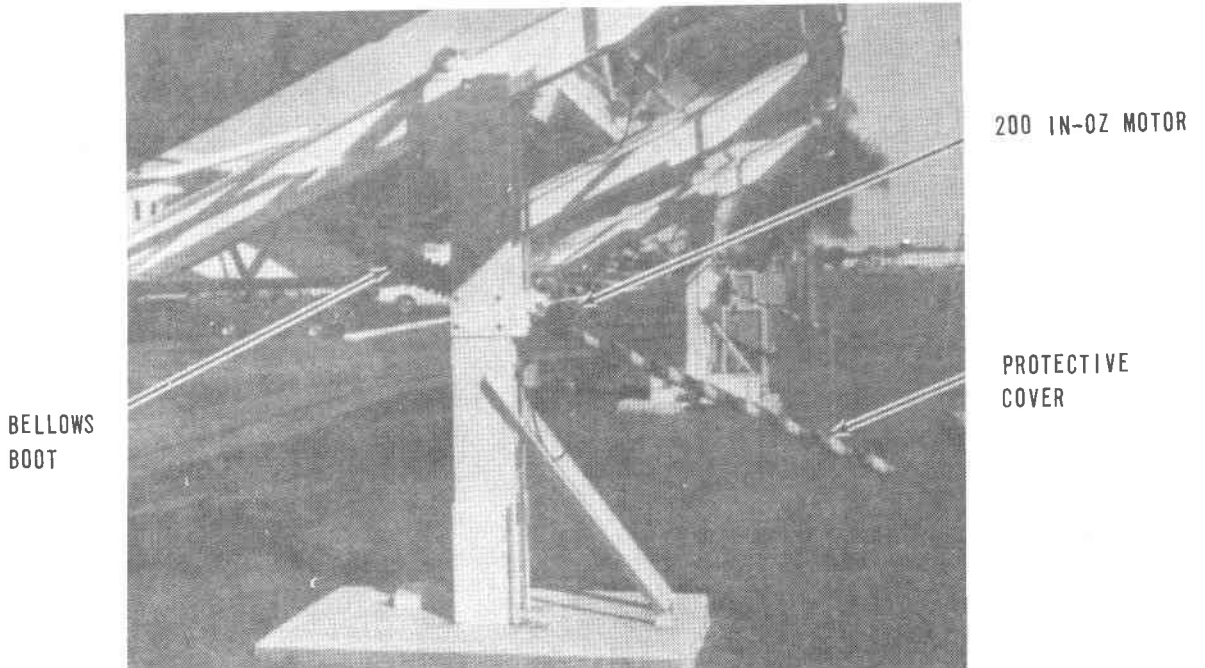


Figure 3-22. Heliostat Actuator

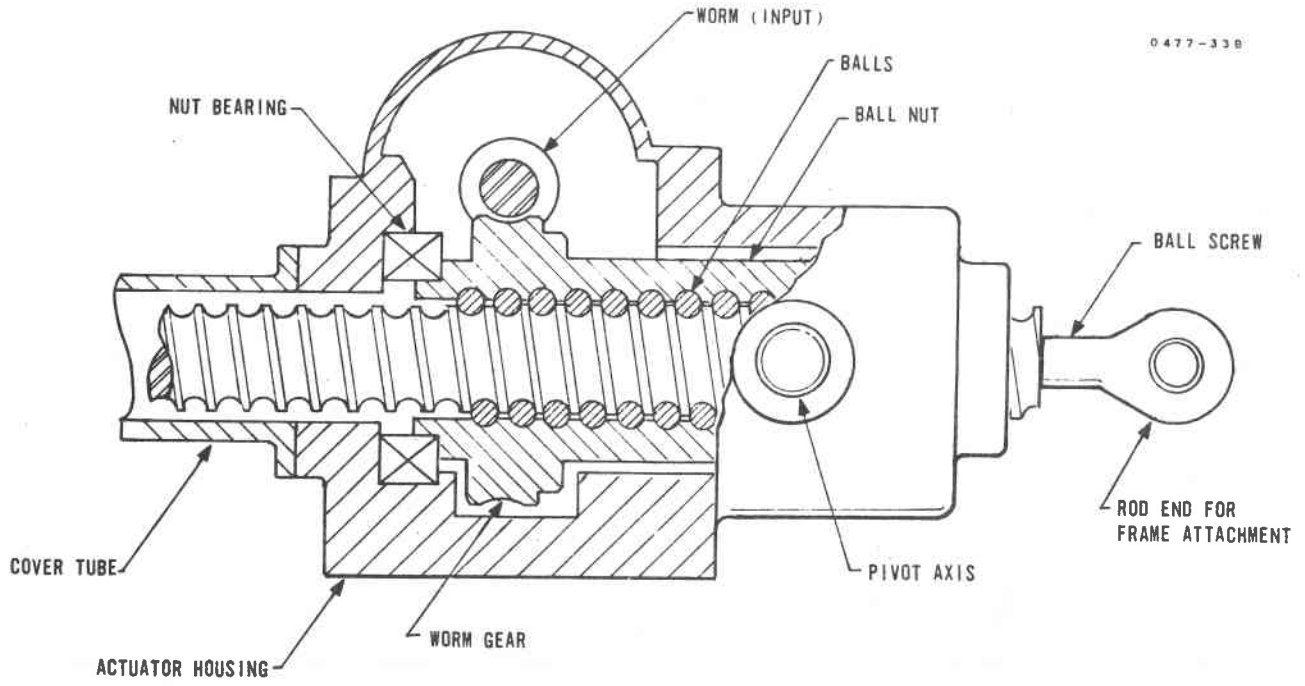


Figure 3-23. Ball Screw Actuator

- Post twist eliminated by symmetrical mount.
- Ground clearance for tip of cover tube.

Standard commercial screws were modified slightly for the pilot plant design. Actuator vendors are:

Pow-R-Jac Division
Limitorque Corporation
King of Prussia, Pa.

Templeton, Kenly & Co.
Broadview, Illinois

Pow-R-Jac ball screw actuators are baselined in the preliminary design. The ball screw has high efficiency and high side load capability.

Screw actuators were selected for the heliostat outer axis drive for the following reasons:

- Inherent stiffness
- Low backlash
- No spring preload required
- Accuracy and repeatability
- Life
- Standard commercial parts requiring minimum modification
- Require only one gear pass

Figures 3-21 and 3-22 show the complete outer axis drive system. Figure 3-23 shows the operation of the ball screw actuator. The dc motor/encoder (200 ounce-inch stall torque) assembly drives the worm directly. The 40:1 worm ratio is self-locking and controls reflected inertia load on the motor. The combination of gear ratio, screw lead (0.474 inch/turn) and pivot geometry provides effective gear ratios from 11,000:1 to 18,000:1 depending on gimbal angle.

Pointing accuracy of this system has been proven during SRE testing. Lot control and assembly/calibration techniques allow the use of standard rolled thread screws for minimum cost. Saginaw Steering Gear, division of General Motors, supplies the ball screw and nut assembly used by Limitorque.

INITIALIZATION SWITCHES

The position of each heliostat throughout the day is not directly monitored in the open loop control scheme successfully developed by Honeywell. The system accuracy is maintained through very precise response of the heliostat to commands from the control computer. To accomplish this, a known starting point for each axis of the heliostat is required. This is known as initialization position and has been defined as both gimbals horizontal with the mirrors face down. This is also the normal storage position for the heliostats. The error budget has set a maximum error of $0.45m+$ (3 sigma) for this condition. At start up, or other times when required, each heliostat is commanded to go to initialization position. Switches on each axis define when this condition has been obtained. These switches are set to the required position during heliostat assembly. These low cost switches are less expensive than shaft encoders.

The initialization electronics is packaged with the other electronics. The switches were comprised of a sensor wheel and two opto-pairs. One switch assembly is integrated into the inner axis drive. Two assemblies are used for the outer axis, one mounted at the top of each post to sense rotation of the frame support pins. The sensor wheels are 18.44 cm (7.26 in.) in diameter. They interrupt the light path of the opto-pairs and when decoded by the logic determine when initialization has been reached. Prototype units have been fabricated and installed on the four heliostats presently in operation. These units, while not packaged for use in a production system, produced test results consistently within the error allowable. Figure 3-24 is a photograph of one of the initialization switches used for development.

Initialization switches for the pilot and commercial plant heliostats will continue to utilize a sensor wheel and two opto-pairs. One unit will be integrated into the inner drive assembly and two units will continue to be used for the outer axis. All units will be located inside sealed assemblies to protect them from the environment (one fact learned from SRE tests was that condensation affects opto-pair performance). The sensor assemblies are very similar in design and construction although the packaging is different for the inner axis and outer axis assemblies. Both units are fabricated and adjustments made to locate the opto-pairs exactly at the edges of the detents on the sensor wheel before shipment to the assembly site. A small micrometer tool will be used to make these settings. After the settings are made the assembly is locked in place until assembled into the heliostat. A definite procedure of assembly and adjustment of the heliostat has been detailed in Page 6-1 of this report. When this procedure has been followed, initialization switches installed and the heliostat at correct position, the initialization switches may be unlocked (that is, shipping chocks removed) thus obtaining proper adjustment. A sketch of the switch portions of these assemblies is presented in Figure 3-25.

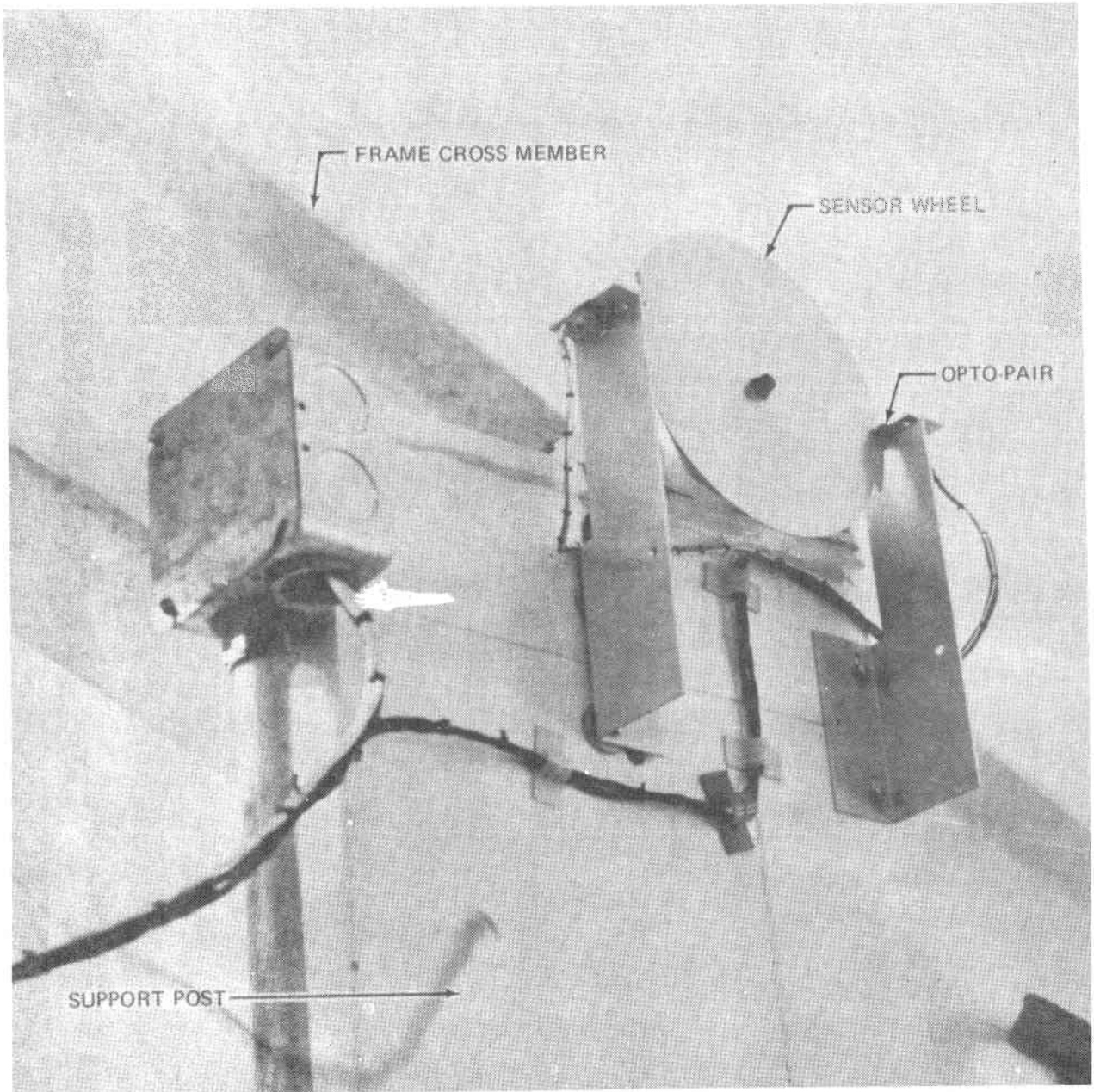


Figure 3-24. Initialization Switch SRE Units

0477-658

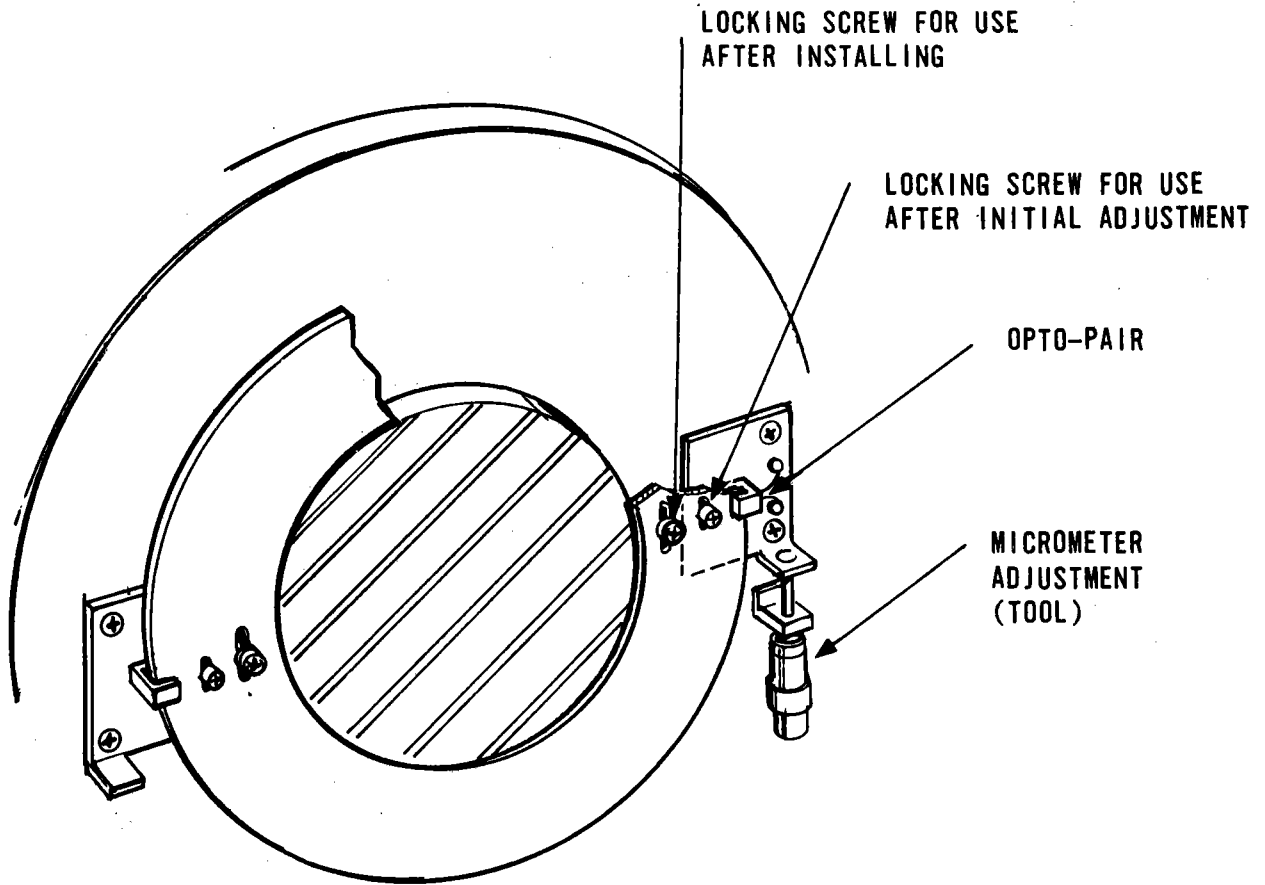


Figure 3-25. Initialization Pilot Plant Units

HELIOSTAT WEIGHT

An estimate of the heliostat component weights is presented in Figure 3-26. This presents gimbaled weight plus the weight of support structure separately to arrive at a total weight for the complete heliostat including foundations. It should be noted that the foundation weight is dependent upon site soil properties. The value used is based on the solar research experiment data at Honeywell's Florida Facility.

PARTS COUNT

A parts count has been conducted based on the solar research experiment heliostat. The count is cursory in that some purchased assemblies are counted as one part and small hardware, that is, nuts, bolts, washers, wire, have not been counted. The parts count obtained are as follows:

Electronics

Power Supplies	2
Diodes	29
Transistors	34
DIP	81
D/A Converter	2
Dual Inline Receiver	1
Oscillator	1
Relay	2
OP Amp	22
Capacitor	53
Resistor	133
Circuit Boards	3
Opto Pairs	12
Connectors	2
Batteries	2
Battery Chargers	2
Weather Proof Enclosure	1

	Solar Research Experiment Model and Pilot Plant (2)	Revised ⁽¹⁾ Pilot Plant	Commercial Plant
Frame	3,923 lbs	1,725 lbs	1,725 lbs
Mirror Module	2,600	2,600	2,500
Mirror Module Bearings	168	25*	25*
Crank Arms	220	180	180
Tie Rods	258	230	230
Inner Axis Drive	<u>75</u>	<u>105*</u>	<u>100*</u>
(TOTAL GIMBALED WEIGHT)	7,244 lbs (3,286 kg)	4,865 lbs (2,207 kg)	4,760 lbs (2,159 kg)
Post Assembly	260	250	250
Outer Axis Actuators	170	150	150
Foundation	<u>5,800</u>	<u>5,800**</u>	<u>5,800**</u>
(TOTAL WEIGHT)	13,474 lbs (6,112 kg)	11,065 lbs (5,019 kg)	10,960 lbs (4,971 kg)

* Inner Axis Drive Contains the Mirror Module Bearings for one of eight positions

** Site Dependent

(1) Estimated after producibility study

(2) Before producibility study

Figure 3-26. Heliostat Weight Estimates

Motors

Brushes	6
Shafts	3
Sensor Wheel	3
Housing	3
Bearings	6
Optal Pairs	3
Armatures	3
Magnets	3

Frame

10 inch Wide Flange	2
10 inch I Beams	3
Bearings	4

Mirror Modules

Structure	4
Hubs	8
Mirrors	(40m ²)

Inner Drive

Spur Gear	1
Crank Arms	8
Tie Rods	6
Rod Ends	12

Outer Drive Actuator

2

HELIOSTAT ELECTRONICS, DETAILED OPERATION

This section contains the detailed description of the Heliostat Electronics (HE). The following paragraphs contains the description of the HE used for the SRE and also describes the additions required for operation at pilot plant level and beyond and contains some of the cost savings ideas contemplated for inclusion in the pilot plant or commercial plant HE.

Heliostat Electronics Overall Operation

A block diagram of the Heliostat Electronics (HE) is shown in Figure 3-27. Two computer controlled operating modes are provided, (1) Initialize and (2) Track. The Initialize Mode provides the means for the gimbals to drive to a known reference position, namely outer axis horizontal, mirror normal face down. Once a set of known gimbal angles is acquired by the computer, the Track Mode is used to incrementally update the gimbal positions as required. Initialization is initiated by the setting of a single bit in the 8 bit command word sent by the control computer to the heliostat. Incremental update commands are coded in combinations of 6 bits in the command word.

A Manual Mode is also provided which allows an operator at the heliostat site to assume command of the gimbals by means of a set of panel switches. The Manual Mode is used for special testing and for gimbal control in the event of a failure in the control hardware.

Tracking Mode

Asynchronous incremental gimbal angle update information is received by the HE from the DDP H-516 where it is converted to parallel form and stored until used. These registers are periodically scanned by the counter control circuitry and new update information is loaded into an up/down counter. The counter is counted up or down 1 or 15 steps depending on the direction and amount of gimbal movement being commanded. One count corresponds to one motor shaft revolution which is approximately 81 arc-seconds of gimbal travel.

The output of the counter is converted to an analog level by a D/A converter and becomes the error signal to the analog servo amplifier. The gimbal torque motor is driven in accordance with the sign and magnitude of the error signal. As the motor shaft is driven, an incremental encoder produces an output pulse per motor shaft revolution on one of two output lines, depending on the direction the shaft is turning. These pulses are fed to the counter control circuitry where they are used to update the up/down counter. One motor shaft revolution will count the counter down one step. When the counter output reaches zero the command has been executed and the servo stops driving.

Two sets of control electronics are provided, one each for the inner and outer axes. The outer axis control electronics differs from the inner in that a two motor drive system is required for the outer axis as compared to only a single motor for the inner. Because of this the outer axis requires two power amplifiers and incremental encoders plus some added circuitry to maintain speed sync between the two motors.

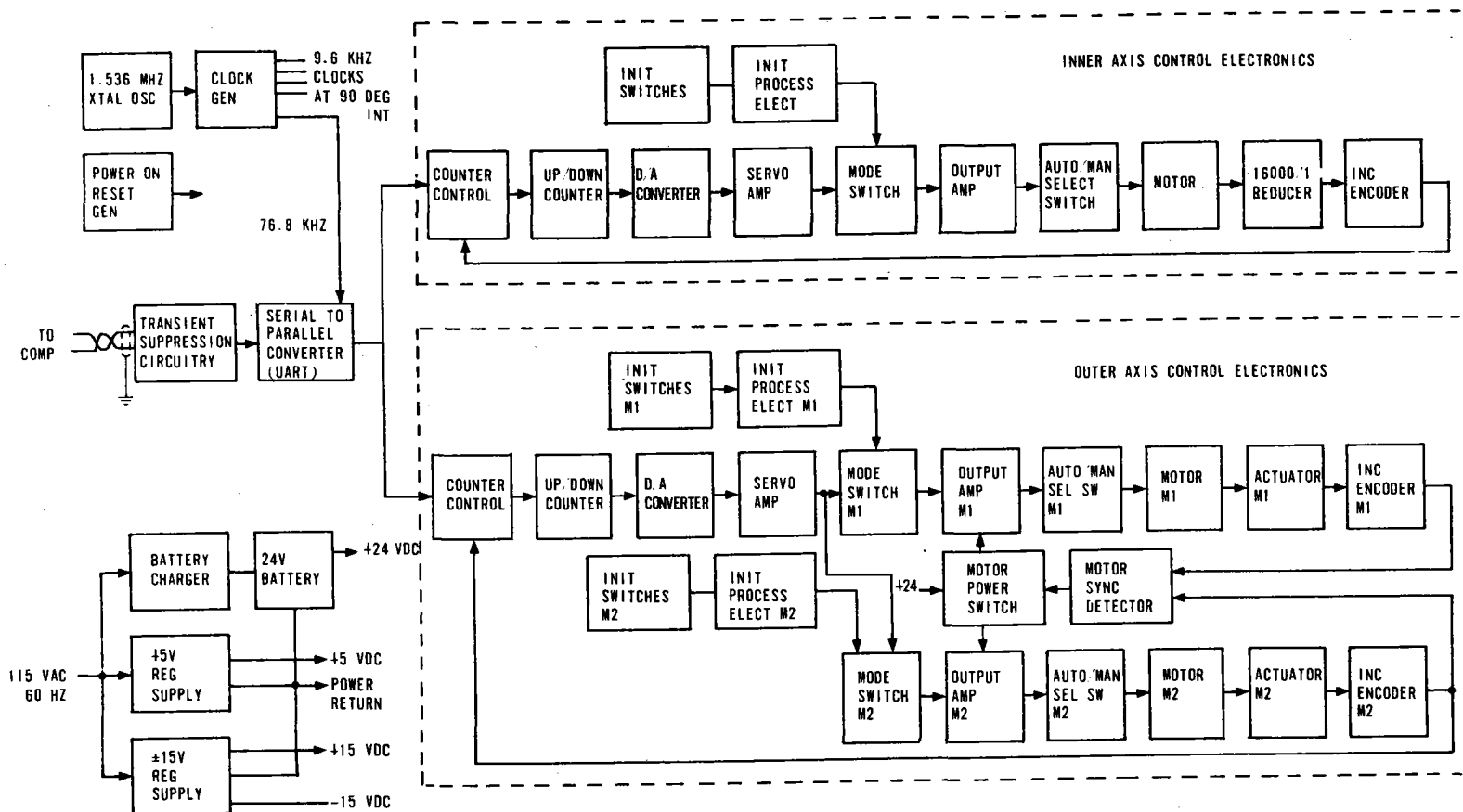


Figure 3-27. Heliostat Electronics Block Diagram

Initialization Mode

When commanded to initialize, the heliostat transfers control of the gimbal drives to the initialization switches. These are optically coupled switches consisting of an infra-red emitting diode and a phototransistor operated by a coded disc mounted on the gimbal. The switches provide the error signal and direction sense to achieve the initialization position by the shortest path. The initialization position is accurate to within 100 arc-seconds.

Since two motors are used to drive the outer axis, separate initialization switches are used for each motor. This assures that both ends of the outer axis frame will be leveled to within the initialization position accuracy every time the heliostat is initialized after which the two motor synchronizer circuits maintain the relationship.

Other Functions

The inner and outer axes control electronics share a common communications receiver, timing control generator and power supply. Power-on resets are used extensively to assure that the logic comes up as desired after power turn on.

The 24 volt supply used to provide the heavy motor currents consists of two 12-volt automobile batteries connected in series. 115 vac, 60 Hz power is brought to each site to power the battery charger, the low voltage regulators, and any on-site test equipment that might be desired.

Gas discharge tubes and resistor-zener diode combinations are used on the communications lines for protection against EMP associated with lightning. To further enhance lightning protection the heliostat frame, support posts, and electronics boxes are all connected with heavy cable to 24 feet deep ground rods.

Subsequent pages describe in detail the operation of the HE on a function by function basis.

Heliostat Electronics Communications Interface Details

A schematic diagram of the Heliostat Communications Interface is shown in Figure 3-28. A standard 8820 differential line receiver is used as an input buffer to accept asynchronous 8 bit serial digital data from the computer output circuits. The output of the line receiver feeds a Universal Asynchronous Receiver Transmitter (UART) which converts the serial data to parallel and stores it in 8 output registers. When data is available, the UART generates a data ready signal which is used to condition the counter control logic. When data has been accepted by the HE, a data ready reset pulse is generated by the counter control circuitry to reset the UART output registers. A complete data word is actually 10 bits in length formatted as a start bit, 8 data bits, and one stop bit. Data bits are assigned as shown in the figure. Data rate is 4800 bps.

The direction of gimbal rotation is according to the following convention. A "1" for the inner axis direction bit corresponds to a clockwise

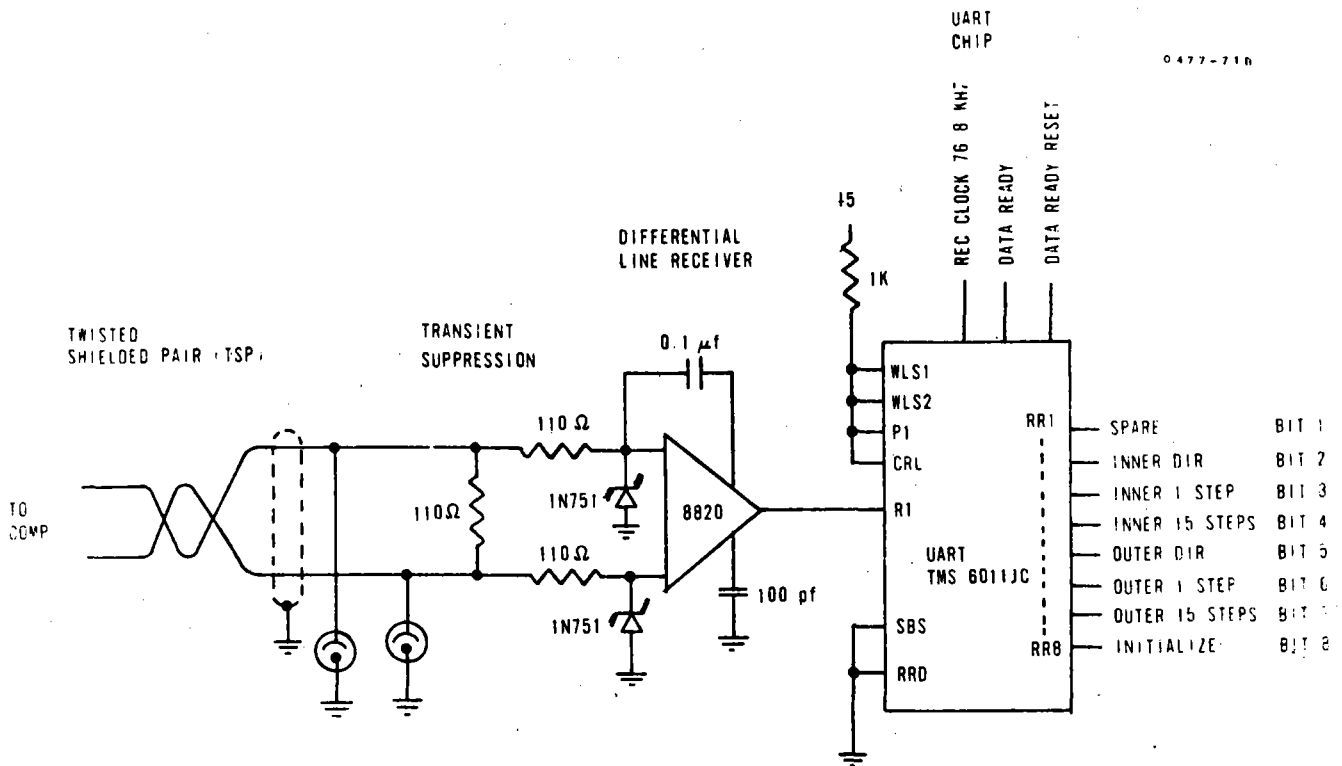


Figure 3-28. Heliostat Communications Interface Schematic Diagram

rotation of the mirror axis as viewed from the heliostat toward the tower. A "1" for the outer axis direction bit corresponds to an up beam rotation when the mirror normal is within the quadrant of the target defined by local horizontal and vertical.

The communications link between the computer and the heliostat is a buried twisted shielded pair up to 5800 feet in length. Because of this, transient suppression circuitry is used on the lines. Transient suppression occurs in two stages. First a 90 volt gas discharge tube is used to clip the transient to a reasonable level. Resistors and zeners further reduce this to a level that is harmless to the logic.

Up/Down Counter and Counter Control Circuitry

The up/down counter keeps track of the commands until they can be implemented by a given axis in the heliostat control servo. The counter control circuitry provides updates to the up/down counter by continuously cycling between UART outputs, looking for new command information from the control computer, and incremental encoder outputs, looking for evidence of implementation of previous commands. The capacity of the up/down counter is 8 bits (127 counts) to provide some reserve capacity beyond the 15 count maximum command requirement. Counter control cycle time is 104 microseconds.

A schematic of the counter control circuitry and up/down counter is shown in Figure 3-29. Operation is as follows.

Control Computer Updates

Updates from the control computer to the up/down counter are controlled by a 4 bit clock counter in the following manner. A Data Ready (DR) signal from the UART signifies that a data word has been received from the computer and is available at the UART outputs. The DR signal is clocked into the HE to synchronize the command data with the HE timing. The leading edge of the clocked DR signal is used to reset the 4-bit clock counter to zero. Should a 1 or 15 step command bit be present in the data word, the appropriate gate monitoring the clock counter output is armed. During that half of the 104 microsecond counter control cycle time that is reserved for command computer updates, 153.6 kHz clocks are allowed to flow to the up/down counter. The direction bit determines whether the count is up or down. The same clocks are also counted by the clock counter. When the gate monitoring the output of the clock counter detects that the commanded number of step counts has been inputted, clock flow to the up/down counter is terminated. When all clock counter monitors for both axes are closed signifying all data has been accepted, a DR RESET pulse is generated to reset the UART output holding registers to await receipt of the next word.

A power-on reset is provided to the up/down counter to insure the output is set at zero counts at power turn on.

Incremental Encoder Updates

As stated earlier, the incremental encoder provides an output pulse for every revolution of the gimbal motor shaft. Since the pulses are asynchronous and only 10 microseconds in width, they are temporarily stored in the counter control circuitry by means of a latch. The output of the latch is then synchronized to HE timing by a clocked flip-flop. During that half of the 104 microsecond cycle time reserved for encoder updates, the contents of the flip-flop are gated into the up/down counter. Separate circuits are provided for encoder cw or ccw pulses which determines whether the count is up or down. After an update has been made to the up/down counter, the temporary storage latch is reset to await later inputs from the encoders. If the motor/gimbal overshoots, an extra pulse from the encoder causes the up/down counter to not be "zero" thus the motor is commanded to "back up".

Digital to Analog Converter

The heliostat D/A converter transforms the digital output of the up/down counter to a bipolar analog signal for use by the servo amplifier. The converter is a 10 bit offset binary type from Analog Devices, Part No. DAC-10Z-3. Since only 8 bits are required to read the up/down counter, the two LSBs of the converter are fixed to a "0" input. The transfer function of the encoder is 78 MV/count. Maximum output is 10 volts. Input codes for outputs of zero and for the first and full count positive and negative output values are given in Table 3-2.

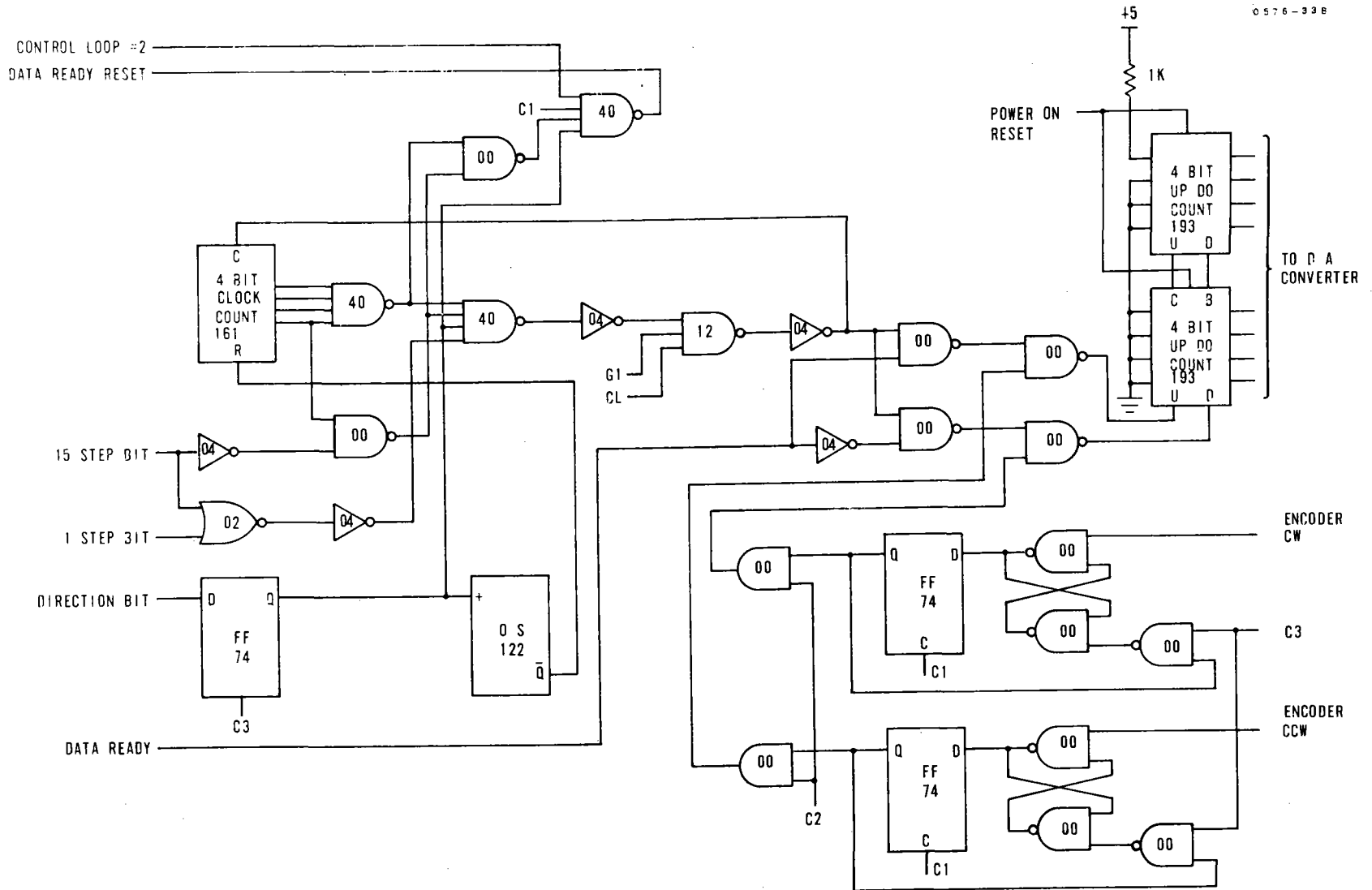


Figure 3-29. Heliostat Counter Control/Up-Down Counter

Table 3-2. Heliostat D/A Converter Operation

M S B	Input Code						L S B	Output Volts
1	1	1	1	1	1	1	1	+9.922
1	0	0	0	0	0	0	1	+0.078
1	0	0	0	0	0	0	0	0.000
0	1	1	1	1	1	1	1	-0.078
0	0	0	0	0	0	0	0	-10.000

Servo Output Amplifier

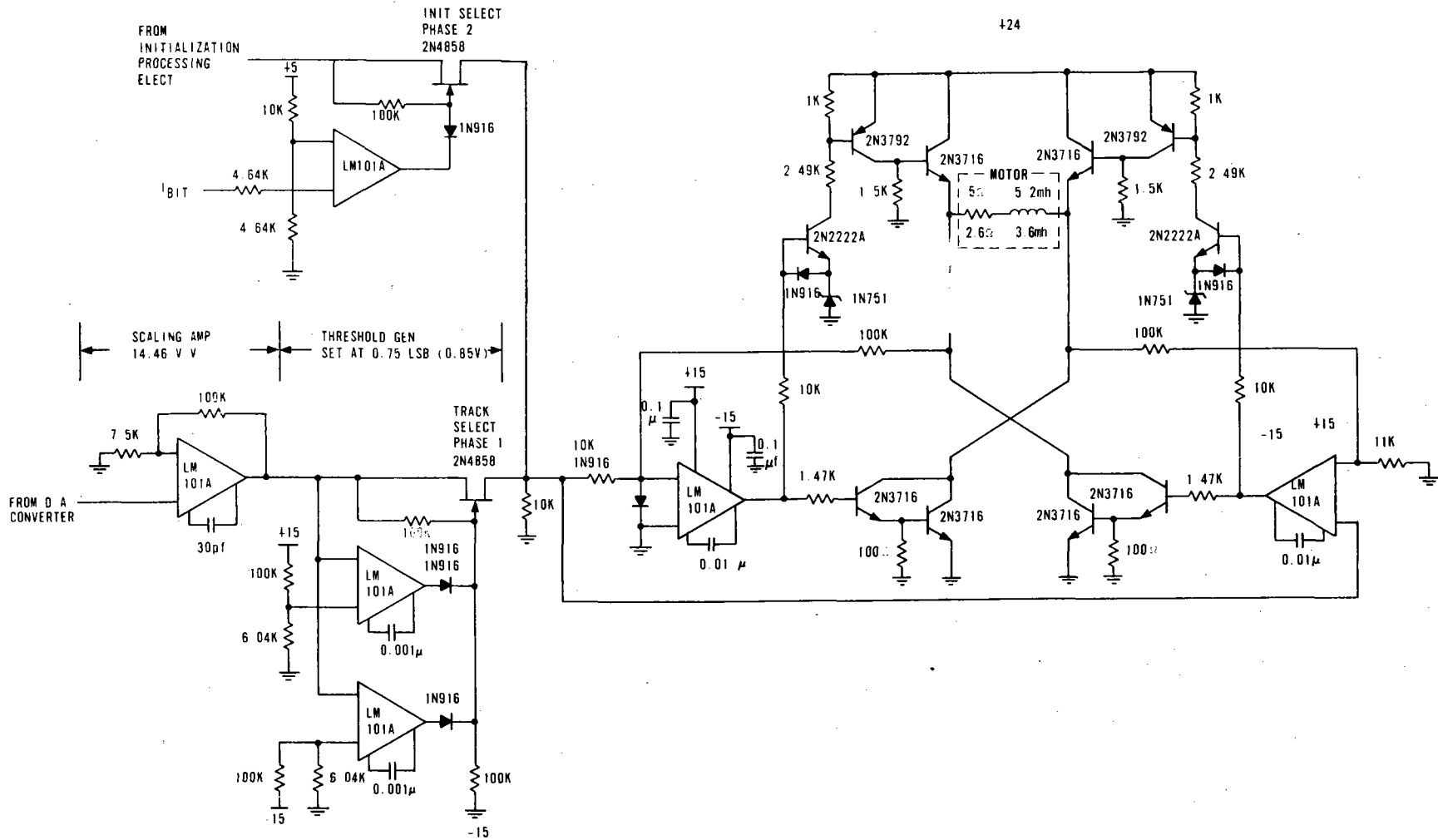
The servo output amplifier interfaces the D/A converter and the initialization processing electronics with the gimbal drive motors. The circuitry consists of a scaling amplifier, a pair of FET analog switches, and an output power amplifier. A schematic of the servo output amplifier is shown in Figure 3-30. Operation is as follows.

The scaling amplifier is a noninverting operational amplifier stage with a gain of 14.3 V/V. This in conjunction with the D/A converter and power amplifier provides for one half peak motor voltage (one quarter motor torque) for a 1 step command.

Two FET analog switches provide for the selection of the track or initialize modes of operation. The switches are 2N4858 field effect transistors operated from LM101A operational amplifiers configured as comparators. A "1" for the initialization bit in the command word turns on Q2 and allows information from the initialization processing electronics to drive the gimbal torque motor through the output power amplifier. A "0" for the I-Bit turns off Q2 and allows track information from the output of Q1 to control gimbal drive.

Q1 is threshold sensitive. The two comparators which control it monitor the output of the scaling amplifier. Q1 is turned on only if the output of the scaling amplifier is greater than 0.75 of the analog weight of one count in the up/down counter. This prevents loop offset from uselessly dissipating power in the motor and eliminates the possibility of a limit cycle oscillation condition existing between loop offset and a one count in the up/down counter.

The I-Bit used to select the initialization mode by turning on Q2 also sets the output of the up/down counter to an analog equivalent of zero volt. Under these conditions the threshold detectors controlling Q1 keep Q1 off and effectively prevent Q1 and Q2 from ever coming on together.



3-42

Figure 3-30. Heliostat Servo Output Amplifier

The output power amplifier is a linear H switch configuration consisting of a pair of solid state switches and a pair of gated linear power amplifier stages, with the motor winding floated between opposing switch/amplifier pairs. The polarity of the input signal determines which switch/amplifier pair is chosen. When a pair is selected, the switch ties one side of the motor winding to ground while the other side is driven by the linear amplifier with a positive drive signal. Reversing the input polarity causes the other switch/amplifier pair to be chosen which reverses the grounded and driven ends of the motor winding. This permits bidirectional motor currents to be driven from the one heavy positive supply available, the 24V battery. This is a very efficient method for linearly driving dc motors eliminating the parts and losses associated with generating a high current negative voltage required by a more conventional power amplifier. Also, because the battery is such a good low impedance source, no heavy 24 volt line filtering is required.

High gain operational amplifiers are used in the feed forward path of the power amplifier to provide good linearity and low threshold. Frequency response is controlled such that step function inputs of reversing polarity cannot cause both amplifier switch pairs to be driving simultaneously. Voltage feedback is used to take advantage of the damping effect of the back EMF of the motor. Gain of the amplifier is 10 V/V. The power amplifier is designed to drive the 4.4 and 6.7 amp peak currents of the inner and outer axes motors respectively without any modifications or value changes.

Incremental Encoder

The Incremental Encoder provides the control mechanism by which the gimbal motor is allowed to turn the number of revolutions equal to the count stored in the up/down counter. It does this by generating an output pulse for every revolution of the motor shaft which is fed to the counter control circuitry to update the up/down counter. As mentioned earlier, when the counter output is reduced to zero, gimbal drive is removed and the motor stops.

The Incremental Encoder consists of a coded disc, two optical pairs and some logic to decode the outputs of the opto-pairs. A schematic of the encoder and a picture of the coded disc is shown in Figure 3-31. The disc is mounted on the motor shaft with the edge allowed to rotate between the two optical pairs. The pairs are Texas Instruments Part Number T1L148 and consist of an IRED and a phototransistor mounted facing each other in a U-shaped plastic housing. When the hole in the disc appears between the pair, a signal is generated in the phototransistor. This output is latched by an LM111 with hysteresis whose output is wired to interface directly with T²L. The follow-on logic decodes the output of the two optical pairs to generate the 1 pulse/revolution output.

Since servo operation is bidirectional, the incremental encoder must not only be able to detect rotation but direction of rotation as well. The key to determining direction of rotation lies in the fact that the holes in the coded disc are offset with respect to the positioning of the optical pairs. This results in a time sequence for the

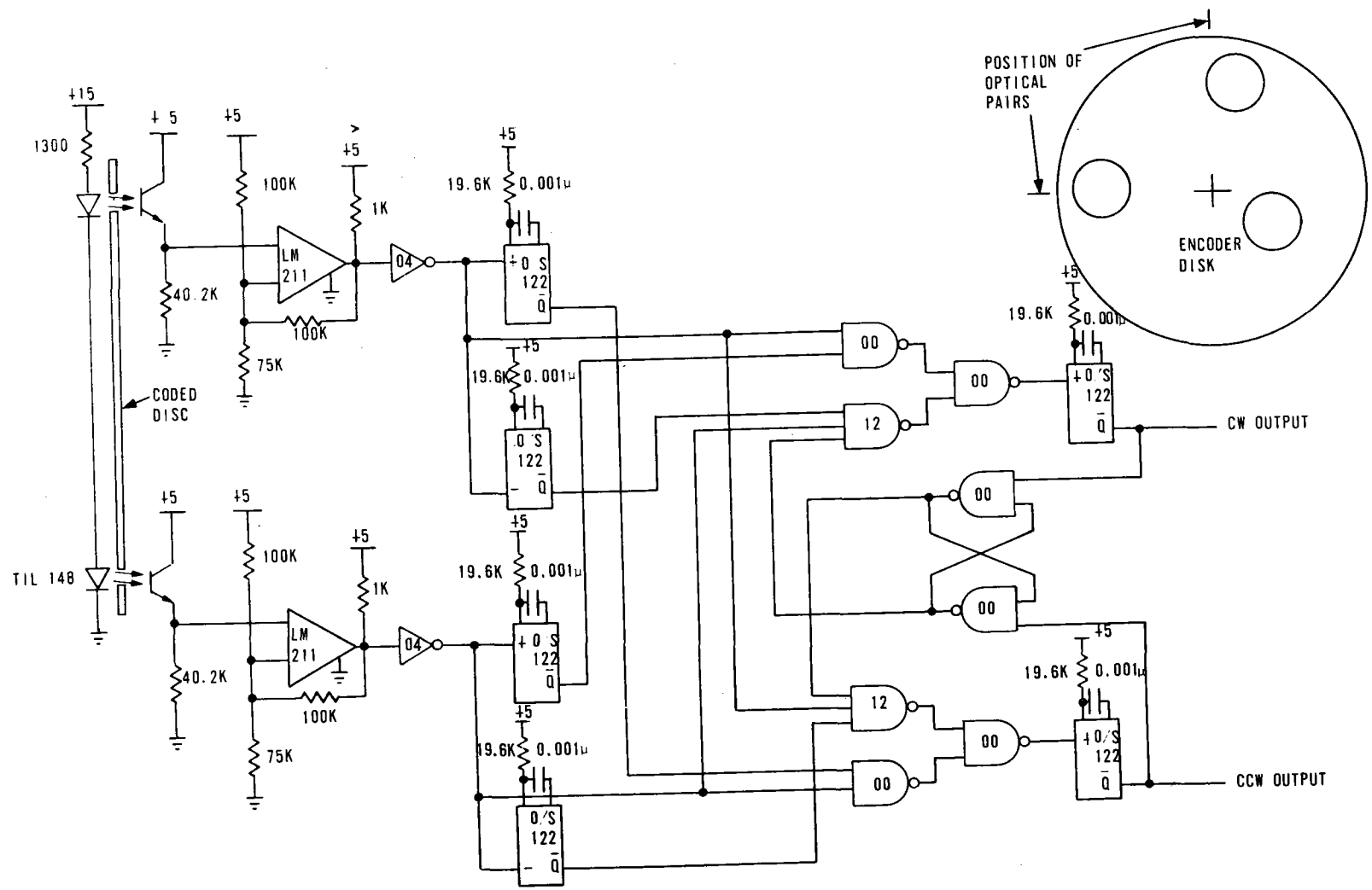


Figure 3-31. Heliostat Incremental Encoder

outputs of the optical pairs during disc rotation that reverses when the rotation of the disc is reversed. This is used by the encoder logic to determine direction of rotation. The encoder generates pulses for cw shaft rotation on one line and pulses for ccw rotation on a separate line. Encoder output pulses occur asynchronously and are negative pulses (+5 to 0) 10 microseconds in width. The encoder logic is so arranged that the disc can be reversed at any time without ambiguity.

The coded disc and optical pairs are mounted in the motor housing. The comparators and follow on logic are contained in the Heliostat Electronics weatherproof box.

Initialization

In the concept of incremental heliostat control, the computer generates and issues a set of incremental gimbals angle update commands based upon current data, updates all records in accordance with the commands issued, and uses the new records as a data base for calculating the next command set. For the system to operate properly, a proper set of conditions must be initially identified or reestablished if for some reason they are lost. Initialization fulfills this requirement by providing the means by which the heliostat gimbals can be driven to a set of predetermined positions which can be used as a reference starting point. All hardware to accomplish this is contained at the heliostat. The computer simply commands the maneuver and waits. No gimbals angle readouts or encoders are necessary and no return communications link to the computer is required. The initialization position is defined as outer axis horizontal, mirrors face down.

Initialization is commanded by the setting of a single bit in the command word. Upon receipt by the heliostat of a "1" for the I-bit, the electronics (1) sets the track servo up/down counter to zero which opens the track loop by means of the threshold detectors in the servo amp and (2) switches control of the gimbals motors to the initialization circuitry.

The initialization hardware consists of a coded disc, two optical pairs, and some processing electronics, all shown in Figure 3-32. The optical pairs are identical to those used in the incremental encoder described earlier. The coded disc is different from the incremental encoders and is mounted to and rotates with the gimbals, passing between the IRED and phototransistor of the optical pair. Depending on the position of the gimbals, the optical pairs generate two state outputs which combine to define gimbals status according to the following Truth Table.

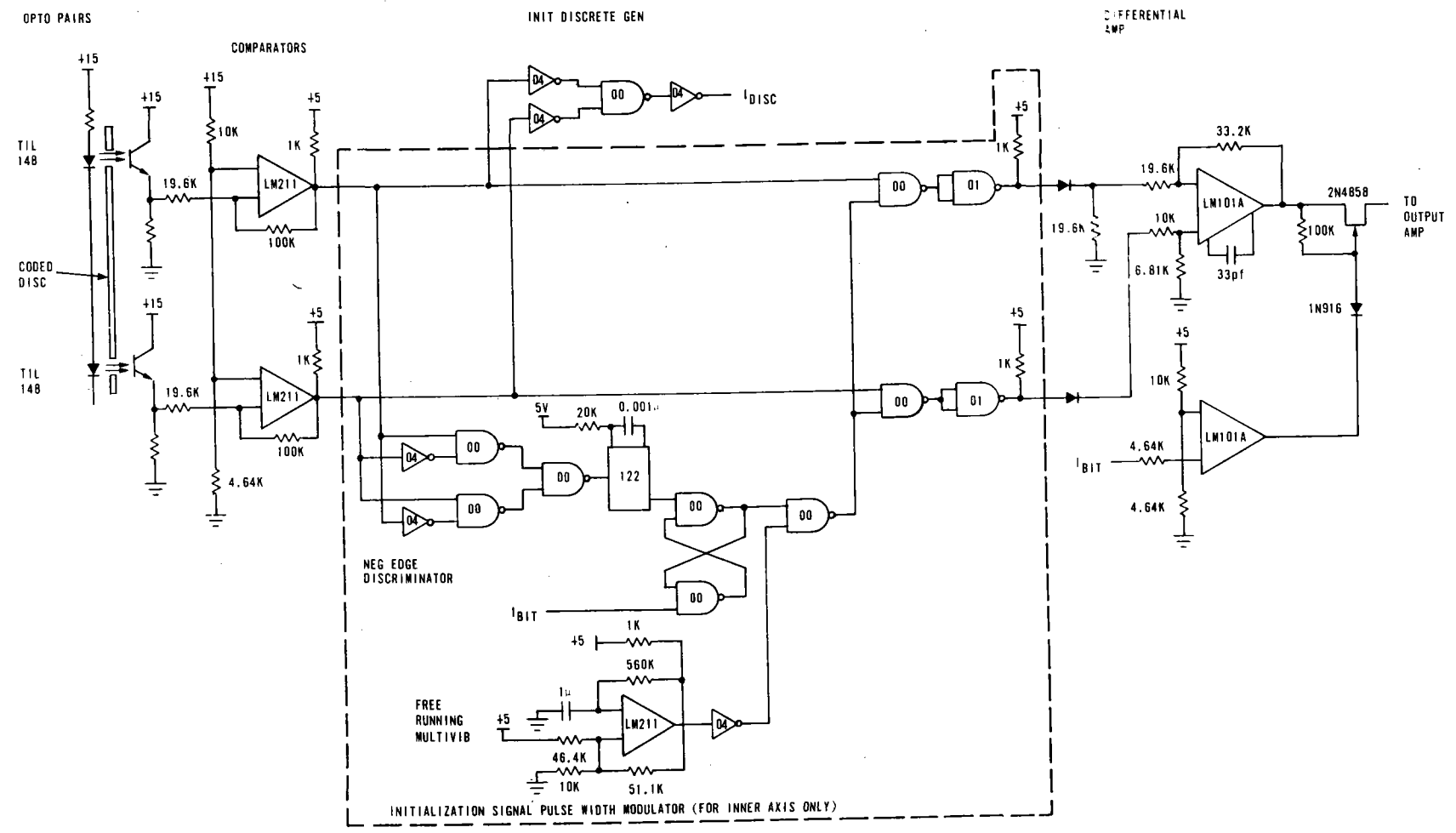


Figure 3-32. Initialization Electronics

Truth Table - Gimbal Status

<u>Output Opto-Pair 1</u>	<u>Output Opto-Pair 2</u>	<u>Status</u>
High	Low	+ Drive required to achieve initialization or stow position
Low	High	- Drive required to achieve initialization or stow position
Low	Low	Initialization position and stow position

The outputs of the opto-pairs are fed to a pair of LM211 comparators designed with a small amount of hysteresis to sharply define the switching point. At this point the initialization mechanization differs somewhat for the outer and inner axes. For the outer axis the comparator outputs are fed directly to a differential amplifier stage which generates the required tri-state output. For the inner axis, the comparator outputs are gated to the differential amplifier. When the mirror modules are a considerable distance from the initialization position, full motor torque is applied to achieve initialization in the shortest possible time. However, when the mirrors are near the initialization position as defined by the appropriate negative edge from one of the opto-pairs, the error is gated to the differential amplifier at a 20 percent duty cycle as determined by the on-off ratio of a free running multivibrator. This is required on the inner axis to prevent limit cycle oscillations through the narrow dead zone caused by the lower torque requirements, backlash, and play of the inner axis drive. A negative edge discriminator circuit is used to distinguish the "appropriate" negative edge, that is, the negative edge associated with reaching initialization as opposed to the negative edge associated with leaving the stow position.

The initialization circuitry also contains the logic to generate a discrete when the gimbal is in the initialization position. This is used by the outer axis control electronics to reset the two motor sync counters so that the outer axis motors are individually initialized and sync reestablished every time initialization is requested. Two sets of initialization electronics are required; one for the inner axis and two for the outer. Initialization accuracy is 100 arc-second for all gimbals.

Outer Axis Two Motor Synchronizer

The motors used to drive the Heliostat gimbals are dc servo motors whose speed is a function of the load. Since two motors are required for the outer axis drive, some means must be provided to keep the two drives tracking within limits. The Two Motor Synchronizer does this by keeping track of the revolutions of both outer axis motor shafts. Should one get too far ahead of the other, the drive is removed from

the leading motor to allow the lagging motor to catch up which effectively keeps the two motors tracking. A schematic of the Two Motor Synchronizer is shown in Figure 3-33. Detailed operation is as follows.

The inputs to the Two Motor Synchronizer are provided by the two incremental encoders associated with the outer axis drives. As with all heliostat incremental encoders, the transfer function of the encoder is one pulse/revolution with each revolution equal to ≈ 81 arc-seconds. The encoder pulses are synchronized to heliostat timing and gated into an up/down counter. Should the motors track perfectly, the output of the up/down counter will remain essentially at zero. Should one motor rotate faster than the other, the counter output will become unbalanced.

The output of the counter is monitored by 4 NAND gates set to sense ± 2 and ± 3 count positions from zero. A two count sensor is used to prevent high speed coasting from reenabling the leading motor drive before the lagging motor catches up. Should the counter monitor detect a two count unbalance, a drive inhibit signal is generated and routed by the direction gates to the proper 24 volt control relay. Since lagging and leading are terms relative to the direction of the drive, the polarity of the analog servo error signal is used to condition the direction gates. The drive inhibit signal deenergizes the relay which removes power from the appropriate power amp thereby disabling drive to the leading motor. Drive is restored when the lagging motor closes to within 1 revolution of the leading motor.

The up/down counter of the synchronizer is reset to zero at every power turn-on whether or not the outer axis frame actuators are equally positioned. However, as explained in the section on initialization, the proper counter output and the positions of the two gimbal drives are reestablished automatically every time initialization of the Heliostat is commanded.

Timing Generator

The Timing Generator provides the timing control signals for the Heliostat Electronics. It consists of a crystal controlled oscillator, countdown logic, and gates for generating clocks. A schematic of the Timing Generator is shown in Figure 3-34.

The frequency of the crystal oscillator is 1.536 MHz. Crystal control is used to provide the frequency accuracy and stability required to synchronize the timing between the Heliostat Communications Receiver, a UART, and the Computer I/O Transmitter, also a UART. No common clocks or timing signals are required between computer and heliostat.

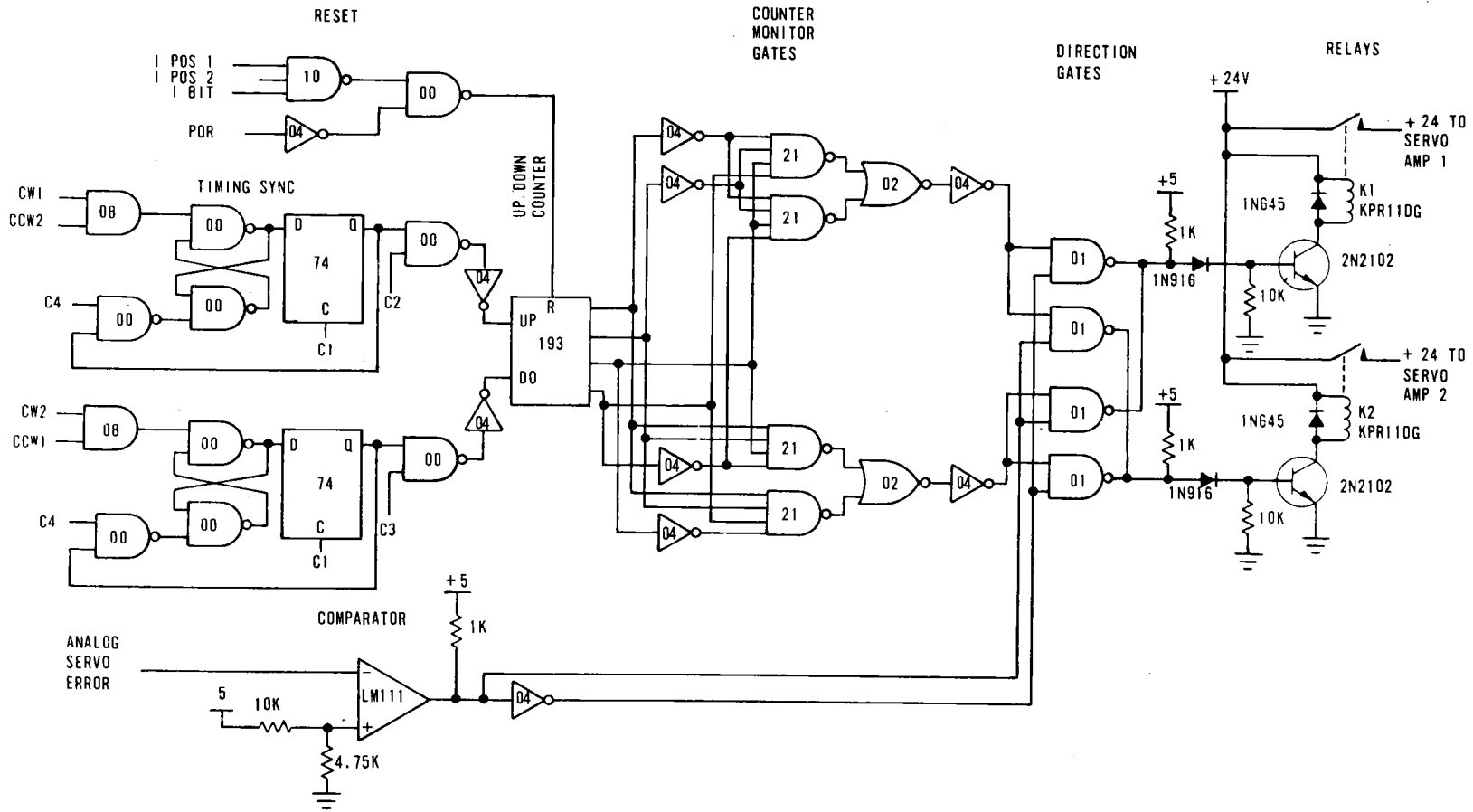


Figure 3-33. Schematic Diagram Outer Axis Two Motor Synchronizer

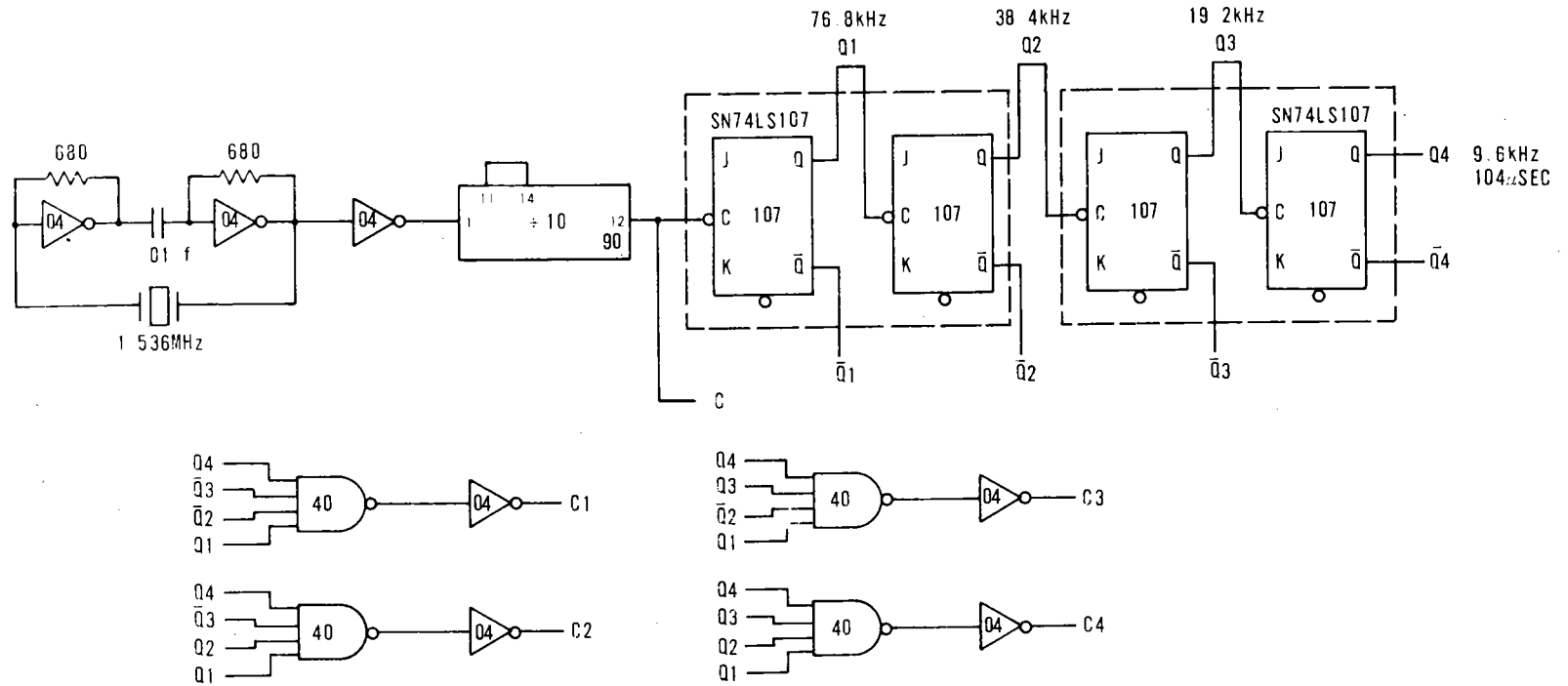


Figure 3-34. Timing Generator Heliostat Electronics

The oscillator output is divided by 10 to 153.6 kHz and further divided by four subsequent binary stages to provide frequencies of 76.8 kHz, 38.4 kHz, 19.2 kHz, and 9.6 kHz. 78.6 kHz is used by the UART, which requires a clock at 16X the data rate, providing for data reception at 4800 bps. The lowest four frequencies are also combined in 4 NAND gates to generate 4 clocks of 104 microsecond period, 6.5 microsecond width spaced at 90 degree increments. These clocks are used by the Heliostat Electronics for general timing control functions.

SRE Heliostat Power Supply AC Power

Each fixed SRE heliostat site has 115 vac, 60 Hz, 20 amp service wired to it. The ac is used to power the battery charger, the Heliostat Electronics regulated power supplies, and any auxiliary test equipment that may be required at the site. A minimum of 4 ac auxiliary outlets is available at each SRE site. AC power is ground fault isolated for safety reasons.

DC Power

Four dc voltages are required by the Heliostat Electronics. The voltages and their primary use are:

1. +5 vdc to power the logic elements
2. ±15 vdc to power the operational amplifier stages
3. +24 vdc to supply gimbal motor drive.

The +5 volt supply on SRE heliostats operates from the 60 Hz line and is a modular supply from AC/DC Electronics Inc. Part Number is IC5N2.7-1. Supply rating is 2.7 amps at 40°C. Actual load is less than 1 ampere. Dimensions are 6.3 by 11.1 by 14.1 cm.

The ±15 volt supply operates from the 60 Hz line and is a modular supply from Burr Brown. Supply rating is ±200 ma. Actual load on +15 volts is 150 ma, -15 ma volts 100 ma. Dimensions are 8.9 by 6.3 by 3.3 cm.

The +24 volt supply is made up of two 12 volt Die Hard automobile batteries connected in series. Two 12 volt battery chargers are provided at each heliostat site in order to be able to recharge the batteries from the 110 vac line. The chargers are from Sears, Part No. 28K517. Batteries may be charged while the system is running. The batteries and chargers are mounted in a separate ventilated wooden box.

An on-off switch for low voltage power is provided on the Heliostat Electronics panel.

See Figure 3-35, SRE Heliostat Power Circuits.

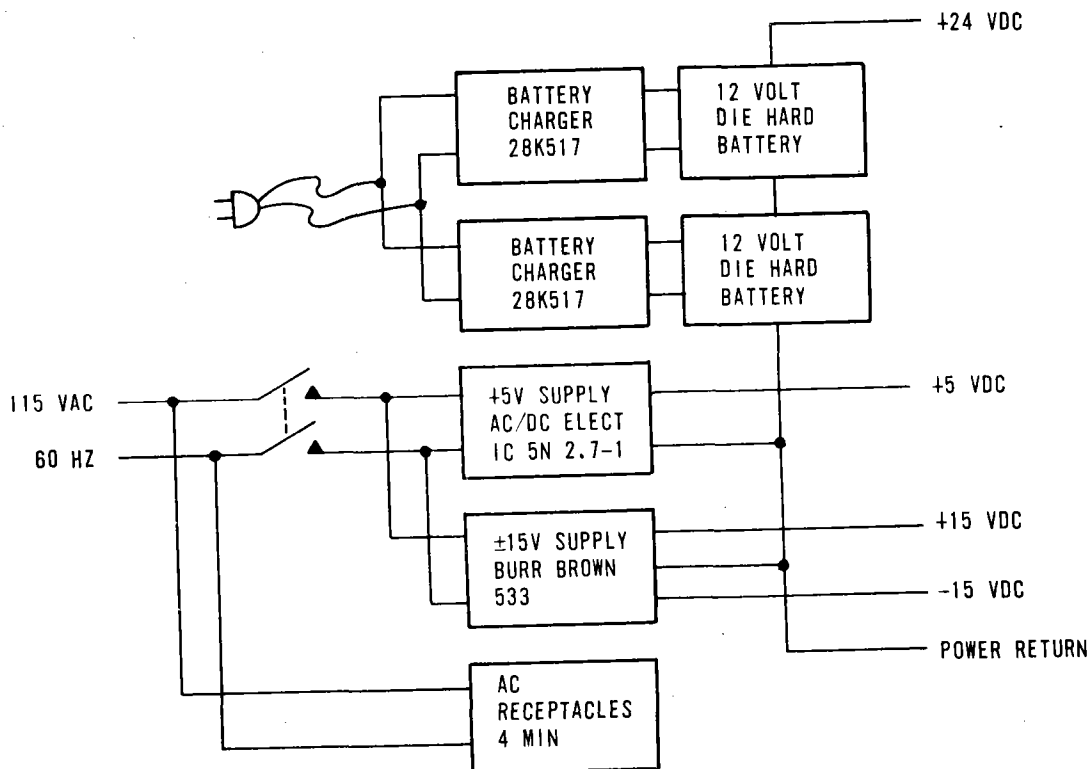


Figure 3-35. SRE HelioStat Power Circuits

SRE Manual Operation

A set of panel switches is provided at each heliostat which allows an operator to assume control of the gimbal motors. Drive for the motor is taken directly from the battery such that no HelioStat Electronics is required. Axes may be driven individually or simultaneously in either direction. Manual control is useful for certain coarse positioning tests, manually checked speed tests, or in the event of a control system failure. A schematic of the manual control mode is shown in Figure 3-36.

For the SRE, the manual control was located in a separate box. For the pilot plant a single box will house both manual controls and electronics but batteries will be housed separately.

SRE Special Test Equipment

A special piece of test equipment called the Solar Test Box is provided which permits an operator to provide the inputs required to exercise all of the HelioStat Electronics except for the communications interface. The box contains 8 SPDT switches which represent the 8 bits in the command word. The switch setting determines whether the respective data bit is a "1" or a "0". A "transmit" button switch is provided which when pressed generates a data ready signal which allows the heliostat to accept the data locked in the switches. Any combination of data bits available to the control computer can be selected by the test box. Data can be changed between "transmissions".

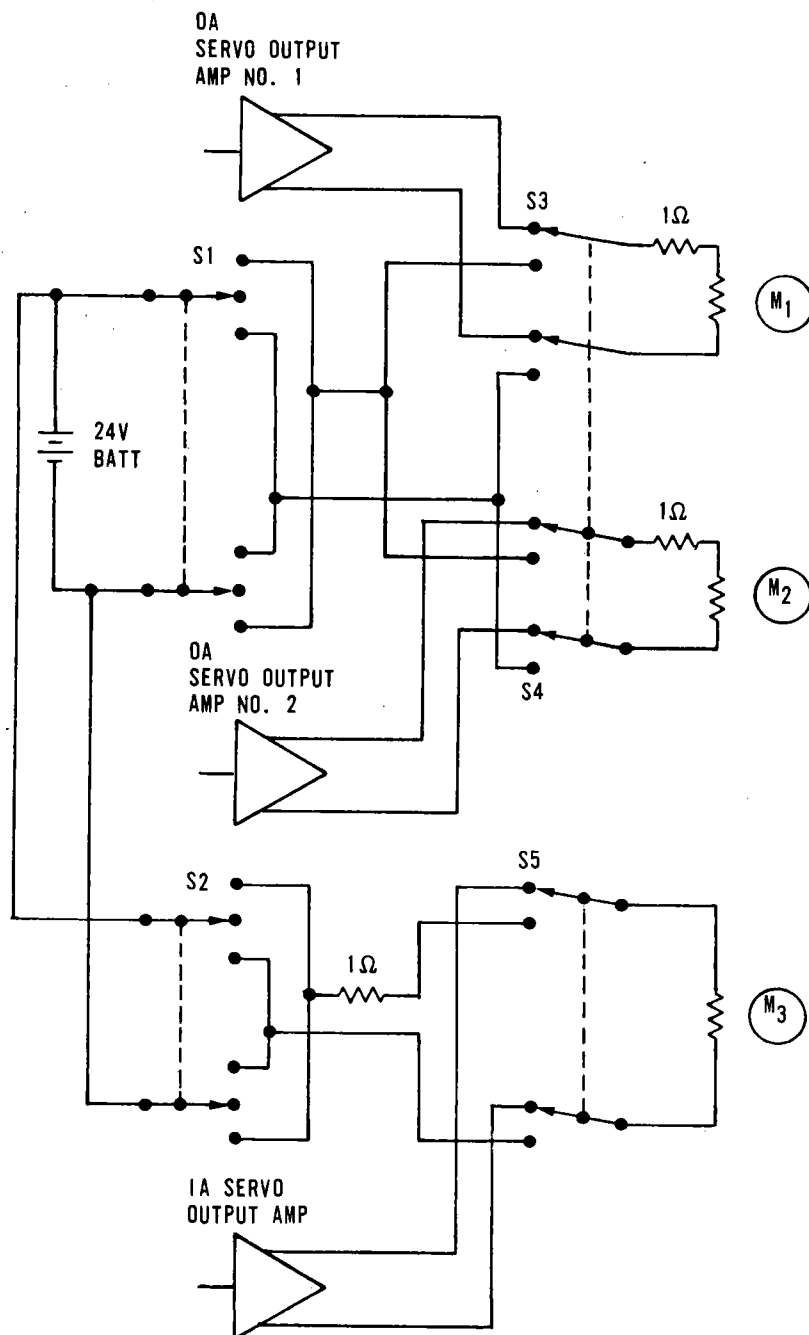


Figure 3-36. Schematic Diagram Manual Mode Operation

The interface between the test box and the HE is by means of a 40 pin dual-in-line carrier which plugs into the 40 pin UART socket. The 5 volt power required by the test box is also accessed through the carrier. Test box dimensions are 22.9 by 17.8 by 5 cm. One test box was built in the SRE program. A schematic of the Solar Test Box is shown in Figure 3-37.

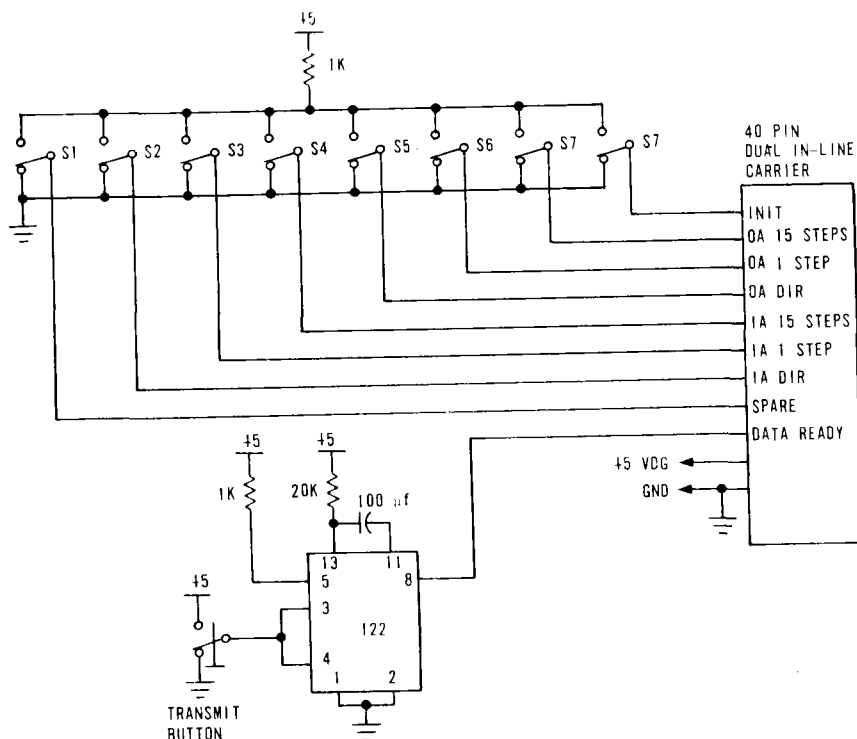


Figure 3-37. Solar Test Box Schematic Diagram

Electronics Packaging

The electronics for the solar research heliostats was packaged in two separate units. Most of the electronics was packaged in a metal weather sealed box (NEMA-12 type) that was installed at one end of the heliostat. The batteries and chargers were packaged in a separate wooden box to prevent corrosion of electronics by battery outgassing. All the electronics were mounted to a foldout panel to provide easy access. A photograph of an electronics assembly is shown by Figure 3-38 with major parts of the electronics indicated.

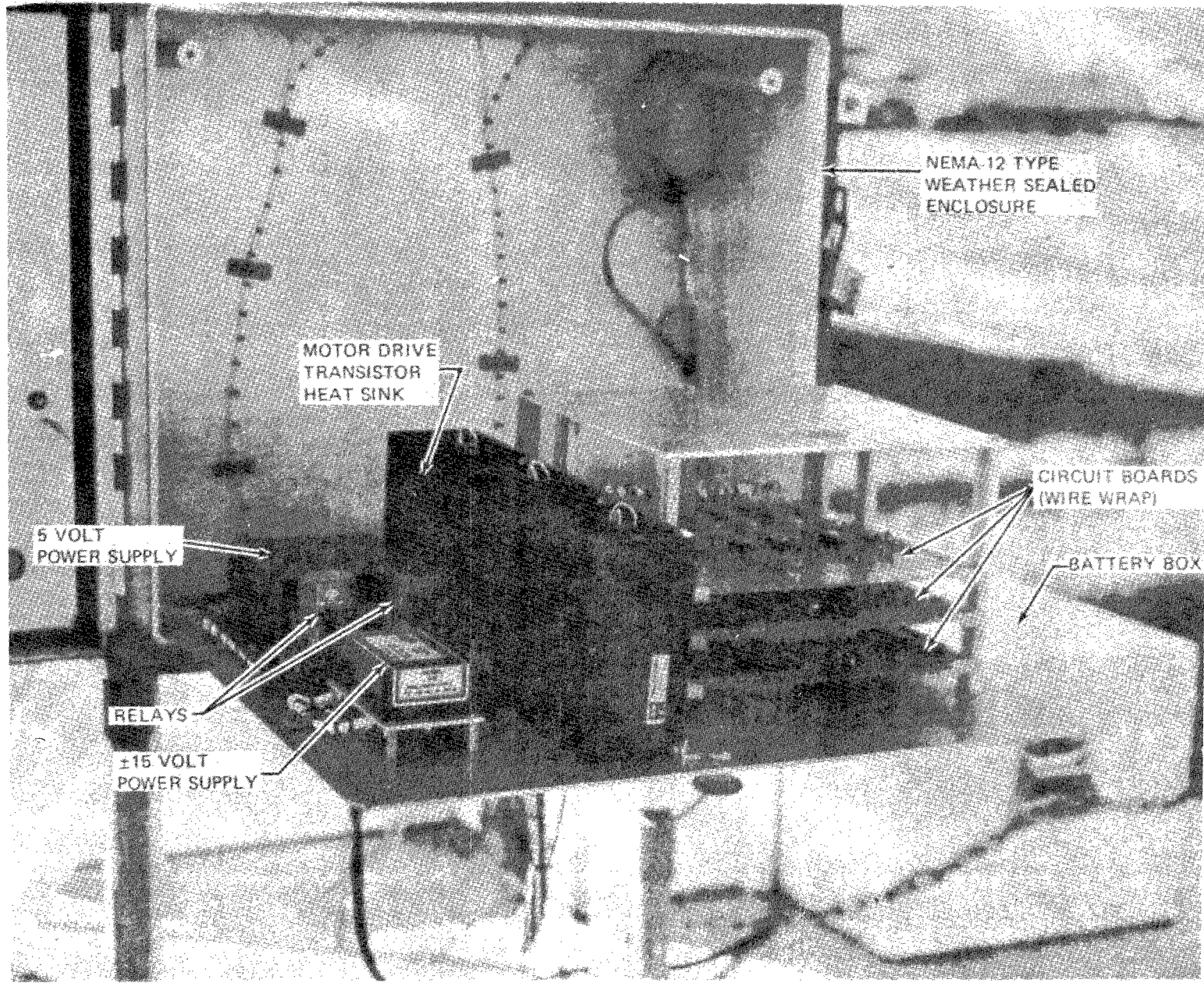


Figure 3-38. Heliostat Electronics Package

Cooling inside the electronics package was accomplished by free convection. A detail discussion of this is contained in Page 4-19. Thermal analysis showed temperature inside the package below component maximum rating of 70°C (158°F) for all environments except with external heating from direct solar radiation. Actual operating experience, without extra protection, indicated no excessive temperatures operating in the Florida environment. In a desert environment the package along with heliostat structure, would need to be painted white to minimize solar absorption. Direct shade will also be provided during high solar intensity periods of day by incorporating an overhanging "roof" above the package.

The packaging technique used for Engineering Model and Solar Research experiment contained three circuit boards for mounting circuit elements. Interconnection was made on the back side of the circuit board using wire wrap technique. Most of the semiconductor devices were mounted in plug in sockets. The circuits boards had edge card connectors and were held in place by plastic card files. Power output transistors for motor drives were mounted to heat sinks. The ± 15 volt and 5 volt power supply, and two relays were mounted directly to the fold out panel.

Electronics packaging proposed for the pilot and commercial plants will remain in two separate boxes. One NEMA-12 type will be used for all the electronics including the battery charger function. A second, separate box, will be used for only the batteries because of their special needs. All the electronics including power supplies and battery chargers will be special designed circuits mounted on two sided printed circuit boards. It is more economical to package commercial, prepackaged, power supplies and battery chargers as an integral part of the electronics in quantities required for the pilot and commercial power plant.

All electronics components, except high power dissipating devices for power supplies, motor drives and battery chargers are mounted on one of four two sided printed circuit boards. All components will be mounted on one side. Cards suitable for automatic component insertion will be used. Edge card connectors will provide interconnection and card files will be used to mount the units. Cooling of the four printed circuit boards will be by free convection. The high power dissipating components are mounted directly to heat sinks which will be integrated into the package to dissipate heat directly outside the weather sealed box. This allows cooler operation of the complete electronics. The package external surface will be painted white and provided with a sun shade to minimize solar radiation load. During low temperature periods with temperatures of -29°C (-20°F), it will be necessary to provide controlled heaters to maintain ambient temperature above the 0°C (32°F) component rated minimum temperature.

Sealed batteries are included in the pilot and commercial plant heliostat. They are mounted, by themselves, in a special battery box designed for use in an outdoor environment.

COMPARISON OF ELECTRONICS FOR SRE AND PILOT PLANT

Some additions and differences will be required to be made to the SRE Heliostat Electronics for operation at the pilot plant level and beyond. These are listed below.

Address Decoder

Dedicated communications lines were used to carry the commands from the control computer to the heliostat for the SRE. For the pilot plant, many heliostats will share the same data bus which will require that an identifying address be used to identify the heliostat being sent the command. An address decoder and data gate is therefore included at each heliostat for the pilot plant.

Uninterruptable Power

Although a large capacity rechargeable battery was used for the SRE, it only supplied the heavy currents to drive the gimbal motors. The low voltage power supplies which were used to power the processing electronics used the 115 vac line for their source of power. The power supply was mechanized in this fashion strictly as a matter of cost and schedule convenience because the ac operated supplies were readily available. For the pilot plant and beyond, all power to operate the heliostat will be drawn from the heliostat battery. The battery will be trickle charged from the ac line to maintain capacity. In the event of a failure in the ac grid, the heliostat battery will be able to supply all heliostat operating power for up to 19 hours.

Other Fail-Safe Feature Additions

A communications loss detector, an ac power loss detector, and gimbal drive motor overtemp detectors will be added as fail-safe features to the pilot plant HE. The communications loss detector is a simple retriggerable one shot which will initiate a stow maneuver should communications be lost for 45 seconds. The ac power loss detector will be an ac detector and timer which will initiate a stow maneuver should the ac grid power be lost for ≈ 20 minutes. The motor overtemp detector will remove drive power from a gimbal motor when a temperature threshold is exceeded so as to prevent damage to the motor winding insulation. Such a condition could result if full power were being applied to drive a stalled motor either against the gimbal stop or because of a mechanical failure.

Power Sequencing to the Heliostat Electronics

For the SRE, a toggle switch was provided at each heliostat site to turn power ON or OFF. For the pilot plant, this function will be performed automatically as part of the normal operating procedure.

A block diagram of the power up and power down sequencing mechanization for the Heliostat Electronics for the pilot plant is shown in Figure 3-39. The mechanization features the following characteristics:

- Individual heliostats or groups of heliostats may be turned on or off as desired under the control of the operator in the tower.
- No additional control lines to the heliostat are required.

- The mechanization permits charging of the heliostat battery without the load of the heliostat electronics such as may be desirable after operating hours.
- In the event of an emergency such as the loss of ac power or communications beyond programmed limits, the mechanization will keep power on only until the fail-safe stow position is reached, after which it automatically turns itself off.

The mechanization accomplishes this in the following manner.

Turning power on at the heliostat really means connecting the 24 volt battery to the DC/DC converter and the output servo amplifier. Switching of the 24 volts is determined by the state of three conditions. They are

1. Presence or absence of the ac line voltage.
2. Presence or absence of communications signals.
3. State of the gimbal positions, that is, stowed or unstowed.

There will be detectors at the heliostat to determine these conditions.

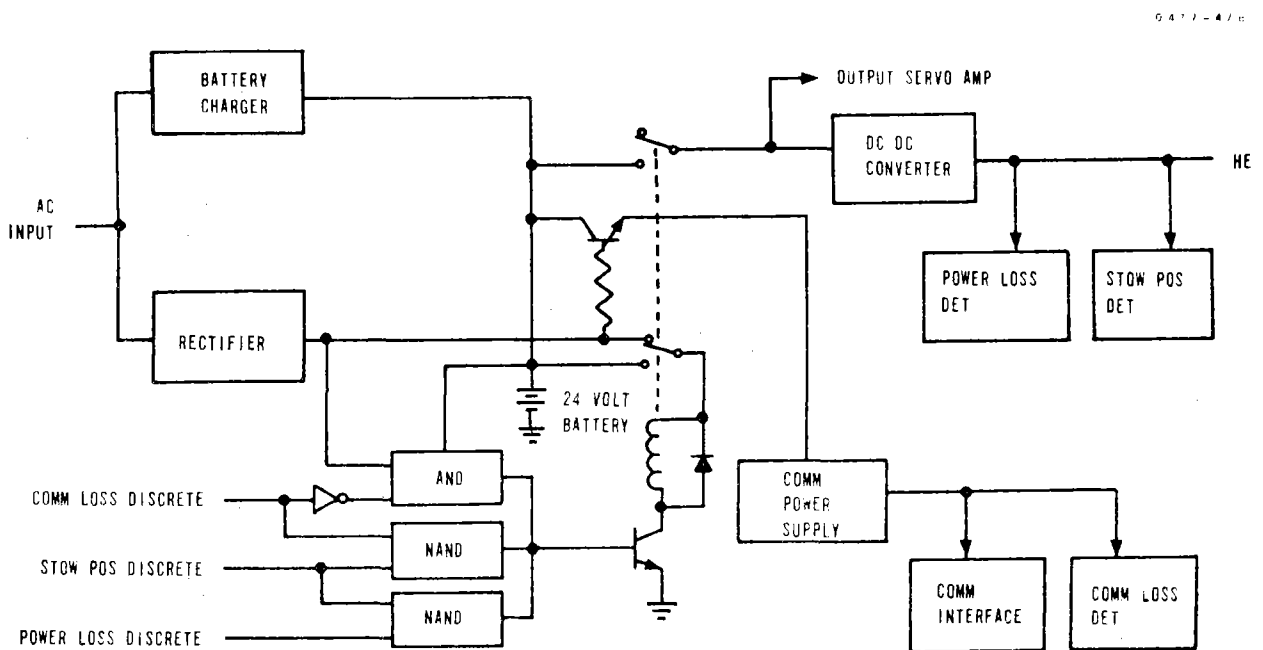


Figure 3-39. Power Sequencing Mechanization

To turn on the Heliostat Electronics will require the presence of ac power and communications. If only ac power is present the 24 volts will not be switched. This will permit charging of the heliostat battery without turning on the Heliostat Electronics.

If both ac power and communications are present, the heliostat will assume a fully powered up condition and be available for operation. Should an emergency arise after the heliostat is powered up resulting in the loss of ac power or communications beyond the acceptable limits, the heliostat, as explained in the section describing the operation of the electronics, will initiate a stow maneuver. The output of the stow position detector will be ANDed with the outputs of the communications and power loss detectors such that heliostat power will be kept on until the stow position is reached after which it will turn itself off.

Summary of Differences Between Electronics for SRE and Pilot Plant

- Address Decoder
- Uninterruptable Power
- AC Power Loss Detector
- Gimbal Motor Overtemp Detector
- Power Sequencing

Future Plans For the Heliostat Electronics

Based on the experience gained during the SRE, some promising cost savings ideas have been identified for inclusion in the Pilot Plant version of the Heliostat Electronics. The details of these ideas are currently being worked under a producibility improvement contract and would be further worked during detail design phases. A general description of these ideas and plans for future versions of the heliostat electronics are given below.

All Digital Gimbal Control Servos

As explained in the detailed description above, the Heliostat Electronics for the SRE was a combination digital/analog system with the circuitry split about 50/50. This mechanization produced a design that could, with simple circuit changes, accommodate a wide range of gimbal step sizes, servo scale factors, motor sizes, and motor torque levels. The flexibility of this approach was appreciated when for example after the engineering model heliostat was built, the outer axis motor and servo scale factor were changed because of unexpected dynamic load friction levels with very little impact on the electronics. The cost of this flexibility however was added complexity. Based on the experience gained during the SRE, it is felt that the circuitry can be somewhat simplified.

The biggest such simplification involves eliminating all linear analog circuitry and replacing it with Class S (switching) types of circuits. The ultimate result of this change is that full motor voltage will be applied whenever motor torque is called for rather than any fraction of full voltage that is possible with the SRE version. While this method would seem to eliminate control of servo scale factor, variations could be effected if required by the use of pulse width modulation techniques.

The parts savings associated with this change is significant. The digital circuitry required to implement this in the inner axis is shown in Figure 3-40 along with the analog circuitry it replaces. For a complete system, it has been estimated that 109 less parts will be required with a piece parts savings of ≈\$100 per heliostat.

Elimination of the ±15 Volt Power Supply

Switching to an all digital servo provides as a secondary benefit, the possibility of a second major electronics functional simplification which is the elimination of the ±15 volt power supply. Elimination of the analog portion of the servo eliminates all LM101A operational amplifier stages which are the primary users of ±15 volt power. All remaining circuitry could be operated from the +5 vdc regulated line or the +24 vdc battery except for the UART, which requires -12 vdc at 7 ma. If a replacement UART not requiring -12 vdc cannot be found, it is felt that this voltage can be supplied by a simple two transistor capacitively coupled inverter/rectifier.

Substitution of a Third Control Loop for the Two Motor Synchronizer

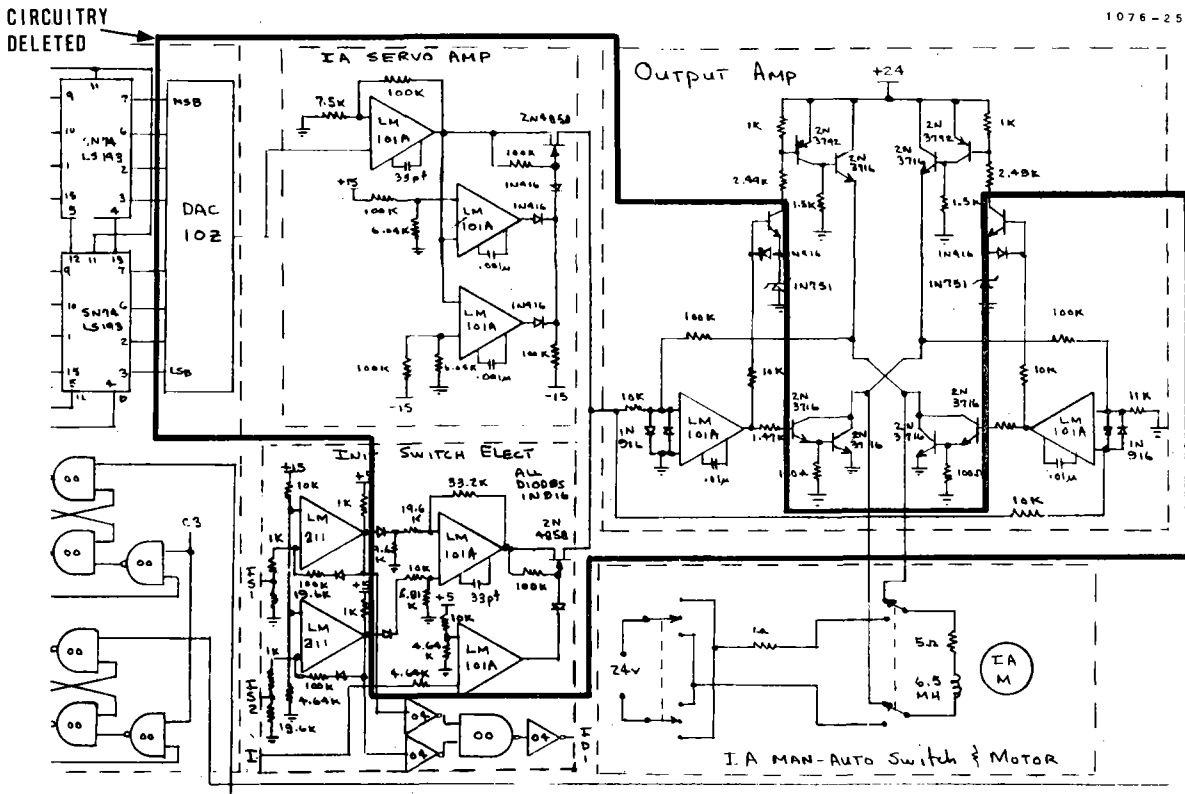
Elimination of the two motor synchronizer circuitry by using separate outer axis control loops is also a simplification possibility. The rationale for this is as follows.

In administering a 15 step command, the two motor synchronizer will keep both outer axis motors within two motor revolutions of each other. In carrying out a one step command, which is the fine track mode, the two motor synchronizer may have no operating effect at all since only a fraction of a second is required to administer a command and commands are several seconds apart. In fact, the two motor synchronizer may allow the outer axis position difference to build up to two motor revolutions and maintain this difference throughout the tracking day, an error though small, that separate control loops will eliminate.

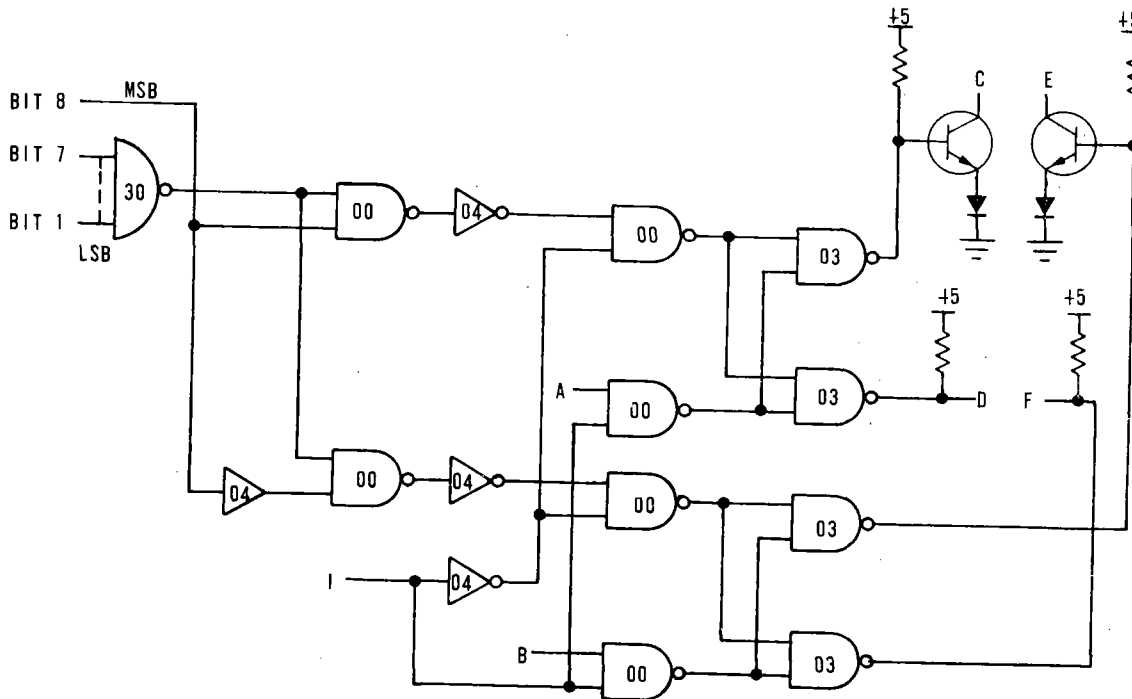
The primary purpose of the two motor synchronizer, therefore, is not to maintain outer axis sync so as to control redirected beam shape and size during track. It does limit the difference during high speed slew to two motor revolutions which prevents a large twisting of the frame. It also serves a limited fail safe function by removing power from the leading motor should one become stalled because of a malfunction.

With regard to failure protection, the motor overtemp detector will provide far more protection capability than the two motor synchronizer. With respect to the twisting of the frame, the experience of the SRE has shown this not to be a concern. Since the circuitry to add a third control loop is simpler than the circuitry for the two motor synchronizer, the synchronizer will probably be eliminated.

Intra-function circuitry will also be simplified as much as possible in the producibility study.



a. Analog Circuitry Replaced (Enclosed in Heavy Line)



b. Digital Replacement for Analog Circuitry
Figure 3-40. Replacement Circuitry

Long Term Improvements

For the long term, major improvements in the cost of the electronics will have to come from techniques such as large scale integration (LSI) or the substitution of a microprocessor for much of the control servo. LSI can probably encompass more of the required circuitry per chip than the microprocessor version but has the disadvantage of having a fairly high front end cost to develop and is somewhat inflexible. The microprocessor being a chip already in production has its development costs spread over many users. It also retains a great deal of design flexibility replacing hardware changes with changes in software and will hopefully be second sourced. Even without using its arithmetic capability, studies have shown that economies can be effected by using microprocessors to replace logic designs employing 30 or more chips. The present Heliostat Electronics uses approximately 100 chips.

A Heliostat Electronics design using microprocessors can probably be ready for the Pilot Plant. An LSI design lies somewhere beyond the Pilot Plant.

Summary of Electronic Improvements

- Conversion to an all digital servo
- Elimination of the ± 15 volt power supply
- Substitution of a third control loop for two motor synchronizer
- Intra-function simplification
- Large scale integration
- Use of microprocessors.

POWER ANALYSIS AND DISCUSSION

The power consumption analysis for the heliostat consists of separate analyses of the continuous and transient power requirements which are then combined to determine the overall power requirements. Continuous power is that power required by the Heliostat Electronics (HE) whether or not a gimbal update is being carried out. Transient power is that additional power required to perform a gimbal update.

The continuous power requirements of the HE are determined by adding up the power drawn by the individual components that make up the HE. The model used for this analysis is the HE from the SRE. Low power Schottky T²L was assumed for all logic elements.

Part 1 of Appendix D contains the details of the analysis showing the parts, the current requirements of each and the totals. Based on this analysis, the total continuous operating power requirement is the sum of the power drawn from each supply and is determined to be 19.80 watts at the battery level. For an assumed operating day of 14 hours, continuous power requirements are $(14)(19.80) = 277.2$ watt hours/day.

The power supply current drains predicted by the analysis are compared to the values measured on the engineering model in Table 3-3. The predicted values have been adjusted to exclude the currents drawn by the initialization electronics and the initialization and incremental encoder opto pairs, which are the conditions under which the measurements were made. The value predicted for the 5 volt supply is less than the measured value probably because a significant number of standard T²L elements were used in the engineering model because of their availability. Standard T²L draws considerably more power than the low power Schottky devices assumed in the analysis.

Table 3-3. Comparison of Measured and Predicted Values of Power Supply Current Drains

Supply	Current Drain, ma	
	Pred	Meas
+5	535	810
+15	102	90
-15	113	100
+24	124	---

The values predicted for the ± 15 V supplies are more than the measured values probably because the quiescent currents of the operational amplifiers were less than assumed in the analysis. The 24 volt current drain was not measured.

The transient power is the additional power required to carry out a gimbal update, that is, the power to drive the motors to move the gimbals. To determine this power, an analysis was done to determine the motor speed, current, and power as a function of time. The power

to carry out a 1 or 15 step command was then determined from which the power to track or slew in watt hours/gimbal degrees was calculated. Only 1 step commands were assumed to be administered in the track mode and only 15 step commands in the slew mode.

Details of the analysis are given in Part 2 of Appendix D. The calculated values for the inner and outer axis track and slew modes can be found in the summary in Table 3-4. The table also shows the amount and type of gimbal travel assumed for an operating day and the power required to perform those maneuvers. Total power for all gimbal maneuvers is seen to be 49.93 watt hours.

Table 3-4. Gimbal Update Power Requirements

<u>Gimbal and Drive</u>	<u>Power Watt Hrs/Deg</u>	<u>Travel Deg/Day</u>	<u>Power Watt Hrs/Day</u>
Inner, Track	0.06341	90	5.707
Inner, Slew	0.01980	450	8.911
Outer, Track	0.14605	90	13.144
Outer, Slew	0.12315	180	<u>22.167</u>
		Totals	49.93 watt hrs/day

The overall power requirement at the battery level is the sum of the continuous power and transient power and is equal to 277.2 watt hrs/day + 49.93 watt hrs/day = 327.13 watt hrs/day. Average power is 327.13 watt hrs/day/14 operating hrs/day = 23.37 watts at battery level. Assuming 20 percent more power has to be put into the battery than can be taken out and a battery charger efficiency of 60 percent, the average line power to operate a heliostat is

$$\frac{(23.37)(1.2)}{0.6} = 46.74 \text{ watts or } 654.36 \text{ watt hrs/day for a 14 hr day}$$

COLLECTOR FIELD ARRANGEMENT

Power Wiring

The field layout for heliostat power wiring is shown in Figure 3-41. For power distribution purposes, the pilot plant is divided in eight sections with approximately 200 heliostats in each section. To reduce transmission losses, high voltage at 2400 vac phase to ground is fed from the tower to transformers centrally located in each section. The transformers convert the 2400V to 120/240 vac, a value that is reasonably safe for general distribution among the heliostats. Two high current row feeder lines fan out from each transformer to provide power to tie points on radial rows of heliostats. From these tie points, heliostat feeder lines distribute power to individual heliostats.

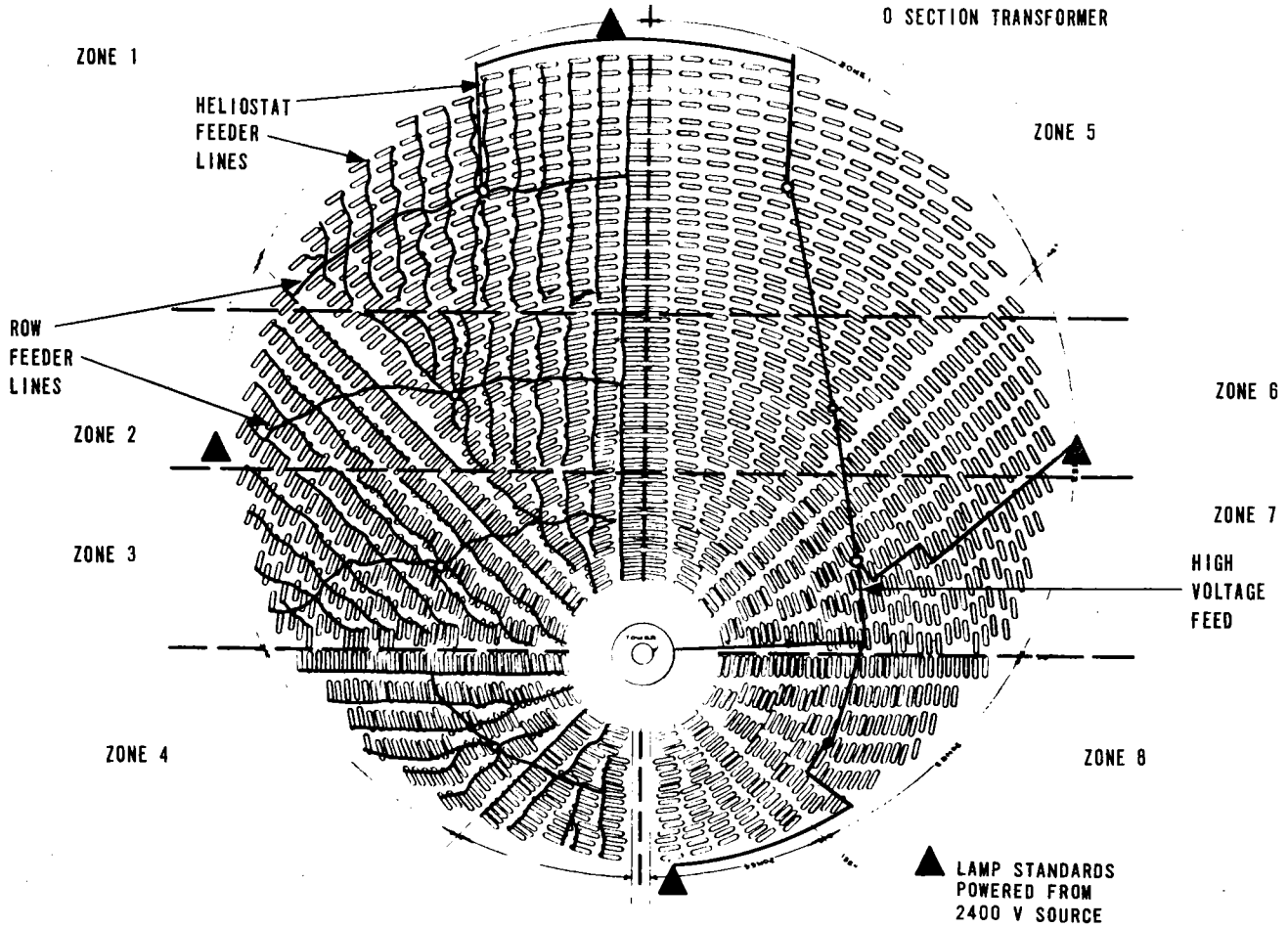


Figure 3-41. Field Layout Showing Low Voltage Feed on Left Side and High Voltage Feed on Right

The high voltage network that interconnects the field transformers forms a ring that completely encircles the tower. To provide for a measure of redundancy, the high voltage connection from the tower to the ring is by means of two separate feeder lines requiring a double break in the system before high voltage is lost to any section.

Average power dissipation for a heliostat is currently estimated to be 46.7 watts. To provide for some margin, line losses were calculated for values 1.8 X this or 86 watts/heliostat. Losses were limited to one percent to the furthest transformer in the high voltage feeder line and five percent to the furthest heliostat in the low voltage system. For the low voltage distribution system, wire sizes were calculated for 120 and 240 volt systems.

Based on the above, 1676m (5500 ft) of AWG No. 2 Aluminum conductor plus safety wire is required for the high voltage feeder lines. For the low voltage distribution system 20575m (67500 ft) of two conductor plus safety line is required. For the 120 volt system wire sizes will range from AWG 000 to No. 14. For the 240 volt system, wire sizes average six to seven sizes less requiring a maximum size of AWG No. 4 for the heaviest feeder. Table 3-5 of the accompanying Figures 3-42 and 3-43 shows the wire sizes and lengths of the various low voltage feeder lines.

High voltage wiring will be buried to a depth 0.9m (36 in.) and low voltage to a depth of 0.6m (24 in.) with signal wires at a depth of 0.46m (18 in.). Enclosures may be used at higher cost but are not included our design.

Control Signal Wiring

The computer/heliostat communications wiring will be radial throughout the field to minimize length and share common trenching as much as possible with the power distribution system. In-line superheater and boiler heliostats will share a common line such that loss of a line will result in a heat loss distributed among the receiver components rather than concentrated in one section. All communications lines will terminate at the tower so that transmitted data can be checked at the end of the line. The accompanying figure shows the routing and lengths of the communications lines.

For the pilot plant field a total of 18 separate lines will be required with an aggregate length of 26173m (86200 ft). There is an average of 94 heliostats on a line with a maximum of 104. Communications lines will be twisted shielded pairs of AWG No. 18 buried to a depth of 0.46m (18 inches).

Field Instrumentation and Calibration Array Wiring

Field instrumentation communication lines will be routed in a manner similar to the method used for the control communications lines, that is, in a radial manner and sharing common trenching. Seven lines will be required with an aggregate length of 4267m (14000 ft). Field instrumentation communications lines will be twisted shielded pairs of AWG No. 22 buried to a depth of 0.46m (18 inches). Shown in Figure 3-43 are the lengths and routing for the various buses.

Table 3-5 . Heliostat Low Voltage Power Wiring

Wire Size (220 Volt System)	4	5	6	6	10	12	14	16	18	20
Wire Size (110 Volt System)	000	00	0	1	5	6	8	10	12	14
Zone 1 (m)	107	171	---	---	---	---	250	608	1036	831
Zone 2 (m)	277	---	---	---	---	---	---	283	1416	581
Zone 3 (m)	---	256	---	---	---	---	291	1309	463	318
Zone 4 (m)	---	---	73	97	158	321	597	230	580	21
<hr/>										
Totals, 1/2 Field (m)	384	427	73	97	158	321	1138	2430	3505	1751
X 2										
Totals, Full Field (m)	768	854	146	194	316	642	2276	4860	7010	3502

3-67

Total composite Heliostat Low Voltage Power Wiring = 20575m (67500 ft).

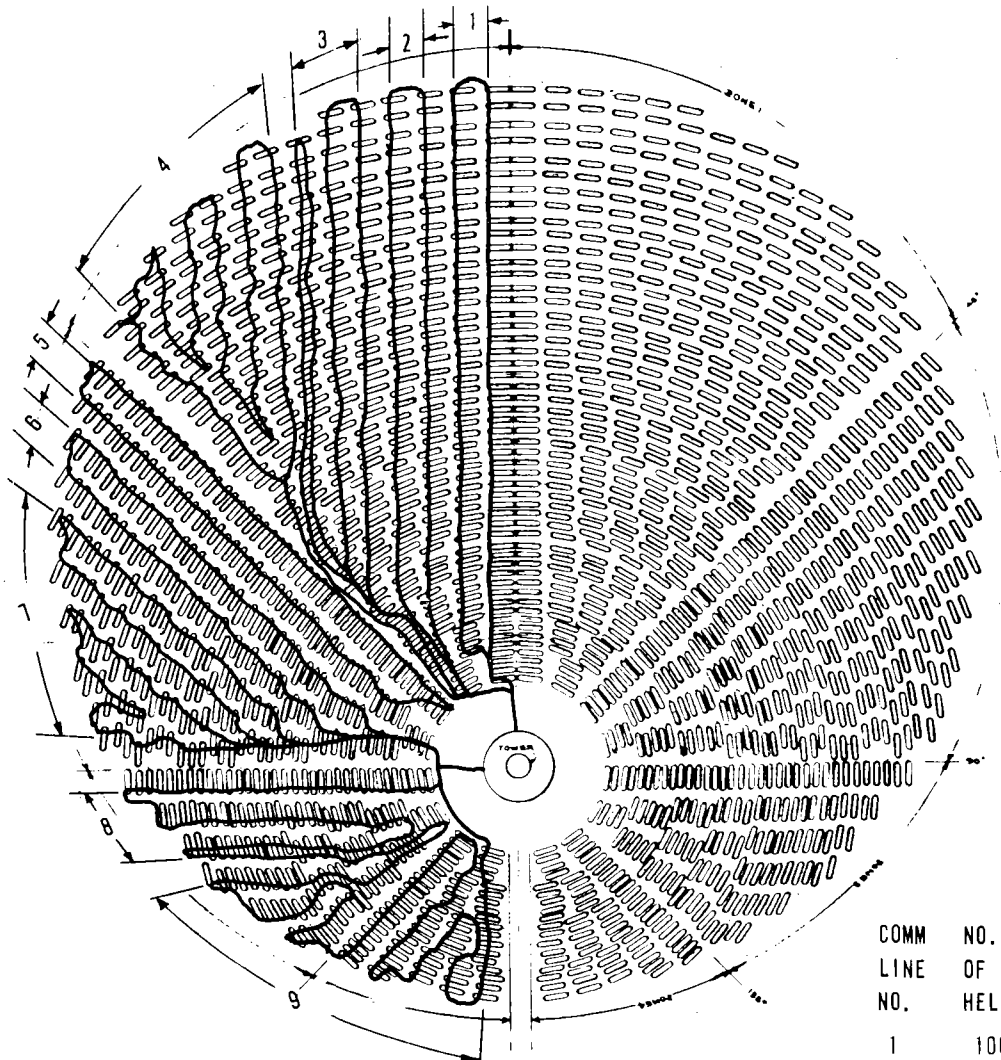
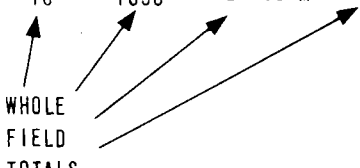


Figure 3-42. Heliostat Communications
Signal Interconnect Diagram and
Communications Wiring Summation

COMM LINE NO.	NO. OF HELIOSTATS	ROUTE LENGTH L1(M)	TOTAL LENGTH L1+3N(M)
1	100	887	1192
2	96	985	1277
3	104	1770	2088
4	93	1737	2020
5	91	853	1130
6	82	789	1039
7	90	1278	1553
8	90	1048	1323
9	103	1169	1513
9	849	10549 M	13137 M
X2	X2		
18	1698	21098 M	26273 M

WHOLE
FIELD
TOTALS



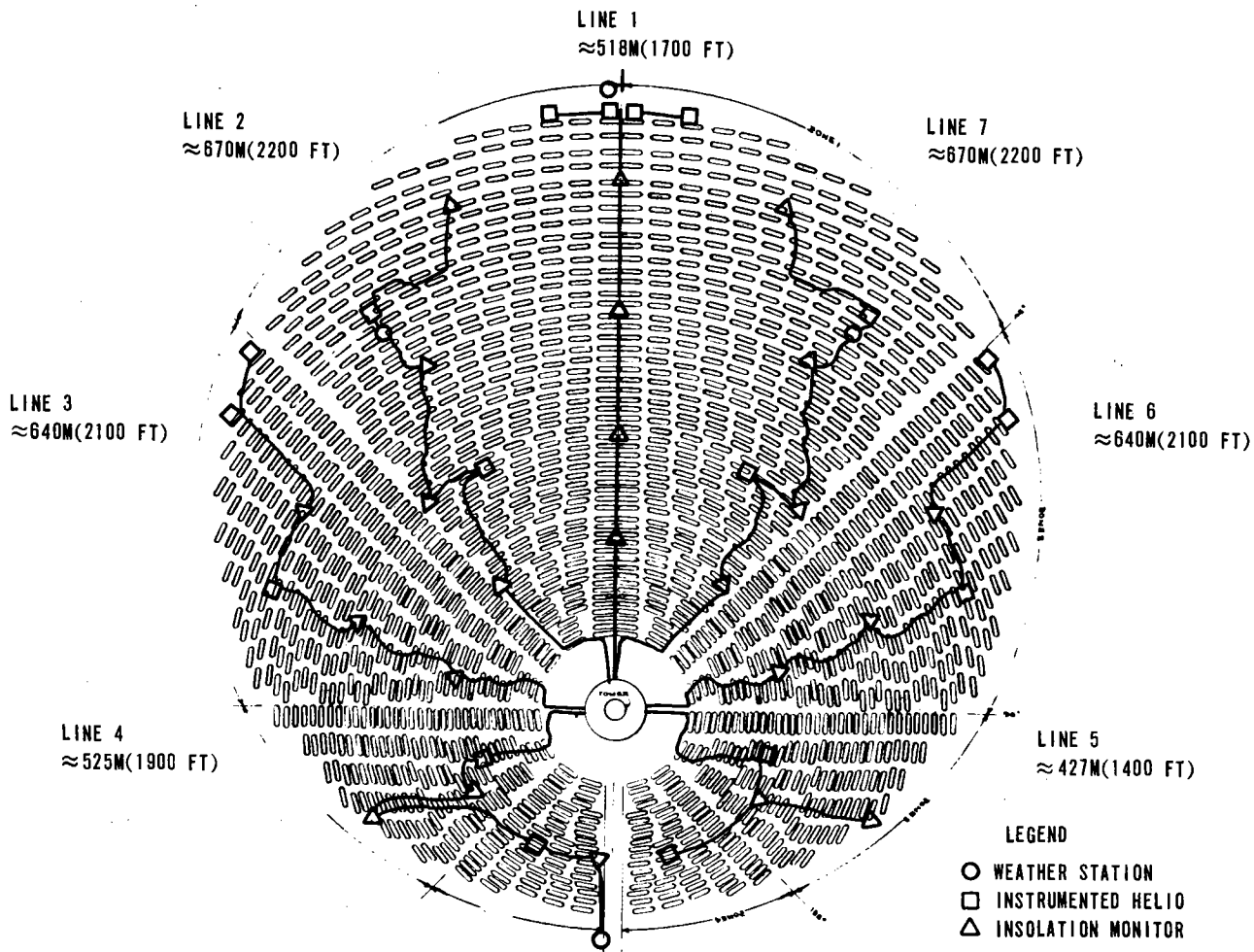


Figure 3-43. Location and Interconnect Diagram Pilot Plant Collector Subsystem Field Instrumentation

Operating power for field instrumentation will be acquired from the closest heliostat site.

The Calibration Array/Control Computer interface will also be by means of twisted shielded pairs. Two pairs of lines are required for each calibration array for a total of 16 lines. Aggregate length of these lines is 2438m (8000 ft). Wire size is AWG No. 22.

Although properly a part of the collector subsystem, the essential calibration array is treated summarily here and in complete detail in Section 5. This is in accordance with an outline which requested treatment there of instrumentation and control equipment.

Overall Operation

The calibration array provides a quick and efficient means to make measurements on the redirected beam. With the beam directed toward the array, a series of photodetectors spread across the array provide electrical signal samples of the energy levels throughout the beam. The samples are scaled, multiplexed to a single line, digitally converted and transmitted in serial fashion to the computer upon request.

Beam shape, size, and intensity information are contained in the data block. The data is used in several ways. Energy centroid calculations permit updates to the computer program to correct for differences between the perceived and predicted beam position. This periodic feedback will provide measured checkpoints of how well the system is operating over long periods of time.

Total energy calculations for the beam can also be made from this data which when compared to the energy available can be used to determine when cleaning may be required. The effectiveness of toe-in and focusing can also be determined by comparing measured shape and size patterns to theoretically determined optimum patterns.

Automatic background suppression was used on the SRE which may not be required at the Pilot Plant and beyond. Background suppression consisted of a series of photodetectors set apart from the main array which looked out over the field to provide a measure of the ambient energy. These signals were averaged, inverted and added to each array detector output to enhance the signal to background ratio. This offset measurement was required for the SRE because the beam tracked the array all day long and background suppression of this type proved quite effective. At the pilot and commercial plants, the array will only be used periodically and a readout of the array before the beam is redirected to it will provide direct measurements at each cell which can be accounted for on a cell by cell basis in the computer. This method should be even more effective than the offset method since the same cell will be used for both measurements.

For the pilot plant eight calibration arrays will be used ranging in size depending on section of the field the array is required to service. The arrays will be placed atop the tower. The same MUX unit will be used to relay receiver data down the tower using a single twisted shielded pair for every 256 sensors.

A block diagram of the calibration array and processing electronics is given in Figure 3-44. Details of the system are contained in the following paragraphs.

COMMAND CONTROL ARRANGEMENT

The open loop command and control scheme of the collector subsystem is basically simple. A central processor complex computes the sun vector and knowing the geodetic geometry of each heliostat and the receiver, calculates the required inner and outer axis rotation for each heliostat and issues the appropriate integer commands over a data bus. At each heliostat, the command word is decoded and the respective axis driven to position by keeping track of integer motor revolutions taken from a known reference or start point (initialization) such that the redirected beam tracks a given point on the receiver's cavity wall. Different modes of operation are under computer and/or operator control depending upon the immediate Pilot Plant System requirements.

Figure 3-8 shows a general functional block diagram of the collector subsystem which emphasizes the control interplay. Figure 3-3 presented a drawing tree of the collector subsystem control subsystem (BG8251B1) showing the heart of the control subsystem is the Level 6/43 computer network. Chosen because of (1) 64 vectored interrupts, (2) automatic context save/restore, (3) high bus bandwidth, (4) number of buses, (5) memory address capability and (6) number of device addresses.

Primary functions performed by the control subsystem are:

- a. Computation of the sun vector to each heliostat. For the pilot plant, one calculation per second common to the entire field of heliostats will be adequate. For the commercial scaled plant, a separate geodetic reference sun vector should be calculated once per second for each commercial plant module.
- b. Computation of the mirror normal vector for each heliostat which will satisfy the mode of operation. The required inner axis and outer axis rotation will be calculated once per second and compared with the present orientations for each tilt-tilt heliostat under the computer's control.
- c. Command and control of the heliostats. Commands will be issued at a maximum rate of once per second to each heliostat. If different heliostats (AZ-EL and Tilt-Tilt) are included in the pilot plant, the commands will be in a "universal" format.
- d. Mode control of the collector subsystem field. Present modes include:
 - Stow (or Safe)
 - Initialization

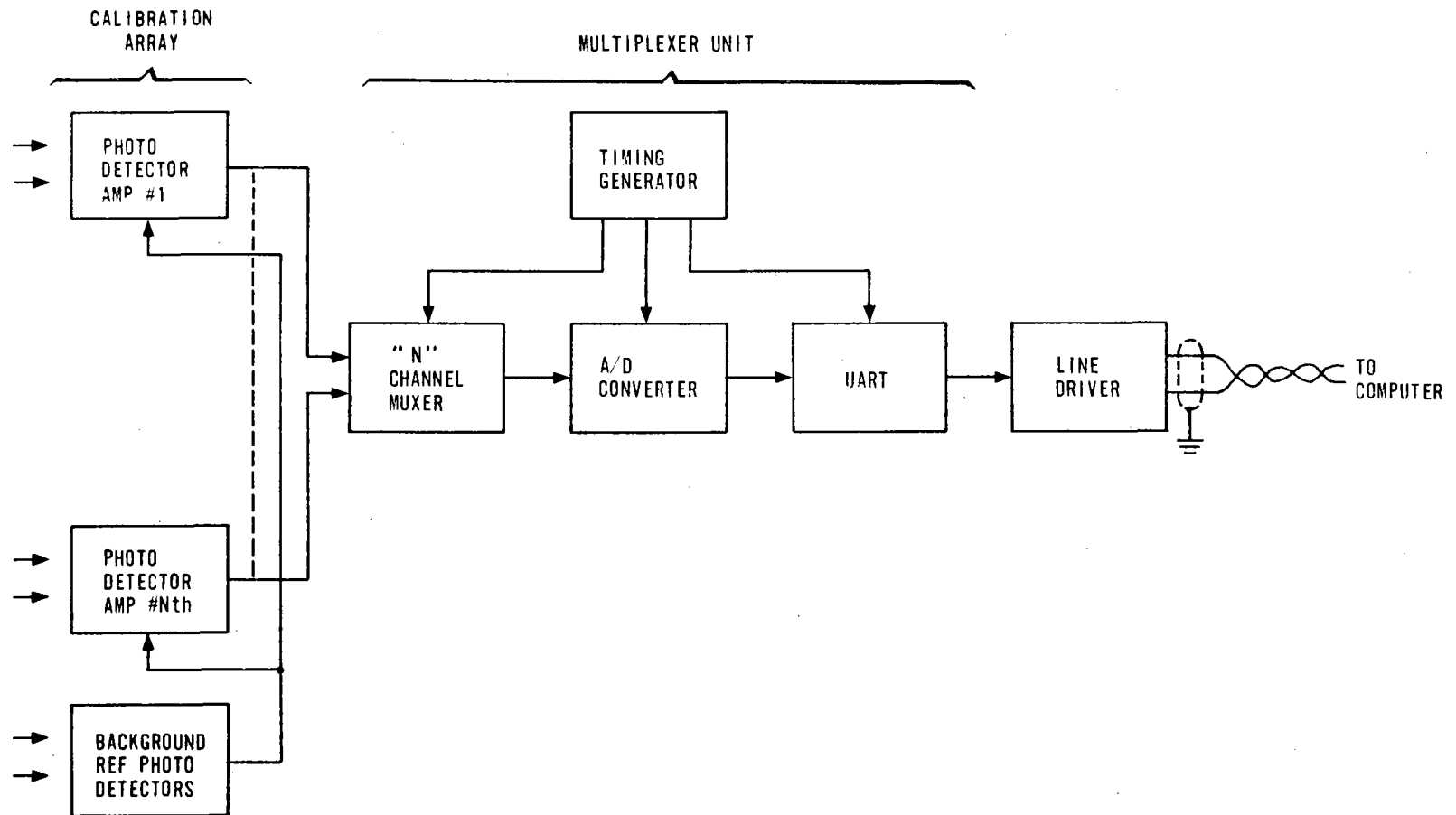


Figure 3-44. Calibration Array and Electronics

- Track Primary Target
 - Track Secondary (or Standby) Target
 - Emergency Defocus
 - Calibrate
- e. Calibration of the heliostats. As required, each heliostat will be sent to a calibration array for accuracy verification and possible offset adjustments made to certain constants.
 - f. Performance monitoring of collector subsystem.
 - g. Provide operator control and interface capability from the operator console.
 - h. Provide displays and visual indicators as required.
 - i. Provide Pilot Plant/Commercial Plant central control computer with the required interfaces and responses.
 - j. Provide the capability for off-line data reduction and analysis.

The overall computer, peripheral, and communication interface is depicted in Figure 3-45.

An artist's conception of the operator Operation Console (PN 34028595) is shown as Figure 3-46.

Computer System Overview

The proposed configuration is a distributed processing system designed for maximum backup, computational capacity, and throughput while keeping cost at a minimum. The primary heliostat control computer configuration consists of dual Level 6/43 central processors with memory management options configured on a single 23 slot megabus (Figure 3-47). This arrangement allows the central processors to share memory and peripherals in a very efficient manner. One Central Processor Unit (CPU) will be dedicated to the computation and initiation of commands to the heliostats, while the second will perform the remaining functions assigned to the control computer system. Both will run self-test routines periodically to verify continued correct operation. Should one of the CPUs fail the self-test, the operator will be notified and its functions will be assumed by the CPU in the Back-up Control Computer System which can interface with all of the devices and memory available to the primary computer via the Inter-System Link (ISL).

The computers, 16 cartridge disks, dual floppy disks, memory and multiline communication controllers will reside in 2 two-bay racks. Two disk drives will be housed separately. An example cabinet is shown in Figure 3-48 surrounded by the chosen peripherals. A recommended floor plan is given in Figure 3-49 and a composite configuration list with part number is shown in Table 3-6. Items indicated with a (•) were not shown within the block diagram of Figure 3-47.

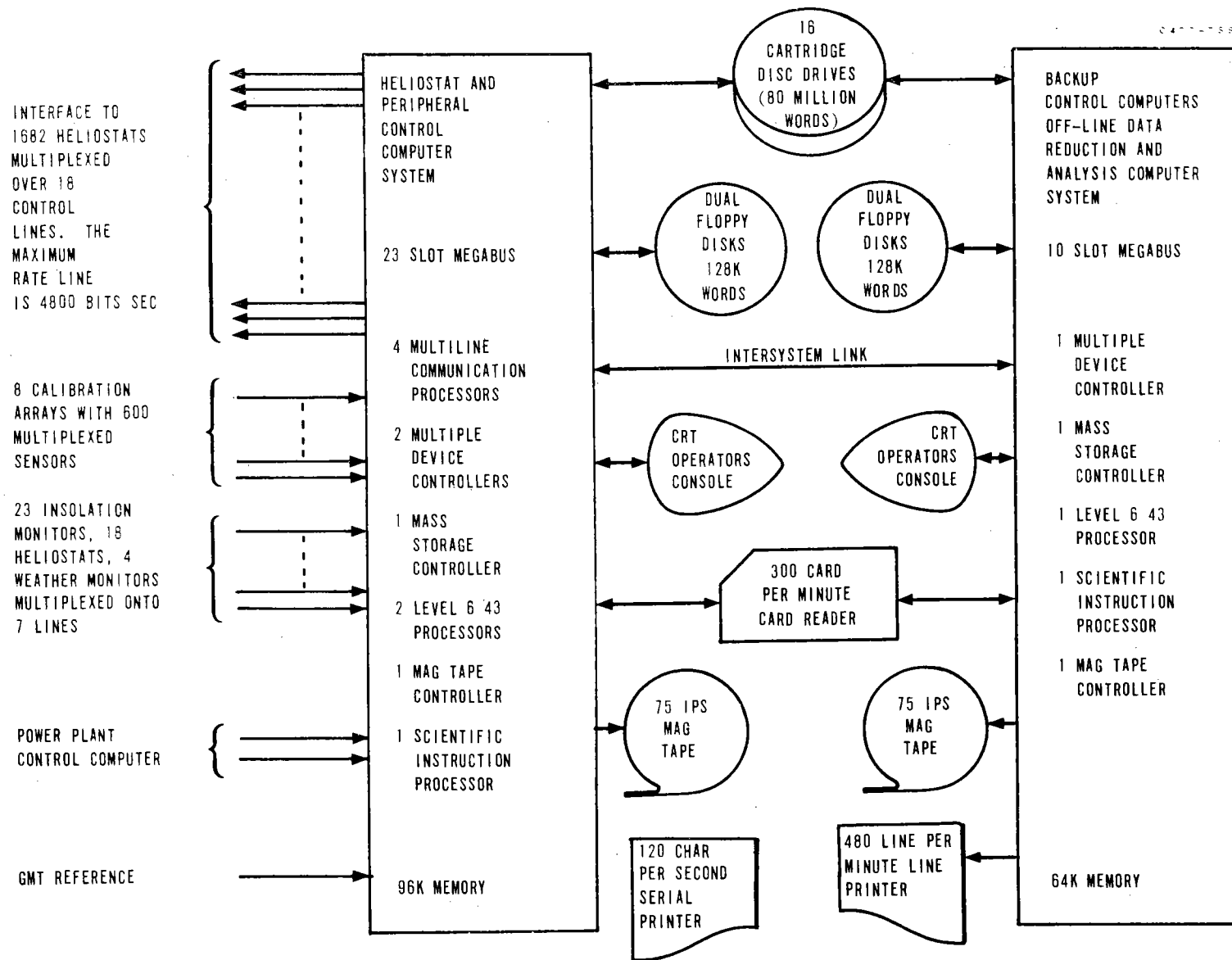


Figure 3-45. Communication Interface

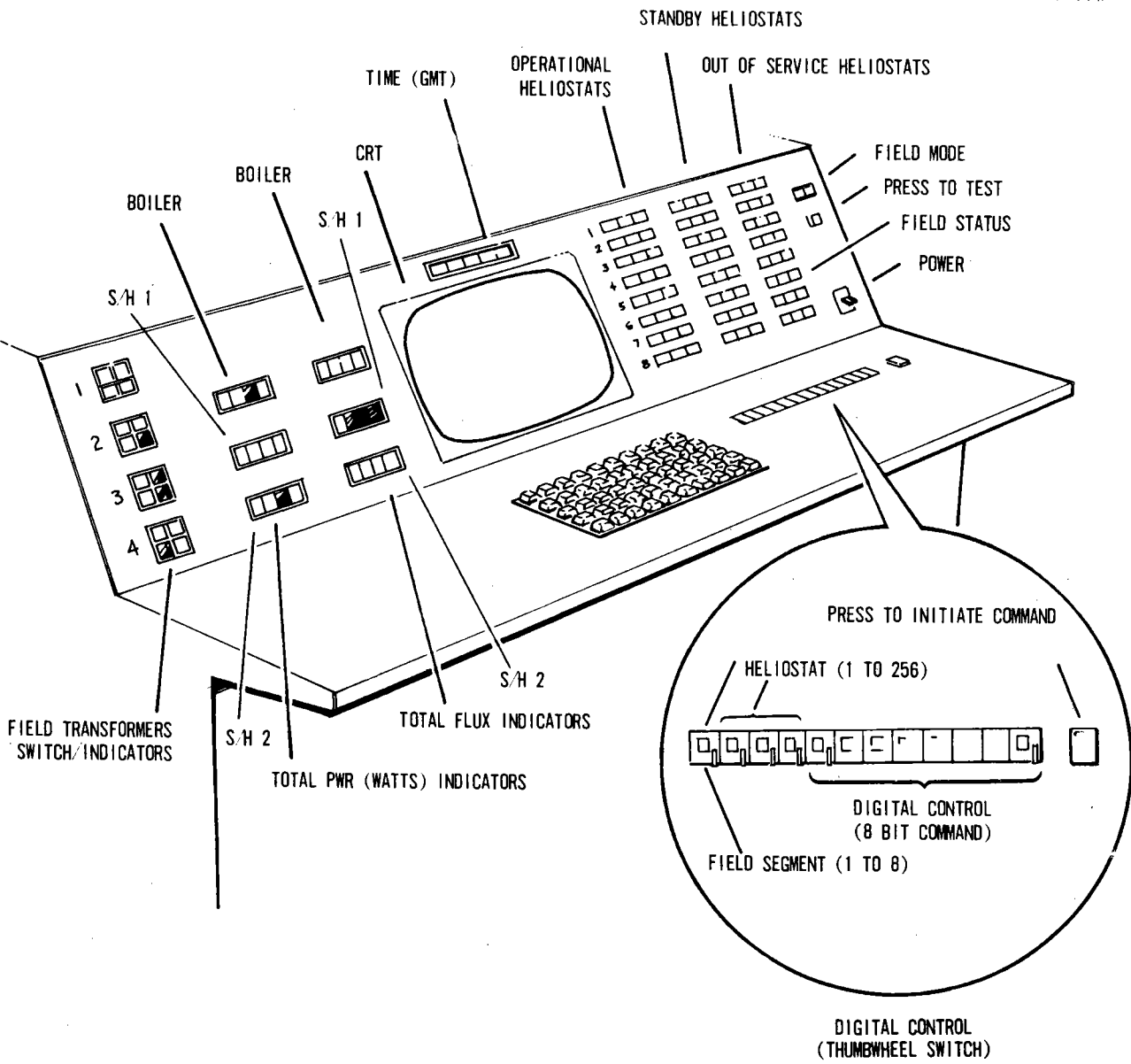


Figure 3-46. Collector Subsystem Operators Console

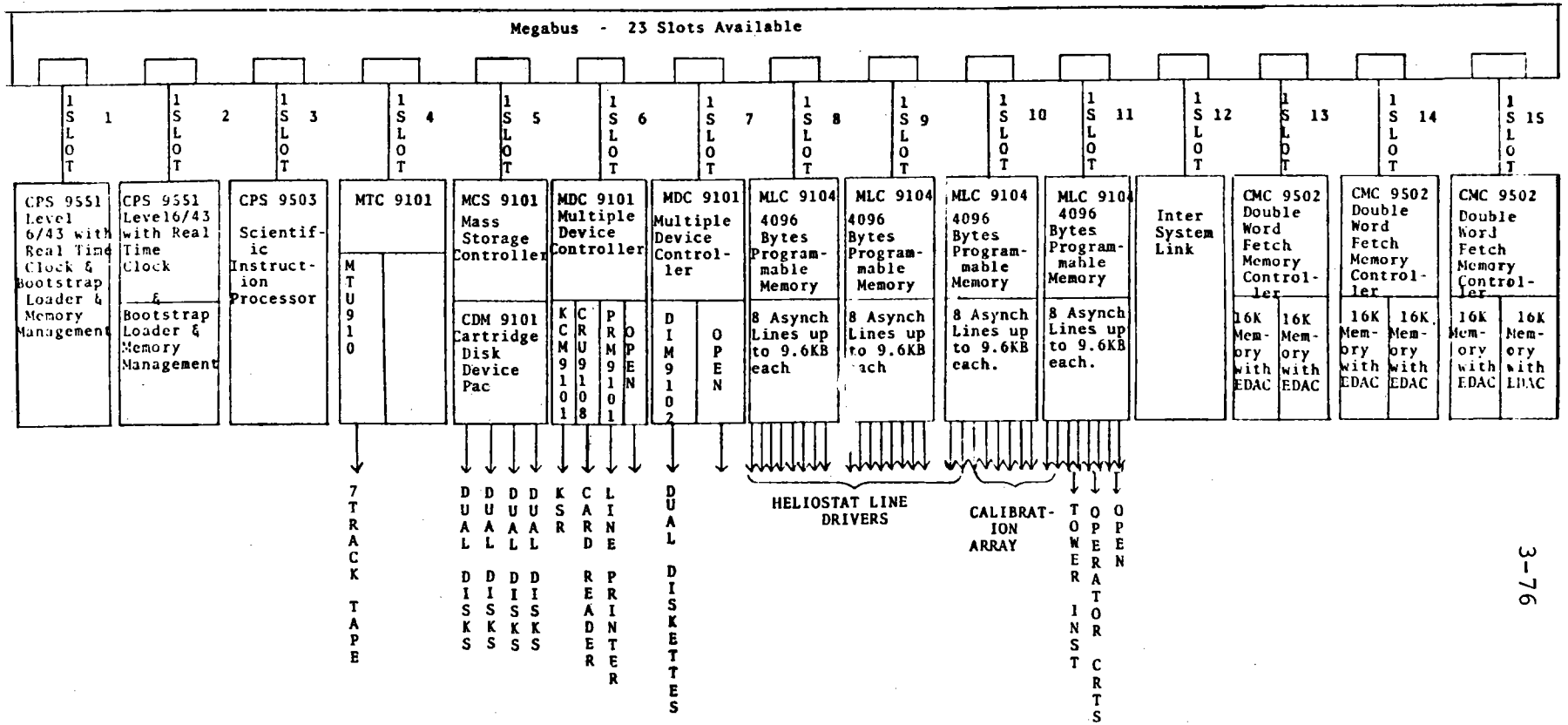
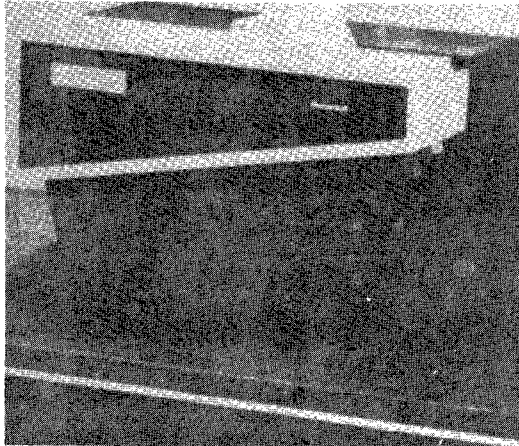
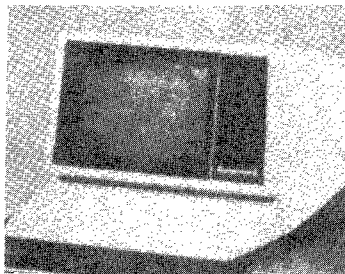


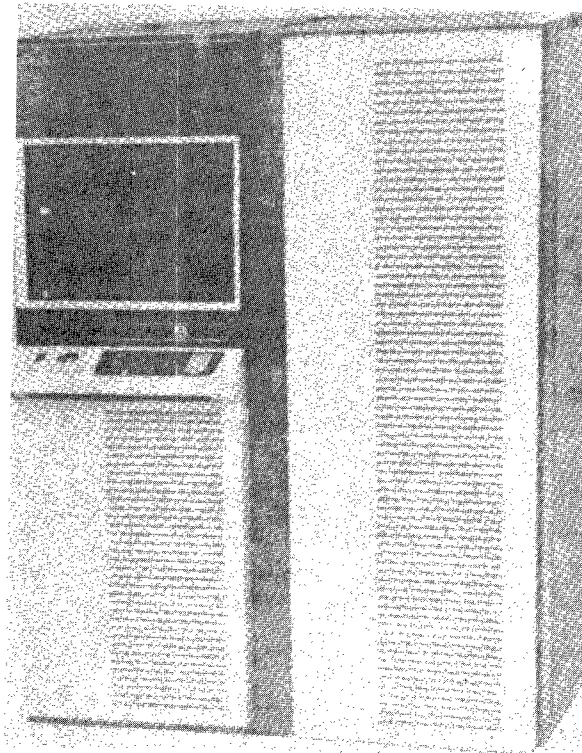
Figure 3-47. Megabus



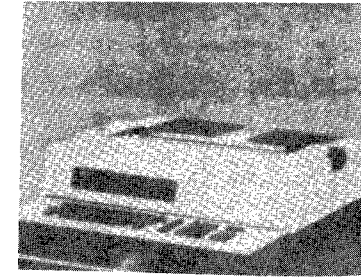
TABLETOP CARD READER



TABLETOP CRT (TTY) AND KEYBOARD



**CAB90003 60 INCH RACK MOUNTED
CABINETS WITH ALL PANELS AND DOORS**



0477-67

**TABLETOP KSR33 120 CPS
KEYBOARD TYPEWRITER CONSOLE**



FREESTANDING LINE PRINTER

Figure 3-48. Rack Mounted Computer and Peripherals

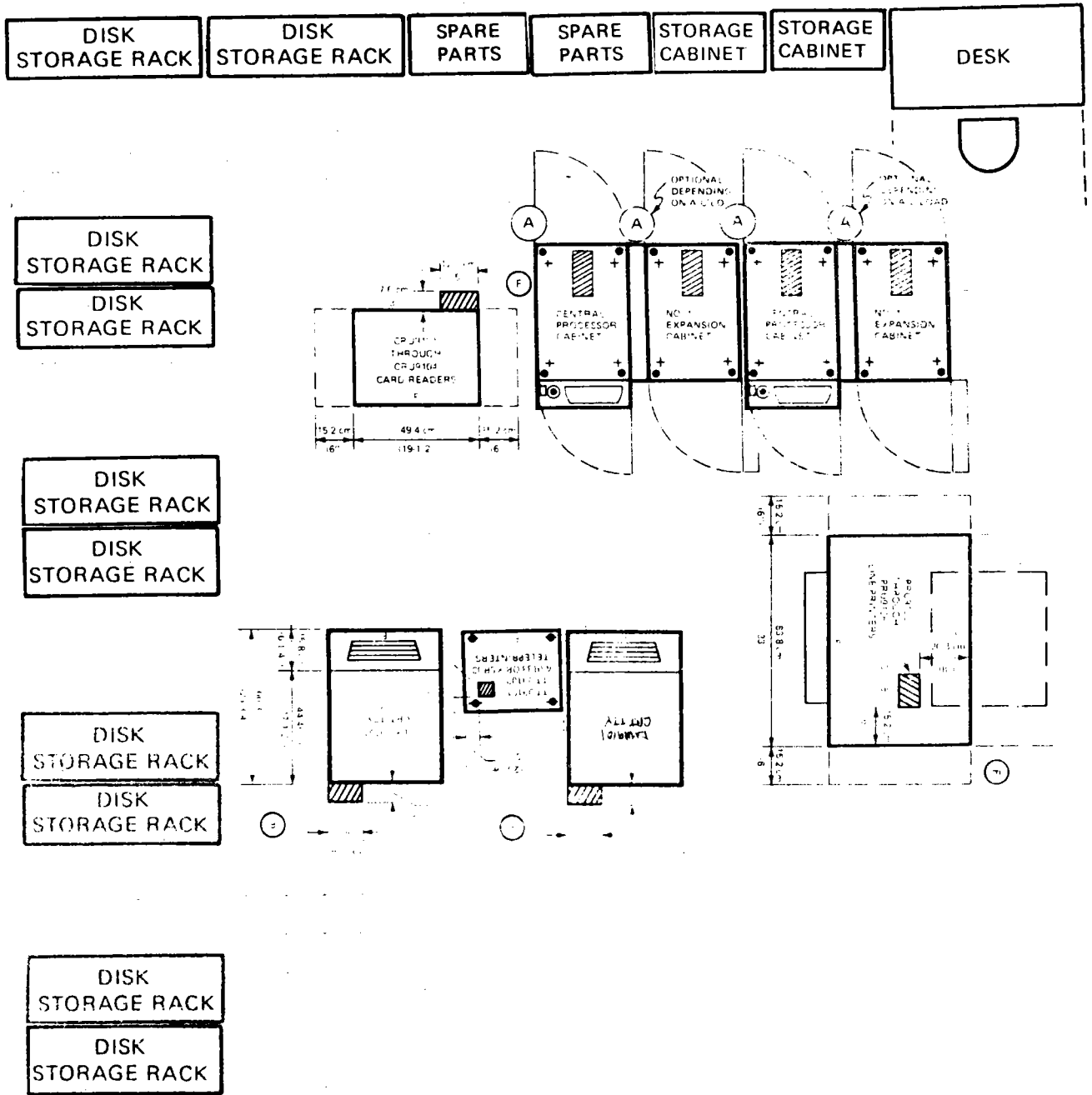


Figure 3-49. Floor Space Plan

Table 3-6. Solar Computer Complex for Pilot Plant
Or One Commercial Plant Module

<u>Part No.</u>	<u>Qty</u>	<u>Description</u>
CPS9551		6/43 in 10 slot megabus
• CPS9552		6/43 in 5 slot megabus
CPF9501	3	Memory Management Option
• CMC9502	3	Double word fetch memory controller with 16KW EDAC memory
CMM9502	3	Additional double word fetch 16KW of EDAC memory
CMC9502	2	Double word fetch memory controller
CMM9502	2	Additional 16KW EDAC memory
CPF9503	2	Scientific Instruction Processor
• PSS9002		Single Phase, 115V, amp PDU (memory save)
CPU9501		6/43 CPU only
• MTC9101	2	Magnetic Tape Controller
• MTU9121	2	7 Track Mag Tape Drive
• MTM9102	2	Device Pac for 7 Track Tape
• CRU9108		300 CPM Card Reader
• CRM9101		Device Pac for Card Reader
• TWU9106		120 CPS Console Typewriter
• KCM9101	2	Device Pac for KSR
MDC9101	2	Multiple Device Controller
• PRM9101		Device Pac for Line Printer
• PRU9105		480 LPM Printer
MSC9101	2	Mass Storage Controller
• CDM9101	2	Device Pac for Cartridge Disk
• CDU9116	8	High density cartridge disk - 1R, 1F
MLC9104		Multiline communications processor with current loop comm pacs with 8 asynch lines up to 9.6KB each, with cables
MLC9104		Multiline communications processor
MLC9104		Multiline communications processor
MLC9104		Multiline communications processor
• VIP7105		Asynchronous CRT/Keyboard Terminal
• CAB9004	2	60 in rack mounted PDU without panels and doors
• CAB9008	2	Panel - one side
• CAB9008	2	Panel - one side

Table 3-6. Solar Computer Complex for Pilot Plant
Or One Commercial Plant Module (Continued)

<u>Part No.</u>	<u>Qty</u>	<u>Description</u>
• CAB9009	2	Door - rear
• CPS946X	2	I/O Channels >48
• CPF9401		Watch Dog Timer
• CPF9402		Multiprocessor Option
• CAB9402	2	9-slot megabus expansion chassis
• DIU9102	2	Dual diskette
• DIM9101	4	Diskette Device Pac
TBD		Inter-System Link

Table 3-7. Priority Levels

INTERRUPTS

Capability	64	
Assigned	18	Heliostat Line Drivers
	1	WDT Watch Dog Timer
	1	CRT/Operator
	2	Disks (Cartridge)
	1	Diskette
	1	ISL
	8	UART for multiplexed calibration data
	1	Serial Printer
	7	UART Multiplexed weather data insulation monitors and heliostats wraparound commands, and selected heliostat resolver data
Total	40	

Computer Architecture

The heart of the Level 6 system proposed for the pilot plant system is the 23 slot Megabus. All elements of the Level 6 central processor, memory, peripheral devices and communication controllers are attached to the Megabus and all transfers (memory, interrupts, instructions) between them take place on the Megabus. It supports high speed asynchronous data transfer between all of the boards plugged into it at rates up to 3 million 16 bit words per second. An extensive use of microprocessors in the design of each motherboard (such as the multiple device controller, multiline communications processor, and mass storage controller) supports input/output to each external noted on Figure 3-47 to proceed simultaneously with internal algorithm computations in the dual Level 6/43 CPU boards and scientific instruction processor. These features plus a large number of program-visible registers, an extensive addressing capability and an instruction set designed for efficient programming make the Level 6 an ideal computer system for the heliostat control problem. Table 3-7 summarizes the primary capabilities of the Level 6 components chosen for the collector subsystem control computer system.

40 of the possible 64 priority levels have been assigned per Table 3-7. There is automatic interrupt identification, as when a device interrupts and identifies itself to the central processor. The Megabus also has an automatic save/restore of context (done normally on other systems by software). This plus parity checking on the Megabus ensures the integrity of data transfers.

The Megabus can transfer either words or bytes. All transfers are of the direct memory access (DMA) type; each device controller maintains its own information about the location in memory to/from which data is to be transferred and accesses that location directly. DMA transfers result in minimal software involvement. Control of the Megabus is distributed; each unit on it contains all of the control and timing it needs to use the bus, without the need for a central control unit of any kind.

A distributed tiebreaking network provides the function of granting Megabus cycles and resolving simultaneous requests. The logic to accomplish this function again resides in every unit on the bus. Priority is granted on the basis of physical position on the bus. Memory is granted the highest priority and the central processor the lowest. Other units are positioned on the bus according to their performance requirements, their priority increasing according to their proximity to memory. Figure 3-47 contains a proposed assignment for the Pilot Plant Primary Heliostat Control Computer System.

Timing

Analysis has shown that the Level 6/43 Processor as previously defined can handle the number of calculations and communications throughput for a field of 1680 heliostats. An analysis for the reduction in the requirements to 1598 heliostats has not been made. For the commercial plant applications, the total computer hardware requirements

will not change even though the number of heliostats per module will increase to 4642 heliostats because no back-up computer will be required for off-line processing within each module. The three CPUs can then be dedicated to heliostat control with a nominal interface of 1548 heliostats per CPU required. The command issue rate can still be once per second update.

The exact timing associated with any Level 6 instruction depends upon the addressing mode associated with it and type of memory in the configuration. The double-pull memory chosen for the Solar Pilot Plant Heliostat Control Computer provides the maximum speed available on the Level 6 today (when the cache memory is formally announced in 1977 it will provide an improvement of approximately 40 percent).

Table 3-8 gives nominal execution times for Level 6/43 instructions using double pull memory. Many of the computations for the heliostat will utilize the scientific instruction processor (SIP) which can execute in parallel with its associated central processor (CPU board).

Table 3-9 gives detailed execution times for a selection of the scientific instructions available with the SIP when double pull memory is not utilized. Its inclusion will result in an improvement of approximately 60 percent. Of special interest is the last column in the table which notes the amount of time available for parallel execution in the CPU and SIP.

Software

There are three groupings of software applicable to the pilot plant or commercial plant:

1. The basic operational program
2. The support software to perform the systems functions
3. Performance analysis off-line software

Operational Program

Experience with the SRE operational program has demonstrated the concept of the majority of the proposed pilot plant and commercial plant operations.

- Open loop tracking via commands to heliostats
- Secondary target attainment
- Calibration via the calibration array
- All required vector calculations and beam correction factors
- Flexible operator responses
- Recording data for off-line data analysis

A listing of the program used in the SRE is provided as Appendix E to this PDR. Additional effort will have to be spent to separate the coding for the following new areas.

Table 3-8. Nominal Level 6/43 Execution Times

Load Index Register	2 μ sec
Load Base Register	2.5 μ sec
Add Subtract	1.2 μ sec
Multiply	8 μ sec
Divide	10 μ sec

Table 3-9. Performance of Scientific Instructions
(Normal Memory)

Instruction	Instruction Address Format	Overall Instr Time (μsec)	Available SIP/CPU (for overlap)
Multiply	SA _D op SA _D	8.15	1.63/6.12
	SA _Q op SA _Q	11.45	1.63/9.42
	R op SA	8.60	1.63/6.01
	RR op SA	12.40	1.63/9.45
	M _D op SA _D	10.04	1.83/6.38
	M _Q op SA _Q		
Divide	SA _D op SA _D	7.17	1.63/5.14
	SA _Q op SA _Q	14.52	1.63/12.49
	R op SA	7.62	1.63/5.03
	RR op SA	15.47	1.63/12.52
	M _D op SA _D	9.06	1.83/5.40
	M _Q op SA _Q	17.64	1.83/13.98
Compare	SA _D op SA _D	3.27	1.63/1.24
	SA _Q op SA _Q	3.27	1.63/1.24
	R op SA	3.72	1.63/1.13
	RR op SA	4.22	1.63/1.27
	M _D op SA _D	5.16	1.83/1.50
	M _Q op SA _Q	6.39	1.83/2.73
Branch	Branch on Indicator	3.23	1.63/0.0
Branch	Branch on Accumulator	3.23	1.63/0.0

op - Operation, SLD (Scientific Load)
 SA_D - Scientific Accumulator (Double word length)
 SA_Q - Scientific Accumulator (Quadruple word length)
 SA - Scientific Accumulator (D or Q word length)
 M_D - Main Memory Location (Double word length)
 M_Q - Main Memory Location (Quadruple word length)
 R - Central Processor Register (Single integer length)
 RR - Central Processor Registers (Double integer length)

Table 3-9. Performance of Scientific Instructions
(Normal Memory)
(Continued)

Instruction	Instruction Address Format	Overall Instr Time (μ sec)	Available SIP/CPU (for overlap)
Load	SA _D SA _D	2.28	1.63/0.25
	SA _Q SA _Q	2.28	1.63/0.25
	R SA	2.73	1.63/0.14
	RR SA	3.23	1.63/0.28
	M _D SA _D	4.17	1.83/0.51
	M _Q SA _Q	6.00	1.83/2.34
Store	SA _D SA _D	2.28	1.63/0.40
	SA _Q SA _Q	2.28	1.63/0.40
	SA R	2.79	1.63/0.0
	SA RR	3.55	1.63/0.0
	SA _D M _D	4.43	1.83/0.77
	SA _Q M _Q	5.73	1.83/2.07
Swap	SA _D SA _D	2.78	1.63/0.75
	SA _Q SA _Q	2.78	1.63/0.75
	R SA	3.79	1.63/0.0
	RR SA	4.55	1.63/0.0
	M _D SA _D	6.67	1.83/3.01
	M _Q SA _Q	9.20	1.83/5.54
Add Subtract	SA _D SA _D	3.75	1.63/1.72
	SA _Q SA _Q	3.57	1.63/1.54
	R SA	4.20	1.63/1.61
	RR op SA	4.52	1.63/1.57
	M _D op SA _D	5.64	1.83/1.98
	M _Q op SA _Q	6.69	1.83/3.03

- Monitor large quantity of meteorological data
- Pilot Plant level control (master control) and interface modules
- Control of beam travel in prescribed sequences and trajectories for safing reasons
- Calibration sequencing of a field of heliostats
- Start-up and shut down sequences
- Control redirected insolation as a function of cloud coverage and receiver constraints
- Revise calibration algorithms
- Maintain status on each heliostat, provide displays to operator
- Computer and console self-tests.

It is envisioned that most of the programming can be done in a higher order language (FORTRAN) using newly developed optimizing Level 6 compilers for improving timing and memory management. In line assembly coding must be used for input/output command formulations and issuance/receipt. The SRE experience has shown that no double precision arithmetic is required.

Level 6 Software Characteristics. Level 6 offers both a basic and an extended software capability.

General Comprehensive Operating System (GCOS) 6/3 performs the chief system functions needed for program development, checkout and support. Figure 3-50 provides an overview of the various modules, languages, programs, and development tools.

The program development tools are comprised of: a Command Processor that interacts with the Loader to bring the other system modules into memory, two language processors; a FORTRAN Compiler and an Assembler for the Level 6 Assembly Language, an Editor for correcting the source text of programs written in either language, a Linker that converts object modules from the Assembler or the compiler into an executable form, and a Cross-Reference Program, which is a utility that relates the symbolic tags of an assembly program to the listing line numbers where they appear. Figure 3-51 summarizes a sequence of events that will take place during the development of the Solar Pilot Plant Program.

Executive Modules

The Executive software is a basic set of support facilities such as peripheral drivers, disk and diskette file managers, buffer manager, clock handler, automatic task scheduler and dispatcher based on a flexible priority/interrupt structure, and the trap manager for certain conditions arising out of program execution, etc. Figure 3-52 shows the interrelationships of the Executive modules with the heliostat control computer programs.

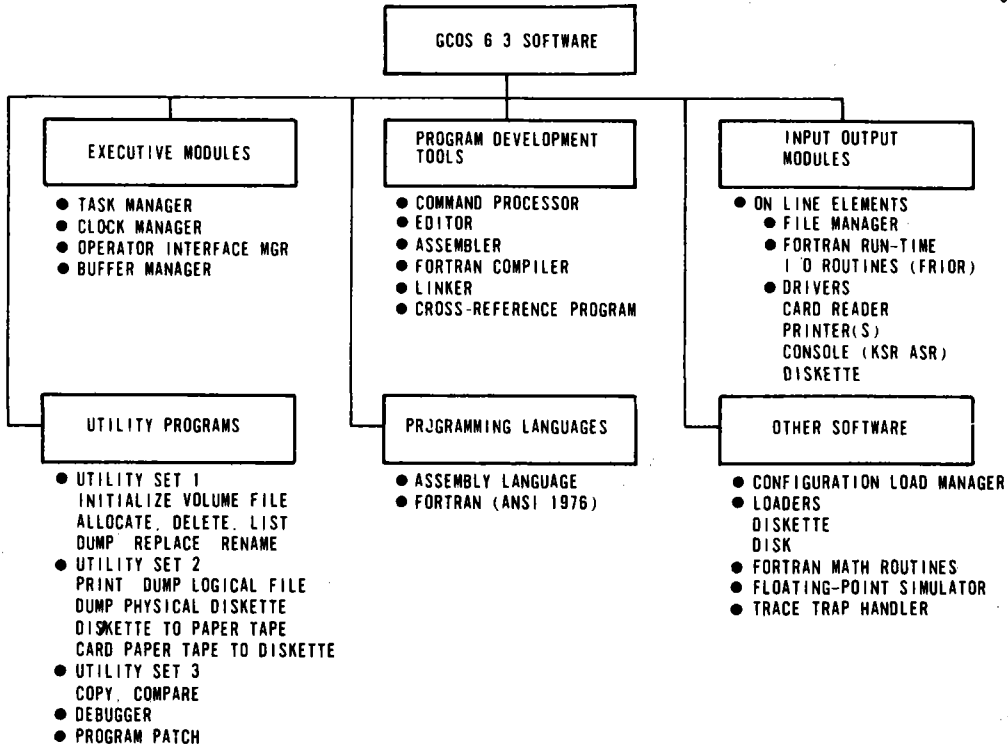


Figure 3-50. Software Overview

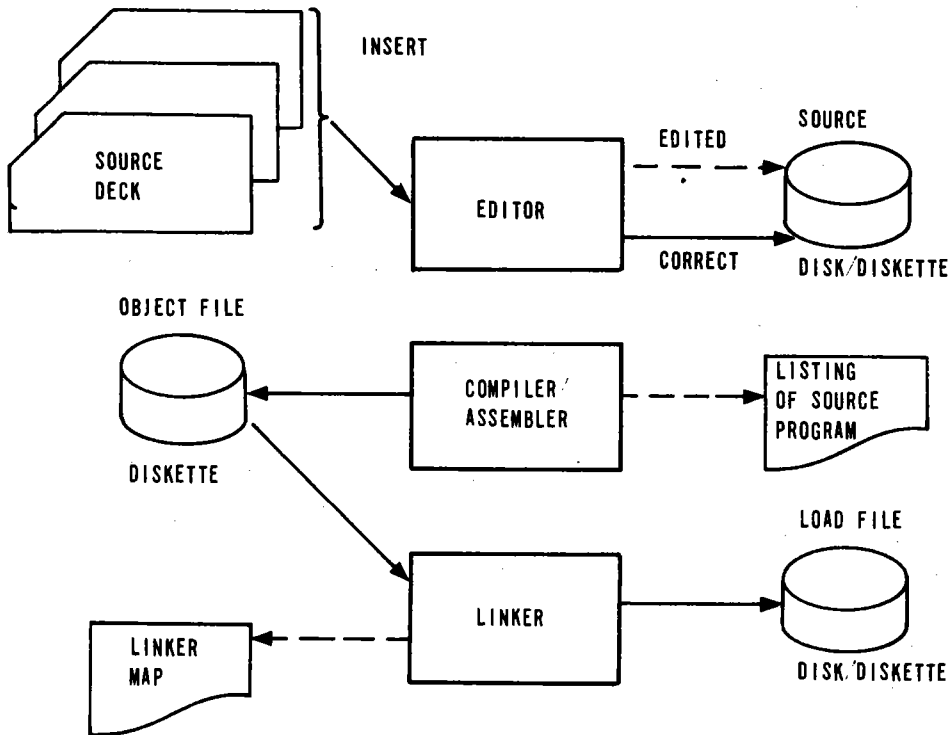


Figure 3-51. Program Development Sequence

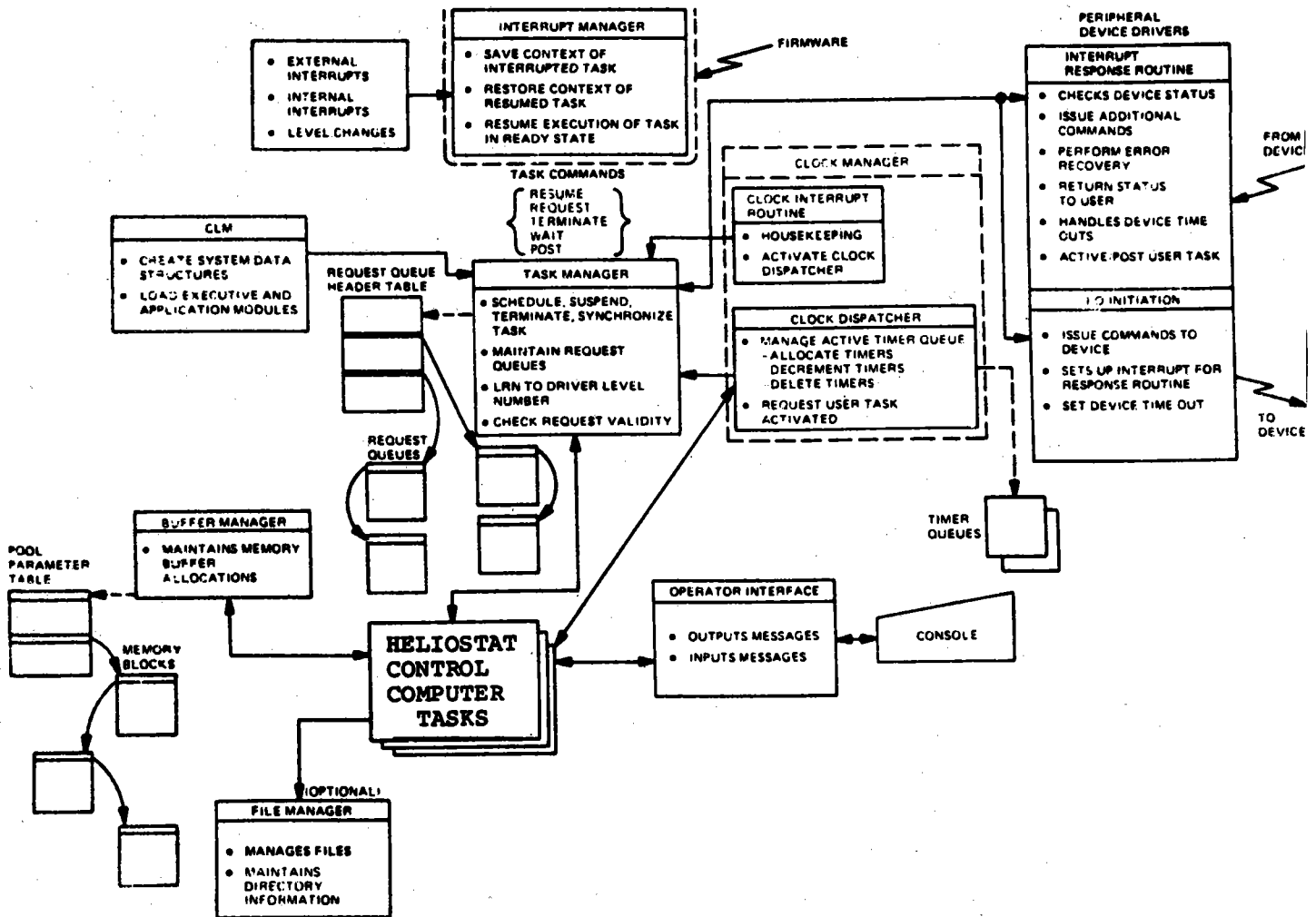


Figure 3-52. Interrelationships of the Executive Modules With the Heliosat Control Computer Tasks

Test Data Reduction Programs

Programs to reduce recorded data were developed for the SRE to evaluate tracking accuracy and redirected energy flux maps. However, the data analysis requirement for the pilot plant applications will be far more extensive. With the back-up Level 6 computer, full consideration was given to provide the computational power be able to

- Reduce daily energy data and calibration, per heliostat, data
- Generate plots and other evaluation tools
- Compile special purpose programs for correlation studies
- Flag trending problem areas
- Store large quantities of intermediate data via disk and tape for future off-line data reduction use and distribution to other interested parties
- Determine better calibration algorithms and/or procedures
- Correlate day to day energy capture with respect to the following influences:
 - Calibration interval
 - Communication link wraparound check failures
 - Temperature
 - Wind
 - Insolation levels
 - Shadowing and blocking
 - Humidity
 - Time of year versus toe-in setting (flux mapping via calibration array)
 - Parasitic power
 - Storage subsystem usage and performance
 - Control philosophy (how early and sequence to get on target, whether to stow or not during short interval rains, etc.)
 - Receiver efficiency.

The detailed requirements for data analysis will be generated during the detail design phase of the pilot plant collector subsystem development. Coding will be done during the period of hardware fabrication and obviously new requirements will materialize as the initial plant integration and checkout start.

Post test data reduction activities for the commercial plant will be obviously reduced because of the non-experimental nature of the commercial plants and many environmental correlation characteristics will have been determined during Pilot Plant testing.

CONCLUSION

All major elements of the collector subsystem have been discussed including heliostats, field computers, and software. All of these elements were proven capable and effective during the SRE efforts. This preliminary design represents a minimum risk and cost effective solution to the pilot plant collector system design problem.

Section 4
PERFORMANCE ANALYSIS AND TRADE STUDIES

The purpose of the first part of this section is to delineate those items of analysis which show our heliostat design is ready to support the pilot plant. Since the same heliostat is used for pilot and commercial plants all of these analyses are equally applicable to the commercial design.

The second part of this section describes trade off studies and design choices which were made during the preliminary design contract.

The following paragraphs treat mechanical and electrical analyses which are followed by the trade offs.

ANALYSIS SUMMARY

Mechanical analysis has provided early operational success (SRE), cost effective design and a foundation for future development. Extensive analysis work has been performed to support the pilot plant preliminary design.

An overview of areas investigated is shown below. Although it would be impossible to present all of the analysis done to date this summary and the following subsections provide a picture of the analytical depth along with key results. Analysis details may be found through the listing of Technical Coordination Letters (TCLs) listed in Section 6.

1. Structural Analysis

• STARDYNE

Deflection and stress under wind loads

Deflection under "g" loading at variable gimbals angles

• Other

Thermally induced stress--Ref TCL-SRE-36

Column loading analysis--Ref TCL-SRE-35

Frame braces

Tie rods

Actuators

Support posts

Reinforced concrete analysis

Torsion stiffness analysis

2. Aerodynamic Loading (Ref TCL-SRE 66)

Wind forces at 13.5 m/s and worst case gimbal angles.

- Total Moment (wind 1 to outer axis) 346 kg-M (30,000 in.-lbs)
- Total Drag (wind 1 to outer axis) 298 kg (658 lbs)
- Total Lift (wind 1 to outer axis) 368 kg (810 lbs)

Total Drag Force at 54 ms 488 kb (1,074 lbs)

(Storage position, wind velocity perp to heliostat outer axis)

(NOTE: Moment are peak values of oscillatory plus center of pressure components. These are used for sizing structural stiffness. Motor torque requirements are based on center of pressure effects only. All values include wind shear effects.)

3. Pointing Accuracy Analysis

Spring rate effects

Manufacturing and assembly tolerances

Backlash effects

Bearing runout and fit effects

Thermal effects

Alignment resolution

Mass imbalance effects

Inner axis mm versus tie rods and crank arms
Actuator imbalance

4. Thermal Analysis

Pointing (toe-in) error due to differential thermal expansion.

Tie rod stress due to differential expansion.

Study of sensitivity to changes in solar heating and ambient temperature. Ref TCL-SRE-36.

5. Drive System Analysis

Bearing loads and life

Friction torque load on motor

Wind torque loads on motor

Variable 'g' torque loads on motor (imbalance effects)

Torque loads due to thermal effects

Reflected inertia

Motor sizing analysis

Reduction ratio of linear actuator drive

6. Mass Properties Analysis

Weight estimate

Center of gravity

Mass moment of inertia reflected at motor

Actuator imbalance versus gimbal angle

Mirror drive balancing

7. Image Analysis

Image size and shapes

Cosine effects

Mirror shape effects

Reflectance effects

8. Coordinate Transformation Analysis

Conversion of pointing error in three different heliostat frames into a target oriented frame.

9. Motor Sizing Analysis

Comparison of load factors (torque, speed, gear ratio, drive train efficiency) to motor capabilities for both inner and outer axis gimbal drives.

10. Control Loop Stability Analysis

Verifies stability of drive system under quantum input commands.

11. Heliostat Servo Output Amp Small Signal Simulation and Analysis12. Analysis of Heliostat Response to Environmental Effects13. Analysis and Prognosis for Commercial Plant Changes14. Calibration Array Analysis15. Heliostat Location Analysis**STRUCTURAL STATES AND DYNAMIC ANALYSIS**

Structural analysis was conducted on the complete heliostat assembly. A large scale digital computer program known as STARDYNE was used for these analyses. The program was written and is maintained by Mechanics Research Inc. It is available for use through remote computer facilities of Control Data Corporation. Honeywell Report 876-13994, dated 29 September 1976 is a complete, detailed, report of analysis techniques and results. Separate analysis was conducted on the mirror modules by Parsons Corporation and a summary of the results are presented.

A complete analysis was conducted for the Parson's mirror modules used on the engineering model heliostat. The changes made in the design of the research experiment heliostats were not of major significance

insofar as structural properties were concerned. The updated analysis was limited to a check of predicted torsional deflection. Mirror modules for the pilot plant will be of similar design. The results of these analyses are:

Maximum Skin Stress	- 129 kg/cm ²	(1837 psi)
Maximum Bending Stress	- 46.5 kg/cm ²	(662 psi)
Maximum Shear Stress	- 386 kg/cm ²	(5492 psi)

The margin of safety for combined bending and shear stress is 2.8. Obviously stress is not a major consideration. Torsional deflection analyses were conducted and predicted 0.7 mr at a maximum torque of 79 kg-m (7500 in-lbs). Tests conducted on two mirror modules confirmed the torsional deflection and indicated stresses were not critical.

In laminated structures exposed to solar radiation and containing several types of materials two potential failure modes require special attention. These are thermal stresses created when materials with different expansion coefficients are rigidly bonded together and creep failure in bond joints where stresses are present with high temperatures. The design and construction of the mirror modules have considered these potential problem areas. The expansion coefficient for the structure in the plane of the mirror has been closely matched to the glass mirror by using aluminum clad steel skins over the honeycomb. This material has only a thin cover of aluminum as a corrosion protection and bonding improver over the basic steel sheet. The expansion coefficient of steel is 16.2×10^{-6} cm/cm - °C (9×10^{-6} in/in - °F) compared to 7.2×10^{-6} cm/cm - °C (4×10^{-6} in/in - °F) for glass. This is a reasonably close match. Analysis and test data has shown satisfactory stress levels in the two bond joints and approximately 0.25 cm (0.1 in.) structural foam in the contoured area between the glass and the front skin of the structure. Creep failures occur when constant strain is present in a structure and the resulting stress is relieved by temperatures above recrystallization temperature for the material. The Honeywell mirror module design does not create stress in the bond joint at the mirror above the almost insignificant stress produced by glass weight of 62.6 kg (138 lbs), supported by 10 m² of bond area (<<1.0 psi). The temperature of this bond will not exceed 60°C (140°F). Creep failures simply do not occur at this insignificant stress level and temperature.

Preliminary analyses were conducted on various parts of the frame and on a complete frame using simulated mirror modules. These preliminary analyses were used in the initial evaluation of the frame. The initial frame concept was a welded bar joist configuration. The most critical portion of the frame was the cantilever beam supporting the two end mirror modules. A STARDYNE computer model of this portion of the frame was made and analyses conducted for vertical loads and loads that exist when the frame was rotated 75 degrees about the axis. The results showed the 15.24 cm (6 in.) by 35.56 cm (14 in.) bar joist design was adequate except for a minor problem relative to rotation

about its length. This could be corrected simply by adding a cross brace. The analysis was repeated for a 25.4 cm - 37.2 kg/m (10 in. - 25 lb/ft) wide flange. The results showed inadequate torsional stiffness which was corrected by welding 0.317 cm (1/8 in.) plates between the flanges on both sides. The analysis then showed adequate torsional design.

A complete frame was modeled on the STARDYNE program. The frame design was for 25.4 cm - 37.2 kg/m (10 in. - 25 lb/ft) wide flange beams with torsional stiffeners. The mirror module were simulated and entered into the model. The analysis showed deflections and stresses within acceptance limits.

The following reported data is a complete structural analysis of the heliostat as finally configured for the solar research experiments. A complete model of the frame, mirror module support posts, crank arms, tie-rods, etc. was used. Static and dynamic analyses were conducted using the STARDYNE programs at two frame positions and for one wind load condition.

The complete model was analyzed considering that the heliostat was in the stowed position. In this position the frame is horizontal and the mirror modules are face down. A one "g" static load was applied to all elements of the structure. The results obtained were deflections, loads and stresses for the structure. All data was within acceptable limits. Deflections, rotations and stresses of various heliostat structural components are presented in Figure 4-1. Maximum stresses occurred in the outer axis bearing pin and was 10, 430 psi. This yields a 2.47 margin of safety. A complete STARDYNE analysis was conducted with the heliostat rotated 75 degrees about the frame axis and the mirror modules face up and parallel to the plane of the frame. Analysis was conducted for a one "g" static load, a 13.35 m/sec (30 mph) wind load and a combination of the static and wind load. Deflections, rotations and stresses of various heliostat structural components are presented in Figure 4-2. The maximum stress of 18,202 psi occurred on the outer axis pin. This yields a margin of safety of 1.0. The steel used in the frame had a yield strength of 36,000 psi.

Dynamic analysis of the heliostat was conducted using the same structural model and position as the original static analysis. This was the stowed position with frame horizontal and mirror modules face down. All eigenvalues (natural frequencies) of the structure were determined by the STARDYNE program. The Householder-QR model extraction technique was used. There were 198 natural frequencies ranging from 2.7 Hz to 1555 Hz. The higher frequencies are not significant in a structure of this size since sufficient energy at the frequency is not normally available to excite them and/or they are insignificant portions of the structure. The first 20 eigenvectors were considered for later stress and deflection analyses. The modes were analyzed to determine major components in resonance at the various frequency. As an example the first mode shapes is presented in Figure 4-3 and Figure 4-4. Figure 4-3 sketches the primary rotation of the four mirrors, in phase. The results of computer graphics presentation is given in Figure 4-4.

Location	Maximum at Mirror Module		Maximum for Frame		Maximum Stress*	
	X3 Deflection (IM)	Rotation About X2 (MR)	X3 Deflection (IM)	Rotation About X2 (MR)	Moment (PSI)	Shear (PSI)
Front Main Beam	0.130	0.75	0.166	0.80	2,143	1,220
Rear Main Beam	0.207	0.035	0.218	1.50	1,993	1,018
Cross Beams	---	---	0.082	--	15,940	3,220
Outer Axis Pins**	---	---	0.0025	--	10,430	5,220

* Maximum moment stress and maximum shear stress did not necessarily occur at same point

** Maximum stress point in frame

Figure 4-1. Summary Heliostat Deflections and Stresses Heliostat in Horizontal Position 1G Static Load

1G STATIC LOAD

Location	Mirror Module Mounts				Maximum For Frame				Maximum Stress*	
	X3 Deflection (in)	X1 Deflection (in)	Rotation About X3 (mr)	Rotation About X2 (mr)	X3 Deflection (in)	X1 Deflection (in)	Rotation About X3 (mr)	Rotation About X2 (mr)	Moment (psi)	Shear (psi)
Front Main Beam	0.022	0.167	2.4	0.25	0.047	0.230	2.45	0.26	7,350	3,680
Rear Main Beam	0.022	0.167	2.3	0.37	0.047	0.230	2.3	0.230	6,206	3,570
Cross Beams	---	---	---	---	0.015	---	---	---	2,741	4,150
Outer Axis Pins**	---	---	---	---	---	0.0085	---	---	16,754	8,390

1G STATIC +30 MPH WIND

Location	Mirror Module Mounts				Maximum For Frame				Maximum Stress*	
	X3 Deflection (in)	X1 Deflection (in)	Rotation About X3 (mr)	Rotation About X2 (mr)	X3 Deflection (in)	X1 Deflection (in)	Rotation About X3 (mr)	Rotation About X2 (mr)	Moment (psi)	Shear (psi)
Front Main Beam	0.007	0.145	2.3	0.63	0.031	0.216	2.4	0.68	7,709	3,860
Rear Main Beam	0.081	0.145	2.3	0.48	0.038	0.216	2.35	0.98	6,396	3,700
Cross Beams	---	---	---	---	0.015	---	---	---	3,438	4,710
Outer Axis Pins**	---	---	---	---	---	0.0097	---	---	18,202	9,110

*Maximum moment and shear stress not necessarily at same point

**Maximum stress point in frame

Figure 4-2. Summary Heliostat Deflections and Stresses, Heliostat at 75 Degrees Outer Axis Rotation

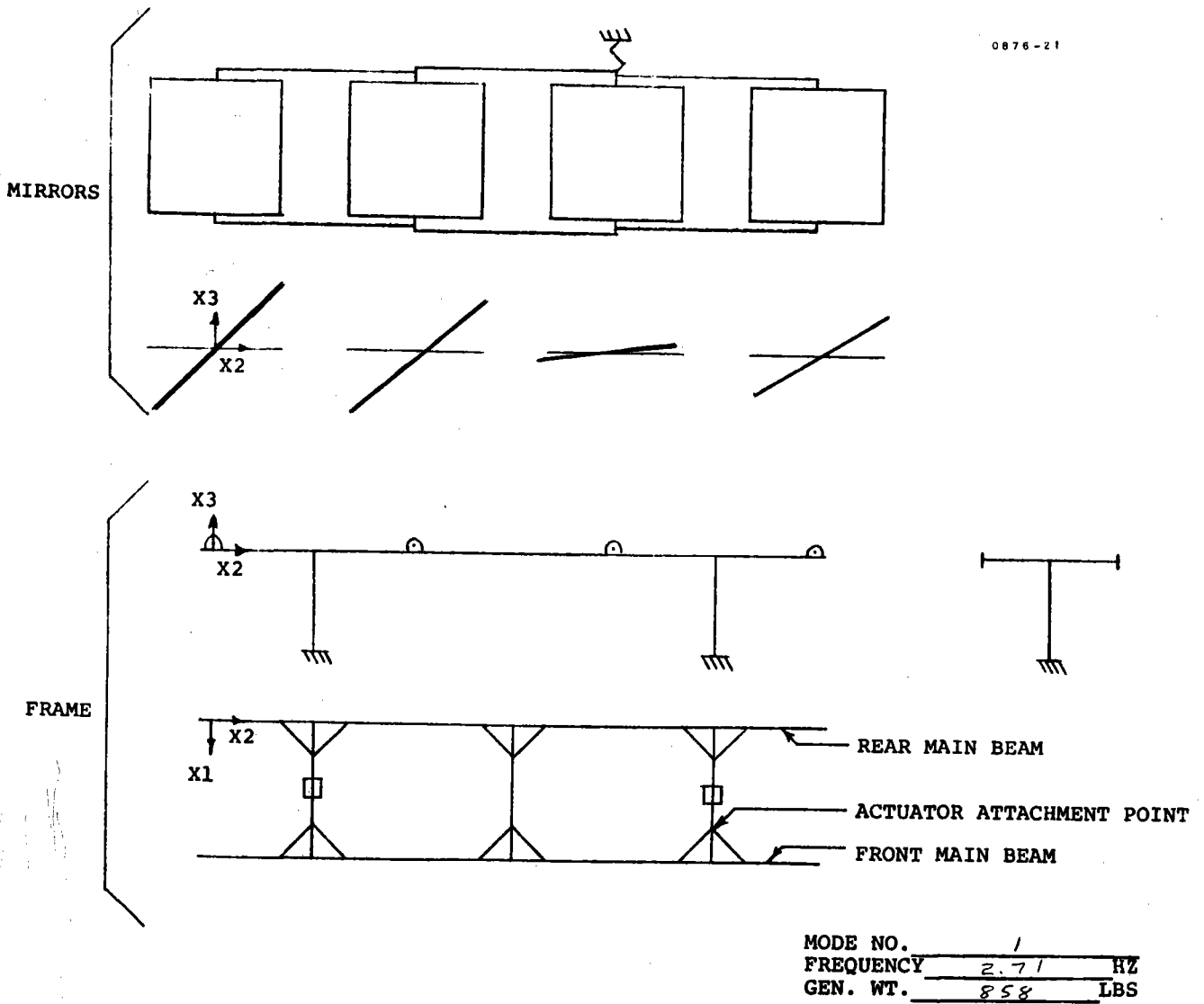


Figure 4-3. Modal Shape Heliostat in Stowed Position

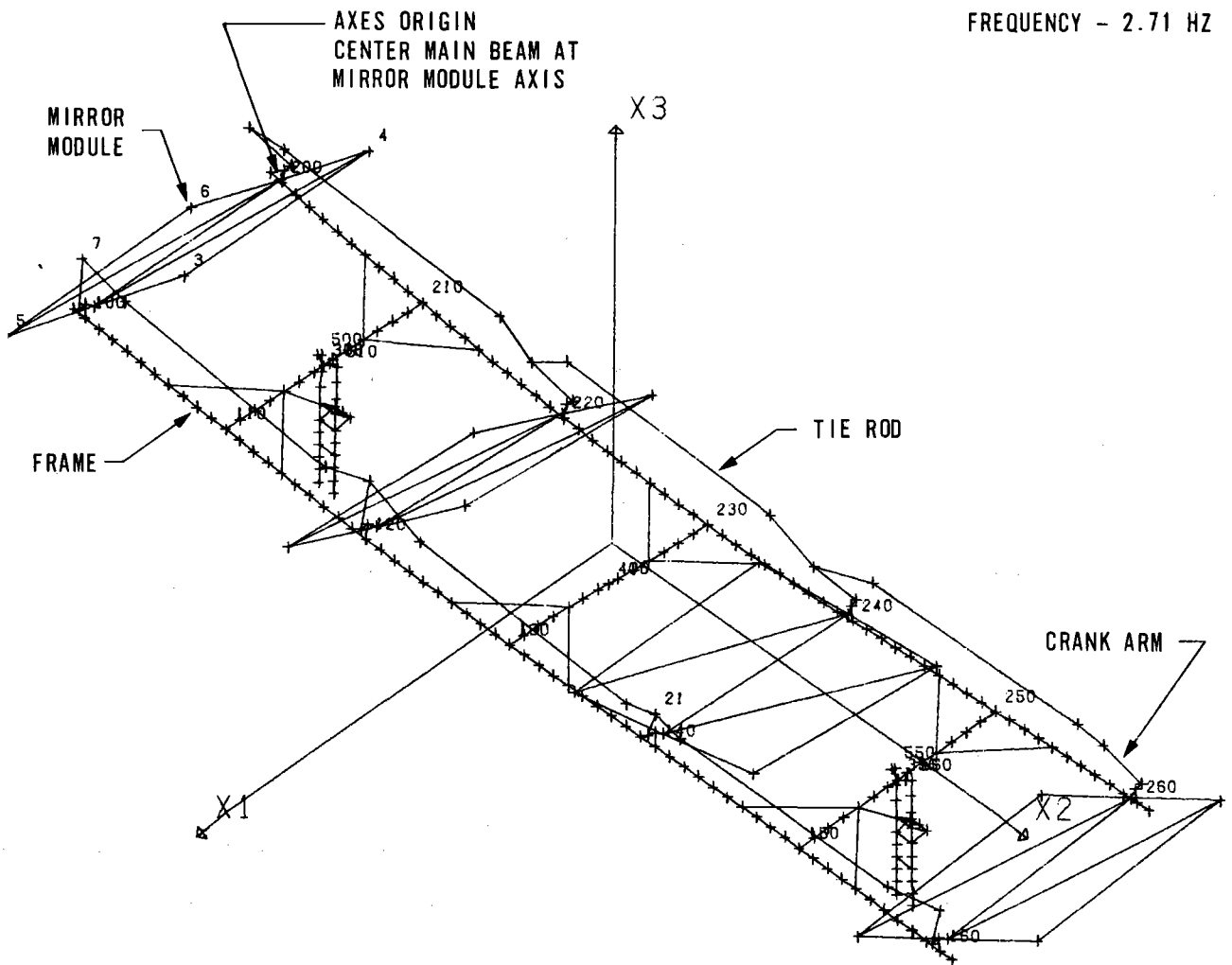


Figure 4-4. Deformed Plot - Heliostat Horizontal - First Mode - Mirror Modules Displacement Case 1

A summary of some of the modes of particular interest follows:

<u>Natural Frequency</u>	<u>Description of Mode</u>
2.7	Mirror Module rotation. Three units in phase.
3.2	Frame bending in X1 direction.
3.9	Frame rotation
4.3	Frame bending in X3 direction
4.60	Frame bending in X3 direction plus mirror module torsion
4.7	Frame bending in X3 direction
4.9	Mirror module rotation. Three units, two in phase with 180 degrees shift to third
4.9	Post bending in X3 direction
6.0	Frame bending in X3 direction
6.2	Mirror module rotation. Two units out of phase.

A survivability analysis was conducted using the finite element model and data obtained in the Householder-QR reported above. The analysis was a transient, time history, of the linear elastic model represented by the first 20 eigenvectors. Model deflections and associated stresses were examined at 400 equally spaced time points between zero and five seconds. Load vectors and element dynamic stresses were obtained at each time point. The input was assumed to be from vortex shedding of the first mirror module and applied simultaneously to the remaining three mirror modules to produce vertical loads and torsion in the mirror module. It assumed 40 percent of free stream velocity (38 m/sec) as the driving force on each mirror module. One quarter of this force was applied as wind load induced torque on the mirror modules at each of the following resonant frequencies.

2.7 Hz	Mirror torsion mode
3.9 Hz	Frame bending mode
4.6 Hz	Frame bending mode
4.9 Hz	Mirror torsion mode

The loads thus simulated are much greater than could be reasonable expected to result. The stresses resulting from these loads are shown for various heliostat elements by Table 4-1. Only one stress point of any significance was noted. This was 27,600 psi at crank arm adjacent to the driven mirror module. This arm was fabricated from steel with a yield strength of 36,000 psi thus presently has a margin of safety of 0.3. Additional margin of safety may be obtained simply for pilot plant heliostats by using higher strength steel. Due to limited exposure to this environment, location in a single component and conservative nature of the assumed input, this is considered satisfactory.

Table 4-1. LG8016B Heliostat Assembly Survivability
Stress (Dynamic Only)

<u>Location</u>	<u>Stress</u>	
	<u>Type</u>	<u>Magnitude (psi)</u>
Outer Axis Pin	Shear	140
	Moment	6,292
Cross Beam (At Front Support)	Moment	1,336
Angle Braces	Axial	856
Outer Axis Drive	Axial	1,248
Tie Rod	Axial	8,508
Crank Arm (IA Drive Position)	Shear	3,053
	Moment	27,600

AERODYNAMIC ANALYSIS

The previously described structural analysis used load calculations made early in the program. These calculations produced data such as that shown in Figure 4-5 and Tables 4-2 and 4-3. The details of these and other aerodynamic analyses are contained in TCL-SRE-66.

COLLECTOR SUBSYSTEM POINTING ACCURACY ANALYSIS

An error budget was presented in Detail Design Report (Reference 6) that indicated we were well within the 2 milliradian 1σ requirement. Experience on the SRE provided new information which has been used to update the error budget. Although several items have been added or deleted and others have changed value, the total RSS values are unchanged within the accuracy of prediction.

Table 4-4 compares the two budgets at a summary level. Figure 4-6 contains heliostat rotation frames described in Tables 4-4 through 4-6. Table 4-5 summarizes the updated independent error sources; while Table 4-6 shows all the elements that comprise just one item (mirror drive backlash) in Table 4-5. Note that some improvement is anticipated for the pilot plant heliostats resulting from detail design changes.

Changes in some items of Table 4-4 deserve mention. Test has shown the total spring rate of the inner drive system plus mirror module deflections under wind load is lower than expected. The spring rate of the gear box was low due to use of a lower cost bearing approach. Additional elements were also discovered as a result of SRE testing. Twist of the mirror module under wind moment was previously omitted. Test also demonstrated a lower sensitivity to solar heat loads. Differential temperatures between the frame side rail and inner drive tie rod were found to be only 3°F instead of the 18°F budgeted value.

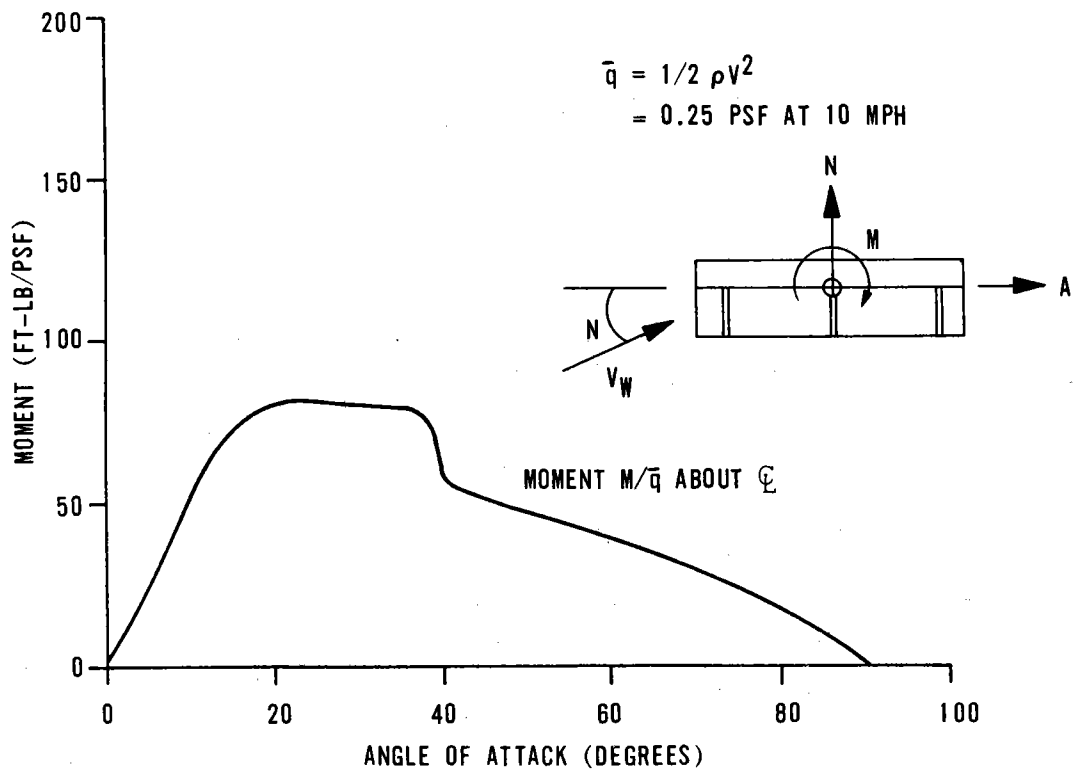
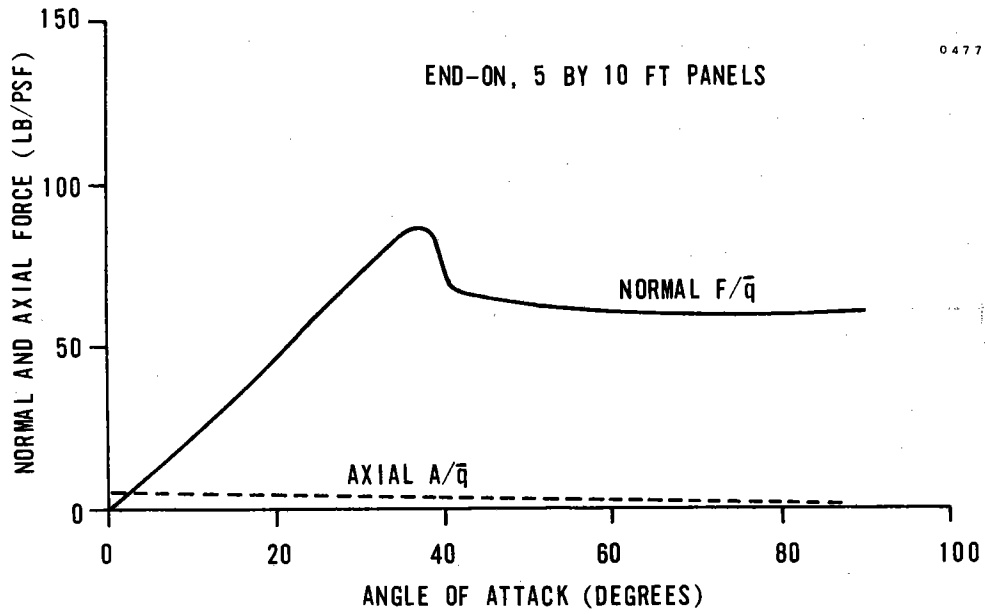


Figure 4-5. Wind Forces and Moment On Mirror-Torsion Tube Assembly

Table 4-2. Torsional Stiffness Parameters

V _{Div} MPH	Static Divergence		Resonant Freq. 30 MPH		Deflection at 30 MPH
	Module -Inner -K _θ Ft-Lb/Rad	Heliostat -Outer -K _θ Ft-Lb/Rad	Module Inner Hz	Heliostat Outer Hz	Either Config. α = 20 deg Millirad
10	38	307			∞
30	345	2,762			∞
60	1,381	11,049	1.06	0.411	116
100	3,837	30,692	1.95	0.754	34.5
150	8,632	69,057	3	1.16	14.5
100√3	11,510	92,076	3.48	1.35	10.8
200	15,346	122,768	4.04	1.56	8
300	34,529	276,228	6.1	2.36	3.52
400	61,384	491,073	8.15	3.15	1.97
500	95,913	767,000	10.2	3.95	1.26
600	138,120	1,104,964	12.2	4.74	0.874
700	187,997	1,503,979	14.3	5.53	0.642
800	245,548	1,964,380	16.3	6.3	0.491
900	310,771	2,486,169	18.4	7.1	0.388
1000	383,668	3,069,344	20.4	7.9	0.314
1200	552,482	4,419,857	24.5	9.5	0.218
1400	751,989	6,015,916	28.5	11.1	0.16
1600	982,190	7,857,523	32.7	12.7	0.122
1800	1,243,085	9,944,677	36.76	14.23	0.97
2000	1,534,672	12,277,379	40.8	15.8	0.78

Table 4-3. Mirror/Heliostat Response To Static Wind Loads and Wind Turbulence

Static Wind Loads

STATIC DEFLECTION

$$\Delta\theta \equiv \frac{(\partial M/\partial\alpha) \alpha_0}{-K_\theta \frac{\partial M}{\partial\alpha}} = \frac{p \frac{S}{2} \bar{c} C_{M\alpha} V_w^2 \alpha_0}{-K_\theta - \frac{pS\bar{c}}{2} C_{M\alpha} V_w^2} = \frac{\alpha_0}{\left(\frac{V_{DIV}}{V_w}\right)^2 - 1}$$

$$\text{or } \left(\frac{V_{DIV}}{V_w}\right)^2 = \frac{\alpha_0}{\Delta\theta_{MAX}} + 1 = \frac{0.34904}{\Delta\theta_{MAX}} = 1 \text{ at } 20^\circ \alpha$$

$$= 3491 \text{ at } 20^\circ \text{ for } 0.1 \text{ millirad}$$

$$\text{or } -K_\theta = \frac{\partial M}{\partial\alpha} \left(\frac{\alpha_0}{\Delta\theta_{MAX}} + 1 \right) = 150 \bar{q} [3491] \text{ for module - inner axis}$$

Wind Turbulence

RMS ROTATION

$$\sigma_\theta \cong \frac{\alpha_M}{-K_\theta - \frac{\partial M}{\partial\alpha}} \cong \frac{\frac{1}{\pi} \sqrt{1 + (2 \alpha_0)^2}}{\left(\frac{V_{DIV}}{V_w}\right)^2 - 1}$$

$$\text{so that } \left(\frac{V_{DIV}}{V_w}\right)^2 = \frac{\frac{1}{\pi} \sqrt{1 + (2 \alpha_0)^2}}{\sigma_{\theta MAX}} + 1$$

$$= \frac{0.3183 \sqrt{1 + (2 \alpha_0)^2}}{\sigma_{\theta MAX}}$$

$$= 3184 \text{ at } 0 \alpha_0 \text{ for } 0.1 \text{ millirad}$$

$$= 3883 \text{ at } 20^\circ \alpha_0$$

where α_0 is nominal angle of attack in radians

Table 4-4. Error Budget Comparison

Errors in Millirads											
Source	3 σ						3 σ		1 σ		
	O ₂	O ₃	O ₁ /I ₁	I ₃	M ₁	I ₂ /M ₂	M _{T1}	M _{T2}	M _{T1}	M _{T2}	
Wind			0.274	0.001	0.124	0.131	0.398	0.131	0.398	0.131	
Temperature	0.02		0.2	0.18		0.9	0.2	0.92	0.2	0.92	
Gravity			0.25			0.085	0.25	0.085	0.25	0.085	
Independent	0.163	0.160	0.446	0.313	0.839	1.120	0.95	1.130	0.317	0.377	
SRE Accuracy 18 May 1976						RSS/Axis		1.08	1.45	0.60	0.99
						Total RSS		1.81		1.15	

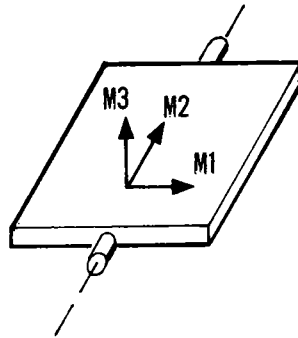
Errors in Millirads											
Source	3 σ						3 σ		1 σ		
	O ₂	O ₃	O ₁ /I ₁	I ₃	M ₁	I ₂ /M ₂	M _{T1}	M _{T2}	M _{T1}	M _{T2}	
Wind			0.39	0.001		0.99	0.39	0.99	0.39	0.99	
Temperature	0.02		0.20	0.03		0.15	0.20	0.15	0.20	0.15	
Gravity			0.25			0.09	0.25	0.09	0.25	0.09	
Independent	0.163	0.05	0.94	0.247	0.452	0.96	1.04	0.97	0.35	0.325	
Pilot Plant Accuracy 21 March 1977						RSS/Axis		1.16	1.40	0.61	1.06
						Total RSS		1.82		1.22	

Table 4-5. Independent Error Sources

<u>Error Source</u>	<u>3σ Errors - Milliradians</u>					
	<u>O₂</u>	<u>O₃</u>	<u>O₁/M₁</u>	<u>I₃</u>	<u>M₁</u>	<u>I₂/M₂</u>
<u>Control</u>						
Quantization			0.200			0.200
Command Lag			0.050			0.050
Computer			0.340			0.340
Initialization			0.45			0.45
<u>Mirror Module</u>						
Opt axis not \perp to axis of rotation					0.450	
Stub Shaft Coning				0.040	0.040	
<u>Frame Drive</u>						
Screw Lead Diff Error			0.130			
Backlash			0.215			
Bearing Runout	0.002	0.002	0.050			
Rod End Axial Play (Axial)			0.144			
<u>Mirror Drive</u>						
Backlash						0.522
Gear Tooth Errors						0.140
Crank Arm Length						0.208
Bearing Runout				0.040		0.040
<u>Foundation</u>						
Random Walk	0.031		0.010			
<u>Assembly and Alignment</u>						
Field Location Accuracy		0.05				
Level of Outer Axis	0.16					
Azimuth of Outer Axis		0.05				
Actuator Geometry Accuracy			0.62			
Level of MMs			0.24			
Orthogonality of Axes				0.24		
Toe-In Adjust						0.44
Tie-Rod Length Adjust						0.176
Total RSS 3 σ	0.163	0.05	0.94	0.247	0.452	0.96

Table 4-6. Inner Drive Backlash Summary

	Backlash Values (Milliradians) 3σ							
	SRE				Pilot Plant			
	No. 1	No. 2 (Drive)	No. 3	No. 4	No. 1	No. 2 (Drive)	No. 3	No. 4
Gearbox		0.30				0.15		
Pivot Pin-to-Bearing Fit		0.275				---		
Pivot Pin-to-Gearbox Fit		0.125				---		
Fit of 4 Inch Bearing to MM Shaft (Drive)		0.250				0.250		
Fit of 4 Inch Bearing to Housing (Drive)		0.150				0.150		
Diam Clearance of 4 Inch Bearing (Drive MM)		0.325				0.325		
Rod End B3 Fit to Pin on Crank Arm	0.176	---	0.176	0.176	0.176	---		
Rod End B2 Fit	0.176	---	0.176	0.176	0.176	---		
Rod End A2 Fit	---	---		0.176		---		
Rod End A1 Fit	---	---		0.176		---		
Fit of 4 Inch Bearing to MM Shaft	0.118	0.00	0.118	0.118	0.118	---	0.118	0.118
Fit of 4 Inch Bearing to Housing	0.070	---	0.070	0.070	---	---	---	---
Diam Clearance of 4 Inch Bearing	0.153	---	0.153	0.153	0.088	---	0.088	0.088
RSS	0.323	0.611	0.323	0.408	0.289	0.462		
	0.691	0.611	0.691	0.735	0.545	0.462	0.545	0.599
RMS of 4 = 0.68 mr.						0.522		



M - FIXED IN MIRROR MODULE
 I - FIXED IN FRAME
 O - FIXED IN POSTS

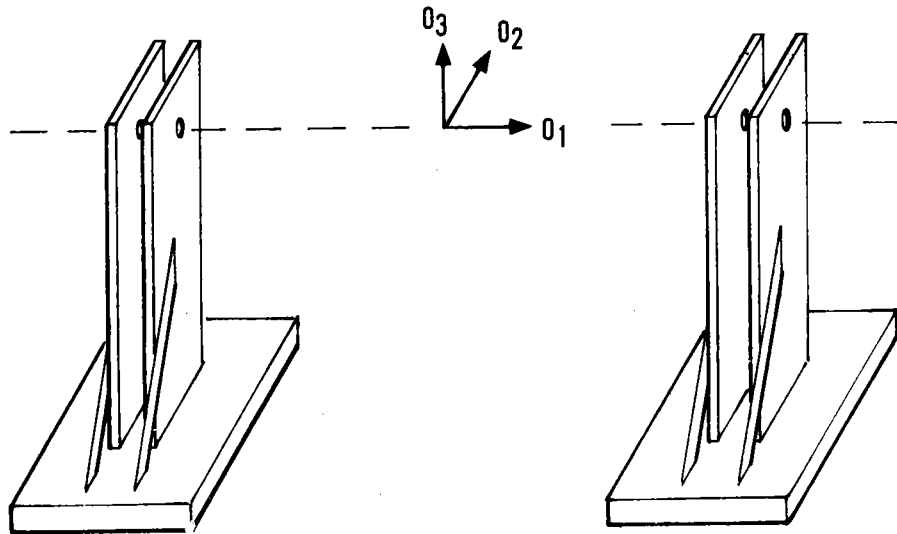
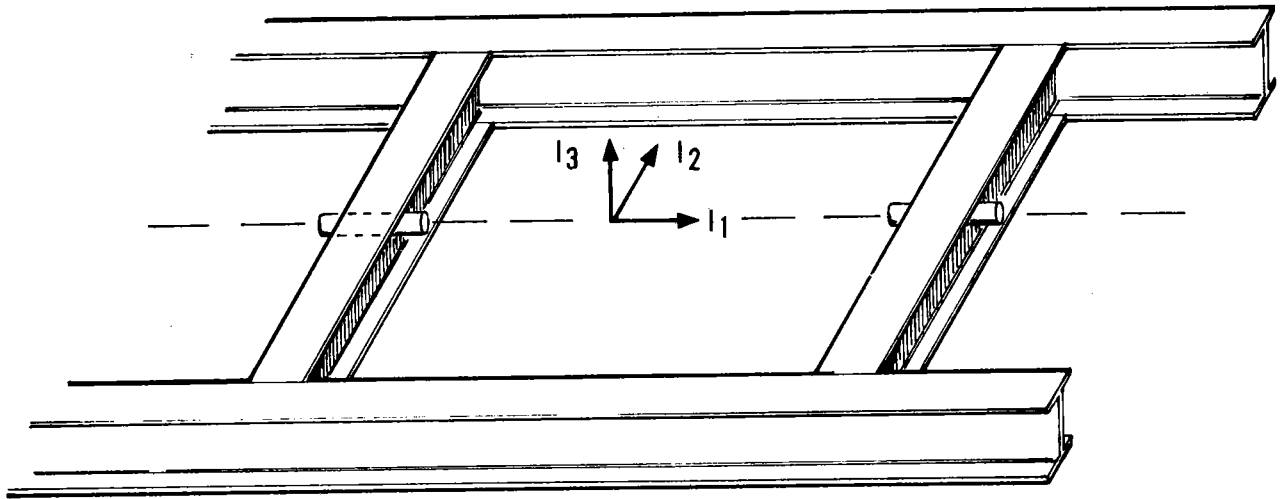


Figure 4-6. Heliostat Rotation Frames

Independent errors about O_1/I_1 increased due to the addition of terms for initialization switches, rod end rotational play and inaccuracies in the setup of the frame drive pivot geometry. Independent errors about axes M_1 and I_2/M_2 were reduced by deleting the optical contour allowance. This belongs in a separate budget. Addition of initialization, toe-in adjustment and tie rod length errors kept the I_2/M_2 term from dropping significantly.

The picture presented by the updated budget is consistent with SRE test results. Both reflect the superior performance about the frame pivot axis as compared to the mirror module axis. Considering the apparent shape of the receiver aperture as seen by a heliostat the distribution of errors between axes is in the right proportion. It should also be noted that the deviations of beams from single mirror modules due to toe-in error also tend to conform to the aperture shape (horizontal spreading with slight downward motion of end beams).

The new error budget will be used to make further cost trade-offs during the producibility study. Torsional stiffness requirements on the mirror module will be relaxed by increasing the total RSS value back up to 2 milliradians as originally proposed. New wind tunnel data is expected to provide additional latitude.

Stress on some components at the higher 40 M/S (survival) wind speed will size some elements previously controlled by the error budget. Thus some errors may change slightly as a result of detail design.

THERMAL CONSIDERATIONS OF HELIOSTAT DESIGN

Two separate areas were given thermal consideration in the design of the heliostat. Temperature change and differences in temperature of various parts in the heliostat have been investigated to determine the effect on heliostat errors. The second thermal consideration investigated was the operating temperatures of electronics and drive motors.

Performance of the heliostat depends upon the ability to establish and maintain very precise positions of the frame and mirror module upon command from the heliostat central computer. Changes in temperature in a static and/or dynamic mode cause changes in the length and shape of heliostat assemblies. These have two effects on the assembly. They create loads in the structure at temperatures other than where the assembly was made and produce angular errors in position when components have different temperatures.

Structural expansion is most pronounced in the frame, post, actuator area. It is reasonable to assume that a frame could be assembled on the two support posts and the outer axis drive connected at ambient temperatures of 0°C (32°F). Under operating conditions, high ambient temperature and high solar insolation, the frame temperature may easily exceed 50°C (122°F). Calculations show frame expansion in the 10.1m (33 feet) between posts to be almost 5.1mm (0.2 in.). Assuming no corresponding expansion of the ground, relative motion between frame and posts and/or loads will be produced. The bearing at the top of the posts are designed to accommodate this relative motion. The design

of the outer axis actuator attaching bracket, on the frame end, keeps the moment load on the ball screw below allowable. For the actuators presently used this is 38.7 kg-m (3360 in-lbs) and 10.4 kg-m (900 in-lbs) on the actuator selected for further development in the heliostat producibility study. Painting the surface with white cellulose lacquer offers an additional factor because it's absorptivity is 0.12 to 0.3 over a life of 5 years.

Thermal distortion has not been proven to be a problem in tests conducted during the solar research experiment. Design considerations have been given to unsymmetrical heating caused by difference in thermal time constants between very heavy beams and lighter tie-rods. Also solar insolation on one side of components such as posts result in differential expansion with resulting bending. During operation different cooling/heating rates of machine elements resulting from cloud passing over or relative motion between parts may cause components to move from full sun to shade with resulting transient temperature differences. In the solar research experiment tests have shown adequate control of this phenomena by the use of high reflectivity paint. Techniques for solar shielding of elements like the support posts have been developed should painting alone prove inadequate. Thermal test data reported in detail by the Solar Research Test Report (277-14333 dated 18 February 1977) have shown adequate operation during normal temperature variations experienced.

Thermal analyses of the Solar Research Experiment have been conducted for the electronics package and the drive motors located on the inner and outer drive assemblies. Analysis has also been conducted for the design to be used in the pilot plant. These analyses of the electronics packages considered heat flow only by free convection. This is a conservative approach since forced convection will be present most of the time and radiation will also dissipate some heat. Adequate thermal design is based on logic elements maximum ambient temperature of 70°C (158°F) and motor winding maximum temperature of 155°C (311°F). Worst case ambient temperature was specified as 49°C (120°F).

Power dissipation in the electronics package for the Solar Research Experiment was 23.4w. The remainder of the 35w total power is dissipated in the battery box and the drive motors. Temperatures rise from ambient to the air in the electronics package was calculated to be 10°C (18°F). Thus components inside the package have a maximum air temperature of 59°C (138°F) air compared to 70°C allowable.

The electronics package proposed for the pilot plant will have a power dissipation of 38w out of the 47w total for a heliostat. Temperature rise from ambient to the air in the electronics package was calculated to be 15°C (28°F). Thus components inside the package have a maximum air temperature of 64°C (148°F) compared to 70°C allowable.

Analysis of the electronics considered the effect of direct solar radiation on temperatures within the box. A white painted box with absorptivity of 0.3 and the size used on the Solar Research Experiment would gain over 200w on the outer surface if exposed to direct

sunlight. This would increase temperatures 43°C (77°F). Sufficient temperature margin does not exist for this much load. The conclusion was that the electronics package must have protection from solar radiation in the form of an awning extending over the top to provide shade during times of high solar radiation. Added heaters or wider temperature margin parts will be required for low temperature operation.

Combinations of analytical and test data were used to determine the effects of input power and time on the motor armature temperature. The motor specification allows a maximum armature temperature of 155°C (311°F). The conductors within the motor are copper and thus have a coefficient of resistance of 0.00393 1/°C. Constant power was applied to the motor and the temperature rise of the armature calculated based on the change in resistance as a function of time. The thermal time constant was 13.25 minutes. Motor power is expected to be approximately 20w maximum. The analysis showed a maximum temperature of 122°C (252°F). The temperature at one time constant was 98°C (208°C). HelioStat operating conditions dictate that in normal operating modes, maximum power will not be applied for one time constant.

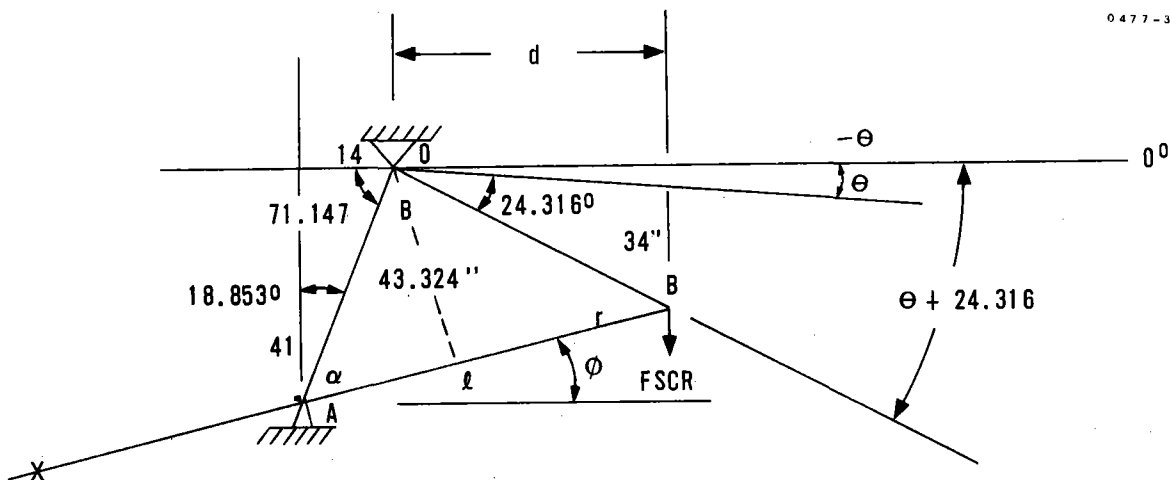
DRIVE SYSTEM ANALYSES

Because both drive systems are linkage assemblies, many of their characteristics are a function gimbale angle.

Drive System characteristics which are angle dependent include:

- Wind loads
- Gimbal residual imbalance
- Actuator imbalance
- Effective reduction ratio (motor to frame axis)
- Effective actuator lever arm
- Actuator column loads and resultant bending stress
- Tie rod column loads
- Actuator column load capability
- Required motor speed and torque
- Effective actuator length
- Linkage spring rate

Analytical software has been developed and used to quantify these effects. Representative math models and computer outputs are attached.



$$\beta = 180 \text{ deg} - 71.147 \text{ deg} - 24.316 - \theta$$

$$\ell = [(43.324)^2 + (34)^2 - 2(43.324)(34) \cos \beta]^{1/2}$$

$$\alpha = \cos^{-1} \frac{\ell^2 + (43.324)^2 - (34)^2}{2(\ell)(43.324)}$$

$$\phi = 90 \text{ deg} - \alpha - 18.853 \text{ deg}$$

$$M_A = [\text{WTMOV}(\ell - \text{LCGM}) - \text{STFIX}(\text{LCGF})] \cos \phi$$

$$\text{FSCR} = M_A / \ell \cos \phi$$

$$d = 34 \cos (\theta + 24.316)$$

$$M_o = \text{FSCR} (d)(\text{in-lbs})$$

M_A = moment about actuator pivot due to imbalance of actuator

FSCR = downward force at B due to actuator imbalance

M_o = moment about heliostat axis due to actuator imbalance

Frame Drive System Geometry

Listing of Drive Geometry Program

```

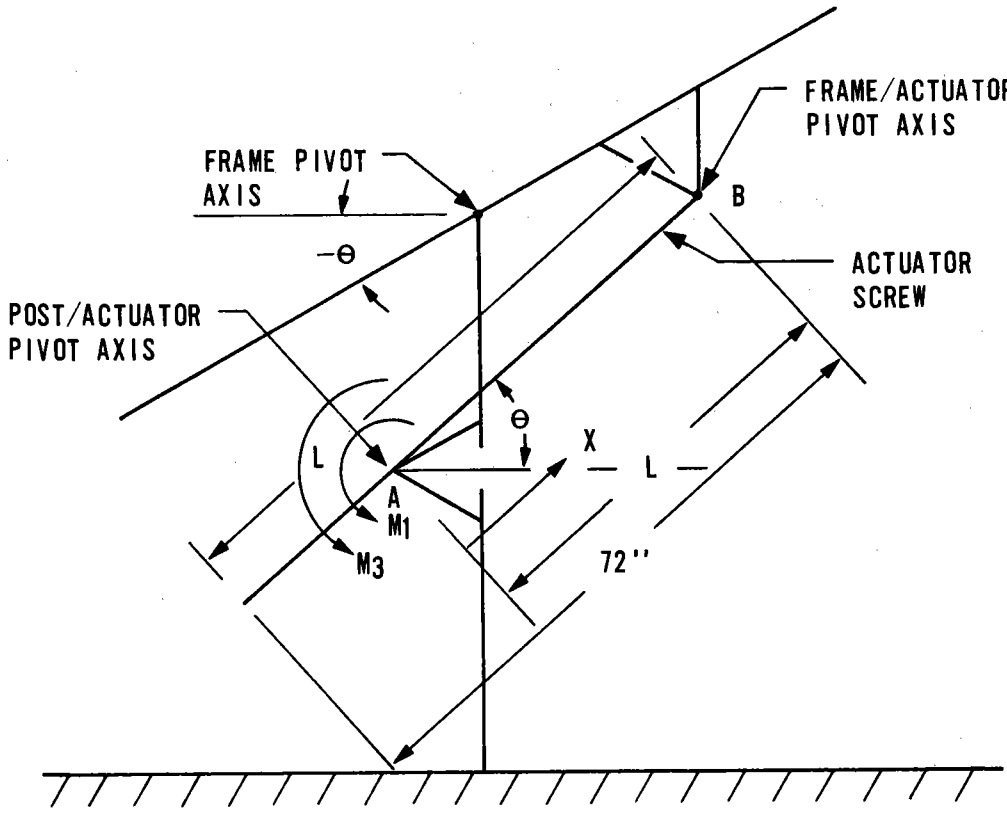
100 *** OUTER DRIVE GEOMETRY, SCREW MOMENT ABOUT AXIS ***
110 READ L,MA,MO,L1,L2,L1TAN,LOGF,MOAVG
120 DATA DTH,RTD,5.,30.,395734
130 DATA MTMOV,MTOT,23.0,25.4
140 DATA L1,L2,43.,324.,34.0
150 DATA LOGM,LOGF,35.,33.,044
160 ***
170 II = 0
180 THETA = -25.
190 MOAVG = 0.
191 WRITE(9,111)
200 22 THETA = THETA + DTH
210 II = II + 1
220 BETA = 180 - 71.147 - 24.316 - THETA
230 L = SQRT(L1**2 + L2**2 - 2.*L1*L2*COS(BETA/RTD))
240 TANALF = L2*SIN(BETA/RTD)/(L1 - L2*COS(BETA/RTD))
250 ALPHA = RTD*ATAN(TANALF)
260 PHI = 90. - 18.853 - ALPHA
270 MA = (MTMOV*(L-LOGM) - (MTOT - MTMOV)*LOGF)*COS(PHI/RTD)
280 FSCR = MA/(L*COS(PHI/RTD))
290 D = L2*COS((THETA + 24.316)/RTD)
300 MO = FSCR*D
310 MOAVG = MOAVG + MO
320 WRITE(9,222) THETA,MO,D,FSCR,MA,PHI,L
330 IF (THETA.LT.75.) GO TO 22
340 MOAVG = MOAVG/FLCAT(II)
350 WRITE(9,333) MOAVG
360 STOP
370 111 FORMAT(//
380 +AX,THETA      MO      D      FSCR      MA      PHI      L (,/)
390 222 FORMAT(7F9.1)
400 333 FORMAT(/// MOAVG = ,F9.1)
410 END

```

Frame Drive Geometry Analysis Results

THETA	MO	D	FSCR	MA	PHI	L
-30.0	601.2	33.8	17.8	250.0	42.8	65.2
-25.0	559.5	34.0	16.5	222.9	40.8	63.4
-20.0	507.7	33.9	15.0	217.3	39.7	61.4
-15.0	446.3	33.6	13.3	132.5	36.7	59.3
-10.0	375.8	33.9	11.4	535.5	34.8	57.1
-5.0	297.2	33.1	9.3	426.9	32.8	54.9
0.0	211.6	31.0	6.8	307.1	31.0	52.5
5.0	120.1	29.6	4.1	176.8	29.2	50.0
10.0	24.4	28.1	0.9	36.6	27.4	47.4
15.0	-73.5	26.3	-2.8	-112.7	25.8	44.8
20.0	-171.4	24.3	-7.0	-270.0	24.2	42.0
25.0	-286.2	22.2	-12.0	-434.4	22.8	39.2
30.0	-354.3	19.8	-17.9	-504.5	21.5	36.4
35.0	-431.1	17.4	-24.8	-578.9	20.5	33.5
40.0	-490.2	14.7	-32.3	-655.9	19.8	30.5
45.0	-523.2	12.0	-43.6	-1122.0	19.5	27.4
50.0	-518.0	9.2	-58.4	-1307.1	19.6	24.6
55.0	-457.2	6.3	-78.5	-1422.7	20.5	21.7
60.0	-314.2	3.4	-99.3	-1430.7	22.4	18.8
65.0	-142.6	0.4	-120.3	-1222.1	25.4	16.0
70.0	396.7	-2.1	-125.0	-1222.7	31.8	13.5
75.0	1153.2	-5.5	-124.7	-1221.5	41.2	11.3

MOAVG = 44.2
 TDR.
 :



Actuator Column Load Math Model

Listing of Program for Analysis of Actuator Bending Stress Due to Column Load

LIST ENDSTR *5 TON ACTUATOR*

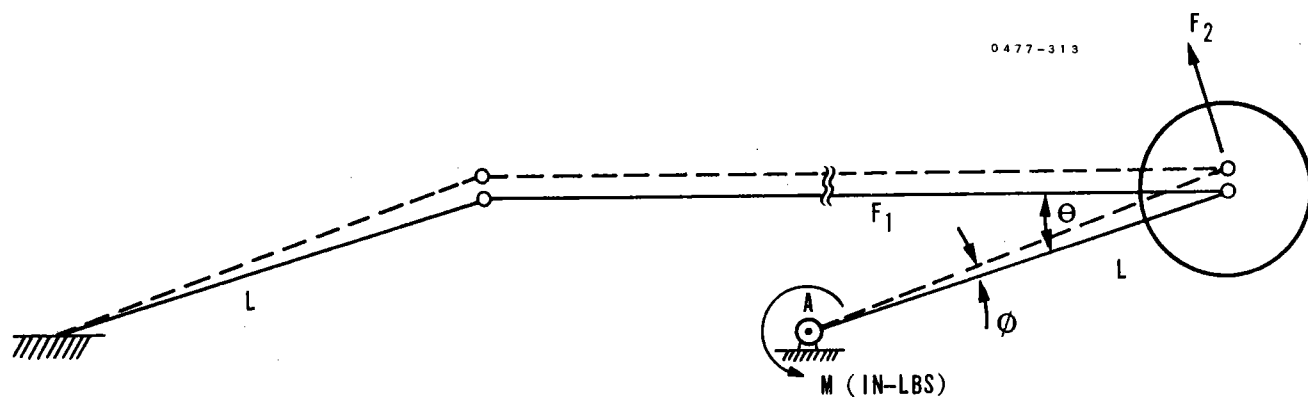
```

10 *** HELIOSTAT E. S. ACTUATOR BENDING MOMENT AND STRESS CALC.
20 *** FORMULATION- R. SNYDER, CODING- J. PROTOLA
30 REAL L,L1,L2
40 DATA L1/43.324/, L2/34.0/, CEULER/1.213E7/, STRMAX/7.0E4/
50 DATA AREA/1.021/, CBND/6.873/, RTD/57.29573/
60 DATA DIAM/1.14/, PI/3.14159/
70 ***
80 AREA = PI*(DIAM)**2/4.
90 CBND = .57/(.0491*DIAM**4)
100 THETA = -35
110 WRITE(9,111)
120 11 THETA = THETA + 5.
130 BETA = 180. -71.147 -24.316 -THETA
140 L = SQRT(L1**2 + L2**2 -2.*L1*L2*COS(BETA/RTD))
150 TANALF = L2*SIN(BETA/RTD)/(L1 - L2*COS(BETA/RTD))
160 ALPHA = RTD*ATAN(TANALF)
170 PHI = 90. - 18.853 -ALPHA
180 BNDMOM = (461. + .32*(72. - L)**2)*COS(PHI/RTD)
190 FSUBB = BNDMOM*CBND
200 *** FIND AXIAL COMPRESSIVE STRESS
210 *** AA*FSUBA**2 + BB*FSUBA + CC > 0.
220 AA = L**2
230 BB = - (CEULER + STRMAX*AA)
240 CC = CEULER*(STRMAX - FSUBB)
250 DISCRM = BB**2 - 4.*AA*CC
260 IF (DISCRM.LE.0.) GO TO 22
270 WRITE(9,222) DISCRM
280 DISCRM = 0.
290 22 SODIS = SQRT(DISCRM)
300 FSUBA1 = (-BB + SODIS)/(2.*AA)
310 FSUBA2 = (-BB - SODIS)/(2.*AA)
320 FCOMP1 = AREA*FSUBA1
330 FCOMP2 = AREA*FSUBA2
340 WRITE(9,333) THETA, L,PHI,BNDMOM,FSUBB,FCOMP1,FCOMP2
350 IF(THETA.LT.75.) GO TO 11
360 STOP
370 111 FORMAT(/,5X,
380 + THETA, L, PHI, BNDMOM, FSUBB, FCOMP1, FCOMP2//)
390 222 FORMAT(/*** DISCRM =/,G11.4// GET TO 2220 ***)
400 333 FORMAT(5F9.1,2*1P511.3)
410 END

```

Actuator Stress (FSUBB PSl) Versus Gimbal Angle

THETA	L	PHI	RNDMMOM	FSUBB	FCOMP1	FCOMP2
-30.0	55.2	42.3	343.7	2395.3	7.155E 04	2.305E 03
-25.0	53.4	40.3	367.0	2522.3	7.157E 04	2.965E 03
-20.0	51.4	38.7	387.5	2653.3	7.158E 04	3.151E 03
-15.0	49.3	36.7	410.5	2821.3	7.160E 04	3.363E 03
-10.0	47.1	34.3	435.7	3001.3	7.162E 04	3.620E 03
-5.0	44.9	32.3	466.3	3205.2	7.165E 04	3.915E 03
0.0	42.5	31.0	500.0	3435.6	7.169E 04	4.263E 03
5.0	40.0	29.2	539.1	3699.4	7.173E 04	4.676E 03
10.0	37.4	27.4	581.0	3993.4	7.179E 04	5.170E 03
15.0	34.9	25.3	629.1	4323.3	7.186E 04	5.766E 03
20.0	32.0	24.2	682.5	4691.4	7.197E 04	6.493E 03
25.0	29.2	22.8	741.6	5097.1	7.210E 04	7.390E 03
30.0	26.4	21.6	806.2	5541.0	7.229E 04	8.513E 03
35.0	23.5	20.6	876.1	6022.0	7.255E 04	9.940E 03
40.0	20.5	19.3	951.0	6535.6	7.293E 04	1.179E 04
45.0	17.6	19.5	1039.3	7073.5	7.350E 04	1.422E 04
50.0	14.6	19.6	1110.9	7635.7	7.440E 04	1.748E 04
55.0	11.7	20.5	1190.9	8135.3	7.539E 04	2.191E 04
60.0	8.8	22.4	1263.7	8636.1	7.659E 04	2.793E 04
65.0	6.0	25.3	1316.6	9049.6	7.794E 04	3.577E 04
70.0	3.5	31.3	1323.6	9097.6	7.911E 04	4.464E 04
75.0	1.3	41.2	1233.3	8476.3	1.159E 05	5.256E 04

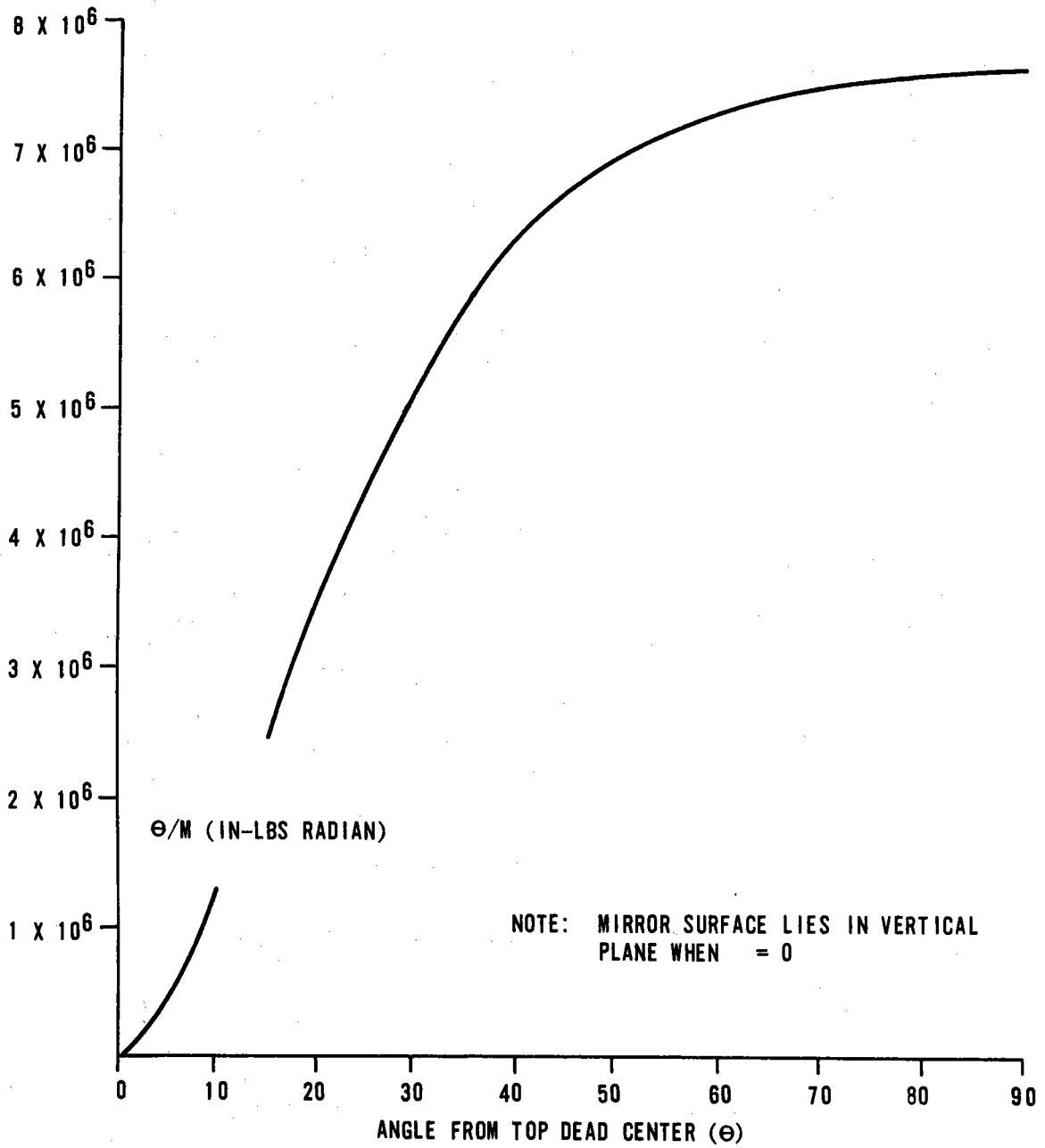


TORSIONAL SPRING RATE AT AXIS A IS M/ϕ (in-LBS/RADIAN)

AT $\theta = 0^\circ$ $M/\phi = 0$

AT $\theta = 90^\circ$ $M/\phi = \text{MAXIMUM}$

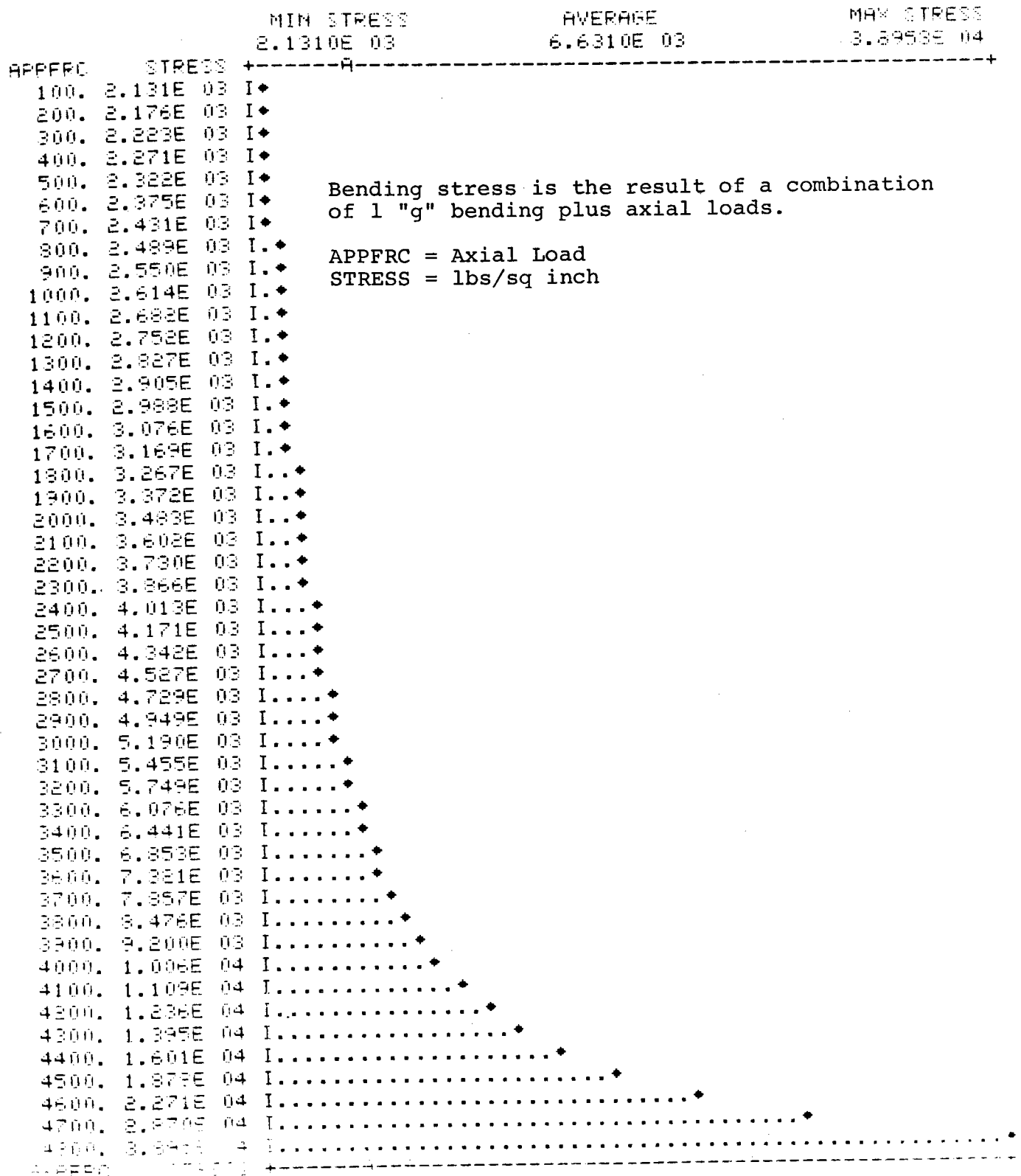
Inner Drive Linkage Model



Torsion Spring Rate of Inner Drive Linkage
Versus Angle (for 4 Inch Crank Arm)

Tie Rod Bending Stress Versus Axial Load

PLOT OF APPFRC VERSUS STRESS



MASS PROPERTIES ANALYSIS

Efficiency of the drive systems depends on our ability to balance the composite rotating masses about their axes of rotation. The inner axis analysis considers the combined effects of crank arms, tie rods and mirror modules. As the result of this analysis a 1,500 inch-pound imbalance is specified for each mirror module to counteract the linkage assembly. This balancing provides the added benefit of making the outer axis balance independent of inner axis position.

Analysis of the outer heliostat axis has also been completed. A related analysis of the frame drive system has defined a residual moment due to a variable imbalance of the actuator about its own pivot axis (see Drive System Analyses). Since the RMS value of this imbalance over the operating angular range is near zero, its effect is disregarded in the CG analysis.

Inner Axis Balance Analysis

$$M_{CA} = \text{moment exerted by one crank arm is} \\ 264^* \text{ in.-lbs (0.707)} = 186.65 \text{ in.-lbs}$$

$$M_{TR} = \text{moment exerted on each MM by each} \\ \text{tie rod is } \frac{45.804}{2} \times 24 \text{ (0.707)} = 388.60 \text{ in.-lbs}$$

$$\text{Imbalance on end MM}^2 = 2(M_{TR}) + 2(M_{CA}) \\ = 2(186.65 + 388.60) = 1150.50$$

$$\text{Imbalance on center MM}^2 = 4(M_{TR}) + 2(M_{CA}) \\ = 4(388.6) + 2(186.65) = \underline{1927.7}$$

$$3078.2$$

$$\text{Total imbalance on inner drive} = 2 \times 3078.2 = 6156.4 \text{ in.-lbs}$$

$$\text{Required imbalance/MM} = 6156.4/4 = 1539.1$$

Therefore:

An imbalance of 1539 inch-pounds is required on each of four mirror modules to balance the inner axis composite. The CG of the mirror module must be moved toward the mirror face as required.

* Measured value.

Heliostat Outer Axis Mass Properties

LIST HMP

```

100 *** HELIOSTAT MASS PROPERTIES
110 . 3923. 78.04 4.923 0.9848E5.
120 . 2880. 78.5 14.5 1.924E4.
130 . 2.2 12 14.5.
140 . 2.2 145 14.5.
150 . 74 11.5 12.6.
160 . 74 145.5 12.6.
170 . 4 11.75 14.5.
180 . 4 145.25 14.5.
190 . 4 11.75 14.5.
200 . 4 145.25 14.5.
210 . 98 7.5 14.5.
220 . 98 149.5 14.5.
230 . 167 6 14.5.
240 . 167 151 14.5.
250 . 22.1 12 5.5.
260 . 60.16 10.75 14.5.
270 . 1.77 111 -4.6.
280 . 1.77 111 -4.6

```

```

PRIN CGI
DEFINE FILE(S)
1-HMP

```

100 *** HELIOSTAT MASS PROPERTIES

NODE	W	X	Z	TYO	MULT
1	3923.	78.04	4.923	0.9848E 05	1.000
2	2880.	78.50	14.50	0.1924E 05	1.000
3	2.200	12.00	14.50	0.0000	1.000
4	2.200	145.0	14.50	0.0000	1.000
5	74.00	11.50	12.60	0.0000	1.000
6	74.00	145.5	12.60	0.0000	1.000
7	4.000	11.75	14.50	0.0000	1.000
8	4.000	145.3	14.50	0.0000	1.000
9	4.000	11.75	14.50	0.0000	1.000
10	4.000	145.3	14.50	0.0000	1.000
11	98.00	7.500	14.50	0.0000	1.000
12	98.00	149.5	14.50	0.0000	1.000
13	167.0	6.000	14.50	0.0000	1.000
14	167.0	151.0	14.50	0.0000	1.000
15	22.10	12.00	5.500	0.0000	1.000
16	60.16	10.75	14.50	0.0000	1.000
17	1.770	111.0	-4.600	0.0000	1.000
18	1.770	111.0	-4.600	0.0000	1.000

```

WTOT = 7587.
W6 = 77.55
WOG = 9.476
TYOG = 0.2446E 06

```

*TDP.

?

Frame Mass Properties

LIST EMP

```

19 *** FRAME MASS PROPERTIES: WT, X, Z, IY
20 , 1272, 12, 5, 64.6,
21 , 1272, 145, 5, 64.6,
22 , 270, 78.5, 5, 1100,
23 , 270, 78.5, 5, 1100,
24 , 96, 78.5, 5, 390,
25 , 101, 31.8, 5,
26 , 101, 125.2, 5,
27 , 193, 12, 5,
28 , 193, 145, 5,
29 , 42, 78.5, 5,
30 , 48.48, 12.22, 3.77, 17.41,
31 , 43.6, 111, -2.75,
32 , 21.4, 77.75, 9.4,

```

FROM CSI

FINE FILE(S)

1=EMP

19 *** FRAME MASS PROPERTIES: WT, X, Z, IY

NODE	W	X	Z	IY	MULT
1	1272.	12.00	5.000	64.60	1.000
2	1272.	145.0	5.000	64.60	1.000
3	270.0	78.50	5.000	1100.	1.000
4	270.0	78.50	5.000	1100.	1.000
5	96.00	78.50	5.000	390.0	1.000
6	101.0	31.80	5.000	0.0000	1.000
7	101.0	125.2	5.000	0.0000	1.000
8	193.0	12.00	5.000	0.0000	1.000
9	193.0	145.0	5.000	0.0000	1.000
10	42.00	78.50	5.000	0.0000	1.000
11	48.48	12.22	3.770	17.41	1.000
12	43.60	111.0	-2.750	0.0000	1.000
13	21.40	77.75	9.400	0.0000	1.000

WTOT = 3922.

XCG = 78.04

ZCG = 4.923

IYCG = 0.9848E 05

STOP.

Heliostat Component Weights

<u>Qty</u>	<u>Description</u>	<u>Weight (lbs)</u>
<u>Mirror Module</u>		
3	Mirror Modules	650
1	Mirror Module	650
1	Spur Gear	60
8	Bearing Support Assembly	1
8	Bearing Retainer	4
<u>Frame</u>		
1	Frame	3,923
<u>Frame Drive</u>		
2	Pivot Pin	1
2	Ball Screw Jack	85
4	Pillow Blocks	2
2	Ball Jack Ends	2
2	Actuator Bracket	20
2	Motor Encoder (Actuates Frame Drive)	5
2	Adapter Motor	1
<u>Mirror Drive</u>		
1	Mirror Drive Gear Box	15
1	Pivot Pin	1
1	Cover, Gear	2
1	Cover, Gear Box	1
1	Drive Motor Assembly (Mirror)	4
1	Pivot Block (Mirror Gear)	10
<u>Foundation Support</u>		
4	Cast Iron Pillow Blocks	8
1	Support and Post Assembly (2)	260
1	Foundation and Support (2)	17,400
<u>Mirror Cranks and Tie Rods</u>		
8	Crank Arm	28
8	Taper Lock	2
4	Tie Rod	46
1	Drive Electronics	60

SOLAR RESEARCH EXPERIMENT IMAGE ANALYSIS

Sun images reflected from a parabolic mirror as projected onto a broad-side surface located at the focal point (target) have been shown* to consist of two parts:

1. A true-shape image of the mirror linearly scaled in size by $1 - \cos\theta$, where θ is the angle between the mirror axis and the sun.
2. A pattern of circles around each point on the mirror image of radius EF where E is half the sun's subtended angle (.00465 rads) and F is the focal length (distance to the tower).

Circular mirror pattern shapes are sketched for several different values of θ in Figure 4-7. It is convenient to think of the patterns as composed of four circles having diameters defined by:

$$\begin{aligned} D_S &= 2EF && \text{sun's image} \\ D_M &= (1 - \cos\theta) D_M && \text{mirror image} \\ D_I &= D_M + D_S && \text{total image outer diameter} \\ D_C &= D_M - D_S && \text{total image core diameter} \end{aligned}$$

In equation form:

$$\begin{aligned} D_I &= (1 - \cos\theta) D_M + 2EF \\ D_C &= (1 - \cos\theta) D_M - 2EF \end{aligned}$$

Outer image diameter is of particular interest to the research experiment since it, together with computation errors of the offset facets and pointing errors, defines the desired size of the target array.

The core diameter is of uniform intensity and for $D_M < D_S$ is constant at maximum value. For $D_M > D_S$ the core intensity is still uniform but of decreasing magnitude with increasing D_M .

The scaled mirror image size part of the equation is seen to be a function only of θ and is, therefore, only weakly related to distance from the target. The sun image portion of the equation is dependent only on the sun's subtended angle and is directly proportional to distance from the target.

* Memo, W. H. Egli to J. C. Powell, 3/4/75, "Performance of Off-Axis Low Aperture Reflectors", S&RC/R.

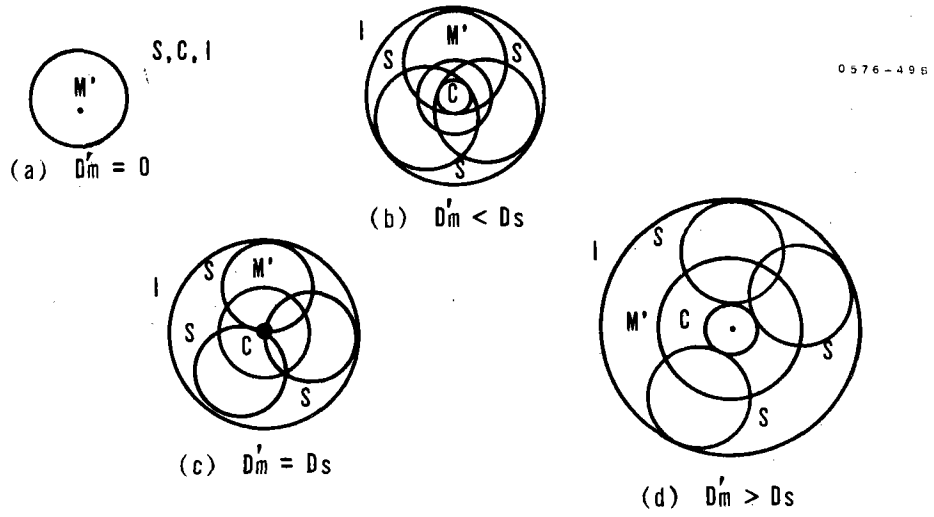


Figure 4-7. Circular Mirror Images

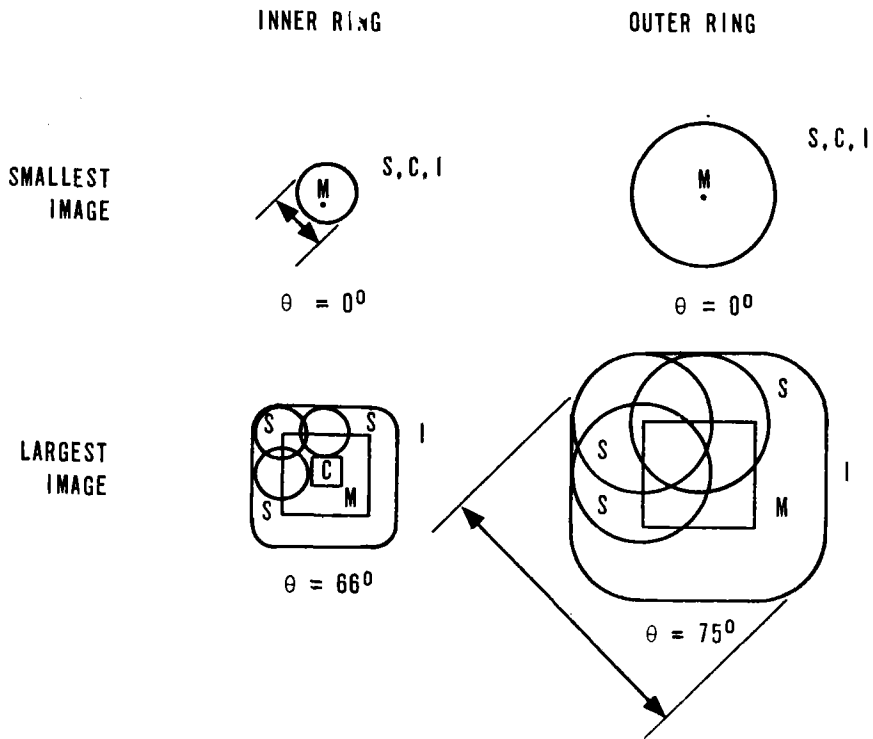


Figure 4-8. Site Images - $10M^2$ Square Facet

Mirror shapes other than circular do not result in nice simple equations, but are just as easily sketched. Image shapes expected from a 10m^2 square mirror at the extremes of the field and for the extremes of θ are sketched to scale in Figure 4-8. The image rotates about its center on the broad-side target plane the same amount as the plane defined by the sun, mirror normal, and target vectors rotates away from vertical.

Total specular reflectance, by taking into account the spectral distribution of the sun's energy, gives a true picture of reflector efficiency.

Reflectance figures can be misleading unless the total (sun's) specular reflectance is used. The example below shows how a mirror, having a maximum reflectance as high as 0.9, has an effective (total specular) reflectance of only 0.68 even though its reflectance appears to track the sun's spectral distribution.

Spectral distribution of the sun's energy per unit wavelength is plotted in Figure 4-9.* Reflectance below 0.3 and above 2.0 microns is of little benefit since 98% of the sun's energy falls within this band, as shown by the cumulative distribution in Figure 4-10.

Reflectance of a 1/4 inch silvered second surface mirror is plotted in Figure 4-11.** When this is multiplied by the sun's irradiance, the reflected spectral distribution per unit wavelength of Figure 4-12 is obtained. Integrating Figure 4-12 gives the cumulative reflected energy of Figure 4-13 showing a total specular reflectance (mirror efficiency) of 68%.

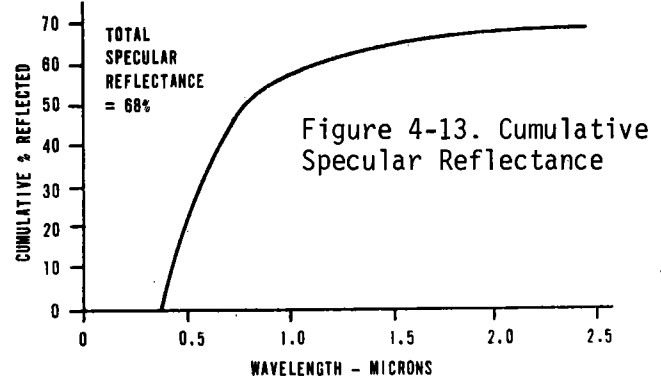
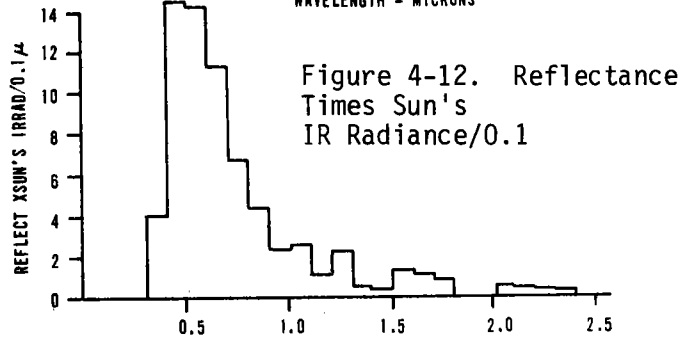
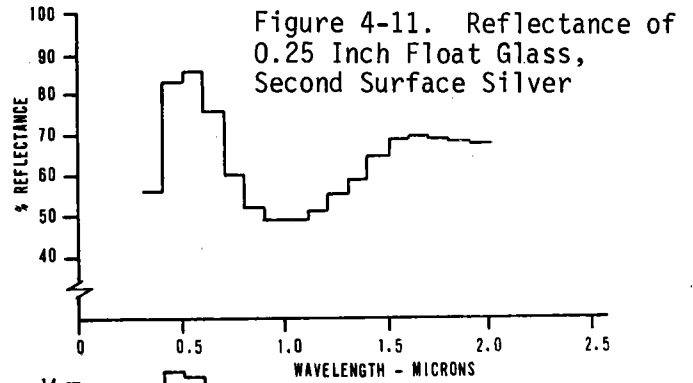
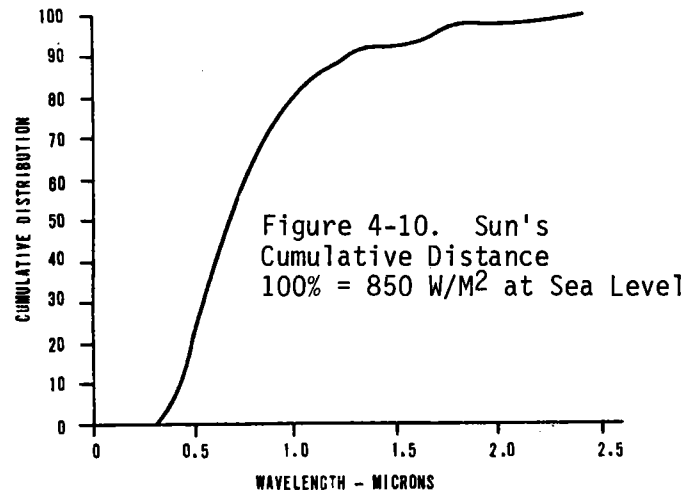
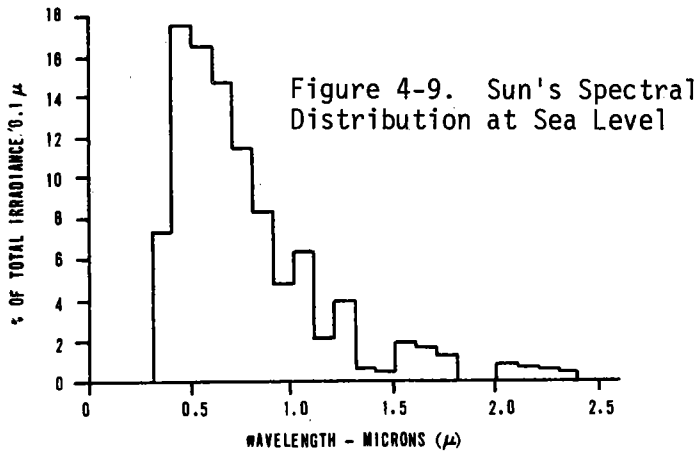
Silicon photo transistors are being used in the experiment calibration array. They have a peak spectral response at .9 microns and taper off to zero below .5 and above 1.1 microns. While they are useful for obtaining relative intensity measurements for determining spot size, the mirror total reflectance should be periodically measured (to determine mirror efficiency). If significant variations are noted, we might also want to periodically measure the mirror reflectance versus wavelength to aid in evaluation.

Cost tradeoffs should use the total specular reflectance of the reflectors. If manufacturer's data is used, the same model for the sun's spectral irradiance must be used. It appears there is considerable latitude possible here; i.e., time of day and elevation above sea level can make significant differences.

* Handbook of Geophysics and Space Environments, Air Force Cambridge Research Labs, Office of Aerospace Research, U. S. Air Force, 1965.

** Design fabrication and testing of a heliostat for a central receiver solar thermal power plant - Final Report by University of Houston and McDonnell Douglas Astronautics Co. under a national science foundation grant for period 5/74 to 9/75.

0576-40R



Angles between facet axes and the sun, important because they define the maximum available power and off-axis aberation of a heliostat, vary between 0 and 74 degrees.

Cosines of facet axes to sun angles, calculated for the field geometry over the course of a day and a year, were found to:

1. Be significantly larger in the North field quadrant.
2. Be significantly larger for inner rings.
3. Have an average yearly value of .78.
4. Be nearly normally distributed; 68% > .73, 95% > .45, 99% > .30.
5. Have a range of 1.0 to 0.28.

Loss of available power and defocusing due to the site geometry is demonstrated in Figure 4-7. Here the average yearly cosines for the heliostats are plotted versus field position. The significantly higher values for the inner rings compared to the outer rings is due to the higher tower line of sight for the inner circles.

The effect of radial distance from the tower (or tower height) on the cumulative distribution of the cosines is demonstrated in Figure 4-8. This curve, together with the field geometry is used to compute the cumulative distribution of the cosines for the entire field, shown in Figure 4-9. These plots are useful for weighing the effects of apertures or targets not capable of receiving the worst case images.

The cosines were calculated each hour for one hour after sunrise to one hour before sunset for three days of the year; equinox, summer solstice and winter solstice. Average yearly values for a particular heliostat were calculated by averaging the values for each hour and the three days.

COORDINATE TRANSFORMATIONS ANALYSIS

Mirror pointing errors are related to error rotations occurring about the three error measurement frames in the heliostat by the equations:

$$\text{Error about } \hat{x}_{11} = M_1 + (I_1 + O_1) C\theta - (I_3 + O_3 c\phi + O_2 s\phi)$$

$$\text{Error about } \hat{y}_{11} = I_2 + M_2 + O_2 c\phi + O_3 s\phi$$

where

\hat{y}_{11} is the unit direction vector along the inner gimbal axes

\hat{z}_{11} is the unit vector along the mirror normal

$$\hat{x}_{11} = \hat{y}_{11} \times \hat{z}_{11} .$$

Error equations are developed by determining the rotation of the mirror caused by small error rotations about the heliostat frames:

O_n fixed in the mounting posts

I_n fixed in the outer gimbal

M_n fixed in the mirror.

The direction cosines of the mirror normal measured on the inner axis are related to the base cosines in an errorless heliostat by the matrix equation

$$|n_m| = |\theta| |\phi| |n_b| \text{ or } |n_b| = |\phi|^T |\theta|^T |n_m|$$

where

$|\phi|$ is the rotation matrix due to the outer gimbal angle

$|\theta|$ the matrix due to the inner gimbal angle.

If we include the error rotations we get

$$|n_m| = |M| |\theta| |I| |\phi| |O| |n_b| .$$

Combining the two above equations gives:

$$|n'_m| = |M||\theta||I||\phi||O||\phi|^T|\theta|^T|n_m|$$

M, O, and I are error rotations about the three axis of each triad which for small angles ($\cos \gamma = 1$ and $\sin \gamma = \gamma$) reduces to:

$$(\gamma) = \begin{vmatrix} 1 & \gamma_3 & -\gamma_2 \\ -\gamma_3 & 1 & \gamma_1 \\ \gamma_2 & -\gamma_1 & 1 \end{vmatrix}$$

The transformation group $|\phi||O||\phi|^T$ then is:

$$|\phi||O||\phi|^T = \begin{vmatrix} 1 & (O_3 \csc \phi - O_2 \sec \phi) & -(O_3 \sec \phi + O_2 \csc \phi) \\ -(O_3 \csc \phi + O_2 \sec \phi) & 1 & O_1 \\ (O_3 \sec \phi + O_2 \csc \phi) & -O_1 & 1 \end{vmatrix}$$

which is the matrix representation of the rotational error vector \hat{O} transformed through a rotation ϕ .

Let

$$|\phi||O||\phi|^T = O'$$

another small angle transformation matrix.

Then

$$|n'_m| = |M||\theta||I||O'|||\theta|^T|n_m|$$

But

$$|\hat{I}||\hat{O}'| = \begin{vmatrix} 1 & +(I_3 + O_3') & -(I_2 + O_2') \\ -(I_3 + O_3') & 1 & (I_1 + O_1') \\ (I_2 - O_2') & -(I_1 + O_1') & 1 \end{vmatrix}$$

which is the matrix representation of the sum of the two rotation vectors \hat{I} and \hat{O}' - another small angle rotation matrix.

Then

$$|n'_m| = |M||\theta||I + O'|||\theta|^T|n_m|$$

But

$|M||\theta||I + O'||\theta|^T$ is exactly the same form as was $|I||\phi||O||\phi|^T$ so that it is the matrix representation of the error rotation vector $\hat{I} + \hat{O}'$ transformed through the rotation θ and summed with the error rotation vector \hat{M} .

Functionally, the above can be represented as shown in Figure 4-14, where the error vector \hat{O}_n is transformed through ϕ , summed with \hat{I}_n , transformed through θ and summed with \hat{M}_n .

Let the resulting matrix, itself a small angle rotation matrix, be $|\beta|$ and defining the error matrix $|\epsilon| = |n'_m| - |n_m|$, then:

$$|\epsilon| = |\beta||n_m| - |I||n_m| = \begin{vmatrix} 0 & \beta_3 & -\beta_2 \\ -\beta_3 & 0 & \beta_1 \\ \beta_2 & -\beta_1 & 0 \end{vmatrix} |n_m|$$

which in vector form is:

$$\hat{\epsilon} = \hat{\beta} \times \hat{n}_m$$

The rotation vectors \hat{O} , \hat{I} and \hat{M} and the mirror normal \hat{n} can be transformed to any convenient computation frame. The target frame is a particularly useful one since the error rotation about the target direction can be dropped and the two remaining cosines are the cross-course and elevation errors in the target frame.

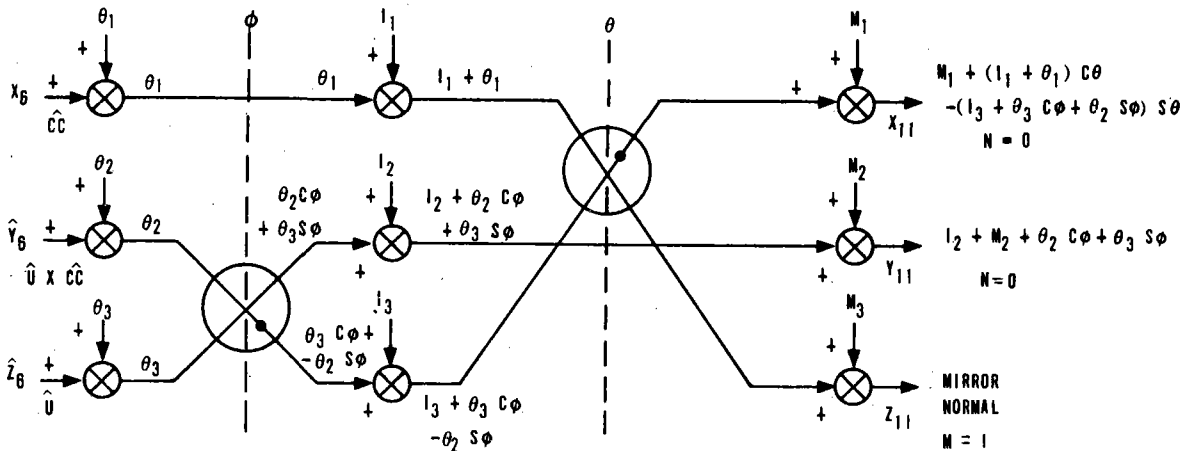


Figure 4-14. Heliostat Pointing Error Flow Diagram

Functional relationships between the coordinate frames used in the analysis and control of the heliostats are defined in Figure 4-15. From left to right the rotations r , w , i , $Lg + \Omega t + 90^\circ$ and Lt define the transformations from inertial to local vertical-north space and give the direction cosines of the sun direction vector. The rotation H gives the base frame for a specific heliostat in terms a cross-course, up, and (cross-course) X (up) frame. E is the elevation angle to the target and provides the transformation to the target frame. The N transformation zeros the sun's cosine on the \hat{x} axis, S zeros the sun's cosine on the \hat{y} axis and F is a 90 degree rotation to realign the inertial frame x axis and the sun's direction vector. The ϕ and θ rotations are the heliostat gimbal angles and provide the transformation from the base frame to the mirror.

The circle diagram of Figure 4-16 provides a summary of the functional diagram. The numbers within the small circles represent the frame, the letters (on the inside of the large circles) are rotation angles and the x , y or z notations outside the circle define the axes about which the rotations occur.

Matrixes relating the frame adjacent to a rotation can be written using the diagram key. For instance, by inspection:

$$\begin{vmatrix} x_{10} \\ y_{10} \\ z_{10} \end{vmatrix} = \begin{vmatrix} 1 & 0 & 0 \\ 0 & c\phi & s\phi \\ 0 & -s\phi & c\phi \end{vmatrix} \begin{vmatrix} x_6 \\ y_6 \\ z_6 \end{vmatrix}$$

Vector direction cosines can also be defined using the diagram. For example:

$$S_1 \hat{x}_6 + S_2 \hat{y}_6 + S_3 \hat{z}_6 = S_1 \hat{x}_{10} + (S_2 c\phi + S_3 s\phi) \hat{y}_{10} + (S_3 c\phi - S_2 s\phi) \hat{z}_{10}$$

Figure 4-15. Computational Frames

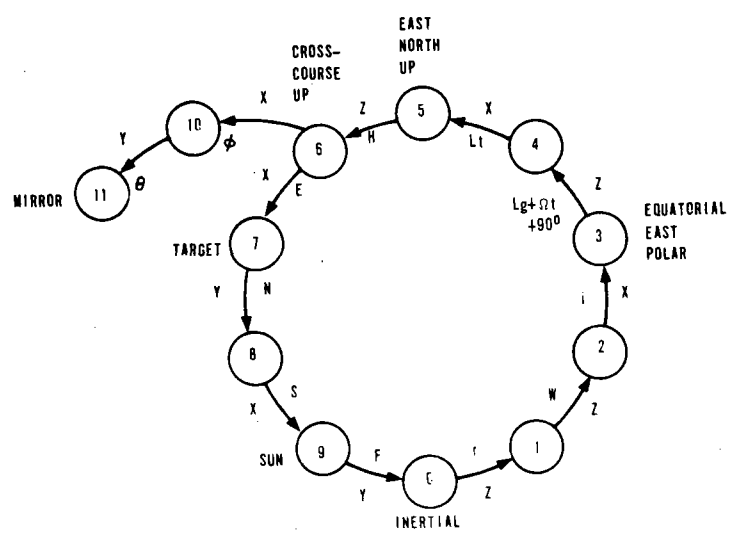
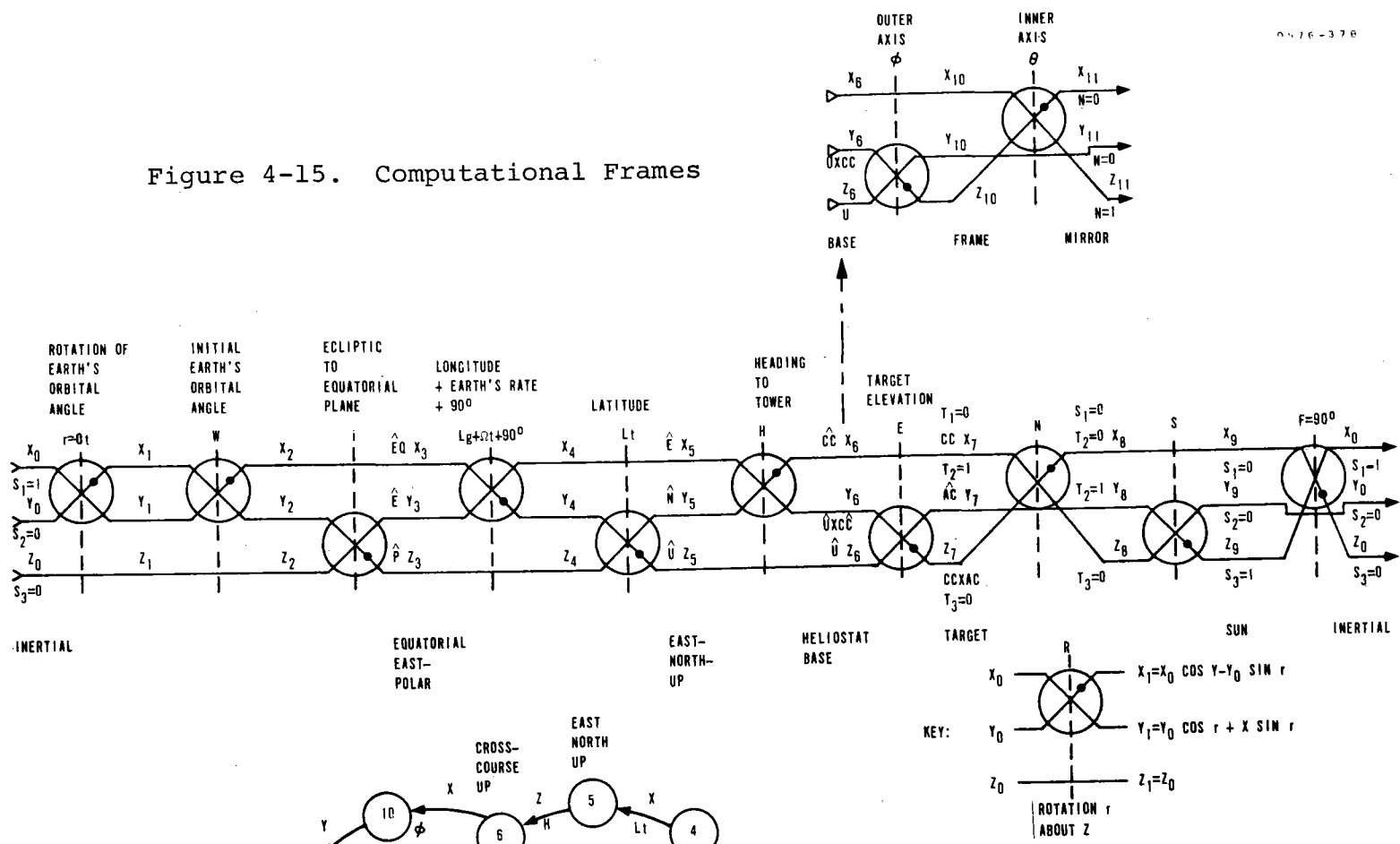


Figure 4-16. Circle Diagram

The equations for computing cross-course* and elevation errors at the target are derived as follows:

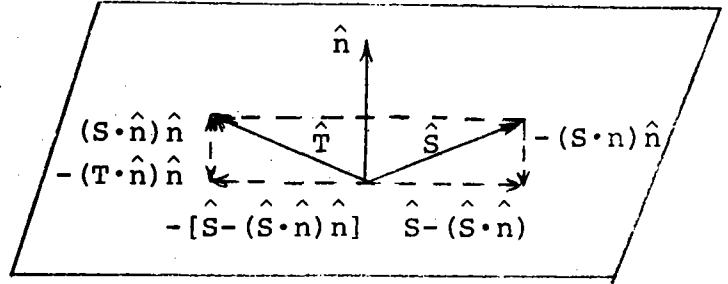
For \hat{T} = Unit Director Vector to Tower

\hat{X} = Unit Sun vector

\hat{n} = Unit Mirror Normal Vector

$$\hat{T} = - [\hat{S} - (\hat{S} \cdot \hat{n}) \hat{n}] + (\hat{S} \cdot \hat{n}) \hat{n}$$

$$\hat{T} = - [\hat{S} - 2(\hat{S} \cdot \hat{n}) \hat{n}]$$



converting to matrix equations

$$(\hat{S} \cdot \hat{n}) \hat{n} = \mathbf{nn}^T \mathbf{S}$$

so that

$$\mathbf{T} = - [\mathbf{I} - 2 \mathbf{nn}^T] \mathbf{S} \quad \text{similarly} \quad \mathbf{S} = - (\mathbf{I} - 2 \mathbf{nn}^T) \mathbf{T}$$

$$\text{Let } \mathbf{T}' = - [\mathbf{I} - 2 \mathbf{n}' \mathbf{n}'^T] \mathbf{S}$$

where $\mathbf{n}' = \mathbf{n} + \delta \mathbf{n}$ and $\delta \mathbf{n}$ is small compared to \hat{n}

$$\text{then } \mathbf{T}' = - (\mathbf{I} - 2 [\mathbf{n} + \delta \mathbf{n}] [\mathbf{n} + \delta \mathbf{n}]^T) \mathbf{S} = -\mathbf{S} + 2 (\mathbf{nn}^T + \mathbf{n} \delta \mathbf{n}^T + \delta \mathbf{n} \mathbf{n}^T + \delta \mathbf{n} \delta \mathbf{n}^T) \mathbf{S}$$

but $\delta \mathbf{n} \delta \mathbf{n}^T$ is second order small

$$\text{therefore } \mathbf{T}' = -\mathbf{S} + 2 (\mathbf{nn}^T + \mathbf{n} \delta \mathbf{n}^T + \delta \mathbf{n} \mathbf{n}^T) \mathbf{S} = -(\mathbf{I} - 2 [\mathbf{nn}^T + \mathbf{n} \delta \mathbf{n}^T + \delta \mathbf{n} \mathbf{n}^T]) \mathbf{S}$$

$$\text{Let } \epsilon \mathbf{T}' = \mathbf{T} - \mathbf{T}' = -\mathbf{S} + 2 \mathbf{nn}^T \mathbf{S} + \mathbf{S} - 2 \mathbf{nn}^T \mathbf{S} - 2 (\mathbf{n} \delta \mathbf{n}^T + \delta \mathbf{n} \mathbf{n}^T) \mathbf{S}$$

$$\text{or } \epsilon \mathbf{T}' = -2 (\mathbf{n} \delta \mathbf{n}^T + \delta \mathbf{n} \mathbf{n}^T) \mathbf{S}$$

$$\epsilon \mathbf{T}' = -2 (\mathbf{n} \delta \mathbf{n}^T + \delta \mathbf{n} \mathbf{n}^T) (-\mathbf{I} + 2 \mathbf{nn}^T)^T$$

$$= -2 (-\mathbf{n} \delta \mathbf{n}^T + 2 \mathbf{n} \delta \mathbf{n}^T \mathbf{nn}^T - \delta \mathbf{n} \mathbf{n}^T + 2 \delta \mathbf{n} \mathbf{n}^T \mathbf{nn}^T)^T$$

But since $\delta \mathbf{n}^T \mathbf{n} = 0$ and $\mathbf{n}^T \mathbf{n} = \mathbf{I}$

$$\epsilon \mathbf{T}' = -2 (-\mathbf{n} \delta \mathbf{n}^T - \delta \mathbf{n} \mathbf{n}^T + 2 \delta \mathbf{n} \mathbf{n}^T)^T = -2 (\delta \mathbf{n} \mathbf{n}^T - \mathbf{n} \delta \mathbf{n}^T)^T$$

$$\epsilon \mathbf{T}' = 2 (\mathbf{n} \delta \mathbf{n}^T - \delta \mathbf{n} \mathbf{n}^T)^T \quad (1)$$

Since $\mathbf{n} \delta \mathbf{n}^T$ and $\delta \mathbf{n} \mathbf{n}^T$ are symmetric with equal diagonals

* Across the course or beam path as opposed to along the beam course.

$n\delta n^T - \delta n n^T$ is a skew symmetric rotation matrix, $[\psi]$, and is small angle since all terms are multiplied by δn or δn^T .

$\epsilon T' = 2 (\psi)T$ which in vector notation gives

$$\hat{\epsilon T} = 2 \hat{\psi} \times \hat{T}$$

letting $\delta \hat{n} = \hat{\phi} \times \hat{n}$ and expanding $n\delta n^T - \delta n n^T$ gives ψ , the elements of which are the rotation vector $\hat{\phi} = [\hat{\phi} - (\hat{\phi} \cdot \hat{n})\hat{n}]$ which can be recognized as the component of the rotation vector \hat{n} so that

$$\hat{\epsilon T}' = 2 [\hat{\phi} - (\hat{\phi} \cdot \hat{n})\hat{n}] \times \hat{T} \quad (2)$$

If we compute the error in the target frame where $T = 0\hat{x}$ and $1\hat{y}$ and $0\hat{z}$

$$\frac{\epsilon T'}{2} = [-\phi_3 + (n \cdot \phi)n_3] \hat{c}\hat{c} + 0 \hat{a}\hat{c} + [\phi_1 - (n \cdot \phi)n_1] \hat{c}\hat{c} \times \hat{a}\hat{c}$$

and the miss distances at the target are:

$2R (\phi_3 + (n \cdot \phi)n_3)$ cross course error and

$2R (\phi_1 - (n \cdot \phi)n_1)$ perpendicular to cross course and along course.

Where R is the slant range to the target.

MOTOR SIZING ANALYSIS

The gimbal drive motor is a permanent magnet dc motor, the current I_M of which is given by:

$$I_M = \frac{V_M - \dot{\theta}_L N K_V}{R_M} \quad (4-1)$$

where

I_M = motor current in amperes

V_M = motor terminal voltage in volts

$\dot{\theta}_L$ = gimbal angular speed in deg/sec

N = effective gear ratio between motor shaft and gimbal

K_V = motor back EMF in volts/deg/sec

R_M = motor winding resistance

The usable motor torque T_M can be found from

$$T_M = I_M K_M - T_{FM} - T_{FG} \quad (4-2)$$

where

T_M = motor torque in ft-lbs

K_M = motor torque sensitivity in ft-lbs/amp

T_{FM} = torque required to drive motor friction

T_{FG} = torque required to drive gear friction

from which the usable load torque T_L becomes

$$T_L = T_M EN \quad (4-3)$$

where

T_L = load torque in ft-lbs

E = efficiency of gear ratio/100

Combining Equations 4-1, 4-2, and 4-3 and solving for $\dot{\theta}_L$, the speed that the motor will run at under load becomes

$$\dot{\theta}_L = \frac{V_M EN K_M - R_M [T_L + EN(T_{FM} + T_{FG})]}{EN^2 K_M K_V} \quad (4-4)$$

The power in the motor W_M , in watts, can be found from

$$W_M = W_M I_M \quad (4-5)$$

Substituting 1 in 5 produces

$$W_M = \frac{V_M^2 - V_M \dot{\theta}_L N K_V}{R_M} \quad (4-6)$$

The power W_L in watts delivered at the motor shaft is

$$W_L = K \dot{\theta}_L \left(NT_{FG} + \frac{T_L}{E} \right) \quad (4-7)$$

where

K = scaling factor to convert FTLB deg/sec to watts and equals 2.367×10^{-2}

The motors used for the inner and outer axes gimbal drives for the SRE are Inland T1806-H and T1804, respectively, with parameters as follows:

	<u>T1806</u>	<u>T1804</u>
Volts at peak torque, V_M , volts	22	17.8
Peak torque, ft-lbs	0.52	1.04
Back EMF, K_V , volts/deg/sec	0.00295	0.00366
Motor Resistance R_M , ohms	5.1	2.65
No load speed, deg/sec	7448	4870
Torque sensitivity, K_M , ft-lbs/amp	0.121	0.155
Motor friction	0.0156	0.026
Maximum winding temp, °C	155	155
Amps at peak torque	4.3	6.7

The remaining parameters complete the definition of the system.

	<u>Inner Axis</u>	<u>Outer Axis Per Actuator</u>
Load, wind, & unbalance, T_L , ft-lbs	238 max @ 13.5 M/S	517 max @ 13.5 M/S
Gear Ratio, N	16000	11450 to 18000, 16000 avg
Gear efficiency, E	0.2	0.25
Gear friction torque, T_{FG} , ft-lbs	0.021 to 0.120	0.260

Based on the above derivations and data, the values appearing in the two tables were calculated for several load conditions. Temperature rise calculations are based upon a thermal resistance of 3.5°C/watt.

Inner Axis Motor Calculations							
T_L ft-lbs	T_{FG} ft-lbs	$\dot{\theta}_L$ deg/sec	W_M watts	W_L watts	Eff %	ΔT Rise, °C	Remarks
0	0.021	0.43	7.3	3.4	47	25	0 wind and unbalance
119	0.070	0.36	21.6	14.7	68	75	1/2 wind and unbalance
238	0.12	0.28	37.9	20.6	54	132	Full wind at 13.5 M/S
476	0.22	0.12	70	16.7	24	245	2X wind and unbalance
660	0.30	0	95	0	0	332	T_L at stall, $\dot{\theta}_L \rightarrow 0$

Outer Axis Motor Calculations							
T_L ft-lbs	T_{FG} ft-lbs	$\dot{\theta}_L$ deg/sec	W_M watts	W_L watts	Eff %	ΔT Rise, °C	Remarks
0	0.26	0.22	33	21.7	66	115.5	0 wind and unbalance
258	0.26	0.20	41	24.6	60	141	1/2 wind and unbalance
517	0.26	0.18	49	26.5	54	171	Full wind at 13.5 M/S
1034	0.26	0.15	63	28.4	45	220	2X wind and unbalance
3014	0.26	0	120	0	0	320	T_L at stall, $\dot{\theta}_L \rightarrow 0$

CONTROL LOOP STABILITY ANALYSIS

Torque motors with position feedback provide efficient, simple control loops that give stable operation with digital commands during tracking and slewing modes and with large windloads.

Stable operation was demonstrated by analysis using

- Quantized position feedback from the motor shaft
- Structural load resonance
- Quantized commands and feedback
- Multiple and three state loops
- 23 degrees/hour and 0.3 degree/second command rates
- Wind loads up to 834 pound-foot

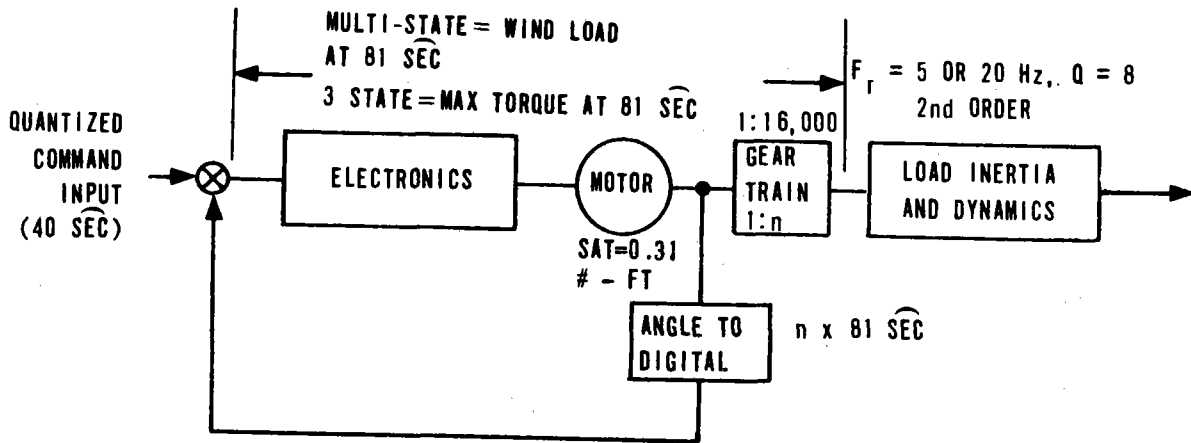
The gear ratio was selected to deliver an 81 arc-second load motion for one revolution of the motor. The resulting gear ratio of 16,000:1 effectively decouples load torques from the motor. With position feedback from the motor, the control loop is essentially independent of load dynamics. Motor back emf provides the damping required to give stable loop operation, so that the loop electronics need provide only a power amplification function.

Simplicity and economy are characteristic of the resulting design shown in functional block diagram form in Figure 4-17. The electronics convert the quantized error signal to a power drive to the torque motor (Inland No. NT1911). The motor drives the load through the gear train. Digital output of the drive No. 1806 motor shaft position is subtracted from the command angle input to generate the error signal.

The first configuration simulated used an electronics gain giving 30 mph wind load torque for each step (81 arc-seconds) of error signal. Stable, well damped response was indicated with feedback from either the load or motor shaft. With feedback from the motor shaft, the loop gain was increased until the 81 arc-second quantization of error signal produced saturated motor torque. This results in three state operation 0, + stall torque or - stall torque output. The loop was run with command rates of 23 degrees/hour and 0.3 degree/second and with up to 30 mph wind loads. No indication of instability was noted.

Printout of a typical outer gimbal run showing response to step 834 lb-ft wind torque and 6 mr step command inputs is presented in Figure 4-17a. Feedback from motor shaft, three state loop gain and a 13 Hz load resonance were used for this run. The oscillation of load position is due to ringing of the load spring-mass system.

Figure 4-17. Functional Block Diagram



SYMBOL-BLOCK #
 + = 99 QUANTIZED INPUT COMMAND
 * = 50 MOTOR SHAFT POSITION
 X = 68 QUANTIZED MOTOR SHAFT POSITION
 O = 40 MIRROR POSITION

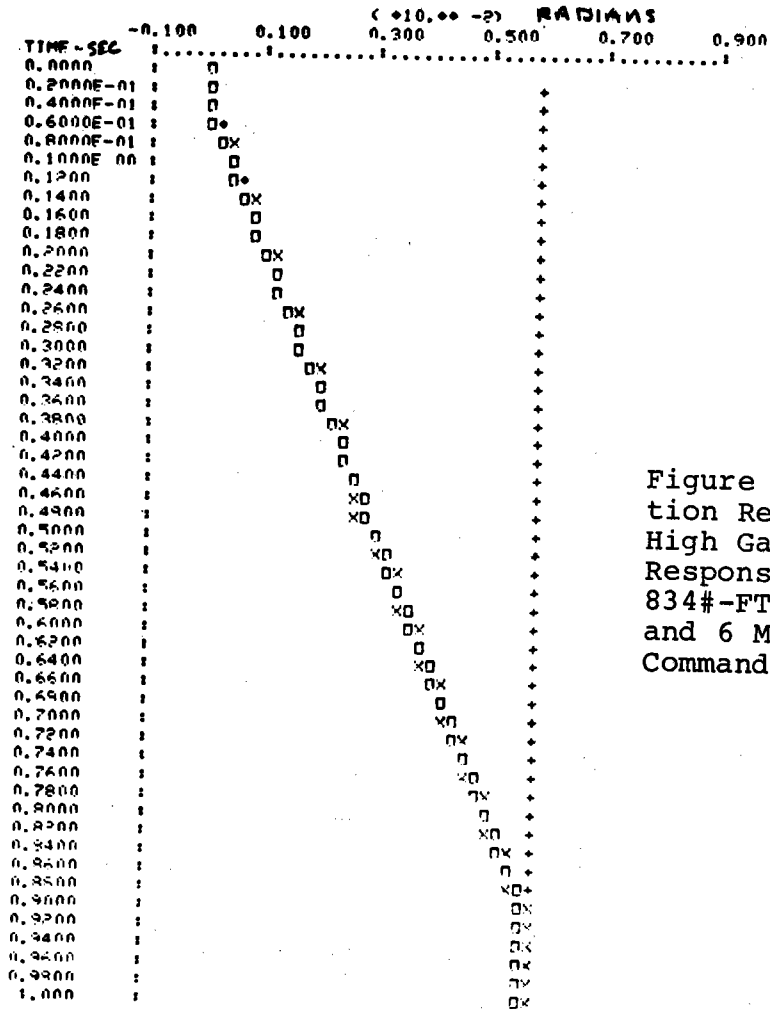
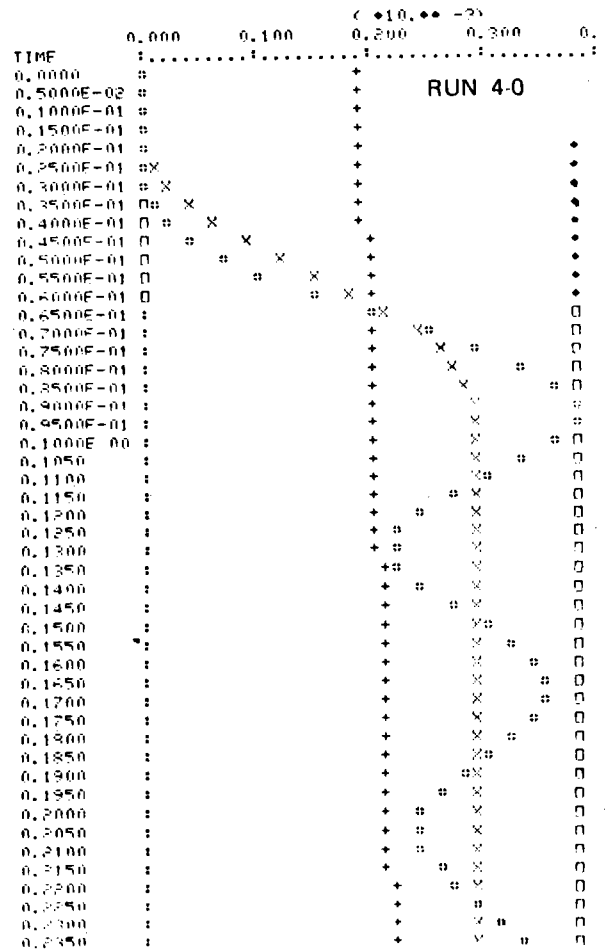
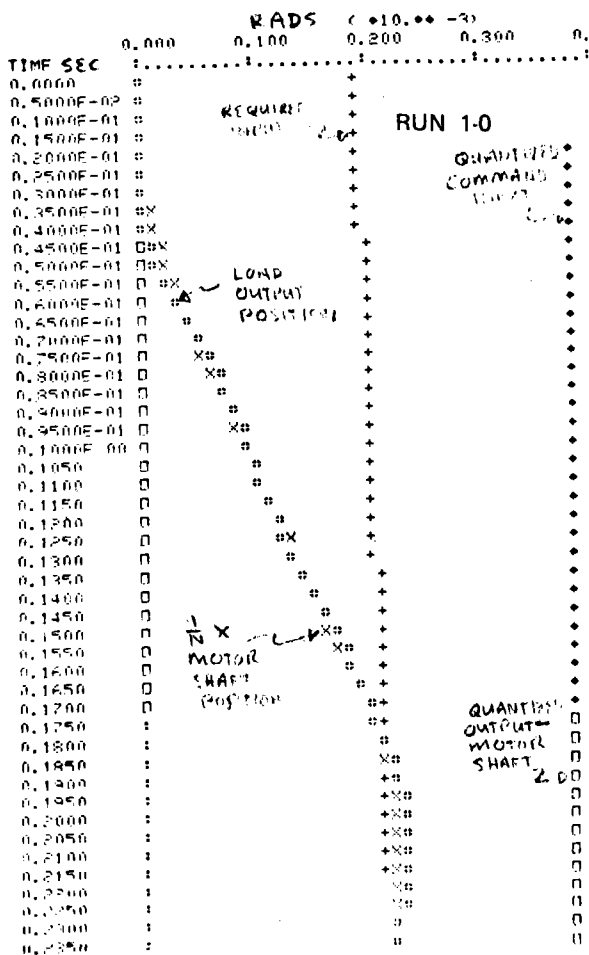


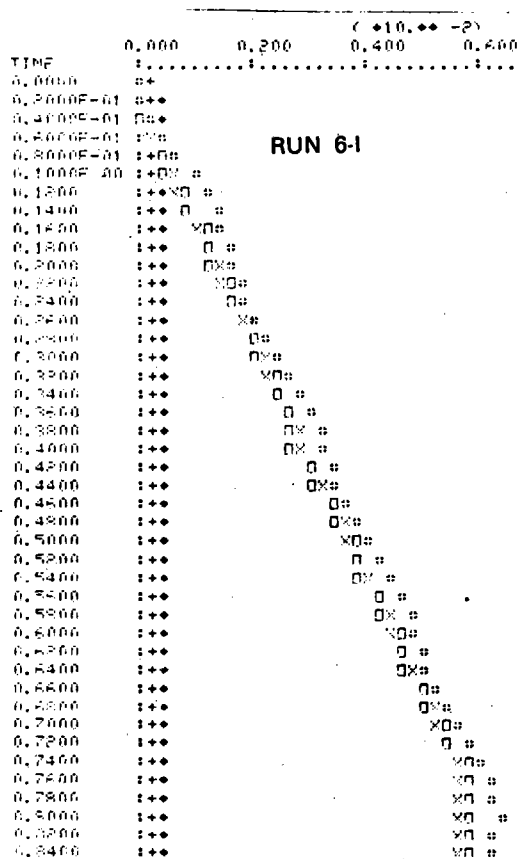
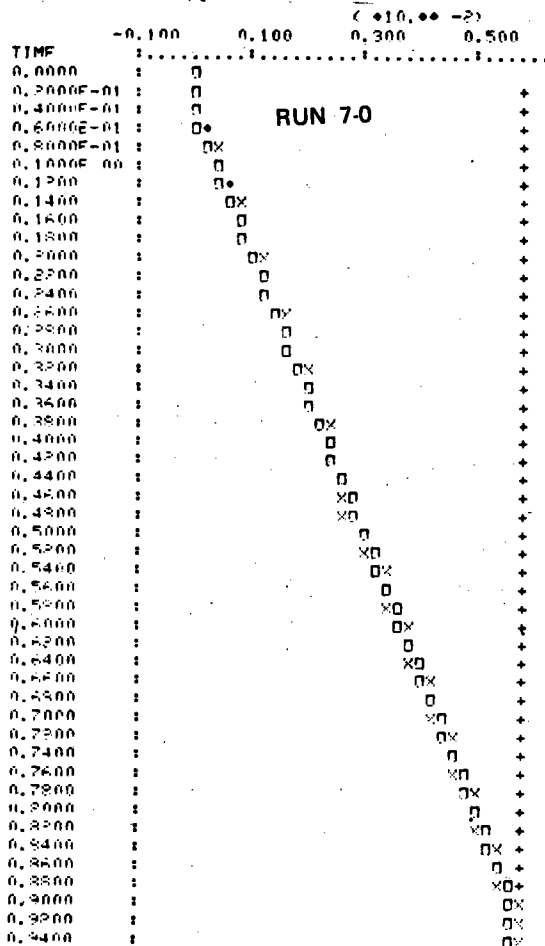
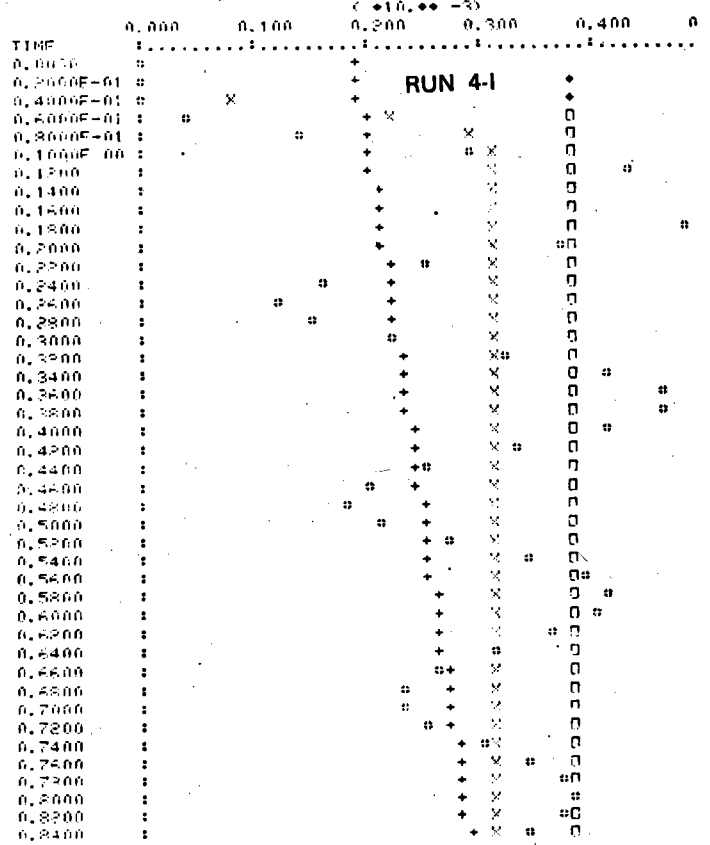
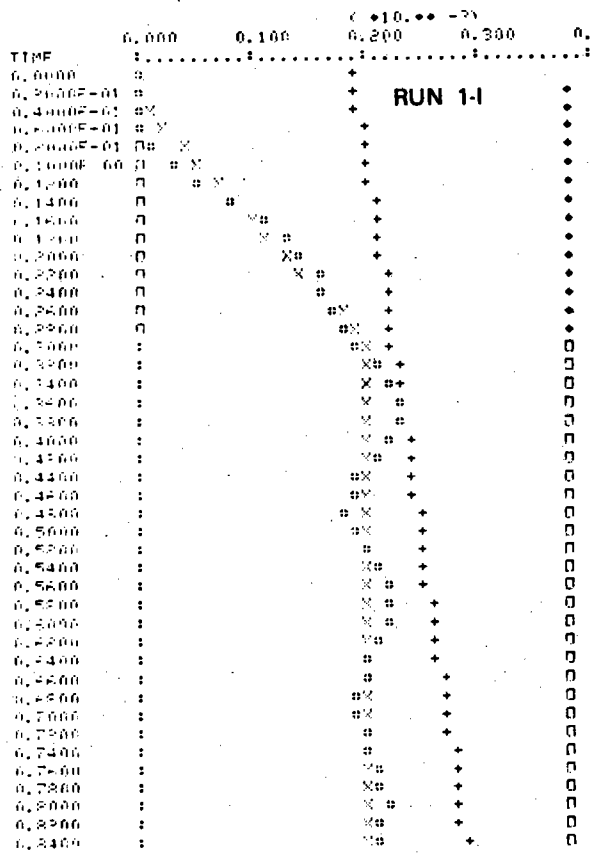
Figure 4-17a. Simulation Results Showing High Gain Loop Response to Step 834#-FT Wind Torque and 6 MR Step Command Inputs

Inner and outer axis transient response to various combinations of command inputs, windloads, and loop gains demonstrated satisfactory response times and stability.

The table below describes the loop inputs and gains used for various transient response runs. The figures show the simulation results for selected runs.

Outer Axis				Inner Axis			
Run	Gain	Step Load Lb-Ft	Step Command Bits	Run	Gain	Step Load Lb-Ft	Step Command Bits
1-O	LO	0	1	1-I	LO	0	1
2-O	LO	834	0	2-I	LO	208	1
3-O	LO	834	1	3-I	LO	208	0
4-O	HI	0	1	4-I	HI	0	1
5-O	HI	834	1	5-I	HI	0	15
6-O	HI	-834	1	6-I	HI	208	15
7-O	HI	-834	15	7-I	LO	208	15





SERVO ANALYSIS AND SIMULATION

The model used in the simulation of the heliostat loop is shown in Figure 4-18. It includes quantization of the input commands and position feedback, torque motor saturation limiting, load spring rate and damping, and worm gear friction.

Parameter values used for the analysis are summarized in the table below.

The simulation uses the "analog continuous systems simulator". This permits application of various input commands and load torques in combination or individually and provides stability verification under these conditions. Outputs from any block within the loop can be obtained.

LOOP PARAMETERS USED IN SIMULATION

	<u>Symbol</u>	<u>Units</u>	<u>Inner Axis</u>	<u>Outer Axis One Motor</u>
Torque Motor				
Max Stall Torque	T_M	lb-ft	0.52	1.04
Gain	K_M	lb-ft/V	$2.17\epsilon-2$	$4.34\epsilon-2$
Elec Time Const	T_M	sec	$1.3\epsilon-3$	$1.3\epsilon-3$
Damping (BEMF)	K_B	lb-ft-sec	$3.91\epsilon-3$	$7.82\epsilon-3$
Inertia	J_M	lb-ft-sec ²	$5.21\epsilon-5$	$1.04\epsilon-4$
Quantization		arc-sec	81	81
Gear Ratio	N	-	$1.6\epsilon4$	$1.6\epsilon4$
Gear Efficiency	E	-	0.25	0.25
Gear Inertia at Motor	J_G	lb-ft-sec ²	3×10^{-8}	2.86×10^{-5}
Load				
Inertia	J_L	lb-ft-sec ²	$7.32\epsilon2$	$2.67\epsilon3$
Spring Rate	K_L	lb-ft/rad	$6.25\epsilon5$	$1.75\epsilon7$
Damping	D_L	lb-ft-sec	$2.67\epsilon3$	$2.70\epsilon4$
Torque				
Wind	T_W	lb-ft	208	834
Mass Unbalance	T_U	lb-ft	30	200
Friction	T_F	lb-ft	2	2

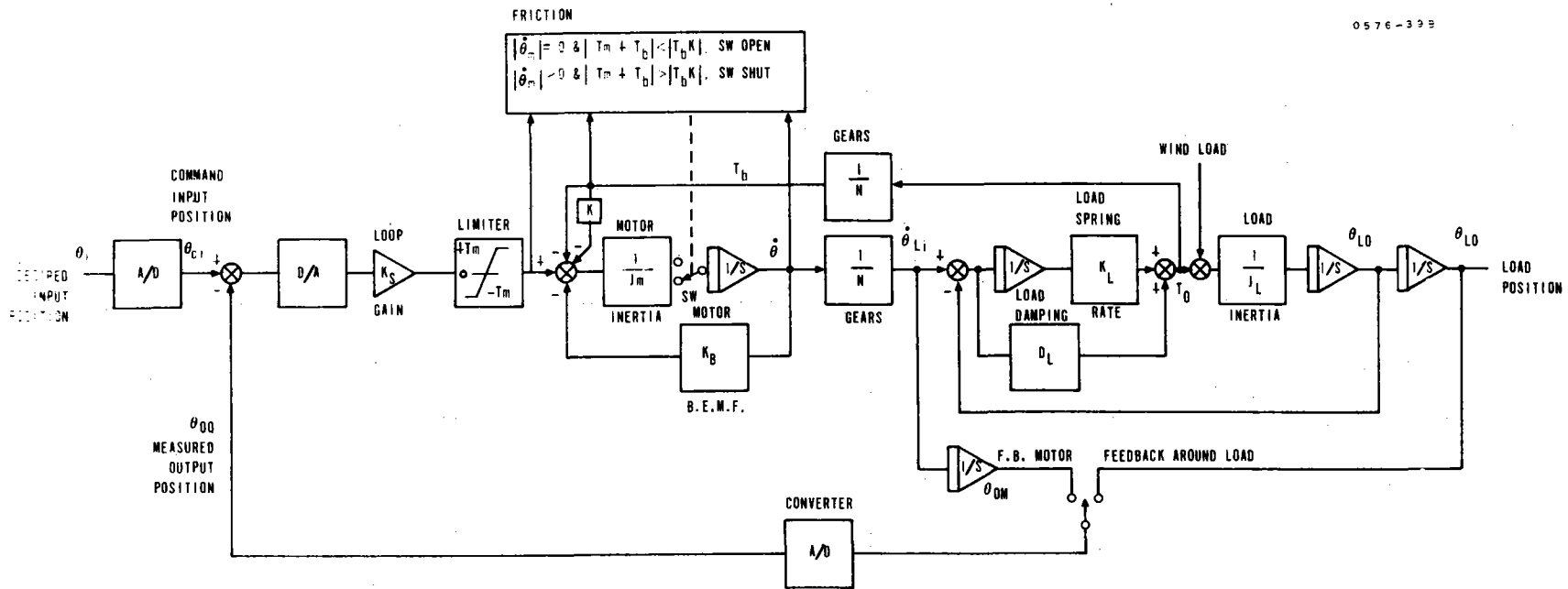
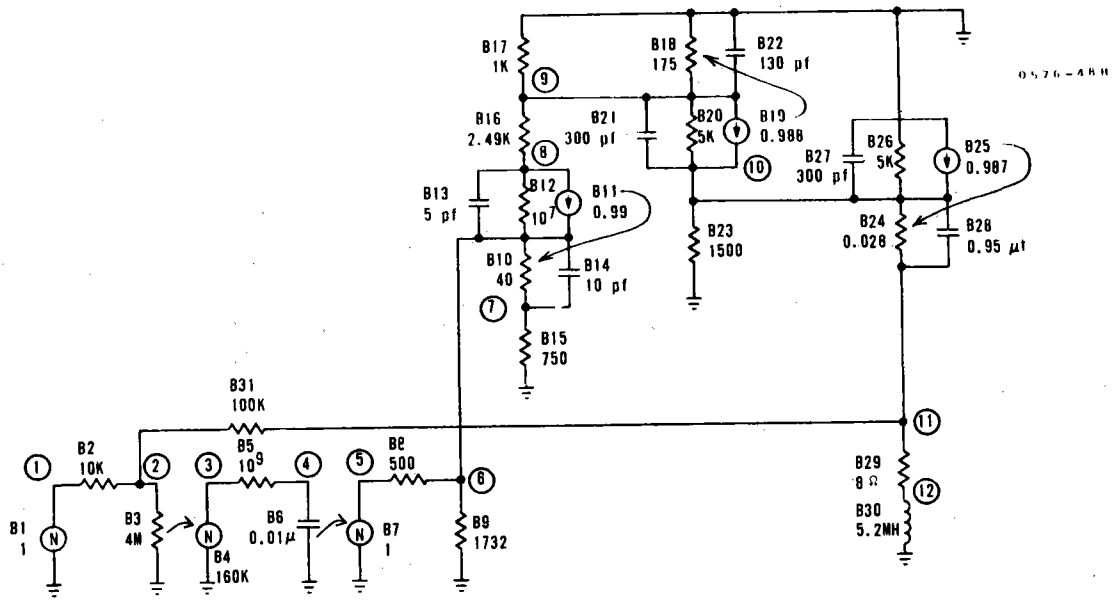


Figure 4-18. Gimbal Control Loop Model Used in Simulation

HELIOSTAT SERVO OUTPUT AMP SMALL SIGNAL SIMULATION AND ANALYSIS
A small signal simulation of the Heliostat Servo Output amplifier showed stable closed loop operation.

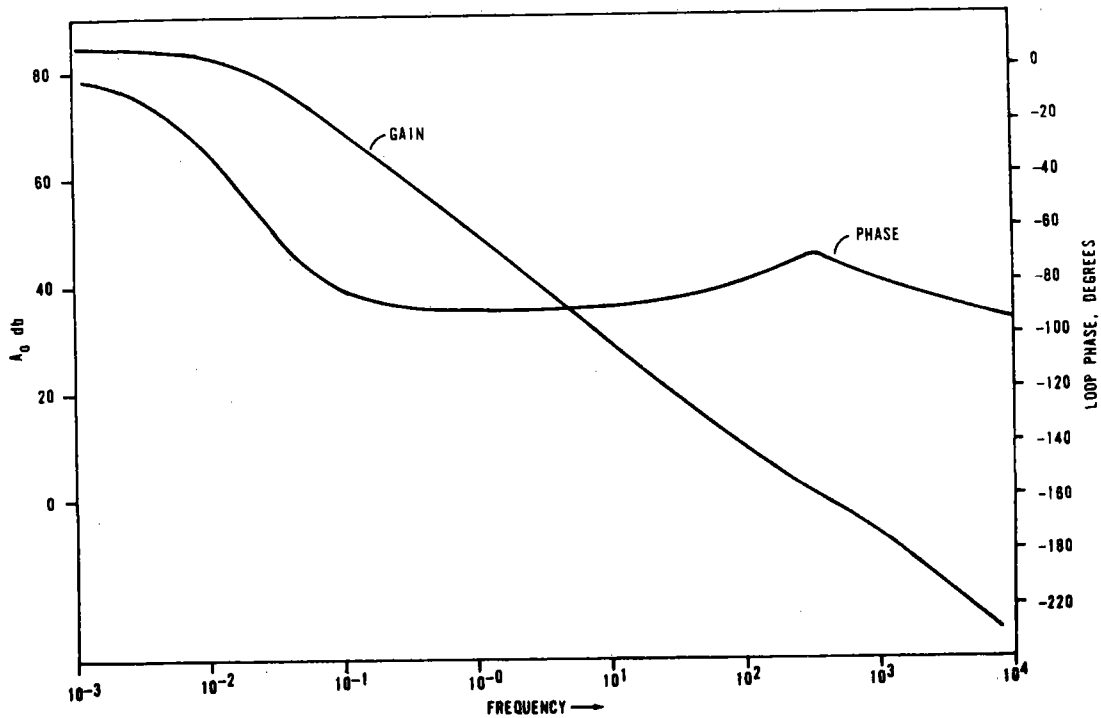
The equivalent circuit for the simulation is shown in Figure 4-19. The model is for a linear simulation of the op amp and the three level shifting and power output transistors. The op amp model considers input R, output R, and voltage gain and uses a single pole low frequency corner for response purposes. All higher frequency breaks occur at 1 MHz and higher and are of no consequence. The transistor models are modified H parameter common base equivalents taking into account input resistance, output resistance, current gain, collector to base transition capacitance, and base to emitter diffusion capacitance. The values shown are nominal values for an output operating current of one ampere.

A Bode plot of the open loop gain and phase calculations is shown in Figure 4-20. Phase margin is >90 degrees. Gain margin is >60 db. Breadboard test data tends to verify these numbers in that no ringing was observed in square wave response tests on the amplifier.



HELIOSTAT SERVO OUTPUT AMPLIFIER
 SMALL SIGNAL EQUIVALENT CIRCUIT
 SERVO OUTPUT AMPLIFIER
 VALUES SHOWN ARE NOMINAL CASE FOR $I_0 = 1$ AMPERE
 PHASE MARGIN >90 DEGREES; GAIN MARGIN >60 DB; BANDWIDTH 250 Hz
 CLOSED LOOP GAIN 10 V/V

Figure 4-19. Small Signal Model



PHASE MARGIN > 90°; GAIN MARGIN > 60 DB; BANDWIDTH 250 Hz

Figure 4-20. Heliostat Servo Bode Plot

ANALYSIS OF HELIOSTAT RESPONSE TO ENVIRONMENTAL EFFECTS

The collector subsystem heliostats are designed to meet a 30 year useful life requirement. Our limited SRE test experience (one year) has not shown anything to the contrary in the design so far. However the only real proof of meeting this requirement along with maintaining long term pointing accuracy requirements will be to start full scale testing under desert operational conditions. Some specific effects, however, with respect to the field environment exposure are discussed below. Subparagraph F. provides a brief list of special purpose testing in addition to daily performance monitoring which will help to fully evaluate the influence of the pilot plant environmental exposure.

A. Thermodynamic Effects

A previous subsection includes a detailed discussion of the thermal environmental effects upon the heliostat with respect to:

- Thermal gradients across the heliostat and resultant induced errors. The SRE test results indicate that the gradients are well within those used within the collector subsystem error budget to retain a 2 mr pointing accuracy.
- Thermal effects upon the structure and enclosed heliostat electronics under maximum temperatures expected.
- Thermal effects upon the enclosed heliostat electronics due to cold temperatures.

In summary, it was found that the thermal gradients are within specification, the electronics box must be shaded during peak insolation levels and be heated during colder temperatures.

Cold weather effects on the experimental model heliostats of the SRE were not determined during the SRE except for the opportunity to evaluate the inner and outer drive system characteristics at near freezing conditions (33°F) in early morning. The power consumption of the inner drive increased about 25 percent and of the outer drive about 70 percent as compared to a 65-70°F day of operation. Lubricant stiffening and possible bearing interface tolerance changes will increase the power required for operation during cold weather. A more quantitative impact has not been empirically determined yet and will be a subject of future test and investigation prior to release of the final pilot plant heliostat detail design. Proposals for additional cold weather testing have already been prepared and submitted to ERDA for approval, which as of this date is still pending.

No temperature effects, shaded or under solar loading, have been noted during the SRE testing that changes our present mirror module design's contour.

B. Cloud Coverage

Cloud coverage will not affect the collector subsystem performance because of the open loop control philosophy except for reducing the

time available for calibration. Scheduling sequences may have to change to accommodate calibration of all heliostats within a week if cloud coverage is extensive. However, the complexity of the collector subsystem control procedures and software requirements is significantly increased.

From a total power plant viewpoint, cloud coverage has a severe effect.

- The thermal energy into the receiver is reduced or completely stopped and the storage subsystem output must be activated.
- Control complexity between the several subsystems is increased.

The collector subsystem control complex will monitor the 24 insolation recording devices. During the detail design phase of the heliostat, full interface will assure complete control despite:

- a. Thermal gradient build-up across the receiver as a function of different nonsymmetrical energy flux inputs and applicable time constants.
- b. Damage to the receiver.
- c. Potential damage to receiver due to instantaneous application of full solar flux near solar noon after an extended cloud coverage interval.
- d. Excess energy losses.

Based upon these time factors, the program requirements document will be generated to include all necessary control constraints for the software to remove sectors of heliostats based upon master control commands derived from cloud coverage over portions of the field and deviations of cloud coverage. Flags will be sent to the operator any time this type of independent activity is initiated by the control subsystem.

Logic of this nature will prevent unnecessary loss of energy input due to premature removal of the heliostat field off the target while insuring that receiver stress limits are not dangerously approached.

The dynamic activity of thin and small clouds does not appear to be a problem due to their normal rapid shadow transient across the Earth's surface, even though direct insolation at a spot can drop from 900 W/m^2 to zero within 20 seconds as observed during the SRE test program. These types of cloud activity shadow a portion of the ground only for a few seconds. The larger cloud which covers only a portion of the field or moves only gradually (gradually would be as compared to the receiver thermal gradient response time) would be the condition where the collector subsystem would initiate heliostat activity if necessary as commanded by the master control system.

C. Wind Effects

Wind loading is the single largest cost driver in designing the structural rigidity and gimbal drive strength to both survive at 40 m/sec winds and meet a 2 mr tracking accuracy under operational wind loading (13.5 m/sec) requirement.

Much analysis and test has been performed on a single SRE configuration heliostat exposed to operational wind loads of 13.5 m/sec (30 mph) assuming free stream conditions with limited data on ground effects.

An extensive structural analysis performed using the STARDYNE program was previously reported. Natural torsional harmonics were obtained and a dynamic varying input force which was a combination of the first 4 most significant (mirror module rotations) harmonics was applied across the heliostat with an average velocity of 13.5 m/sec. Also static loads associated with 13.5 m/sec were applied to the analytical model. In all cases, stress or loads never exceeded hardware limitations.

The SRE test effort spent considerable effort to determine wind effects upon heliostat operations. Individual mirror modules were loaded with uniform loads representing worse case pressure drag values for 13.5 m/sec. Worse case torsion loads were applied and mirror module deflections recorded. The moments were based on a combination of moment coefficients determined from an earlier wind tunnel test and flat plate free stream theoretical values. In all cases the mirror structures and contour control exceeded design requirements (1 mr or less deflection).

At the heliostat level moment loads were again applied on the inner axis and outer axis. The results compared favorably with the initial error budget except where the inner drive lash exceeded design goals.

Visual monitoring of the SRE heliostats with wind gusts of approximately 13.5 m/sec, the peak instantaneous deviation was 2.9 mr. Off-line analysis of rapidly recorded (once per 2 seconds) calibration array data showed that peak oscillations were ± 1.2 mr about the nominal beam direction.

Before addressing the field effects one other area should be mentioned. Three wind specification changes have occurred since the conception of the SRE which are applicable to the pilot plant or a commercial plant collector subsystem design.

- The wind profile was changed from a $V = V_{\infty} \left(\frac{H/S \text{ Height}}{10m} \right)^{0.2}$ profile to a 0.15 power profile.
- Due to the possibility of a rapidly approaching thunderstorm front, the heliostats may be exposed to a 22.5 m/sec wind load while at any operational gimbal orientation. Tracking does not have to continue, but slewing must be accomplished and no catastrophic damage occurs to the heliostat. Previously maximum wind velocity of 13.5 m/sec was peak.

- While in the stow position, the heliostat can be subjected to a 40 m/sec wind at 10 degree angle of attack (previously treated as zero) from horizontal. This requirement comes from the data presented in a TWX from Sandia. Previous requirements were a 45 m/sec survivability wind parallel to the ground.

Table 4-7 shows how the new requirements introduce individually additional loading stresses on the inner axis. Where the original design provided a comfortable margin against the original requirements (3.15:1 being the least), the subsequent additions completely negates the margin. This is especially true if 40 m/sec wind strikes each of the four mirror modules simultaneously in a stowed position, as shown in the last column of Table 4-7.

The field effects of the wind are relatively nebulous. Request for proposals were requested by ERDA to perform field effect wind tunnel testing on arrays of heliostats. This effort has been delayed due to scheduling changes. Field effects will include the following:

- Influence of the outer perimeter barrier upon the wind flow for the outer radii heliostats. The wind will create lift and become turbulent, thus inducing non-horizontal velocity vectors at points within the field. The vortex shedding from the fence could cause induced worse case moments on individual mirror modules.
- Influence of the receiver tower. The tower will cause separation and an increased wind velocity before reattachment or reaching free stream characteristics. The inner rows of heliostats may be affected.
- Influence of the ground effects and 0.15 power profile. It is difficult to predict the pressure gradients and subsequent induced moments on the inner and outer axis even for one heliostat because of the low profile of Honeywell's tilt-tilt design. In some orientations portions of a mirror module may be as close as 0.6m to the ground while other portions of the same mirror module may be as far as 4.9m from ground level. The irregular vortex shedding from one mirror module to another complicates even this situation. The effect of the low profile will be to reduce loads on the heliostat compared to a configuration that protrudes higher into the boundary layer.
- Influence of one heliostat upon another. The loads experienced by a single heliostat in an open field will be greater than that experienced by a heliostat in a group of heliostats.
- Influence of the different heliostat orientations on adjacent heliostats with respect to shedding frequencies and vortex magnitudes.
- Influence of the 10 degree angle of attack across the entire field during 40 m/sec winds.

Table 4-7. Stress Margin Versus Inner Axis Moment Loading

	Baseline 13.5 m/sec Oper 45 m/sec Surv and 0.20 Profile Exp; Load One MM Only	Oper 0.15 Exp	Oper 17 m/sec WCAOA	Oper 25 m/sec WCAOA	Surv 40 m/sec 10 Deg AOA	Surv 40 m/sec 10 Deg AOA 4 MM
Ratio by which moment loads increase	1	1.15	1.58	3.43	6.32	25.3
Moment (kg-m)	86.4	99.4	136.6	66	546.3	2185
MM stub shaft torque margin to σ_{su}	24	20.9	15.2	7	3.79	0.95
MM bearing load margin for 630.4 lbs at 86.4 kg-m	4.71	4.09	2.98	1.37	0.75	0.19
Crank arm stress margin to 2461 kg/cm ² ultimate shear stress	5.24	4.55	3.32	1.53	0.83	0.20
Taper lock shear stress margin to 2461 kg/cm ² σ_{su}	7.14	6.21	4.52	2.08	1.13	0.28
Tie rod column load margin	3.15	2.74	2.0	0.921	0.50	0.25
Spur gear tooth stress margin	5.33	4.64	3.37	1.55	0.84	0.21
Motor torque margin	4.0	3.48	2.53	1.17	N/A	N/A

NOTE: Margin values are ratio of failure load to expected load under condition shown.

- Effect on the average energy input to the receiver from the composite collector field heliostat. Statistical analysis of the collector field performance for various wind loads will be conducted after field array testing results are available. Heliostats will not all be affected in the same way by wind from a given direction. They will oscillate, not necessarily in phase, at the inner axis natural frequencies of 2 Hz to 4 Hz. The net energy loss will be very small when the damping influence of the field effects is included. An analysis will be made in detail design, on a field wide basis to evaluate the wind speed frequency profile against heliostat structural requirements to meet the 2 mr tracking under wind loads. For instance if wind speeds greater than 10 m/sec occur less than 9 percent of the time (and those instances are in late afternoon) then the 2 mr pointing accuracy requirements can be maintained up to 10 m/sec and the average resultant energy input be applied during the 9 percent of the time. Very little flux will be lost by completely missing the boiler. The heliostats must still meet the survivability requirements without catastrophic failure.

The wind rise rate of 0.01 m/sec^2 poses no additional problem. Neither does the 17 m/sec dust devil requirement when compared to the 25 m/sec steady state requirement.

In November 1975, Honeywell ran a small field effects test where 1/96 scale models were subjected to varying wind speeds with different barrier heights. No attempt was made to generate a scaled boundary layer profile. The heliostat models (1/96 scaled, 3-8 foot square facet heliostats) were not the same as the present configuration. None of the facets were instrumented. The results may be used qualitatively to demonstrate that at various stations within the field the dynamic pressure varies greatly, even to the point of flow reversal.

Honeywell will, during detail design, run a fully instrumented 1/10 scale model wind tunnel test using a properly scaled boundary layer. Each of the outer axis bearings and each mirror module will be instrumented with strain gages to obtain direct moment readings. Nine pressure taps per mirror module will also be incorporated. The model will be tested alone and with another 1/10 scale model upstream at different scaled distances (1.6 ft to 3.6 ft) to evaluate directly the influence of one heliostat upon another.

This testing should bracket all worse case loading on a heliostat very similar to the PDR baseline discussed in this document. The model is scaled from the SRE experimental model configuration. Slotted mirror modules with an approximate 94 percent solidity ratio will also be evaluated while on the heliostat model.

The results from the preliminary wind tunnel tests, additional monitoring of the SRE heliostats, and future scaled wind tunnel test will provide a complete envelope of field conditions and heliostat response. The result of these tests will be used to determine the most cost effective design for pilot plant heliostats based on redirected energy.

D. Humidity and Atmospheric Effects

Humidity effects will be monitored within the field by the ground level dewpoint indicators at the weather stations and dewpoint indicators near the receiver aperture. Dewpoint indicators are preferable to relative humidity devices because they are inherently more accurate and cheaper. It is important to understand these additional near-ground attenuation losses since almost all of the atmosphere's water vapor lies within the first 2-3 km of altitude.

Line-of-sight losses typical of a pilot plant and commercial plant field have been evaluated based on present design and available data. Figure 4-21 shows different results for the same heliostat field conditions representing the SRE setup of heliostats 147m, 260m and 314m from a target 15.8m high. Computed analytical atmospheric effects for 55 percent relative humidity are also shown. After correcting for known instrumentation scaling errors, the SRE results show a higher percent loss at the longer line-of-sight distances due to atmospheric attenuation (combined effects of atmospheric water and turbidity).

Additional tests will be performed at various atmospheric conditions. These tests will use the equipment that uses a direct on-line compensation of the calibration array photocells to obtain total reflected energy. This calibration compensates the photocells which are sensitive to only a limited band (0.5μ to 1.1μ) to account for the effects of atmospheric attenuation on the total solar spectrum. It is proposed to use this same technique for monitoring energy flux inputs during pilot plant testing.

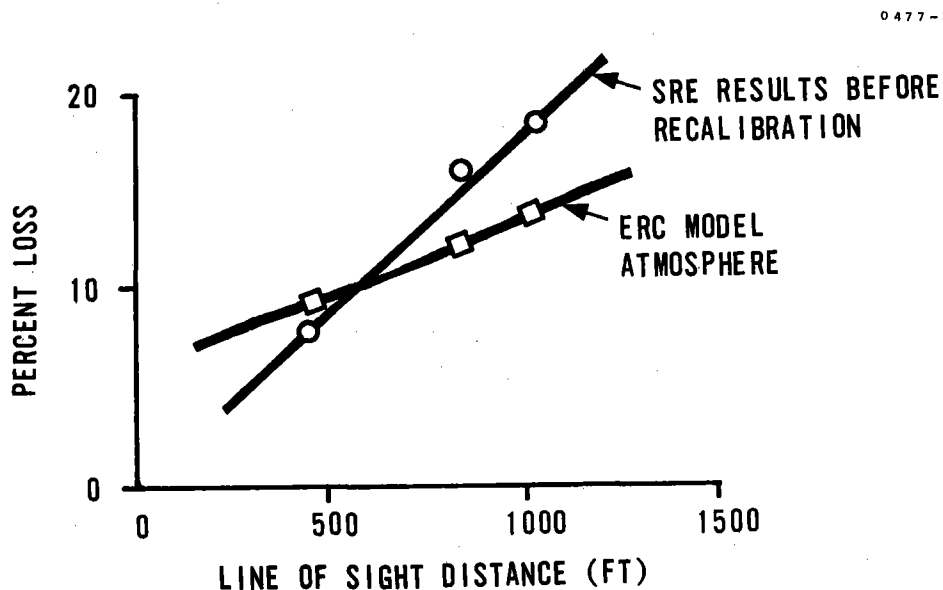


Figure 4-21. Percent Energy Losses Versus Line-of-Sight Distances for Humidity 55 Percent

As a result of additional testing and improved atmospheric model development, the line-of-sight attenuation due to scatter and absorption will be evaluated to determine the exact collector field size for a 10 mw pilot plant output on 21 December with a clear day index of 1.0.

E. Other Environmental Effects

1. Blowing Sand, Dust, Rain

The PDR heliostat design includes protection from blowing sand, dust and rain in the form of seals on motor housing, electronics, gear housing, and initialization mechanism housings. Internal moisture relief is provided where required. These concepts will be further evaluated during the detail design phase and on one prototype heliostat build.

2. Erosion of Mirror Module Reflectivity

Honeywell presently has a test of silvered glass mirrors underway near Phoenix, Arizona. They had controlled mirror samples exposed to the desert environment since February 1977. Initial results of reflectivity and surface erosion will be available in September 1977. This information will also be available for final collector subsystem design.

3. Lightning protection is discussed on pages 3-37 and 3-38.

ANALYSIS AND PROGNOSIS FOR COMMERCIAL PLANT CHANGES

Based on the performance of the SRE collector subsystem, we have seen no significant problems. The challenge remains to obtain acceptable performance at lower cost. Design evolution has been the key to cost reduction to date and is expected to continue on through the pilot plant phase.

The Honeywell pilot plant heliostat incorporates several concepts which are lower cost ways to meet the same specifications. The hybrid frame, self-aligning mirror module bearings and smaller actuators are prime examples. The next major iteration is expected when real wind load design criteria can be quantified. Honeywell is planning wind tunnel tests which will provide coefficients for a single heliostat. A stronger driver however is the actual value of wind velocity at the heliostat level considering effects of other heliostats, wind fences ground effects, etc. Our prediction is that actual wind moments will be less than those used for present designs to the point where gravity effects and stress levels at 40 m/sec winds will become the design driver in some cases presently designed by deflections.

Since the mirror modules represent approximately 40 percent of the heliostat cost and because they are now designed by wind moment loads, there is reason for optimism about their cost. Lower wind moments on mirror modules also result in lower loads on nearly all other components.

Ray trace analysis and SRE test experience have shown that control of focal length of heliostats with distance from the tower is not critical. This may change at the larger commercial scale but the heliostat design is flexible enough to have several fixed focal lengths.

Torsional stiffness of mirror module stub shafts has a strong effect on the minor support structural cost. Aluminum stub shafts used on SRE heliostats put increased demands on the honeycomb panel structure. Steel hubs (modulus 3X that of aluminum) will be used on all future units to reduce the cost driving torsional stiffness requirement on the sandwich panel.

Vented mirror modules (with pressure relief slots) offer a possibility for reducing wind moments further but are not baselined for the pilot plant. This approach may be a key to reducing commercial cost by increasing the cost optimal heliostat size. This approach does not have the 120 inch size tooling constraint in one direction which not applies to the honeycomb module. A reiteration of the parametric analysis will be appropriate for the commercial heliostats when new wind load data is available.

Low iron float glass mirrors will of course be available when quantities are sufficient to get the glass manufacturers to convert their lines. Low iron will increase reflectivity by 3 percent for clean mirrors. However the average loss due to "dirt" may swamp out this gain.

Calibration techniques should be fully explored in terms of alleviating error budget cost drivers. White paint, for instance, is the baseline technique for controlling errors due to thermal distortions. It is possible that software algorithms could be used to compensate cyclic errors as a function of sun position, if pre-rusted steel were used.

Error budget trade-offs can also be performed to minimize cost. Mirror contours for instance have proven far superior to the budgeted one milliradian/1 σ allowable deviation. This could be used to alleviate torsion stiffness requirements on the mirror module structure. Backlash on the inner drive linkage, on the other hand, has been difficult to hold to budgeted values. This is a second area where additional error allowances could be cost effective.

Large volume manufacturing techniques will reduce commercial plant costs. Die cast aluminum will replace machined parts on several drive unit parts. Powdered metal will replace cast iron on bearing housings and will drive costs down by reducing machining costs. Forging and stamping will be used extensively where appropriate. Manufacturing and assembly tooling will continue to evolve to obtain required accuracies with less labor cost.

It is also important to note those areas where further cost reductions (beyond pilot plant) are not expected. Hybrid steel frames, posts, concrete slabs, float glass mirrors, and bearings fall in this

category. These items are based on existing production rates and market competition that will not be impacted significantly by heliostats. Quantity price breaks will be the only factor.

CALIBRATION ARRAY ANALYSIS

The design, sizing and location of the calibration arrays for both pilot and commercial plants are based on analyses supported by SRE test results. TCLs SRE 99 and 115 document this work.

The array location is controlled by ray blockage considerations. Figure 4-22 shows that if the arrays are located below the receiver, far heliostat rays are blocked by other heliostats in adjacent rows; rays from near heliostats are blocked by the arrays themselves. The result of this was to mount the arrays on the receiver at the top.

An image size analysis was completed next to determine the required size and pitch angle of each of the eight arrays. Figure 4-23 shows the model used to define the beam size equations.

The equations quantify the following effects:

- Sun cone angle.
- Line-of-sight (LOS) distances.
- Cosine effects (azimuth and elevation).
- Azimuthal range of heliostats served by each array.
- Spreading of images (vertical and horizontal) due to constant toe-in angles used on each heliostat.
- Heliostat pointing accuracy.
- Mirror module contour accuracy.
- Change in image size as a function of LOS due to use of a common focal length of all mirrors.
- Span of time (centered on solar noon) over which calibration capability is desired.

Table 4-8 summarizes the results showing optimum sizes and pitch angles for each array. For the preliminary design however, a common frame size and pitch angle are used to simplify construction and improve aesthetics. Experience with pilot plant operation will provide data to cost optimize the arrays for commercial plants.

Structural analysis of the array frame has also been completed based on stress under survival wind conditions. Weights of these assemblies including the sensors and wiring have also been determined.

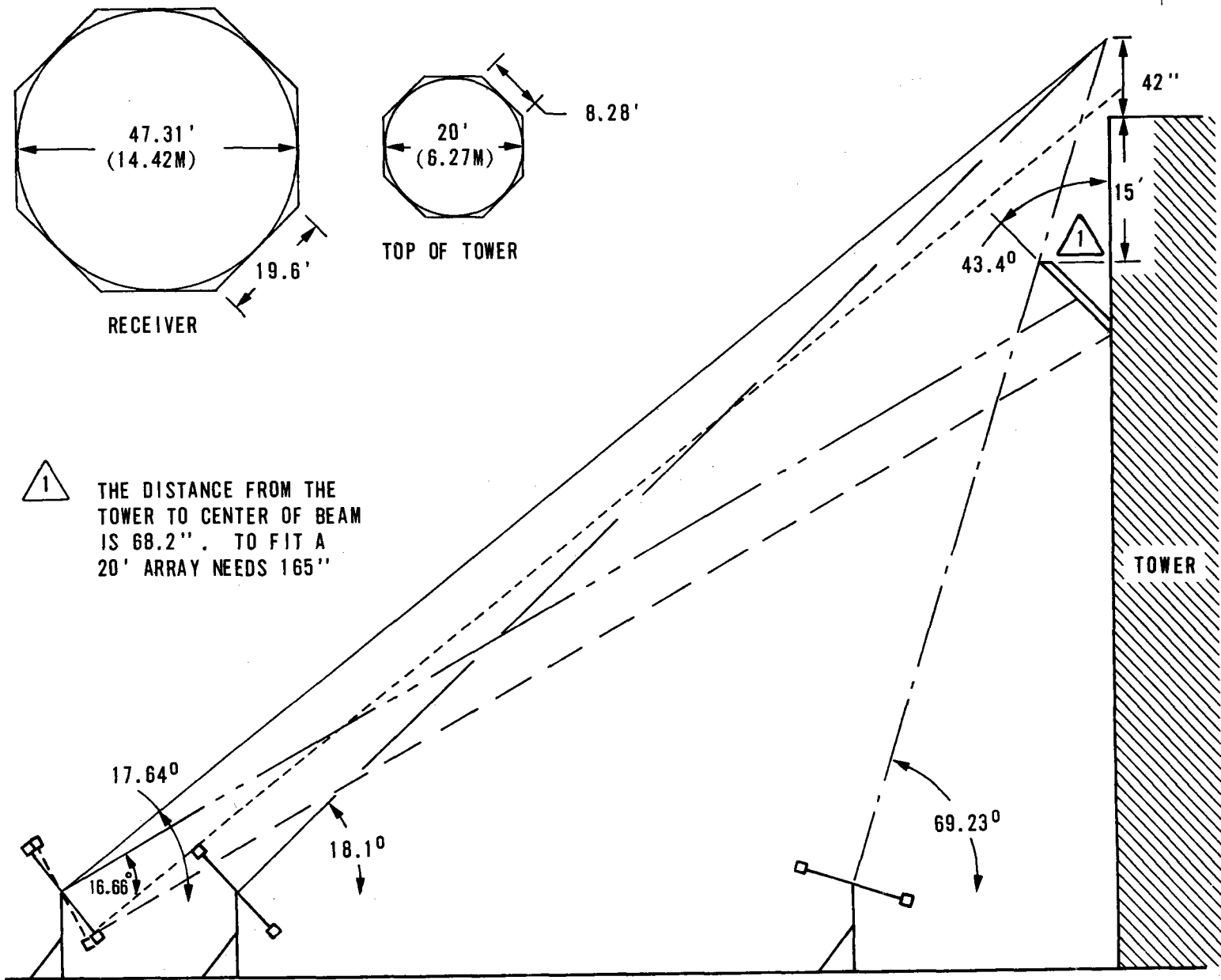


Figure 4-22. Ray Blocking During Heliostat Calibration

0477-1988

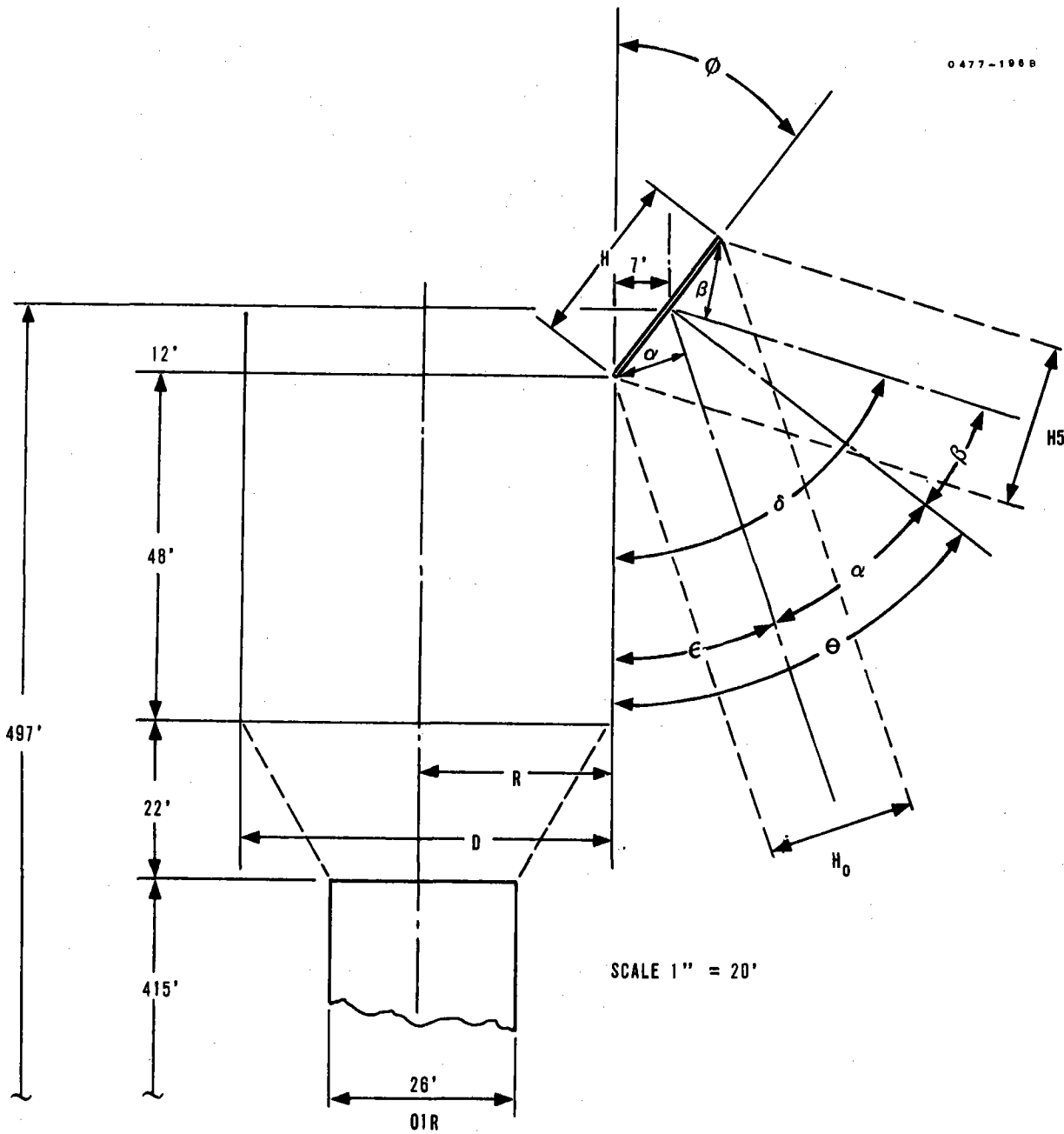


Figure 4-23. Array Analysis Model

Table 4-8. Calibration Array Parameters

<u>Cal Array No.</u>	<u>Width (ft)</u>	<u>Height (ft)</u>	<u>Phase (deg)</u>	<u>No. of Sensors</u>	<u>Weight (lbs)</u>	<u>Drag Force (lbs)</u>
1,8	25.55	23.54	31	624	803	4307
2,7	27.77	24.53	38	700	900	5256
3,6	23.02	20.62	48	483	621	2831
4,5	23.54	20.78	56	504	648	2469

Maximum wind velocity at the 500 foot elevation is:

$$V_{500} = 90 \text{ mph} \left(\frac{500}{32.81} \right)^{0.15} = 135 \text{ mph}$$

This velocity is combined with solidity ratios and drag coefficients from S. F. Holmes's "Fluid Dynamic Drag" to define the total wind drag values shown in Table 4-8. Three sizes of square aluminum were selected based on allowable bending stresses.

Figure 4-24 shows the pilot plant frame design.

HELIOSTAT LOCATION ANALYSIS

Ray trace optimization has determined that variable spacing of heliostats in the field is optically the most efficient scheme. Radial spacing therefore increases as a function of distance from the tower. The attached computer output is a sample of the data used to generate the field layouts in other sections of the report. This data was generated by ERC in Minneapolis.

Azimuth zone 1 is from 0 degrees to 45 degrees; zone 2 is from 45 degrees to 90 degrees. Numbers to the right of the equal signs are radii in feet. Numbers in parentheses are row numbers.

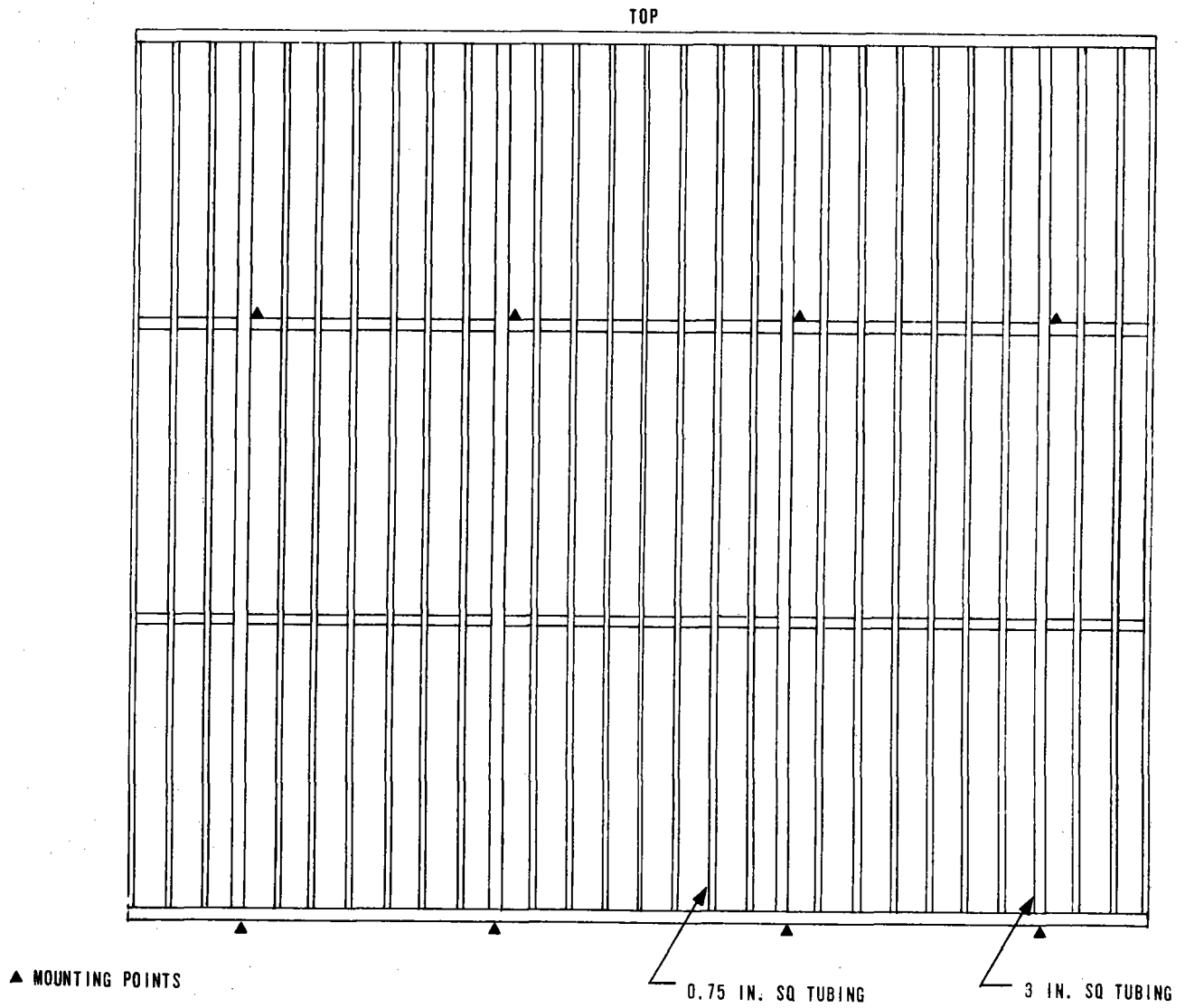


Figure 4-24. Calibration Array Frame

POLAR RADII IN AZIMUTH ZONE 1

R(1) = 165.0	R(2) = 141.6	R(3) = 148.3	R(4) = 215.1	R(5) = 232.0	R(6) = 249.1	R(7) = 266.3	R(8) = 283.6
R(9) = 301.2	R(10) = 314.9	R(11) = 336.7	R(12) = 354.7	R(13) = 372.9	R(14) = 391.2	R(15) = 409.9	R(16) = 428.5
R(17) = 447.4	R(18) = 466.6	R(19) = 485.9	R(20) = 505.4	R(21) = 525.2	R(22) = 545.2	R(23) = 565.4	R(24) = 585.9
R(25) = 606.6	R(26) = 627.6	R(27) = 648.8	R(28) = 670.4	R(29) = 692.2	R(30) = 714.4	R(31) = 736.8	R(32) = 759.6
R(33) = 782.8	R(34) = 805.3	R(35) = 830.2	R(36) = 854.5	R(37) = 879.3	R(38) = 904.5	R(39) = 930.1	R(40) = 956.3
R(41) = 983.0	R(42) = 1010.3	R(43) = 1034.2	R(44) = 1066.7	R(45) = 1096.0	R(46) = 1126.0	R(47) = 1156.8	R(48) = 1188.5
R(49) = 1221.1	R(50) = 1254.9	R(51) = 1289.7	R(52) = 1325.9				

POLAR COLLECTOR COUNT IN AZIMUTH ZONE 1

N(1) = 2	N(2) = 2	N(3) = 2	N(4) = 2	N(5) = 3	N(6) = 3	N(7) = 3	N(8) = 3
N(9) = 3	N(10) = 4	N(11) = 4	N(12) = 4	N(13) = 4	N(14) = 5	N(15) = 5	N(16) = 5
N(17) = 5	N(18) = 6	N(19) = 6	N(20) = 6	N(21) = 6	N(22) = 7	N(23) = 7	N(24) = 7
N(25) = 7	N(26) = 8	N(27) = 8	N(28) = 8	N(29) = 8	N(30) = 9	N(31) = 9	N(32) = 9
N(33) = 9	N(34) = 10	N(35) = 10	N(36) = 10	N(37) = 11	N(38) = 11	N(39) = 11	N(40) = 11
N(41) = 12	N(42) = 12	N(43) = 12	N(44) = 13	N(45) = 13	N(46) = 14	N(47) = 14	N(48) = 14
N(49) = 15	N(50) = 15	N(51) = 15	N(52) = 16	N(53) = 16			

POLAR RADII IN AZIMUTH ZONE 2

R(1) = 165.0	R(2) = 141.6	R(3) = 147.9	R(4) = 214.3	R(5) = 230.8	R(6) = 247.4	R(7) = 264.2	R(8) = 281.1
R(9) = 294.2	R(10) = 315.6	R(11) = 337.4	R(12) = 350.3	R(13) = 367.9	R(14) = 385.4	R(15) = 407.8	R(16) = 422.0
R(17) = 440.3	R(18) = 454.8	R(19) = 477.6	R(20) = 496.5	R(21) = 515.5	R(22) = 534.9	R(23) = 554.4	R(24) = 574.2
R(25) = 594.1	R(26) = 614.3	R(27) = 634.8	R(28) = 655.5	R(29) = 676.5	R(30) = 697.7	R(31) = 719.2	R(32) = 741.1
R(33) = 763.2	R(34) = 785.6	R(35) = 808.4	R(36) = 831.5	R(37) = 855.0	R(38) = 878.9	R(39) = 903.2	R(40) = 927.9
R(41) = 953.1	R(42) = 978.4	R(43) = 1004.9	R(44) = 1031.6	R(45) = 1058.8	R(46) = 1086.7	R(47) = 1115.2	R(48) = 1144.4
R(49) = 1174.3	R(50) = 1205.1	R(51) = 1236.7	R(52) = 1269.3	R(53) = 1303.0			

POLAR COLLECTOR COUNT IN AZIMUTH ZONE 2

N(1) = 2	N(2) = 2	N(3) = 2	N(4) = 2	N(5) = 3	N(6) = 3	N(7) = 3	N(8) = 3
N(9) = 3	N(10) = 4	N(11) = 4	N(12) = 4	N(13) = 4	N(14) = 5	N(15) = 5	N(16) = 5
N(17) = 5	N(18) = 6	N(19) = 6	N(20) = 6	N(21) = 6	N(22) = 6	N(23) = 7	N(24) = 7
N(25) = 7	N(26) = 7	N(27) = 8	N(28) = 8	N(29) = 8	N(30) = 9	N(31) = 9	N(32) = 9
N(33) = 9	N(34) = 9	N(35) = 10	N(36) = 10	N(37) = 10	N(38) = 11	N(39) = 11	N(40) = 11
N(41) = 11	N(42) = 12	N(43) = 12	N(44) = 12	N(45) = 13	N(46) = 13	N(47) = 13	N(48) = 14
N(49) = 14	N(50) = 14	N(51) = 15	N(52) = 15	N(53) = 16			

POLAR RADII IN AZIMUTH ZONE 3

R(1) = 165.0	R(2) = 141.6	R(3) = 147.4	R(4) = 213.8	R(5) = 229.9	R(6) = 246.2	R(7) = 262.5	R(8) = 279.0
R(9) = 295.7	R(10) = 317.4	R(11) = 324.4	R(12) = 346.4	R(13) = 363.6	R(14) = 380.9	R(15) = 398.4	R(16) = 416.1
R(17) = 433.9	R(18) = 451.9	R(19) = 470.0	R(20) = 488.4	R(21) = 506.9	R(22) = 525.6	R(23) = 544.5	R(24) = 563.6
R(25) = 582.4	R(26) = 602.3	R(27) = 622.1	R(28) = 642.0	R(29) = 662.2	R(30) = 682.6	R(31) = 703.3	R(32) = 724.2
R(33) = 745.4	R(34) = 766.9	R(35) = 788.7	R(36) = 810.8	R(37) = 833.2	R(38) = 856.0	R(39) = 879.1	R(40) = 902.5
R(41) = 926.4	R(42) = 950.6	R(43) = 975.3	R(44) = 1000.4	R(45) = 1026.0	R(46) = 1052.1	R(47) = 1078.7	R(48) = 1105.9
R(49) = 1133.6	R(50) = 1162.1	R(51) = 1191.2	R(52) = 1221.1	R(53) = 1251.7	R(54) = 1283.3	R(55) = 1315.7	R(56) = 1348.9

TRADE OFF STUDIES

Certain trade studies which support pilot plant choices are sufficiently important to warrant treatment here. Without question the parametric trade study (performed during the first six months of the preliminary design phase) influenced the Honeywell heliostat more than any other technical work. This attempt at conceptual optimization is treated first because of its preeminent position. Following this is the summary treatment of the foam versus honeycomb mirror module. This trade study also involved hardware. The results of the study were sufficiently important that a special report was issued. The next two trade studies are design choices involving component selections (battery versus other storage and ball screw versus machine screw). Following these is a brief treatment of indoor versus outdoor assembly. Finally is a summary of our choice of measurement technique and computer.

PARAMETRIC TRADE STUDY

A parametric trade study was completed in December 1975 which showed the tilt-tilt heliostat to be less expensive (\$/unit energy) than the "Az-El" configuration. The study further defined a 40 m², 4 square facet heliostat with a 2 milliradian (1σ) pointing accuracy and 13.5 M/S operating wind speed capability as being cost optimal.

Honeywell's approach to heliostats has always leaned toward "low profile" concepts to minimize the effects of wind loads. Two primary concepts were identified early during the SRE contract. These concepts were identified early during the SRE contract. These concepts are referred to as "Az-El" and "Tilt-Tilt" after their gimbal orientations and are described in reference 17. Cost per unit of thermal energy into the receiver was the obvious selection criteria. However, cost and energy output could not be obtained until the two concepts had been designed. Moreover, the quantity and range of both configuration and requirement variables would require many design iterations.

A joint effort was completed in 1975 by Honeywell Energy Resources Center (ERC) and Honeywell Avionics which provided the desired data. Avionics generated software to get \$/m² impacts of varying the following items:

- Total mirror area per heliostat.
- Number of mirror modules (facets).
- Aspect ratio of facets.
- Spacing between facets.
- Pointing accuracy.
- Operating wind speed capability.

ERC developed the variations in net annual energy (thermal) into the receiver. Figure 4-25 shows how the two outputs were married to get the cost per unit of thermal energy into the receiver. The software was designed in both cases to suboptimize individual parameters during

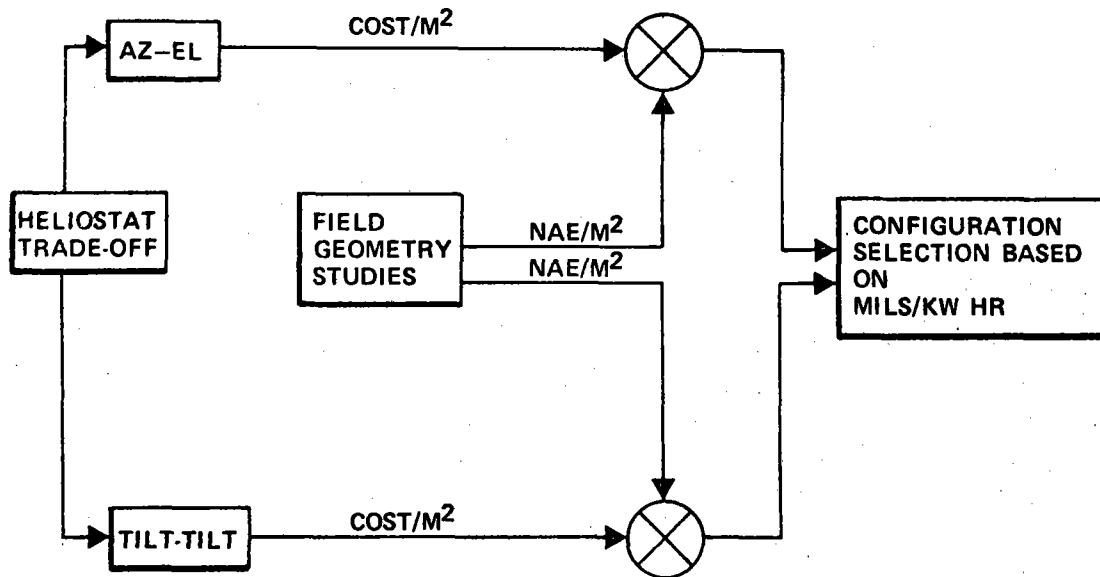


Figure 4-25. Heliostat Evaluation Process

each iteration. The end result was an optimal configuration for each of the two gimbal arrangements shown in Figure 4-26. The 13.5 M/S wind speed capability and 2 milliradian (1σ) pointing accuracy were optimal for both.

A complete description of software generated for this effort by Avionics is provided in reference 2.

Although there are numerous design requirements and configuration elements that could have been used as input (independent) variables, the six listed above were judged to have the greatest impact on cost and energy. Figure 4-27 shows a simplified flow chart of the software. The chart shows the process for only one design iteration. Nested loops were used to iterate on any or all input variables automatically.

The actual software consisted of an executive routine, eight major subroutines and eight function subroutines. Figure 4-28 describes the function of each and the internal flow of information between them.

The cost sensitivities of sample variables are shown in Figures 4-29 through 4-32. The costs shown in these curves are at LBM level assuming commercial quantities and learning curves. The complete results were provided in reference 17.

Actual costs which come out of the SRE detail design have been higher than those estimated for the parametric study. The mirror module cost is three times higher while the outer axis (frame) drive is actually

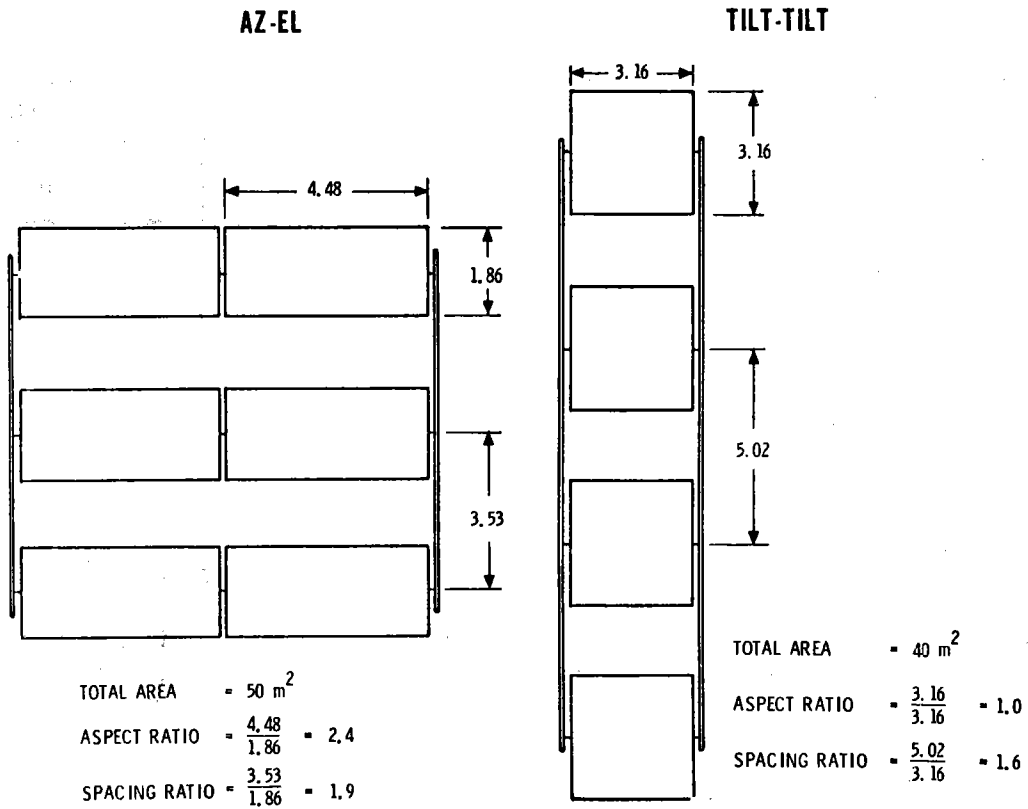


Figure 4-26. Gimbal Configuration

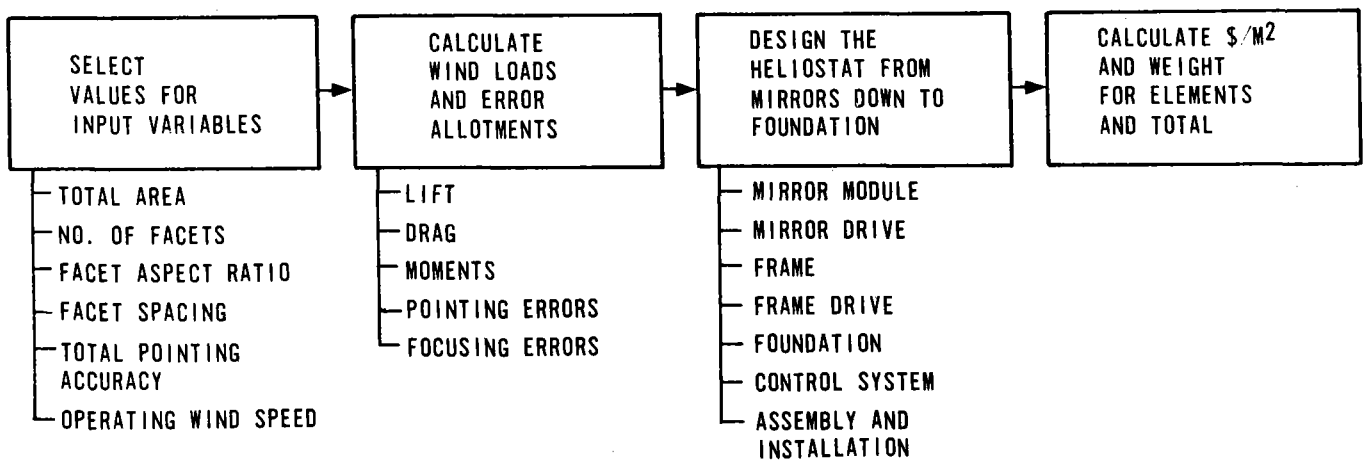


Figure 4-27. Parametric Analysis Flow Diagram

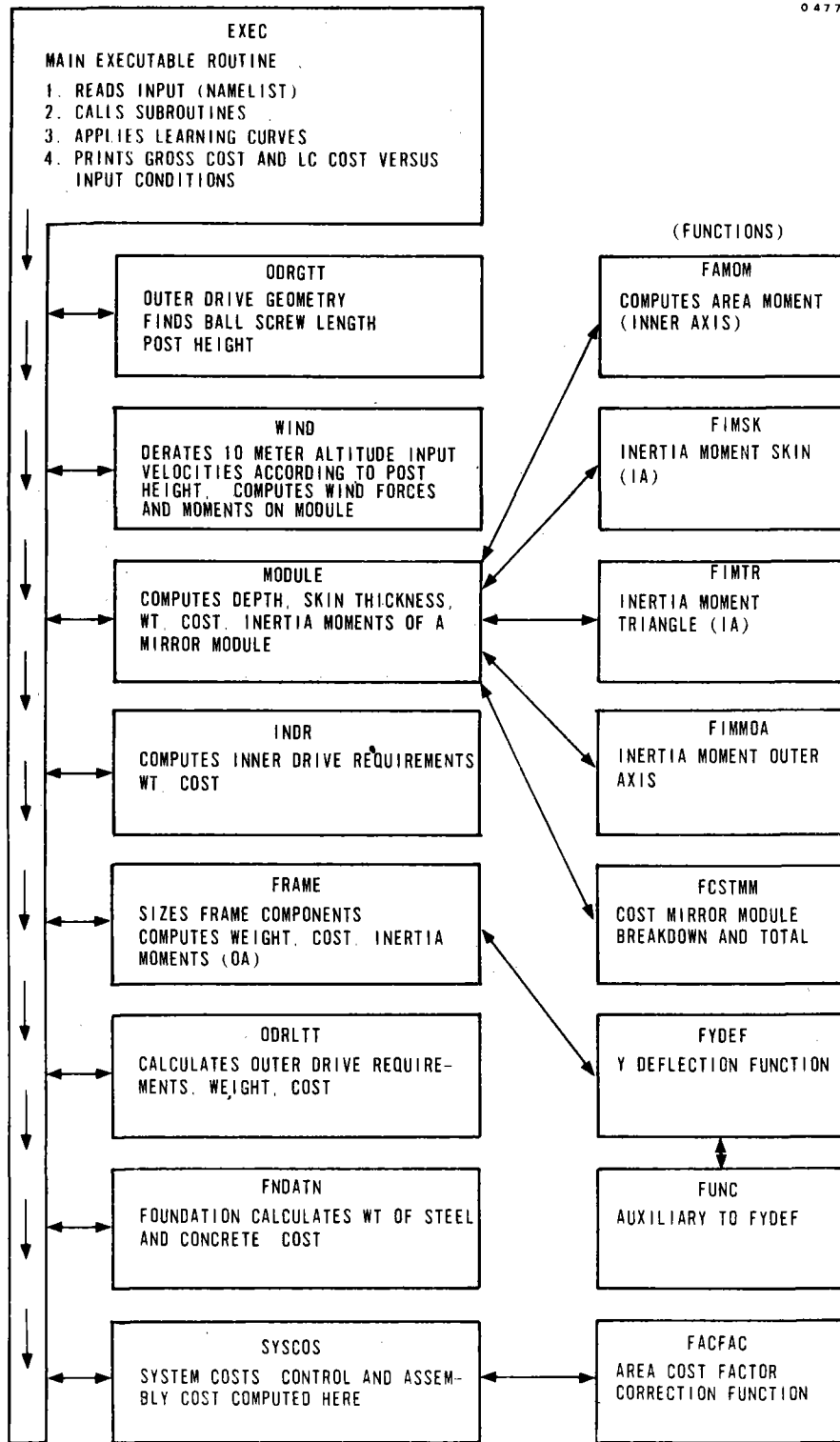


Figure 4-28. Flow Chart for Tilt-Tilt Heliostat Computer Program

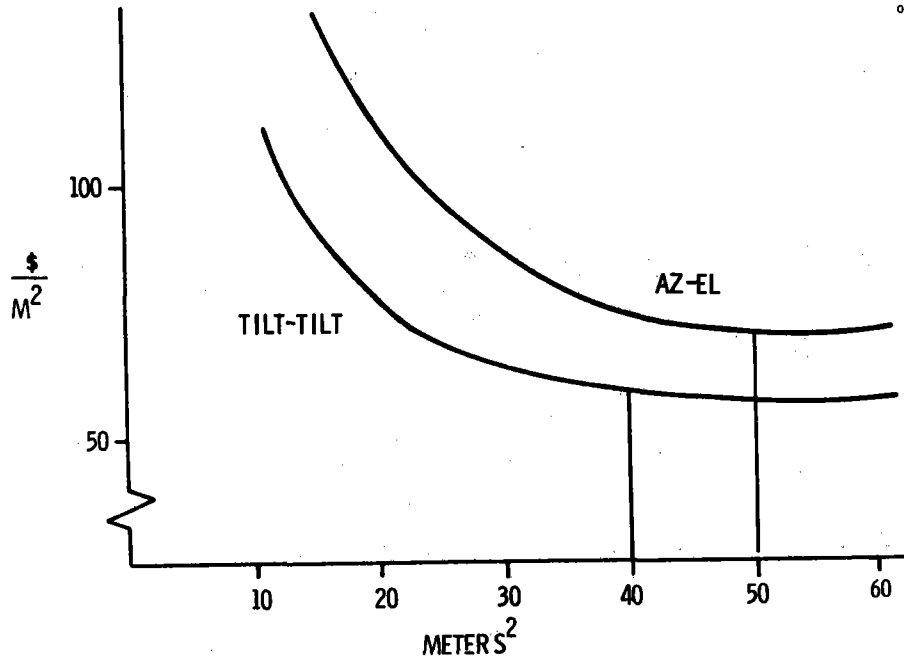


Figure 4-29. Sensitivity To Area

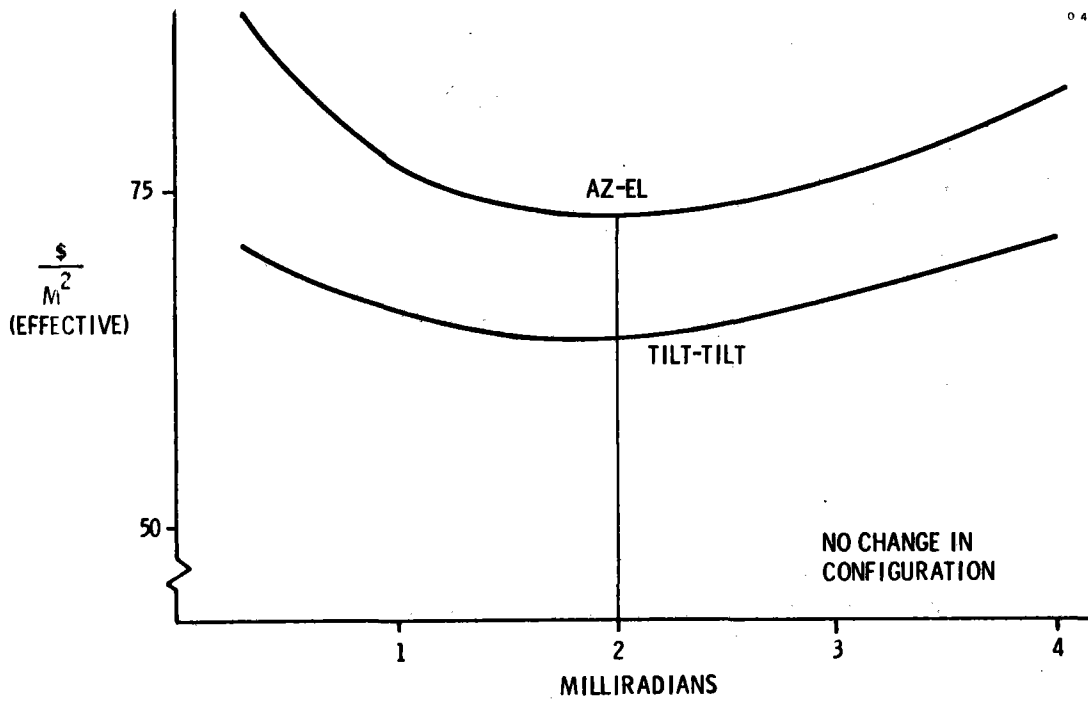


Figure 4-30. Sensitivity to Pointing Accuracy

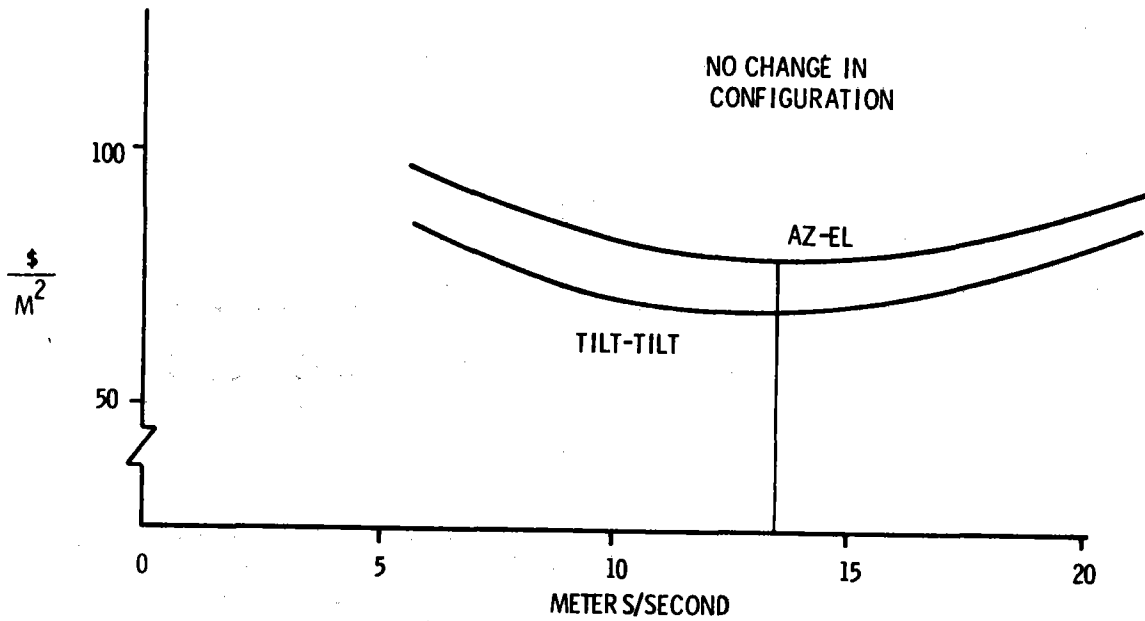


Figure 4-31. Effective Cost Versus Heliostat Wind Speed Capability

AZ-EL TILT-TILT

AREA (m ²)	50	40
WIND (M/S)	13.5	13.5
POINTING ACC (mr)	2	2
ASPECT RATIO	2.4	1.0
FACETS	6	4

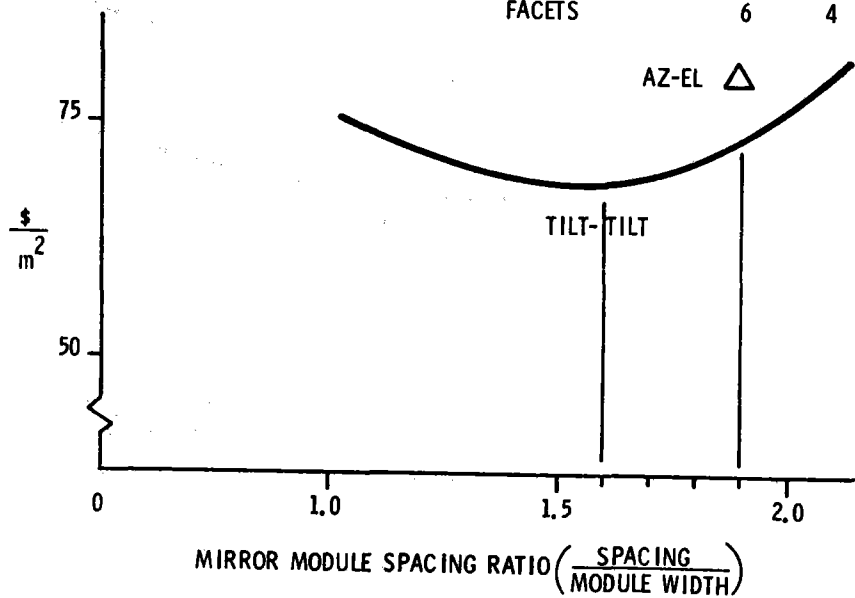


Figure 4-32. Sensitivity to Mirror Module Spacing

less. If the study was rerun using today's pilot plant estimates the optimal heliostat size would increase significantly, possibly double. Preliminary work on the producibility study however has revealed numerous ways to drive costs back down through design evolution (see reference 16).

Our prediction is that the heliostat total area will eventually optimize for commercial scale at no less than 40 square meters and may be larger to an extent consistent with final component costs.

A minor change in aspect ratio of the mirror module will be required for the pilot plant. Bonding presses require a maximum dimension of 120 inches in one dimension requiring an aspect ratio of 130/120 = 1.08 instead of the 1.0 value to get a full 10 square meters. The spacing between mirror modules may also be affected. The cost sensitivity curves show no cost impact for these changes.

The remaining parameters which were set by the study are:

- Number of facets = 4
- Pointing accuracy = 2 milliradians (1σ)
- Operating wind speed capability = 13.5 M/S

No data has come out of the SRE contract effort which shows a need to change these from a heliostat point of view. In fact, the latest error budget (<2 mr) combined with the latest cost data (> study estimates) demonstrates the impact of not having the design at the optimized level.

A high priority task in the producibility study will be to drive mirror module costs down with larger error allotments.

FOAM VERSUS HONEYCOMB MIRROR MODULES

Two materials received major consideration as the core of sandwich type construction for the mirror modules used in the engineering model heliostat. They were Type 300 Owens/Corning Urethane Foam with a density of 32 kg/m³ (2 lbs/ft³) and aluminum honeycomb with a density of 41.6 kg/m³ (2.6 lbs/ft³). Two mirror modules were designed and fabricated by companies specializing in lightweight construction to detail requirements established by Honeywell Drawing 34026575.

Brunswick Corp., Lincoln, Nebraska designed and fabricated two mirror modules using the urethane foam as a core material. Serious problems were encountered in obtaining the 677.9m (2,224 feet) spherical radius and in bonding the steel skin to the urethane foam. Both mirror modules were tested and produced unsatisfactory results. Changes in contour fabrication and bonding techniques may result in significant structural improvements.

Further investigations into urethane properties in relation to its use in this type of structure have brought out additional problems.

The dimensional stability of urethane is not good when subjected to temperatures of 60°C (140°F). Permanent increase in volume of up to 15 percent has been observed. In addition, the thermal coefficient of expansion is nearly 10 times that of steel. These combined will result in large internal pressure forces in the mirror module structure with resulting dimensional changes. Urethane foam, while called closed cell, will absorb moisture from the atmosphere and with temperature cycling this causes deterioration of the foam to the point where it is not a satisfactory structural material. This deterioration occurs in much less than the 30 year life requirement. No practical means of sealing the urethane foam from this moisture has been found. The combination of bad experience with engineering model mirror modules and detrimental material properties have resulted in urethane foam not being considered further.

Parsons Corp., Stockton, California has designed and fabricated two engineering model mirror modules using the 41.6 kg/m³ (2.6 lbs/ft³) aluminum honeycomb and 14 mirror modules for the solar research experiment using 32 kb/m³ (2.0 lbs/ft³) aluminum honeycomb. Two of the 14 mirror modules from the solar research experiment were used to replace the urethane foam units on the engineering model heliostat.

Structural tests completed on the 2 engineering model mirror modules and 2 of the 14 solar research experiment mirror modules fabricated by Parsons gave excellent results. Contour was initially well within specification and did not change significantly under simulated wind loads. Torsional deflection was 0.7 to 0.8 mr at maximum applied torque compared to a specification requirement of 1.0 mr.

The pilot plant mirror modules are aluminum honeycomb units which, produced by Parsons, have exhibited in-specification performance. Efforts are underway to reduce the cost of this type. Fabrication of mirror modules using urethane foam cores has been discontinued. Investigations of other cost effective structures will be researched in detail in Honeywell's Heliostat Producibility Program.

LINEAR ACTUATOR TRADEOFFS AND SELECTION (BALL SCREW VERSUS MACHINE SCREW)

The ball screw (BS) linear actuator has been selected over the machine screw (MS) because of its torque efficiency and backlash/life characteristics. The two actuator styles are shown in Figures 4-33 and 4-34.

Experience in designing the SRE heliostats has shown that even though commercial components appear usable in most cases, our design requirements differ markedly from those used by the vendors. The actuators are a case in point. The actuators were originally selected for their repeatability, accuracy and low backlash and because the commercially available jacks could be readily adaptable to our needs. These have proved out as expected in prototype tests. The challenge has been to obtain reasonable mechanical efficiency in the face of the unique

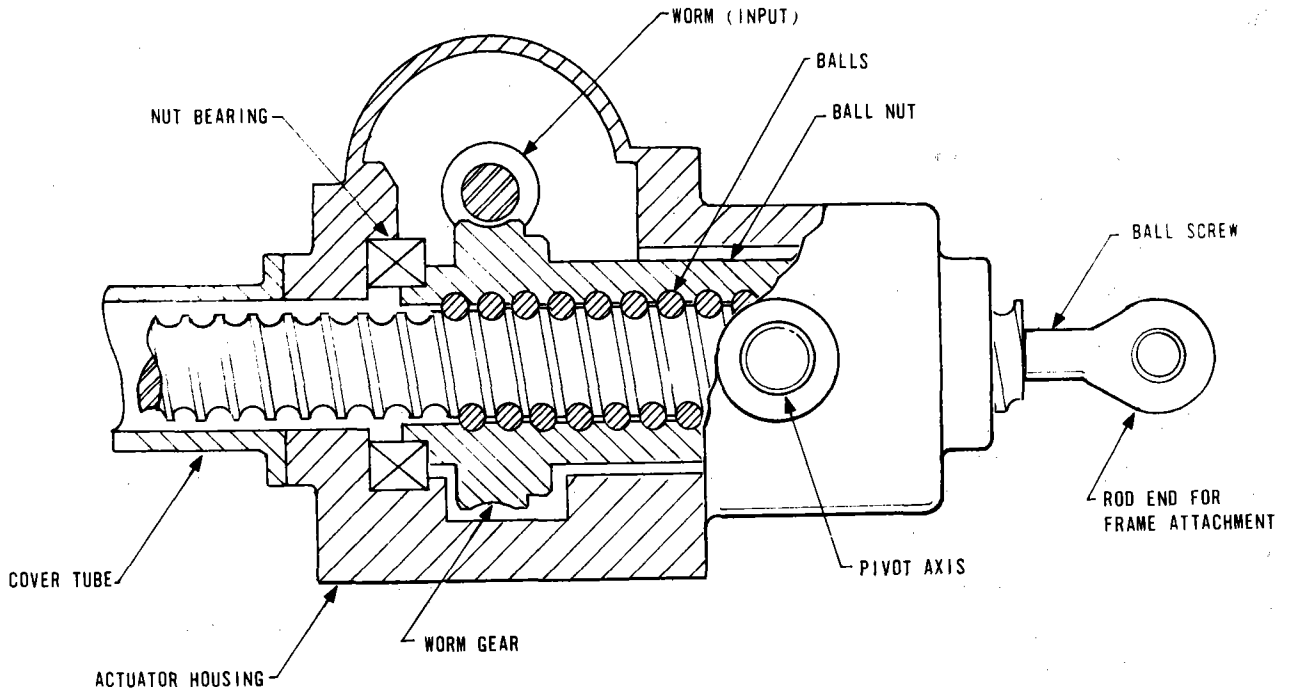


Figure 4-33. Ball Screw Actuator

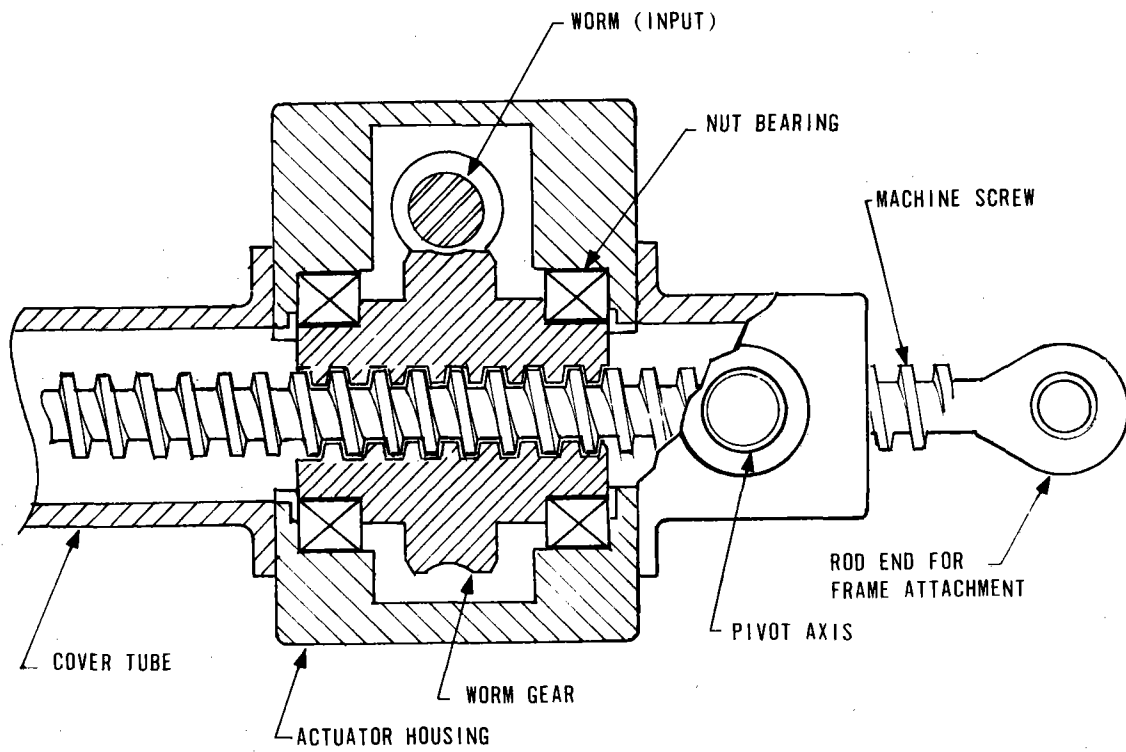


Figure 4-34. Machine Screw Actuator

heliostat application requirements. These requirements are listed here briefly and will be discussed in detail later.

1. Pulse operation
2. High compressive spring rate
3. Column buckling stress
4. High gear ratio (motor shaft-to-actuator nut)
5. Need for self-locking feature
6. Side loads from various sources
7. Large dynamic range (0-900 rpm motor speed)

A hypothetical actuator with a mechanical efficiency of 100 percent would require less than 10 in-oz of input (motor) torque under worst case combinations of wind moments, imbalances, drive geometry, and friction. Yet testing of the machine screw prototypes shows input torques had to be as high as 80 in-oz with no external load at 900 rpm (Reference 19). This low torque efficiency must be overcome by larger motors, electronics and batteries with higher current capacities and more electrical power consumption. All of these increase the total drive system to be nearly equal for both actuator types. The detail description of the design requirements show there is technical risk associated with the machine screw units.

Performance over life is the other major criteria which favors the ball screw unit. Because of the rolling contact interface between the screw and nut (see Figure 4-33) the life can be predicted just like a ball bearing. Limitorque has performed this analysis to show the backlash limit of 0.010 inch will be maintained in excess of 30 years for our predicted loads and travel.

The machine screw unit (see Figure 4-34) can be manufactured to easily meet the 0.010 inch requirement but no supplier will attempt to predict how long it will continue to meet it. They all agree it won't last 30 years. Backlash unfortunately cannot be calibrated out either by our calibration arrays or by a fully closed loop drive system. The cost of even one teardown/rebuild cycle per actuator would significantly increase the life cycle cost of the machine screw unit.

The following paragraphs will review the design criteria listed previously and how they affect the efficiency/performance of the two actuator types.

Pulse Operation

In the tracking mode the motors turn one revolution at intervals from a few seconds to 60 seconds or more. The motor must overcome static friction and reflected inertia torque with each pulse input. Static friction is obviously less for the BS unit; the real advantage is its higher gear ratio. The 40:1 worm gear ratio used on the proposed actuator is a result of slow speed and motor constraints combined with higher leads on the BS unit. The MS by comparison has a 24:1 ratio and reflected inertia is $40/24^2 = 2.78$ times greater.

The smaller actuator proposed for the low cost study has an 84:1 ratio which significantly reduces friction and inertia loads at the motor.

Compressive Spring Rate

The actuator has a requirement of 180,000 lbs/in minimum (per error budget) including housings, gears, pivot pins, etc. This determines a minimum diameter for the screw itself. The present 1-1/2 inch screw is sized by column loads and exceeds this requirement. The 1 inch screw planned for the low cost unit will just meet it. (Note that a screw, sized for tensile stress only, could be as small as 0.09 inch in diameter.) The larger screw results in larger nut and nut bearings and larger friction and viscous drag torques. The MS unit is more sensitive to increases in diameter due to thread friction torques.

Column Buckling Stress

Required screw travel is set by the angular range of the gimbal and the pivot geometry. The actuator is inefficient from a column loading stress standpoint because it is pivoted at both ends, has a high slenderness ratio (length/rad of gyration) and has moment loads at the nut. The 1-1/2 inch diameter screw is also the minimum size expected to meet heliostat requirements. Planned wind tunnel tests on instrumented scale model(s) will provide the data needed to establish actual column loads.

Gear Ratio

Constraints of dynamic range, motor characteristics and actuator/frame pivot geometry set allowable limits for actuator mechanical gain. The ratio of worm gear ratio to screw lead must fall in the range of 75 to 100 (motor revolutions per inch of screw travel). Practical limits on the lead (inches of travel per revolution of the nut) of machine screws dictates lower gear ratios which have the adverse effects described above.

Leads of one half to one inch are standard for the proposed ball screw actuators while 0.25 inch is the maximum allowable for machine screw units.

Self-Locking

At a 40:1 ratio used on the SRE BS actuators, there was some question as to their ability to self-lock under wind conditions which might induce oscillatory loads. (Tests to date at 40:1 show no problem.) The proposed 84:1 ratio for the low cost actuators would leave no question. The ball/nut unit alone reverses easily and depends on the worm to hold it. The machine screw on the other hand depends on the friction in the screw/nut threads to lock.

Side Loads

Side loads are defined as any load perpendicular to the axis of the actuator screw. These come from three different sources, all detrimental to machine screw efficiency. The first is a horizontal load at the end of the screw (frame attach point) which can result from frame thermal expansion, wind deflections of frame and post and assembly tolerances. The result is a moment at the screw/nut interface which is resisted by high radial loads at each end of the nut. The

MS actuator binds under this condition and stalling of the 200 in-oz motor has been observed under test. The second side load is also a moment and is due to the imbalance weight of gear housing and cover tube. The third is a gravity effect when the screw is retracted. The nut acts as a fulcrum for the overhung screw and sees 70 pounds of radial load. The machine screw thread amplifies this by the slope of the teeth generating friction torques. Note: The machine screw prototypes were reworked by adding bronze bushings to try to control side load. There was no significant change in no load torque. (See Reference 19.)

Tests have verified that ball screw input torque is insensitive to side loads. Overstressing of the ball/nut interface is avoided through the use of an actuator pivot bracket which has designed-in compliance in a direction perpendicular to the screw axis.

Dynamic Range

The ball screw unit has been key in our ability to both track (pulse operation) and slew at high speed (900 rpm) with one small motor. If a motor were to be sized to obtain the 900 rpm speed with a machine screw the external loads on the end of the screw would be insignificant compared to the internal friction and viscous drag of the actuator itself. This is like sizing a motor for a go-kart with a transmission out of a full size automobile.

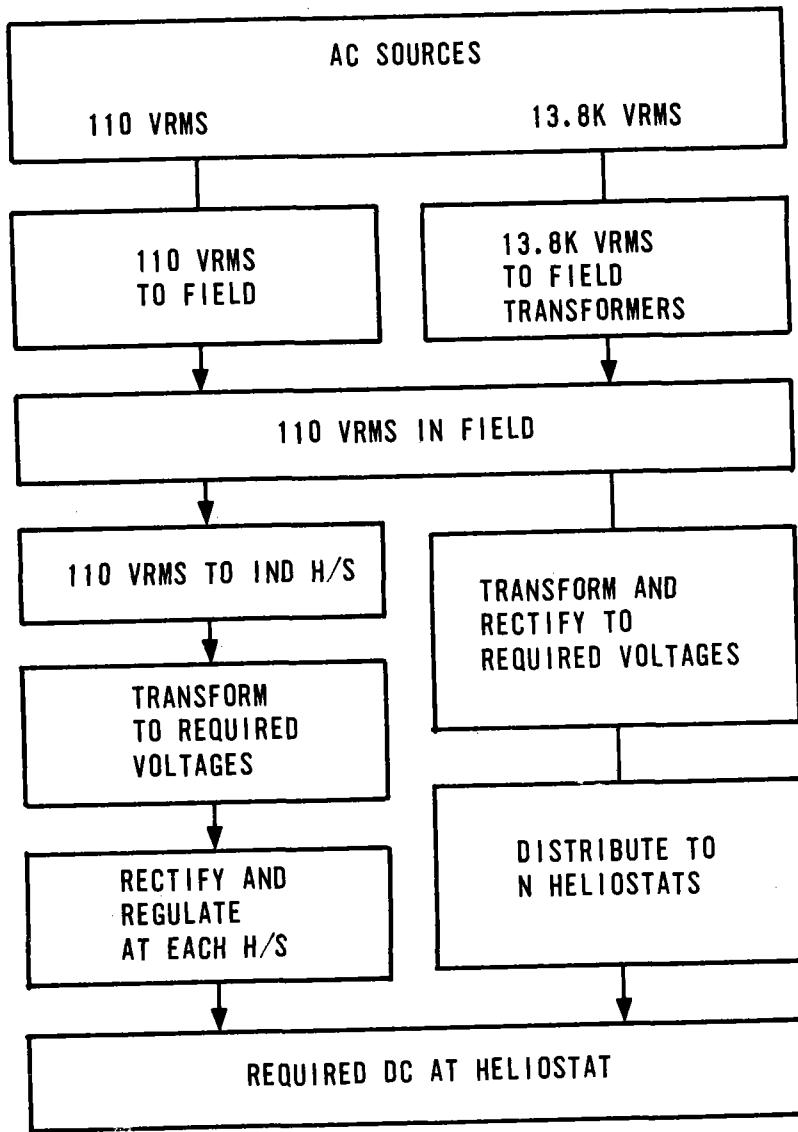
Power Distribution Trade-Off

A power distribution trade-off was performed early* in the SRE program. After cursory analysis nonelectrical techniques were discarded. After further analysis other techniques such as solar cells and motor generators were dropped. Remaining were (1) ac distribution, (2) dc distribution, and (3) ac/dc system with ac distribution to a battery charger and dc operation of the H/S.

1. The ac system does not require much maintenance but requires distribution wires sized for peak loads, for example, all heliostats maximum demand at once.
2. DC system could avoid the expense of the grid by frequent service/charging of batteries. This approach would also require a large overbuy.
3. The ac/dc system operates batteries in a "float" condition thereby keeping maintenance requirements low. The ac distribution system reduces copper costs by reducing peak load in accordance with good load management practices.

The result of the trade-off was selection of the ac/dc system for the pilot plants and finding the dc system unacceptable from a cost/performance standpoint (see Figure 4-35).

* Reference TCL SRE-005.



USE OF
AUX EQUIPMENT
DRILLS, SPRAYERS,
ETC.

Figure 4-35. AC/DC Power Distribution

Indoor Versus Outdoor Heliostat Assembly. Honeywell conducted a cursory analysis pertaining to the differences between indoor and outdoor assembly. Each step in the assembly process was defined and "standard hours" were determined. Based upon industrial engineering standards these hours or times are indicative of the time required for a skilled fully trained operator to accomplish the indicated task with no mistakes.

Each task is such a low level of detail that the summation of the tasks is fairly accurate despite small inaccuracies which may exist in each task. A total of 260 odd tasks were estimated for the outdoor build analysis and 60 odd tasks for the indoor tasks. The outdoor assembly assumed similar tasks to the SRE while the indoor tasks were not so well defined.

Based upon these analyses it was concluded and is our recommendation that outdoor assembly be undertaken to accomplish the assembly with least risk and at lowest cost. This conclusion was verified by a visit to the Barstow site where generators are actually outdoors. The tables (4-9 and 4-10) summarize the details of each approach.

The main driver for the conclusion was found to be the number of times a part or subassembly had to be handled. Since indoor assembly required more handling it was more time consuming. Many parts, it was found, could be off loaded and stored in the field until assembly could be accomplished.

This trade study clearly shows that the use of outdoor assembly techniques is a saving in number of hours as well as total costs even including premium rates for outside labor.

Table 4-9. Indoor Build

Summary of Total Assembly Operation
for Total Fabrication Plus On-Site Installation

Type of Activity	Activity Occurrence by Work Crew Function				Activity Totals			
	Sub- Assy	Main Assy	Matl Hndl	Adj/ Algn	Tot DCC	Dist Feet	Std Hrs	% of Time
Operation	25	10	8	3	46	372	35.04	82.5%
Transport	4	0	10	0	14	2360	2.66	6.3%
Inspect	1	0	0	0	1	0	0.19	0.5%
Delay	1	0	0	0	1	0	4.60	10.8%
Storage	0	0	4	0	4	0	0.00	0.0%
Work Crew Totals:								
Distance-Ft	1080	0	1652	0		2733		
Std Hrs	30.03	4.02	6.04	2.40			42.49	
% of Time	70.7	9.5	14.2	5.6				100.0%

Total Standard Hours = 42.49 to Build One Heliostat

Table 4-10. Outdoor Build
Summary of Total Heliostat Assembly Operation
for Solar Power Plant (Pilot Plant)

Type of Activity	Activity Occurrence by Work Crew Function				Activity Totals			
	Sub- Assy	Main Assy	Matl Hndl	Adj/ Algn	Tot. DCC	Dist Feet	Std Hrs	% of Time
Operation	7	198	0	0	205	65	22.48	84.4%
Transport	0	20	14	0	34	1270	2.70	10.1%
Inspect	0	8	0	1	9	0	1.46	5.5%
Delay	0	2	0	0	2	0	0.00	0.0%
Storage	0	2	9	0	11	0	0.00	0.0%

Work Crew Totals:

Distance-Ft	0	645	690	0		1335		
Std Hrs	1.57	23.71	1.07	0.29			26.64	
% of Time	5.9	89.0	4.0	1.1				100.0%

Total Standard Hours - 26.64 to Build One Heliostat

CALORIMETRY VERSUS CALIBRATION ARRAY MEASUREMENT

A trade study was conducted to select a method of accurately measuring the reflected solar insolation at the receiver in energy terms. Specifically it was desired to develop a technique that could be used to evaluate heliostat reflectance and transmission of the reflected energy to the receiver. Three basic forms of calorimetry were considered. These are (1) sensible heat absorption calorimeter, (2) thermo-electric calorimeter and (3) optical calorimetry.

Sensible Heat Absorption Calorimeter

Energy absorbed by a material without undergoing a change in state is defined as sensible heat. A calorimeter using this principle could be used to determine reflected energy. The desired data would be the energy absorbed by a quantity of fluid circulated through the surface of the calorimeter. To minimize reradiation, convection and conduction losses, it would be necessary to control temperatures of the fluid to near ambient by controlling the mass flow rate. Even with this precaution it would be necessary to determine heat loss and/or gain with the environment by analytical means to improve the accuracy of reflected energy data. A major concern in this regard is that no material has the properties of a "black body". In fact reradiation of 3 to 5 percent is common even for special materials. This method would also integrate the heat flux over the total area and hence lose pattern variation information. Figure 4-36 presents a block diagram for such a calorimeter.

The major consideration in design of this type of calorimeter is to control the mass flow rate of the fluid to maintain temperatures within

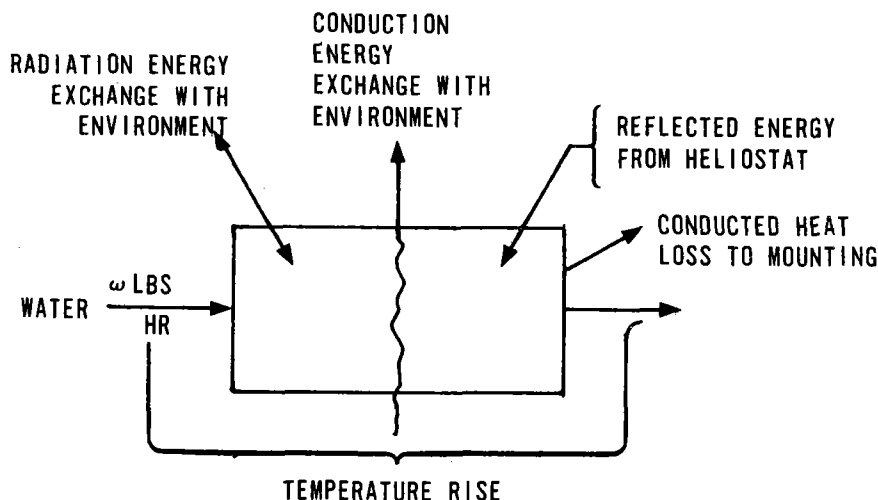


Figure 4-36. Block Diagram for Sensible Heat Absorption Calorimeter

2°F to 5°F of ambient to minimize losses. This must be an active flow control system to maintain the collector near ambient temperature during changes in reflected energy such as that occurring when clouds are passing over. Assuming clear day solar intensity of 1000 watts per square meter and total heliostat efficiency of 80 percent the water flow rate must be 14.5 kg/min (32 lbs/min) to maintain 2°F temperature rise and 39.5 kg/min (80 lbs/min) to maintain 5°F temperature rise.

Difficulty in either eliminating heat exchange with the environment or analytically compensating the data makes this method expensive to implement with potential large error sources. For these reasons Honeywell has not chosen this type of calorimeter.

Thermo-Electric Calorimeter

Small circular copper plates exposed to the reflected energy of a heliostat can be used as a calorimeter if the edge is grounded and thermocouples used to measure temperature differential between the center and the edge. Instruments of this type are available from several sources typified by Thermogage Inc., Frostburg, Maryland.

The instruments are satisfactory for energy intensity levels up to 15 suns, 15,000 w/m², without auxiliary cooling. Above this level deterioration of the instrument occurs due to high temperatures. The instrument does not account for reradiation or convection losses thus provides only net energy data. Without some type of cooling this would be unsatisfactory for heliostat evaluation. Analytical data would be required to determine reradiated energy from the instrument.

The instrument could be installed in a grid pattern either with or without other surrounding material. When corrected for losses it

would produce total reflected energy as well as pattern information. The \$200 cost per instrument and need for a large number is a major problem with this approach.

Optical Calorimeter

The optical calorimeter approach uses a single very accurate solar insolation instrument, Eppley Pyrheliometer, as an "on-line" standard and inexpensive silicon solar cells for the large quantity of sensors. If continuous calibration of the solar cells against the pyrheliometer is used very accurate data may be obtained. There is a limit to silicon solar cell temperature thus the number of heliostats being tested at one time must be limited or the silicon cells cooled. The cooling is to prevent excessive temperatures and has little effect on data when the device is maintained below maximum temperature.

Refer to Figure 4-37 for a block diagram of the optical calorimeter and explanation of the following symbols. The silicon solar cells are sensitive to light in the 0.5 to 1.1 micron (μ) wavelength with a center at 0.8μ . The calibration array used in the solar research experiment contained silicon cells on 0.3m (1 foot) centers and was 4.27m (14 feet) high and 4.88m (16 feet) long for a total of 224 cells. An auxiliary array containing 5 silicon cells, aimed in the same direction as the main array but out of the reflected beam, was used to compensate for the background energy not attributed to reflection from the heliostat. Thus the output of the instrumentation is a measure of the energy in the 0.8μ band of the reflection from the heliostat.

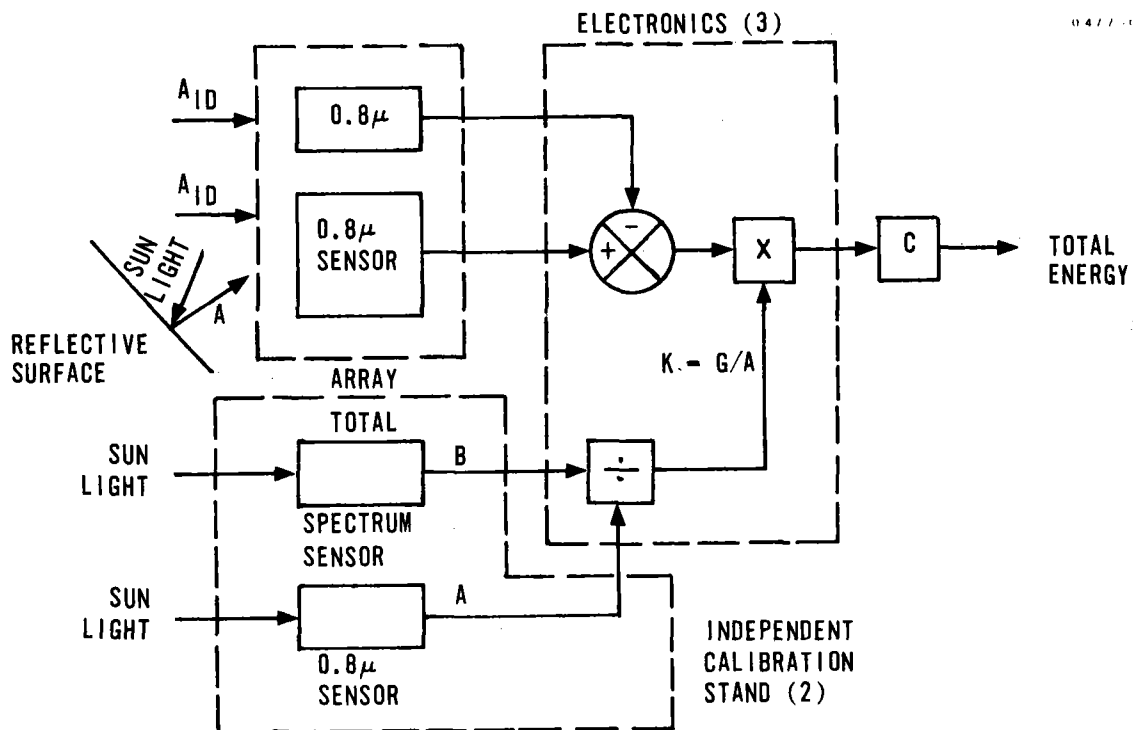


Figure 4-37. Block Diagram for Optical Calorimeter

To obtain energy level over the total solar spectrum (approximately 0.2μ to 2.4μ) a continuous calibration scheme has been developed. The output of a total spectrum sensor, Eppley Pyrheliometer, is divided by the output of a silicon solar cell while both are tracking the sun. The resulting b/a gives a calibration constant, k . (See Figure 4-15.)

The output of the independent calibration stand multiplied by the output of the array summer for each of the 224 solar cells produces a signal proportional to the reflected energy at each segment of the array. Proper manipulation of this data through a computer represented by C then produces accurate pattern data and total energy in any desired units or display fashion.

The overall accuracy of this system approaches that of the total spectrum sensor. It provides total and pattern energy data in any desired form and is not effected seriously by temperature, reradiation or convection. If it is desired to exceed flux density of approximately 15 suns ($15,000 \text{ w/m}^2$) cooling may be required to prevent damage to the silicon solar cells. This is the system that has been selected and used for solar research experiments at Honeywell.

Calibration Array Grid Spacing

An analysis was performed to determine the degradation of image centroid location as a function of increasing the grid spacing between photodetectors on the calibration array.

An expression to relate the intensity profile (either horizontally or vertically) across a gridded calibration array was generated. Coefficients were varied to simulate different peak intensities, different image skew and centroid offsets across a theoretical 20 by 20 foot array:

$$y(x) = \text{Intensity} = \frac{1}{A(X+D)^2 + B(X+D) + C}$$

where

$$-10 \leq X \leq 10 \text{ along the X axis.}$$

Coefficients were chosen to give representative scatter and intensity magnitude ranges expected at the calibration array (0 through 9) X 1000 watt/m² for different heliostat field positions.

In the cross axis (that is, vertical or Z) a linear degradation from $Y(X_i)$ along the vertical centerline of the array to zero at $Z = \pm 10$ feet is assumed and these values of $Y(X_i)_{Z_0 \rightarrow Z_{10}}$ are used in the centroid calculations

$$Z(X_i) = \frac{Y(X_i)}{\frac{10}{\Delta X}} \cdot N(\Delta X)$$

where

$$N = 1, 2, 3, 4 \dots$$

$$N\Delta X < 10 \text{ and}$$

ΔX = grid spacing size (i.e., number of data points used in centroid determination)

Grid spacing versus number of sensors used in the 400 ft² grid would be:

<u>ΔX (grid spacing of sensors) (feet)</u>	<u>Number of sensors in 20 by 20 foot grid</u>
0.05	160,801
0.10	40,401
0.20	10,201
0.40	2,601
0.50	1,681
1.00	441
2.00	121
5.00	25

This spacing obviously assumes sensors along the outer edge of the 20 by 20 foot grid and along the center lines of the array. A grid spacing of 0.05 foot will be considered the accurate location.

Figure 4-38 shows a very concentrated, slightly skewed image using coefficients:

$A = 0.2$, $B = 0.05$, $C = 0.11$, $D = 0.3$ as might be seen from a North side.

Figure 4-39 shows a more flat, more skewed distribution as might be seen from a South site at a non-optimum time of day using coefficients:

$A = 0.02$, $B = 0.05$, $C = 0.25$, $D = 1.0$

The centroid location and error from the centroid computation using $\Delta X = 0.05$ foot is shown in Table 4-11. $|\Delta|$ represents the calculated difference in feet from the true centroid.

The centroid locations noted in the above table were made using the number of sensors (data points) indicated previously per the defined grid spacing (for example, 1681 samples for the 0.50 foot spacing).

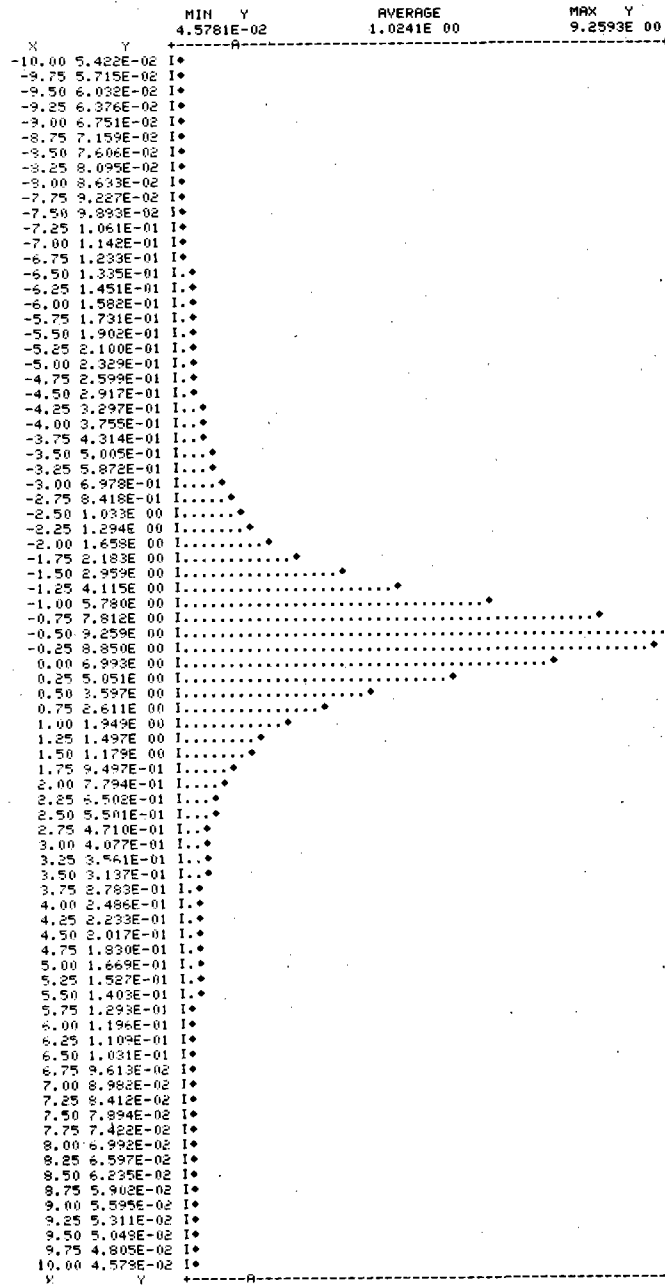
The nearest heliostat will have a line of site distance of approximately 140 meters (460 feet). An error of 0.46 foot in the centroid calculation will result in error of 1 mr. The calibration scheme itself should not introduce more than 0.05 mr, implying that the centroid accuracy itself should be no more than 0.023 foot in error.

570 444 FORMAT(F7.2,1PE10.3,1X,56A1)

0
NAME OUTPUT FILE
GRID

FORMAT GRID=6

PLOT OF X VERSUS Y

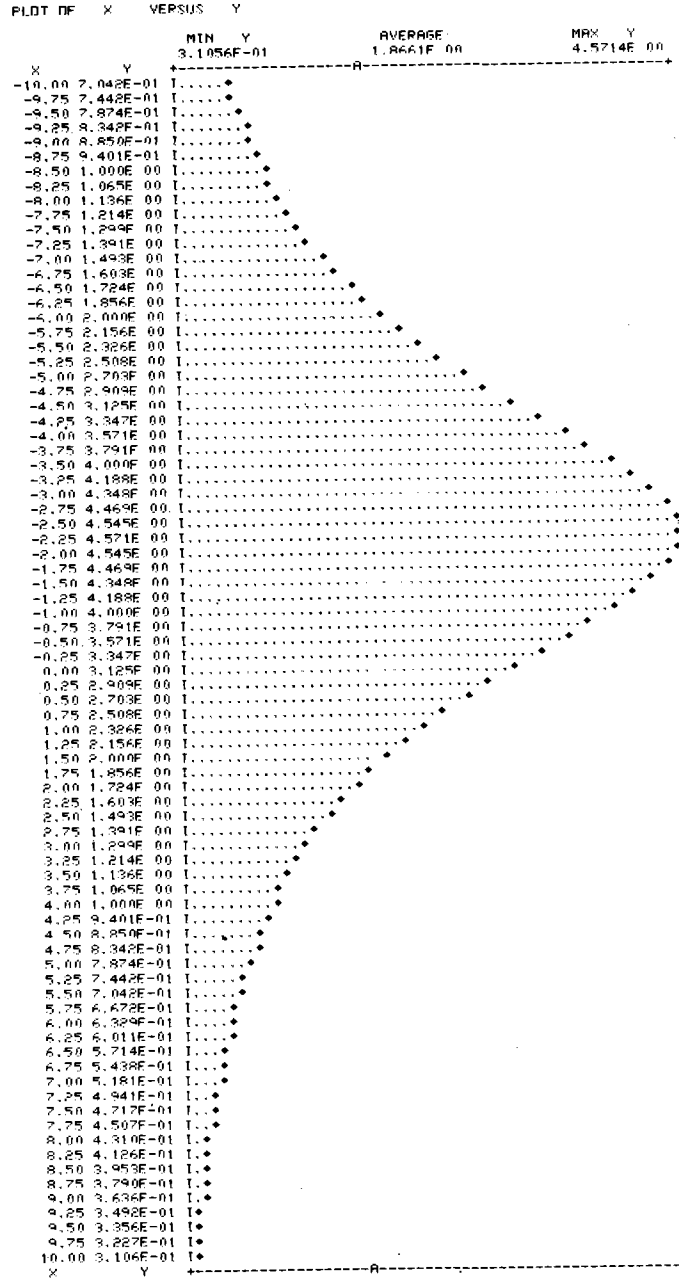


CENTROID = -0.4046
TOP:

Figure 4-38. Concentrated Image Using Coefficients

```

?EDIT GRID
EDIT
FLN 30
 30 DATA A/.02/.8/.05/.0/.25/.D/1./
C 1.021.021
 30 DATA A/.02/.8/.05/.0/.25/.D/1./
D
NAME OUTPUT FILE
GRID
?SAVE GRID
OK TO DESTROY OLD FILE?
Y
?FORTRAN GRID+.6
    
```



```

CENTRION = -1.7102
STOP
?OFF
OFF AT 07:06 03/28/77
COMPUTE SEC. - 17.2
CONNECT MIN. - 08
    
```

Figure 4-39. Flat Distribution Using Coefficients

Table 4-11. Centroid Computation

Grid Spacing (Feet)	Ref Figure 4-16		Ref Figure 4-17	
	Centroid Location	$ \Delta $ (feet)	Centroid Location	$ \Delta $ (feet)
0.05	-0.404408	0	-1.704372	0
0.10	-0.404461	0.00005	-1.705839	0.000147
0.20	-0.404567	0.000159	-1.708757	0.0004385
0.40	-0.404772	0.000364	-1.714526	0.010154
0.50	-0.405010	0.000602	-1.717378	0.013006
1.00	-0.39797	0.006429	-1.731311	0.026939*
2.00	-0.256203	0.14820*	-1.757467	0.053095
5.00	-0.055357	0.34905	-1.771083	0.066711

*Introduces >0.05 mr error into heliostat tracking.

As can be seen from the previous table representing two different profiles and other profiles run, at a grid spacing of one foot, the 0.05 mr criteria is reached for the inner most heliostats. Therefore it is recommended that a one-foot grid be retained even though some money savings could be made by going to a larger grid pattern. A smaller grid interval is not considered necessary from an accuracy standpoint.

If a 0.10 mr resolution is desired (0.046 foot centroid error), a one foot grid spacing will still be necessary to handle the concentrated peak image configuration.

One additional point needs to be made. This analysis does not address resolution of the input energy flux determination. With a larger grid size, the flux density maps would be coarser and therefore not as accurate. This accuracy degradation would be proportionally greater than the centroid calculation since it is in essence a straight integration of the sensor field data rather than a statistical treatment (for example, centroid calculation) of a large quantity of data points.

COMMAND COMPUTER CHOICE

Honeywell has analyzed several competitive minicomputers and has chosen the Honeywell Level 6 minicomputer because it is competitive and much data about it was readily available for preliminary design.

While acknowledging that several minicomputers are capable of performing the pilot plant task we have delineated a few of the competitive advantages of the Level 6 over some competitive machines. The interrupt structure, Automatic Context Save/Restore and other functions and the Level 6 comparison to other machines is described below.

INTERRUPT STRUCTURE

Function. Refers to the actions the CP takes when an event of importance to a program takes place outside the CP. (Such an event might be the end of a peripheral operation.) Items to note here are the number of priority levels in the system; the speed with which the interrupt handling program can be entered; and the degree to which the system automatically saves the state of the program which was interrupted, so it can be restarted later.

Benefit. An adequate number of such levels permits the hardware to control the prioritized execution of tasks, thus eliminating the need for complex software to perform this function. The results are: (a) fast response time for real time applications, and (b) greater throughput through reduced overhead.

Level 6 Capability. There exist 64 interrupt priority levels. The user can assign a distinct priority to a device. A device can break into (interrupt) a program running at a lower priority level. When the hardware services an interrupt it automatically saves the state of the running program in a predefined area of memory. It then restores the state of the device specific program from a predefined memory area, one area for each priority level. This eliminates the need for software polling to identify the interrupting device.

<u>Level 6</u>	<u>DEC</u>	<u>H.P. 21MX</u>
6/06 TBD	11/03/04/05/10	05A
6/34 } 64 (Vectored	11/35/40	08A
6/36 } Interrupt)	11/45/50	12A
	11/70	
	Variable	60 vectored
	0 - 8	
	<u>DATA GENERAL</u> ⁽¹⁾	<u>TEXAS INSTRUMENTS</u>
	Nova 2	990/4 - 8 vectored
	Nova 3	990/10 - 16 vectored
	Eclipse	

Level 6 Competitive Advantage. In addition to providing Vectored Interrupts, Level 6 has the maximum number of interrupt levels (64) competitively available. This feature, coupled with Automatic Context Save/Restore far exceeds competitive offerings.

BUS BANDWIDTH

Function. Bus bandwidth may be expressed as the number of bytes of data or commands which can be transferred between any two points in the system per second via the bus.

(1) Not vectored.

Benefit. The higher the bus bandwidth, the larger the system you can practically configure, the less likely you are to become bus limited and the more practical it is to use the same bus over the whole range of a product line (that is, very small to very large).

Level 6 Capability. The Level 6 bus bandwidth is at least 6 million bytes/second, probably closer to 6.5 million.

<u>Level 6</u>	<u>DEC</u>	<u>Data General</u>
6/06 } 6/34 } 6 MB 6/36 }	11/03/04/05/10 - 5 MB 11/35/40 - 5 MB 11/45/50 - 5 MB, Unibus	Nova 2 - 2.5 MP I/O BUS Nova 3 - TBD Eclipse S/100 } Eclipse S/200 } 2.5 MB Eclipse C/300 } I/O BUS

<u>H.P. 21 MX</u>	<u>TEXAS INSTRUMENTS</u>
05A } 08A } 5 MB 12A }	990/4 - NA 990/10 - 6 MB

Level 6 Competitive Advantage. The Level 6 bus has the highest real bandwidth of any minicomputer bus today. The benefit to the user comes in several ways:

- (1) The ability to configure a larger single bus system than the competition before running into performance limitations.
- (2) The ability to replace the current CP with a future higher performance CP with the knowledge that the bus has the needed extra capacity.

NUMBER OF BUSES IN BASIC SYSTEM

Function. Refers to the number of distinct data buses used to connect system elements.

Benefit. The use of one bus reduces cost and increases configurability. With slow technologies, some earlier systems needed two or more buses to achieve a desired data transfer rate.

Level 6 Capability. Level 6 uses a single bus for all traffic as compared to many competitive systems, which either require more than one or which resort to special buses for high speed transfers.

LEVEL 6 MEGABUS ^T SUMMARY COMPETITIVE COMPARISONS

<u>Functional Area</u>	<u>Level 6</u>	<u>PDP-11</u>	<u>Nova 2</u>	<u>Nova 3</u>	<u>Eclipse</u>	<u>Texas Instruments</u>	
						<u>990/4</u>	<u>990/10</u>
*Asynchronous Bus	Yes	Yes	Yes	Yes	Yes	No	Yes
*Bus Bandwidth	6 MB	5 MB	2.5 MB	2.5 MB	2.5 MB	NA	6 MB
Number of Buses	1	1 ⁽¹⁾	2	2	2	1	2
*Bus Memory Address Range	16 MB	256K	33KW	32KW	32KW	NA	1 MW
*No. of Controller/ Device Addresses	1024	NA	59	59	60	NA	1024
Word/Byte Transfer Modes	Both	Both	Both	Both	Both	NA	Word
Data/Address Integrity	Yes	Yes	No	No	No	NA	TBD
*Split Read Cycle	Yes	No	No	No	No	NA	TBD
Driver Speed/ Technology	1975	1970	1968	1975	1968	1975	1975
DMA	Yes	Yes	Yes	Yes	Yes	No	Yes
*Bus Control (Distributed)	Yes	No	No	No	No	NA	Distributed
Bus Time-out	Yes	Yes	TBD	TBD	TBD	NA	TBD
Number of Priority Interrupt Levels	64	Variable	16	16	16	8	16

(1) See detail sheet

* Areas of Level 6 Competitive Advantage

<u>Level 6</u>		<u>DEC</u> ⁽¹⁾	<u>Data General</u>
6/06	} 1	11/03/04/05/10 - 1	Nova 2 } 2
6/34		11/35/40 -1	Nova 3 }
6/36		11/45/50 } 1 Unibus	Eclipse S/100 } 2
		2 Solid State	Eclipse S/200 }
		11/70 - 2-32 bit internal buses	Eclipse C/300 }

H.P. 21MXTEXAS INSTRUMENTS

05A	} 2	990/4 -1
08A		990/10 - 2
12A		

Level 6 Competitive Advantage. Equal. The use of one bus reduces cost and increases configurability. With slow technologies, some earlier systems needed two or more buses to achieve a desired data transfer rate.

BUS MEMORY ADDRESS RANGE

Function. Refers to the amount of memory that can be addressed by controllers and other units in transferring data over the bus.

Benefit. A large range permits using large memories without imposing artificial restrictions on the location of I/O buffers in memory, etc.

Level 6 Capability - Over 16 million bytes.

<u>Level 6</u>		<u>DEC</u> ⁽¹⁾	<u>Data General</u>
6/06	} 16 MB	11/03/04/05/10	Nova 2 } 256KB
6/34		11/35/40	Nova 3 }
6/36		11/45/50	Eclipse S/100 } 256KB
		11/70	Eclipse S/200 }
			Eclipse C/300 }

H.P. 21MXTEXAS INSTRUMENTS

05A	} 32k - 131k	990/4 - NA
08A		990/10 - 2MB
12A		

(1) No standard bus on 11/03.

Level 6 Competitive Advantage. The Level 6 bus has the capacity to address 2^{24} bytes of memory (24 control lines). All I/O controllers are designed to support the full 2^{24} bytes of address. A user can be sure that as his need for memory space on a system increases, the bus and all I/O devices will present no problems to him. Whereas the CPUs come in various performance and functional ranges, the bus and the I/O controllers are designed for the "top of the line" and guaranteed long useful life.

Data General I/O devices use the memory management unit to address more than 32k. This means all I/O buffers must be in a designated 32k area (though this area may be scattered over memory) and is awkward.

NUMBER OF CONTROLLER/DEVICE ADDRESSES

Function. Refers to the number of unique "end points" (communication lines or peripherals) that can be addressed by a program.

Benefit. A large number of channel numbers permits the support of very large I/O configurations.

Level 6 Capability - 1024 devices.

<u>Level 6</u>	<u>DEC</u> ⁽¹⁾	<u>Data General</u>
6/06	11/03/04/05/10	Nova 2 60
6/34	11/35/40	Nova 3
6/36	11/45/50	Eclipse S/100
	11/70	Eclipse S/200 60
		Eclipse C/300
<u>H.P. 21MX</u>	<u>TEXAS INSTRUMENTS</u>	
05A	990/4 - NA	
08A N/A	990/10 - 1024	
12A		

Level 6 Competitive Advantage. The ability of the Level 6 bus to directly address I/O commands to 1024 end points has advantages both in the size of the system that can be realistically configured, and, in programming ease. Every end point in a system is a channel whether it be a communication line, a tape drive, a printer, etc. Older architectures which limit device address to 64 or so generally have to resort to a different software visibility for communications or data acquisition systems because they simply run out of addresses.

Because of the foregoing advantages Honeywell believes the Level 6 computer is an exceptional choice for the pilot plant control computer.

(1) No address parity

CONCLUSION

The foregoing analyses and trade studies are not exhaustive but are indicative of analyses, trade offs, and design selections made during the preliminary design phase. Space does not permit a complete listing of all design choices which have previously been presented to and approved by Sandia and ERDA.

Section 5 OPERATION, INSTRUMENTATION AND CONTROL

INTRODUCTION

This section describes normal operations, off normal operations, and preliminary scenarios for collector subsystem operation. Since great flexibility exists in the system several special tests are briefly discussed for performance during the first two years of pilot plant operation. One of these special test outputs will be the best start-up procedure. Figure 5-1 shows standby positions outboard of each corbel. The beams from certain sections of the field travel from the ground up three imaginary lines to these standby positions. From these positions the beams can easily be moved onto and off of the receiver in very short times. Note the beams cross only protected positions of the structure to move on and off the steam generator.

The operation and control arrangement is discussed first. The second section discusses the operator versus computer initiated commands. The third topic is instrumentation and is followed by the detail discussion of our calibration array and associated electronics. The final section discusses maintenance and logistics before a concluding paragraph.

OPERATION AND CONTROL ARRANGEMENT

Control of the collector subsystem can be functionally categorized into three areas:

- A. Control during normal operational modes.
- B. Control to protect pilot plant equipment and personnel from damage due to the environment, equipment malfunction, or incorrectly applied redirected insolation.

Each area is discussed below.

A. Control During Normal Operation

Normal operation will involve the full integration of control features to include all field instrumentation for performance monitoring, checking the status of communication links, comparing performance of the 18 instrumented heliostats, software program safing and mode control, start-up and shutdown sequences, and collector subsystem calibration.

1. Start-Up and Shutdown Control

Start-up sequences will commence early enough in the morning such that the entire heliostat field can be placed upon the receiver 1/2 hour after sunrise. Normal shutdown will begin 1/2 hour before sunset or earlier depending on the time of

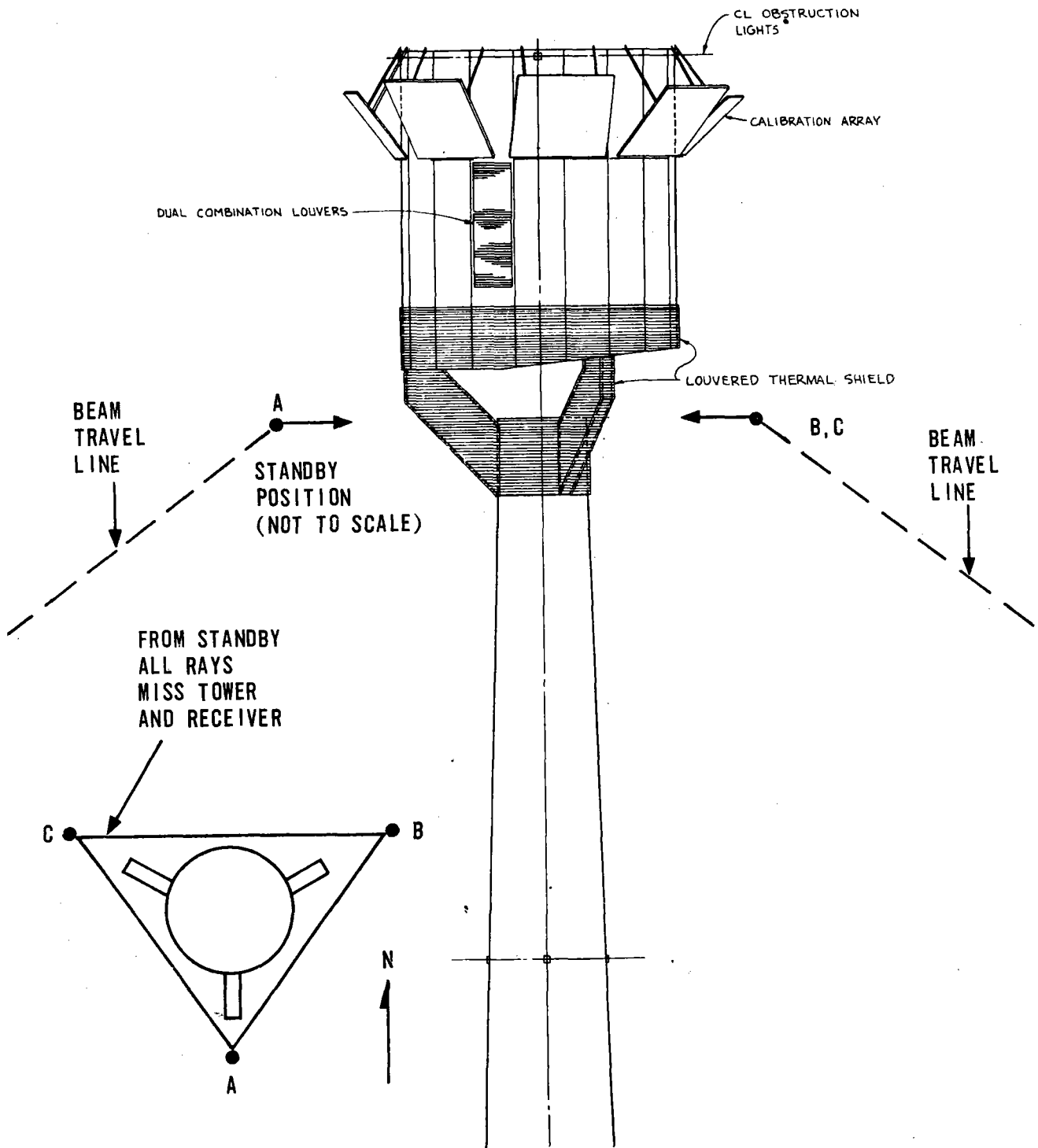


Figure 5-1. Standby Position

year (sun's elevation) and outer axis travel restrictions (+30 deg to -75 deg rotation range). Before commanding the heliostats to initialize the control subsystem will be sequenced through several checks such as:

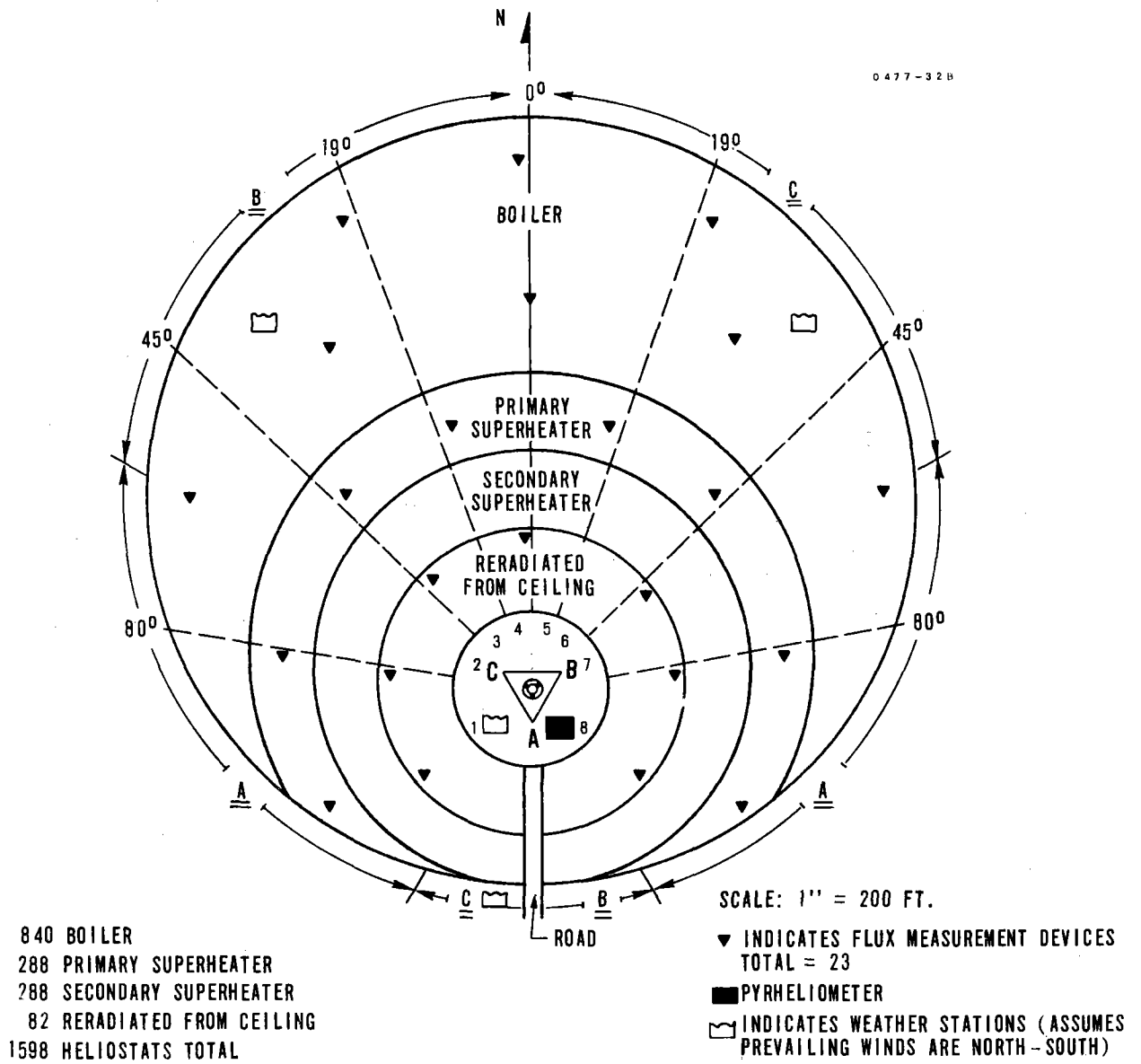
- Bringing the data processing hardware on line.
- Run self-tests.
- Confirm that winds, weather forecasts, etc., allow for proper operation.
- Confirm that field power transformers are operational.
- Confirm that anticipated insolation flux densities will be adequate for operation. It would not be necessary to have adequate insolation to generate steam at 1/2 hour after sunrise as a precondition to bring the heliostat field to a standby position per Figure 5-1. For instance, if a morning cloud or fog coverage was expected to lift at some time, the heliostats should already be prepositioned such that the redirected beams will be on the boiler and superheaters as the coverage dissipates.

After these checks have been successfully passed, the operator would command all heliostats to turn on power and initialize. In the early morning before, or at dawn, no danger will result from redirected images affecting aircraft overhead. However, if for some reason the field must start up at some other time, controls are included in the software such that the airport is not affected. Part of the detail design phase will address accuracy effects, if any, resulting from initializing with the mirror surface down which assists in solving the overhead safing problem.

From initialization each heliostat will be brought to a standby position near the tower, represented by A-B-C around the tower on Figure 5-2. A different standby pattern may be developed during the detail design phase based upon actual travel requirements of each heliostat to its primary target area such that movement across the receiver structure members will be minimized. The command to go to the standby target could be either under software control for each heliostat after initialization is reached, or by operator control, commanding sectors of heliostats at a given time. After the operator initiates the mode to go to standby targets, the central processor will control the trajectory.

Under operator control, the heliostats will be commanded to track their primary targets in the following sequence:

- First - boiler heliostats
- Second - first stage superheater heliostats
- Third - second stage superheater heliostats



Heliostats in Zone

Point to Standby Target

C
A
B

C
 A
 B

Figure 5-2. Standby Pattern

2. Daily Monitoring, Checks, and Control

During the course of the day, the monitoring functions of the power plant master controller or the collector subsystem control system can direct heliostats to retreat to their standby (secondary) target due to detected adverse reactions of the receiver (thermal gradients across boiler, pressure too high, etc.) or field conditions (cloud coverage over part of the field). Any change of status of any heliostat due to automatic control will be displayed on the operator console.

The operator has the option, from the console to direct a mode change (for example, go to standby positions) of any selected heliostat or any group (sectors) of heliostats.

The fact that each heliostat has not fallen behind in slewing from any position to its commanded position under high slew rates (1200 arc-sec per second) is assured by the 8 bit up-down counter within the heliostat electronics, one for each axis. These counters will not overflow unless the slew rate falls 5.7 degrees behind. The SRE test results (Section 7) show that the inner axis averages 0.6 deg/sec and has never dipped less than 0.4 deg/sec under wind loading. The outer axis maintains an average of 0.3 deg per second rate under operational conditions. If due to a combination of a large wind gust (22 M/S) and momentary worse case gimbal orientation with respect to the wind velocity and direction, loading causes a temporary lag the overflow counter will keep track of the lag and cause the axis to catch up.

An additional control feature is the wrap-around communication link check discussed on page 3-66. The control subsystem will check each command sent to each heliostat on each of the 18 communication data buses. If the received bit train is not identical to the transmitted data, the operator will be flagged. Erroneous returned signals could be caused by:

- Noise induced while being routed to the heliostats (causing erroneous heliostat response)
- Noise induced while the signal is returning to the computer complex (no impact upon heliostat positions)
- Erroneous data sent by transmitter
- Error in the computational check of the returning signal.

During the detailed design phase, a more extensive analysis will be made with regard to potential data transmission error rates and methods of performing statistical checks per communication theory techniques. For instance, the two on-line Level 6/43 CPUs may both check the returning wrap-around transmission and if either check OK, then the transmission will be assumed to be good.

Another control feature will be utilization of feedback from the 18 instrumented heliostats. For these selected heliostats, one per each data bus, a precision resolver (minimum resolution of 360/16 or 20 arc-seconds for the inner axis) on each axis will be monitored by the control subsystem for two purposes:

- Provide short term performance monitoring data. The precision angular readout will be compared both on line and off line (with analysis routines) with the commanded position (resolution of 80 arc-seconds). Short term movements due to wind loads, local thermal gradients, etc., will be detectable. This activity per heliostat will give a good feel as to the short term responses to environmental effects of the total field.
- If a transmission error is detected, the instrumented heliostats' resolver positions can be compared with the previous position and the command issued (if any) to that heliostat. If there has been no unaccounted for disturbance of gibal position, this is an indication that noise was induced into the transmission on the return route. However, since only 1.13 percent of the heliostats are instrumented, this check will not be conclusive.

Note that if control of any one heliostat is lost, the initialization bit can be set and control regained from which the heliostat can be redirected to its assigned target.

Twenty-four insolation sensors as placed throughout the field. Four calibrated pyrhelimeters will obtain absolute insolation levels from which the other 19 sensors (one spare) can be calibrated and corrections made for variations in CO₂, H₂O, pollutants and other atmospheric attenuation. The sensors will be used for two purposes:

- Compare the flux received throughout the day throughout the field with the energy input to the receiver subsystem.
- Anticipate potential problems with respect to inducing thermal gradients across the boiler based upon detected partial cloud coverage in portions of the field. During the detailed design phase, full interface with the receiver subsystem vendor will be made to derive thermal gradients and time constant margins such that control software can be specified which can perform monitoring and control logic to provide operator awareness and remove potentially hazardous conditions by automatically slewing selected heliostats to a standby position.

3. Calibration

Calibration will actually be a normal, periodic mode of operation. The SRE test results indicate that a weekly calibration interval per heliostat should be adequate. During the Pilot Plant integration and checkout phase, this interval may be determined to have to be more frequent or a longer interval may be adequate.

Selection of a heliostat to be calibrated can be under the control of either the console operator or software. After the system integration phase is complete, the rotation of heliostats to be calibrated could be completely under software control except for particular heliostats being investigated for trouble or showing trending errors larger than normal.

Because of the image spread of some South, West and East heliostats due to the toe-in phenomena, a good, overlapped spot to calibrate with may exist for only 4-5 hours depending on the time of year. Assuming five available hours over the field of 1600 heliostats for seven days a week using eight calibration arrays, this results in a capability or requirement of having to calibrate only six heliostats per hour per array which will have little impact with regard to loss of redirected insolation from the field due to calibration. A heliostat can be brought to the array within 15 seconds, the centroid location and image quality be monitored for one minute (that is, 60 samples) and be back on its assigned target within 15 seconds for a total loss time of only 1.5 minutes. At six per hour, it can be seen that much spare time will be available for the more busy sectors (North) and catch-up in case of inclement weather the previous day's allocated time slot. As a result of calibration, a heliostat's offset constants will be modified and applied until next calibration, insuring good control over the field's tracking performance. Off-line analysis will be used to detect any long term trending or sudden shift errors.

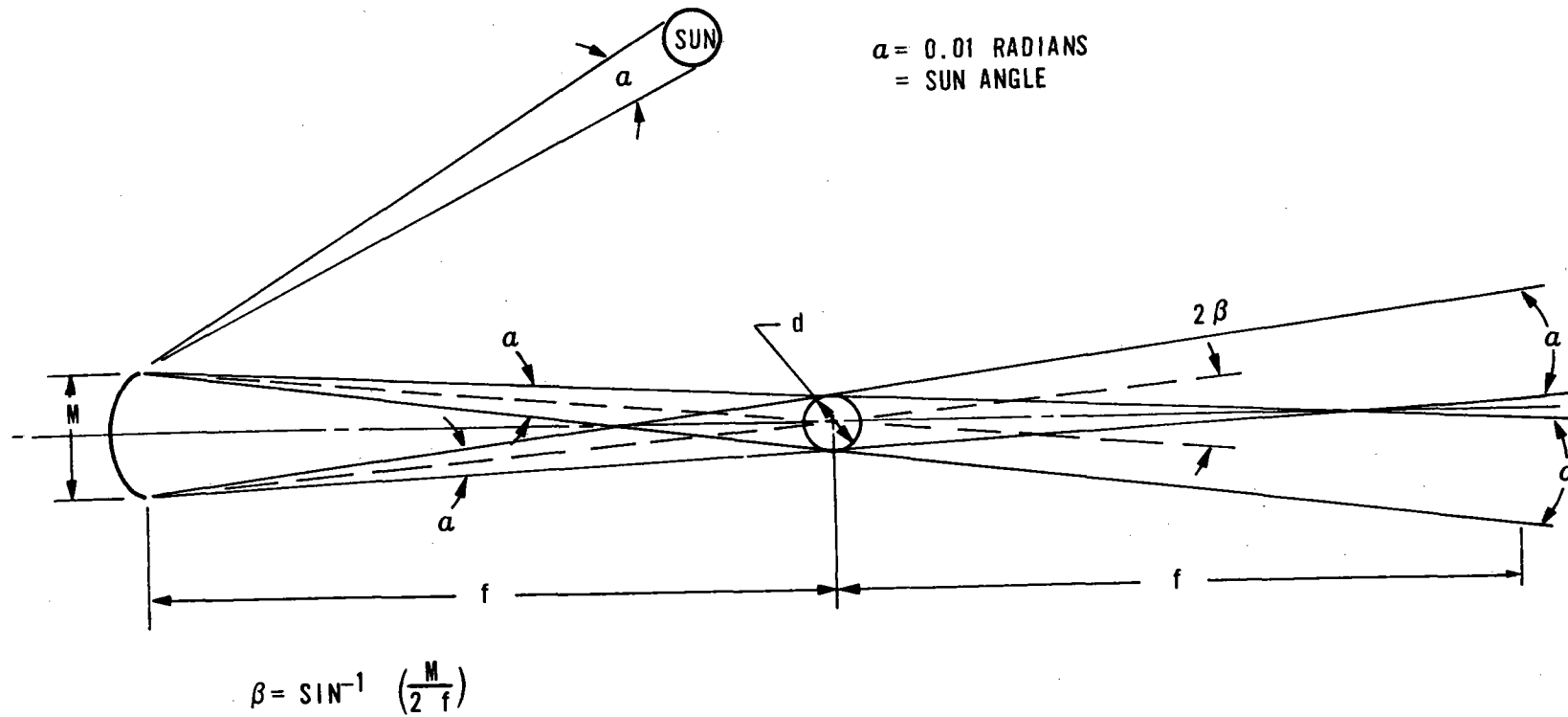
Because of the octagon pattern of the calibration arrays, the spill over from one adjacent, array to another due to an off-center heliostat could erroneously affect the centroid calculation of the second array. Because of the large amount of available time on a weekly basis, the software will be programmed to insure that two adjacent arrays are not being used simultaneously for the minute of data sampling to determine precise error corrections to be applied.

Based upon past performance history of the different heliostat sites, a unique required calibration interval could be generated for each heliostat and also be under software control, with all changes made apparent to the collector subsystem operators.

B. Control to Protect Equipment and Personnel

Protection must be afforded to personnel and equipment from potential damage or injury due to misdirected radiation from the collector subsystem. This section generates a rationale to discuss actual zones of concern. Damage to personnel eyes is the primary concern.

Figure 5-3 shows a single facet curved for focus and illuminated by an area source (the sun). From the figure it should be clear that the beam angle γ is the sun angle (α) plus twice the focal half angle (here defined as β). Thus an approximation of "beam" diameter is γ (in radians) times the slant range (in meters). Since the maximum



$\alpha = 0.01$ RADIANS
= SUN ANGLE

$$\beta = \sin^{-1} \left(\frac{M}{2f} \right)$$

γ = BEAM ANGLE BEYOND FOCAL POINT IS

$$\gamma = \alpha + 2\beta$$

Figure 5-3. Single Facet Curved Mirror

energy is the insolation (incident on the mirror) times the mirror area this number will be used. Thus the following calculations:

$$\text{Insolation} = 1000 \text{ w/m}^2$$

$$\text{Mirror} = 10 \text{ m}^2$$

$$\text{Total Energy} = 10 \times 1000 = 10 \text{ kw}$$

At Slant Range of 345m Beam diameter is

$$\text{Dia} = \gamma \times \text{SR} = 0.01947 \times 345 = 6.7\text{m}$$

$$\text{Area} = \frac{\pi C^2}{4} = 35.4 \text{ m}^2$$

$$\text{Flux} = \frac{10 \text{ kw}}{35.4 \text{ m}^2} = 282 \text{ w/m}^2 \text{ compared}$$

to incident sunlight of 1000 w/m^2 . Using this number and the calculations of Table 5-1 we conclude the zone of concern to be two focal lengths (or less) away from the heliostat mirror.

Consider now Figure 5-4 which shows the Four facet geometry. Note since the facets are spaced on 1.6X facet size dimensions that there appears to be a larger spread angle beyond the focal area. Again consult Table 5-1 for γ and at the distance f_0 past the focal area the spot or beam diameter is

$$\text{DIA}_4 = \gamma_4 \times \text{S.R} = 0.03308 \times 408 = 13.5$$

$$\text{AREA} = \frac{\pi (\text{DIA})^2}{4} = 143 \text{ m}^2$$

Using four facets at 10m^2 each and insolation of 1 kw/m^2 yields:

$$\text{Flux} = 40\text{kw} \div 143\text{m}^2 = 279 \text{ w/m}^2$$

again a relatively safe level compared to the basic 1 kw/m^2 available from the sun.

Therefore it can be concluded that the zone of concern should not be more than two focal lengths from the heliostat. This is shown pictorially in Figures 5-5 and 5-6. Table 5-2 provides the data points shown in Figure 5-6.

Protective techniques will consist of both passive and active measures.

Passive measures to protect personnel and property within and immediately near the power plant facilities will consist of:

1. Enforced personnel standing operating procedures (SOPs) to prohibit access to dangerous areas during specific periods of operation, in particular the tower. Prescribed sun glasses will be required for all personnel.

Table 5-1. Focal Area

<u>Characteristics*</u>	<u>Units</u>	<u>Figure 1 Dimensions</u>	<u>Figure 2 Dimensions</u>
M*	Meters	3.16 x 3.16	3.16 x 2.16
f	Meters	345	345
β	Radians	0.00947	N/A
α	Radians	0.01	0.01
γ	Radians	0.01947	N/A
M_o	Meters	N/A	9.4
f_o	Meters	N/A	408
β_4	Radians	N/A	0.01153
γ_4	Radians	N/A	0.03308

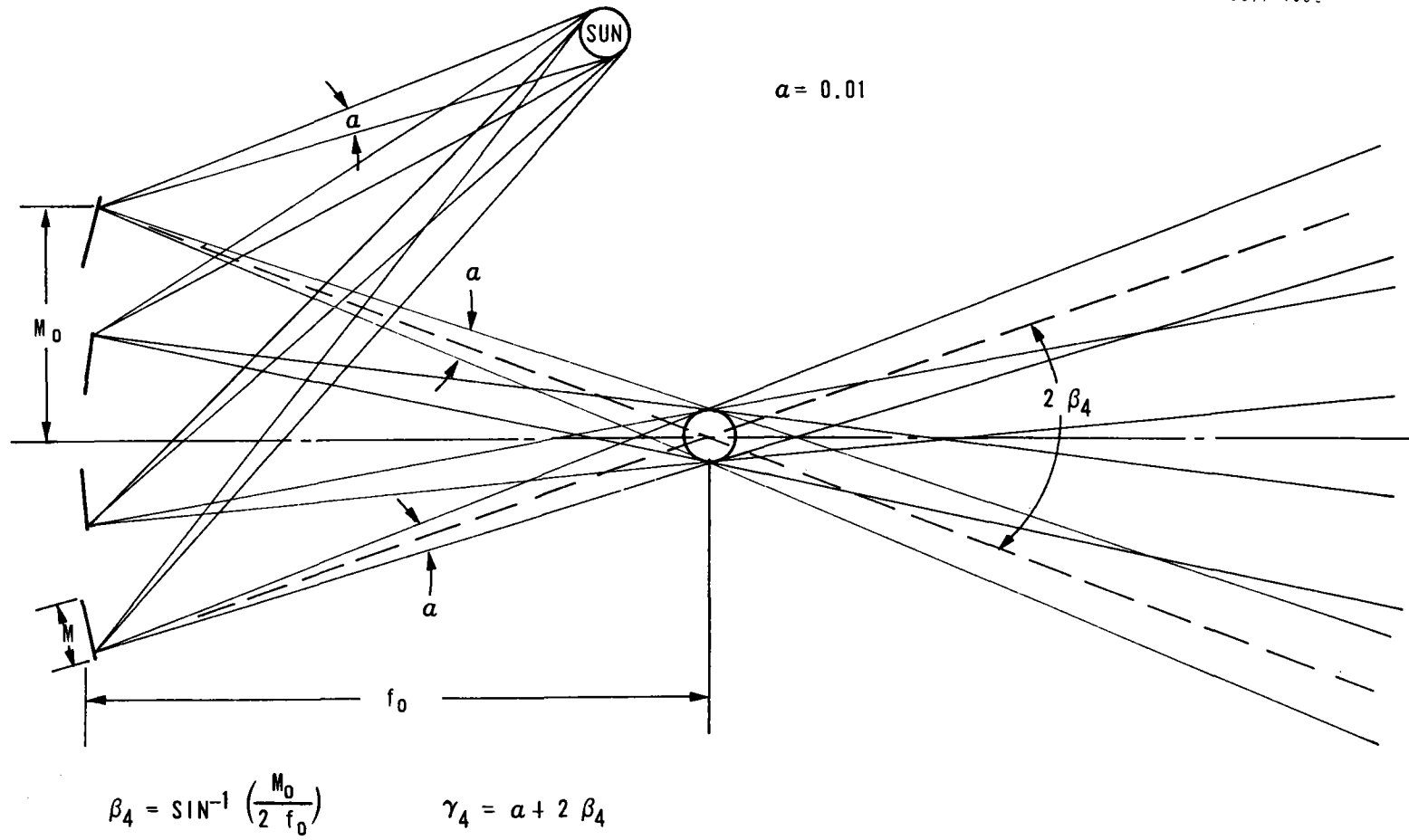


Figure 5-4. Four Facet Mirror

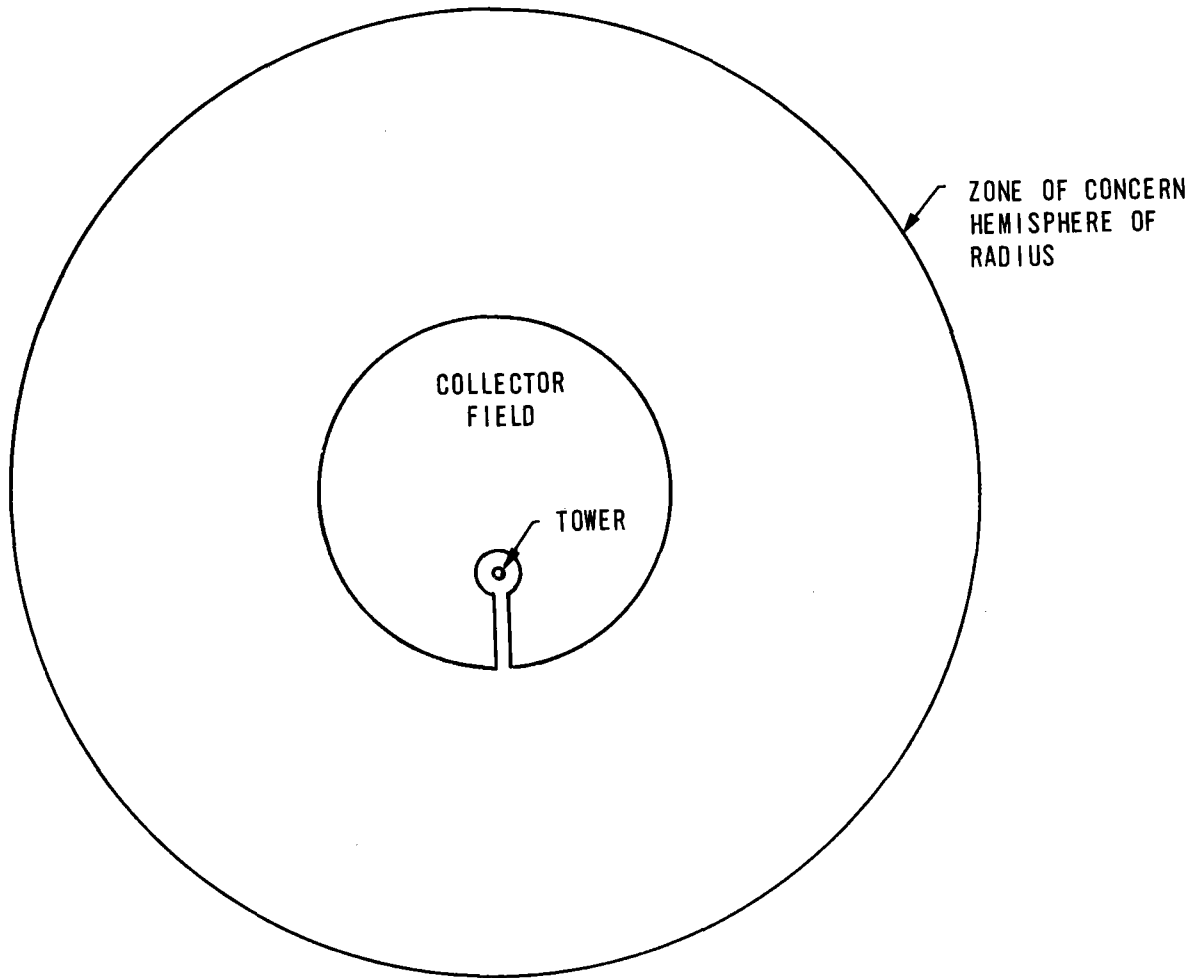


Figure 5-5. Zone of Concern

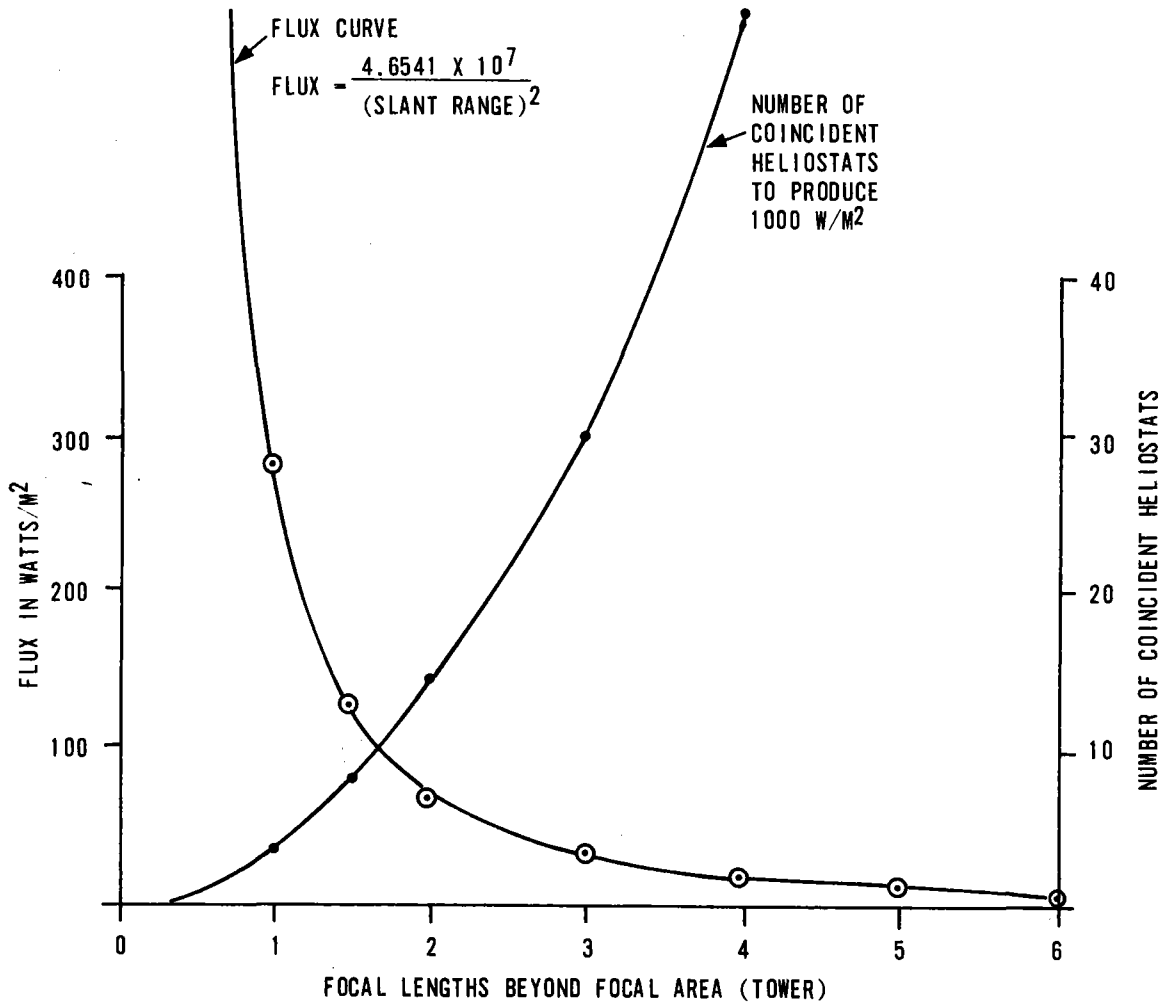


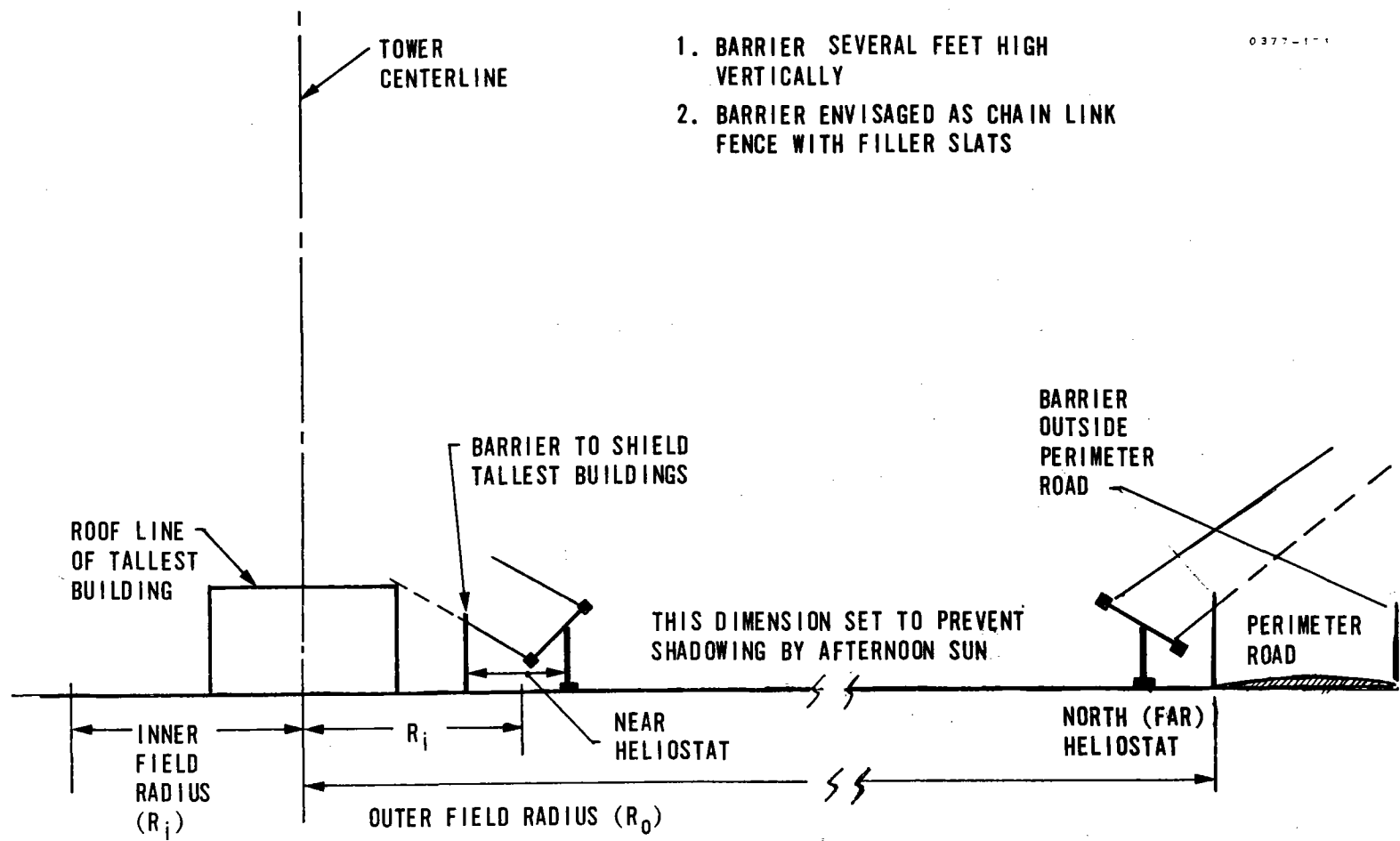
Figure 5-6. Flux Versus Distance

Table 5-2. Flux Versus Slant Range Four Facets

<u>Focal Length</u>	<u>Slant Range</u>	<u>Flux</u>	<u>No. of H/S To Produce 100 w/m</u>
1/2	204	1118.35	0.9
1	408	279.59	3.5
1 1/2	612	124.26	8.1
2	816	69.90	14.3
3	1224	31.07	32.3
4	1632	17.47	57.2
5	2040	11.18	89.5
6	2448	7.77	128.7

2. Barriers. The barrier shall be opaque to sunlight but shall also not cause substantial structural loads from wind environments. To meet these goals a chain link fence with filler slats or attached nylon mesh (for example, wind breakers for tennis courts). The nylon mesh may be preferred because of being cheaper and offering less resistance to high wind loads. However long term maintenance costs may be higher. Detail calculations have not been possible but it is estimated that a barrier could be incorporated in the security fence such that both functions are provided. Care must be taken such that no shadows are cast by the barrier on heliostats in the innermost row. The inside barrier shall protect buildings and grounds near the base of the tower. The outside barrier shall protect external facilities as well as the perimeter road. Figure 5-7 shows this concept. Additional lower barriers could be placed within the field along selected radial access lanes if the need becomes apparent.

3. Reflective paint and thermal insulating material will be used to protect the tower structure, corbels, support and calibration array supports.



1. BARRIER SEVERAL FEET HIGH VERTICALLY
2. BARRIER ENVISAGED AS CHAIN LINK FENCE WITH FILLER SLATS

0377-111

Figure 5-7. Barrier Concept

Active measures include:

1. Software control of heliostat beam trajectory throughout the field to insure high concentrations do not overlap at any one time when start-up or shutdown must be accomplished during times of large impinging flux levels. As Figure 5-6 shows, beyond focal lengths of two tower heights, it would take a coincidence of 15 or more heliostats overlapping to produce only 150 watt m⁻² insolation flux. The additional time to sequence the trajectory from inner to outer gimbal rather than both random and simultaneously would be minimal. Only during emergency shutdown (15 minutes maximum) due to sudden winds or hail would a controlled trajectory not be feasible.

Around the Barstow Pilot Plant area, it appears that elevated roads which vehicular traffic may be impinged by redirected insolation coming over the barrier tops are at such a distance that the flux levels will not cause eye damage or temporary blindness. Commercial plant site selections should also retain this safety consideration.

2. Under normal operations, the heliostat field will be brought up to position before 1/2 hour from sunrise and after 1/2 hour before sunset.

OPERATION INSTRUMENTATION AND CONTROL

This section ties together operational control considerations which are applicable to either the pilot plant or the commercial plant modules. The available field instrumentation is related to the various safing, calibration, and normal operation modes that the collector subsystem must be capable of performing.

OPERATION INSTRUCTIONS*

One of the difficult design decisions for the pilot plant is the degree of automation implemented in the master plant control system. Certain functions can either be manually or automatically performed. In the collector subsystem case there are many functions not possible through manual techniques. This makes the collector subsystem at once easier and harder design. The design challenge is to give the operator supervision capabilities while not slowing down collector command control subsystem operation. Our blend of automatic operations, commands, and alarms provides efficient automation without sacrificing essential human decision involvement.

To incorporate full control over the collector subsystem, the following table (Table 5-3) identifies the control commands or instructions that will be a part of the software package and whether the initiation of the specific control is under operator jurisdiction or computer control or either. Operator control functions will be entered via the command

* An Operating Instruction Document (No. 1176-14147) was published 25 October 1976.

Table 5-3. Command Initiation

<u>Description of Control Function</u>	<u>How Initiated</u>	
	<u>Operator Control</u>	<u>Software Control</u>
A. Mode Control		
1. Normal Primary Target Tracking		X
2. To calibrate selected heliostats based on:		
• Routine operations (once/week)	X	X
• Control of beam time on calibration array	X	X
• Special troubleshooting	X	
• Update site parameters	X	X
3. Track standby target		
• During start-up (all heliostats)		X
• Special reasons (for example, experimentation, receiver evaluation, etc.) (individual and all heliostats)	X	
• During standby after unexpected event (receiver problem, after peculiar environmental condition, etc.)	X	
4. Safing		
• Beam control during routine start-up - shutdown		X
• Beam control during emergency defocus (3-4 degrees offset)	X	X
• Heliostat field sector emergency defocus	X	
• Initiate emergency defocus (receiver thermal stress, insolation gradients due to partial cloud coverage, etc.)	X	X
• Equipment safing (GO TO STOW due to wind or hail conditions)	X	X
• Beam control during emergency stow		X
5. Initialize (that is, go to initialize)	X	
• Selected heliostats	X	
• During start-up sequence - all heliostats	X	X
6. STOW (END OF DAY, or ample weather warning)		
• Selected heliostats	X	
• Entire field of heliostats	X	X
7. Point Mirror Normal in given direction (No Tracking)	X	
8. Control of rate to reach a given position or target	X	X

Table 5-3. Command Initiation (Continued)

<u>Description of Control Function</u>	<u>How Initiated</u>	
	<u>Operator Control</u>	<u>Software Control</u>
9. Testing		
• Wrap-around <u>commo</u> check (Normal Operation)		X
• Wrap-around <u>commo</u> check (Special Request)	X	
• Self-test of control subsystem	X	
• Lamp test, etc.	X	
10. Data Output		
• Normal Operation		
Disk		X
Displays	X	X
Special Requests	X	
11. Control interface with master plant controller	X	X
12. Display field ac power monitors	X	X
13. Compare resolver data of 18 instrumented heliostats with calculated gimbal position		
• Routine		X
• Special request for display	X	
14. Update time		X
15. Switch or update operational program	X	
16. Display particular operational or meteorological data		
• Routine		X
• Special Requests	X	

console. It should be noted that after the operator initiates a particular action, then the Level 6 computer control subsystem will carry out the actual task under its control via issuing the appropriate sequence of commands over the communication links to the heliostats or other equipment to decode and execute.

This paragraph does not include the case where an individual heliostat has been placed under local manual control for maintenance or other reasons. Further definition of our preliminary design will be performed in the next phase.

INSTRUMENTATION

Field instrumentation for the pilot plant field will consist of meteorological stations, insolation monitors and gimbal angle readout devices on selected heliostats. The purposes of these devices are as follows.

The meteorological stations will provide wind speed, wind direction, temperature, and humidity inputs to the control system. This data will be used to help evaluate operation under varying ambient conditions. The stations also provide the means to detect the severe conditions under which operation should be discontinued and the heliostats stowed. Four stations will be used in the pilot plant placed throughout the field as shown in Figure 5-8 of the accompanying figures.

The insolation monitors will consist of silicon phototransistors and linear amplifiers which will provide a measure of the available sun's energy at specific sites throughout the field. The monitors will provide inputs to help evaluate system performance with respect to unbalanced conditions caused by intercepting clouds and might even be used to alter the control strategy to help accommodate such conditions. Twenty three monitors will be used in the pilot plant placed in the field as shown in Figure 5-8.

Eighteen heliostats, one from each command communications line will be selected for sample performance monitoring at the pilot plant. Gimbal angle readout devices will provide the means to be able to compare actual gimbal position with commanded position. This data will provide another checkpoint on whether or not at least one heliostat on each communications lines is receiving and properly executing commands from the control computer.

The data from the field will be returned to the control computer by means of half duplex serial digital data buses with several ports sharing the same data link. Communications traffic control will originate with a common request for data sent by the computer to all taps on a given line. Each tap will then use a different delay to respond. The computer will recognize the sequence of the returned data to identify its origin. No addressing will be required. All taps on a line will respond whenever a request for data is sent. Data requests and data will be sent over the same twisted shielded pair. Each tap will contain all of the electronics required to be a complete sending station. A block diagram of such a system is shown in Figure 5-9 of the accompanying figures.

Note that some ports such as the insolation monitors will not require a local multiplexer. Also note that some functions such as the power supply, XTAL oscillator, timing generator and transmitter section of the UART exist at every heliostat and may be combined to save hardware costs.

The complete system will require seven data buses with an aggregate length of 4267m (14000 ft).

CALIBRATION ARRAY AND ELECTRONICS

Overall Operation

The cal array provides a quick and efficient means to make measurements on the redirected beam. With the beam directed toward the array, a series of photodetectors spread across the array provide electrical

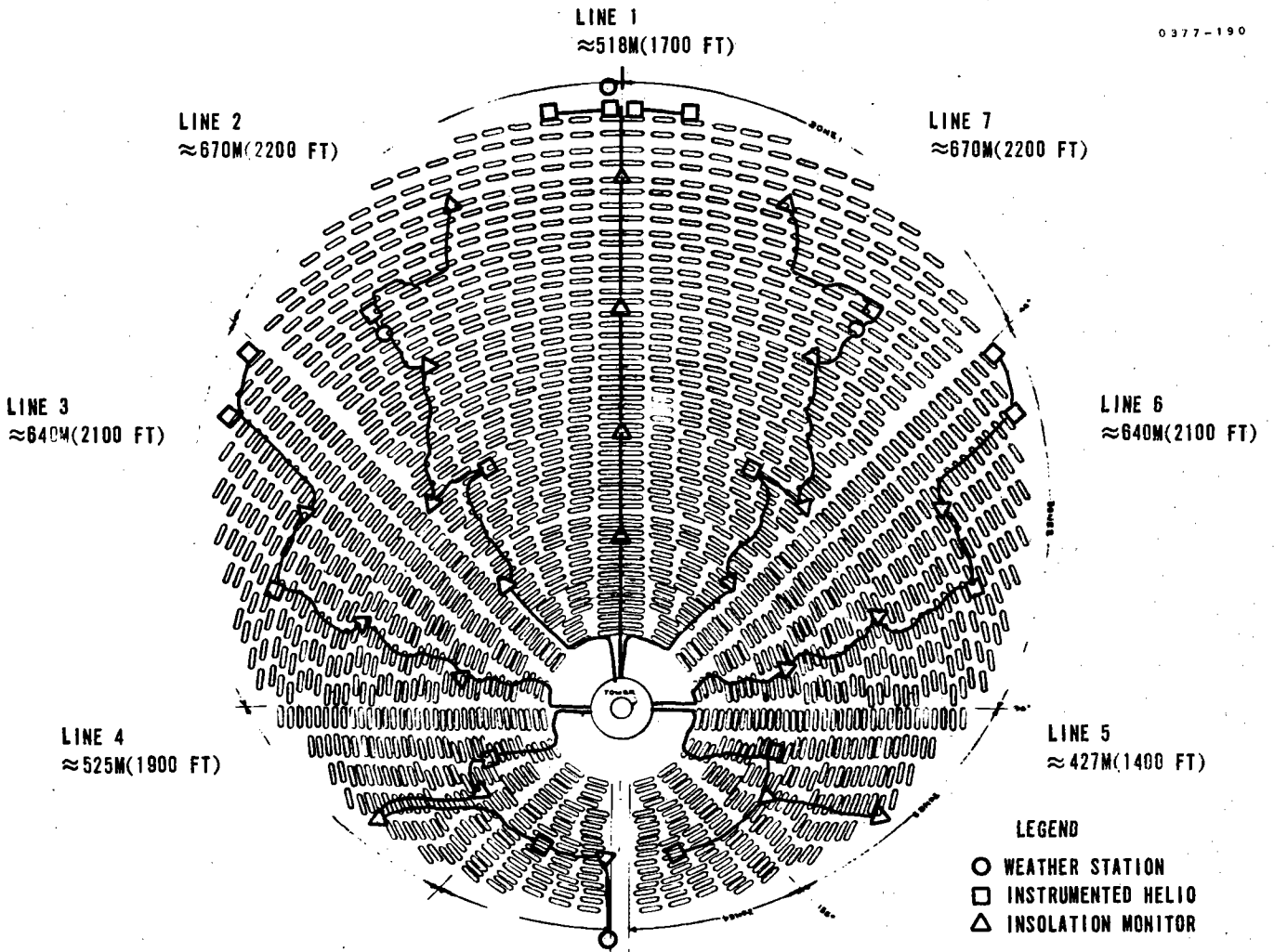


Figure 5-8. Location and Interconnect Diagram
Pilot Plant Collector Subsystem Field Instrumentation

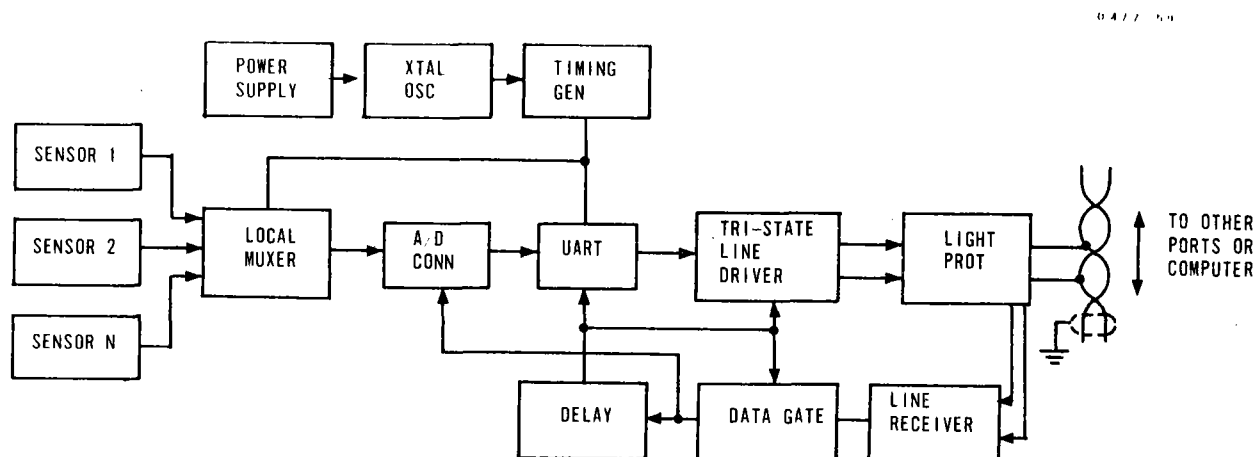


Figure 5-9. Field Instrumentation Data Processor and Transmitter

signal samples of the energy levels throughout the beam. The samples are scaled, multiplexed to a single line, digitally converted and transmitted in serial fashion to the computer upon request.

Beam shape, size, and intensity information are contained in the data block. The data is used in several ways. Energy centroid calculations permit updates to the computer program to correct for differences between the perceived and predicted beam position. This periodic feedback will provide measured checkpoints of how well the system is operating over long periods of time.

Total energy calculations for the beam can also be made from this data which when compared to the energy available can be used to determine when cleaning may be required. The effectiveness of toe-in and focusing can also be determined by comparing measured shape and size patterns to theoretically determined optimum patterns.

Automatic background suppression was used on the SRE which is not required at the Pilot Plant and beyond. Background suppression consisted of a series of photodetectors set apart from the main array which looked out over the field to provide a measure of the ambient energy. These signals were averaged, inverted and added to each array detector output to enhance the signal to background ratio. This offset measurement was required for the SRE because the beam tracked the array all day long and background suppression of this type proved quite effective. At the pilot and commercial plants, the array will only be used periodically and a readout of the array before the beam

is redirected to it will provide direct measurements at each cell which can be accounted for on a cell by cell basis in the computer. This method should be even more effective than the offset method since the same cell will be used for both measurements.

For the pilot plant eight cal arrays are used ranging in size depending on section of the field the array is required to service. The arrays will be placed atop the tower. A separate multiplexer/processor is provided for each array.

A block diagram of the cal array and processing electronics is given in Figure 5-10. Details of the system are contained in the following paragraphs.

Cal Array Mechanical

Eight calibration arrays consist of tubular aluminum frames mounted on top of the receiver outer housing as shown in Figure 5-11. The size of these arrays was determined by a detailed analysis which provided the maximum image height and width expected at each array. Sun cone angle, pointing accuracy, contour accuracy, toe-in spread error and slant range were included in the calculations. Cosine effects from the various field locations served by each array were also considered.

The structural design of the array frames uses square aluminum tubing for minimum weight and maintenance cost. The various tubing sections are sized by stresses due to wind drag loads (assuming peak velocity at pilot plant array height of 60 m/sec (135 mph)). These stresses may however be sized by seismic loads depending on tower/receiver response characteristics.

The analysis resulted in four different combinations of array size and slant angle which were optimized for the quadrant they serve. Our design approach however will be to make all frames the size of the largest unit which also allows them all to be set at the same slant angle. Array numbers 3, 4, 5 and 6 will have fewer sensors because of the smaller image sizes.

Pilot Plant arrays (eight required) are 8.54m (28 ft) wide by 7.32m (24 ft) high. Commercial plant arrays (32 required) are 13.4m (44 ft) wide by 12.2m (40 ft) high. All arrays will slant 0.66 radians (38°) off of vertical. Assuming photodetectors are on 0.3m centers the pilot plant arrays weigh 400 kg (900 lbs) each including the sensor assemblies and wiring harnesses. The structure required to mount the arrays to the receiver housing is not included in this estimate.

The commercial plant arrays will weigh approximately 1050 kg (2300 lbs) each.

Analysis of the resolution of the arrays as a function of sensor density (number of sensors/m²) has since shown that lower densities are possible. This will not affect overall frame size but will reduce cost and weight.

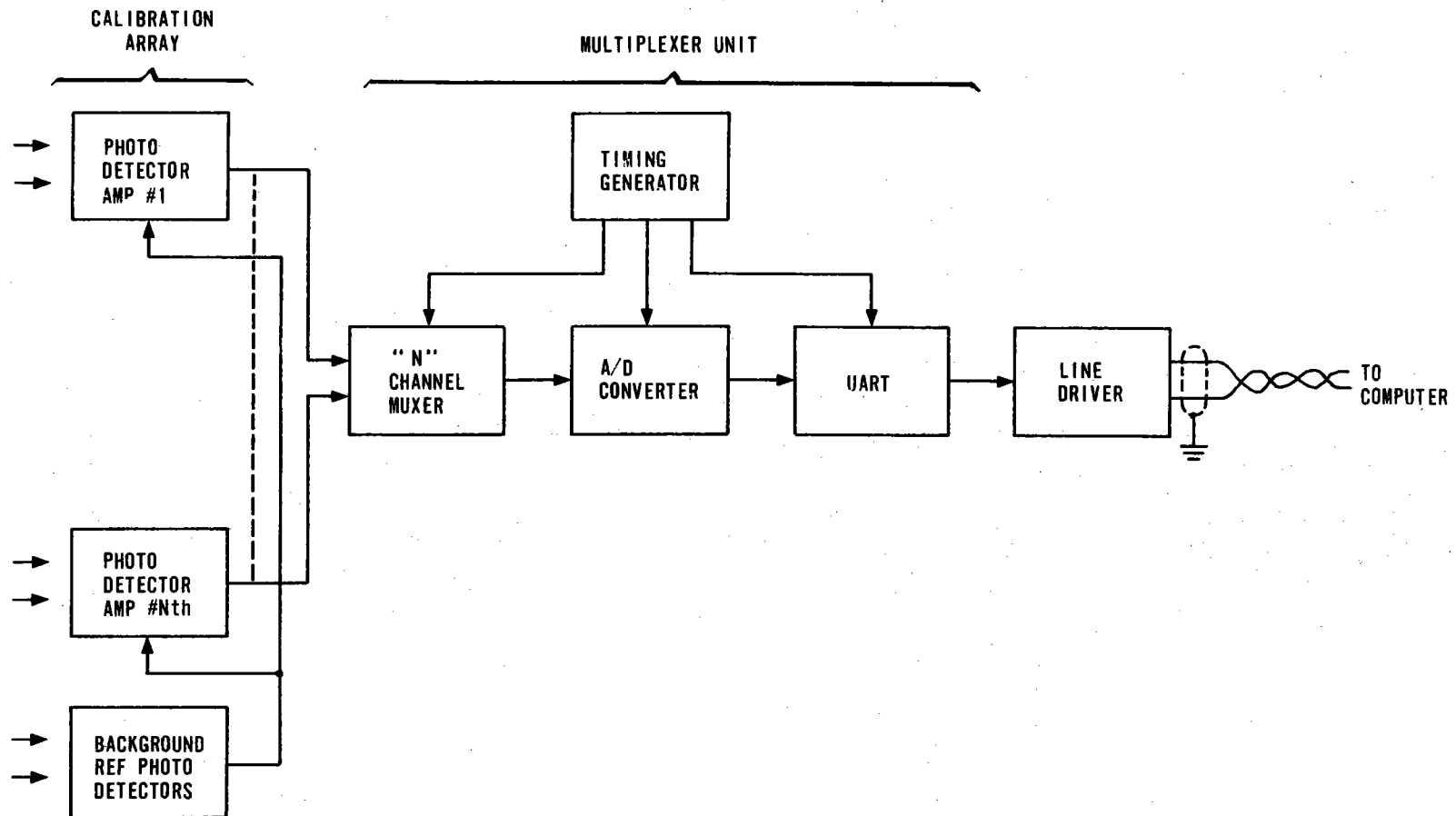


Figure 5-10. Calibration Array and Electronics

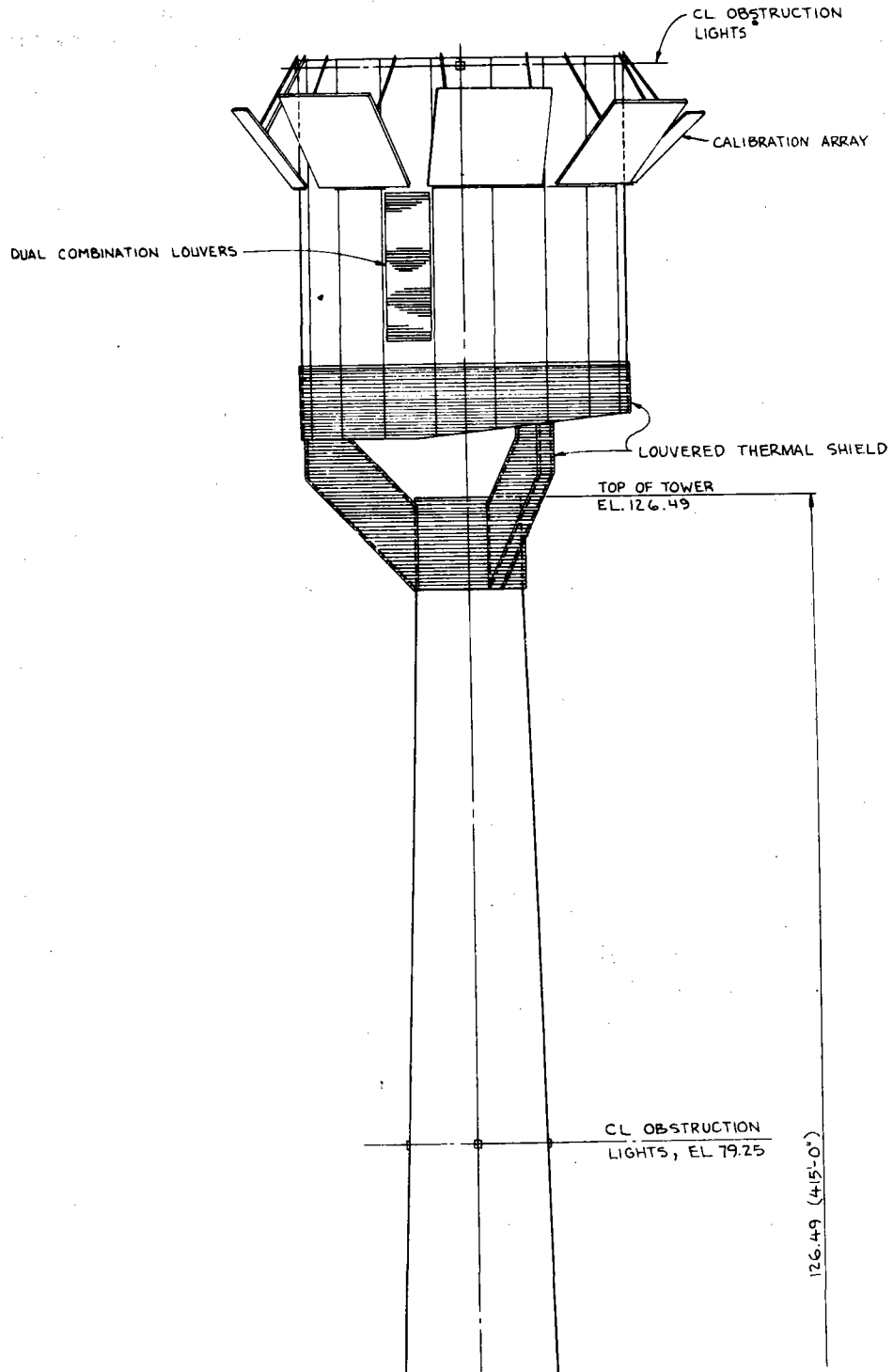


Figure 5-11. Receiver and Calibration Array

The packaging and circuit description for calibration array sensors used during engineering development and solar research experiment has been shown in Figure 5-10. The calibration arrays for a pilot or commercial plant will use the same components in a more permanent package. The cost of these devices is low enough to make it feasible to use a potted module packaging concept for packaging. Replacement will be as a complete unit. This technique will provide adequate support and environmental protection for all electronic components. The potted module will mount directly to the calibration array structure. Interconnection to calibration array wiring will be by solder terminals located in a small cavity that can be protected from the ambient environment after wiring is completed.

Photodetector Operation

The array photodetector consists of a silicon phototransistor and an operational amplifier with feedback, a schematic for which appears in Figure 5-12. The phototransistor is operated as a photodiode and is forced by the feedback to operate in the short circuit mode. Maximum junction operating voltage is limited to the offset voltage of the op am (2 mv max). Operation in this fashion provides for excellent linearity and stability with age and variations in temperature. The following analysis is provided to support these contentions.

The two big variables that could offset operating performance are the β and leakage current of the phototransistor. First consider leakage current.

The leakage current I_L of a PN junction is the sum of three currents and is given by:

$$I_L = I_D + I_G + I_S$$

where

I_D = diffusion current due to diffusion of minority carriers across the junction

I_G = charge generation current due to impurity ions in the depletion layer

I_S = surface leakage current

The contribution due to I_D can be found from the classic diode equation which is given by:

$$I = I_D \left(e^{\frac{qV}{MKT}} - 1 \right)$$

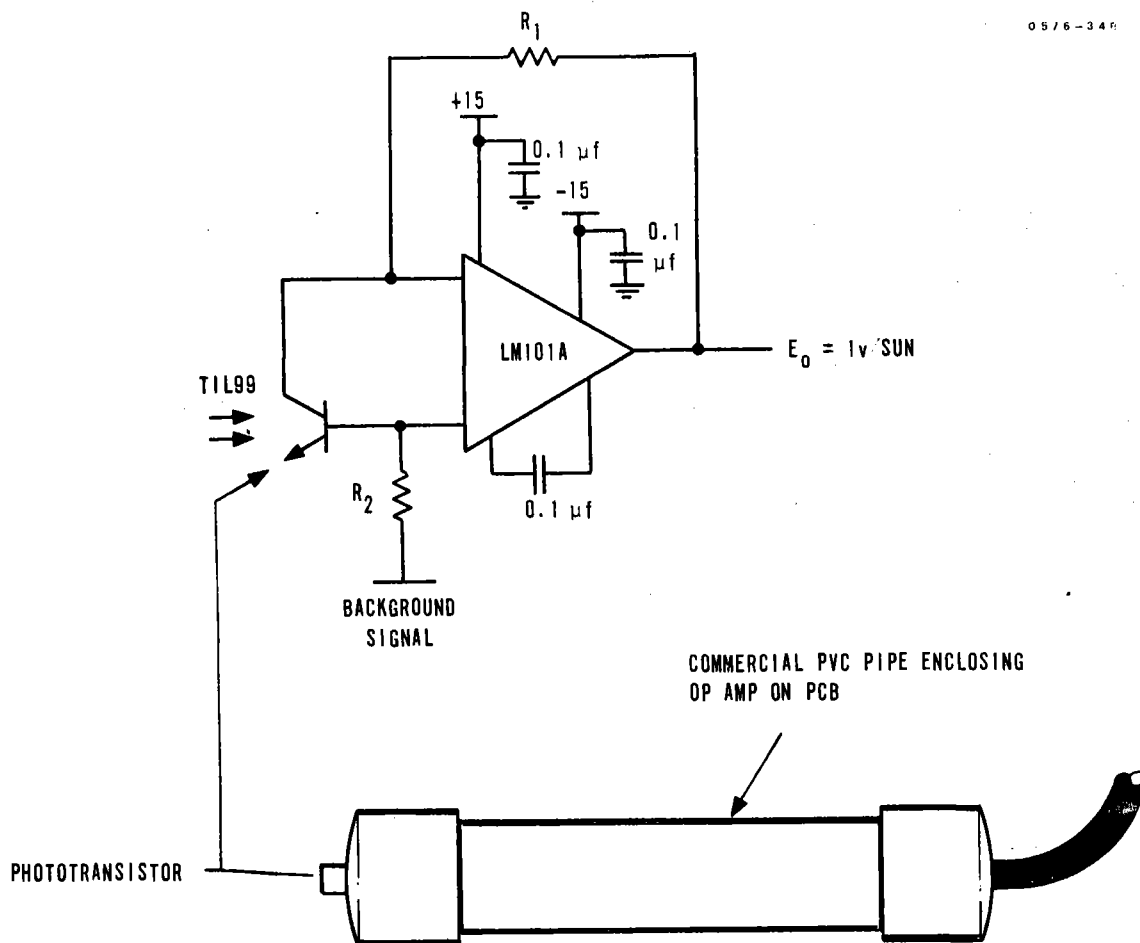


Figure 5-12. Photodetector Circuit

where

q = electron charge (1.60199×10^{-19})

V = junction voltage

M = scaling constant (1 to 2 depending on construction)

K = Boltzmann's constant (1.38032×10^{-23})

T = absolute temperature in degrees Kelvin.

By evaluating the equation at $V = 10$ volts where the TIL99 photo-transistor is specified and at $V = 0.002$ volt, the maximum voltage at which it will be operated, that part of the leakage current due to I_D is found to be reduced by a minimum of 92.5 percent.

The calculation of the charge generation current I_G depends on several physical parameters not available for the TIL99. However, extrapolation of a curve showing a plot of I_G versus voltage* shows that the contribution of I_G at 0.002 volt will be reduced to ≈ 0.6 percent that of I_G at 10 volts.

Surface leakage current I_S results from the resistance path across the junction and as such is directly proportional to the applied voltage. Comparing 0.002 volts to 10 volts, this component becomes vanishingly small. Based on a total leakage current made up of one-third diffusion current and two-thirds charge generation current, the maximum leakage current at 0.002 volts is (7.5 percent) (0.33) + (0.6 percent) (0.66) or 2.9 percent of that at 10 volts. Spec for TIL99 at 10 volts is 100 nanoamps at 25°C. Since both diffusion and charge generation currents are bulk currents, they follow the general rule of doubling every 10 degrees Celsius increase in junction temperature.

At 125°C, the maximum junction operating temperature, maximum leakage is:

$$\begin{aligned} I_{L_{\max}} &= 2^{10} (0.0029) (100 \times 10^{-9} \text{ amp}) \\ &= 297 \text{ nanoamps} \end{aligned}$$

To determine the significance of this number it must be compared to the signal level current.

Signal current I is given by:

$$I = I_{SO} \text{ KAR}$$

* Motorola High Speed Switching Transistor Handbook, Second Edition, page 50.

where

I_{SO} = solar insolation incident on active area of the phototransistor in mw/cm^2

K = factor to modify spectral response of the transistor compared to sunlight (≈ 0.26)

A = active area of chip in cm^2 (nom 0.076 cm square)

R = Responsivity of chip (500 $\mu\text{a}/\text{mw}$)

Nominal signal current I at one sun incident input is:

$$\begin{aligned} I &= (100 \text{ mw}/\text{cm}^2) (0.26) (0.076 \text{ cm})^2 (500 \mu\text{a}/\text{mw}) \\ &= 75 \mu\text{a}/\text{sun} \end{aligned}$$

Compared to a worst case leakage current of 0.3 μa , leakage current is no problem.

Note that in the equation for signal current, no β term is included. This is because the device is operated as a diode and hence no β multiplier is used. β variations with age, temperature or signal level are therefore eliminated. Since K and R are basic physical constants, the only variable is A which affects scale factor and not linearity. A has been found to vary ≈ 3 to 1 and is compensated for by selecting the resistors in the amplifier so that all amplifiers have the same scale factor.

Amplifier scale factor for the SRE has been chosen at 1 volt per sun. Saturation occurs at approximately 15 suns input. The scale factor may be reduced slightly at the pilot and commercial plants to increase the upper range power handling capability. This is accomplished by reducing the resistor values in the amplifier.

The phototransistor case temperature rise measured during the SRE was found to be $\approx 6.1^\circ\text{C}$ (11°F) for a one sun input. Linearly extrapolating this to a maximum junction operating temperature of 125°C shows that the maximum input handling capability in an ambient air temperature of 37.7°C (100°F) without cooling is $(125 - 37.7)/6.1 \approx 14$ suns.

If it was deemed necessary to increase the power handling capability of the detector at the pilot plant, a scheme, planned for further study in the detail design phase, which does not use active cooling would be considered. It involves using fiber optics to carry a small sample of energy from the face of the array to the photodetector which would be removed from the direct beam. Only the energy required to illuminate the chip would strike the photodetector. Since the collector of the transistor is in direct contact with the case, less temperature rise would result than if the entire photodetector were in the beam and the power handling capability would increase.

The background signal input in Figure 5-12 is where the measured background signal is summed into the photodetector for suppression purposes.

Multiplexer Operation

The cal array for the SRE was 4.9m (16 ft) by 4.3m (14 ft) with photodetectors spaced horizontally and vertically 0.3m (1 ft) apart, resulting in 224 signals to complete one electronic "snapshot" of the redirected beam. To efficiently transfer this information to the computer which was remotely located, the signals were multiplexed to a single line, converted to an 8 bit digital word and transmitted in serial fashion to the computer over a twisted shielded pair. Figure 5-13 of the accompanying figures shows a block diagram of the cal array electronics as well as a diagram of the multiplexer switching, details of which are given in the following paragraphs. This same multiplexer scheme will be used to transmit boiler, superheater, and piping temperatures, flow rates, pressures and other data such as valve position to the master control subsystem.

The analog multiplexer was designed around the Harris Semiconductor HI 506A which is a 16 channel single ended integrated analog multiplexer. The switches were arranged in a two-tiered fashion with 16 input channels for each output channel as shown in the figure. Fifteen input chips provided for a total input capacity of $15 \times 16 = 240$ channels. Capability exists to add one additional chip for a total of 256 channels.

A differential amplifier was used to interface the analog multiplexers with the A/D converter. Since only single ended switching was used to multiplex data, the array common line was returned to the low side of the differential amplifier to reduce offset.

The A/D converter was a Hybrid Systems ADC 540-8 which is an 8 bit converter with a 3 μ sec convert time. At a scaling of 1 volt/sun (on a clear cloudless day at 28° North latitude 2/27/76 St. Petersburg, Florida), the LSB of the converter at 10 volts per 2 to the eighth power (2^8), ie, $10 \div 2^8 = 0.039$ volt, corresponded to a resolution of 0.039 suns (approximately 35 watts per square meter). In the pilot plant calibration arrays, more accurate data will be taken so that relative accuracy of each sensor approaches 2 percent or better.

The UART (Universal Asynchronous Receiver Transmitter) is a TMS 6011 dc which is a standard integrated chip and is the same device used in

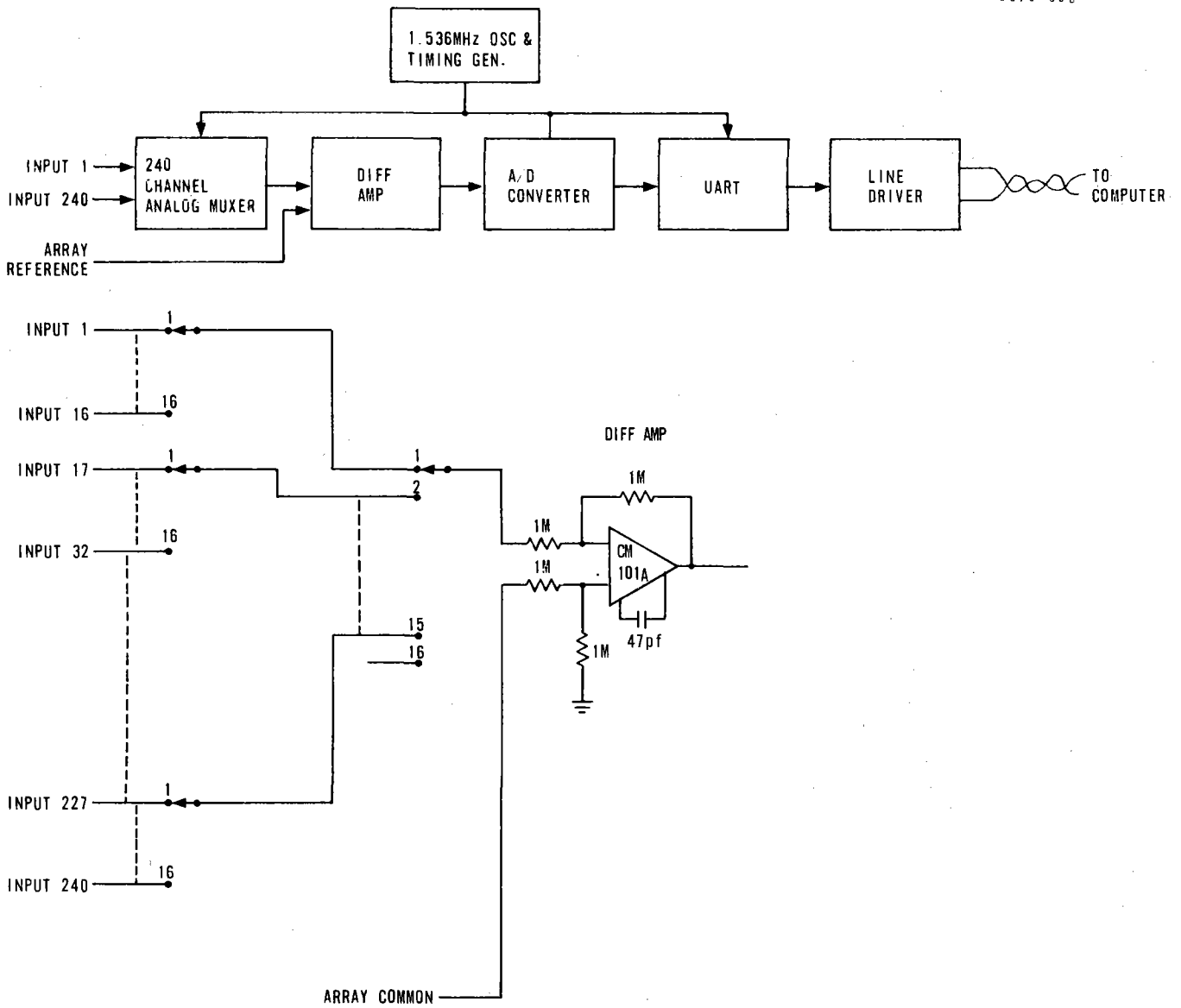


Figure 5-13. Cal Array Electronics and Multiplexer Switching Diagrams

the Heliostat Electronics. The purpose of the UART was to accept the 8 bit parallel output of the A/D converter, format the data with start and stop bits, and clock out the complete word in serial fashion to the line driver. The line driver was a standard 8830 five volt differential driver. Transmission to the computer is by means of a twisted shielded pair.

Timing for the control of the cal array electronics was derived from a 1.536 MHz crystal oscillator and some countdown circuitry. Crystal control was required to provide the accuracy and stability to synchronize the UART Cal Array transmitter with the UART computer receiver. Multiplexer sequence time was 1.67 ms per channel requiring (240 channels) (1.67 ms/channel) = 0.4 sec to transmit a complete data block. Transmission rate was 9600 bps.

Lightning protection on the communications lines in the form of series resistors and shunt zener diodes proved marginally effective. Losses attributable to lightning included two line drivers and one line receiver over a period of one year. However the St. Petersburg area is noted for its summer thunder showers and the equipment survived many intense lightning storms.

As the SRE progressed, more and more information was being sent to the computer through the Cal Array electronics including background level measurements, weather data, pyrhelimeter data, and radiometer data. By the end of the SRE, 239 of the 240 available channels were assigned.

With regard to the Pilot Plant and beyond, the size of the cal array will be increasing requiring an increase in the number of data channels to as many as 700. To accommodate this increase the multiplexer will be arranged in a three-tiered design as shown in Figure 5-14. Maximum input capacity of this arrangement is $16^3 = 4096$ channels. Except for the timing which will have to be expanded to accommodate the larger number of channels, the remainder of the cal array electronics is expected to remain as the SRE except for packaging. Each sensor for the pilot plant will be carefully assembled and conformally coated prior to assembly into a weather tight case. The PVC pipe provided adequate protection for the SRE but is not suitable for long term performance. In detail design hermetic seals and encapsulation will be examined but maintenance will be fully considered.

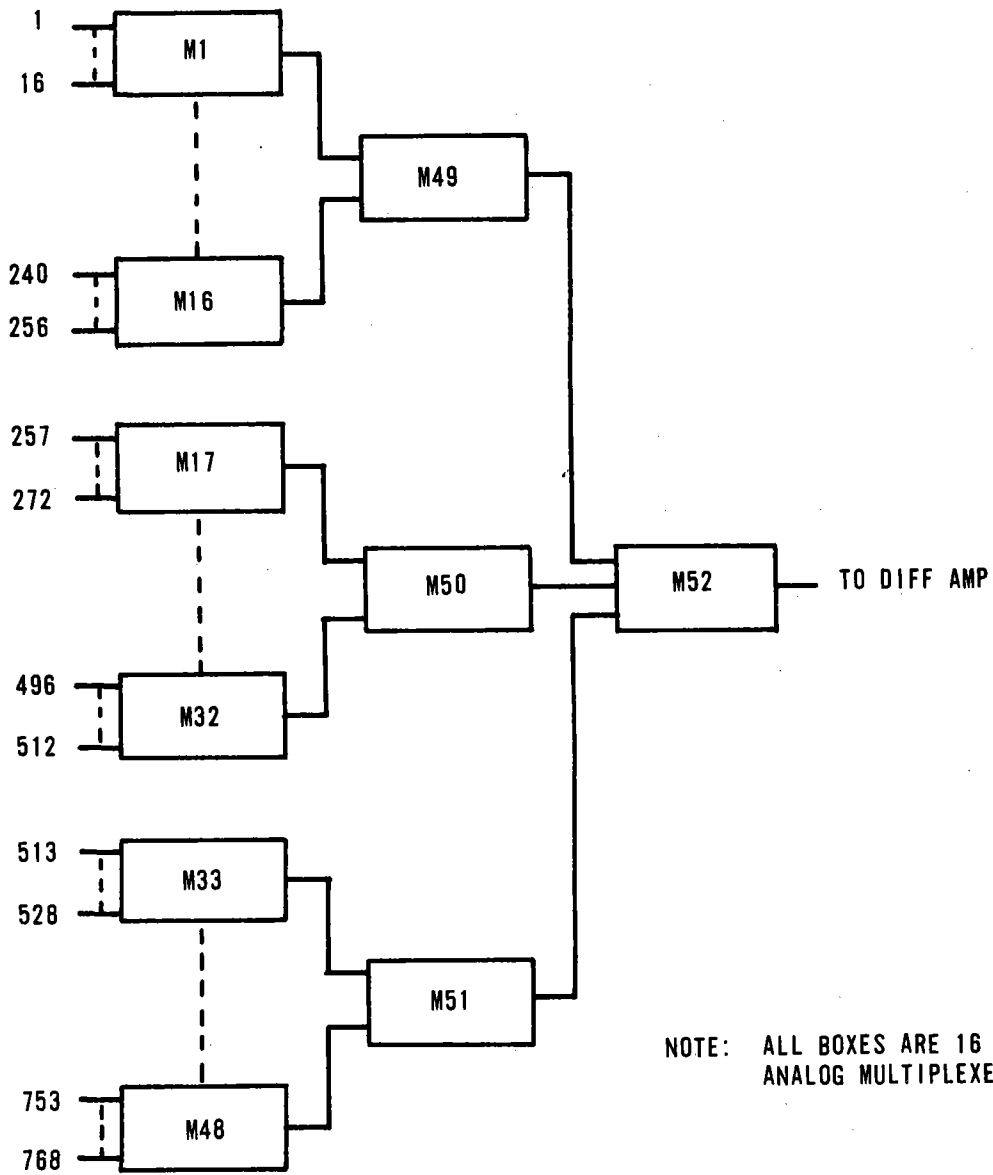


Figure 5-14. A Three Tiered Multiplexer with 756 Channel Capacity

TWO YEAR SPECIAL TESTS

Because of its crucial nature in providing some basis for the commercial plant operational requirements, some attention was felt necessary to the kind of tests expected for the collector subsystem. It is felt that the following periodic and one-time tests are representative of those necessary to gain full benefit of pilot plant experience applied to commercial plant design.

Many functions and operations will be automatically recorded by the plant computers. These extensive data files are expected to provide a wealth of data for reduction and analysis both on and off site.

Extensive on-line and off-line performance monitoring will be conducted during the pilot plant integration and checkout phase and the two year operational phase. In addition to this analysis, it is suggested that certain special tests be conducted to help fully evaluate the field effects.

Special Long Term Tests

The following tests will be those of a periodic nature:

1. At the end of one year and then again at the end of two years, inner drive gear boxes and actuator assemblies will be removed and replaced with spares. Prior to removal, lash at each site will be determined and compared with original values. They will be carefully stripped down and fully evaluated with regard to wear and environmental effects on surface materials (screw, gear teeth) and the change in lash, etc.
2. Once each three months, the output levels of all photo-optical pairs on four selected heliostats (12 per heliostat) will be recorded to determine long term degradation characteristics.
3. The foundations of four heliostats will be permanently instrumented with precision levels. Monthly night readings should be taken along with the temperature. The levels will be shielded from direct solar insolation. Two outer perimeter heliostats, one mid-interval, and one inner heliostat should be instrumented.
4. Effects of the Barstow site exposure should be determined periodically on the following:
 - a. Paint wear and thermal reflectivity characteristics.
 - b. Dust erosion upon mirror module reflectivity.
 - c. Mirror module and outer axis bearings and stub shaft material degradation.
 - d. Rubber seals for the electronics enclosure and the actuator protective bellows, spur gear housing seals.

5. Select four mirror modules at random and measure the contour at the beginning of the test effort, at the end of one year and again after two years to determine any long term effects on the contour shape due to thermal cycles and solar loading.
6. Monitor, on two selected heliostats, the power required per drive mechanism and per total heliostat once per three months to obtain temperature and time influences.
7. Four to six heliostats will be selected and outer axis alignment and toe-in setting reconfirmed with precision measurements twice per year.
8. Six sites will be selected and initialization setting stability evaluated (has deadband opened or decreased any due to mechanical shifts of adjustments).

Special One-Time Tests

1. Instrument one heliostat fully with thermal couples and record the thermal gradients every one-half hour for three or four representatively clear, hot days. Compare with estimated worse case numbers.
2. Based on a site noise survey (airport radars, transmission lines, etc.) EMI testing should be conducted at the determined frequencies and amplitudes. These noise characteristics should then be induced above ground and into the control system at various junctions to determine potential susceptibility levels.

Additionally, the maximum level of induced current due to local lightning should be determined from power companies or cable companies. Applicable reduced levels should be induced into one heliostat area to demonstrate the capability to shed induced voltages and protect the semiconductor components.

MAINTENANCE AND LOGISTIC SUPPORT

Pilot plant maintenance is addressed and followed by logistic support for the Level 6 computer. The Honeywell collector subsystem design, and especially the heliostat, is comprised of easily replaceable modular elements. These elements are designed for long trouble-free life. In the remote and unlikely event of a failure, any part or assembly can be quickly changed to maintain high levels of in-service performance.

Using night and cloudy days for servicing heliostats seems to provide plenty of time for maintenance and repair. A superficial analysis was made of reliability and maintainability of the heliostat. This analysis resulted in the availability analysis following. It is anticipated that frame, post, and foundation repairs would be made on-site and replacement of these parts would be unnecessary. A representative list of spare heliostat parts is shown in the spares table. Exact quantities will vary depending on lead time, failure experience, etc.

Spares Table

<u>Typical Quantity</u>	<u>Item</u>
92	Photosensors for Cal Array
2	Mux Electronic Boards
5	Inner Gear Box Drives
6	Inner Linkages
3	Inner Drive Motors
3	Outer Drive Motors
7	Actuator Assemblies
5 Sets	Heliostat Electronics
5 Dry	Batteries

The quantity stocked on site is also a function of repairability, service life test equipment, item cost, and availability of substitutes. The shelf life only affects batteries but is a factor there. This list of spares provides parts for the highly maintainable heliostat.

AVAILABILITY

Based on a 1,600 heliostat field operation and the information developed for Table 5-4, the availability per unit exceeds 99 percent for a year of operation. The corrective maintenance per year can be completed in the time interval when the heliostats are not in operation. Expected operation is 14 hours per day for a 360 day period.

Repair Time per Failure in Hours = percent of time required for maintenance available time.

100 percent - percent of time required for maintenance
= availability

Frame	100 - 24/8760 = 99.997% availability per year per unit
Mirror	100 - 72/8760 = 99.992% availability per year per unit
Inner Drive Gear Box	100 - 4/8760 = 99.9995% availability per year per unit
Inner Drive Linkage	100 - 8/8760 = 99.9991% availability per year per unit
Inner Drive Motor	100 - 4/8760 = 99.9995% availability per year per unit

Table 5-4. Solar Pilot Plant Preliminary MTTR and MTBF Predictions

Unit	MTBF (Hrs)	Failure Rate (λ) ($\times 10^{-6}$)	Qty	Contribution of Total Failures	Repair Time (Rp) (Hrs)	Σ (λRp)
Frame	100,000,000	0.01	1600	16	24	384
Mirror	10,000,000	0.1	6400	640	72	46,080
Inner Dr Gear Box	66,667	15	1600	24,000	4	96,000
Inner Dr Linkage	25,000	40	1600	64,000	8	512,000
Inner Dr Motor	100,000	10	1600	16,000	4	64,000
Outer Dr Motor	100,000	10	3200	32,000	4	128,000
Actuator	100,000	10	3200	32,000	4	128,000
Heliostat Elec.	250,000	4	1600	6,400	10	64,000
Central Processor	25,000	40	4	160	4	640
Peripheral Equipment	15,000	67	4	268	4	1,072
Cal Array	13,884	72	8	576	24	13,824
P/S Batteries	500,000	2	1600	3,200	2	6,400
Field XMFR	100,000	10	8	80	10	800
				$\Sigma \lambda = 179,340$		$\Sigma \lambda Rp = 1,061,200$

$$MTTR = \frac{\Sigma \lambda Rp}{\Sigma \lambda} = \frac{1,061,200}{179,340} = 5.92 \text{ hours}$$

$$MTBF = \frac{1}{\Sigma \lambda} = \frac{1}{106} = 5.576$$

$$\frac{\text{Failures}}{\text{Day}} = \frac{1 \text{ Solar Pilot Plant} \times 420 \text{ hrs/mo} \times 1 \text{ mo/30 days}}{5.576 \text{ hours/failure}} = 2.51 \text{ Failures Day}$$

Corrective Maintenance Per Year = 5,349 hours

Outer Drive Motor	100 - 4/8760 = 99.9995% availability per year per unit
Actuator	100 - 4/8760 = 99.9995% availability per year per unit
Heliostat Electronics	100 - 10/8760 = 99.999% availability per year per unit
Control Processor	100 - 4/8760 = 99.9995% availability per year per unit
Peripheral Equipment	100 - 4/8760 = 99.9995% availability per year per unit
Calibration Array	100 - 24/8760 = 99.997% availability per year per unit
Power Supply Batteries	100 - 2/8760 = 99.9997% availability per year per unit
Field Transformer	100 - 10/8760 = 99.999% availability per year per unit

LOGISTICAL SUPPORT OF LEVEL 6 COMPUTER SYSTEM

The Level 6 design concept, based on containing functional system modules on single boards, not only reduces module interconnections to the Megabus and power (eliminating intra-module connections) but also enhances system availability. First, the existence of functional boundaries simplifies the procedures required to diagnose faults. In turn this means that execution of these procedures should require very little downtime, on the order of minutes, and that the attempt to isolate a fault to board level should normally be successful. Secondly, "repair" of the fault requires simply unplugging the failed unit and plugging in a replacement.

Another very important maintenance feature of the mainframe is the set of built-in tests. Each microprogrammed bus attachment (for example, CPU, Controller) has a portion of its microprogram space (10 percent to 20 percent) reserved for self-test. This self-test is executed as a by-product of the control panel operations used in system initialize and bootstrap. By this method, the tests are executed frequently so that otherwise undetected faults will be less likely to propagate errors into user output. And, as stated earlier, detection equals diagnosis. In addition to the self-test, the CPU provides a permanently stored program (assembly language level) which will test memory.

For maintenance purposes, all system modules that can be easily removed and replaced at the customer site are called Optimum Replacement Units (see table attached) or ORUs. ORUs include the following.

- Primary boards that connect into the Megabus and similar boards that form part of a Level 6 component (for example, Memory-or-Device-Pacs).

Optimal Replacement Unit Spares List

Model Number	Description
Controller and Processor Boards	
CMC9003	Parity Memory Controller with four connectors for mounting Pac adapter CMM9001; same as CMC9001 without CMM9001
CMC9004	EDAC Memory Controller with four connectors for mounting Pac adapter CMM9002; same as CMC9002 without CMM9002
CPU9201	Central Processor for CPS92XX systems
CPU9401	Central Processor for Model 6/34 systems
CPU9402	Central Processor with Watchdog Timer Option (CPF9401) for Model 6/34 systems
CPU9403	Central Processor for Model 6/36 systems
CPU9404	Central Processor with Watchdog Timer Option (CPF9401) for Model 6/36 systems
GIY9001	General Purpose DMA Interface; same as GIS9001 less paddle boards
GIY9002	System 700 Bus Interface for CPS92XX systems, for Level 6 chassis; same as GIS9002 less ribbon cables and board for S700 drawer
MDC9101	Multiple Device Controller
MLC9103	Multiline Communications Processor
Memory-Communications-Device-Pacs	
CMM9001	8K Word Memory-Pac with parity, with mounting hardware
CMM9002	8K Word Memory-Pac with EDAC, with mounting hardware
CRM9101	Card Reader Device-Pac, with mounting hardware
DCY9101	Communications-Pac, 2 asynchronous lines up to 9.6KB each, with mounting hardware; same as DCM9101 but without cables
DCY9102	Communications-Pac, 1 asynchronous line up to 9.6KB, with mounting hardware; same as DCM9102 but without cables
DCY9103	Communications-Pac, 2 synchronous lines up to 10.8KB each, with mounting hardware; same as DCM9103 but without cables
DCY9104	Communications-Pac, 1 synchronous line up to 10.8KB, with mounting hardware; same as DCM9104 but without cables
DIM9101	Diskette Device-Pac (takes two spaces on Multiple Device Controller MDC9101), with mounting hardware
KCM9101	Device-Pac for teleprinter, typewriter, and CRT consoles, with mounting hardware
PRM9101	Printer Device-Pac, with mounting hardware
CPF9201	Extended Memory and Memory Lockout Option-Pac with mounting hardware
Devices	
DIY9101	Diskette Unit, without power supply for peripheral devices DIU9101, DIU9102; standard is 60 Hz 120 V; available also at 50 Hz 220 V, and 50 Hz 240 V
Power Assemblies	
DIY9102	Diskette Power Supply assembly for peripheral devices DIU9101, DIU9102
PSS9002	Memory Save with Autorestart for up to 64K words, with hardware for rack mounting, and battery
PSS9401	Power Supply for 4 or 5 slot Megabus chassis (9 or 10 slot chassis requires two power supplies)
Cabinetry/Hardware	
CPE9411	Full Control Panel Electronics for 6/30 Models, rack mountable or tabletop CPS's; excludes housing, power switch and lock assembly
CPF9210	Full Control Panel Electronics for 6/06 CPS's; excludes housing, power switch and lock assembly

*Refer to Power Frequency explanation in Heading Information Section for ordering rule

- A power supply, control panel, or peripheral device.
- Fuses for power; air circulating fans.

The actual ORU isolation is carried out in two steps. First, the resident hardware/firmware performs the go/no-go test of basic data paths to verify that ORU Isolation Test Routines are loadable and that their execution can be initiated. This test is executed automatically each morning at system turn-on. Second, the test and verification software tests are performed, completing the ORU isolation and causing the results to be displayed.

The display of results indicates (1) the unit to be replaced. (2) the case of no fault detected, or (3) the case in which the fault cannot be resolved to an ORU. In the vast majority of cases the result will be isolation of the fault to an easily replaced ORU.

Large Level 6 configurations such as the Pilot Plant configuration are expected to require special consideration in order to maintain an adequate level of system availability. In particular, the maintenance of peripheral and communication units in such a system may require diagnosis, repair, verification and preventative maintenance to be performed without shutting down the system. The T&D software components related to Level 6 peripherals and communications have been designed to operation under GCOS (the disk based operating system) simultaneously with the execution of other tasks.

Mean Time to Repairs (MTTR)

The MTTR for a unit or a system is the sum of the mean time to diagnose, the mean time to fix, and the mean time to verify that the fix was proper. The generalized objectives met by the Level 6 are listed below and are applicable to each major unit individually.

Unit MTTR Goal - 1 Hour

This goal is for mature systems (2-3 years after first ship) and applies only to those faults which are diagnosed and repaired by qualified personnel.

Preplanned Diagnosis - 30 Minutes

Maximum, 90 Percent Effective

Preplanned diagnosis includes use of Quality Logic Tests (firmware), T&Ds (software), and step by step instruction (cookbooks). For mature systems, 2-3 years after first ship, 90 percent of the faults in any major unit (for example, device, controller, etc.) should be able to be resolved to the proper corrective action (for example, replace ORU(s), make adjustments, replace unit, etc.) using only these facilities. Thirty minutes is the maximum time to execute preplanned diagnosis and determine either:

- a. The corrective action necessary, or
- b. The problem is outside the scope of preplanned diagnosis.

Replacement of ORU - 15 Minutes Maximum

The time required for qualified personnel to replace any module which is considered to be an "Optimum" Replaceable Unit (ORU) is 15 minutes or less.

CONCLUSION

Pilot plant operations and strategy have been briefly covered in the preceding paragraphs. The operations provide safe beam control during start-up and shutdown. In some rare instances individual heliostats can stow without absolute beam control. Instrumentation has been provided for in a flexible cost effective manner. Brief discussion was made of specific tests to be performed on the pilot plant collector subsystem and maintenance operations necessary to keep the plant operating at peak efficiency.

While necessarily brief and cursory it is concluded that our preliminary design can be effectively detailed without substantial problems in the detail design phase.

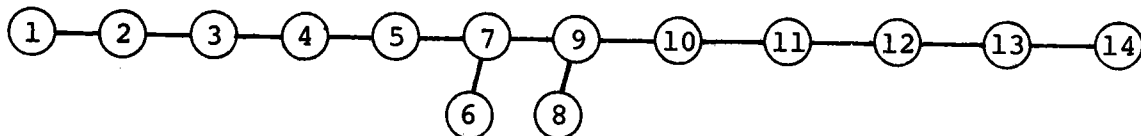
Section 6 SUPPORTING DATA

FIELD ASSEMBLY PROCESS

The heliostat assembly basically is completed in the field with a few of the minor subassembly operations done indoors. The mechanical installation and assembly of each heliostat is identical in sequence and structure. The following discussion, therefore, provides a step by step installation and assembly procedure to form a single heliostat. A condensed flow chart appears below to show the sequence. Operations are keyed to the text by the circled numbers.

Additional information on the special tools used and rationale is provided in a subsequent section on focusing and alignment.

- ① Ground Preparation
- ② Foundation and stub post installation
- ③ Support post assembly and alignment
- ④ Frame assembly
- ⑤ Electronics, wiring harness and ground strap installation
- ⑥ Actuator subassembly
- ⑦ Actuator installation and alignment
- ⑧ Subassembly of mirror module bearings
- ⑨ Assembly of mirror modules to frame
- ⑩ Assembly of mirror drive unit
- ⑪ Mirror module leveling and toe-in
- ⑫ Crank arm and tie rod assembly
- ⑬ Installation of initialization switches
- ⑭ Actuator lead calibration and heliostat checkout



- ① Ground preparation is a pacing item that must be accomplished in advance of all succeeding operations. The activities for ground preparation are:

1. Layout and mark heliostat sites
2. Layout and mark utility routes
3. Dig utility trenches
4. Lay in utility lines (power and signal)
5. Check out utilities
6. Bury utilities

The equipment required for this operation are three small tractors with blades and four "ditch witches".

- ② Foundation and stub post installation consists of the following activities:

1. Move backhoe to site
2. Dig two holes
3. Prepare hole bottom (remove loose soil)
4. Move two stud post and re-bar assemblies to site
5. Position weldments in holes
6. Position concrete forms
7. Move assembly jig to site
8. Position jig level and on azimuth
9. Check post alignment and center-to-center spacing
10. Pour concrete
11. Remove forms

The hole digging operation requires a backhoe, a pair of concrete forms, concrete vibrator.

It is assumed that the concrete is available from the same source used in the tower construction. The liquid concrete is vibrated immediately after pouring to relieve any stresses that may have been introduced to the posts while pouring.

- ③ Assembly and alignment of support posts consists of the following operations:

1. Assemble and bolt posts to stubs previously set in concrete
2. Level tops of posts with respect to each other
3. Plumb posts
4. Measure and record actual azimuth of outer axis using tooling pads at top of each post.

- ④ The assembly of frame to the posts consists of the following activities:

1. Move small parts to site
2. Move frame trailer beside slabs
3. Assemble pillow blocks to pivot rods
4. Secure pillow block locking collars
5. Move double gantry over frame and slabs

6. Lift frame
7. Slide frame to position over posts
8. Lower frame onto posts lightly
9. Align bolt holes and machined surfaces
10. Assemble nuts and bolts loosely
11. Reposition hoists to hook one side of frame
12. Raise hoists to tilt frame 75 deg. in direction of target
13. Measure and shim pillow blocks A/R
14. Torque down pillow block bolts
15. Lower hoists and release from frame
16. Leave frame in free position temp.

Equipment required consists of a double gantry and frame semi-trailer/tug (Figure 6-1), rolling ladders and cable sling (2).

For safety the frame should be restrained from rotating during assembly.

- ⑤ The electrical assembly operation consists of the following activities:

1. Move parts and tools to site
2. Install control and electrical box to foundation
3. Install battery box
4. Install conduit on underground wires
5. Connect underground wires to box
6. Tie heliostat ground strap into ground mat
7. Connect ground strap to post
8. Assemble ground straps to frame and posts
9. Temp. hand harness to frame
10. Wire frame actuators
11. Wire harness to control box
12. Prepare stress loops and clamp
13. Drill holes and install harness cover
14. Check for proper elec. operation

Ground strap installation needs to be performed prior to general electrical installation.

- ⑥ Frame drive actuator subassembly may be assembled in a covered preassembly area. Activities include:

1. Actuator parts in storage
2. Move parts to subassembly station
3. Assemble rod ends to actuators
4. Assemble brackets to rod ends
5. Assemble flange bearings to pivot pins
6. Assemble motor/encoder to actuator
7. Move assemblies to inventory

Anticipated tools consist of trammel tools, a small dolly, work bench, hand tools and 24 vdc power.

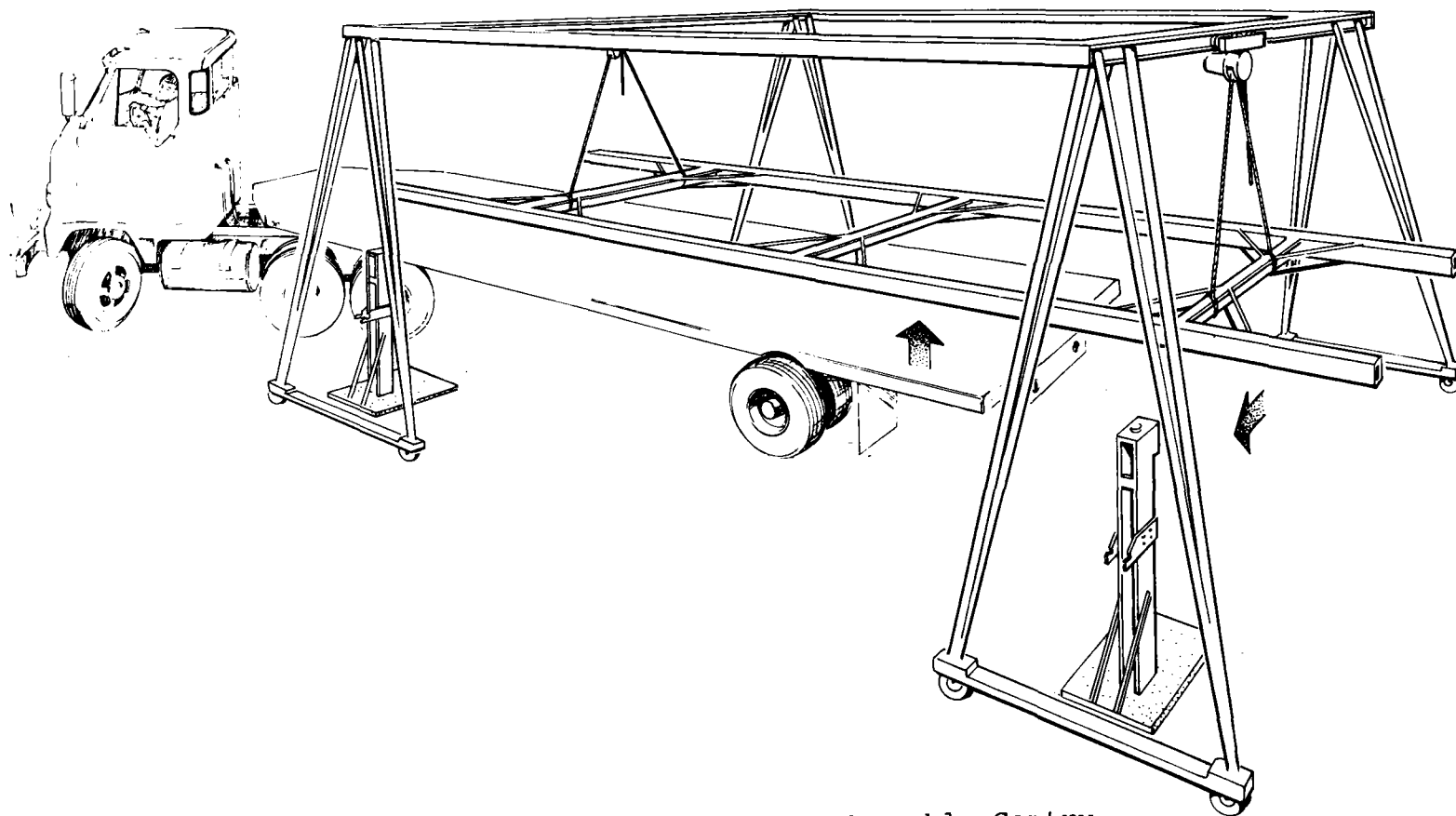


Figure 6-1. Concept of Double Gantry
For Assembly of Frames to Posts

⑦ The assembly of actuators to frame and posts consists of the following activities:

1. Move actuator assemblies to site
2. Slide actuator flangettes on post plates
3. Bolt flangettes loosely to plates
4. Bolt brackets to frame loosely
5. Set 34 inch dimension and torque down bracket
6. Repeat above for second actuator
7. Set 43.32 dimension at plates and flangettes and set angle
8. Repeat above for second actuator
9. Ready for next operation

The equipment required includes five foot rolling ladders and 34 inch and 43.32 inch trammel tools.

Actuators are preassembled with rod ends, brackets and flangettes attached at a prior subassembly operation. Extra outer flangette shells are carried by the crew because this part cannot be secured by preassembly.

The trammel tools are double sided to hold pivot axes parallel to each other.

The 43.32 inch trammel tool has a precision bubble level to set the lower actuator pivot at a predetermined angle from the upper pivot.

⑧ The mirror module bearing support subassembly operations consist of the following activities:

1. Parts in inventory
2. Move parts to subassembly station
3. Assemble parts for eight bearing supports
4. Move assemblies to inventory
5. Bearing assemblies in inventory

A work bench and hand tools are utilized here and this operation can be located in a shed or building where the small parts are received/stored in order to minimize parts handling.

⑨ Assembly of the mirror modules to the frame consists of the following activities:

1. Move spur gear and parts to site
2. Move two rolling scaffolds to site
3. Drive frame actuators to spec length
4. Move gantry to site
5. Position gantry over No. 2 mirror location
6. Move M/M trailer under gantry
7. Disassemble holding bracket from four M/M hubs
8. Move hoist over M/M and lower
9. Position spreader bar hooks to hubs

10. Lift M/M approximately 12 inches
11. Assemble gear and O/parts on one hub
12. Assemble bearing on other hub
13. Move M/M laterally off trailer
14. Index M/M 90 degrees and turn horizontally
15. Move M/M into position over frame
16. Lower M/M and guide onto studs
17. Insert tooling pins in both sides
18. Center spur gear in frame hole
19. Lower full weight of M/M on frame
20. Loosely assemble eight nuts on studs
21. Lower spreader bar and remove hooks
22. Raise spreader bar to clear M/M
23. Reposition gantry over No. 1 location
24. Move M/M trailer under gantry
25. Move hoist over M/M and lower
26. Position spreader bar hooks to hubs
27. Lift M/M approximately 12 inches
28. Assemble bearings onto hubs
29. Move M/M laterally off trailer
30. Index M/M 90 degrees and turn horizontally
31. Move M/M into position over frame
32. Lower M/M and guide onto studs
33. Insert tooling pins in both sides
34. Lower full weight of M/M on frame
35. Loosely assemble eight nuts on studs
36. Lower spreader bar and remove hooks
37. Raise hoist to clear M/M
38. Rotate MM 1 and 2 face up and clamp
39. Reposition gantry over No. 3 location
40. Move M/M trailer under gantry
41. Move hoist over M/M and lower
42. Position spreader bar straps
43. Lift M/M approximately 12 inches
44. Assemble bearings onto studs
45. Move M/M laterally off trailer
46. Index M/M 90 degrees and turn horizontally
47. Move M/M into position over frame
48. Lower M/M and guide onto studs
49. Insert tooling pins in both sides
50. Lower full weight of M/M on frame
51. Loosely assemble eight nuts on studs
52. Lower spreader bar and remove hooks
53. Raise hoist to clear M/M
54. Reposition gantry over No. 4 location
55. Move M/M trailer under gantry
56. Move hoist over M/M and lower
57. Position spreader bar hooks on hubs
58. Lift M/M approximately 12 inches
59. Assemble bearings onto hubs
60. Move M/M laterally off trailer
61. Index M/M 90 degrees and turn horizontally
62. Move M/M into position over frame
63. Lower M/M and guide onto studs

64. Insert tooling pins in both sides
65. Lower full weight of M/M on frame
66. Loosely assembly eight nuts on studs
67. Lower spreader bar and remove hooks
68. Raise hoist to clear M/M
69. Rotate MM 3 and 4 face up and clamp

The equipment consists of single gantries, rolling ladders, spreader bards and a semitrailer tug.

The semitrailer will be loaded with 16 mirror modules (4 sets) located on the trailer by the vendor in a manner which permits unloading of the modules in a prearranged sequence.

⑩ The assembly of the mirror drive unit consists of the following activities:

1. Parts in inventory
2. Move parts to site
3. Move rolling scaffold to site
4. Assemble pivot block to frame
5. Assemble mirror drive gearbox to frame
6. Install pivot pin
7. Install spring and shoulder washer
8. Install spring support assembly
9. Align assembly and preload spring
10. Torque bolts down
11. Grease moving parts
12. Assemble cover
13. Connect wiring from harness

Rolling ladders are required. The spur gear cover is bolted together vertically.

⑪ The next operation of leveling the mirrors and adjusting the toe-in consists of the following activities:

1. (Actuator length preset from previous operation)
2. Recheck actuator length and adjust
3. Move gantry over mirror No. 2
4. Move two rolling scaffolds to site
5. Position precision level on M/M
6. Move hoist over M/M hub
7. Attach hoist hook to hub
8. Use hoist to adjust level
9. Measure and select shims
10. Position shims under bearing support
11. Release hoist and recheck level
12. Torque down four nuts on studs
13. Reposition gantry over M/M No. 1
14. Reposition precision level on M/M No. 2
15. Reposition hoist over hub
16. Attach hoist hook to hub
17. Use hoist to adjust level

18. Measure and select shims
19. Position shims under bearing supports
20. Release hoist and recheck level
21. Torque down four nuts on studs
22. Reposition gantry over M/M No. 3
23. Reposition precision level on M/M No. 3
24. Reposition hoist over hub
25. Attach hoist hook to hub
26. Use hoist to adjust level
27. Measure and select shims
28. Position shims under bearing supports
29. Release hoist and recheck level
30. Torque down four nuts on studs
31. Reposition gantry over M/M No. 4
32. Reposition precision level on M/M No. 4
33. Reposition hoist over hub
34. Attach hoist hook to hub
35. Use hoist to adjust level
36. Measure and select shims
37. Position shims under bearing supports
38. Release hoist and recheck level
39. Torque down four nuts on studs
40. Wire initialization sensors
41. Position level perp to axis on MM No. 1
42. Unclamp M/M - position to spec - reclamp
43. Position level perp to axis on MM No. 2
44. Unclamp M/M - position to spec - reclamp
45. Position level perp to axis on MM No. 3
46. Unclamp M/M - position to spec - reclamp
47. Position level perp to axis on MM No. 4
48. Unclamp M/M - position to spec - reclamp

Equipment required consists of single gantries, rolling ladders, precision levels and mirror clamps.

Mirror leveling requires a predetermined amount of forward tilt (toward the tower) of the frame as controlled by the trammel tool setting. This forces all shimming for leveling purposes to be done on one side of the frame (opposite the mirror drive side). Adjustable mirror clamps are still in place from the preceding operation.

⑫ Crank arm and tie rod assembly activities include:

1. Move rolling scaffold to site
2. Move arms and rods to site
3. Assemble alignment tools in four M/M hubs
4. Assemble rod ends to three tie rods
5. Adjust rod length to fit alignment tools
6. Tighten lock nuts on six rod ends
7. Temp store rods on scaffold
8. Remove alignment tools from hubs and set a side
9. Assemble four crank arms to M/M hubs
10. Loosely assemble four taper locks

11. Position No. 2 arm at 45 degrees W/special tool
12. Torque down taper lock on No. 2 hub
13. Assemble rod end to No. 2 arm
14. Assemble O/end of rod to No. 1 arm
15. Secure rod end on No. 1 crank arm
16. Torque down taper lock on No. 1 hub
17. Position rod at opposite end to No. 3 arm only
18. Position center rod between No. 2 and No. 3
19. Secure rod ends on No. 2 crank arm
20. Torque down taper lock on No. 3 hub
21. Position remaining rod end on No. 4 crank
22. Secure rod end on No. 4 crank arm
23. Torque down taper lock on No. 4 hub
24. Move scaffold to opposite side of site
25. Assemble alignment tools in four M/M hubs
26. Assemble rod ends to three tie rods
27. Adjust rod lengths to fit alignment tools
28. Tighten lock nuts on six rod ends
29. Temp store rods on scaffold
30. Remove tools from hubs and set a side
31. Assemble four crank arms to M/M hubs
32. Loosely assemble four taper locks
33. Position No. 2 arm at 45 degrees W/special tool
34. Torque down taper lock on No. 2 hub
35. Assemble rod end to No. 2 arm
36. Assemble O/end of rod to No. 1 arm
37. Secure rod end on No. 1 crank arm
38. Torque down taper lock on No. 1 hub
39. Position rod at opposite end to No. 3 arm only
40. Position center rod between No. 2 and No. 3
41. Secure rod ends on No. 2 crank arm
42. Torque down taper lock on No. 3 hub
43. Position remaining rod end on No. 4 crank
44. Secure rod end on No. 4 crank arm
45. Torque down taper lock on No. 4 hub

Equipment consists of 12 foot high rolling scaffolds, alignment tools (rod ends) and taper arm angle (45 degrees) indicators.

⑬ The initialization operation consists of the following activities:

1. Move initialization equipment to site
2. Secure sensor wheel to rotating shaft
3. Secure housing to structure
4. Remove tooling screws
5. Install cover

Rolling ladders and hand tools are required. Harness wiring consists of mating previously installed cables to sensor contacts

⑭ Checkout of the completed heliostat consists of the following activities:

1. Move equipment to site
2. Connect test equipment
3. Operate outer axis full travel
4. Operate inner axis full travel
5. Initialize outer axis
6. Check four M/M for level
7. Initialize inner axis
8. Check toe-in of four M/M
9. Measure actuator lead (cm of travel per motor revolution)

A precision level and test equipment is required. The test equipment is a "block box" hooked up to the control box to allow manual control of actuators and mirror drive components.

HELIOSTAT FOCUSING AND ALIGNMENT PROCEDURE

The Honeywell heliostat has been designed such that all focusing and alignment is an integral part of the assembly procedure. Where critical dimensions or angles are involved, the accuracy is built into the heliostat components or special tools and fixtures.

The Pilot Plant focusing and alignment procedure is outlined in detail below. The sequence of events shown must be followed to assure a smooth flow of operations. This also assures a minimum of back-tracking, handling, and consequently, minimum cost.

Those steps noted "A" in the following procedure involve alignment operations. Rationale for the various alignment steps is provided following the procedure. "T" numbers refer to tools or special equipment described in attached sketches.

Assembly and Alignment Procedure

1. Install reinforced concrete slabs at surveyed locations.
- T1 A 2. Install prefabricated post weldments. (Precision level tool assures alignment of frame pivot axes).
- T1 A 3. Measure and record azimuth of frame pivot axis. (Theodolite)
4. Preassemble pillow blocks on frame pivot pins. Also secure wiring harness to frame.
5. Install frame on posts and secure pillow blocks against tooling pads.
6. Install electronics assembly to post and tie in power and signal wires from field and harness leads.
- T2 A 7. Install and align actuator bracket to frame.

- T3 A 8. Install actuators to frame pivot brackets and to posts. Align actuator pivot axis with combination level/trammel. Actuators are matched by lot number. Connect harness wires to motor/encoder assemblies.
- T4 A 9. Using motors or electric drill adapter set actuator lengths using trammel tool. (The specified length will cause the frame to tilt slightly toward the tower to assure the mirror modules can be adjusted to level.)
- A 10. Seal actuator motor shafts. Assemble outer axis initialization switches at their zero positions, remove tooling screws, and secure covers. NOTE: Actuators are not to be moved until assembly/alignment of heliostat is complete (therefore they are sealed or tagged as above).
11. Install inner axis gear drive unit on frame and connect harness wires.
12. Assemble tail bearings to four mirror modules.
13. Assemble drive mirror module to frame with mirrors face down and horizontal. Secure tail bearing to frame temporarily. Note tooling holes in frame assure perpendicularity of frame and drive mirror module axes.
- T5 14. Assemble bearings to the other three mirror modules and install on frame with mirrors face down and horizontal. Secure MMs to frame temporarily to prevent rotation. NOTE: MMs have a built-in imbalance.
- T6 A 15. Level four mirror modules with precision beam level and shim under tail bearings. Secure tail bearing of drive MM using tooling holes to assure perpendicularity to outer axis.
16. Secure gear drive unit to frame.
- A 17. Set center-to-center spacing of three MMs with respect to drive MMs (axes parallel) with trammel tool similar to T4 except with five meter spacing.
- A 18. Set toe-in and initialization switch on drive MM.
- a. Secure disk to standoffs temporarily with two screws.
- b. Loosen four screws which secure disk to spur gear.
- c. Determine toe-in angle from tab run.
- T6 d. Assemble precision beam level to tooling pads of MM.
- e. Use manual control box to pulse inner drive motor until desired angle is reached.

- f. Torque four screws to secure disk to spur gear.
 - g. Remove two tooling screws.
 - h. Install cover/seal assembly.
- T6 A 19. Set toe-in on the remaining three MMs using the precision beam level and clamps. Secure MMs to frame using special clamps provided until crank arms and tie rods are installed.
- T5
- T7 20. Install tooling pins to primary end of each MM.
21. Install crank arm to drive MM - no angular adjust here. Torque bolt on crank arm taper lock.
22. Assemble crank arm to the other inside MM bearing with the bolts finger tight.
- A 23. Set tie rod length on tooling pins by rotating the rod end and torque jam nuts.
24. Assemble tie rod to crank arms and torque bolts on second crank arm.
- A 25. Install two remaining crank arms and tie rods on primary drive side in similar manner. Remove tooling pins.
26. Install secondary crank arms to ends of MMs nearest the tower. These crank arms are to be set level with a carpenter's bubble level. Torque bolts on taper locks.
- A 27. Set lengths of three secondary tie rods using pins in crank arms by rotating threaded rod ends. Torque jam nuts. Install three tie rods.
28. Remove clamps that hold MMs to frame.
29. Measure and record actuator lead (Motor Rev/Inch of Travel).

Alignment Procedure Rationale

Ref. Step Number(s)

- 1 Self evident
- 2,3 Tool T1 performs the dual function of leveling the frame pivot axis and mounting the theodolite for measuring the actual azimuth angle of the axis. Constraints placed on post installation already include center-to-center spacing, plumb in two axes, parallelism and field location. Control of the azimuth angle of the frame pivot axis (established by the tooling pads at the top of each post) would be undue burden on the assembly crews. The theodolite provides greater accuracy than assembly tolerances would allow (less than 0.05 milliradians). The measured azimuth angle will

be stored in the computer memory for each heliostat and will be used to correct pointing commands.

- 4,5,6 Preparatory steps for frame assembly and alignment.
- 7,8,9 These steps set up a unique non-right triangle at each actuator. The legs of these two triangles are formed by the post, frame and actuator. The precision oil level (T3) used in Step 8 provides a unique orientation of the triangles with respect to local vertical. The object is to obtain agreement between the hardware and the constants used in the computer.

Another approach might be to measure and record actual values of the four constants for each heliostat but this method is more error prone. In addition, the computer would have to calculate lengths for both actuators which in turn would require more electronics at each heliostat.

- 10 The initialization switches themselves are set at the factory. The field operation simply locks the interrupter wheel onto the pivot shaft at the "zero position". The switch housing is secured to the post next. Two tooling screws (used to maintain the alignment during shipping) are then removed and the cover and gasket are installed.
- 11,12,13, Inner Drive must be assembled before alignment
14
- 15 This operation assures that the MM axes are level at the frame drive "zero" position. The precision beam level mounts to tooling pads which are preset at the factory to define a line perpendicular to the optical axis of the mirror module. The pivot axis of the MM is also controlled with respect to these pads to minimize coneing effects.
- 16 Secure gear to prevent loss of adjustment.
- 17 The object of this step is align the axes of each MM perpendicular to the frame pivot axis; another software assumption. The drive MM is aligned using tooling holes drilled in the frame at the factory using a special drill jig. Before the tail bearings are locked down a trammel point tool is used to set the axes of the three slaved MMs parallel to the drive MM.
- 18,19 This operation is similar to the outer axis initialization except that the drive MM is not level. The object is to "zero" the initialization switch when the optical axis of the heliostat (4 MM composite) is true vertical. Ray trace tradeoff studies have shown that the toe-in angles need to vary with field location to get optimum energy efficiency. The angles are optimum when they are set for a 21 March noon sun position. Since it is not practical to set all

heliostat toe-in angles on one day, the relative angles will be calculated and provided to the construction crews. The problem with trying to set toe-in at a time other than during the normal assembly sequence is that the entire linkage assembly must be loosened or dismantled and then realigned.

Note that there is no adjustment of focus on the mirror modules themselves. Each one has a built-in spherical radius which gives a focal length of 418 meters. Steps 15, 17, 18 and 19 are designed to assure that the four focused images overlap at the receiver aperture.

Sample heliostats will be checked during the construction process using the calibration array to assure proper beam alignment. Special tools will also be checked periodically for accuracy.

There is a low probability that the sun will be at the optimum position (for toe-in) when any one heliostat is checked. However, software has already been developed by Honeywell Energy Resources Center to predict deviations of each of the four beam centroids as a function of time of day, day of the year and relative positions of heliostat and target. This software will be used on-line with the calibration array software to obtain net deviations for each mirror module. Portable shades will cover the three panels not under test.

23,25,27 Tie rod length must be set accurately to assure bind-free motion through the top-dead-center position of the linkage, that is, when crank arms and tie rods are parallel. The tie rod length is set to match the MM stub shaft c-c distances directly. This eliminates the uncertainty due to tolerances on crank arm length.

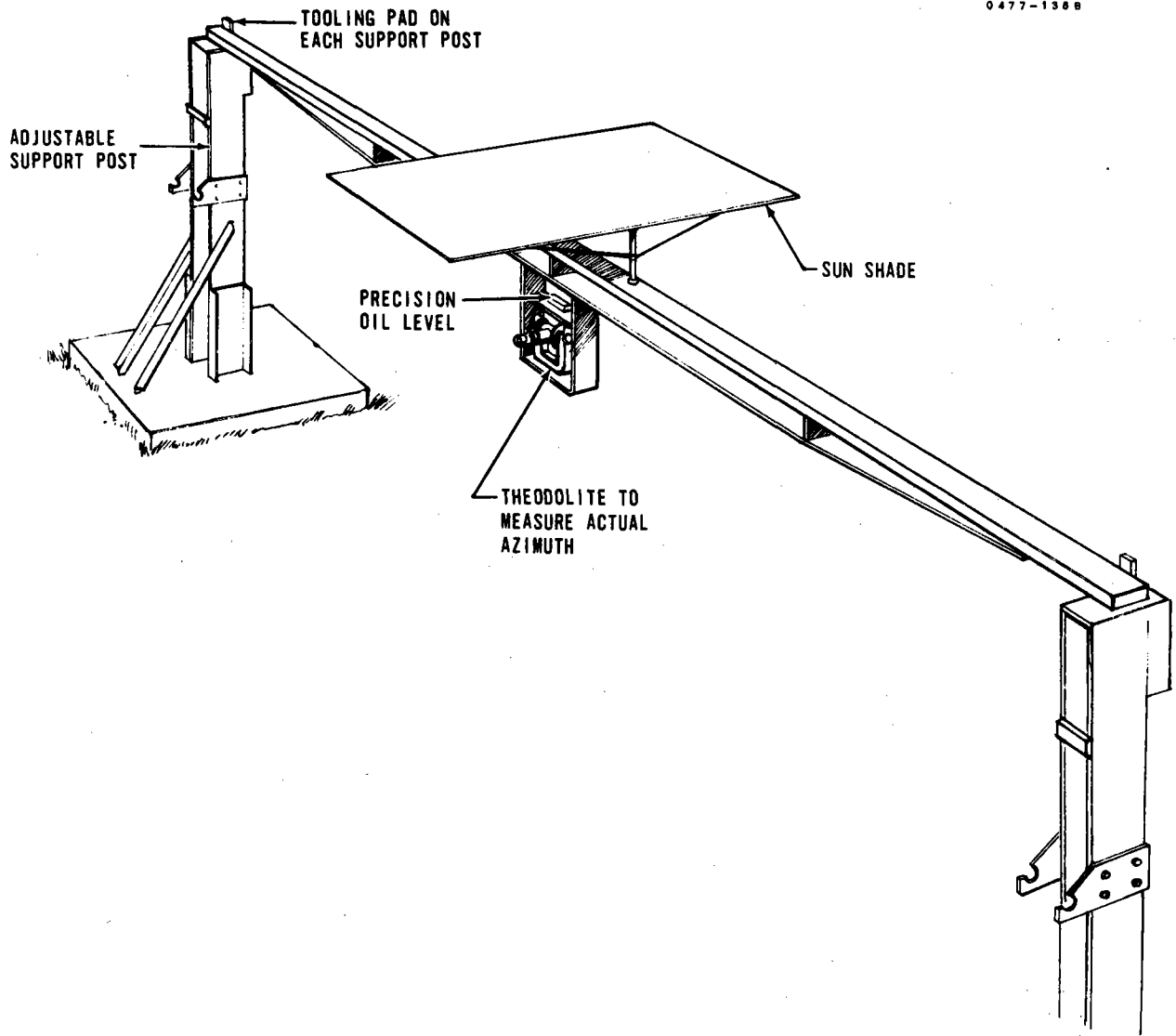


Figure 6-2. (T1) Frame Pivot Axis Leveling and Azimuth Measuring Tool

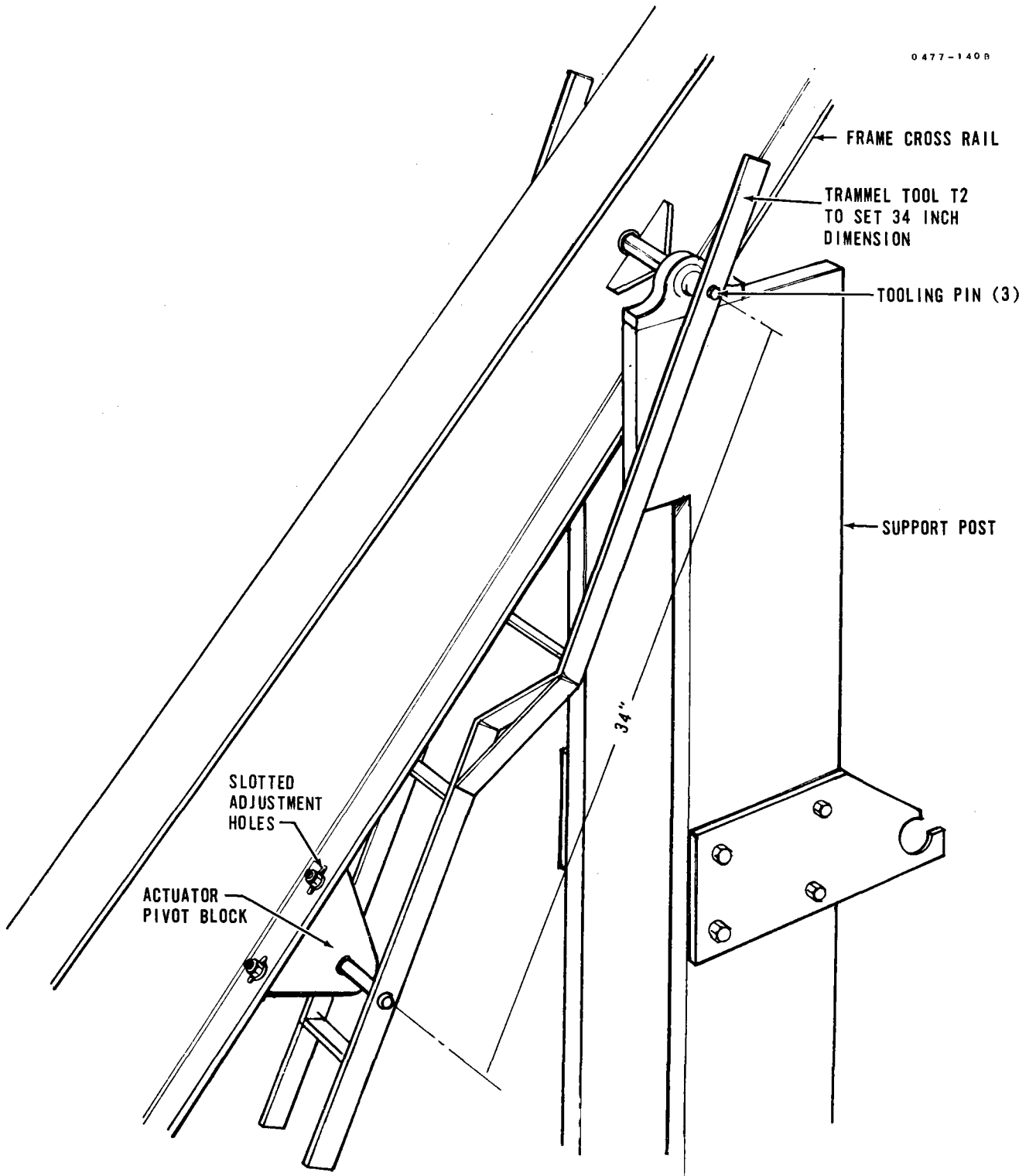


Figure 6-3. (T2) Actuator Pivot Bracket Alignment Tool

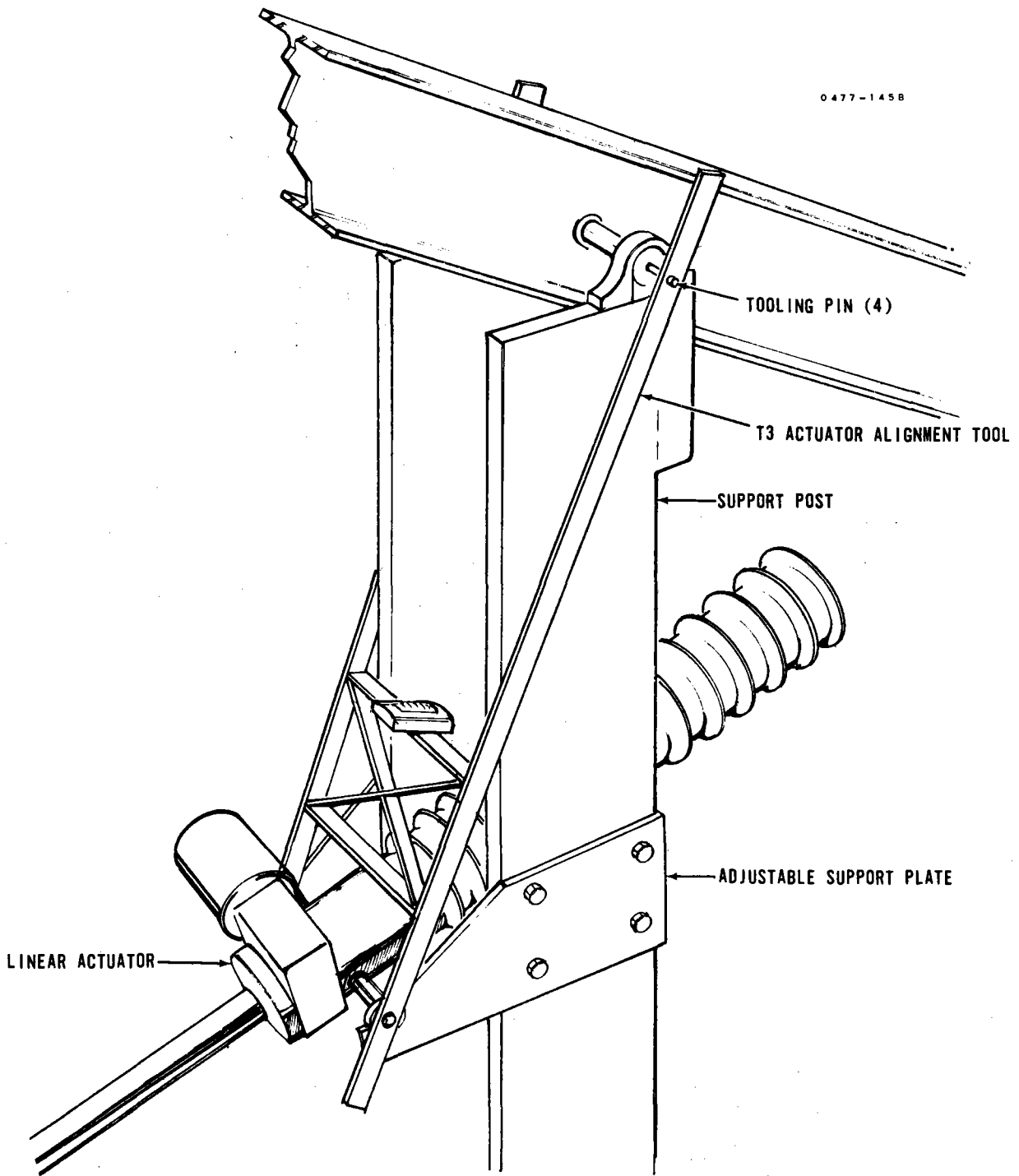


Figure 6-4. (T3) Actuator Pivot Axis Alignment Tool

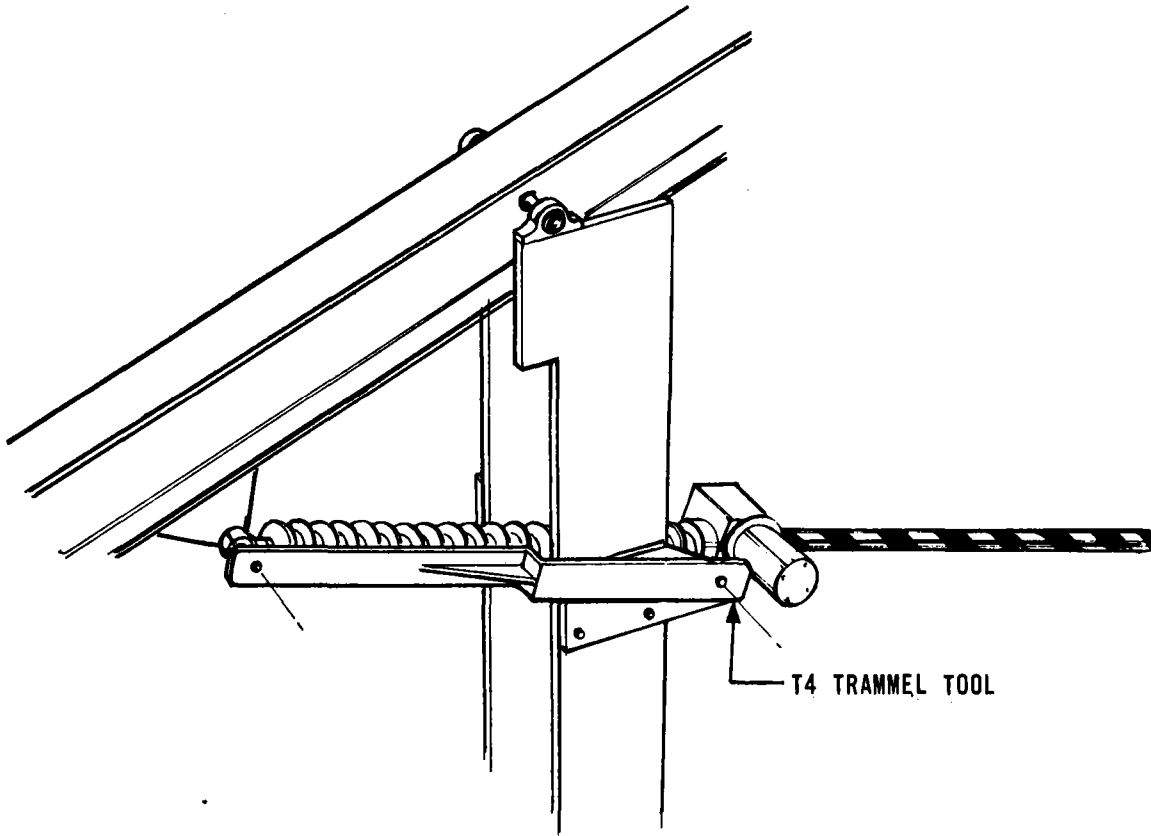


Figure 6-5. (T4) Fixed Length Trammel Tool

0477-139B

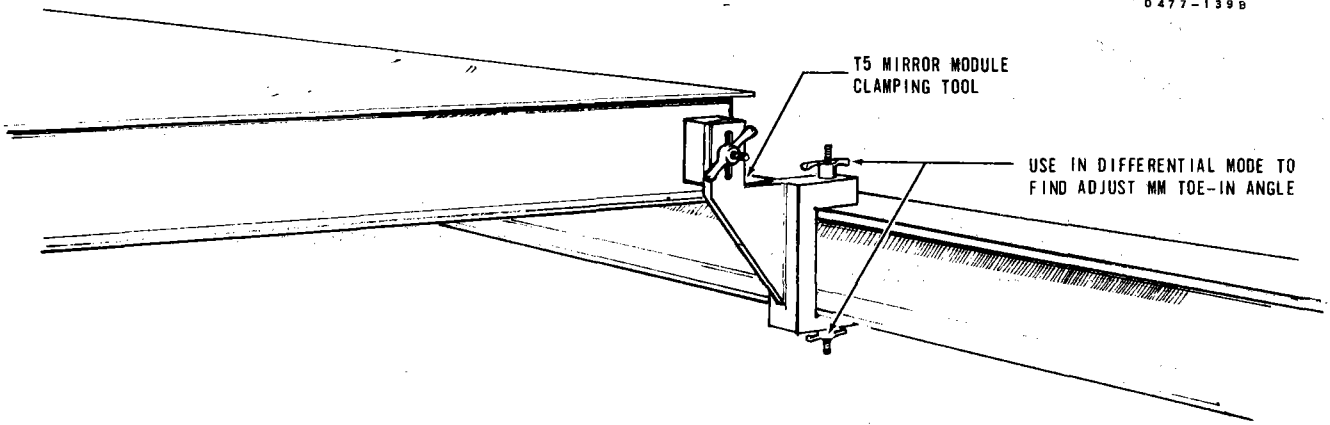


Figure 6-6. (T5) Mirror Module Clamping Tool

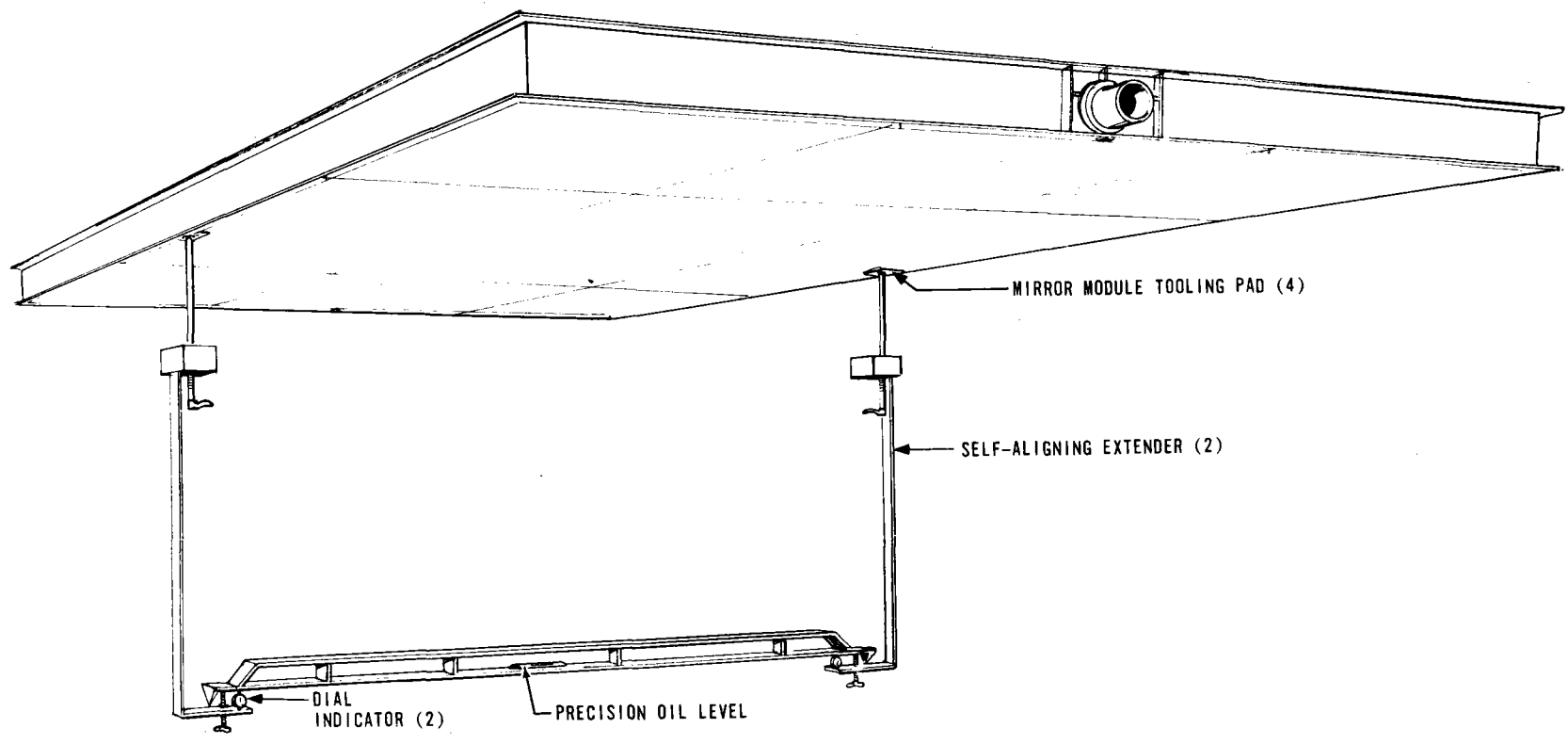


Figure 6-7. (T6) Precision Beam Level

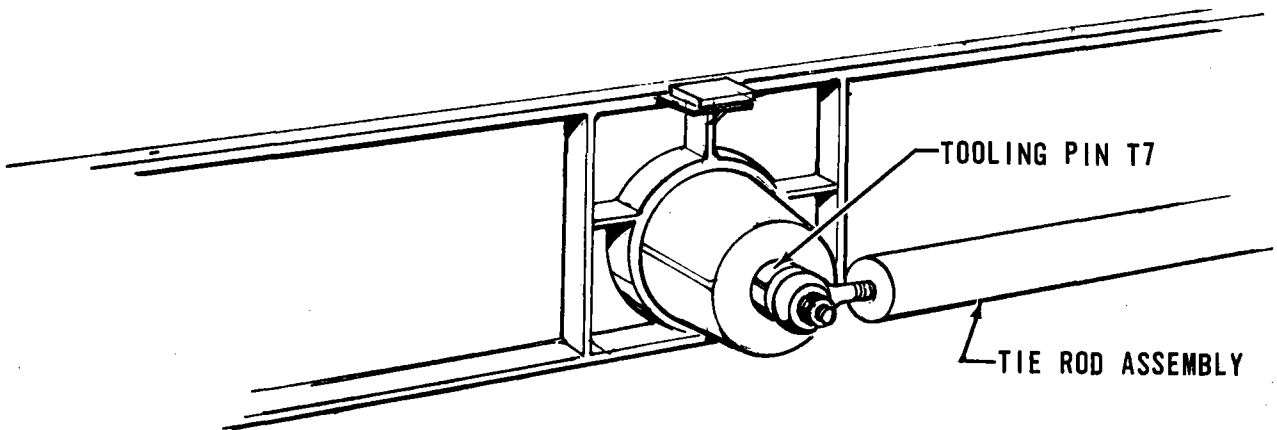


Figure 6-8. (T7) Tooling Pin

MIRROR CLEANING METHOD

A Pilot Plant with an electrical output of 10 mw will require approximately 65,000 m² of mirror surface. To be efficient as solar energy reflectors mirrors must be clean. Data from the solar research experiment indicates overall efficiencies of 80 percent can be maintained by weekly cleaning of mirrors. The quantity and frequency of cleaning of mirrors make it obvious that some type of semiautomatic equipment is required.

Mirror cleaning will be conducted during nonoperating periods when unrestricted access to the field of heliostats may be permitted. Conducting this type of operation during times of no sun will greatly simplify personnel safety requirements and eliminate necessity to control reflected energy. The heliostats scheduled for cleaning should be placed in the required position. Depending on the equipment and techniques developed this could be heliostat horizontal with mirrors either up or down or mirrors parallel to plane of the frame and the frame rotated to maximum angle.

The experience gained on solar research indicates that mirrors will accumulate dirt in the form of dust, water spots and atmospheric residue even with the mirrors stowed face down. This dirt will not be removed by spraying water on the mirrors. Mechanical scrubbing and detergent are required. Commercial window washing products have given excellent results. Superior results are obtained by removing excess moisture immediately.

A study of possible techniques resulted in selection of a procedure where the heliostat is rotated to a maximum angle (approximately 70 degrees) about the outer axis with the mirror surface parallel to the frame. In this position easy access is obtained using a semiautomatic, one man operated, washer driven in front of the heliostat. Devices to guide the brushes and other parts of the equipment will be implemented to prevent damage to mirrors by improper operation. The washing equipment may be thought of as car wash mounted on wheels. Initial spraying with water/detergent solution, mechanical scrubbing with rotating brushes and blow drying to prevent water spots will all be incorporated in a single piece of equipment. The concept of this equipment in operation is presented in Figure 6-13. An alternative concept is a straddle style washer with horizontal brushes and vacuum removal of the water. Water and detergent recycling and reuse would be cost effective from a life cycle cost standpoint.

DEGRADATION RATES

Material degradation rates are a strong function of the environment. The Florida environment is a severe test of all components. While the SRE did not provide direct data on degradation rates of mirrors, paint, bearings, etc., the simple fact that the mirrors have survived provides a key to the quality of the heliostat design

White epoxy paint was used to protect the exposed heliostats parts for the SRE. In the Florida humid environment rust spots appeared

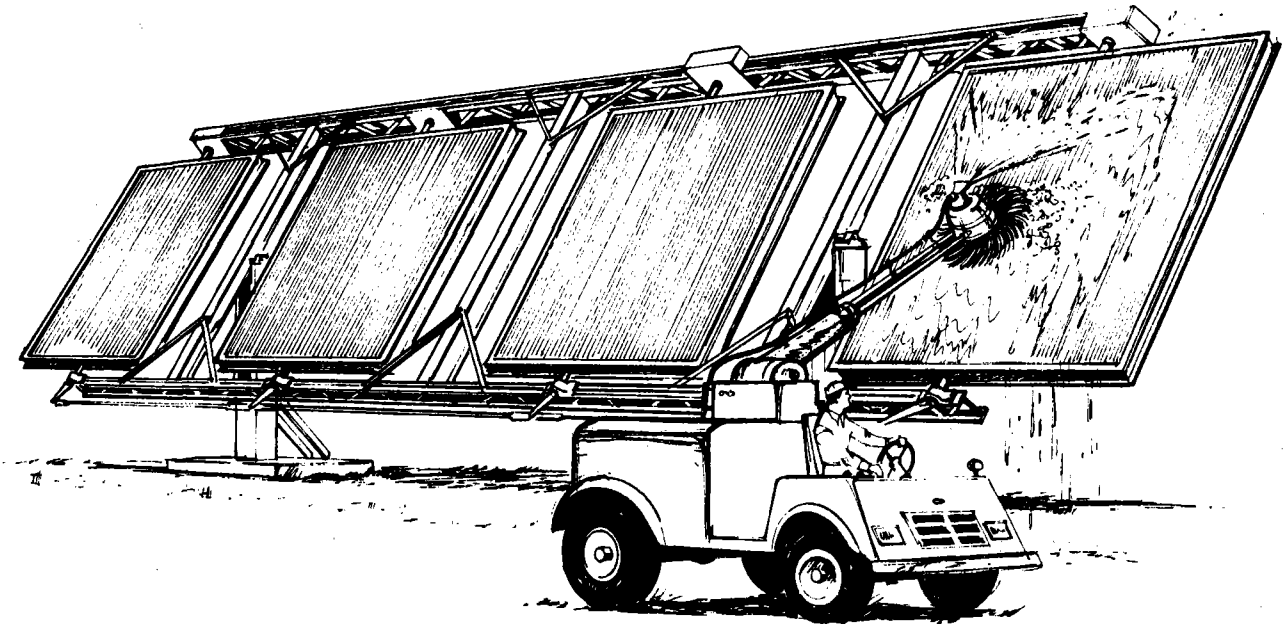


Figure 6-9. Semiautomatic Mirror Cleaning Concept

less than one year after painting. In general these spots were associated welded areas and it is noted that they were rusty prior to painting. The problem appears to be one of application not coating quality as most areas are holding up well from a weatherability standpoint. The protection requirements may be in conflict with the high reflectivity (to avoid thermal induced errors) requirements.

Mirror life degrades extremely rapidly in Florida due to tarnishing of the reflective surface. This is amply borne out by the fact that certain samples tested in Florida failed in 105 days (Reference Research applied to Solar Thermal Power Systems Progress Report No. 2, Report Number NSF/RANN/SE/GI-34871/PR/73/2 prepared under Grant 29726 by the University of Minnesota and Honeywell. The SRE mirrors have experienced some degradation despite being sealed on all edges. The tarnish of the silver is all within 1/4 inch of the edge and there is no tarnish in the center of the mirrors. The SRE mirrors with nine facets have much more area exposed than the pilot plant. The losses of the pilot plant will thus be considerably less.

In detailed design much more effort will be spent in determining degradation rates and means to retard or eliminate them.

a. Mirrors

These three types of mirror module degradations are:

- Contour change.
- Reflectivity degradation - permanent.
- Reflectivity degradation - temporary.

Contour Change

Honeywell feels that bonding the mirror to the structural backing with the silicon adhesive discussed in Section 7 and Appendix (F) along with retaining the structural rigidity exhibited during the SRE program, the mirror modules will retain a 30 year contour life. SRE mirror surfaces have retained their contour control where only regular contact cement was used after a year's exposure to the Florida sun and very heavy humidity. Also much of the time for the engineering model heliostat, the modules have been faced down under constant "g" loading with no relief for extended periods of time (3 to 4 months).

Permanent Reflectivity Degradation

As was mentioned on Page 3-17, long term exposure to the desert will have a presently unknown effect to our glass. However a long term test is being conducted and initial results will be known in September 1977 such that they will be incorporated into our final pilot plant proposal considerations. This study will provide information regarding glass erosion (increased scatter) and silvered surface reflectivity degradation.

First, a few mirror module glass facets will become cracked due to handling errors. Instances of being hit by vehicular machines nudging

against the edge of a module and hand tools slipping while heliostats are being worked on have occurred at Honeywell. Over a two year pilot plant operation, human error (washing modules, during assembly, etc.) it can be assumed that a small number will be damaged. Here the crack will often spread across the width of the individual facet. Therefore, the surface area lost will be the glass thickness X the width of the facet for each crack unless stress relief holes are quickly drilled.

Secondly, if any moisture seeps between the silver coating and the protective backing paint, the reflective material will tarnish. Within the last 6 months about 8 to 10 spots along the edge of various facets have appeared-- most less than the area of a 50 cent piece. This problem will be lessened by two efforts:

1. Insure the protective paint covers up along the entire edge of all facets to reduce the chances of moisture penetration starting.
2. Evaluating the virtues of not applying sealant between facets. If moisture does seep between facets around the gap fillers, it can escape.

Temporary Degradation

Dust, dirt spots due to moisture condensation then evaporation, and bird dropping can reduce the average reflectivity from 4 to 6 percent within two weeks of operation. It is estimated that weekly heliostat mirror washings will be required to maintain efficient solar power plant operations. Again the degradation due to the desert type environment will be known better after the results from ERCs desert experiment are known and feedback is obtained from the NTF experience.

b. Drive System

The actuators used for the outer drive have exhibited life spans of 30 years during operation and testing during operations other than the heliostat application. The inner drive was designed for a 30 year life expectancy. Lubricants used will have 5 year shelf life and because of the low rpm rates, a 5 year life should be retained. However, the heat and other environmental effects (moisture, sand seeping through the seals, etc.) may require a closer relubricating schedule than 5 years. At the present there is no reason to assume that an interval of less than once per 2 years will be necessary.

Actual wear effects are unknown due to the unusual operational environment where relatively very little daily movement is required (e.g., spur gear rotates once per day, a point on the actuator screw is passed twice a day, etc.) but the wind will introduce some rocking motion. The actuator ball nut will receive the most wear. Our specification required a tolerance of only 0.010 inch, but as a normal tolerance, the present Limitorque actuator provides a 0.005 inch tolerance. Therefore, some degradation is even allowable, and the normal daily loads are less than the actuator design goals.

In conclusion, with no firm system level data to prove otherwise, we feel that both inner and outer drive systems will retain their

specified tolerance and accuracy during the 30 year life expectancy of an operational plant.

c. Motors

Present estimates indicate that due to temperature extremes and motor aging, the present Permanent Magnetic Direct Current Motors (PM DC) will last 15 years before recharging the magnet is required. Even then equipment can be brought to the heliostats to remagnetize the magnets after removal of the motors from the drive mechanism. A 30 year life can be expected using more expensive ceramic cased motors but the cost will be more than doubled. The detailed design will address this trade-off more carefully.

Optimistic estimates on armature brush wear is 2^8 motor revolutions. With a typical 16,200 revolutions per day for the inner drive (10,000 per day for the outer drive), we have a 1.25×10^4 operational days. Assuming additional slews other than once a day onto target and off again of 20 percent we have 10,400 days of operation or 28.5 years of operation. However, with the fact that most of the wear and tear will occur due to starting friction due to the starts upon each individual command the 28.5 years is unrealistically high. During the detail design, concepts such as using specially designed brushes with larger surface areas will be investigated. It does not appear unreasonable to expect brush life to maintain a minimum of 10 years of usefulness. This is a conservative factor of 1/3 of the present design's optimistic life span.

d. Paint

The SRE heliostats were painted with a high gloss white zynolyte epoxy paint, chosen for this area because of its high adherence properties and lack of chalking. However, significant rust has formed across parts of the frame, some forming within the I-beam stiffeners and running out to discolor the surface. Operational heliostat exposed surfaces will be primed differently-- completely immersed--and will probably be painted with a white cellulosic lacquer paint. The longevity of this method will far exceed the SRE performance; however, to what extent is presently uncertain. The moisture factor will be less in the desert environment, but dust and sand erosion will be greater therefore exposing bare metal sooner. An evaluation of our proposed materials will be made by our Materials lab as part of future investigations. However, from a touchup and repainting standpoint we have assumed the requirement of one gallon of paint per heliostat per two year operational life based upon our limited experience so far.

INFANT MORTALITY AVOIDANCE

Infant mortality refers to part failures in early operating life and is primarily an electrical part phenomena. There are several ways to deal with the problem. One way is to ship the system as soon as it is operational and repair field failures as they occur. Another way is to operate the system in-house for a period of time to catch and repair early failures before the equipment is in the hands of the customer.

A third way is to purchase piece parts that have already been conditioned to eliminate most of the weak parts before assembly such that after assembly infant mortality is reduced considerably. The most cost effective method to deal with the particular problem can be any of these, depending on the situation.

Note that the method of screening parts addresses a cost problem that the others do not, and that is the rework cost required to get the equipment to an operational status after assembly. This is more precisely defined as a quality problem as compared to infant mortality which is a reliability problem, but both affect ultimate cost. Screening eliminates many bad parts before they are put into the equipment and also the costs associated with finding and replacing them. Screening, and in particular burn-in, affects infant mortality by accelerating failures, causing them to occur before the part is ever assembled into the equipment, again saving trouble shooting and replacement costs.

Screening obviously adds to the price of the piece parts and the real question is, do the parts cost more than they save? First let's examine what we get and then how much it will cost.

Figure 6-10 shows a plot of different AQLs (Acceptance Quality Levels) on functionality for logic devices and their affect on board rework rates. The screening program at Signetics⁽¹⁾ called SUPR II guarantees a functionality AQL of 0.1 percent. For a packing density of 50 elements per board, which is the density for the heliostat electronics for the SRE, a 0.1 percent AQL when compared to the industry standard level of 1.0 percent is seen to reduce rework required from 55 percent to 5 percent of the assembled boards.

The SUPR II program at Signetics involves two levels of processing, Level A and Level B. Level A testing involves the following:

- Visual check.
- Stabilization bake, 6 hours at 150°C.
- Temperature bake, 0 to 100°C, 3 cycle minimum or thermal shock
0 to 100°C, liquid, 15 cycles.
- DC functional test, 100 percent at 25°C.
- Continuity test, 100°C.

Level B testing adds burn-in to Level A. Burn-in is the equivalent of 168 hours at 125°C. Fairchild, Motorola, National Semiconductor and Texas Instruments all have programs similar to the Signetics SUPR II program. A comparison of some of these programs is shown in the attached Table 6-1, Vendor Parts Programs comparisons. Figure 6-11 shows a plot of relative failure rates of integrated circuit parts

(1) Every vendor has similar programs. Each program is slightly different but has a high degree of similarity.

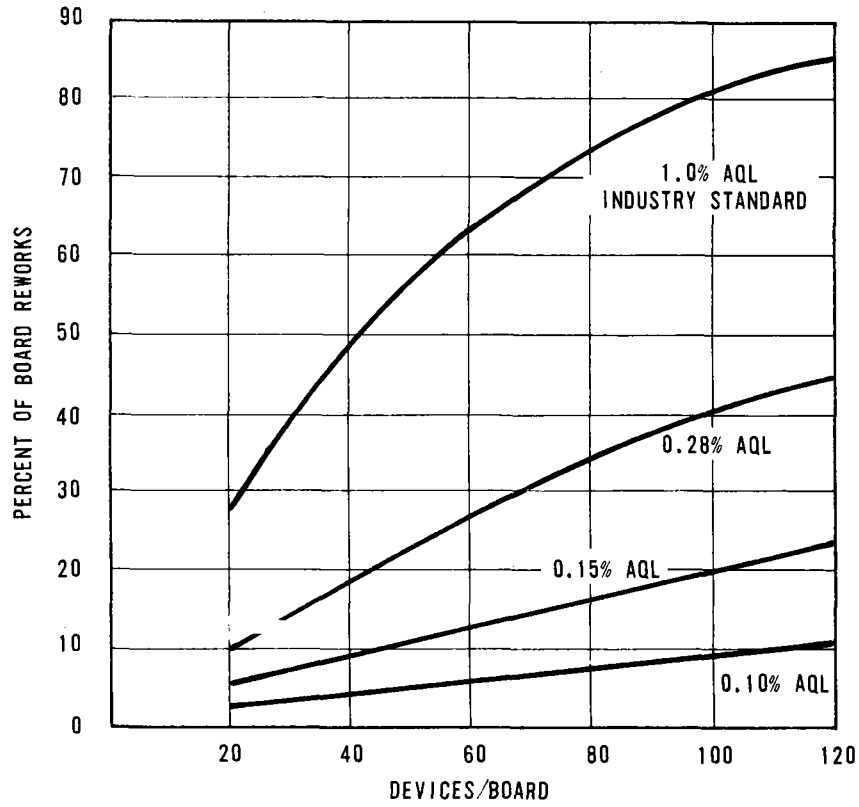


Figure 6-10. AQL Levels on Functionality Versus Board Rework Rates

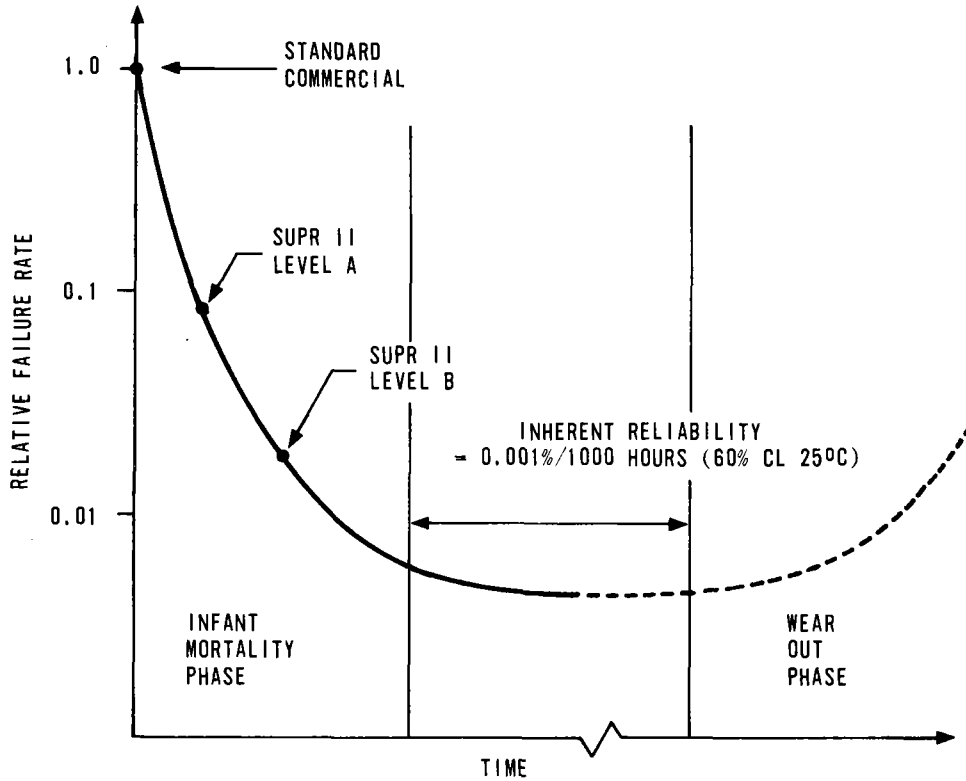


Figure 6-11. Relative Failure Rate Versus Time

Source of Curves: Sinetics Inc.

Table 6-1. "Enhanced-Quality" Vendor Process Programs

Fairchild Level 5 Process (PCQR)	Motorola "BETTER" Level III	National A+ Process Flow	Signetics SUPR II-2 Process	Texas Instrument PEP 3 Level
		"Standard Processing"	38510 Wafer Fab SEM	38510 Wafer Fab SEM Auger Analy/ X-ray
Die Visual 883/2010.1/B		"Standard Processing"	Die Sort Visual 883/2010B	Die Sort 883/2010B
Preseal Visual 883/2010.1/B		"Standard Processing"	Precap Visual 883/2010B	Precap Visual 883/2010B
		HI Temp Storage 6 hr at 150°C	Stab Bake 175°C - 4 hr	Stab Bake 175°C, 4 hr
Temp Cycle (CERAM) 883/1010/C, 5 cycles	Temp Cycle 883/1010	Temp Cycle 0-108°C, 5 cycle		Temp Cycle 883/1010, 10 cycle, 0-100°C
Thermal Shock 0-100°C 883/1011/A			Thermal Shock 883/1011A	
			Centrifuge Monitor (Seal) 1x10 ⁻⁷ : 883/1014B 1x10 ⁻⁵ : 883/1014C	X
25°C DC and Functional				25°C DC and Functional
Burn-in 168 hr at 125°C ea	Burn-in 168 hr at 125°C ea	Burn-in 168 hr at 125°C ea 883/1015.1	Burn-in 168 hr at 125°C ea 883/1015F	Burn-in 168 hr at 125°C ea 883/1015F
25°C DC and Functional		DC & Functional 25°C	DC & Functional 25°C	DC & Functional 25°C
100°C Functional	100°C Functional	100°C Functional	Hot Rail; 100°C Functional	Hot Rail; 100°C Continuity
QC & Symbolization	QC	QC	Tightened QC Symbolization	QC & Symbolization
MARK 74XXXPCQR	MARK MC8XXPRS	MARK (TBD)	MARK N74XXX-B	MARK P3 SN74XXXX
Applicable Types: Plastic or Ceramic	Applicable Types: Digital DIPS	Applicable Types: "N&J" Pkg Products	Applicable Types: Analog, Digital, Memory, MOS	Applicable Types: Plastic DIP ONL Logic, OMOS,

versus time. From points plotted on the curve, the relative failure rate for SUPR II Level A screened parts is seen to be an order of magnitude better than that for standard commercial unscreened parts. For Level B burned-in parts, it is more than 50 times better.

Level B screening is estimated to add ≈ 30 percent to the cost of a part, i.e., 5 cents additional for a simple circuit such as NAND gate to 15 cents additional for a more complicated circuit such as a flip flop. From experience on other large part quantity programs, namely communications equipment, Honeywell has determined that using screened logic elements is a cost effective solution and recommended for the Heliostat Electronics.

With regard to discrete semiconductors, i.e., transistors and diodes, parts can be purchased in unscreened, JAN, JANTX, and JANTXV versions. JAN parts are sample lot tested while JAN TX and JAN TXV parts are screened to include 100 percent testing including burn-in. Relative average costs for various semiconductors and levels of processing are shown compared to a normalized unscreened part in the following table.

SEMICONDUCTOR RELIABILITY LEVELS

	<u>Diodes</u>	<u>Small Signal Transistors</u>	<u>Power Transistors</u>
Unscreened	1.0	1.0	1.0
JAN/Unscreened	1.15	1.12	1.4
JANTX/Unscreened	1.5	1.4	1.8
JANTXV/Unscreened	2.2	2.5	10.8

An AQL figure for discrete semiconductors is somewhat misleading in that the part must adhere to specific parameter specifications which may or may not be important in a particular circuit application. In any event, AQLs average 1.4 percent for JAN parts and 0.85 percent for JANTX and JANTXV parts depending on the sample size. An AQL figure for unscreened parts was not obtained commercial parts (no screening) are nominally accepted as 1 percent AQL.

Based on the above, JAN parts are recommended for discrete semiconductors:

With respect to all semiconductors, both discrete and integrated, Honeywell has compiled and maintained an approved vendor list from whom parts are purchased. The list has evolved from inspection trips to vendors facilities with regard to parts for other programs. Even though many vendors may be qualified to make a given part, only those with the best process control in manufacture are put on the list. This provides further assurance that the best parts are being procured for the money.

With regard to resistors, three types were considered: (1) RLR07, (2) RNC types with established reliability and (3) RNR hermetic types. RLR07 resistors have burn-in and are 100 percent tested. With a ± 1 percent tolerance and a failure rate of 0.01 percent/1000 hrs, cost is \$0.08 each. RNC types are ± 1 percent and with a failure rate of 0.001 percent/1000 hrs cost \$0.32. RNR types cost $> \$1.00$ each. Though RLR07 resistors are not hermetically sealed, moisture should be no problem because of the operating environment, the weather tight enclosure, and the fact that the part will be operated for many hours every day. Based on the above, RLR07 resistors will be the general purpose resistor used in the Heliostat Electronics.

The basic capacitor used in the Heliostat Electronics will be a ceramic capacitor purchased to M39014/05. Purchased to a failure rate spec of 0.1 percent/1000 hrs, cost is \$0.40 each. Power supply capacitors are provided by the vendor and are a special case.

Other parts such as motors and actuators will be similarly treated during detail design including burn in where necessary.

METHOD OF SAFE CONTROL OF REFLECTED LIGHT

It has been shown that focused heliostats are able to concentrate power densities in the redirected beam which are the equivalent of several suns. Overlapping beams can further increase the energy concentration level. Should this energy be directed at some point other than the aperture, power densities at these levels could cause discomfort or even be hazardous to people and/or equipment in, around, or above the facility. The operating system must minimize this potentially hazardous condition to the greatest extent possible.

Ideally it would be highly desirable to not only defocus the field but to defocus or shut off the individual heliostat as well. Unfortunately, no practical, low cost, way to do this has been found. For example, fixed focus mirrors preclude any attempt to alter mirror focus; no reasonable method to provide an electronic "shutter" could be found; spraying mist did not seem practical; and a "window shade" apparatus that could be pulled across the mirror and withdrawn on command that would last 30 years in the environment was prohibitively expensive. Based on the above, it appears that safety will have to depend on the control of the redirected beam.

In the Honeywell open loop control system, the reflected beam may be redirected to any position, constrained only by the limitations on the freedom of the gimbals and the position of the sun. To redirect the beam to a given point the computer uses the position of the sun, which is calculated in real time at 1 sec intervals, and the coordinates of the target with respect to the heliostat (base distance, height, and azimuth), to calculate a set of required gimbal angles. Incremental commands are then issued to the Heliostat Electronics to drive the gimbals from their current position to the desired ones.

If the actual gimbal positions are substantially different from the desired positions, such as at start up in the morning, or in changing from aperture tracking to the stow position, the gimbals can be commanded to take the shortest path to the new position. Or as an

alternative, they can be commanded to take any permissible route to the new position simply by changing target coordinates in piece-wise fashion to correspond to points along the intended route. The latter method will be the baseline approach. This method is used to make the redirected pilot plant beam avoid buildings or other prohibited areas in its travel to its intended destination.

There are conditions; however, that preclude positive control of the redirected beam. With regard to the individual heliostat, failures can be postulated which will render the heliostat inoperable. The redirected beam position will then be a function of the sun position and the uncontrolled mirror position. The heliostat may be covered, repaired, or manually stowed, but for a period of time the beam will be uncontrolled.

With respect to groups of heliostats, there are emergency situations that can result in an indeterminate number of heliostats performing maneuvers that can, for a short period of time, result in the uncontrolled slewing of multiple beams. For example, if a communications bus is broken, the heliostats beyond the break will sense the loss and begin the fail safe maneuver to achieve the stow position. This maneuvering is under the control of the heliostat and not the computer, and the route to the stow position is the shortest path route. With respect to beam positioning this must be considered an uncontrolled maneuver. In performing this maneuver; however, note that the beams will not remain stationary so as to concentrate and remain on a given target but will be constantly slewing. The maximum time a slewing beam will remain outside the confines of the plant perimeter will be 5 minutes.

Even with a perfect control system, however, start up and shutdown during daylight hours will result in beams being redirected outside the perimeter of the facility. To eliminate ground level reflections outside the facility, a high fence will be built around the perimeter of the heliostat field. A fence will also be built around the inside perimeter of the heliostat field to prevent reflected beams from sweeping the building cluster at the tower base. Within the heliostat field, protective glasses will be recommended for all personnel during daylight hours.

FAIL SAFE FEATURES

The SRE involved only four heliostats and these were given constant attention during operation by the test crew. Because of this and for economic reasons, not many fail safe features were built into the SRE heliostat and no serious consequences resulted. However, because of the large number of heliostats required for a power generating plant, fail safe features will be included to protect the heliostat and other plant equipment. These features are described below.

Heliostat Battery

A rechargeable heliostat battery was included in the SRE and is included in the pilot plant design. However, the battery was used only to supply the gimbal motor drive power. The remainder of the Heliostat Electronics operated from power supplies using the 110 volt ac line as the input source. This allowed an operator to stow the heliostat manually in the event of an ac power failure but did not permit continued operation through the failure.

For the Pilot Plant and beyond, all power to operate the heliostat will be drawn from the heliostat battery. The battery will be trickle charged from the ac line to maintain capacity. In the event of a failure in the ac grid, the heliostat battery will provide power for continued operation for up to 19 hours.

Power Loss Detector

A power loss detector will be included at each heliostat. If ac power is lost for 20 minutes, the heliostat will automatically initiate a stow maneuver. All the logic to perform this maneuver will be contained at the heliostat. Under this condition the stow maneuver will be an uncontrolled maneuver, i.e., the gimbals will take the shortest path to the stow position. Should a power loss be detectable by the control computer, such as a catastrophic power loss at the tower, the stow maneuver is done in a controlled manner by the computer through the normal command link.

Communications Loss Detector

A communications loss detector is included at each pilot plant heliostat. If communications are lost for 45 seconds, the heliostat initiates the stow maneuver. Since by definition communications have been interrupted, this maneuver is an uncontrolled maneuver as defined above. To help evaluate the adequacy and effectiveness of the design of the communications link, all data buses to the heliostats will ultimately return to the tower so that checks may be made on transmitted data as seen at the end of the data bus. Thus making highly unlikely "bad commands" to large numbers of heliostats.

Motor Overtemp Detector

The heliostat inner axis is free to rotate with a full 360 degrees of freedom and has no cabling which could wind up and bind the gimbal. However the outer axis has a limited range of freedom and the motors for both axes are subject to stall under sufficient load or because of a failure. Full power to a stalled motor for a sufficient length of time can result in a motor overtemp condition which could damage motor winding insulation. A motor overtemp detector will sense this condition and remove power from the motor to prevent this type of compounding failure.

Manual Control

In the event of an electrical control system failure, a set of switches allow the manual stowing of the heliostat. No cranks or shafts through which auxiliary motors could be used to drive the gimbals are provided. In the event of a gimbal motor failure, the motor will have to

be replaced before the gimbals can be moved. Special tools (electric hand drills) are used in the remote and unlikely event that motors are unavailable and the heliostat must be moved.

Non-Reversing Gears

Self-locking (non-reversing gear trains under load) are used on both axes such that with or without power, wind loads cannot cause the heliostat gimbals to rotate.

Redundant High Voltage Power Feed

The high voltage line that inte-connects the field transformers completely encircles the tower. Redundant feeder lines using separate routing will be used to connect this network to the tower requiring a double break in the high voltage system before high voltage power is lost to any segment of the field.

Summary of Fail Safe Features

- Heliostat Battery
- Power Loss Detector
- Communications Loss Detector
- Motor Overtemp Detector
- Manual Control
- Non-Reversing Gears
- Redundant High Voltage Power Feed

MAKE OR BUY ANALYSIS POTENTIAL

Prudent use of capabilities requires the subcontracting of substantial portions of the heliostats and collector subsystem. The attached map Figure 6-12 shows some potential vendors and indicates how these preliminary subcontracts are distributed throughout the country. Note the transportation sensitive elements (frame and mirror modules) (one vendor are situated close to the pilot plant site. This is felt mandatory to limit transportation costs for these two largest and heaviest assemblies.

Honeywell has begun using our West Covina facility to identify potential local small vendors for miscellaneous piece parts such as tie rods, crank arms and similar items. Vendors cost estimate will be compared to in-house cost estimates and the make or buy decision made primarily on the basis of cost. Transportation costs to the site will be included in these comparisons. When a buy decision is made it will be made on the basis of cost unless some critical parameter is overwhelmingly against this basis. An example might be risk of vendor bankruptcy. If the vendor was nearly insolvent he might not be chosen despite being low bidder. Another philosophy will be the parts where no cost penalty exists (for example, standard bearings, tie rod ends, and bolts).

Honeywell intends to buy most of the heliostat hardware but electronics and other hardware will be manufactured in-house where it is competitive to do so.

PROCUREMENT PLANS

It is the goal of Honeywell to purchase the best product available based on evaluations of price, delivery, and quality consistent with the lowest ultimate cost.

To obtain this goal, it is our plan to follow the formal policies and procedures established and published by Procurement management and monitored for compliance on an on-going basis by Honeywell Internal Audit and DCAS. Our department and system continues to receive the highest level of approval.

It is Honeywell's policy to place purchase orders only with those suppliers who have proven their reliability and capability. Objective evidence supporting the supplier's previous record of supplying high quality articles of the type being procured is reviewed prior to their being approved. Each approved supplier's performance is summarized in computerized reports on a monthly and quarterly basis, the data is reviewed by quality and purchasing management on a regular basis. New sources of supply are constantly being developed to avoid sole source procurement and to foster competitive bidding.

It is our plan to subcontract on a module basis much of the heliostat such as mirror module and drive unit, the frame assembly and drive unit, and the support assembly.

We will select the source(s) for the major subcontracted modules based on the evaluation of potential suppliers by a team consisting of representatives from Procurement, Engineering, Manufacturing, Quality Assurance, and Finance. The team will establish weighted point totals for each potential supplier based on the following criteria:

1. Technical design
2. Facility survey-equipment, capacity, labor relations
3. Vendor quality and reliability survey
4. Vendor committed delivery schedule and our confidence in meeting it
5. Vendor price and substantiation - including freight cost
6. Fabrication site location
7. Amount of subcontracting to be done
8. Vendor management - includes financial condition, previous experience with similar product, and experience with Federal regulations
9. Maintainability and warranty of the item supplied.

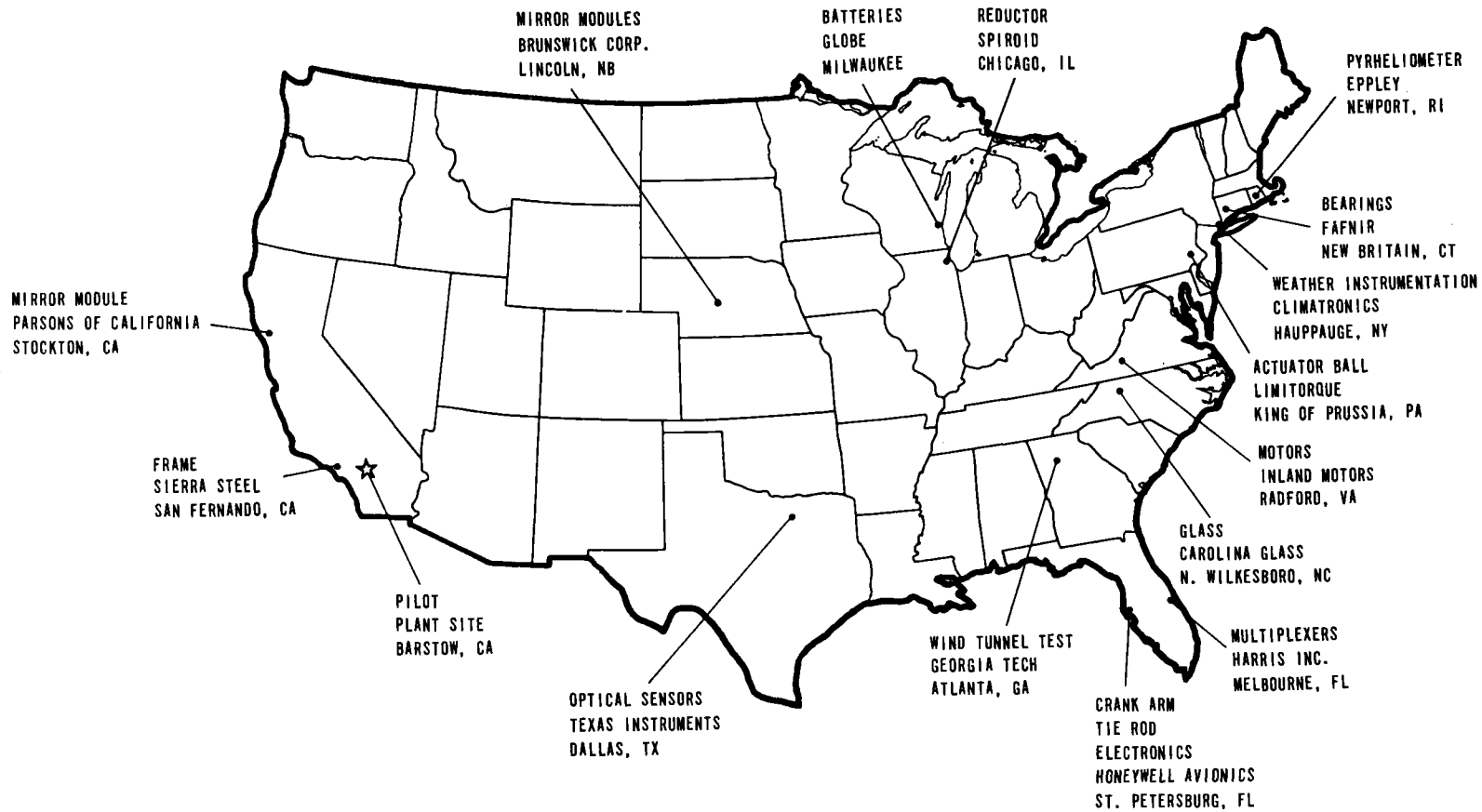


Figure 6-12. Collector Subsystem Vendors

The Procurement buyer(s) are accountable for all aspects of the procurement, including delivery performance. Our Procurement Department maintains one of the best performance ratings in industry relating to our vendors meeting committed delivery schedules. On-time delivery is consistently above 90 percent for all items and has been as high as 96 percent.

The quality levels for the program will be developed to establish appropriate quality and certification criteria based on contractual requirements. These requirements become part of the purchase order specification package.

Our computerized supplier performance summary, reported monthly and quarterly, and reviewed by Procurement and Quality management on a regular basis, enables us to readily determine problem areas and take appropriate action as required. Where required, we will place Quality representatives at the supplier's plant to inspect product as it is being manufactured, and in the final assembled state prior to shipment.

The following is a listing of the potential parts procurement. They are identified as Single Source Parts, (SS), Nonstandard Parts, (NS), Long Lead Parts, (LL), and by lead time required on long lead items:

<u>Part Number</u>	<u>Description</u>
34027499	Tie Rod Assembly (NS)
34027498	Bracket Assembly - Actuator (NS)
34026587	Shoulder Washer (NS)
34027497	Pivot Block (NS)
34026581	Spring Support Assembly (NS)
34027495	Support & Post Assembly (NS)
RAK-1 15/16	Pillow Block (SS)
SPM-10	Ball Joint Rod End (SS)
RR 3/4	Pillow Block (SS)
01-504-0120-4	Linear Actuator, Ball Screw (NS) (LL - 18 weeks)
34027500	Pivot Pin Assembly (NS)
34026600	Taper Lock (NS)
34026579	Crank Arm (NS)
MHP-23	Spring, Preload (SS)
D51-10245-02	Reductor (NS) (SS) (LL - 18 weeks)
34026616	Bearing Retainer, Inner (NS) (SS) (LL - 20 weeks)

<u>Part Number</u>	<u>Description</u>
34026615	Bearing Support Assembly (NS(SS) (LL - 20 weeks)
34026613	Spur Gear (NS)
34027496	Frame Assembly (NS)
34026575	Mirror Module (NS)(SS)(LL) Lead Time - 12 weeks - prototypes and engineering 10-12 months full production

REFERENCE DOCUMENTATION

During performance of the preliminary design contract three primary documentation techniques were used. The first is bound documents with numbers and dates. The second is technical coordination letters (TCLS) Now numbering over 130 letters documenting noncontractual aspects of the design. The final documentation was drawings. All drawings produced under this contract are available and have been transmitted to Sandia. It is emphasized that these drawings are suitable for prototype build only.

These three types of documents are listed in the following tables.

SUPPORTING DATA

1. Preliminary Design Baseline Report (FINAL), CDRL No. 1, 30 Jan 1976
2. Computer Program for Heliostat Parametric Trade Study, Honeywell Avionics Doc. No. 76-856-4-V&H-20, SRE-CD-1, 13 Feb 1976
3. Program Review Presentation Document, Honeywell Avionics Doc. No. 376-13634, March 1976.
4. Engineering Model Plan - Collector Subsystem Research Experiment, Honeywell Avionics Doc. No. 376-13639, 5 March 1976.
5. Detail Design Review Presentation Document, Honeywell Avionics, 22 April 1976.
6. Detail Design Report - Collector Subsystem Research Experiment, CDRL No. 6, 18 May 1976.
7. Proposal for Increased Scope - Heliostat Testing, Collector Subsystem Research Experiment, Honeywell Avionics, 25 June 1976.
8. Final Report on Foam Mirror Module, Honeywell Avionics Doc. No. 676-13890, 9 July 1976.
9. Program Plan - Collector Subsystem SRE, Honeywell Avionics Doc. No. 176-13542, 30 July 1976.
10. Program Review Presentation Document, Honeywell Avionics, 11 Aug 1976.
11. Structural Analysis Report (2 Parts) LG8016 Heliostat Assembly, Honeywell Avionics Doc. No. 876-13994, 29 Sept 1976.
12. Experimental Model Plan - Collector Subsystem (SRE), Honeywell Avionics Doc. No. 576-13699, 1 Oct 1976.
13. Program Review Presentation Document, Honeywell Avionics Doc. No. 1076-14116, 26-17 Oct 1976.
14. Operating Instructions - Collector Subsystem Research Experiment, CDRL No. 13, 8 Nov 1976.
15. Engineering Data - Heliostat Cost, CDRL No. 11, 12 Nov 1976.
16. Producibility Study Proposal, Honeywell Doc. No. 1276-14191, 3 Dec 1976.

17. Preliminary Design Baseline Report Supplement, CDRL No. 1, 17 Dec 1976.
18. Concept Design Report (REVISED), CDRL No. 3, 17 Dec 1976.
19. Test Report - Collector Subsystem (SRE), Honeywell Avionics Doc. No. 277-14333, 18 Feb 1977
20. Baseline Characteristics Document - Solar Pilot Plant, Honeywell ERC Doc. No. F3419-D-101, 2 Mar 1977.
21. NASA CR-2635, A Numerical Investigation of Severe Thunderstorm Gust Fronts, Kenneth E. Mitchess, Dec 1975.
22. ANSI A 58.1-1972 American National Standard Building Code Requirements for Minimum Design Loads in Buildings and Other Structures - Approved, 20 July 1972.
23. TWX from Sandia Laboratories, 24 Dec 1976, R232309Z, Subject: Clarification of ERDA Letter, "Pilot Plant Site Parameters".
24. Honeywell Interoffice Correspondence, R.E. Rose to D.E. Waters, Wind Effects in the Heliostat Field, 11 Dec 1975.

TCL LIST

Technical Coordination Letters (TCLs) are the chief means of non-contractual communication between Avionics (HI Fla) and our customers (ERC). The attached list of TCLs, published during the Preliminary Design Phase of the program, shows number, date, and subject. The list is provided as a reference to many analyses and considerations which are not documented elsewhere. Copies of any or all of these letters will be made available upon request.

LIST OF TCLs

<u>TCL #</u>	<u>Date</u>	<u>Subject</u>
SRE-1	1/15/76	L/C 403127 Use of Honeywell Technical Coordination Letter (TCL)
-2	1/14/76	Request for Data - Fire Code Cooling Water and Compressed Air
-3	1/16/76	Heliostat Bed Location Study of Inyokern, CA & Albuquerque, NM
-4	1/16/76	Pilot Plant Cost Estimate (Part I)
-5	1/16/76	AC Power Distribution Study Report
-6	1/19/76	Transmittal of Solar Collector Subsystem Spec. YG8112A1
-7	1/28/76	Program Plan Revision
-8	1/28/76	CDR Action Item Response
-9	2/2/76	Design Approval
-10	2/03/76	Heliostat Position Loop Simulation
-11	2/19/76	Calibration Array; Cal Array - Computer Interface
-12	2/20/76	Engineering Model Actuator Description and Build Plans
-13	3/11/76	Collector Subsystem Research Experiment Detail Spec., Part 1
-14	3/11/76	ERDA Questions in TWX 17 of 2/17/76
-15	3/12/76	Request for Drawing Approval
-16	3/22/76	Rationale for Pilot Plant Learning Curve
-17	3/22/76	Baseline Characteristics Document
-18	3/23/76	Error Analysis
-19	3/24/76	Actuator Design Trade-Offs
-20	3/29/76	Solar Energy Program, Mirror Modules Transportation
-21	3/31/76	Solar Collector Subsystem Baseline Definition Summary

LIST OF TCLs (Cont'd)

<u>TCL #</u>	<u>Date</u>	<u>Subject</u>
SRE-22	4/1/76	Request for Drawing Approval (Frame)
-23	4/1/76	List of TCL's Issued
-24	4/1/76	Mirror Sample
-25	4/6/76	Document Transmittal
-26	4/14/76	Collector Subsystem Research Experiment Detail Spec. Part I Rev. C
-27	4/14/76	UPC Status On Solar Pilot Plant Heliostats
-28	4/26/76	Request for Drawing Approval (Trailer) (Frame) (Spur Gear)
-29	4/28/76	Request for Drawing Approval (Bearing Support Assy)
-30	4/30/76	Minutes of Internal Detail Design Review
-31	5/5/76	Target Aperature Shapes
-32	5/10/76	Drawing Approval (Heliostat Assy) (Shoulder Washer - for Inner Drive Preload Spring)
-33	5/21/76	Solar Pilot Plant Collector Subsystem Spec. SK133098, Rev. A dated 20 April 76
-34	5/12/76	Drawing Approval (Shaft Motor) (Housing Detail Assy - Motor)
-35	5/17/76	Heliostat Foundation and Support Analysis
-36	5/17/76	Mechanical Analysis of Heliostat Experiment
-37	5/21/76	Baseline Characteristics Document, Rev. 1, 21 April 1976
-38	6/3/76	Direct and Total Insolation Measurements
-39	6/9/76	Use of Rectangular Steel Tube to Fabricate Heliostat Frame
-40	6/16/76	Heliostat Actuators
-41	6/16/76	ERDA Questions on Heliostat Design

LIST OF TCLs (Cont'd)

<u>TCL #</u>	<u>Date</u>	<u>Subject</u>
SRE-42	6/23/76	Mirror Module Construction Samples
-43	7/14/76	Final Report on Form Mirror Module
-44	6/30/76	Heliostat Support Post Configuration
-45	6/30/76	Heliostat Location Survey
-46	7/13/76	Heliostat Dynamic Analysis
-47	7/6/76	Heliostat Wind Loads
-48	7/7/76	Test Data
-49	7/8/76	Engineering Model Heliostat Testing
-50	7/12/76	Test Data
-51	7/12/76	Drawings: Foundation & Support Detail Assy., Support & Post Detail Assy., and Frame Detail Assy.
-52	7/14/76	Transmittal of Collector Subsystem Baseline Summary
-53	7/15/76	Drawings: Crank Arm Detail Assy., Drive Motor Assy., Brg. Support Assy., Housing Detail Assy - Motor
-54	7/15/76	Data Reduction Output
-55	7/16/76	Heliostat - Areas of Possible Cost Reduction Through Redesign
-56	7/16/76	Drawings: Spring Support Detail Assy., Spur Gear, Tie Rod Detail Assy.
-57	7/19/76	Test Data
-58	7/20/76	SRE Experimental Model Assembly Plan
-59	7/22/76	List of TCL's
-60	7/23/76	Test Data

LIST OF TCLs (Cont'd)

<u>TCL #</u>	<u>Date</u>	<u>Subject</u>
SRE-61	7/29/76	Drawings: Heliostat Assy, Retainer Detail Assy - Brg, Pibot Pin Detail Assy.
-62	8/3/76	Trip to Spiroid (Inner Drive Gearbox Supplier)
-63	8/3/76	Trip to Inland Motor Corp., Radford Virginia
-64	8/10/76	Trip to Limatorque Div. of Philadelphia Gear
-65	8/30/76	Heliostat Pointing Error Analysis
-66	8/30/76	Heliostat Aerodynamic Load Analysis
-67	8/30/76	Heliostat Outer Gimbal Drive Analysis
-68	8/30/76	Heliostat Inner Gimbal Drive Analysis
-69	8/30/76	Heliostat Structural Analysis
-70	6/30/76	Heliostat Mass Properties Analysis
-71	8/10/76	Heliostat Wind Environment Requirement
-72	8/10/76	Backlash in Heliostat Inner Drive Gearbox
-73	8/19/76	Low Cost Mirror Modules
-74	8/23/76	Severe Environmental Conditions
-75	8/24/76	Cursory Investigation of Gypsum Core Mirror Modules
-76	8/25/76	Transmittal of Documents from 8/11 Meeting
-77	8/26/77	Material Creep of Heliostat Frame
-78	9/1/76	Mirror Adhesive Bond Test Report
-79	9/8/76	Heliostat Documentation
-80	9/14/76	Dust Devils and Thunderstorm Gusts
-81	9/29/76	SRE Control Software Status

LIST OF TCLs (Cont'd)

<u>CL #</u>	<u>Date</u>	<u>Subject</u>
RE-82	10/6/76	Paper for Presentation to Professional Society
-83	10/7/76	Economics of Mirror Module Size
-84	10/18/76	Heliostat Structural Analysis Report
-85	10/28/76	Revised SRE Collector Subsystem Test Plan dated 10/1/76
-86	10/29/76	Minutes of October 26 & 27 Meeting
-87	11/10/76	Trip Report to Spiroid for Gearbox Failure Investigation
-88	11/15/76	Field Layout And Control Concepts
-89	11/17/76	Comparison of Optical Calorimetry to Sensible Heat Absorbtion Calorimetry or Thermo-Electric Calorimetry
-90	11/19/76	Actuator Selection
-91	11/22/76	Operating Power Estimate for Pilot Plant Heliostat Control Computer
-92	11/23/76	Aerospace Lessons Learned
-93	11/30/76	Preliminary Collector Subsystem Start-up Scenario
-94	12/8/76	Operation and Accuracy of Heliostat Initialization Sensor Assembly
-95	12/9/76	Pilot Plant Collector Subsystem Operator Console
-96	12/17/76	Preliminary Equipment List Action Item Closeout
-97	1/18/77	Transmittal of One Line Drawing SK137130 and Pilot Plant Collector Field Heliostat Arrangement SK137131
-98	1/19/77	Pilot Plant Environmental Specifications and Site Parameters
-99	1/24/77	Calibration Array for Pilot Plant
-100	1/28/77	Photo Transmittal

LIST OF TCLs (Cont'd)

<u>TCL #</u>	<u>Date</u>	<u>Subject</u>
SRE-101	1/31/77	Mirror Modules for Producibility Study
-102	1/31/77	Transmittal of Viewgraphs & Charts Used in Presentation to C. Selvege at Aero on 28 January 1977
-103	2/2/77	Trip Report to Safety Meeting
-104	2/3/77	Pilot Plant Field Power Wiring
-105	2/4/77	Response to PEL (No Number), Dated 21 January 1977, Re: Criteria for Selection of Pilot Plant Systems
-106	2/4/77	Impact of New ERDA Wind Criteria on the Honeywell Tilt-Tilt Heliostat
-107	2/4/77	Request for Barstow Site Map
-108	2/4/77	Photo Transmittal
-109	2/9/77	Long Range Heliostat Development Program
-110	2/9/77	Pilot Plant Communications Wiring
-111	2/10/77	Safety Analysis (HA-75 PEL 83)
-112	2/11/77	Pilot Plant Scheduled Maintenance Requirements
-113	2/11/77	Estimate Loss Due to Dirty Mirrors For Commercial Plant Operations
-114	2/14/77	Pilot Plant Field Instrumentation Communications Systems and Interconnect Wiring
-115	2/14/77	Calibration Array Design Details
-116	2/14/77	Auxiliary Power Requirements
-117	2/15/77	Action Item HA9 Closure
-118	2/15/77	Operating Power Estimate For Pilot Plant Heliostat Control Computer
-119	2/16/77	Instrumentation & Calibration Requirements for Pilot Plant Operations

LIST OF TCLs (Cont'd)

<u>TCL #</u>	<u>Date</u>	<u>Subject</u>
SRE-120	2/17/77	Operating Power Estimate for Pilot Plant Collector Subsystem
-121	2/18/77	Redbook Data Sheet Submittal
-122	2/22/77	Pilot Plant Master Program Schedule for Phase 2
-123	2/22/77	Pilot Plant Collector Subsystem Power, Shielding, and Grounding Plan
-124	2/22/77	Avionics Document 277-14333 Test Report, Solar Research Experiment, Solar Collector Subsystem, Dated 18 Feb 1977
-125	2/22/77	Pilot Plant Test Program
-126	2/22/77	Additional Power Measurement Requirements for Collector Subsystem
-127	2/25/77	Collector Subsystem Consumables for Pilot Plant Operations
-128	2/25/77	Transmittal of Computer Control Room Floor Plan
-129	2/25/77	Copies of Insolation Strip Chart Recordings
-130	2/25/77	Conceptual Filed Layout for Commercial Power Plant
-131	3/21/77	Commercial Plant Design

DRAWING LIST

<u>Number</u>	<u>Description</u>
34026575	Mirror Module
34027496	Frame
34026598	Actuator
34026579	Crank Arm
34026608	Tie Rod
34026615	Bearing Support
34026616	Bearing Retainer
34026613	Spur Gear
34027498	Pivot Block
34026617	Housing Assembly
34026600	Taper Lock
34026583	Motor Mount
34027497	Pivot Block
34026612	Cover
34027500	Pivot Pin
34026581	Spring Support
34026584	Shaft
34026612	Terminal Board
34026587	Washer
34027494	Foundation and Support

CONCLUSION

This section has described in detail the assembly and alignment procedures. The subsequent sections have dealt with mirror cleaning methods, degradation rates and other miscellaneous details supporting our design. The documentation listed and other data should make it clear that much remains to be done in detail design.

Section 7 SRE TEST RESULTS

Applicable pages from the SRE Test Report, Reference 277-14333, are attached within this section to help support our findings that relate to our pilot plant preliminary baseline decisions. The section on Redirected Energy Measurement (Page 7-155) was substantially revised from that initial document.

This section briefly describes the Test Hardware used and provides a detail discussion of the applicable subassembly and system level test results.

SRE SYSTEM DESCRIPTION

Basically Honeywell's SRE Collector Subsystem consists of four low profile, tilt-tilt heliostats (one mobile engineering model and three permanent experimental models) under one central computer control (open look tracking) with a 16 foot by 14 foot photocell grid as the primary method of detecting heliostat performance. Figure 7-1 shows a functional block diagram of the Collector Subsystem SRE. See Page 7-21 for an updated description of the heliostat hardware.

Figure 7-2 shows an aerial view of the actual test layout. The three experimental heliostats are located (clockwise from North):

North Site. 482 feet from the center of the North side of Building E-2. AZ of heliostat to center of E-2 is 190.9483 degrees.

East Site. 852 feet from center of East side of Building E-2. AZ of heliostat to center of E-2 is 270.4558 degrees.

South Site. 1030 feet from Building E-1. AZ of heliostat to center of E-1 is 337.1836 degrees.

Engineering Model. In photo, the engineering model is shown parked about 50 feet behind (South) of the South site.

Building E-2. Is shown near the center of Figure 7-2. A spot from the South heliostat is shown on the South wall and a redirected image is shown on the calibration array which is facing East. The height of the center of the array is 51.9 feet from the center line of the East heliostat outer axis.

The major items are discussed briefly below.

Honeywell DDP516 Computer with 32K Memory and Peripherals

The standard 0.96 μ s cycle time computer is centrally housed in Building E-2 of the St. Petersburg complex and is used to generate and issue heliostat tracking commands, provide the real time clock, and dump raw data and processed data to the ASR-35 or magnetic tape

units once per minute. Figure 7-3 shows the computer facility. More detailed operations are given under Software (Paragraph 3.1.1.4), Program Software Update (5.2.7) and the operating instructions (Reference 2.5) of Document 277-14333. Peripherals include the following.

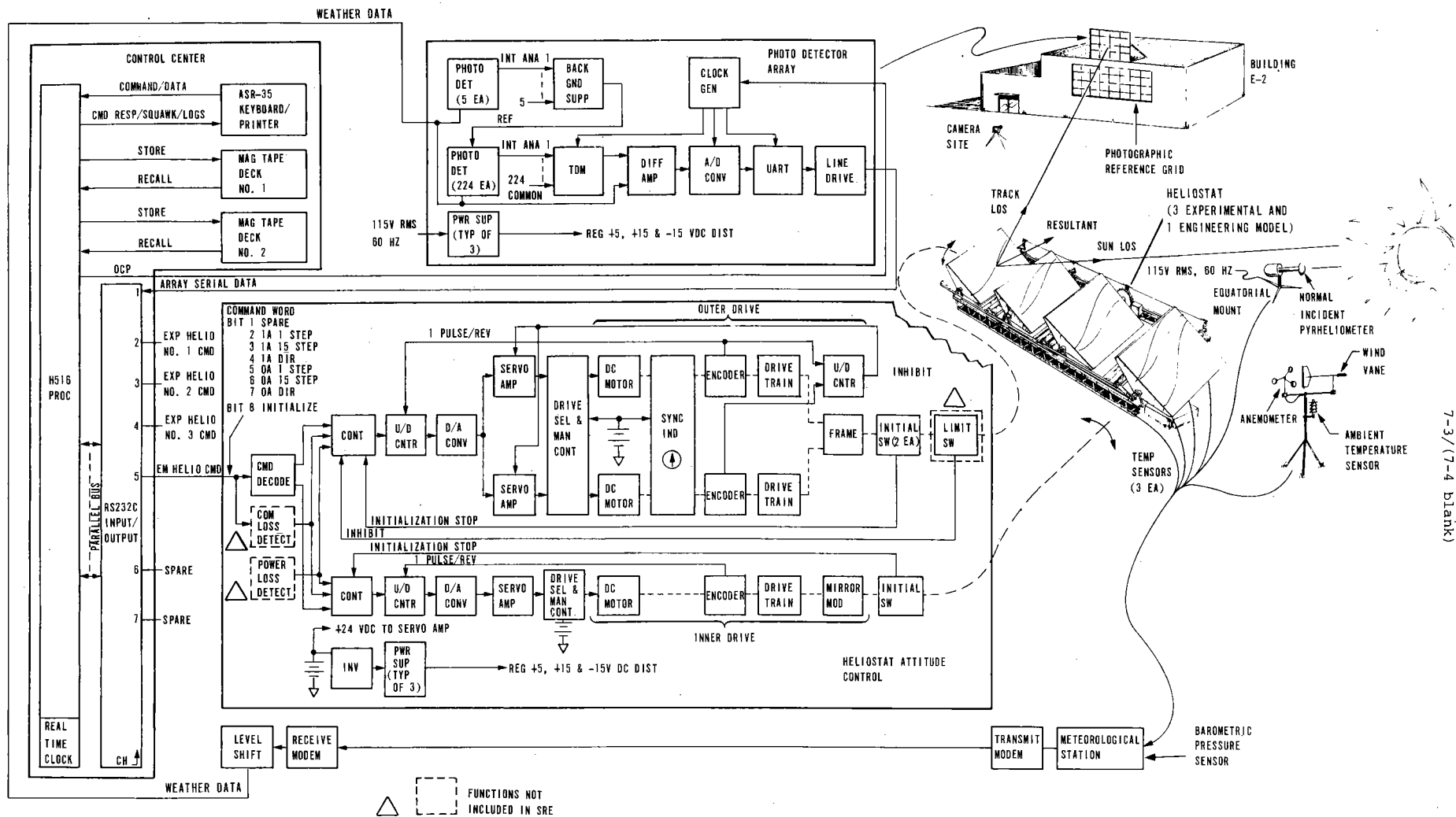
Two 7-Track Magnetic Tape Units (Honeywell Model 10C)

Operational programs are loaded into core, and data (raw and calculated) is dumped for permanent storage and/or subsequent off-line processing. Most data is recorded at 800 bpi. The following data is recorded:

- Time of Day, GMT Days, Hours, Minutes, and Seconds.
- Operational mode of each heliostat (4).
- Base, height, and AZ to target for each primary and secondary target associated with each heliostat.
- Inner gimbal angle of each heliostat.
- Outer gimbal angle of each heliostat.
- Outer drive screw length of each heliostat.
- Three direction cosines for each heliostat associated with its primary target.
- Three direction cosines for each heliostat associated with its secondary target.
- Sun's AZ, elevation, and refraction correction.
- Vertical and horizontal location of the centroid of the redirection image upon the photocell array.
- 224 photocell readings from the array.
- Five background sensor readings used to compensate the calibration array for background radiation levels.
- One background average reading.
- Ten weather channels of information to include wind, temperature, pressure, and global, normal incident, and single photocell solar radiation levels.

One ASR-35

Site parameters and variable scale factors are loaded into the program from the ASR. Also, options within the software are controlled



7-3/(7-4 Blank)

Figure 7-1. Research Experiment Collector Subsection Functional Diagram

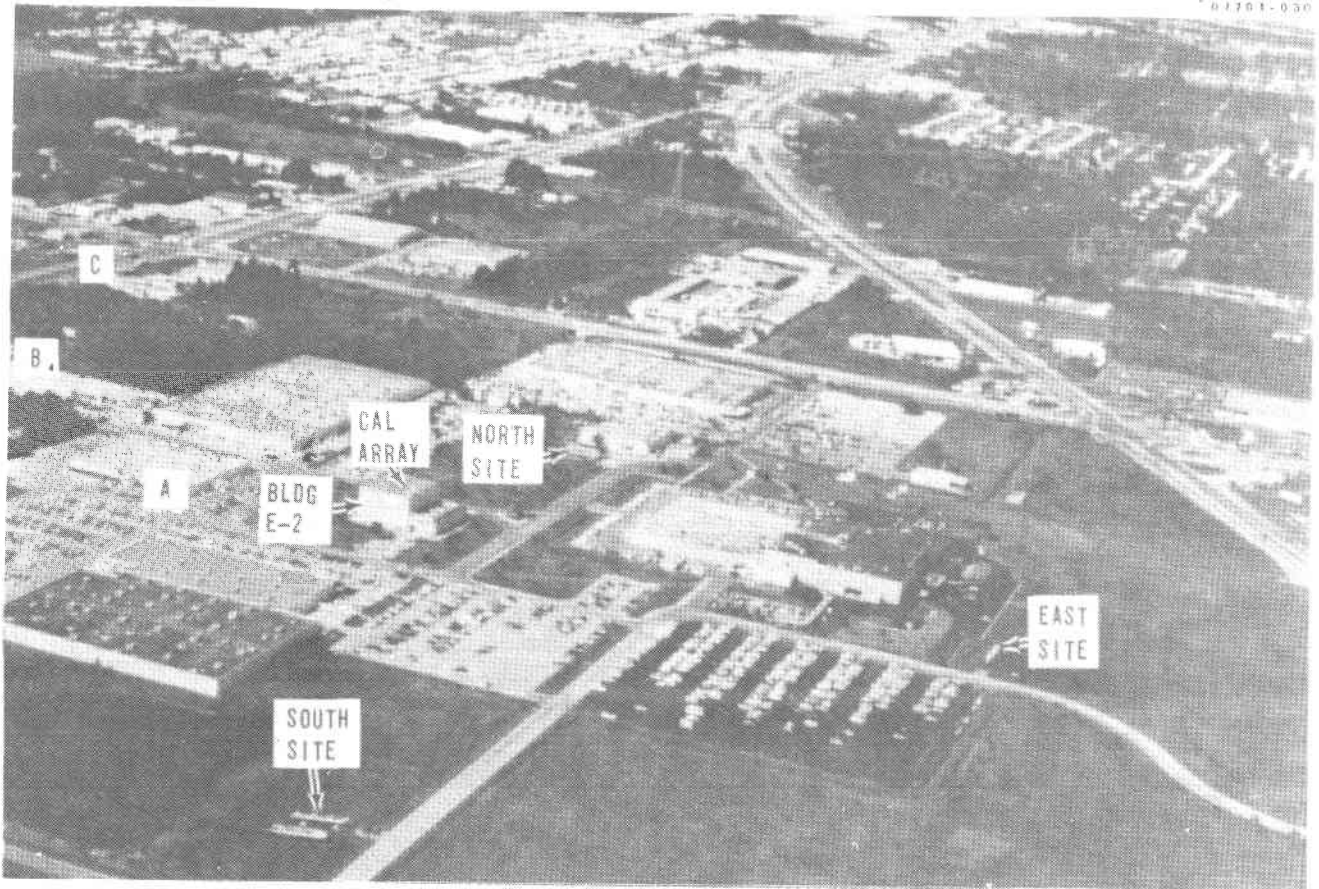


Figure 7-2. Aerial Photograph, Honeywell Complex

SPECIAL EQUIPMENT
ALL ELSE IS STANDARD
COMMERCIAL COMPUTER

A7701-044



Figure 7-3. SRE Computer Facility

via the ASR. During normal operation, all data associated with each heliostat, time of day, calibration array data, and all weather information can be printed on-line once per minute. Figure 7-4 demonstrates sample output during operation.

Special RS232C Interface Box

Special RS232C interface box is used for input/output conversions and data formatting for commands to the heliostat and receiving 240 channels of information (229 photocells and 11 weather channels) from the test instrumentation hardware.

0277-070

```

17.41. 3 2 -55.8411 34.5769-170.5050 38.6667 2.30 -2.06
        -2602 1509 51.5000 265.1169 4874
RATIO= 0.0058,ENERGY=402513.,COSSVN= 0.5530 0.0000 0.7454 0.4015
1 1 1 1 1 1 0 224 198 105 21 160 103 18 0 120
17.42. 3 2 -55.9431 34.5121-170.2274 38.6536 1.48 0.26
        -2608 1507 51.5000 265.1165 5102
RATIO= 0.0054,ENERGY=422513.,COSSVN= 0.5537 0.0000 0.7467 0.4025
1 1 1 1 1 1 0 224 195 82 20 165 159 21 0 120
    
```

S

DAYS/HOURS/BINS = 352.7 17.7 42.

```

1 1 1 3 5 5 15 0 23 24 19 15 11 6 3 2
1 1 2 5 12 21 30 30 41 42 35 28 19 12 6 2
1 2 4 10 23 39 54 63 68 63 52 44 30 0 8 3
1 3 3 19 37 58 69 83 88 86 69 55 35 24 11 5
1 4 14 33 50 65 58 55 97 95 76 61 41 25 9 5
2 6 18 37 51 59 87 101 92 94 75 62 42 26 13 5
3 7 19 33 47 69 82 92 0 89 33 47 37 23 10 5
2 7 17 30 0 58 71 79 63 73 57 27 28 17 7 3
2 6 13 23 18 41 52 62 63 49 34 25 19 11 5 2
2 4 8 15 24 27 33 36 35 27 20 15 7 5 3 1
2 3 5 9 11 15 17 12 14 11 9 7 5 3 2 1
1 2 0 5 6 7 7 6 5 5 4 3 2 2 1 1
0 1 2 2 2 3 3 2 2 2 1 0 1 1 1 1
0 1 1 1 2 2 1 1 1 1 1 1 1 1 1 1
    
```

DELVER= 1.48 DELHOR= 0.26 CALSUM= 5102
AZSUM= -175.464 HELSUM= 38.669

```

17.44. 3 2 -50.2855 34.7110-175.4377 38.6070 1.50 -0.15
        -2684 1551 51.5000 265.1165 5112
RATIO= 0.0055,ENERGY=420017.,COSSVN= 0.5542 0.0000 0.7505 0.4058
1 1 1 1 1 1 0 224 200 131 22 160 150 21 0 120
17.45. 3 2 -50.3312 34.6670-175.0759 38.5977 -0.30 1.59
        -2687 1550 51.5000 265.1165 5150
RATIO= 0.0056,ENERGY=435053.,COSSVN= 0.5543 0.0000 0.7510 0.4064
1 1 1 1 1 1 0 224 200 131 22 160 150 21 0 120
17.46. 3 2 -50.3820 34.6747-175.1157 38.5970 -0.04 -0.02
        -2688 1550 51.5000 265.1165 5218
RATIO= 0.0056,ENERGY=437147.,COSSVN= 0.5544 0.0000 0.7510 0.4065
1 1 1 1 1 1 0 224 200 131 22 160 150 21 0 120 S
    
```

Figure 7-4. ASR Output

DESCRIPTION OF FIGURE 7-4

The preceding ASR output was obtained while the three experimental heliostats were under simultaneous operational control. Data printed is that associated with the East heliostat, even though on-line data associated with all four heliostats can be obtained.

From left to right for each minute.

Line 1:	GMT (Hr/Min)	H/S #	Mode of H/S	Outer Axis Angle	Inner Axis Angle	Sun AZ	Sun Elev	Vertical Location of Centroid	Horizontal Location of Centroid
Line 2:	Integer Outer Axis Commands Accumulated	Integer Inner Axis Commands Accumulated	Height of Target	AZ of Target	Sum of All Photocell Readings				
Line 3:	Ratio of Pyroheliometer to Photocell Reading	Energy Delivered to Target	Percent of Mirror Normal to Sun H/S #1, H/S #2, H/S #3, H/S #4						
Line 4:	Digital representation of 16 channels of background and weather information								

The printout in the center of Figure 7-4 is an optional display of each of the 224 photocells on the 16 foot by 14 foot calibration array.

Figure 7-4. ASR Output (Continued)

Software

A listing of the present version of the operational program (TRACKO) is given in Appendix E. It is coded primarily in FORTRAN for the DDP 516 with interspersed assembly language to handle the high input data rates (240 channels in 400 milliseconds) and to issue the formatted commands to each heliostat. See Page E-1 for a listing of changes made during the conduct of the test program.

The program allows changing site parameter and scale factors from the ASR and initialization of time with respect to actual GMT. It computes the actual apparent sun position, all direction cosines of heliostats to targets, computes the required inner and outer axis angles in order to redirect the sun's radiation, and sends integer

pulses (8 bit command) to each heliostat to obtain the required orientation. Mode control is also under ASR control:

<u>Mode</u>	<u>Condition</u>
1	Calibrate (close loop)
2	Track open loop Primary target
3	Track open loop Secondary target
4	Point at Secondary target
5	Stow (in Home) position
6	Go to initialization position

Various output options to the ASR and magnitude are under program control-- as directed from the ASR. Once per minute, the program samples the calibration array and weather channels, computes the image centroid, calculates energy related information and controls output to mag tape.

The present program sends update commands to each heliostat as often as once per 2 seconds or whenever needed to track within a one-bit resolution (nominally 80 arc-seconds).

Heliostats

Four heliostats were built and tested under the SRE: one mobile engineering model and three fixed site experimental models. Each is separately connected by underground cabling to the RS232 parallel/serial I/O box. Telephone quality, shielded twisted pair cabling is used.

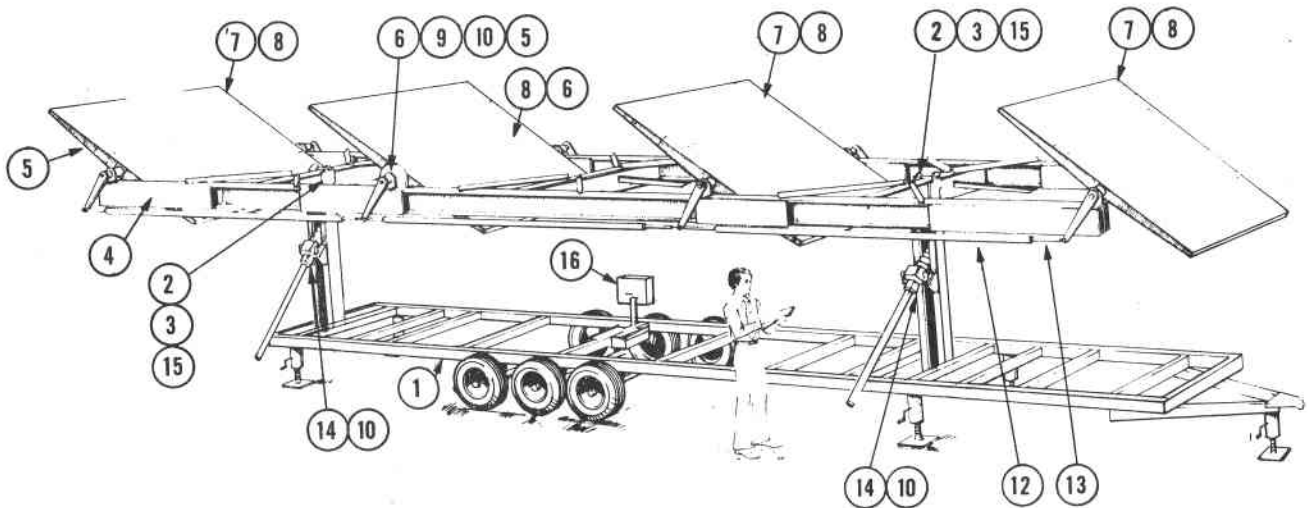
Engineering Model

Figure 7-5 shows a drawing of the trailer-mounted Engineering model. Mirror modules are 125 x 125 inches (3.18 meters) or 10.08 M² for a total reflected area of 40.3 M². The modules used were tapered aluminum honeycomb and tapered foam filled modules.

No initialization hardware is incorporated into the engineering model. Otherwise its characteristics are very nearly the same as described for the experimental model below. Figure 7-6 shows the engineering model in its stowed (safed) configuration. The outer axis is considered to be 0 degree and the inner axis is at 180 degree rotation. Figure 7-7 shows the engineering model in a tracking orientation.

Experimental Model

Three experimental models were built and installed onto 181 kg (400 pounds) U-channel posts attached to two permanent concrete foundation slabs (3 feet by 5 feet by 1 foot). The center line of



- | | |
|------------------------------------|--|
| 1. ENGINEERING MODEL TRAILER | 9. GEAR REDUCTION ASSEMBLY (INNER DRIVE) |
| 2. FRAME BEARING ASSEMBLY | 10. MOTOR/ENCODER ASSEMBLY |
| 3. POST SUPPORT ASSEMBLY | 11. CRANK ARM ASSEMBLY |
| 4. REINFORCED FRAME ASSEMBLY | 12. TIE ROD ASSEMBLY |
| 5. MIRROR MODULE BEARING ASSEMBLY | 13. TIE ROD ADJUSTMENT |
| 6. MIRROR MODULE WITH SPUR GEAR | 14. LINEAR ACTUATOR ASSEMBLY (OUTER DRIVE) |
| 7. MIRROR MODULE WITHOUT SPUR GEAR | 15. SHIMS AS REQUIRED |
| 8. REFLECTIVE SURFACE | 16. ELECTRONICS AND CONTROL BOXES |

0576-42B

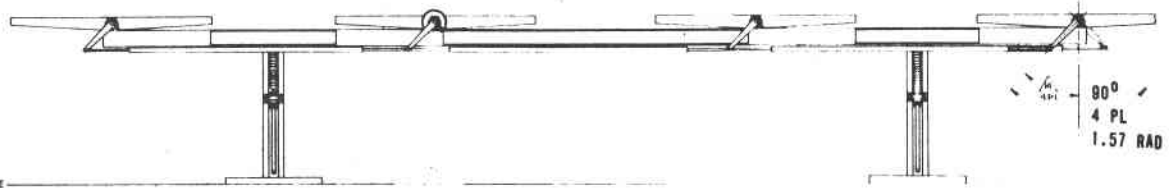
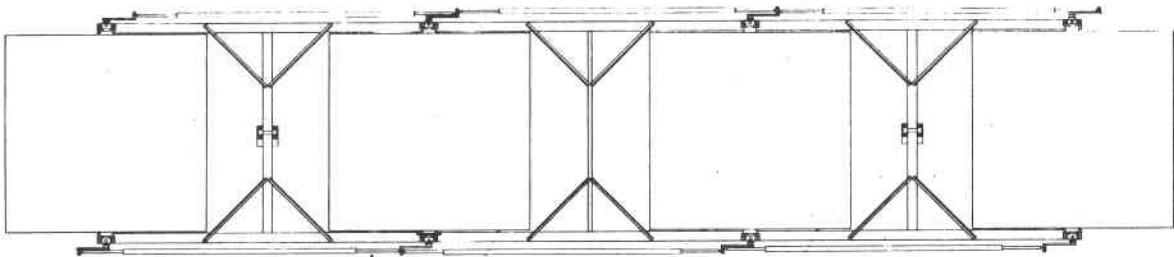


Figure 7-5. Engineering Model Heliostat Assembly and Alignment

A7606-071

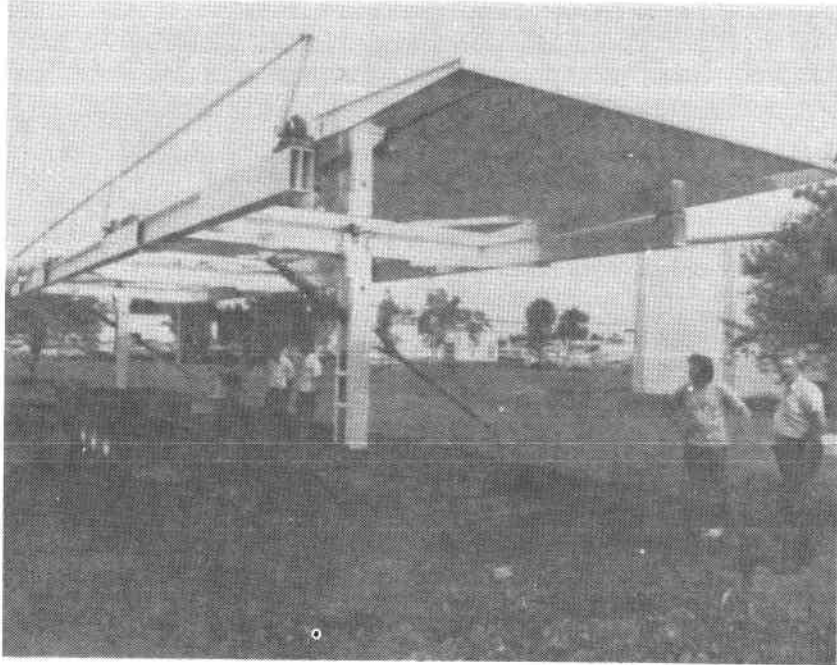


Figure 7-6. Engineering Model in Stowed Position

A7606-75

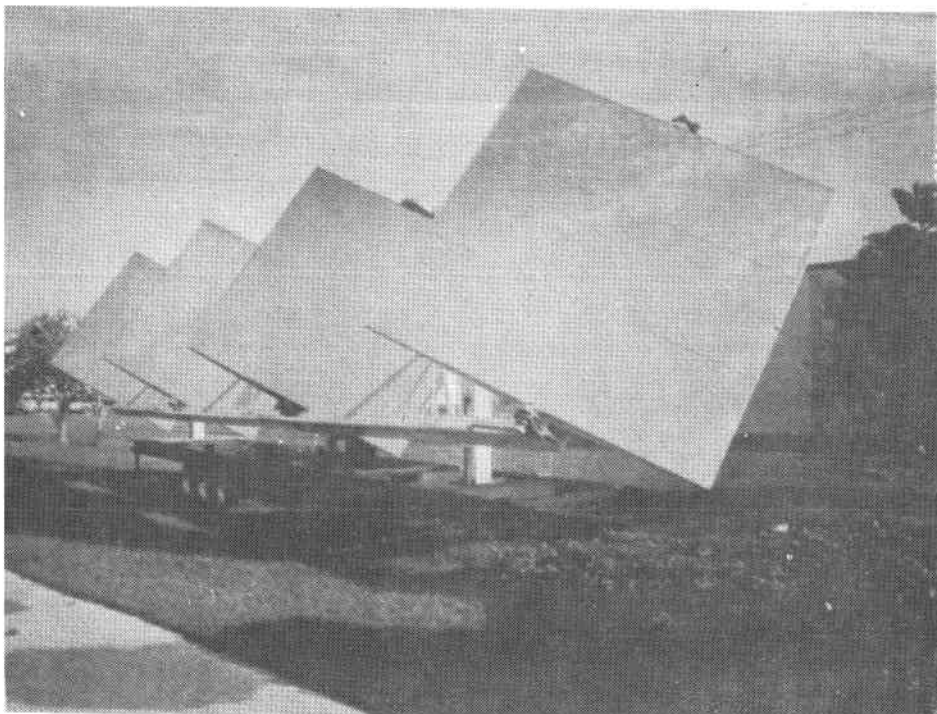


Figure 7-7. Engineering Model Tracking

the frame is mounted approximately 2.3M (7.5 feet) above the foundation top. The four mirror modules are 120 inches by 120 inches (9.3 M² surface area) each.

A summary of its design characteristics is given on Page 3-15. Figure 7-8 shows a line drawing of the Experimental Model and Figure 7-9 shows a photograph of the East site during operation.

Test Support Hardware

In addition to normal general purpose test equipment, a calibration array with the associated electronics and remote weather station was incorporated to greatly enhance data collection for the SRE.

Calibration Array

The calibration array consists of 224 analog photodetectors using TL199 phototransistors mounted on a rectangular grid 4.9 meters (16 feet) wide by 4.3 meters (14 feet) high. Grid line spacing is 0.3 meter (1 foot). The outputs of the photodetectors are fed to a 240 channel analog multiplexer where they are sequentially switched to a common output bus. The analog output of the multiplexer is digitized by an 8-bit analog to digital converter and is outputted in parallel to the Universal Asynchronous Receiver Transmitter (UART). The UART formats the data with start, stop and parity bits and transmits it serially to the heliostat control computer (DD8516) via a line driver and twisted shielded pair. At the computer, another UART receives the serial digital data and converts it back to parallel form where it can be read by the computer at high speed and can be recorded or processed as desired. The entire array is read out by a single command from the computer. All 240 channels are read within 400 ms. This raw digital data can now be used for on-line processing or dumped onto magnetic tape for off-line processing.

Figure 7-10 shows the calibration array on the roof of Building E-2 with a redirected image from the Engineering Model (27 September 1976). The array can be manually repositioned to face any direction. Figure 7-11 is a photograph of the back side of the array showing the supports and multiplexer electronics box.

Five additional photodetectors are set off to the side of the array, spread from approximately 20 feet to 32 feet, and are used to provide a measure of the background radiation from the direction in which the array is facing. The outputs of these detectors are averaged, inverted, and summed with the outputs of each of the 224 array elements to suppress background and enhance the signal to background ratio. The five background detectors along with the average level signal are multiplexed into the 240 channels of digital data.

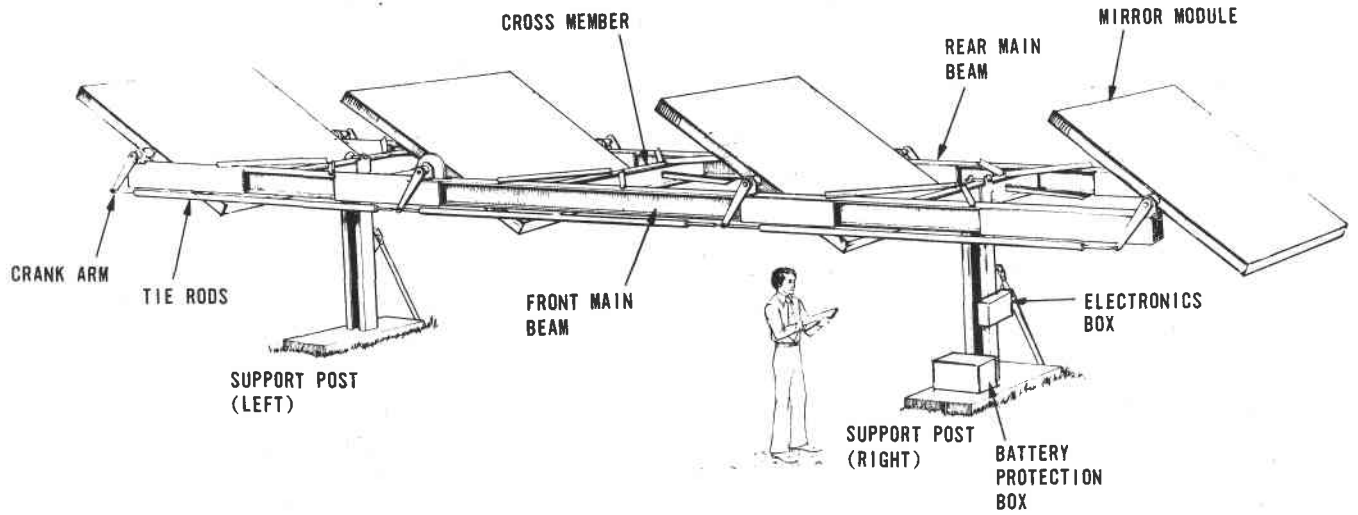


Figure 7-8. Experimental Model Heliostat Assembly

A7701-022

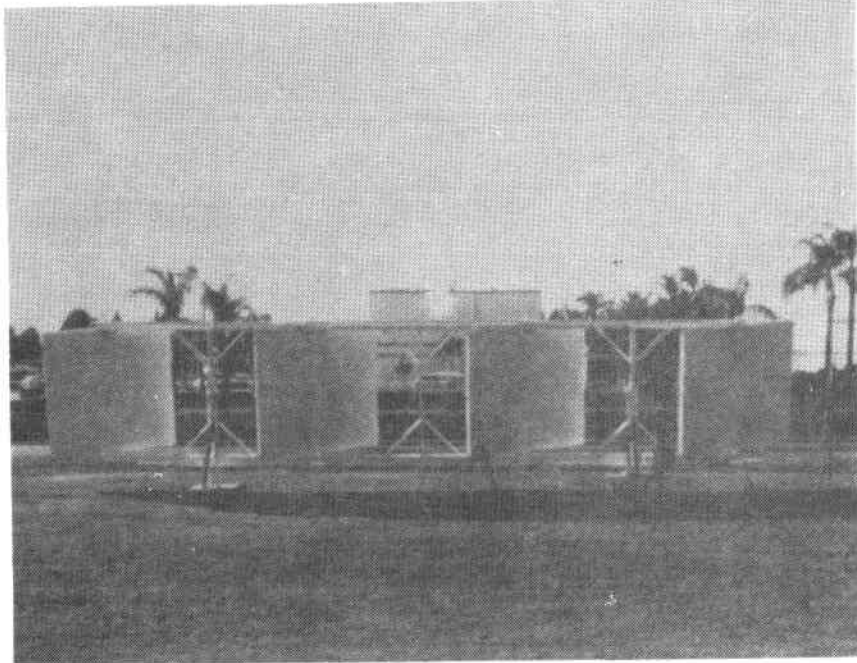


Figure 7-9. East Experimental Model During Operation
12/17/76, 1930 GMT

PHOTO DETECTORS ARE
AT 1 FT GRID INTERVALS

A7701-023

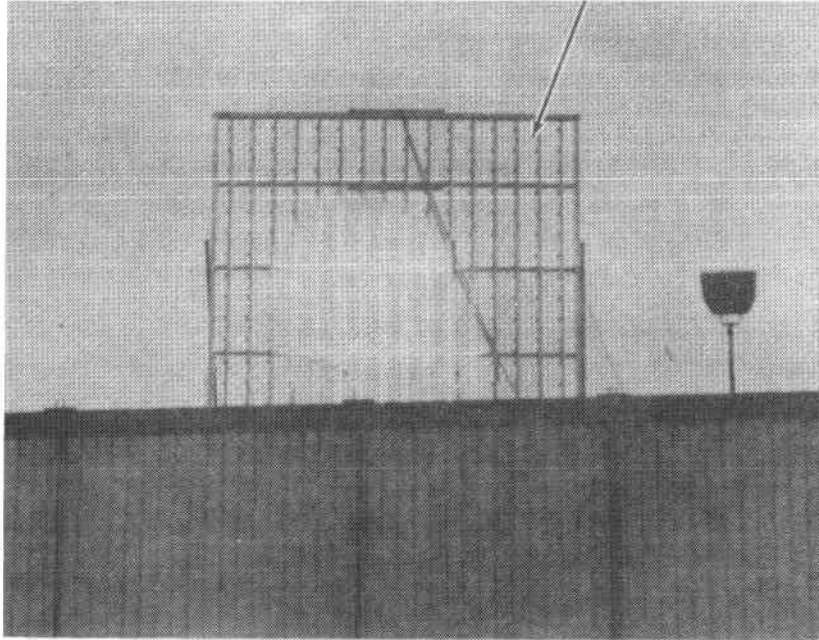
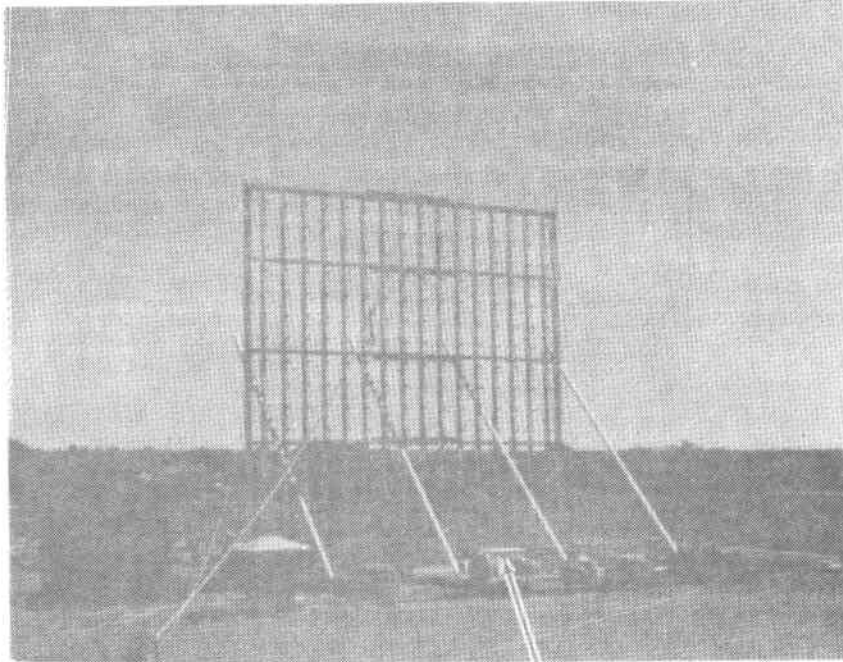


Figure 7-10. Calibration Array Facing North,
9/27/76, Engineering Model Image

A7701-036



MULTIPLEXER

Figure 7-11. Backview of Calibration Array

Since the detector outputs are analog levels of incident insolation power, information on size, shape and intensity are contained in a sampled data block. The weighted geometric (or energy) centroid, radius of gyration, etc., can be calculated with respect to the center of the fixed grid spacing and, thus, drift rates and disturbances can be detected along with total intensities.

Weather Data

A Climatronics 470 weather station and some hardwired instrumentation occupies the remaining 10 channels of the 240 channel multiplexed data into the computer. A normal incident pyroheliometer which continually tracks the sun, a photodetector identical to those used on the array which track the sun with the same field of view as the pyrhelemeter, and a global pyranometer to measure total insolation are hardwired into the multiplexer from the roof of E-2.

The weather station obtains wind speed, wind direction, barometric pressure, and temperatures from any selected heliostat site and provides input via twisted pair shielded cable to the multiplexer.

Figure 7-12 shows the 17 foot wind tower and encoder/transmitter station that also contains the translator cards.

This weather station hardware was operational only during a relatively small period of time covered by the SRE.

Figure 7-13 provides a block diagram of the total automated data collection system.

TEST APPROACH

Basically the SRE Test Program involved the design, build, and test of four heliostats in order to demonstrate specification performance. Component level and system level testing was performed to help determine the validity of the estimated error budget contributions to the 2 mr, one sigma, pointing error.

From testing considerations, the following chronological time sequence depicts some of the more significant milestones.

<u>Date (1976)</u>	<u>Event</u>
2 March	Plywood Mirror Module (MM) available for evaluation.
15 April	Variable focus MM available for evaluation. Calibration array operational.
30 April	First software available to: <ul style="list-style-type: none"> (a) display calibration array on ASR (b) open loop track up to 4 H/S Trailer for engineering model arrived.

A7701-042



WEATHER
STATION
BOX

Figure 7-12. Weather Tower At
Experimental Model Heliostat

0277-088

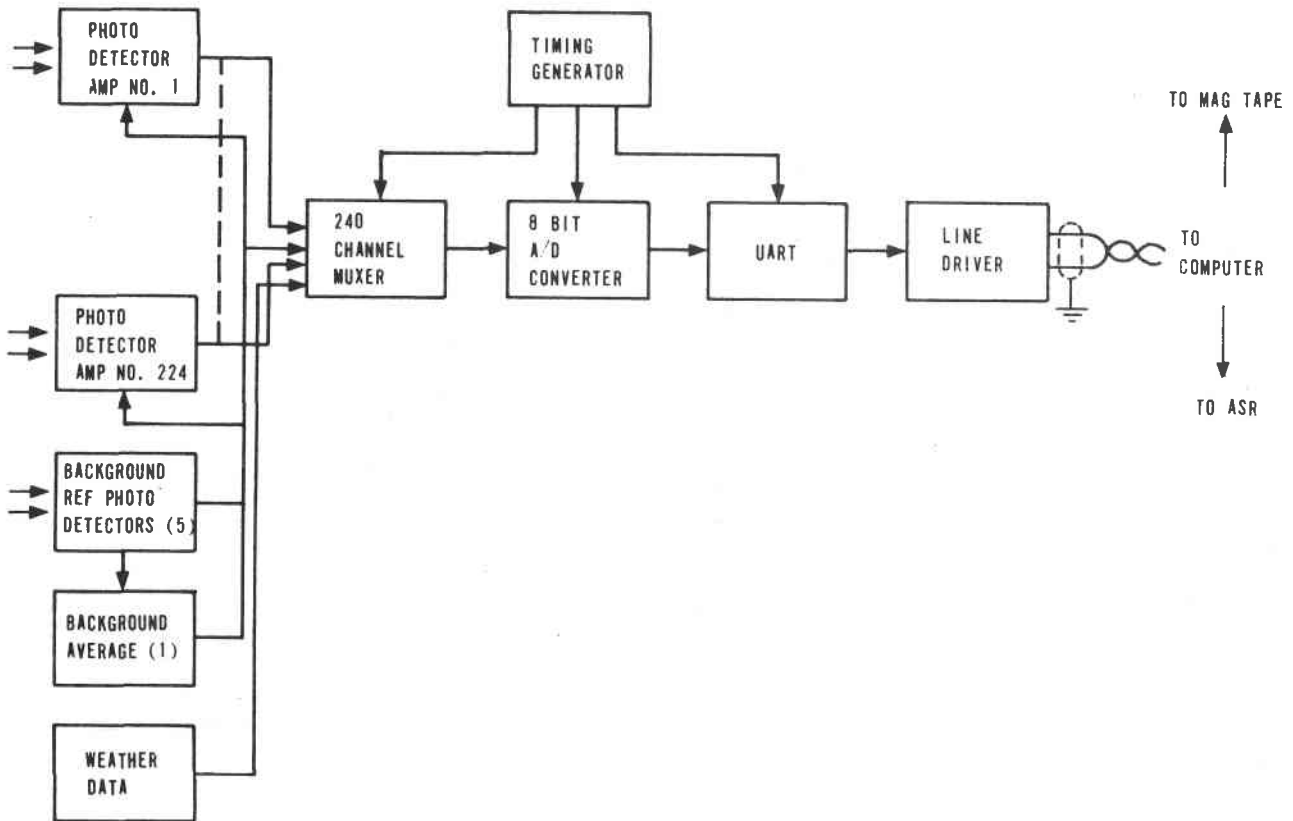


Figure 7-13. Data Collection System

<u>Date (1976)</u>	<u>Event</u>
6 May	Frame for engineering model arrived.
11 May	2 Parsons, aluminum honeycomb tapered MM available.
18 May	Detailed Design Review
25 May	Moved engineering model H/S to North site and started alignment, component testing, etc.
2 June	Started testing 2 Brunswick, foam filled tapered MM - performed component tests and load tests from this time till 7 October on engineering model.
21 June	Collected photographic images of manually controlled heliostat during summer solstice.
19 July	Started recording via strip chart global and normal incident radiation.
8 August	Software and hardware completed and compatibility established. Entered open loop track for first time.
10 August	Lightning struck near heliostat.
11 August	Technical Coordination Meeting with ERDA.
12 August	Tornado fringe struck Honeywell complex.
18 August	Three experimental model frames placed on permanent posts.
15 October	14 new 9-inch thick rectangular honeycomb Parsons MM arrived.
25 October	South Experimental Model operable under DCU control.
26 October	North site operable.
5 November	East site operable.
28 December	Last data obtained.

NOTE

Most testing was curtailed 17 December 1976.

As the testing effort progressed, information and performance data obtained dictated additional design changes, and highlighted the need for additional testing, as well as numerous software improvements both in needed corrections and in increased operator flexibility.

COMPONENT AND SUBASSEMBLY LEVEL TESTING

The paragraphs herein summarize test results obtained from component level (e.g., motors) and subassembly level (e.g., mirror module) level testing performed under the SRE contract.

Mirror Modules

The key to the concept of central solar energy is the reflective surface and its control. Ironically, we found that the actual mirrored surface is less than 2 percent of the total cost of the heliostat. The remainder comes from the structural rigidity and pointing accuracy requirements.

To gain some hands-on experience with mirror modules, a plywood model was fabricated in February 1976 and evaluations were made. Also, a variable contour mirror module was built and some evaluation made. Subsequently, two tapered aluminum honeycomb and two tapered foam-filled modules were delivered from Parsons and Brunswick, respectively, for utilization on the engineering model heliostat in May and June 1976. In October 1976, 14 additional rectangular aluminum honeycomb modules were delivered from Parsons. Some evaluation on other potential materials has been performed under internal development funds.

Table 7-1 gives an overall test data summary of all mirror modules. The specification contour for each is 339M (1112 ft) focal length or 678M spherical radius with no more deviation than 0.001 inch/inch slope variation and no absolute error of 0.062 inch within 60 inch radius. Maximum rotation of the mirror module (MM) including shaft torsion is specified as 1 mr.

Both optical techniques and measuring height with respect to a taut piano wire were used in determining mirror contour as described within subsequent paragraphs.

Shaft loads and edge loads, to determine torsional rotation under simulated aerodynamic induced moments, were used to determine the rotation of a mirror module. These techniques are described on Page 7-31 and applied to potential candidates for operational heliostats.

One problem continued to recur during mirror module load testing and it appeared on a few occasions with the mirrors mounted on the heliostat. Initially, the taper locks, which attach the crank arm assembly

Table 7-1. Engineering Model Mirror Module Test Data Summary

Parameter	Mirror Module						Rectangular	
	Plywood MM1	MM2	MM3P (SN P01)	Parson's MM3P (SN P05)	Brunswick 3B-001	Brunswick 3B-002	Parson's SN001	Parson's SN005
Focal Length	<1000 ft overall 500-600 ft along axle >1000 ft normal to axle	Variable	Close to nominal 1112 ft	Close to nominal 1112 ft	Poor	Poor	Close to nominal 1112 ft	
Redirected Image Shape	Per analytical model as modified by con- tour deviation	Per analytical Model	Per analytical Model	TBD	Scattered	Scattered	Per analytical Model	
Contour Deviation					Poor	Poor		
Manufacturing Accuracy and Short Term Aging (Spec: 0.001 in./in. max 0.062 in. within 60 in. radius)	2 to 1 deviation after 2 month natural environment exposure	0.021 in. max deviation (9 data points)	0.015 in. max deviation (52 data points)	.035 in. max deviation (52 data points)	0.124 out of 24 data points	0.050 out of 24 data points	0.010 max deviation. Did not exceed 0.001 inch/inch	
*G-Sensitivity (Spec: none)	No data	Not used	NA	NA	--	--		
*Wind Sensitivity (Simulated load) (Spec: none)	No data - mirror fractured while attemptin measurement	Not used	0.008 in. max deviation at 2 lbs/sq ft and not to full solar load (22 data points)	Not performed	0.045 in. max deviation	NA	0.004 inch max deviation at 2 lbs/sq ft	
*Solar Load Sensitivity *Sum Total of Environ- mental Condition Not to Exceed an Additional 0.001 in./in.	>0.030 in.	Not used	See wind sensitivity	0.006 in. max deviation partial to full solar load (11 data points)	Not performed	NA		
Weight	842 lbs	1125 lbs	665 lbs (500 lbs design goal)	698 lbs (500 lbs design goal)	690 lbs	690 lbs	690 lbs (at vendor only)	
Edge Load (Spec: 0.5 mr)	NA	NA	0.39 mr at 7500 in./lbs	Not tested	NA	NA	0.24 mr at 7500 in./lbs	
Crank Arm Load (Spec: 1.0 mr)	NA	NA	0.70 mr at 7500 in./lbs	Not tested	11.7 mr at 7896 in./lbs resulted in permanet de- formation of ≈30 arc-min	NA	0.80 mr at 7500 in./lbs	
Imbalance (Spec: 3175 to 1625 in./lb)			+1129 in./lb	+1129 in./lb	+1303 in./lbs	+1241 in./lbs	Not tested	

to the mirror module stub shafts, were torqued to 150 ft-lb. During torsion testing they would slip, thereby, negating that test. The torque was increased to 200 ft-lb on all taper locks. There was one additional slippage during testing and two slippages on the heliostats. The problems were found to be:

1. Rust or dirt forming on the steel taper locks not allowing insertion of the shaft into the taper lock.
2. Scoring of the aluminum shaft.

Solutions were found to be:

1. Completely clean all taper locks before coupling.
2. Torque locks to 225 ft-lb.
3. Use steel shafts (to be incorporated in future designs).

Plywood Mirror Module (MM1)

A plywood MM was constructed February 1976 with a theoretical focal length of 339M (1112 ft). Figure 7-14 shows the structural foundation and contour being formed with plywood; masonite was used as the covering skin; mirror modules were glued to the skin; and the complete structure was painted with epoxy based paint for protection.

Figures 7-15, 7-16 and 7-17 show measured contour points superimposed upon the nominal contour. All measurements were taken with a height gauge being viewed by a theodolite which remained in a shaded area. Figure 7-18 shows a typical contour measurement being taken. Figures 7-19 and 7-20 show MM1 under test and a detail of the diffused image (approximately 14 ft x 17 ft) from the 10 ft x 10 ft mirror module.

Numerous data samples, with photographs, were taken-- some with partial blockage of selected facets. However, the main benefit was obtaining experience in measuring, building, and handling techniques. Figure 7-21 shows surface degradation due to cracks developing as of early May 1976, 2 months after build completion. Environmental exposure was continuous. There were two causes:

1. A non-white tarpaulin was used to cover and protect the MM while not being used. Over the weekend of 24 April 1976, temperatures (estimated less than 150°F) reached by the glass surface caused some cracking due to thermal gradients introduced at the bond-line.

From this point on, either no cover protection was used on any mirror modules except for selected tests, and then a reflective white cover was used.

A7602-058

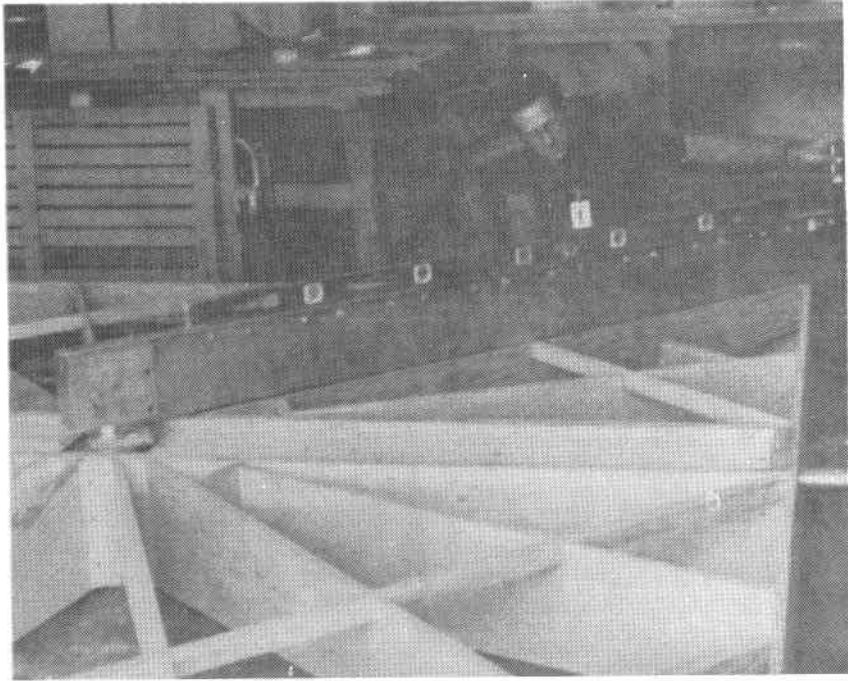


Figure 7-14. Plywood Mirror Module Construction

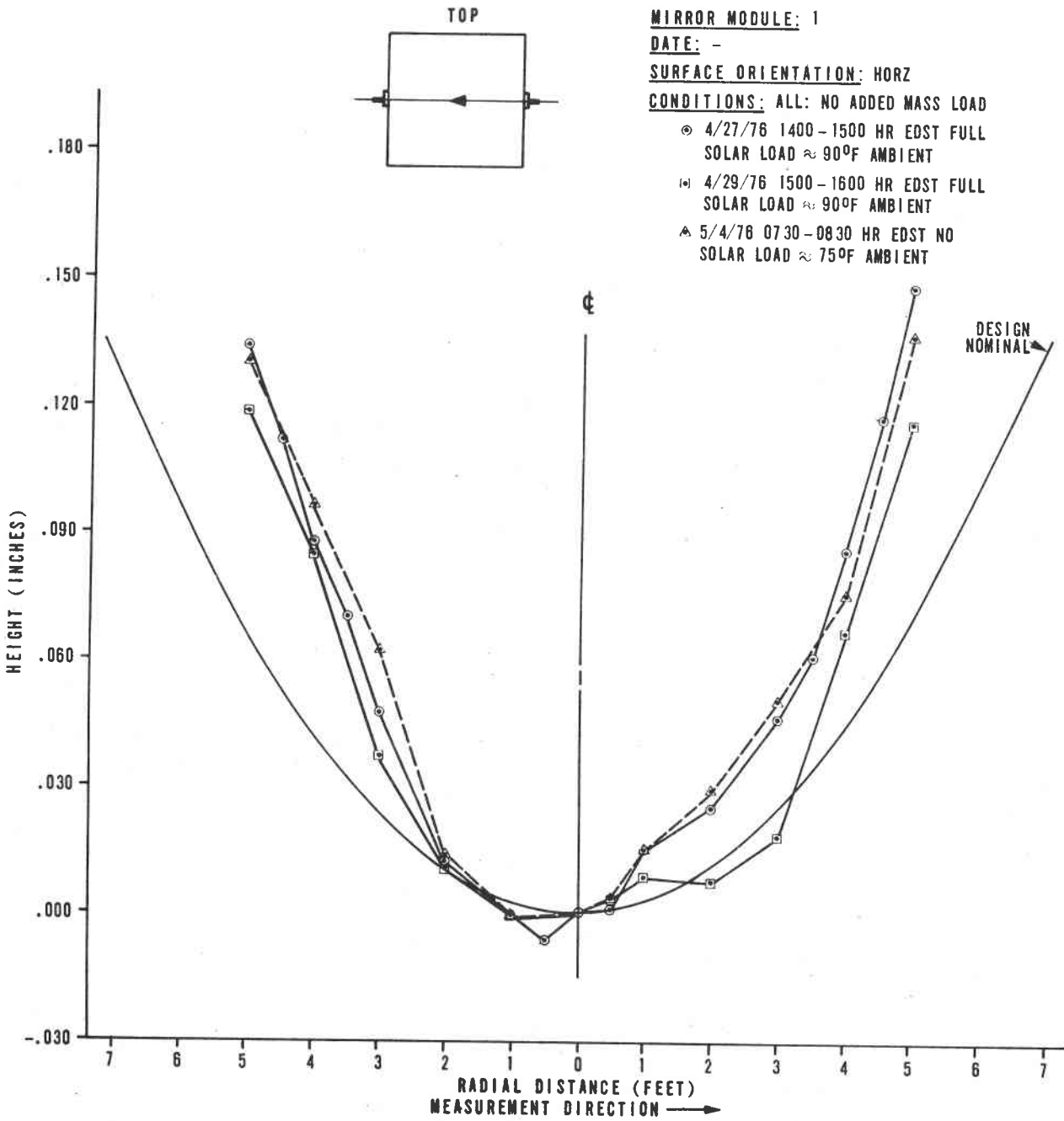


Figure 7-15. Contour Data Plywood Data

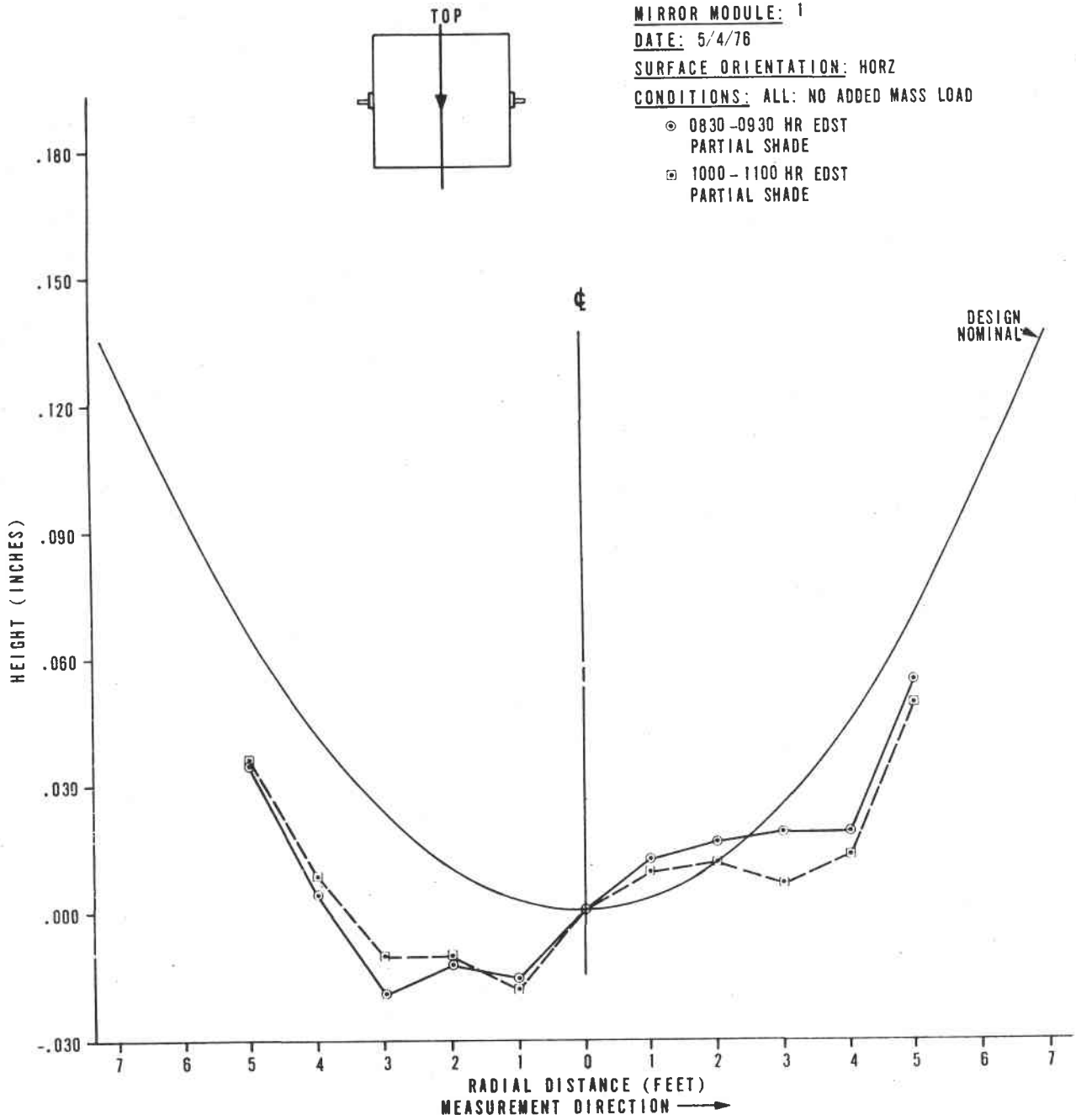


Figure 7-16. Contour Data Plywood MM

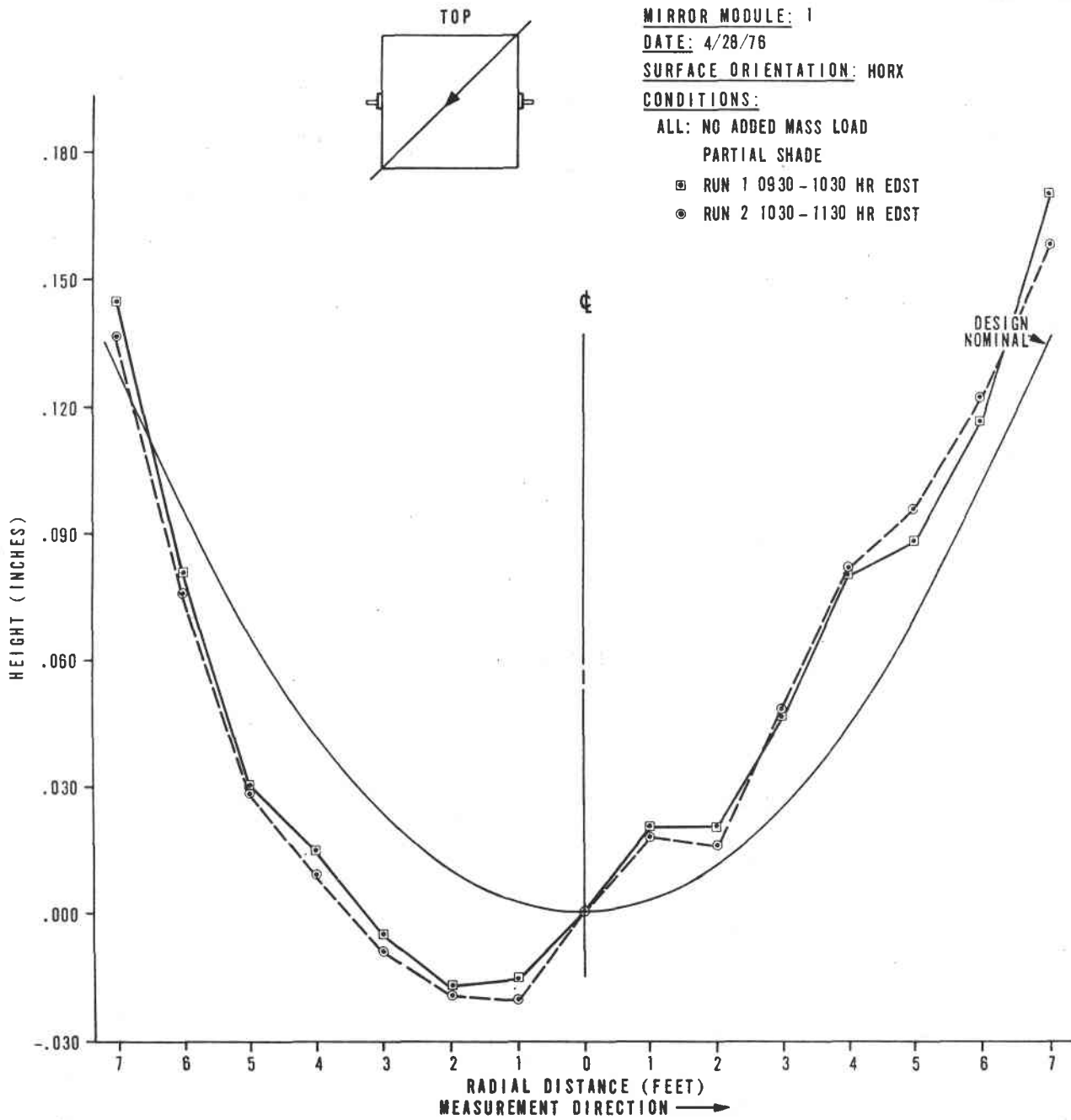


Figure 7-17. Contour Data Plywood MM

LADDER SPAN USED TO SUPPORT MAN
WHEN WORKING NEAR CENTER OF
10 FT X 10 FT MIRROR MODULE

THEODOLITE SHADED
TO ELIMINATE
SOLAR INDUCED
INSTRUMENTATION
BIAS CHANGES

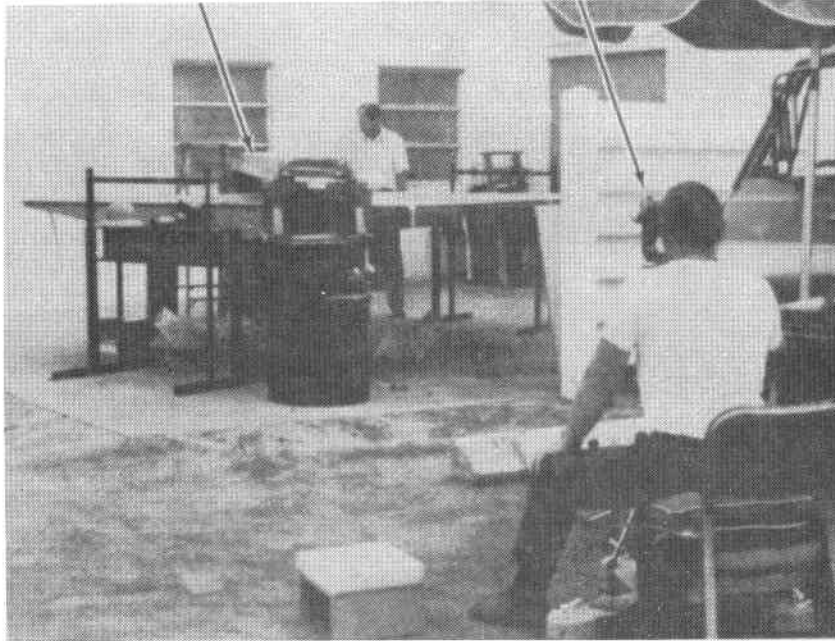


Figure 7-18. Contour Measurements Via Theodolite With Mirror Module Under Solar Loading

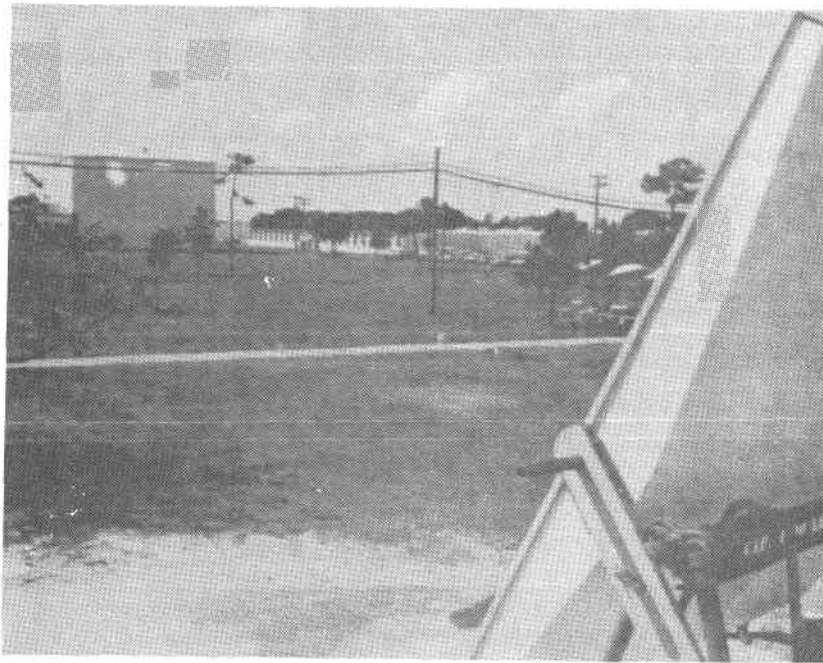


Figure 7-19. Plywood Mirror Module Focused On North Side of Building E-2.

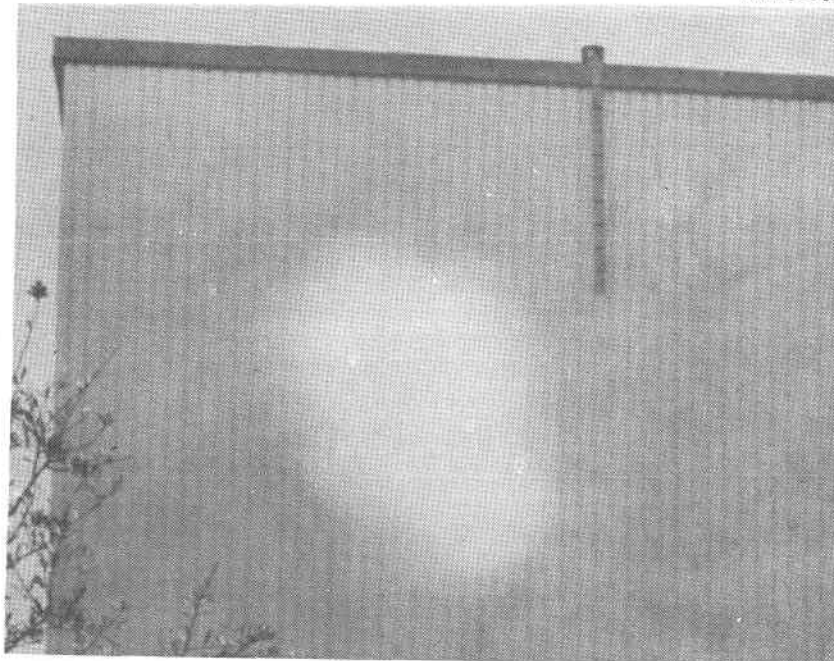


Figure 7-20. Scattered Image From Plywood Mirror Module

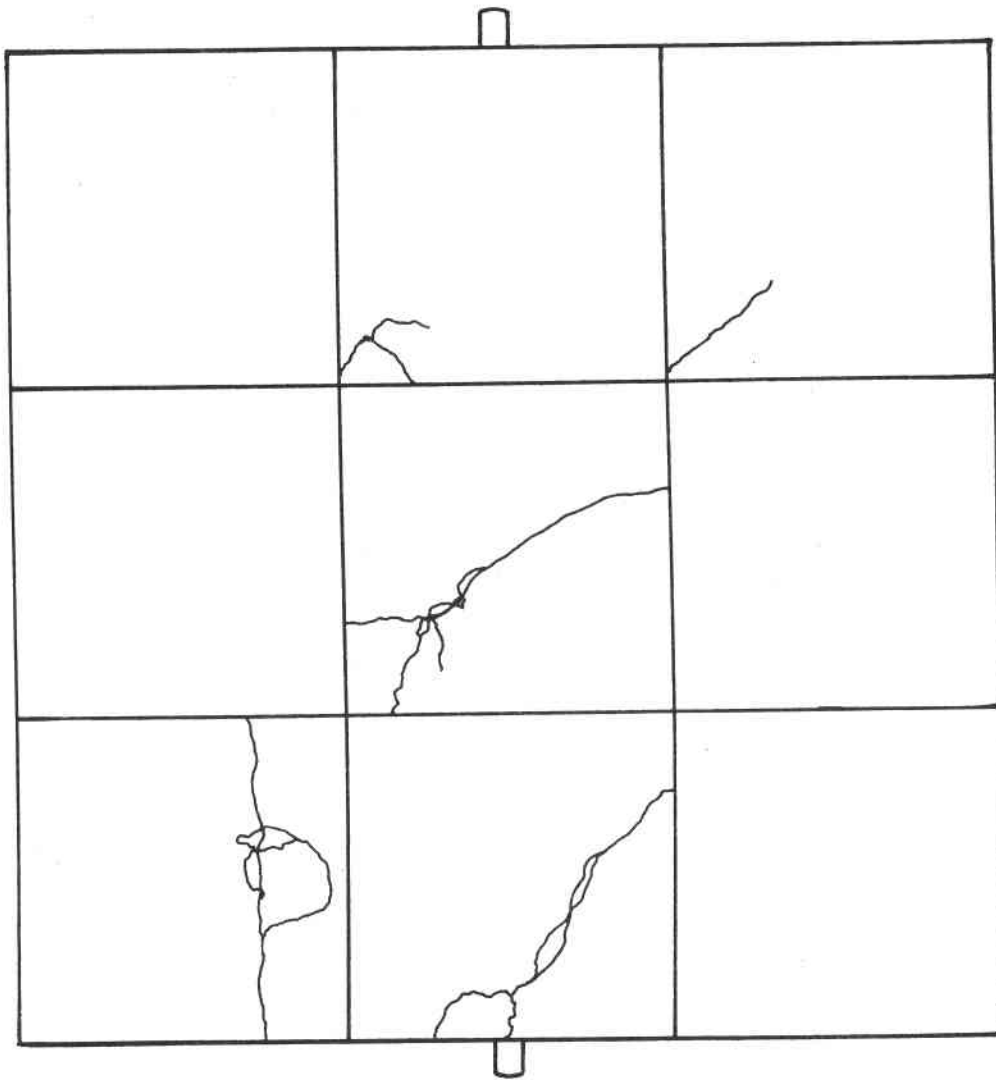


Figure 7-21. Drawing of Cracks Developed in Plywood
MM as of 5/4/76

2. The masonite layer started to degrade. By the end of 1976, degradation (due to moisture and temperature) was bad enough to make the MM completely useless.

Variable Focus Mirror Module (MM2)

A 6-foot square variable focus mirror module was built for additional experience. Figure 7-22 shows the mirror surface which is mounted to circular steel tubing which is in turn welded to a rectangular steel beamed cross structure. The focal length is variable by adjusting a locking nut at the center of the steel tubing, pulling in the center, thereby changing the contour of the mirrored surface.

Initially, the contour would vary under solar loading and 'g' loading due to gaps developing in the mechanical adjustments. Figure 7-23 shows a typical contour measurement demonstrating non-uniformity in control of the contour. Repeatability of measurements was only 0.004 inch from run to run. The weight of the MM itself caused an additional 0.032 inch to 0.036 inch sag from the middle to outer edge from a supported (vertical) to a horizontal position.

Figure 7-24 gives a calibration array intensity map taken on 28 April 1976, in the A.M. with MM2 north of the array. The grids are 1 foot apart in both directions. Notice that there is very little scattering about the nominal 6-foot square redirected image along the principal axis of the image (angle of principal axis is the angle between the mirror normal axis and the sun).

At the center of the image, intensities of a little greater than the equivalent of one sun are reached.

In the latter part of 1976, slippage of locking mechanisms was corrected but no additional testing was conducted because of arrival of the procured engineering model mirror modules in early May 1976.

Foam Filled Mirror Modules (MM3B)

Mirror modules constructed from carved urethane foam appeared to have cost advantages and would be structurally rigid enough with steel skin backing to meet deflection requirements under wind loading. Brunswick Corporation was funded to build two MM to Honeywell drawing 34026575. Figure 7-25 shows the edge profile of the 125 inches x 125 inches (10M²) module. Note that the contoured surface is dished only 0.12 inch from the outer edge. The purpose of the wedge shape was to reduce material costs. Figure 7-26 shows the foam contour being formed by sweeping the contour tool across built-up block sections of foam. Mirrors are glued directly to sheet steel skins bonded to the contoured foam.

At the center of each edge a precision machined 1 inch x 1 inch steel gauging pad is installed. Mirror level and angular settings about the axis are set using these references.

A7604-081

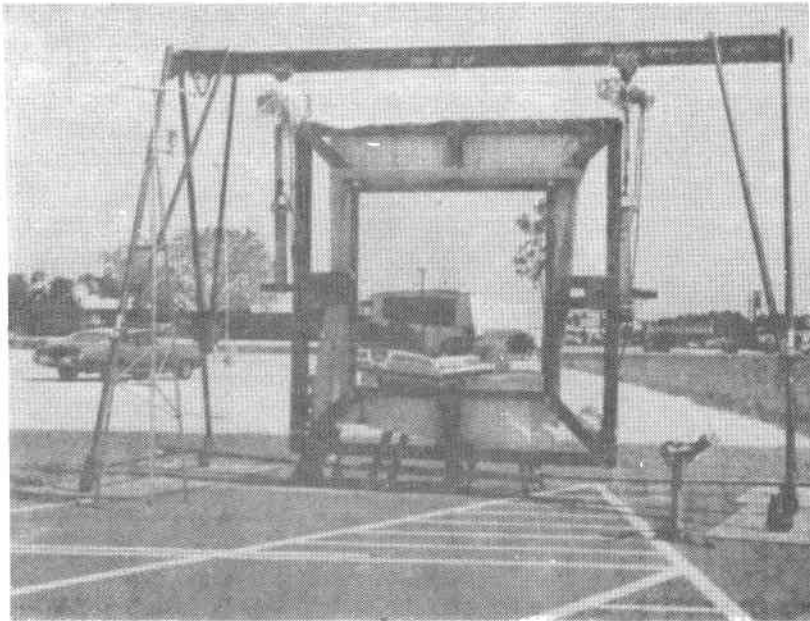


Figure 7-22. Variable Focus Mirror Module Under Test

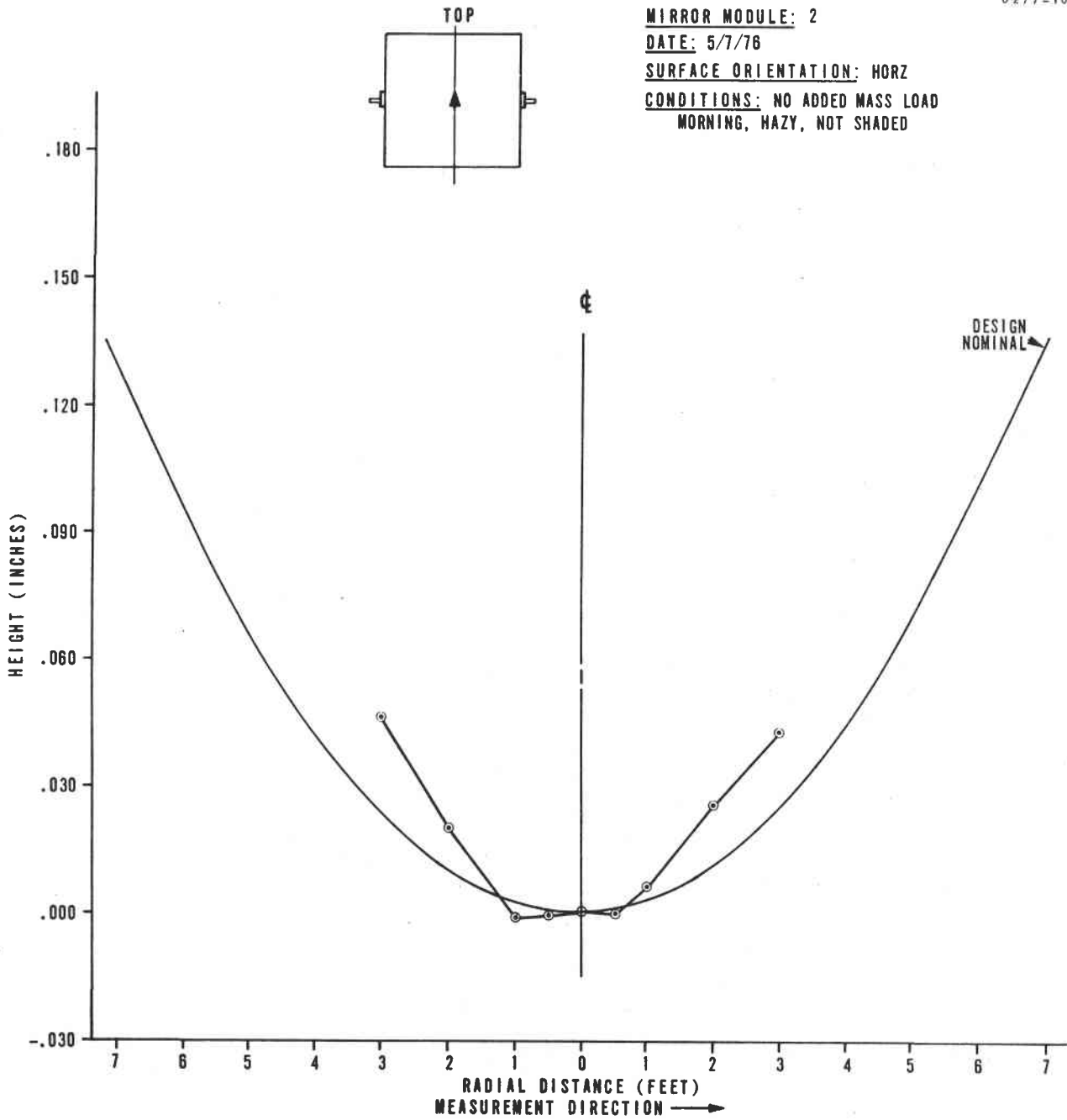


Figure 7-23. MM2 Contour Data

3 3 3 3 3 1 2 3 3 3 3 2 2 3 3
 3 2 3 2 3 3 2 2 3 2 2 3 2 3 3 2
 2 3 3 2 2 3 3 2 2 3 3 3 3 2 2 2
 3 3 1 3 2 2 2 2 3 2 2 3 2 3 3 3
 3 1 3 3 2 3 2 3 3 3 3 3 3 3 2 3
 2 3 3 3 2 3 3 3 2 3 2 2 3 3 3 2
 3 2 3 3 3 4 3 2 2 3 2 1 3 3 2 3
 2 3 3 2 3 3 2 2 3 3 3 2 3 3 2 3
 3 3 3 3 1 3 2 3 2 3 2 3 2 3 3 3
 3 2 3 2 3 2 3 3 3 3 2 3 2 3 3 2
 4 3 2 3 2 3 3 2 2 3 3 2 3 3 3 3
 2 2 3 3 3 3 3 3 2 3 3 3 2 3 2 3
 2 3 3 3 3 3 3 2 2 3 3 3 3 2 3 3
 2 3 3 3 3 3 3 3 3 3 3 2 3 3 3 3

Background Light
 (1 = 0.04 suns)

3 3 3 3 3 2 2 3 3 3 3 3 2 3 3
 3 2 3 2 3 3 2 2 3 2 3 4 4 4 3 2
 2 3 3 2 2 3 3 2 2 4 5 9 10 8 5 2
 3 3 1 3 2 2 2 2 3 4 8 15 16 15 11 5
 3 1 3 3 2 3 2 3 4 7 15 23 24 20 12 5
 2 3 3 3 2 3 3 3 4 9 18 26 27 22 13 4
 3 2 3 3 3 4 3 3 4 10 10 23 24 20 9 4
 2 3 3 2 3 3 2 3 5 10 15 14 18 12 5 3
 3 3 3 3 1 3 2 3 3 7 10 12 10 7 4 3
 3 2 3 2 3 2 3 3 4 5 6 7 4 3 3 2
 4 3 2 3 2 3 3 2 3 3 4 3 3 3 3 3
 2 3 3 3 3 3 3 3 2 3 3 3 2 3 2 3
 2 3 3 3 2 3 3 2 2 3 3 3 3 2 3 3
 2 3 3 3 3 3 3 3 3 3 3 2 3 3 3 3

Redirected Pattern
 Sample 1
 Height 8 ft Width 8 ft

3 3 3 3 3 1 2 3 4 4 4 3 2 2 3 3
 3 2 3 2 3 3 3 3 6 7 7 5 2 3 3 2
 2 3 3 2 2 3 4 6 11 15 13 10 4 2 2 2
 3 3 1 3 2 3 5 11 21 22 18 13 5 3 3 3
 3 1 3 3 2 4 5 16 25 28 22 13 5 3 2 2
 2 3 3 3 3 4 9 18 25 26 20 10 4 3 3 2
 3 2 3 3 3 5 9 15 20 21 8 5 3 3 2 3
 2 3 3 2 3 4 6 11 15 13 9 3 3 3 2 3
 3 3 3 3 1 4 5 7 8 8 4 3 2 3 3 3
 3 2 3 2 3 2 4 4 5 3 2 3 2 3 3 2
 4 3 2 3 2 3 3 2 3 3 3 2 3 3 3 3
 2 3 3 3 3 3 3 3 2 3 3 3 2 3 2 3
 2 3 3 3 3 3 3 2 2 3 3 3 3 2 3 3
 2 3 3 3 3 3 3 3 3 3 3 2 3 3 3 3

Redirected Pattern
 Sample 2
 Height 9 ft Width 7 ft

Figure 7-24. MM2 Beam On Photodetector Array Range:
 Approximately 500 Ft. Date: 4/28/76

0277-071

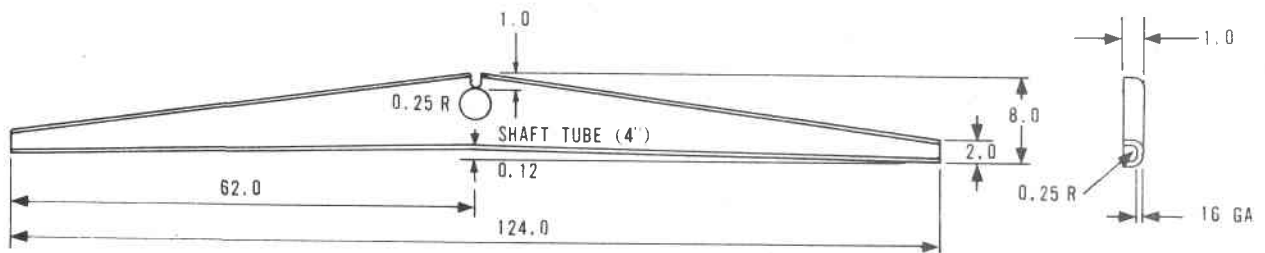


Figure 7-25. Mirror Module MM3B End View

0676-709

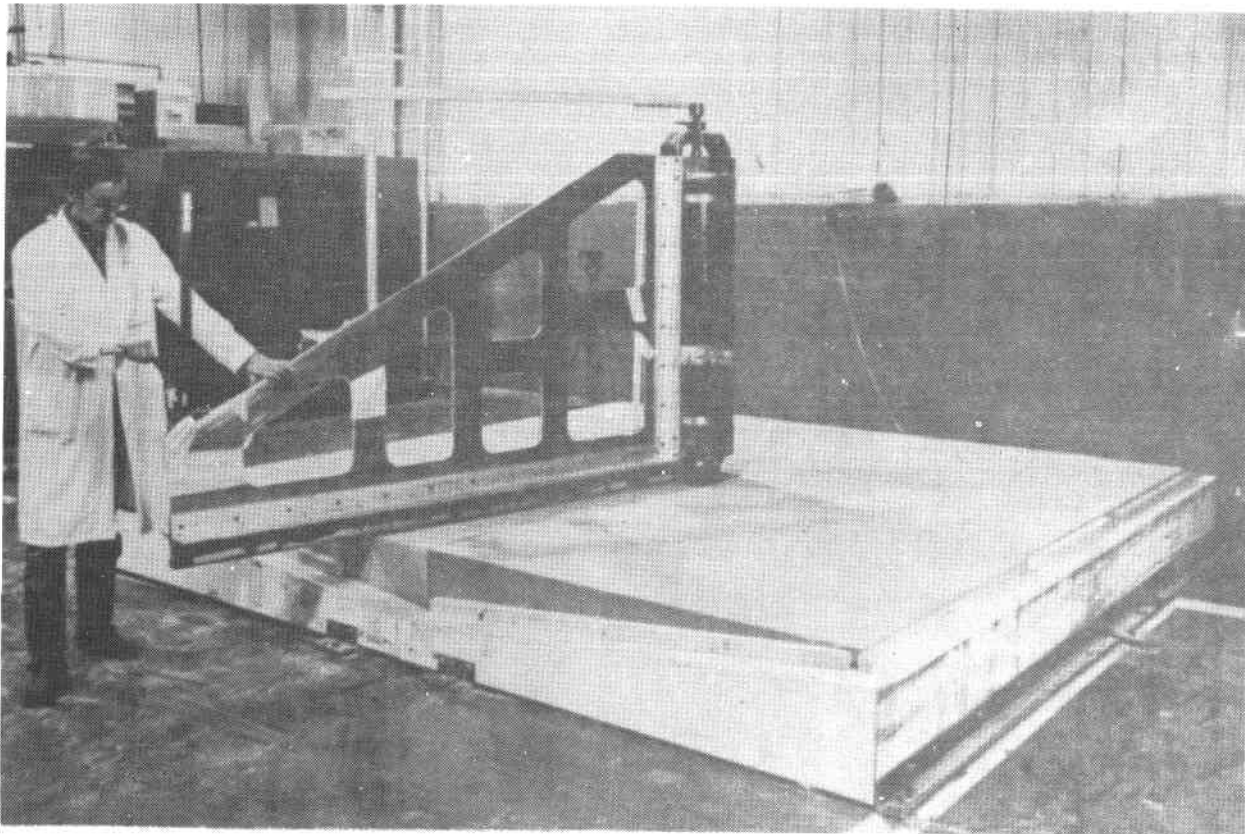


Figure 7-26. Foam Blocks Being Carved

Two different modules were constructed; one with a center beam through the structure (-002) and one without (-001).

Mass properties were:

	<u>Part -001</u>	<u>Part -002</u>	<u>Specification</u>
Weight	690 lbs	690 lbs	500 lbs (design goal)
Mass Imbalance	1303 in.-lbs	1241 in.-lbs	1375 to 1625 in.-lbs

Poor contour control and torsional failure under load caused further build and contractual efforts to discontinue with Brunswick. A final report was prepared and sent to ERC. One crack developed over two different mirror sections. However, each was a result of the edge being struck during handling and assembly. Eventually all cracks elongated across the total width of their respective facets.

Figure 7-27 shows the engineering model heliostat 140M (460 ft) from the target under test in July. The mirror module alignment was set as best as possible, yet note the scattered image caused from the foam structure mirror modules (two lighter colored modules at each end of the heliostat). This image can be compared with the spot from the four modules on the east experimental model 259M (850 ft) from the target (Figure 7-9). Because the scatter would negate good tracking information, during engineering model system level tracking tests the Brunswick modules were either removed or toed 4 degrees outward from the centroid.

Figures 7-28 through 7-31 show the measured contour unloaded and uniformly loaded with 2 lbs/ft² to simulate the aerodynamic loading (pressure drag) expected at 13.5 M/S (30 mph). On all uniform loading tests, 2 pound sand bags are placed on a 1-foot grid over the total mirror surface. As much as 0.040 inch contour deviation was measured under loading. All contour measurements were taken optically. Contour deviations probably resulted from three factors:

1. Poor bonding of mirrors to foam.
2. Poor initial contour shaping of the foam.
3. Separation of the foam from the back steel skin.

Mirror modules were subjected to two types of torsional testing to determine if a 86.6 kg-meter (7500 in.-lb) crank arm load or a 7500 in.-lb edge load causes deflections greater than 1 mr. The 7500 in.-lb results from the theoretical worse case induced moments due to aerodynamic loading at 13.5 M/S. Module -002 (with center tube) was tested.

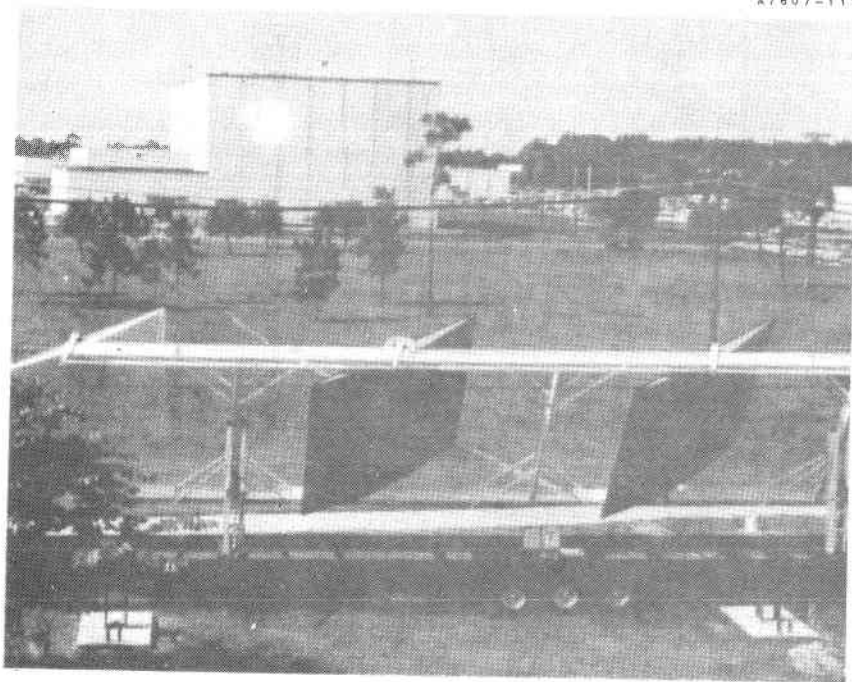


Figure 7-27. Engineering Model Heliostat
Showing Effect of Foam Mirror Module

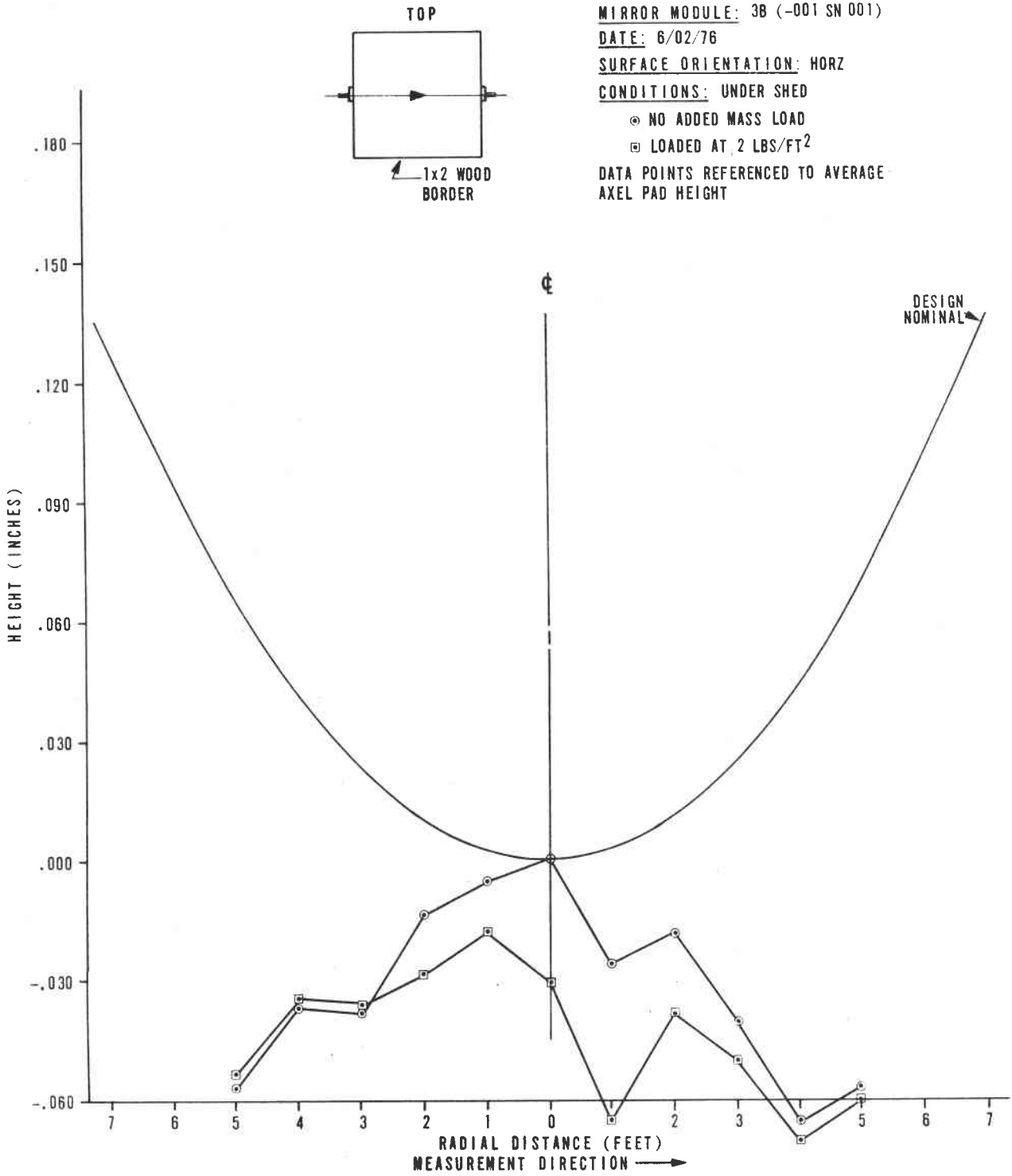


Figure 7-28. Contour Data (Replot)

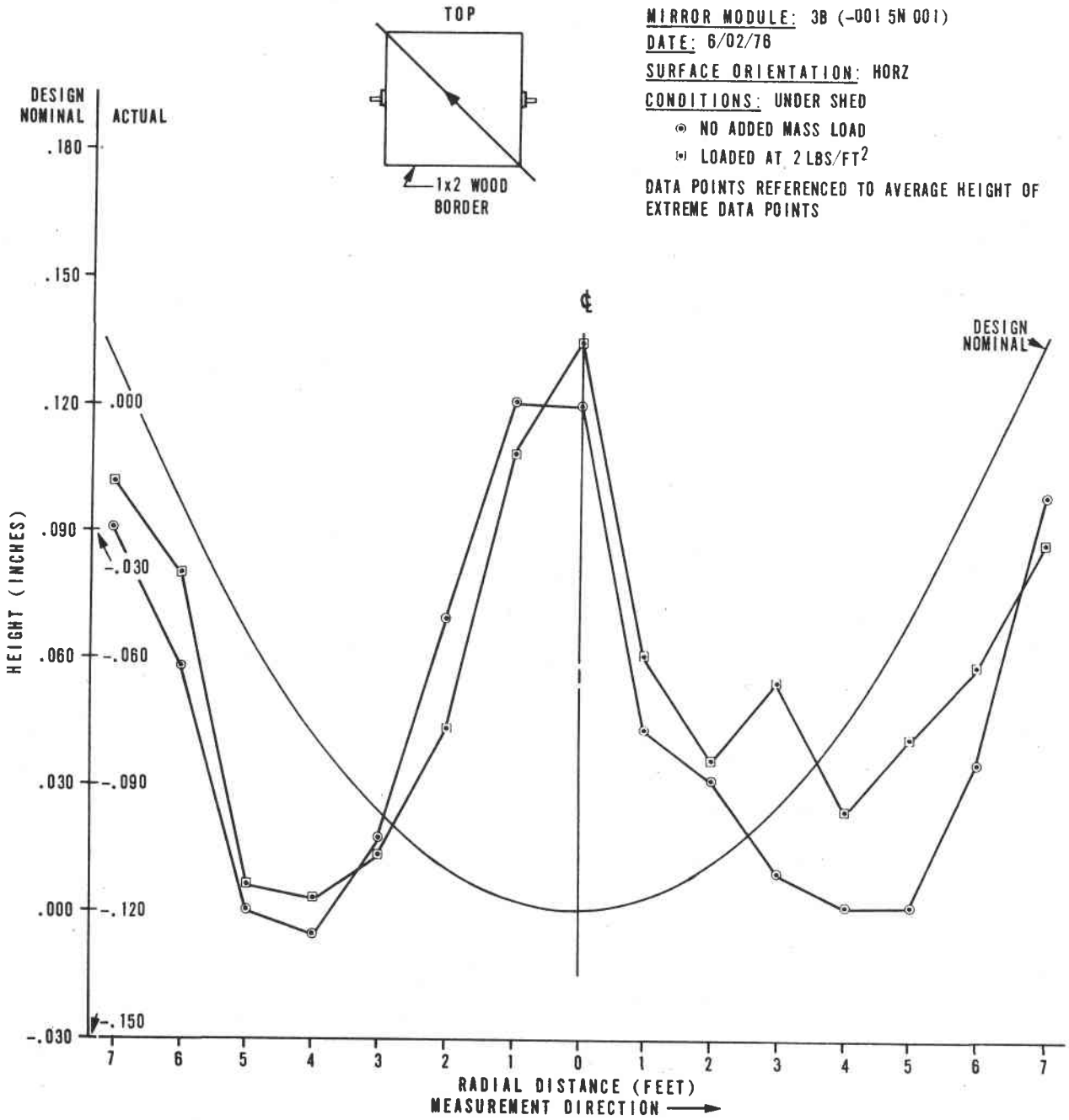


Figure 7-29. Contour Data (Replot)

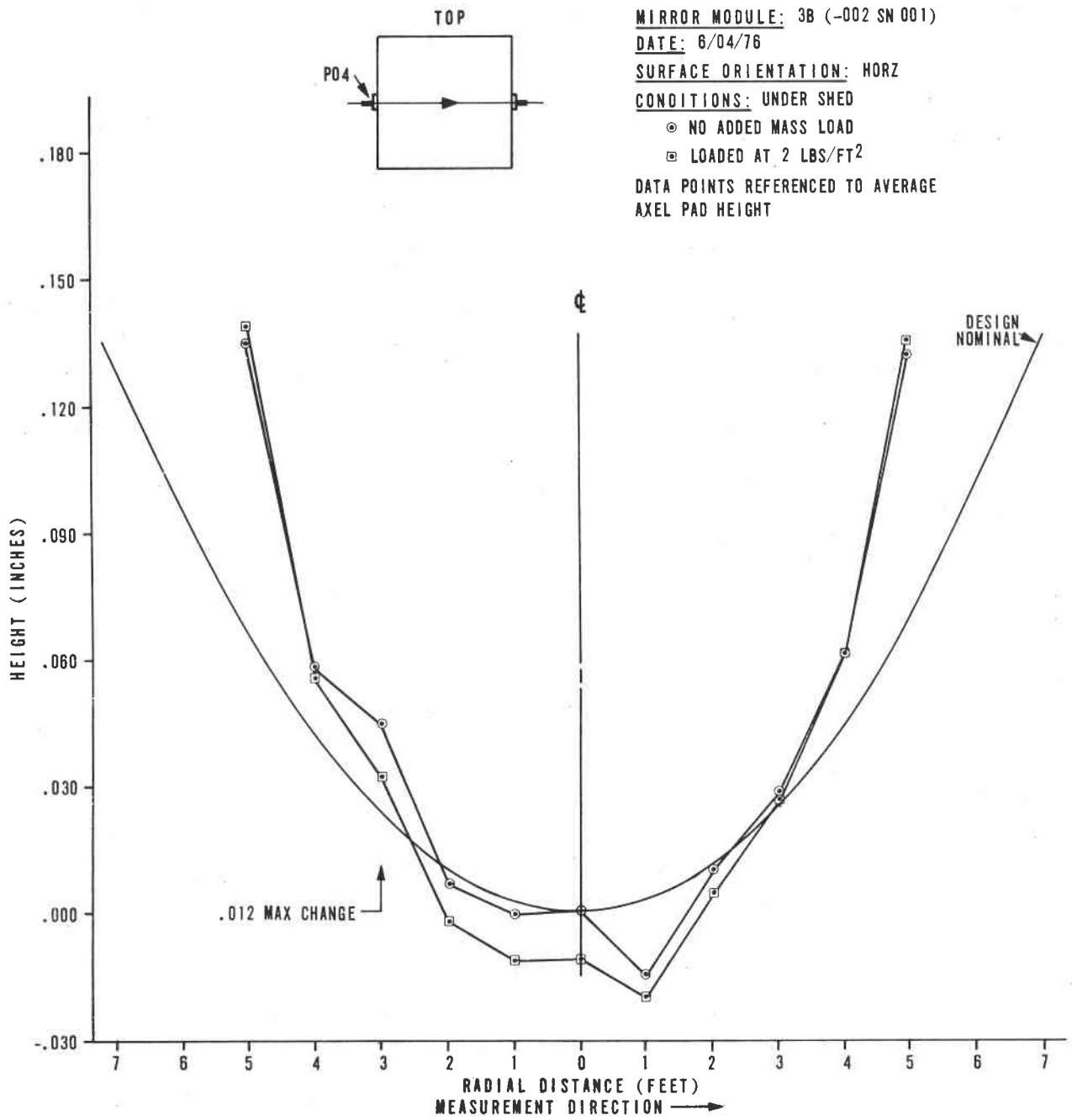


Figure 7-30. Contour Data

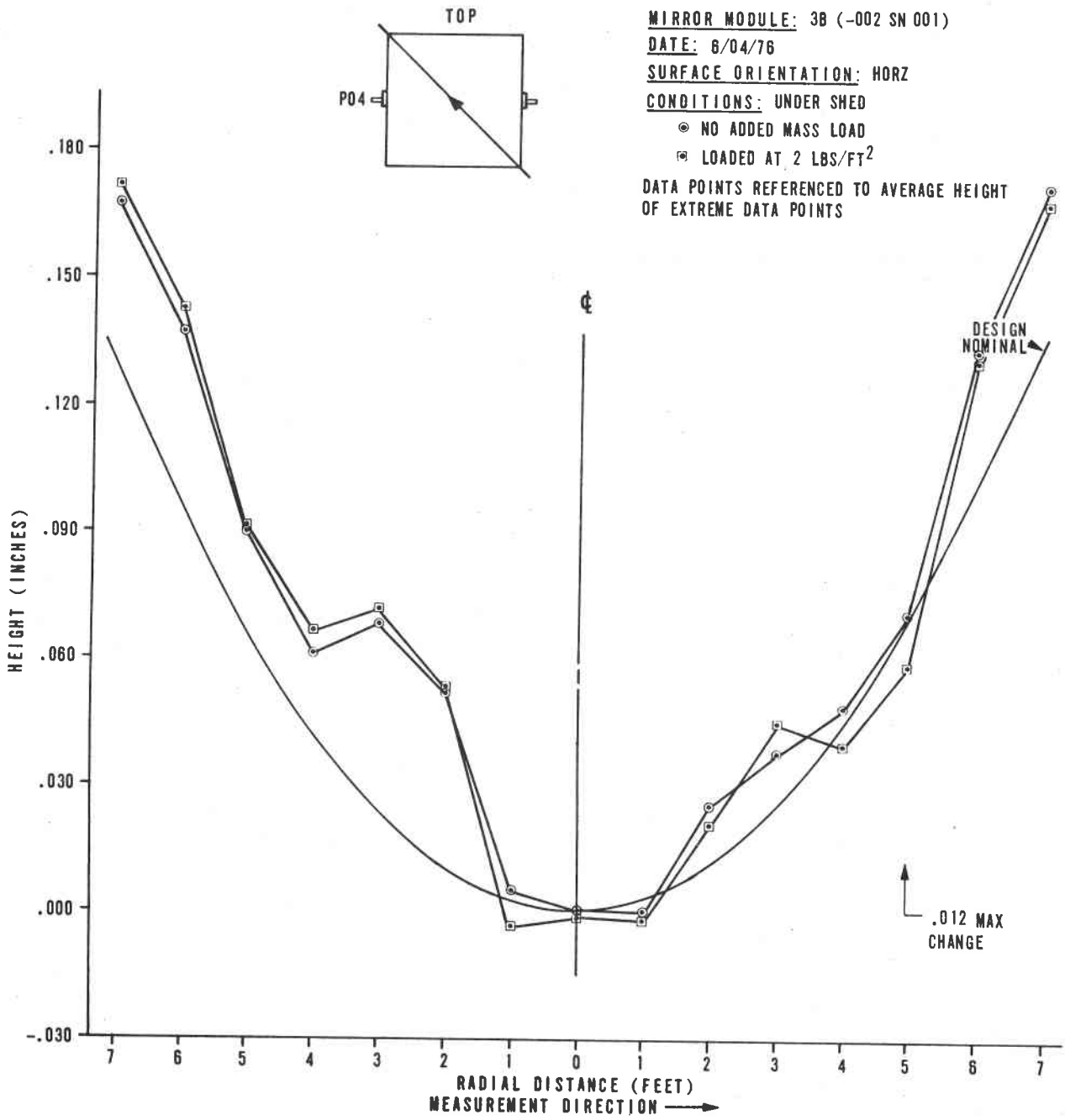


Figure 7-31. Contour Data

Edge load deflections are determined by applying 125 pounds of weight (125 lbs x 60 in. = 7500 in.-lbs) uniformly along one edge of the MM while the crank arms are clamped to a support structure. See Figure 7-32A for a schematic representation. Figure 7-33 is a photograph of a test in sequence (not Brunswick MM). Mirror blocks are monitored with the theodolite before, during, and after load application.

Crank arm load tests are performed by securing one crank arm to a support and suspending a load from the other crank arm (see Figure 7-32B).

A 144.5 Kb (318 lbs) load was hung from one crank arm. The net resultant torque along the shaft was 91.2 kg-meter (7896 in.-lbs) which also includes a 3 Kg-M torque from the crank arm itself.

At a 52.9 Kg-m (4580 in.-lbs) torque, the loaded end of the shaft twisted 1.25 mr with respect to the clamped end, exceeding the 1 mr requirement before full 13.5 M/S wind load condition was reached. At worse case loading a 11.7 mr deflection was measured and a permanent 10.1 mr residual deflection remained. The exact yield point is unknown.

Starting in July, no additional testing on these modules was done. They were placed in an outside environment for storage and at a future date aging characteristics can be obtained.

All raw data was recorded in Data Book 0548.

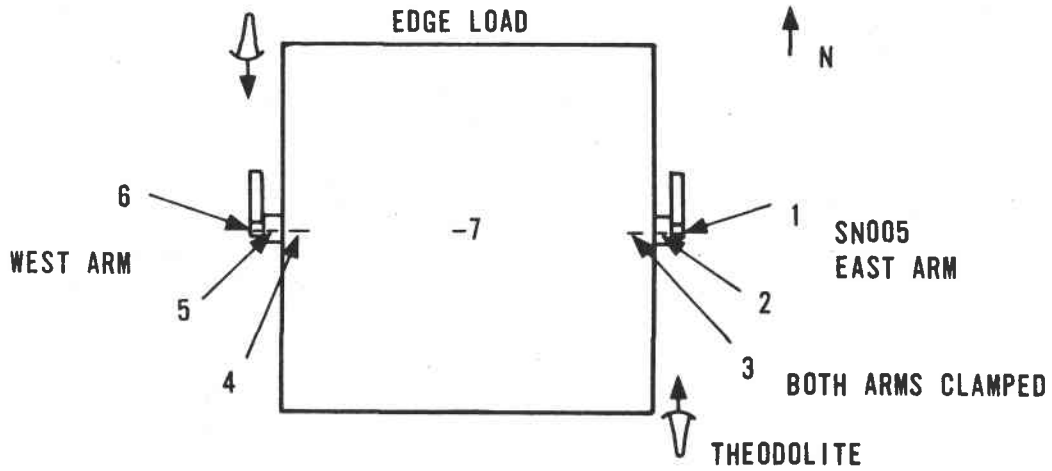


Figure 7-32A. Edge Load Mirror Module Torsional Test Set-Up

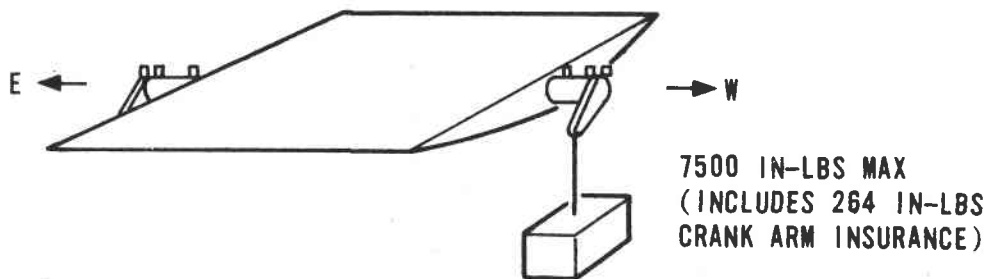


Figure 7-32B. Crank Arm Torsional Test Set-Up

2-POUND SAND BAGS TO
INCREMENT EDGE LOADS
UNIFORMLY ALONG ONE
MIRROR MODULE EDGE

A7701-33

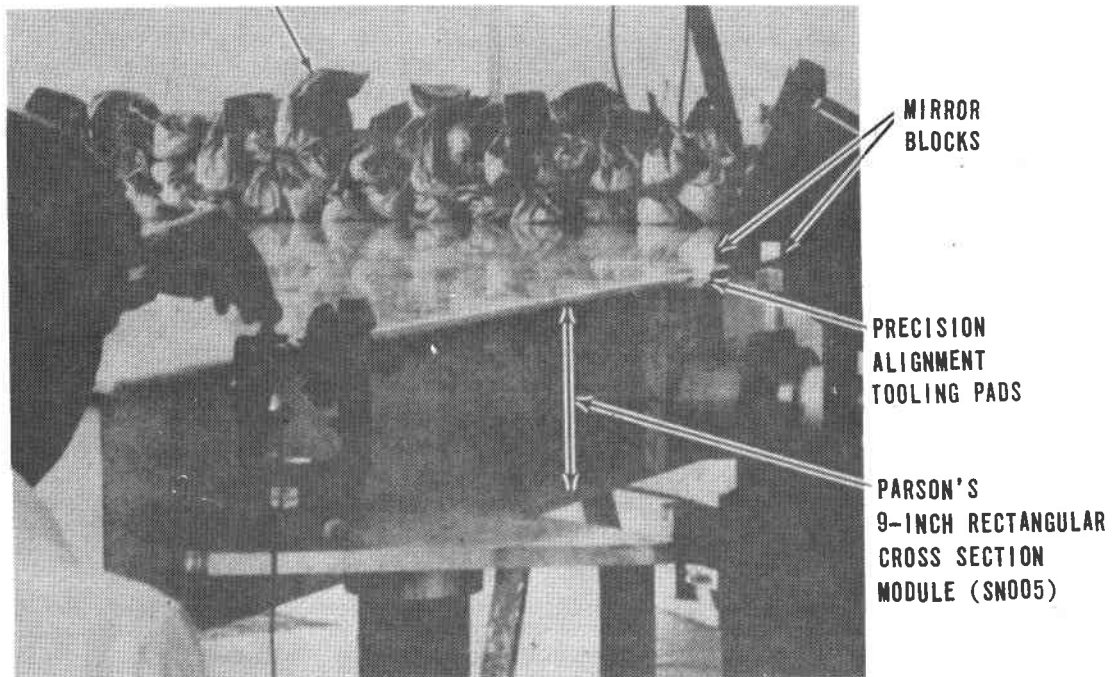


Figure 7-33. Deflection Measurement Due to Edge Load

Aluminum Honeycomb Mirror Modules

A total of 16 aluminum honeycomb mirror modules were procured from Parsons. Two arrived in early May 1976 with a tapered cross section like the Brunswick modules (Figure 7-25) and a surface area of 125 inches by 125 inches (10.1 M^2). These were used on Engineering Model testing.

The cross sectional build-up on the initial two is demonstrated in Figure 7-34A and the last 14 delivered in October 1976 in Figure 7-34B (see also Figure 7-33). The latter configuration was designed with a 120 inch by 120 inch surface area (9.3 M^2) to make use of standard mirror facet sizes. The wedge shape cross section was eliminated because the savings from reduced honeycomb material is offset by the additional labor required to taper the honeycomb fill. Notice also that the later design uses a thin section of carved foam filled aluminum honeycomb for contour control as opposed to piece of cast foam. Both designs used contact cement as bonding adhesive.

The two tapered honeycomb mirror modules were tested (SN P01 and P05) for contour and loading characteristics. Two of the experimental model mirror modules were selected at random (SN 001 and SN 005) and measurements taken.

Mass Properties - Aluminum Honeycomb

	P01	P05	-001	-005
Weight (lb)	665	698	Not	obtained, 690 at vendor
Mass Imbalance (in-lb)	1,129	1,129	Not	obtained

Tapered Cross Section Honeycomb Mirror Module

Theodolite/height gauge measurements were taken to obtain the contour measurements on the first two Parsons mirror modules. Typical contours are shown in Figure 7-35. The distributed loadings (2 lb/ft^2) and solar loading (directly exposed to sunlight) when compared to non-loaded measurements taken under a shaded shed show no significant changes to the manufactured profile on off-normal mirror focus.

From the contour data the maximum off-normal axis is approximately 0.15 MR. At no place do local gradients exceed the 0.001 inch per inch error in slope requirement when compared to a 12 inch span. Very local irregularities, if any, of significance were not determined. Since the contour was specified on a spherical radius basis (maximum deviation of 0.062 inch in a 60 inch radius), it is possible that the corners of module along the diagonal may be outside the specification accuracy.

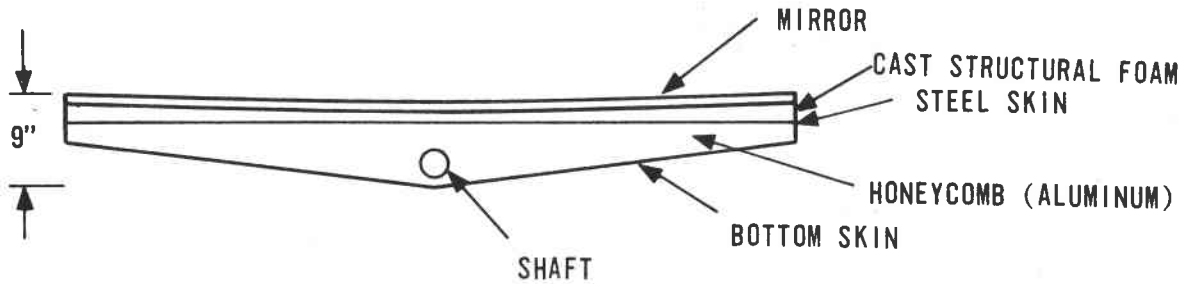


Figure 7-34A. Aluminum Honeycomb 125 by 125 Inch Mirror Module
(2 Procured)

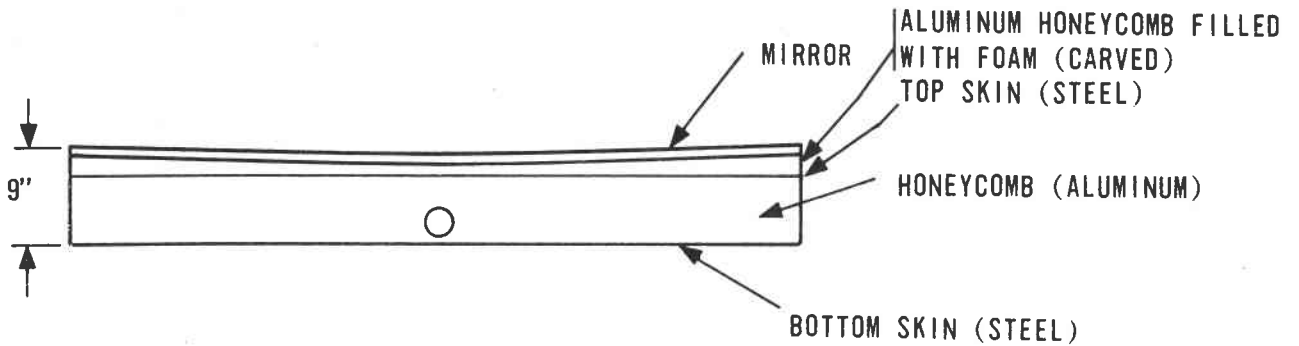


Figure 7-34B. Aluminum Honeycomb 120 by 120 Inch Mirror Module
(14 Procured)

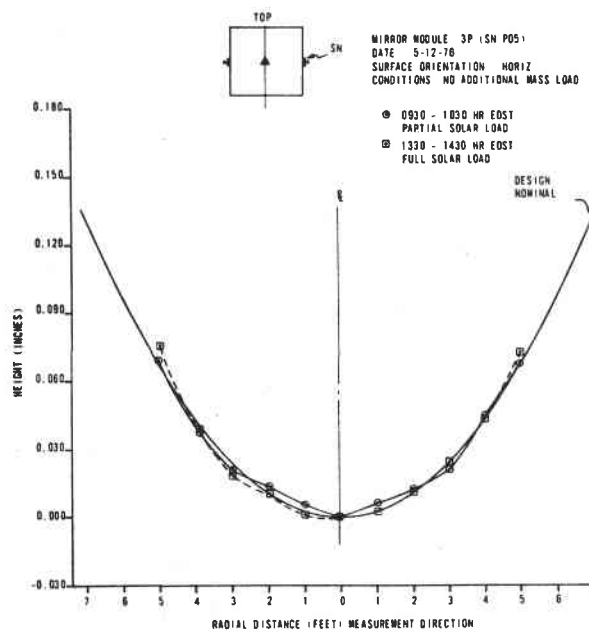
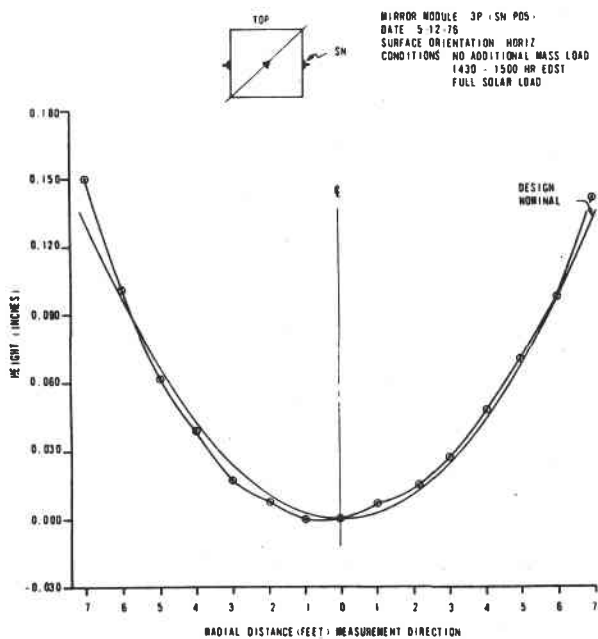
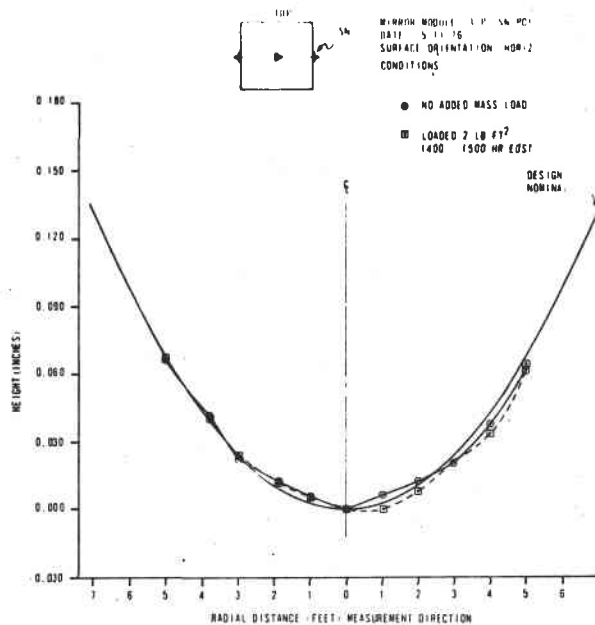
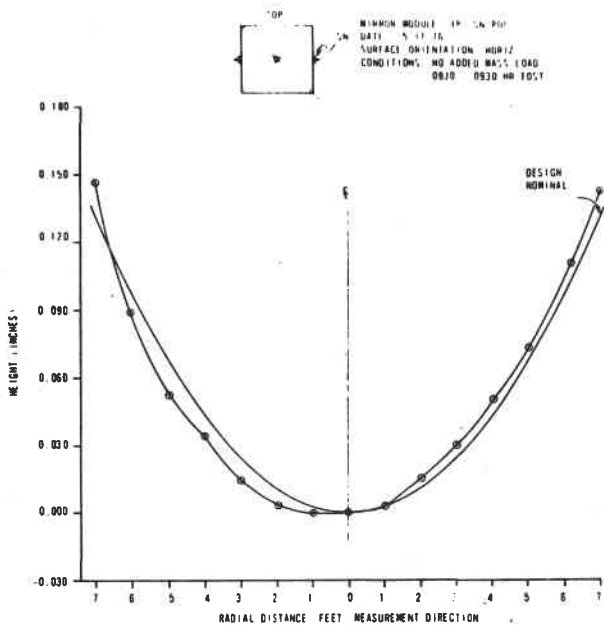


Figure 7-35. Contour Data - Parson's Mirror Modules (Tapered Cross Section)

Some of the nonuniformity that appears to occur near the center results from the following:

- Local flatness
- Measurement tolerance - accuracy of measurement is 0.002 inch, causing error amplification at the center due to small gradient
- Converting all measurements to be with respect to the center of the mirror module.

Under uniform edge loads of 7500 in-lb, SN P01's optical axis deflected less than 0.4 mr (Table 7-2). Under a crank arm load of 7500 in-lb, the optical axis deflected 0.70 mr (from east shaft to west shaft). Typical data is shown in Table 7-3. A 4584 in-lb crank arm load caused a shaft deflection of 0.47 mr. An optical axis deflection of 1.0 mr or less is within Honeywell design specification. Initially, several tests had to be repeated because the taper locks slipped. Over a period of time, including mirror module testing on the heliostats, the torque placed upon the taper locks was increased in increments from 150 ft-lbs to 225 ft-lbs. No slippage has been observed at this level. Several problems were found:

- Rust and dirt prevented smooth seating of the taper locks onto the mirror module shafts.
- The aluminum shafts would gouge causing additional slippage.
- Repeated loosening and tightening of the lock during toe-in adjustments aggravated the problem.

The solution is to use taper locks with additional slits, use hardened steel mirror module shafts, and torque to 200 ft-lbs.

It is anticipated that a full year's environmental exposure aging data will be obtained in May 1977. As of the reporting date, no physical degradation has been observed except a slight darkening at some of the facet edges.

Rectangular Cross Section Mirror Module

Contour and stiffness measurements made on two of the 14 delivered Parson's mirror modules indicate compliance to requirements. All contour measurements were within 0.010 inch of the desired spherical contour and in no case did the error accumulation exceed 0.001 in/in. Gravity force and solar loading effects were within specified requirements. A uniform load of 2 lb/ft² produced contour variations <0.003 inch from baseline measurements. Stiffness measurements gave a 0.81 MR optical axis deflection with maximum torque of 7500 in-lb applied about the axle.

Table 7-2. Mirror Module Static Stiffness Due to MM3P SN P01
Taper Locks Torqued to 150 Ft-Lbs

Δ Load (lbs) at 60 in Lever Arm	Deflection						
	E Arm	E Shaft	E Pad	Center	W Pad	W Shaft	W Arm
0 \rightarrow 20	0'0"+	+0'2"	+0'12"	+0'38"	+0'35"	+0'21"	+0'16"
20 \rightarrow 125	+1'10"	+2'7"	+2'52"	+2'59"	+2'34"	+2'4"	+1'0"
125 \rightarrow 20	-1'14"	-1'58"	-2'14"	-2'51"	-3'46"	-1'56"	+0'7"
					Bad Data Point		Bad Data Point
20 \rightarrow 0	-0'18"	-0'24"	-0'28"	-0'34"	+0'52"	-0'22"	-1'33"
0 \rightarrow \dots \rightarrow 0	-0'22"	-0'13"	+0'22"	+0'12"	+0'15"	+0'7"	-0'10"

Results: Optical axis deflected 0.39 MR at 7500 in-lbs.
(Design goal: 1 MR at 7500 in-lbs)

0277-054

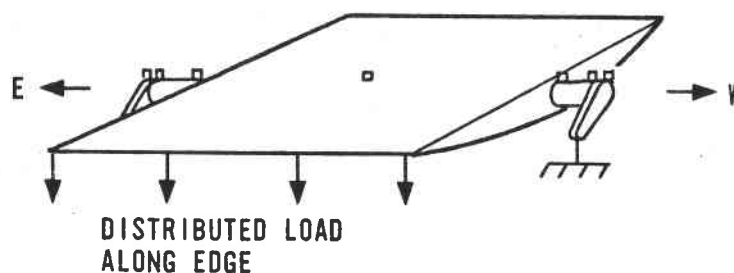
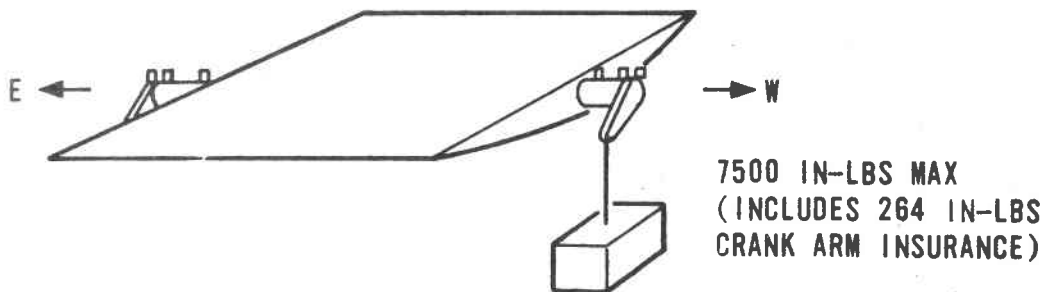


Table 7-3. Mirror Module Static Stiffness MM3P SN P01
Taper Locks Torqued to 200 Ft-Lbs

Δ Load (lbs) at 24 in Lever	DEFLECTION					
	E Arm	E Shaft	E Pad	W Pad	W Shaft	W Arm
0 \rightarrow 30	+0'1"	+0'23"	+0'29"	+0'53"	+1'2"	+1'13"
30 \rightarrow 312	+4'10"	+7'6"	+7'46"	+10'3"	+11'15"	+13'25"
312 \rightarrow 30	-3'54"	-5'8"	-6'18"	-8'40"	-9'49"	-11'30"
30 \rightarrow 0	-0'18"	-0'27"	-0'34"	-0'48"	-0'59"	-1'7"
0 \rightarrow ... \rightarrow 0	-0'1"	+1'54"	+1'23"	+1'27"	+1'29"	+2'1"
30 \rightarrow ... \rightarrow 30	+0'18"	+1'58"	+1'28"	+1'22"	+1'26"	+1'55"

Results: Optical axis deflected 0.70 MR at 7500 in-lbs.
(Design goal: 1 MR max at 7500 in-lbs). E&W crank arms
slipped \approx 100 arc-sec and 30 sec, respectively. Investigation
showed taper locks did not bottom out.



Test Method

Two Parson's mirror modules, SN001 and SN005, were evaluated for compliance to contour and stiffness requirements. These mirror modules were randomly selected from a shipment of 14 units received about 12 October 1976.

Contour measurements were made with the mirror module horizontally supported at the axle. A 0.008 inch piano wire was stretched across the mirror surface in the measured axis to provide a reference for measurements. Parallels placed on the mirror surface were adjusted until electrical contact was made with the wire as indicated by a lamp connected such that contact of the parallel and the piano wire closes the circuit. See Figure 7-36. Repeatability measurements made indicated that data measurements can be repeated within 0.002 inch total error. Measurements made with the sample mounted vertical indicated that any sag in the piano wire was negligible.

Measurements were made at 12 inch increments along 4 axes on MM SN005 with no load applied. Two axes were measured (diagonal and along axle) with 2 lb/ft² loading. Loading was accomplished by applying 2-pound sand bags at 1-foot intervals over the mirror surface as on previous modules. Measurements were made on MM SN001 along one diagonal and both centerline axes with no load applied.

Stiffness measurements were made on MM SN005. With both crank arms clamped on edge load of 130 pounds was applied at MM edge (58 inches from axle center). See Figure 7-33. Angular deflection was measured at each axle and their associated alignment pads using a theodolite and reflective mirror. Additional stiffness measurements were made with one crank arm clamped and 7500 in-lb applied to the opposite arm. Here again deflection was determined optically.

The data is recorded in Engineering Data Book No. 1127.

Data Discussion

The graphs of Figures 7-37 through 7-39 are plots of contour measurements showing the error from the desired theoretical contour. These can be compared with the same data plotted in Figures 7-41 and 7-42. Figures 7-37A and B, and 7-41 and 7-42 show the negligible effects of loading MM SN005 with a distributed load of 2 lb/ft². Figure 7-40A data points were taken with MM SN005, mirror surface down, while mounted on the engineering model heliostat. Data points are the same as those in Figure 7-37A. The variations observed are attributed to difficulty in taking the measurements (operator had to stand on ladder and adjust parallels above head, wind gusts moving piano wire, etc.) rather than sag in the MM.

Figure 7-40B shows the effects of solar loading on MM SN001. Here again wind gusts caused repeatability problems in measurements. Data points are the same as those of Figure 7-39B.

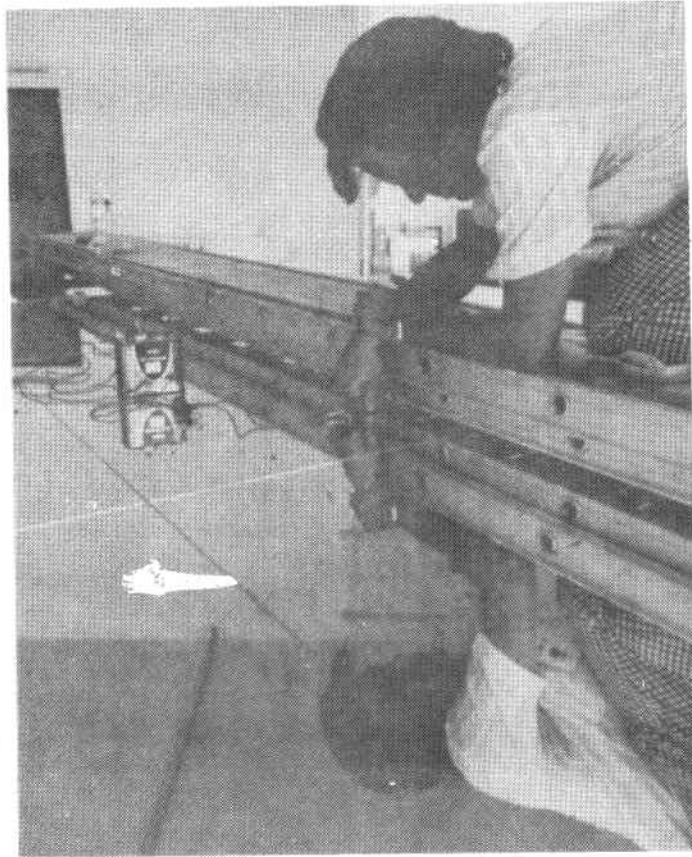


Figure 7-36. Contour Measurements With Piano Wire

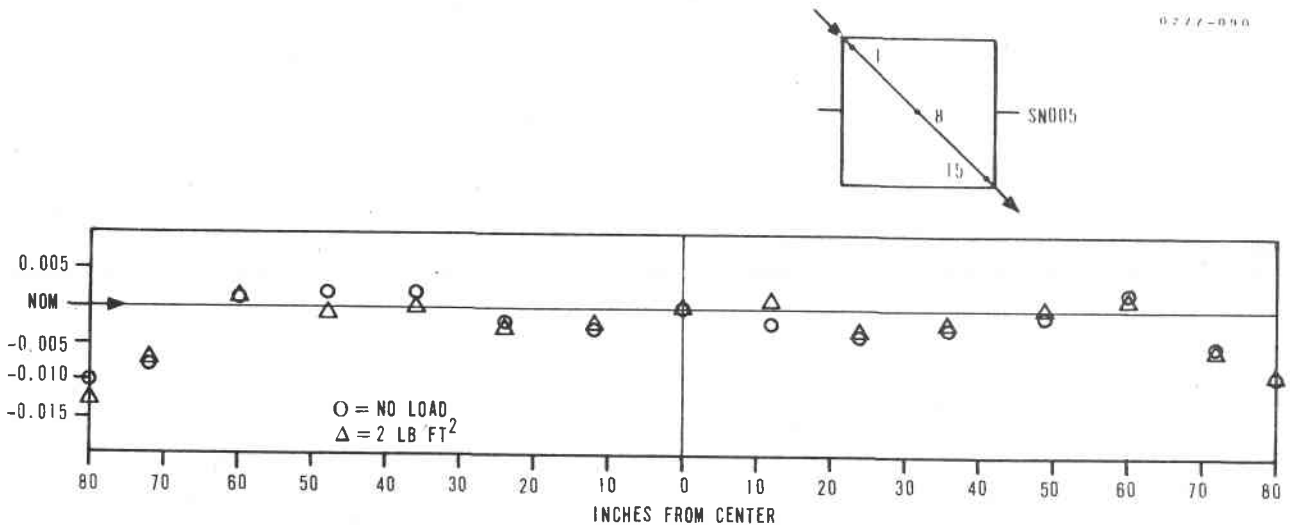


Figure 7-37A. Contour Deviations Parsons Mirror Module, SN 005, Loaded and Unloaded

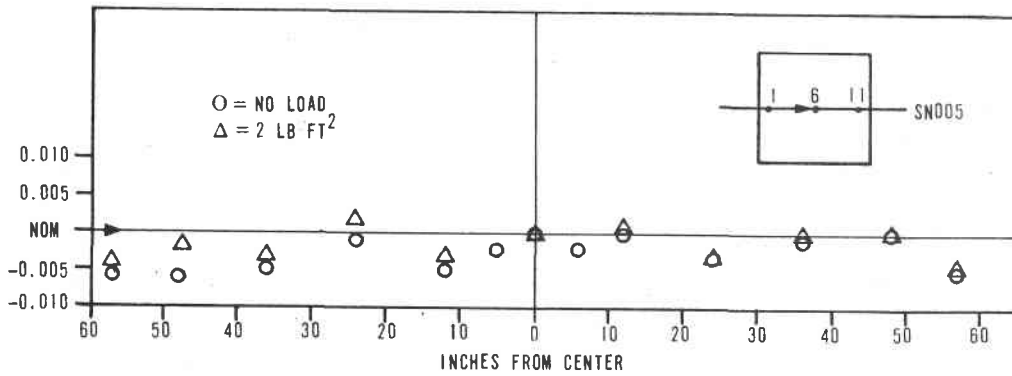


Figure 7-37B. Contour Deviations Parsons Mirror Module, SN 005, Loaded and Unloaded

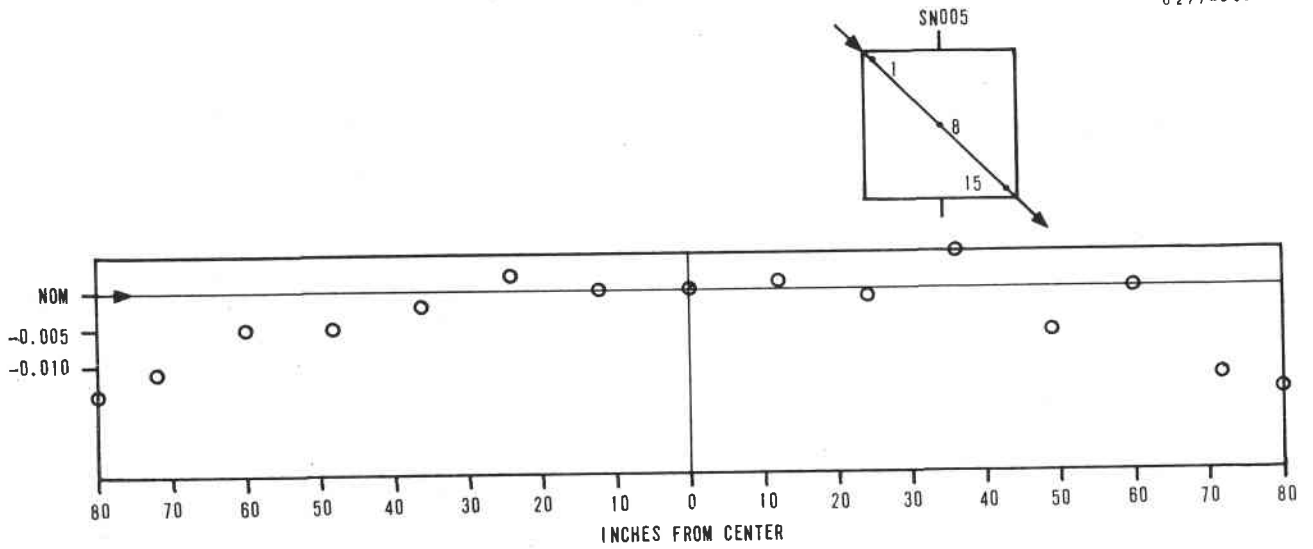


Figure 7-38A. Contour Deviations Parsons Mirror Module, SN 005, Unloaded

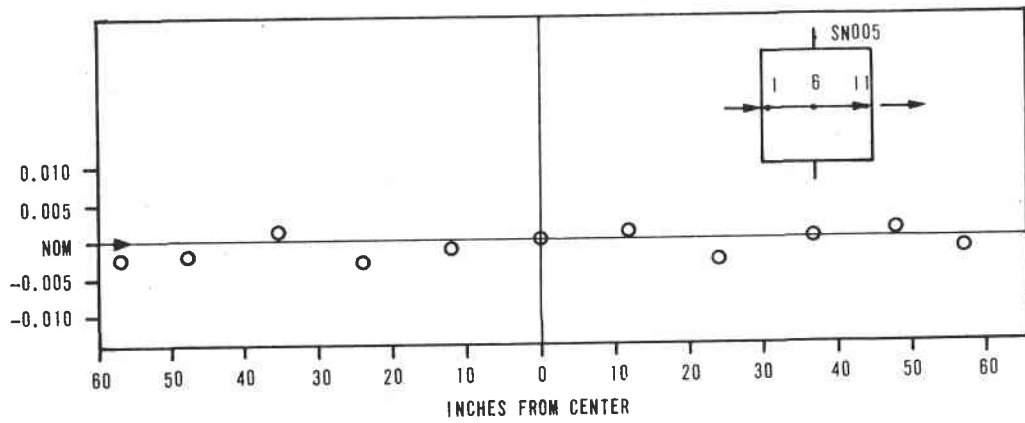


Figure 7-38B. Contour Deviations Parsons Mirror Module, SN 005, Unloaded

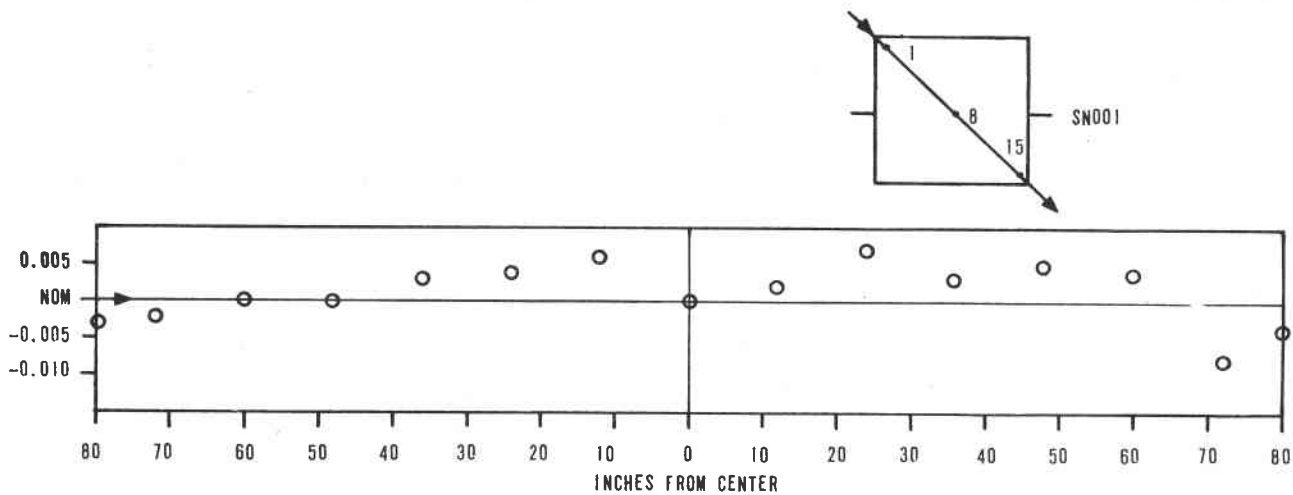


Figure 7-39A. Contour Deviations Parsons Mirror Module, SN 001, Unloaded

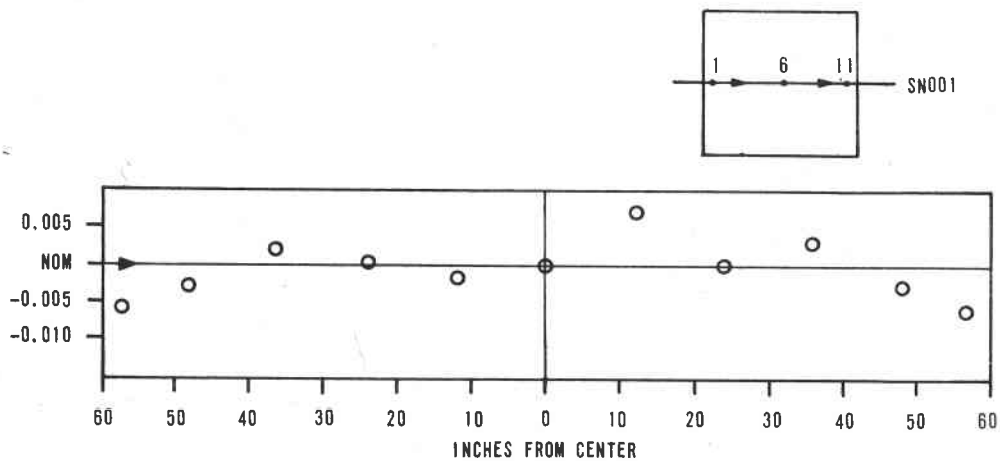


Figure 7-39B. Contour Deviations Parsons Mirror Module, SN 001, Unloaded

0277-056

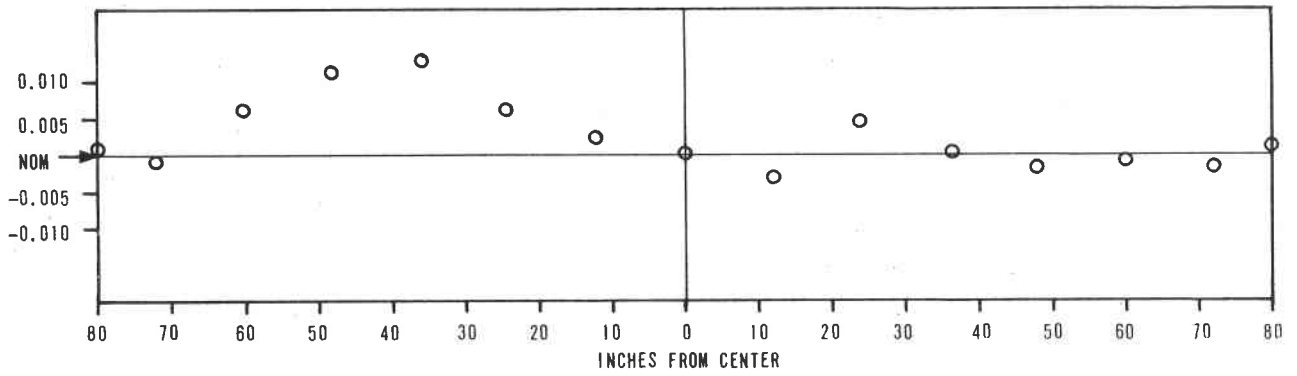
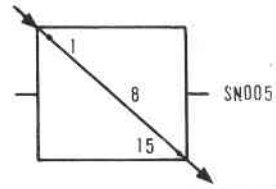


Figure 7-40A. Contour Error Mirror Surface Down

0277-055

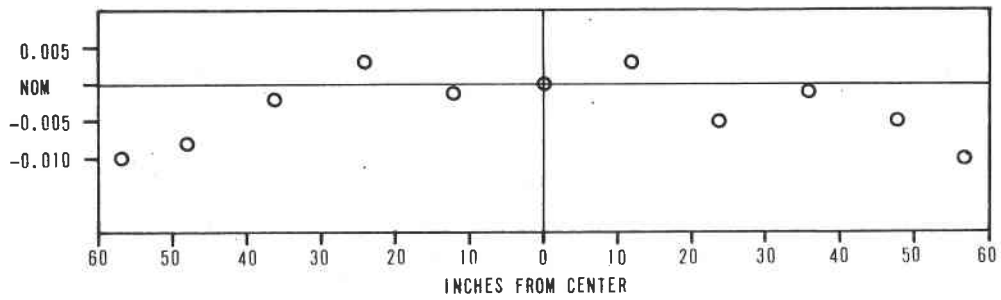
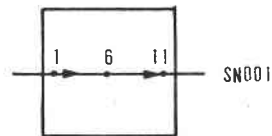


Figure 7-40B. Contour Error Solar Load

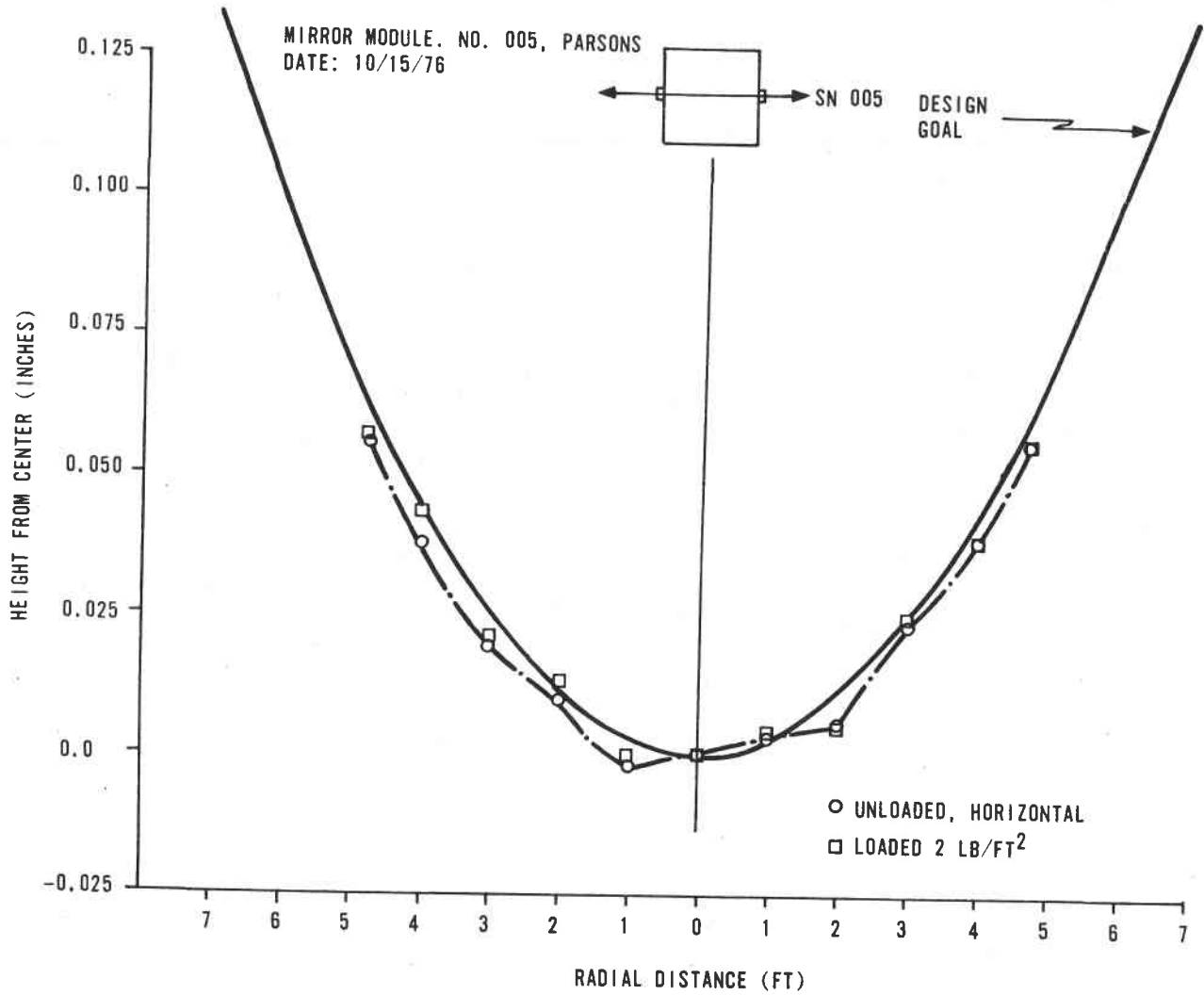


Figure 7-41. Mirror Contour Data

MIRROR MODULE: NO. 005, PARSONS
 DATE: 10/18/76

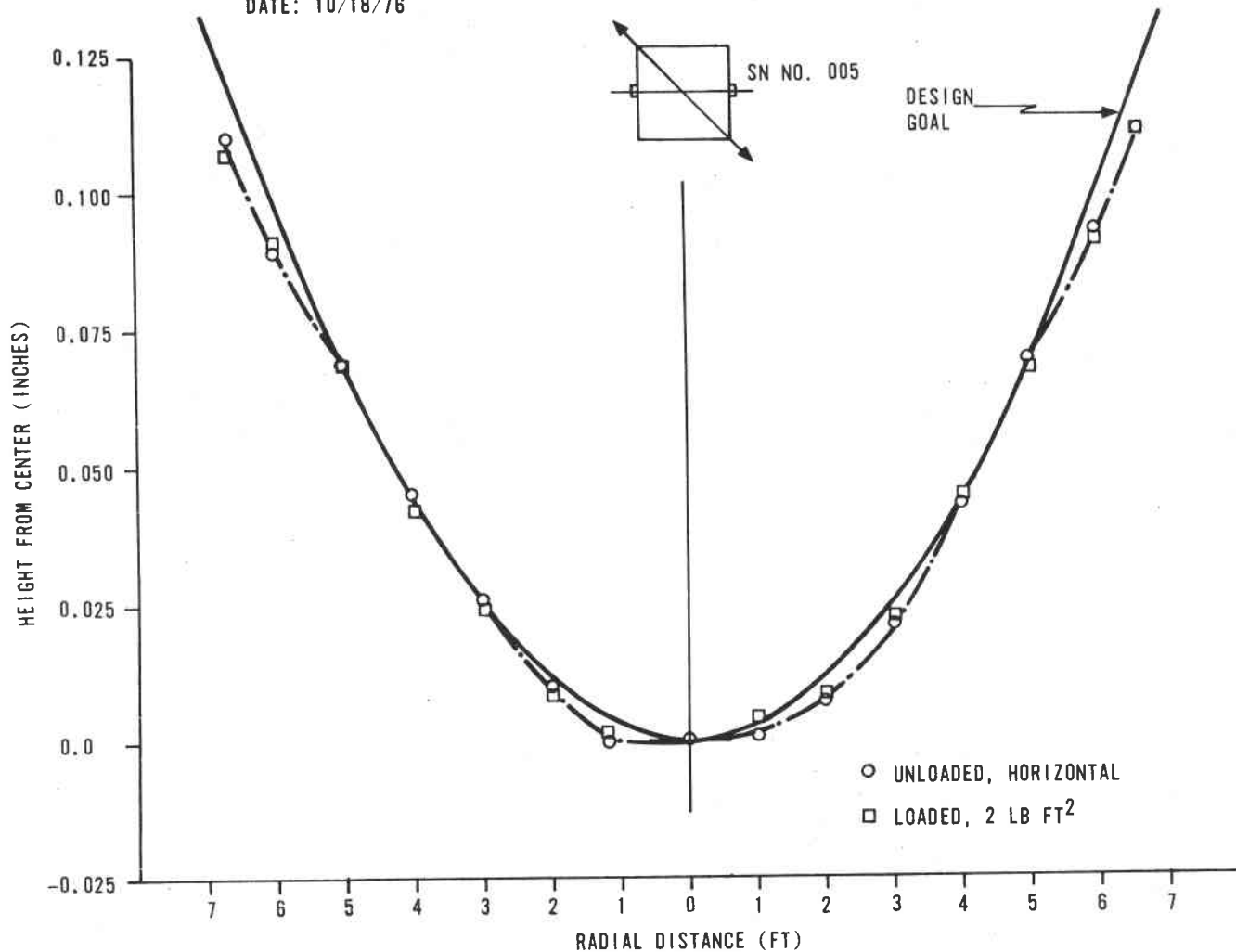


Figure 7-42. Mirror Contour Data

Table 7-4 is a summary of the deflections observed due to an edge load of 130 pounds (7540 in. lb). Deflections were determined optically as illustrated by Figure 7-43. Table 7-5 and Figure 7-44 show MM deflections when a 7488 in-lb (312 lb at 24 in) torque is applied about the axle. MM SN005 was used in all stiffness measurements. Preload of 20 to 30 pounds was used to remove any slop in setup that may affect repeatability.

0 277 - 060

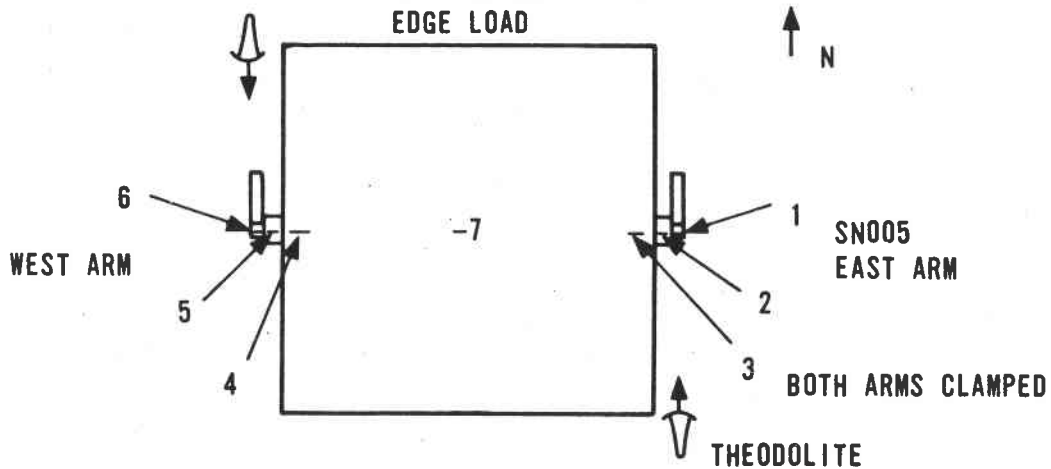


Figure 7-43. Edge Load Deflection Test Set-Up

Table 7-4. Edge Load Deflection

<u>Measurement</u>	<u>0-30 lb</u> <u>Load</u>	<u>0-130 lb</u> <u>Load</u>	<u>30-130 lb</u> <u>Load</u> (7500 in-lb)
E Arm - E Align Pad	59 arc-sec	126 arc-sec	67 arc-sec
W Arm - W Align Pad	23 arc-sec	89 arc-sec	65 arc-sec
MM Center - W Axle	26 arc-sec	75 arc-sec (0.36 mr)	49 arc-sec (0.24 mr)

Points 1-7 indicate reflective mirror locations

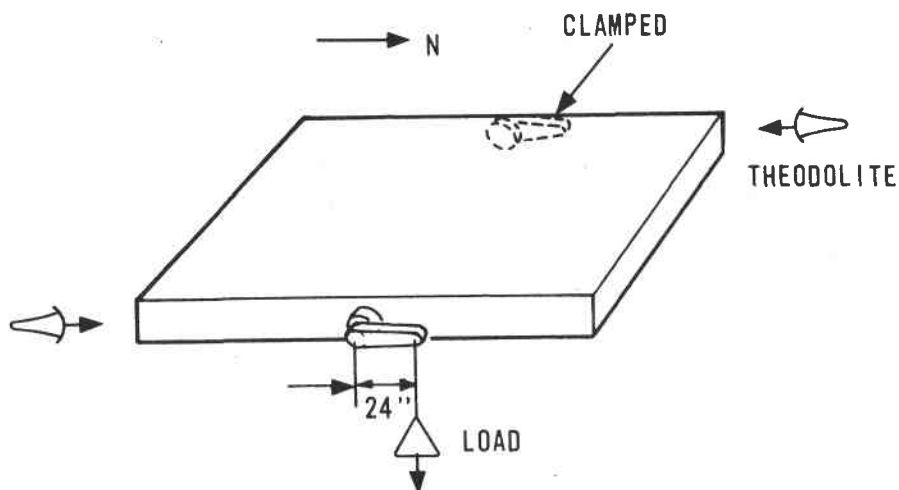


Figure 7-44. Crank Arm Torsion Test Set-Up

Table 7-5. Deflection Due to Crank Arm Load

<u>Measurement</u>	<u>0-20 lb Load</u>	<u>0-312 lb Load</u>	<u>20-312 lb Load</u> (7500 in-lb)
E Axle - E Align Pad	10 arc-sec	123 arc-sec	113 arc-sec
W Axle - W Align Pad	9 arc-sec	121 arc-sec	112 arc-sec
E Axle - W Axle	26 arc-sec	353 arc-sec	320 arc-sec
Optical Axis Deflection			160 arc-sec (0.81 mr)

Mirror Adhesive Bond

Honeywell's Material Engineering Lab tested a series of adhesives for potential mirror module construction to achieve a 30-year life.

The report is included as Appendix F. Whereas we used contact cement for the SRE and it has shown no signs of degradation, it will be necessary to use silicone adhesive materials. Epoxy adhesives may be available for usage with a 30-year life within a few years. The tensile strength of either is strong enough to meet all bonding requirements.

Mirror Module Reflectance

The Detailed Design Report (see Page 6-39) provided spectral reflective measurements taken on film reflectors and mirror glass reflectors. The samples were provided by Avionics Division, but all testing was actually performed by ERC in a laboratory environment over 0.3 to 2.5 MM wave length range. As expected, thin (0.025-0.030 inch) 2nd surface low iron glass provides the greatest reflectance (94-98 percent). Additional samples representing our Parsons' mirror modules were sent to ERC for additional tests to include time and different environmental exposure effects. See Table 7-6. The 87 percent - 87.1 percent reflectivity numbers compare well with Honeywell Avionics numbers of 87.2 percent to 88.2 percent reflectivity.

All measurements taken locally consisted of looking directly at total insolation reflectivity as a function of various cleanliness conditions.

Table 7-6. Reflectances at Various Wave-Lengths For Parsons Mirror Samples. Measured at Energy Research Center

Wavelength (Microns)	Reflectances	
	Sample 'A'	Sample 'B'
0.40	0.885	0.885
0.45	0.917	0.917
0.50	0.946	0.946
0.60	0.951	0.953
0.65	0.942	0.936
0.70	0.918	0.921
0.90	0.890	0.890
1.10	0.791	0.798
1.10	0.770	0.774
1.30	0.792	0.792
1.50	0.842	0.842
1.90	0.870	0.865

Ave = 0.870

0.871

On clear days the calibrated pyrheliometer, which measures the composite of the total solar energy spectrum, was used to obtain the incident insolation and then directly, the reflected insolation. The

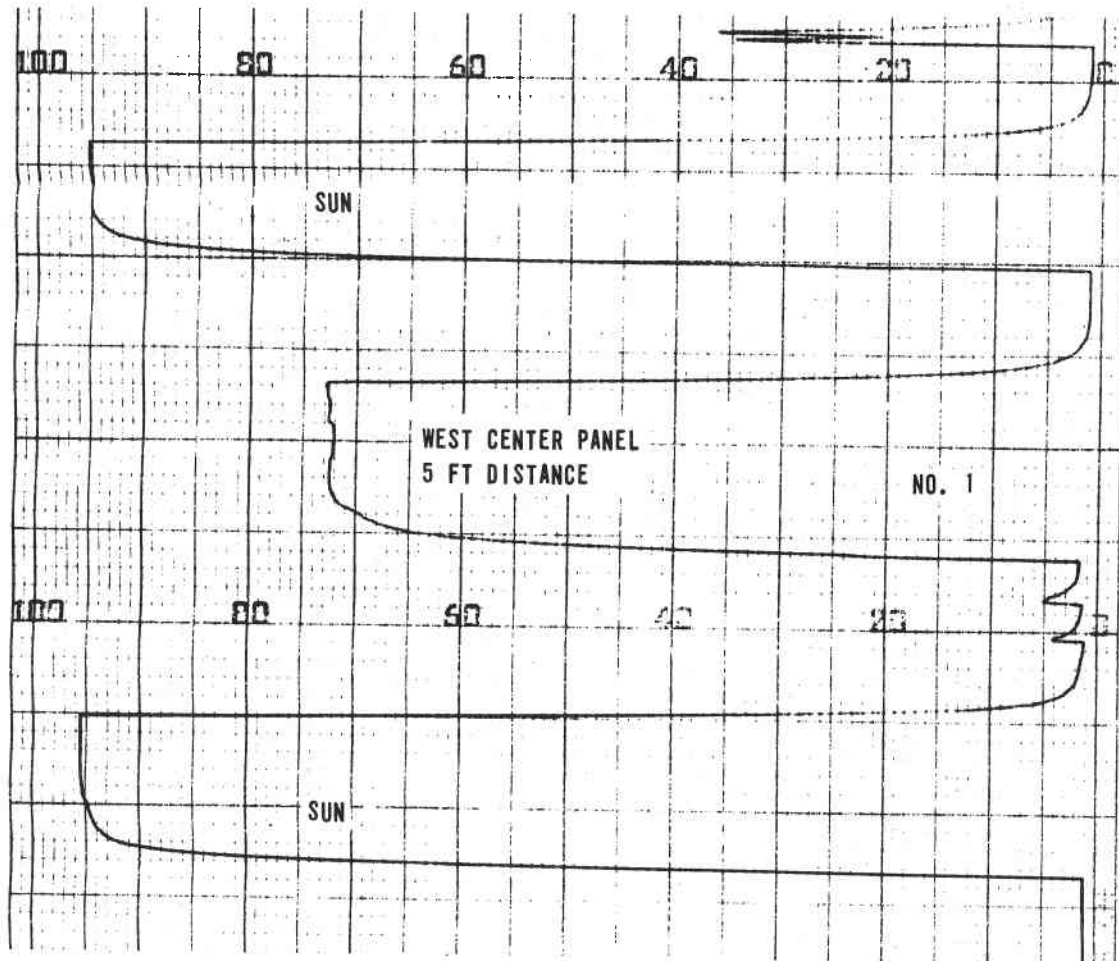
field of view with the sun image (direct or reflected) centered encompasses 5.7 degrees. Figures 7-45A and 7-45B show representative recorded data for clean and dirty facet areas. The clean glass measurements of Table 7-6 are probably smaller than the internally obtained numbers because the pyrliometer integrates the total spectrum and averaging discrete data points on the solar energy profile tends to reduce the actual total.

On the facets tested at random from the experimental mirror modules, the following reflective characteristics were obtained for the described conditions:

<u>Condition</u>	<u>Resultant Reflectivity/Change</u>
1. Clean facets	10.8 - 12.8 percent loss (88-89 percent reflectivity was expected)
2. Dirty facets having been exposed to environment, mirrored surface up for one week. Primary influence upon dirt accumulation is humidity and dew causing collection of dirt. Figure 7-46 shows the dirty mirror used in this test.	18.8-24.0 percent loss. The average <u>additional</u> decrease in reflectivity loss was 9.2 percent.
3. Dirty facets - accumulation over one month during normal day-time operation. Non-streaking adhering dust is predominant characteristic.	15.1-22 percent loss. 15.1 to 16 percent was the dominate range.
4. Dusty mirror during operation exposed to light rain (did not stow heliostat). Energy measurements taken from calibration array at identical direct solar insolation levels before and after rain. Decrease in image quality due to smearing and streaking of mirror module.	24 percent additional reduction in reflectivity. Image quality defined by radius of gyration of weighted image intensity across calibration array deteriorated by 9.1 percent larger image.

Measurements using the pyrliometer compared exactly with the expected reflectivity of our low-iron glass. Reflectivity can be increased from 91 to 93 percent by going to water white 0.098 inch float glass mirrors.

Figure 7-47 shows the large quantity of water droplets remaining 26 minutes after a brief light rain and the sun had reappeared 21 September 1976. Humidity remained at about 70 percent. Clean water droplets seem to reduce solar reflectivity by about 5 percent and significantly increased the scatter. Information of this nature is important to



0952
CHART RATE = 40 SECONDS/INCH
INSOLATION = 8.76 WATT/M²/DIVISION
4 NOVEMBER 1976

Figure 7-45A. Typical Reflectance Measurement on Dirty Mirror Module Facet-Mirror Module SN P001

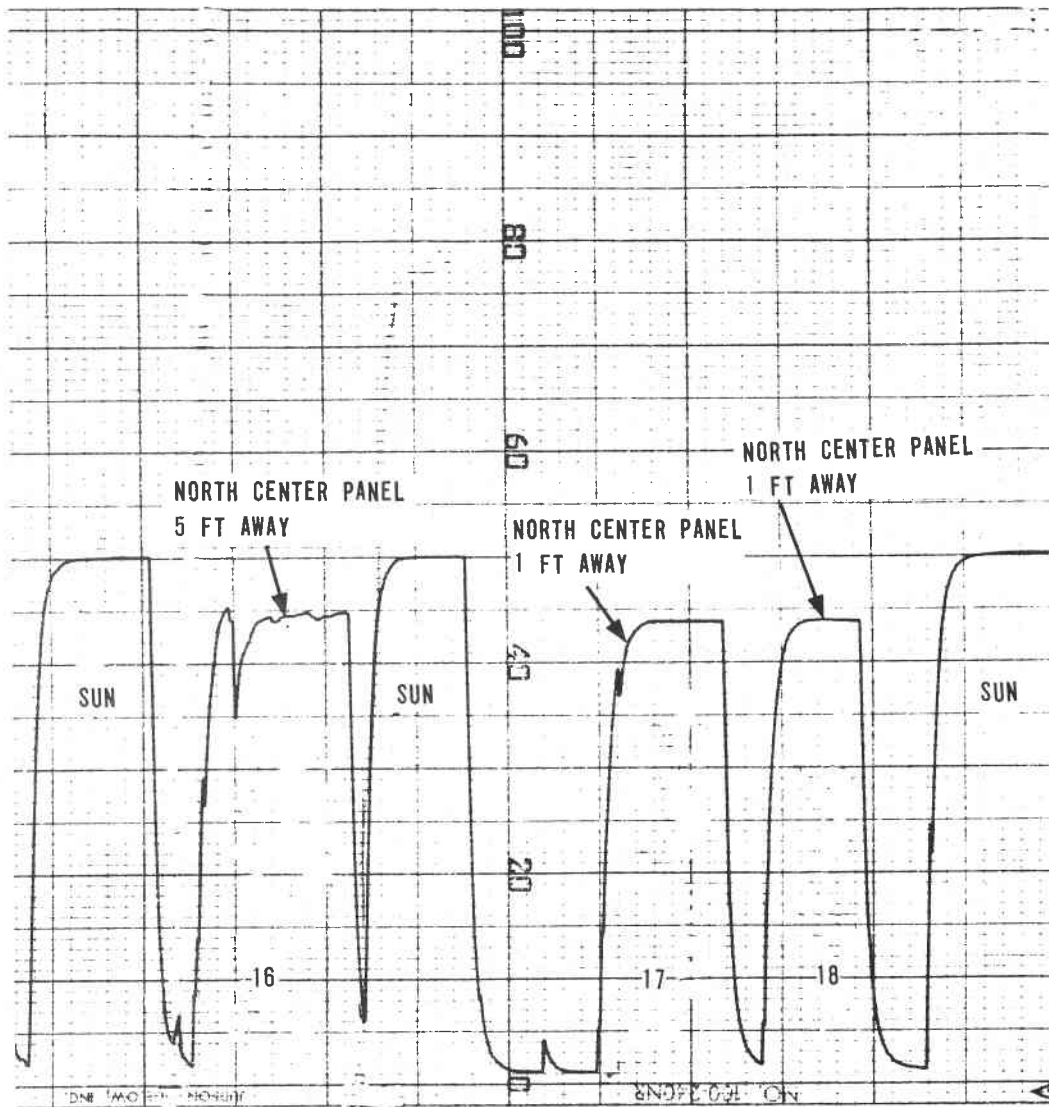


CHART RATE = 40 SECONDS/INCH
 INSOLATION = 17.5 WATT M⁻²/DIVISION
 4 NOVEMBER 1976, SUN ELEVATION = 39.5°

Figure 7-45B. Typical Reflectance Measurement on Clean Mirror Module Facet

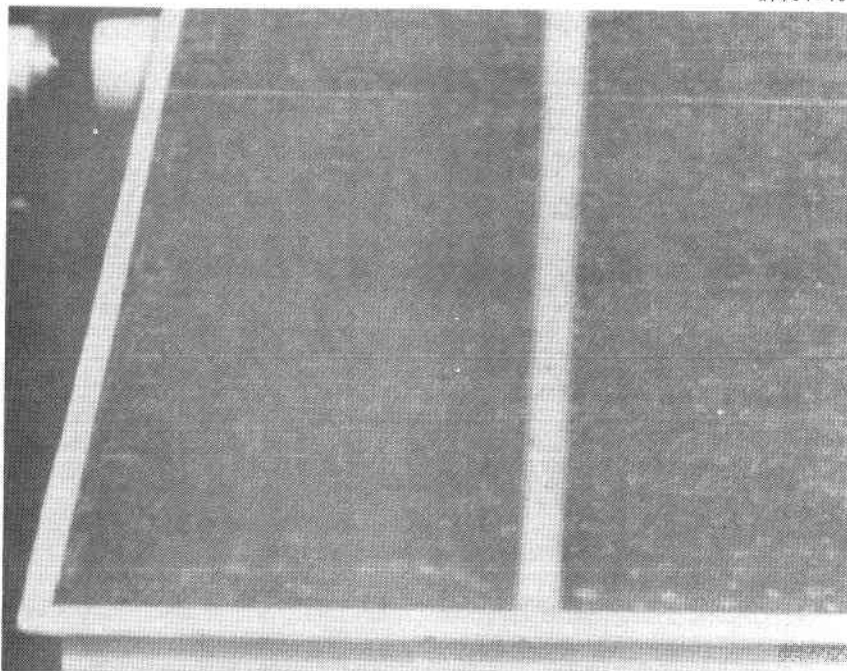


Figure 7-46. SN 001 Dirty Mirror Module

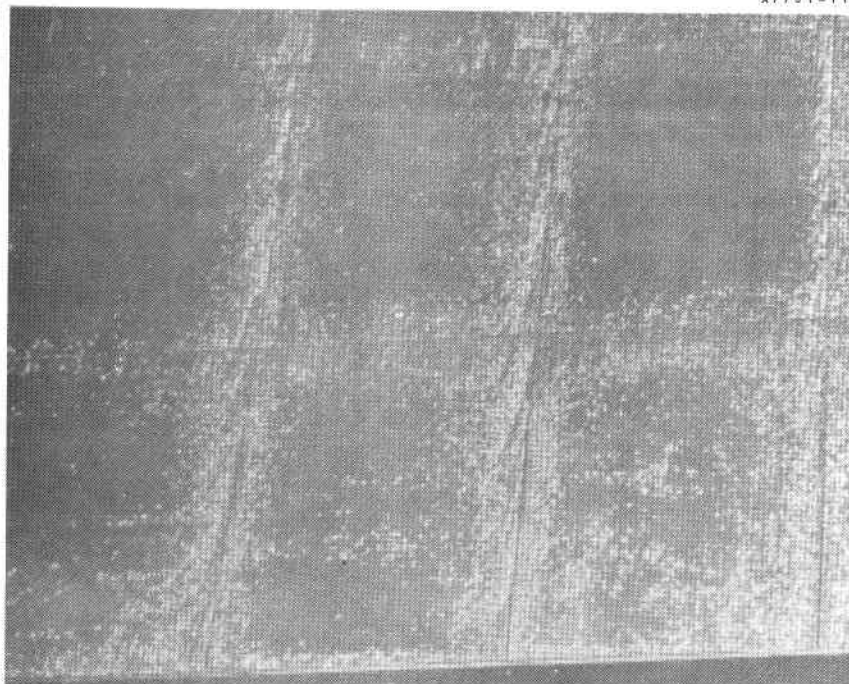


Figure 7-47. Water Droplets 26 Minutes After
Light Rain

establish optimum procedures for pilot plant or commercial plant normal operation (to stow or not to stow with an approaching light, short rain). The temporary degradation (30 to 40 minutes) of reflectivity must be related to the time required to go to stow before a shower and return to operation after a shower.

Motor Characterization

A significant amount of effort was expended to obtain proper drive motors for the inner and outer axis drives. Initially it was calculated that with the loading expected, 100 inch-ounce stall torque permanent magnet dc (PMDC) motors would be adequate for both drives to produce the required torque to generate specification maximum emergency slew rates (0.3 deg/sec) at 900 motor rpm. However, it turned out that what is considered zero viscous drag and zero static torque to a manufacture of 5-ton linear ton actuators using 1/3-3/4 horsepower electric motors was not negligible to our configuration. Static friction torque of the initial machine screw actuators reached >90 inch-ounce alone at some orientations and extensions and slow rates of 100-200 rpm were being reached. These loads do not include the frame imbalance, wind, or bearing friction loads from heliostat operation.

The final solution for the SRE experimental models was to retain the 100 inch-ounce stall torque PMDC motors for the inner drive and use a 200 inch-ounce stall torque motor for the outer drive coupled with utilizing ball-screw linear actuators rather than the machine screw actuators. At the heliostat level the outer axis net torque loads were reduced by a factor of up to 2.4:1 by changing to ball-screw actuators.

Motor rate requirements to achieve a 0.3 deg/sec slew rate at the gimbal axis are as follows:

810 rpm for the inner drive.

545-902 rpm for the outer drive, depending on gimbal angles.

Each motor (four 100 inch-ounce motors and nine 200 inch-ounce motors) purchased from Inland Motor Corporation was characterized at the component level with respect to power/stall torque/speed properties. Then at heliostat level testing, the power input to the motors was used to derive the torque required for gimbaling.

Figure 7-48 shows typical CW/CCW stall torque values obtained for three of the 100 inch-ounce motors. Data is estimated to be within 5 percent accuracy because of the force gage and changing voltage uncertainties. A constant voltage of 22 volts dc was used which would be typical for the 24 volt dc batteries used at system level after drops through the electronics. No load speeds typically ran from 1440 rpm to 1880 rpm at 22 volts dc drawing currents from 0.28 amp to 0.32 amp during July testing. However, under actual heliostat outer actuator loads, speeds averaged as low as 360 rpm.

One motor (No. 1) which was removed from the Engineering Model actuator and used as the inner drive on the East experimental site was re-characterized again 30 November 1976. Figure 7-49 shows there was no degradation over 5 months of use and environmental exposure. The clockwise data points from 1 July are assumed to be erroneously low

MOTOR TORQUE SENSITIVITY (K_T)
(INLAND MOTOR P/N T-1806-H)

0277-109E

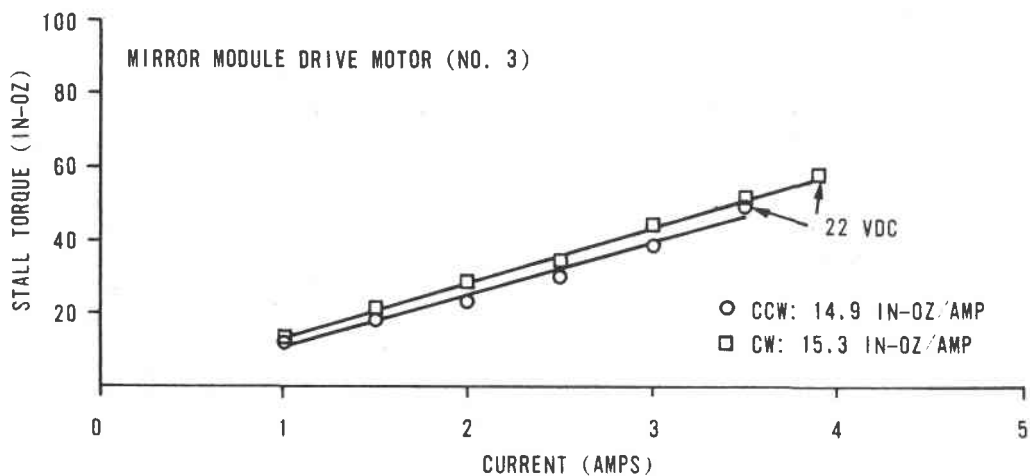
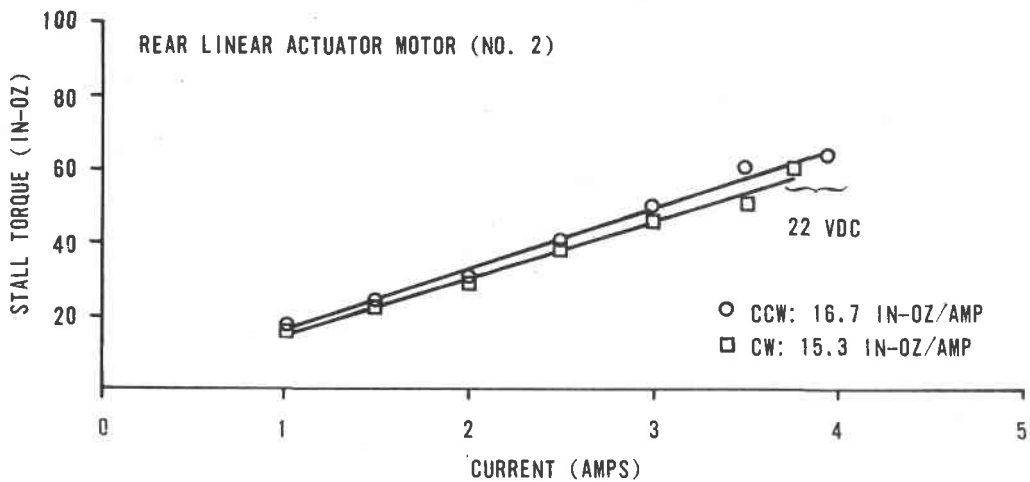
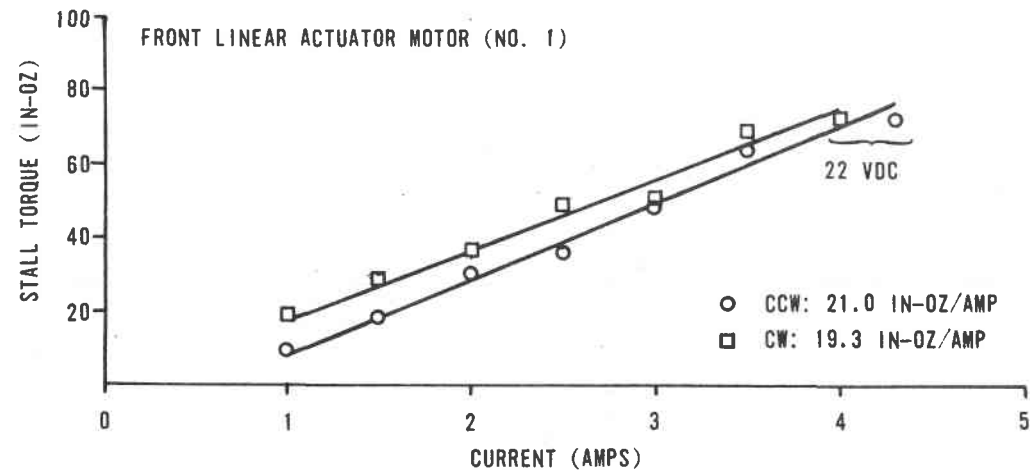


Figure 7-48. 100 In-Oz Motor Characterization

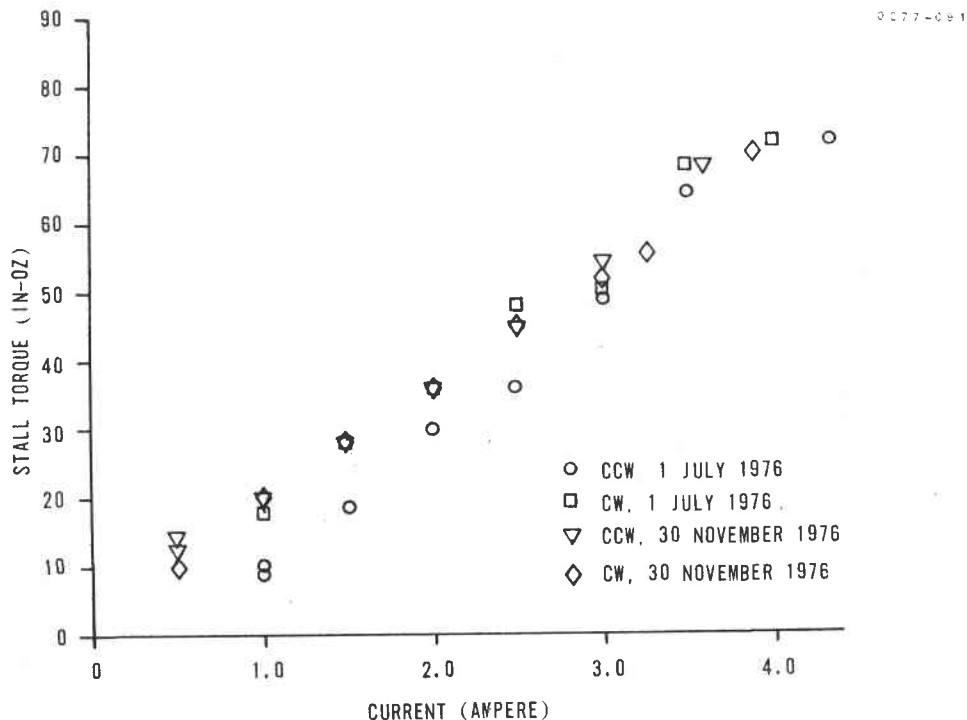


Figure 7-49. Stall Torque - Inland Motor T1806-H (No. 1) -
As a Function of Time

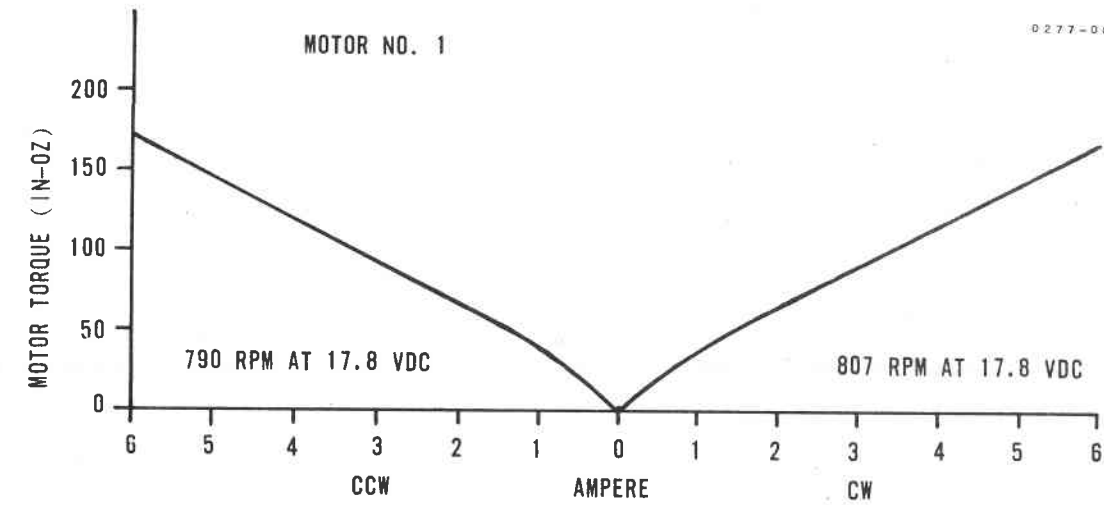
due to measurement technique. At no-load conditions, the CCW and CW speed was 1500 rpm in November at 0.184 to 0.188 amp compared to 1450 rpm in July.

If degradation to a permanent magnet motor does occur, restoration can be made by replacing the magnet with a spare. Stabilization of motor properties is accomplished by applying the full rated current (4.3 amperes for 100 inch-ounces, 6.7 amperes for 200 inch-ounce motor), rotating the shaft discrete rotations of 90 degrees each, and then removing the current.

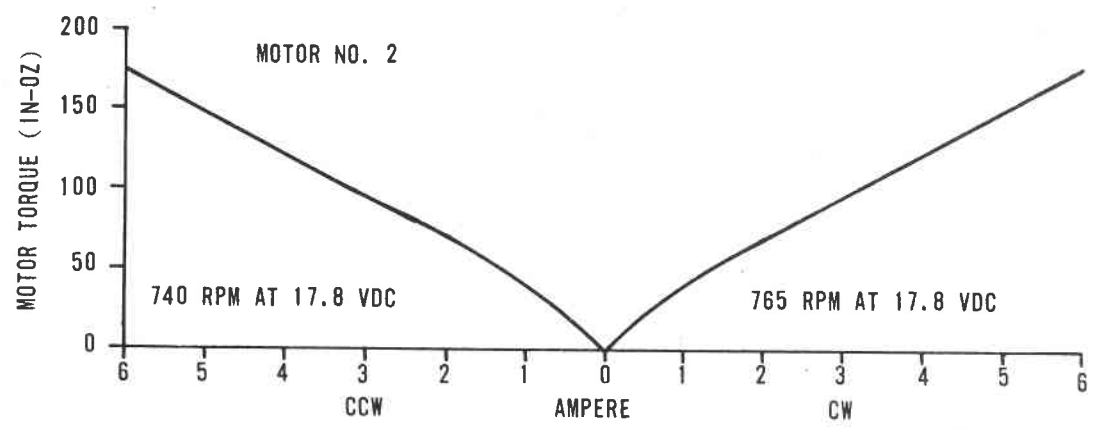
Figures 7-50A through 7-50I show the stall torque characteristics for the 200 inch-ounce Inland motors ultimately used on the heliostat outer drive. No load speeds varied from 740 rpm to 830 rpm.

It is estimated that the total heliostat field plant parasitic power will be increased from 0.72 percent to 0.83 percent of total generated electrical power because of the larger loads for outer axis slew and tracking during daily operation than anticipated as of the Detail Design Review.

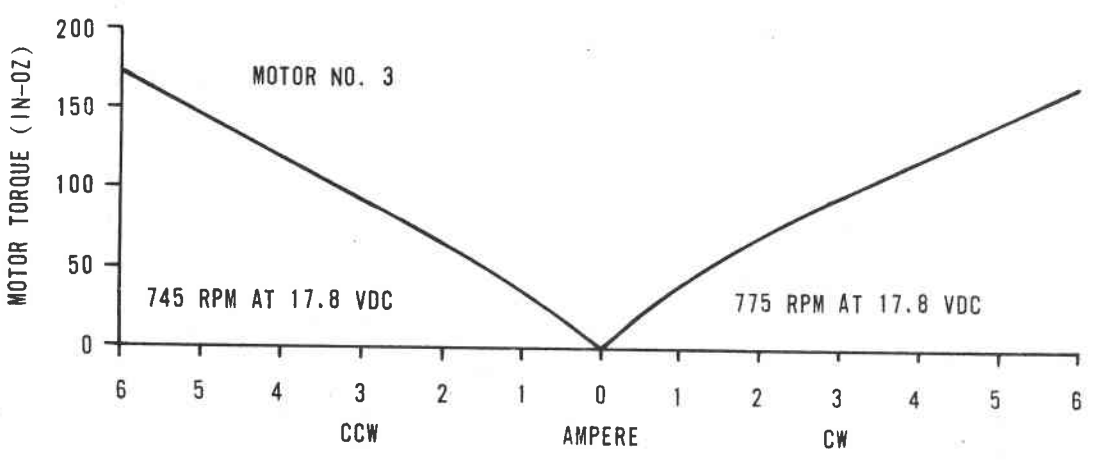
Motor thermal responses were evaluated to determine the feasibility of installing thermocouple cutoff devices on the motor case or winding for hardware safing. In case either the inner or outer axis stalled (hitting OA stops or binding within the IA drive mechanism) motor damage could be precluded if power were removed. Figure 7-51 shows a typical response curve with an outer case one thermal time constant of approximately 13.25 minutes.



A

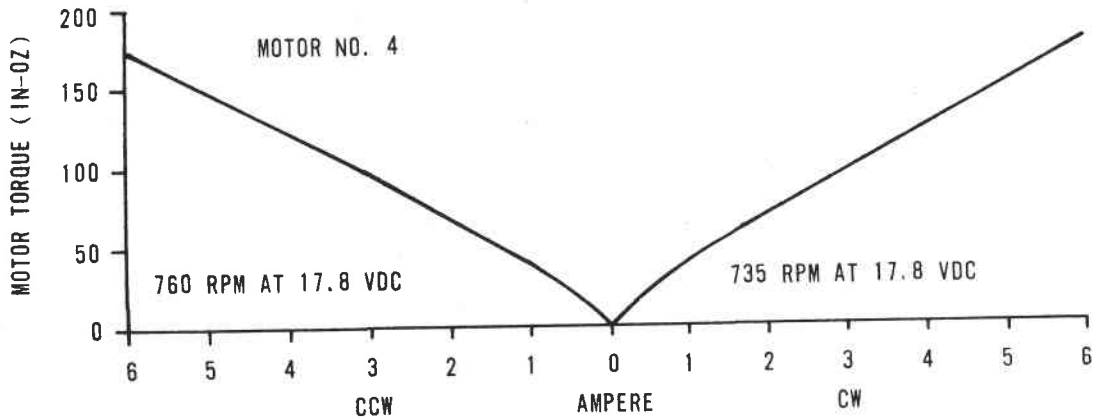


B

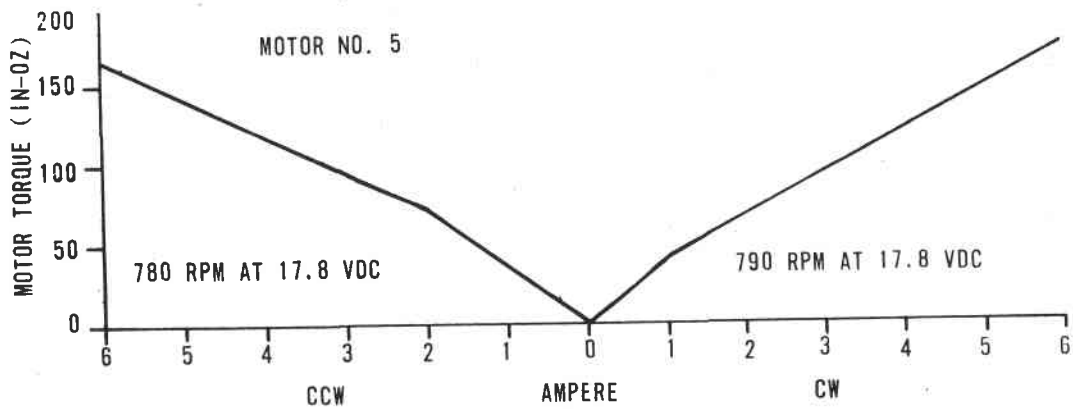


C

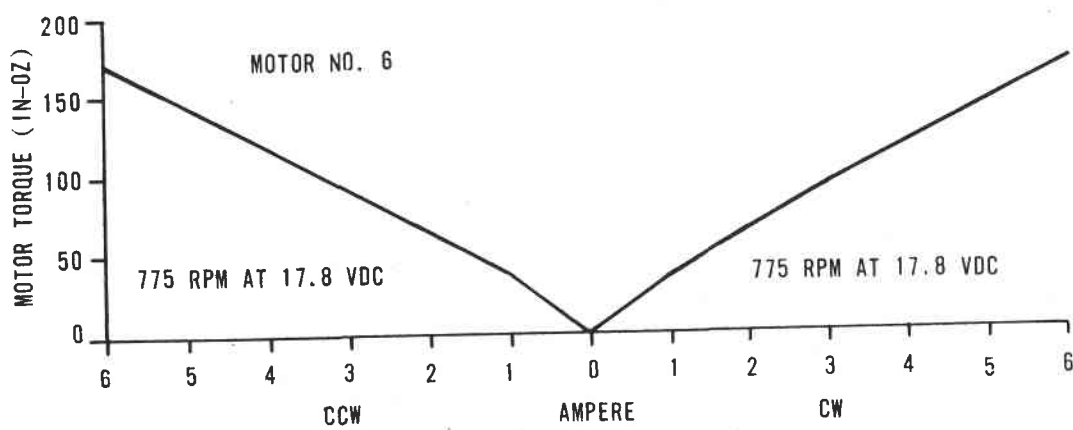
Figure 7-50 (A-I). 200 In-Oz Inland Motor (P/N T1811-B)
 Characterization Data Taken at 1, 2, 3, 6 Ampere in
 CCW and CW Direction



D

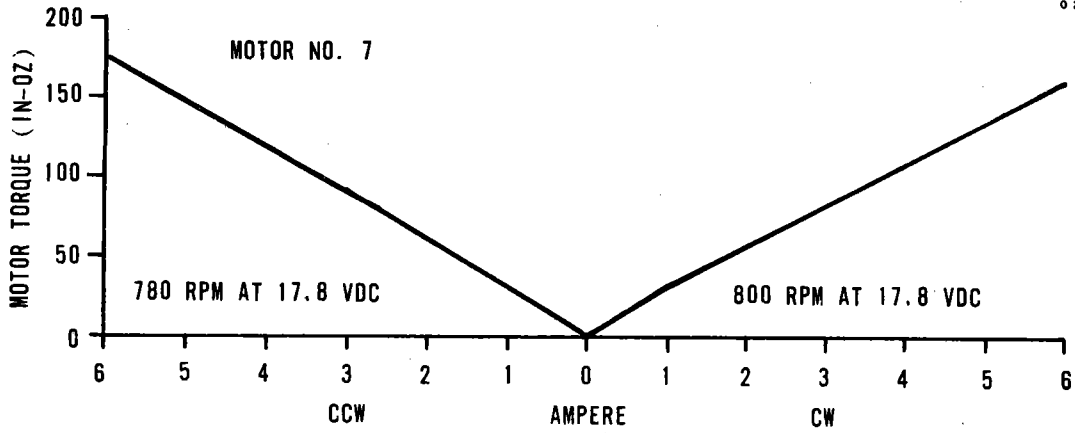


E

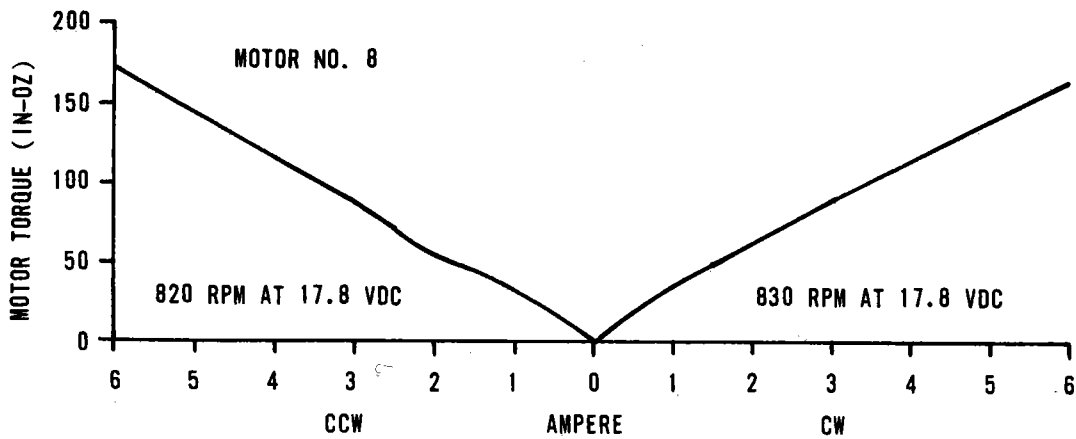


F

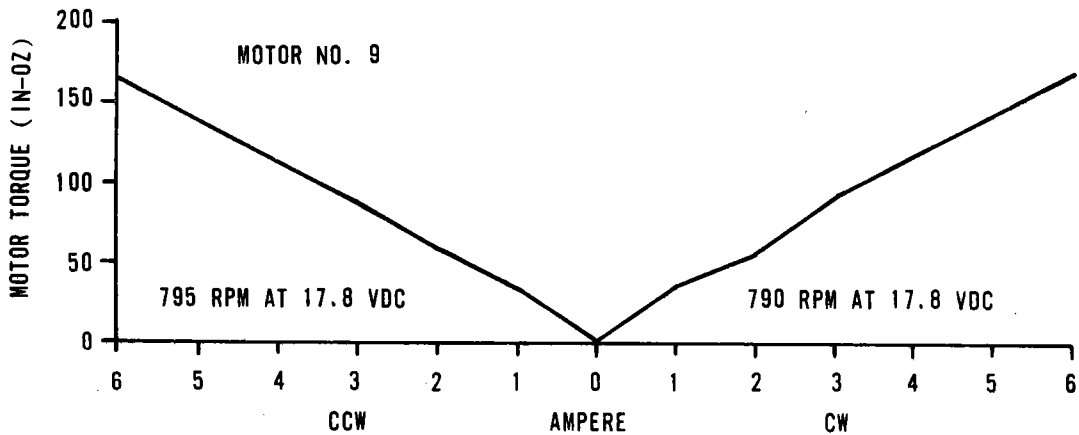
Figure 7-50 (A-I). 200 In-Oz Inland Motor (P/N T1811-B)
 Characterization Data Taken at 1, 2, 3, 6 Ampere in
 CCW and CW Direction



G

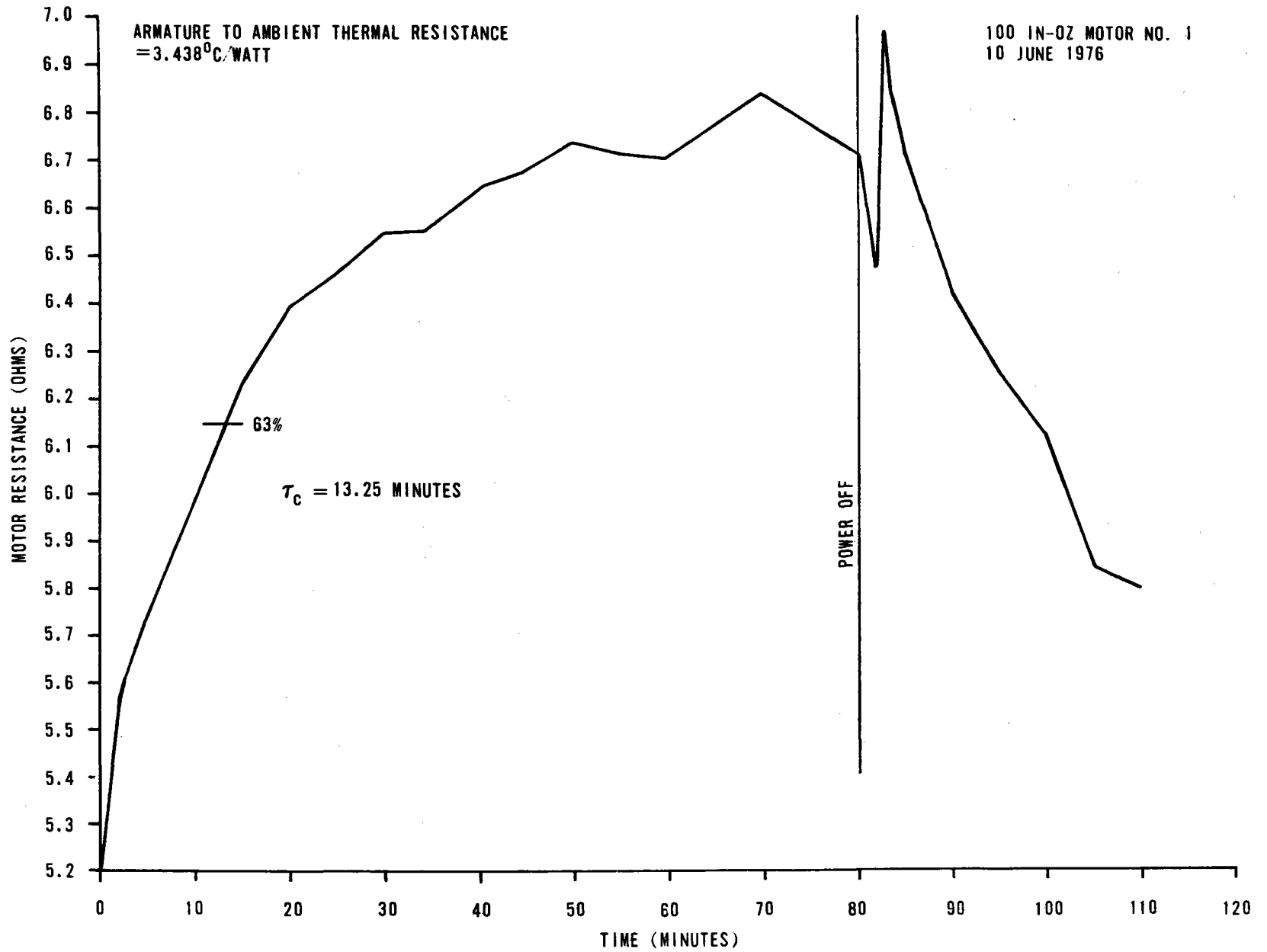


H



I

Figure 7-50 (A-I). 200 In-Oz Inland Motor (P/N T1811-B)
 Characterization Data Taken at 1, 2, 3, 6 Ampere in
 CCW and CW Direction



7-72

Figure 7-51. Motor Thermal Response Characteristics

Thermal Gradient Test

One test was run on the engineering model to determine thermal gradients across the heliostat due to solar insolation loading. Shadowing of metal hardware (e.g., front I-beam to back of I-beam, tie rod to I-beam gradient) will cause relative expansions on the bearing and drive assemblies, thereby inducing rotations and beam deflections. The error budget (Page A-4) assumed a worst case 10°C variation across the cross section of the support posts. Here a maximum of 3°C temperature differential was expected.

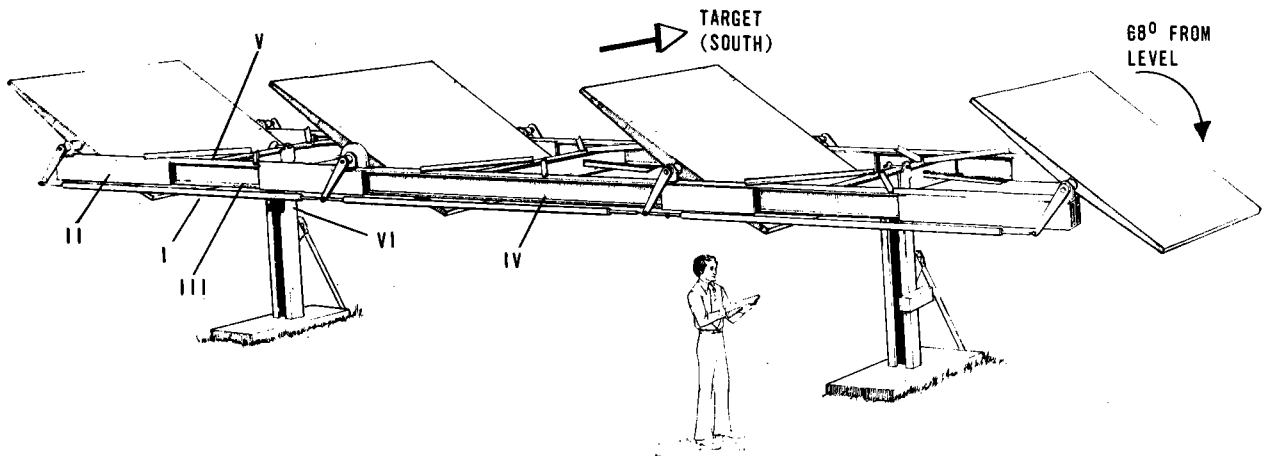
During the test, the relative humidity varied from 60 to 75 percent, winds were from 2.7 to 5.8 M/S (6 to 13 mph), peak insolation about 850 watts/m², and some partial cloud coverage.

Figure 7-52 shows a sketch of the general grouping of thermocouple locators. Table 7-7 gives the location of each thermocouple along with the raw recorded temperature data. Figures 7-53A through 7-53C plot the data as a function of time and location.

After compensating for initial differences in thermocouple biases, it is seen that no differentials which reflect relative expansion resulting in pointing errors exceeded the 18°F (10°C) per the error budget. Across the boxed I-beam 13°F was reached as a worst case. The critical tie rod distribution was more uniform than anticipated with little gradients. The posts did exhibit a maximum of 7°F gradient exceeding the 5.5°F error budget value. This gradient would cause a theoretical 0.26 mr deflection about the outer (O₁) axis. However the frame induced gradients would cause a theoretical 0.4 mr deflection about the inner axis (I₂) rather than the estimated 0.9 mr at a 10°C gradient.

All metal surfaces were painted with common high gloss Zynolyte epoxy enamel white paint. For operational field heliostats, a white cellulous lacquer should be used. Between 88 percent and 70 percent of solar radiation will be reflected, including long term oxidation effects.

It is expected that additional data will be obtained in the future to further confirm the thermal gradient error sources.



1	NE PUSH ROD E END	I	15	FRAME OPEN TOP	IV
2	NE PUSH ROD W END	I	16	FRAME OPEN N SIDE	IV
3	NE PUSH ROD CENTER TOP	I	17	FRAME OPEN BOTTOM	IV
4	NE PUSH ROD CENTER N	I	18	CROSS RAIL TOP	V
5	NE PUSH ROD CENTER BOTTOM	I	19	CROSS RAIL W SIDE	V
6	NE PUSH ROD CENTER S	I	20	CROSS RAIL BOTTOM	V
7	FRAME NE END TOP	II	21	POST E N SIDE	VI
8	FRAME NE END N FACE	II	22	POST E S SIDE	VI
9	FRAME NE END BOTTOM	II	23	AMBIENT ABOVE CROSS RAIL RADIATION	
10	FRAME NE END S FACE	II	24	AMBIENT BELOW CROSS RAIL SHADED	
11	FRAME NE END INSIDE BOX	II			
12	FRAME OPEN TOP	III			
13	FRAME OPEN N SIDE	III			
14	FRAME OPEN BOTTOM	IV			

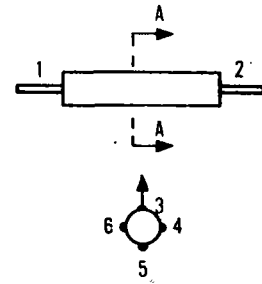
Figure 7-52. Engineering Model Heliostat Temperature Monitor Points

Table 7-7. Thermal Gradient Data

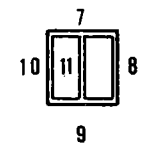
Sensor Time (EDT)	Tie Rod						Frame Box Sec					Frame at Cross Rail			Frame Center			Cross Rail			Post		Ambient		
	E 1	W 2	T 3	Center N 4	B 5	S 6	T 7	N 8	B 9	S 10	I 11	T 12	N 13	B 14	T 15	N 16	B 17	T 18	W 19	B 20	N 21	S 22	EX 23	SH 24	
1000	82	84	84	84	84	84	83	89	84	82	84	84	84	84	84	85	84	85	84	84	84	80	80	80	80
1030	83	84	84	84	83	83	85	88	84	83	84	85	86	85	86	87	85	85	85	84	84	83	84	83	83
1100	86	87	87	86	87	87	88	91	86	86	86	88	89	88	88	91	87	88	88	86	86	85	85	85	85
1130	90	90	90	91	89	88	91	97	88	88	89	91	92	91	91	94	91	90	90	90	88	86	84	85	
1200	92	94	94	95	92	92	95	100	92	90	92	95	96	94	95	98	94	94	94	94	94	87	87	87	
1215	93	95	93	95	92	92	97	103	93	93	92	96	98	96	97	100	96	95	94	94	94	88	92	89	
1230	91	93	94	94	92	94	96	97	93	92	93	96	96	96	97	99	96	94	94	93	94	89	90	88	
1300	97	98	98	99	96	97	100	106	97	94	97	100	102	100	100	104	100	98	98	98	98	92	93	90	
1307	94	97	97	97	94	96	99	104	96	94	96	99	100	99	100	101	99	95	95	95	96	91	88	87	
1318	92	92	92	93	91	92	96	99	93	91	93	96	97	96	96	97	96	94	93	93	94	90	88	86	
1330	88	90	90	90	88	89	92	94	92	88	92	93	93	92	92	93	92	91	91	90	91	89	87	85	
1335	89	90	91	91	89	90	92	95	91	88	91	93	93	92	93	93	93	91	90	90	91	88	87	87	
1348	88	87	89	89	88	89	91	92	88	88	90	91	91	91	91	92	91	90	90	89	88	89	86	87	
1400	94	94	95	96	93	93	94	100	89	89	93	94	95	94	94	97	93	91	91	91	88	89	86	88	
1405	90	89	91	92	91	91	92	95	88	88	91	92	93	92	93	95	93	90	90	91	88	89	88	89	
1430	92	93	92	95	92	92	96	103	90	91	96	95	96	95	96	98	95	92	93	93	89	89	87	88	
1500	92	93	92	94	92	91	95	101	89	90	93	94	95	94	95	96	94	91	93	93	89	90	87	89	
1530	92	93	92	94	92	92	94	99	90	90	92	95	95	94	95	96	94	92	94	93	90	91	88	90	
1600	93	93	93	95	93	93	95	99	91	91	93	95	96	95	95	97	94	93	95	95	91	92	91	87	

Partial Cloud Coverage
Cloud Coverage

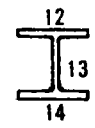
Partial Sun
Sunny



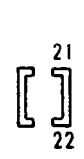
SECTION A-A



I-BEAM BOXED OFF WITH STIFFENER



OPEN I-BEAM



CROSS RAIL EXPOSED

NOTE: TEMPERATURES °F

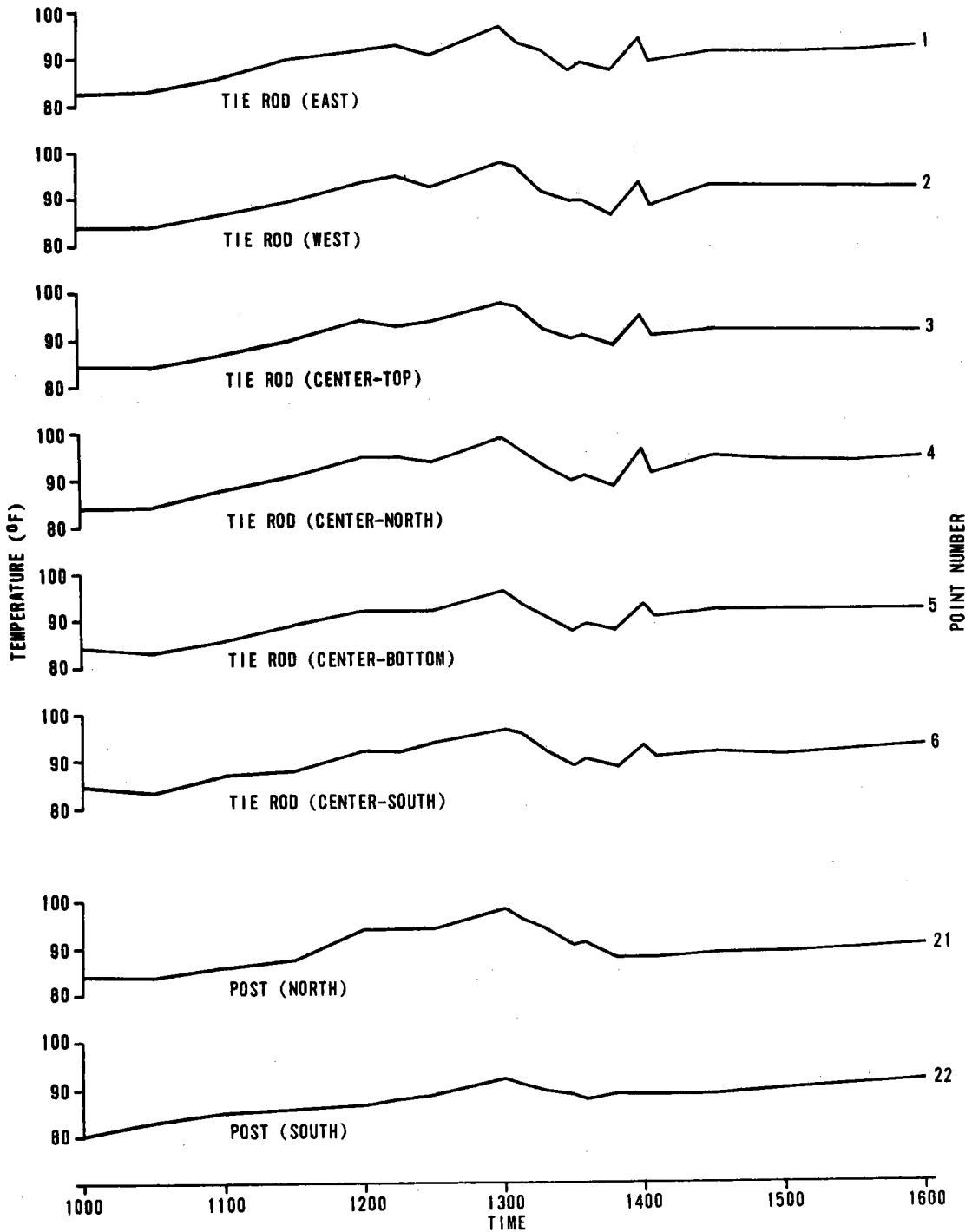


Figure 7-53A. Typical Thermal Time History for Selected Heliostat Points

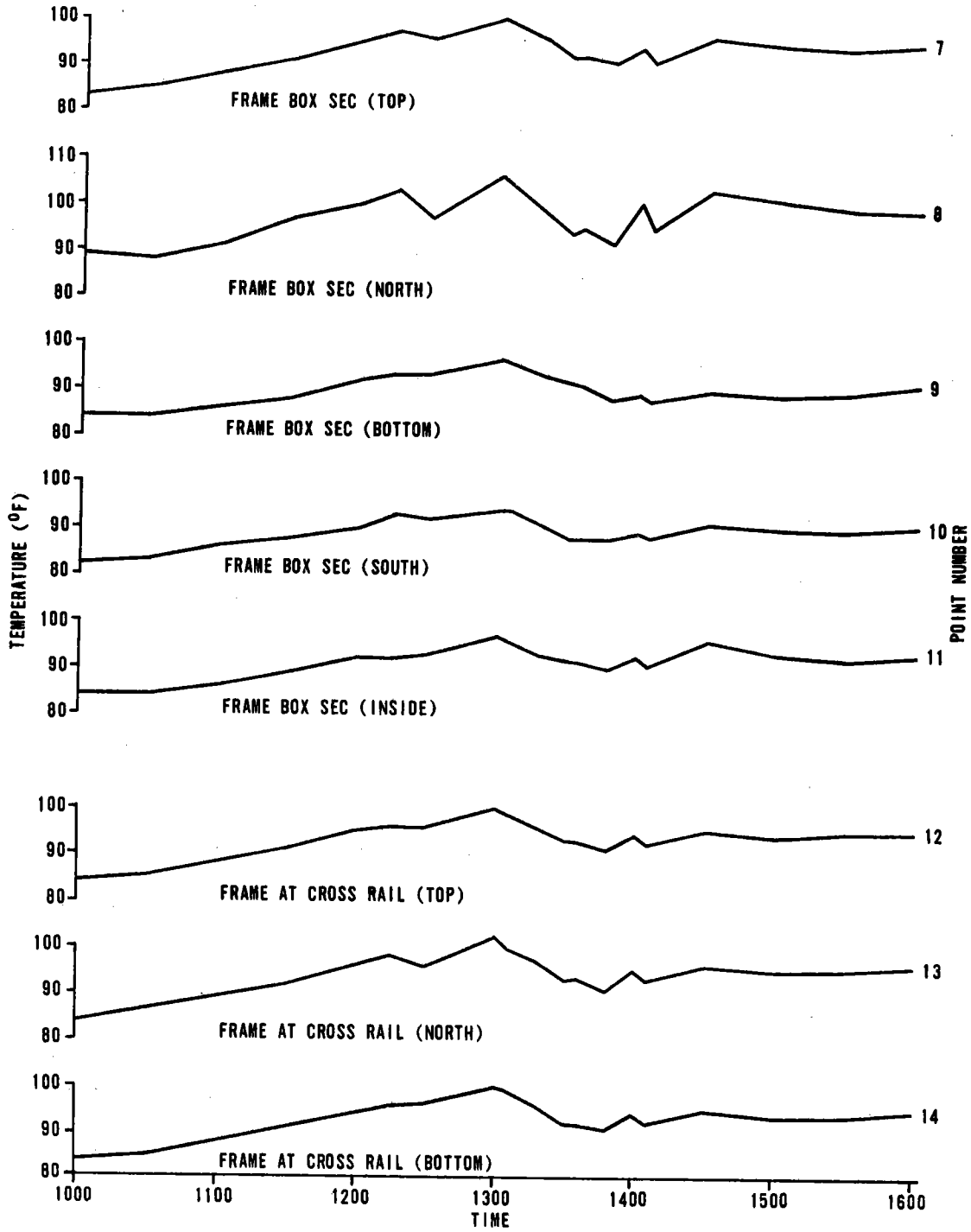


Figure 7-53B. Typical Thermal Time History for Selected Heliostat Points

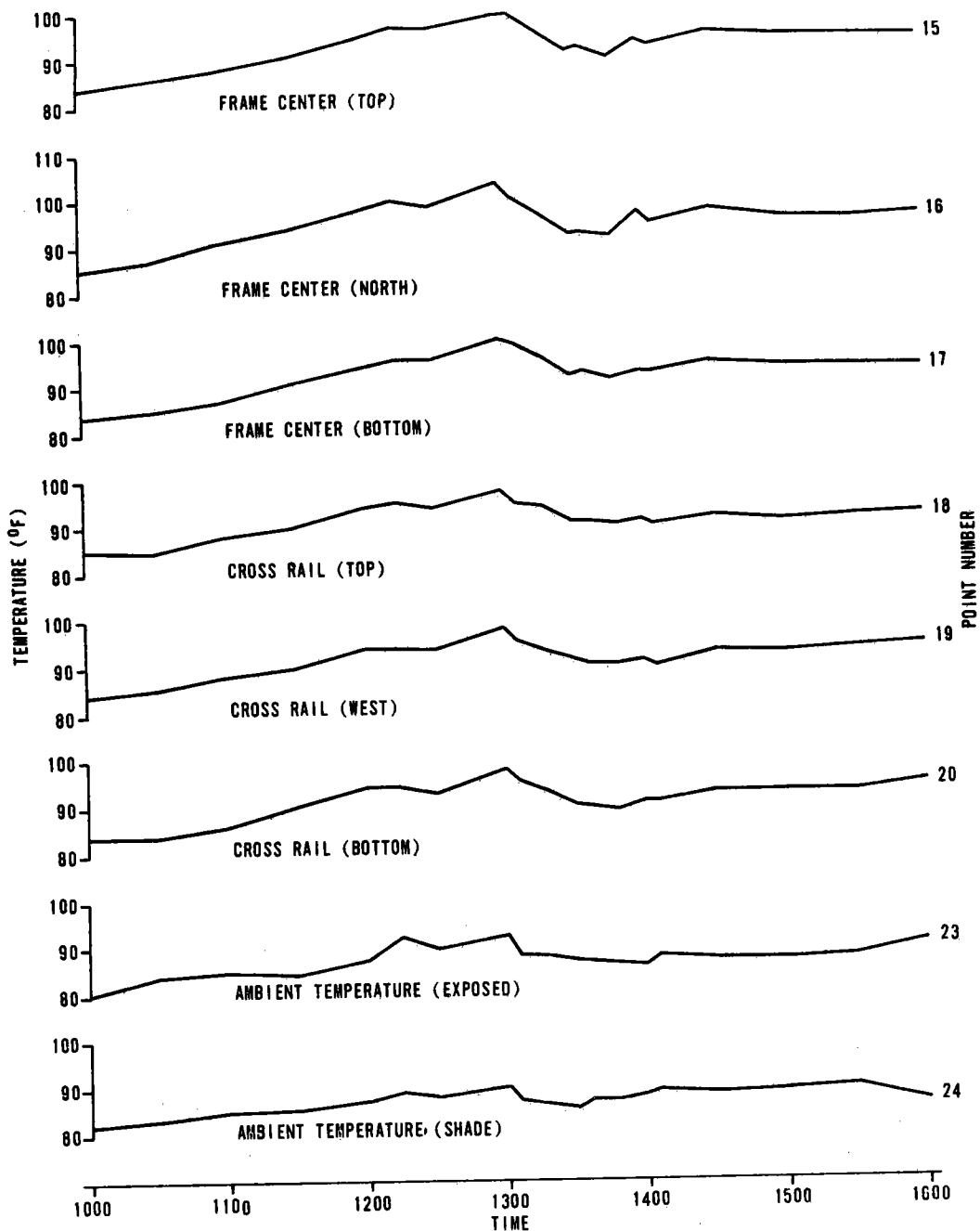


Figure 7-53C. Typical Thermal Time History for Selected Heliostat Points

Heliostat Actuators and Outer Gimbal Drive Characteristics

Two types of linear actuators were tested for use as the outer axis drive:

1. Machine Screw Actuators from Templeton Kenly & Company.
2. Ball Screw Actuators from Limitorque Corporation.

Figure 7-60 shows a photograph of actuators (ball screw) mounted on an experimental model heliostat.

For Commercial Plant and Pilot Plant applications, the ball screw actuators were selected even though the initial cost is greater (\approx \$70 per actuator). The ball screw linear actuator has a proven 30 year life while the machine screw will not provide the life cycle requirements without, at a minimum, increasing backlash and thereby reducing tracking accuracies. Lash cannot be calibrated out and removed by tracking software computations as can most other error sources.

Machine Screw Actuators

Initially, no-load torques at the input motor shaft from the machine screw actuators varied from 49.7 inch-ounces to 73.8 inch-ounces depending on the angle of the actuator screw with respect to horizontal, the amount of extension of the screw, and direction of travel. Without the Inland motor attached, the least no-load torque was 32 inch-ounces.

The machine screw actuators were reworked in-house several times to reduce actuator loads (lubricant changed, bronze bushings used, the steel screw cover replaced with lighter PVC to reduce side loads). Figures 7-54 and 7-55 show that the no-load and loaded RPM versus torque characteristics of the machine screw actuators could not be expected to operate with the 100 inch-ounce motors due to low rpm and limited torque capability.

Actuator efficiency is defined as ratio of output load to input torque.

$$\text{Efficiency} = \left[\frac{\text{Load Weight (\#)} \times \text{Lead of Screw (inch)}}{\text{Gear Reduction} \times 2\pi} \right] \text{Torque Input}$$

The torque input is determined from the motor characterization (inch-ounce per ampere at operating voltage),

For the machine screw; nominally:

Lead = 0.333

Gear reduction = 24

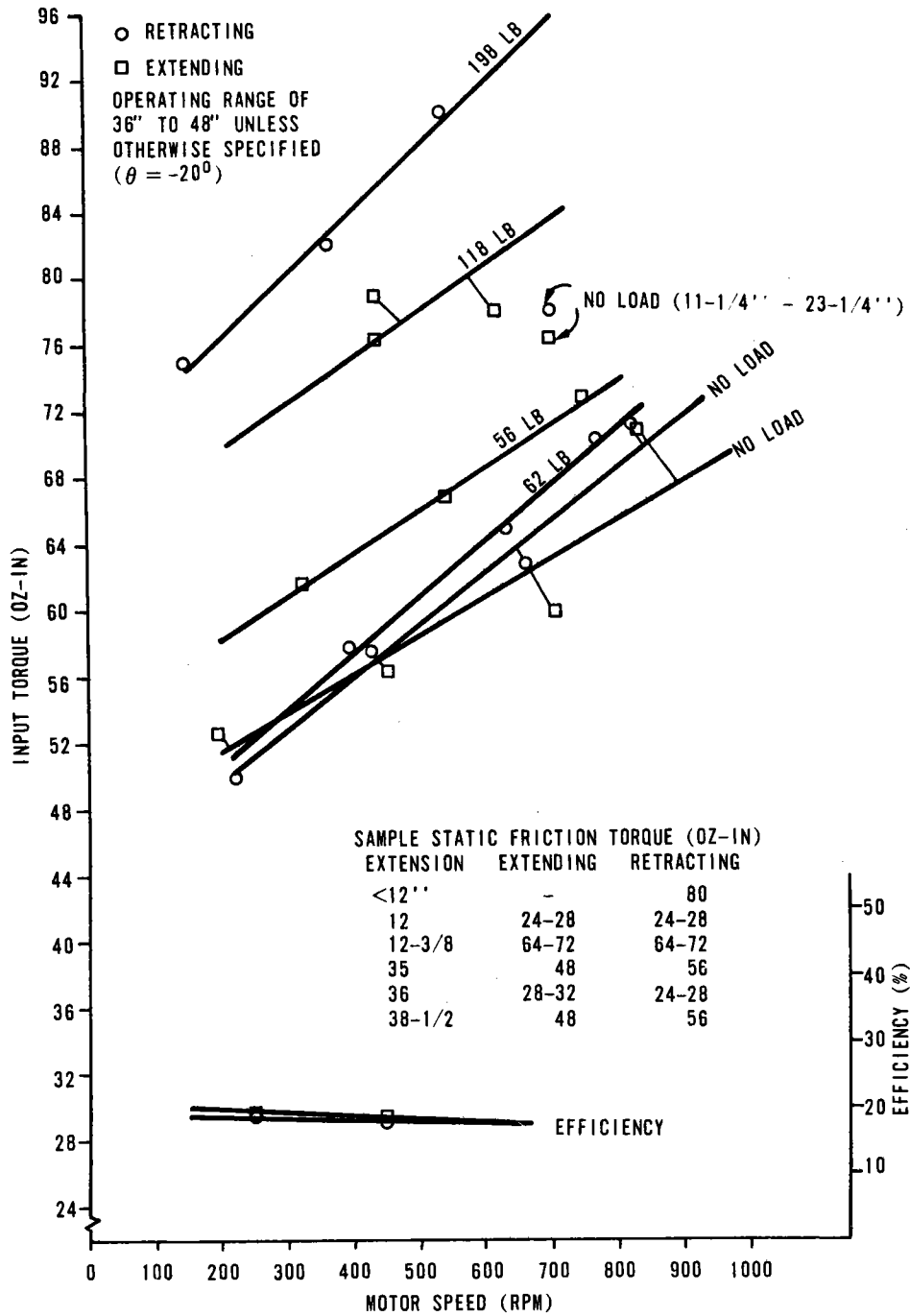


Figure 7-54. Engineering Model Heliostat Machine Screw Actuator No. 1

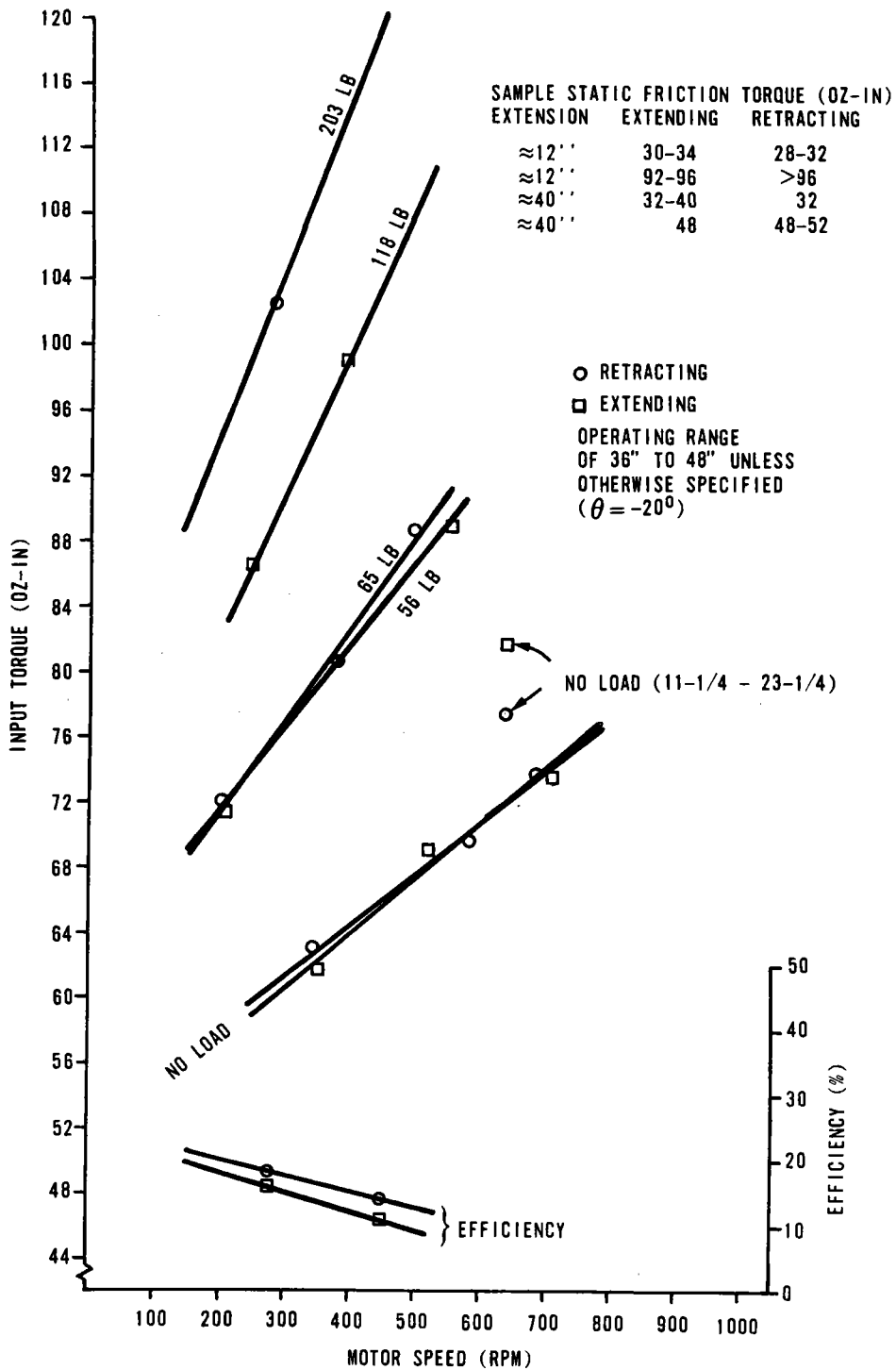


Figure 7-55. Engineering Model Heliostat Machine Screw Actuator No. 2

For the ball screw; nominally;

Lead = 0.474

Gear reduction = 40

On Page 7-147, it is explained that the actual actuator end-to-end gear ratio had to be calibrated to improve tracking accuracy.

The machine screw actuators were especially sensitive to side loads. In a horizontal plane, under its own weight, an extension of less than 16 inches caused frequent stall of the motor due to the weight of the trailing edge of the screw hitting the cover inside.

Power requirements reached 70 watts under certain loading conditions.

Ball Screw Actuator - Comparison with Machine Screw

Initially the ball screw actuators received showed no-load torques up to 60 inch-ounces. With additional in-house work (e.g., changing the input shaft bearing seals, different lubricants, decreasing the imbalance about the pivot axis, increasing the gap between the worm gear and bell housing, increasing the bell housing inner diameter), the performance of the first two ball screw actuators was significantly improved. Compare Figures 7-56 and 7-57 taken 27 May 1976 with Figures 7-58 and 7-59 taken one month later, 29 June 1976. These data are using actual engineering model frame gimbals loadings. The input power was reduced about 10 watts and gimbal rates increased in both directions. Actuator efficiencies ranged from 33 to 38 percent.

The improvements in no-load torque/speed as of early July 1976 of the ball screw actuators is shown by relating Figure 7-60 back to Figures 7-54 and 7-55. Lowering the static and viscous friction torques of the ball screw actuators increased their performance while the machine screw could not be improved any more than shown. For instance at 900 rpm the average no-load torque for the ball screw is 32 inch-ounce while the machine screws average 74 inch-ounce no-load torque.

For the next six ball screw actuators, Limitorque significantly redesigned their actuators incorporating the changes we recommended based on our experience. These were used on our three experimental models.

On five of the new linear actuators, the viscous, no-load torque was 5 inch-ounce or less. The sixth actuator (SN 241844) bound up under operation once and was returned to the vendor. Rework had reduced its no-load viscous torque to 16 to 20 inch-ounces ccw and 22 to 24 inch-ounces cw which is 4X typical new values.

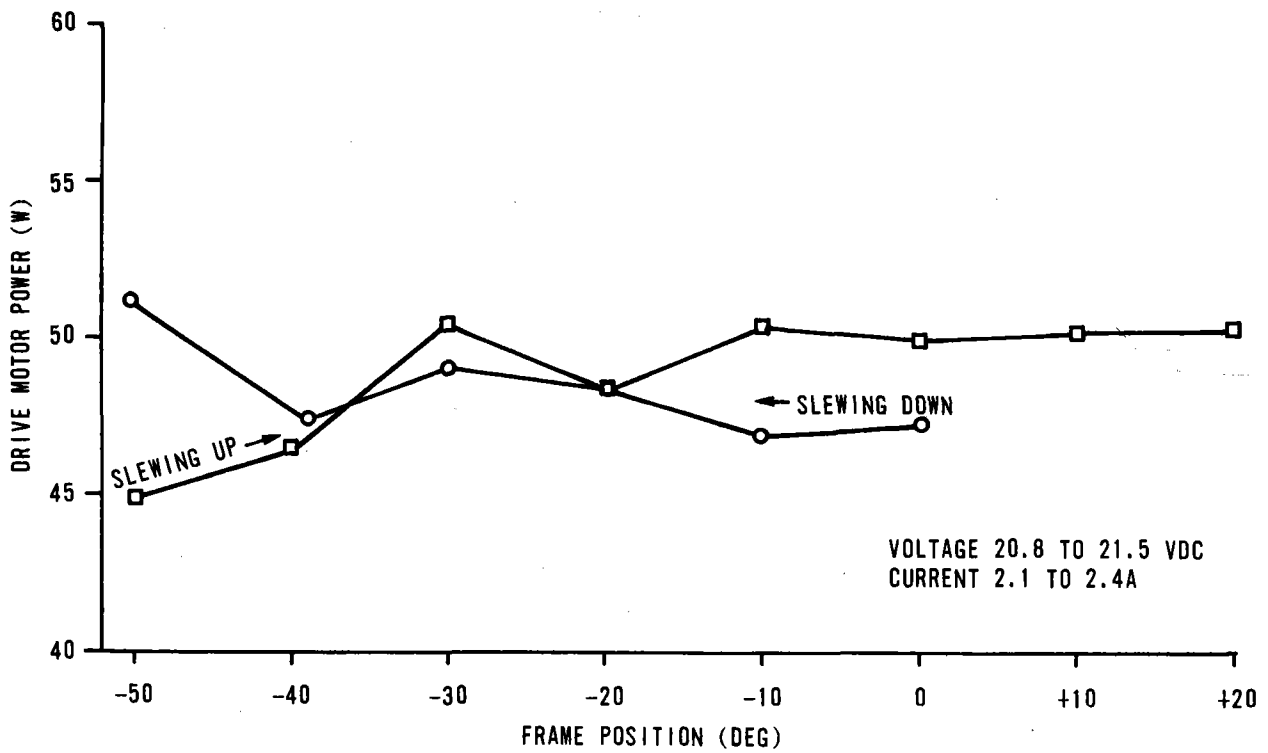
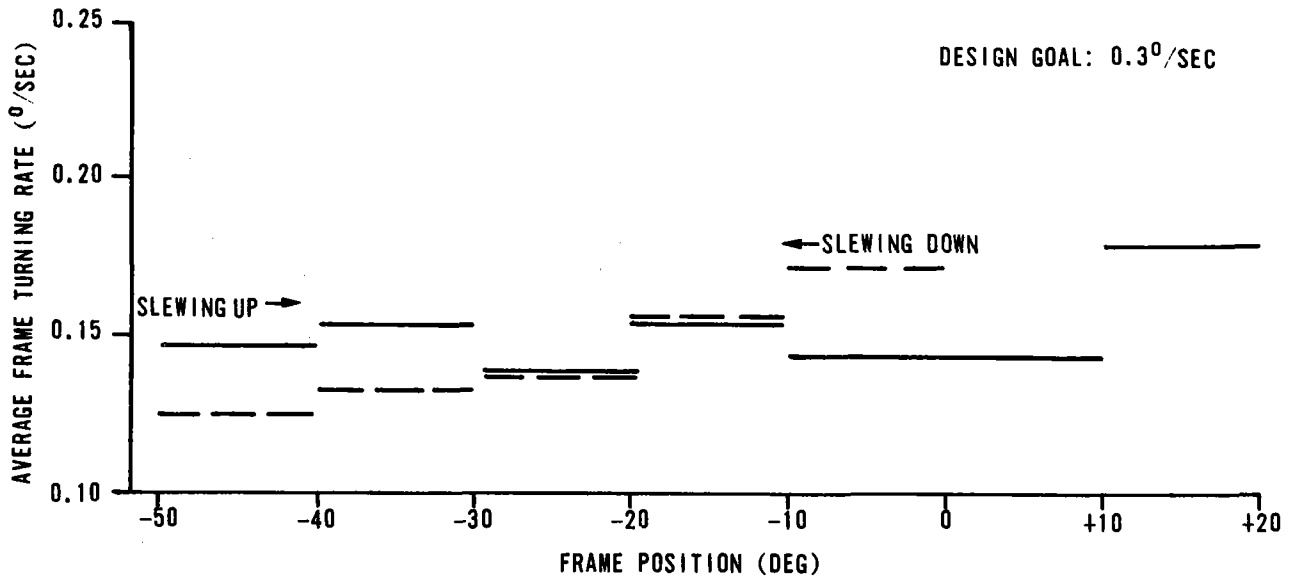


Figure 7-56. Engineering Model Heliostat Front (Tung End) Frame Drive Motor $R_{DC} = 6.66\Omega$

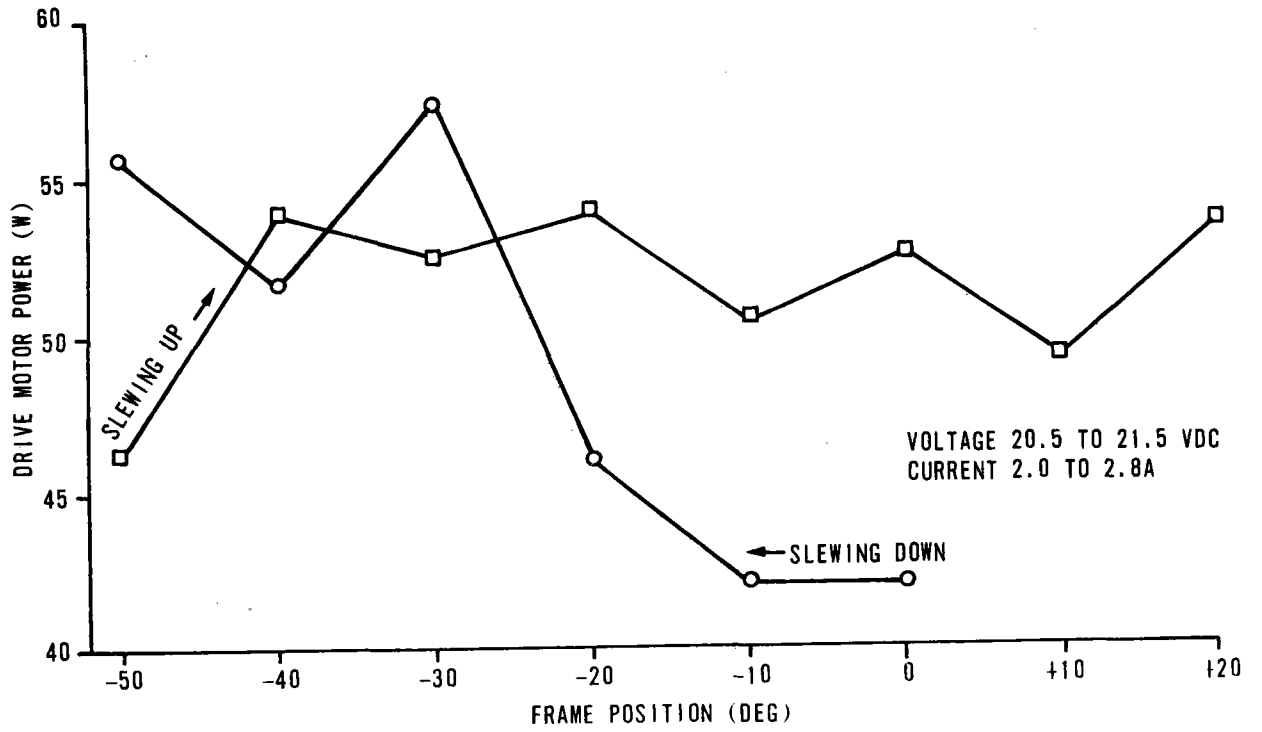
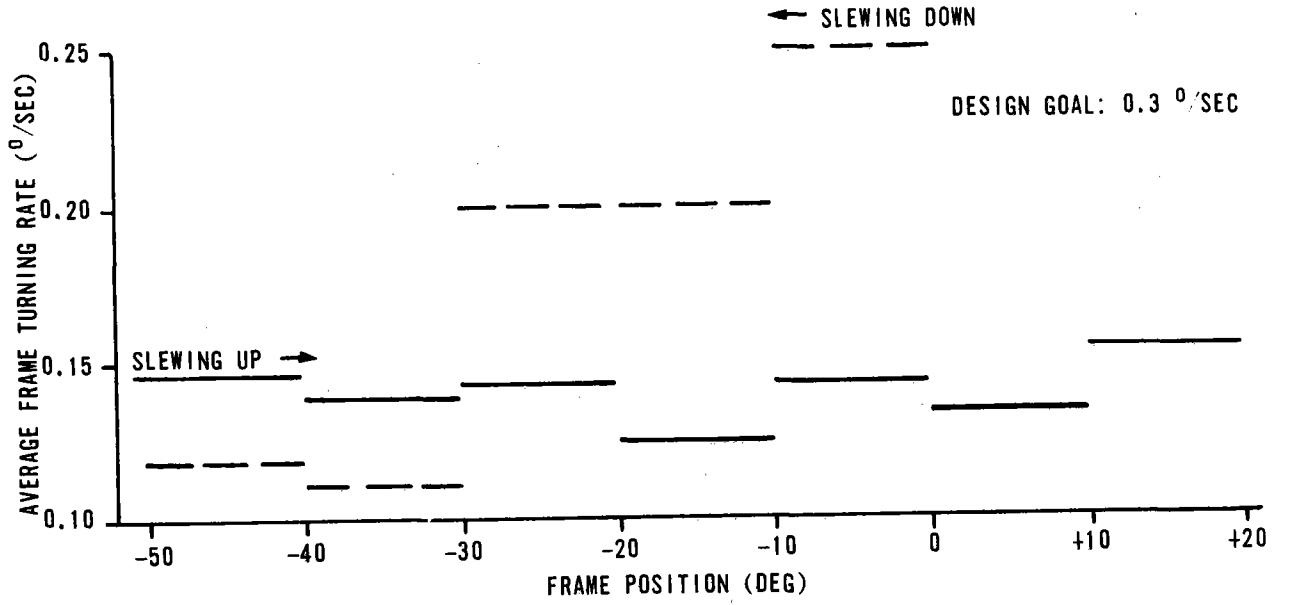


Figure 7-57. Engineering Model Heliostat
Rear Frame Drive Motor $R_{DC} = 8.06\Omega$

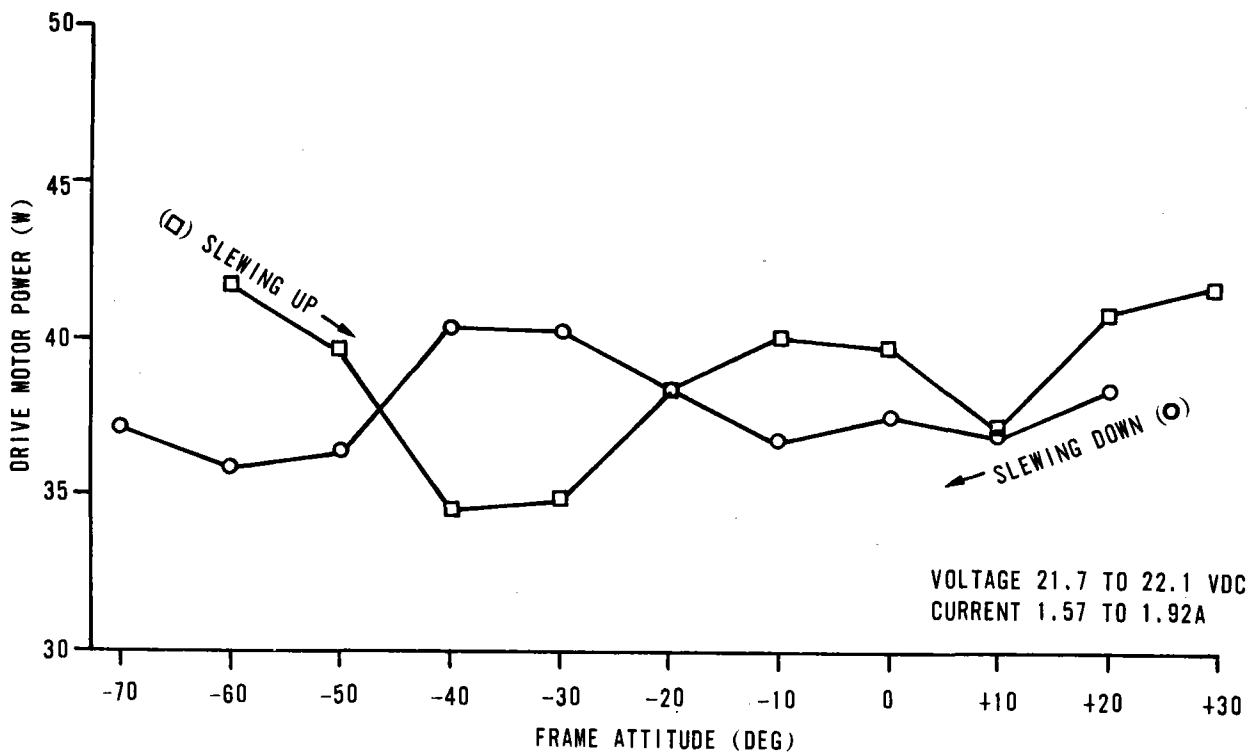
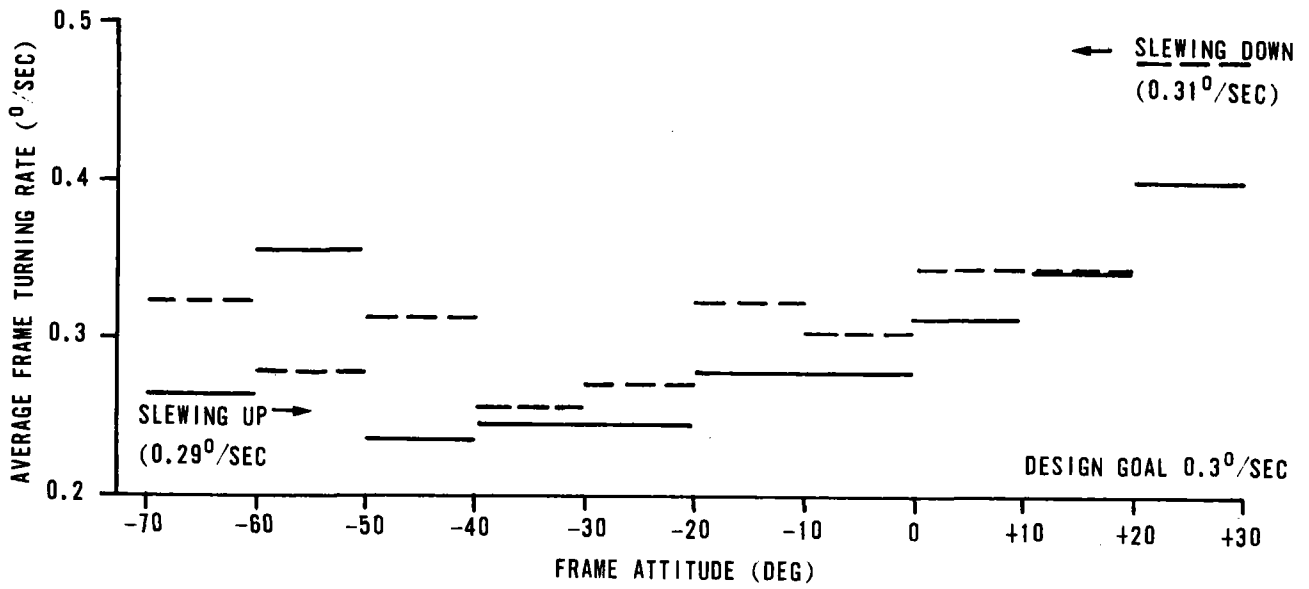


Figure 7-58. Engineering Model Heliostat
Front (Tung End) Frame Drive Motor
(Data Taken Following Actuator Overhaul)

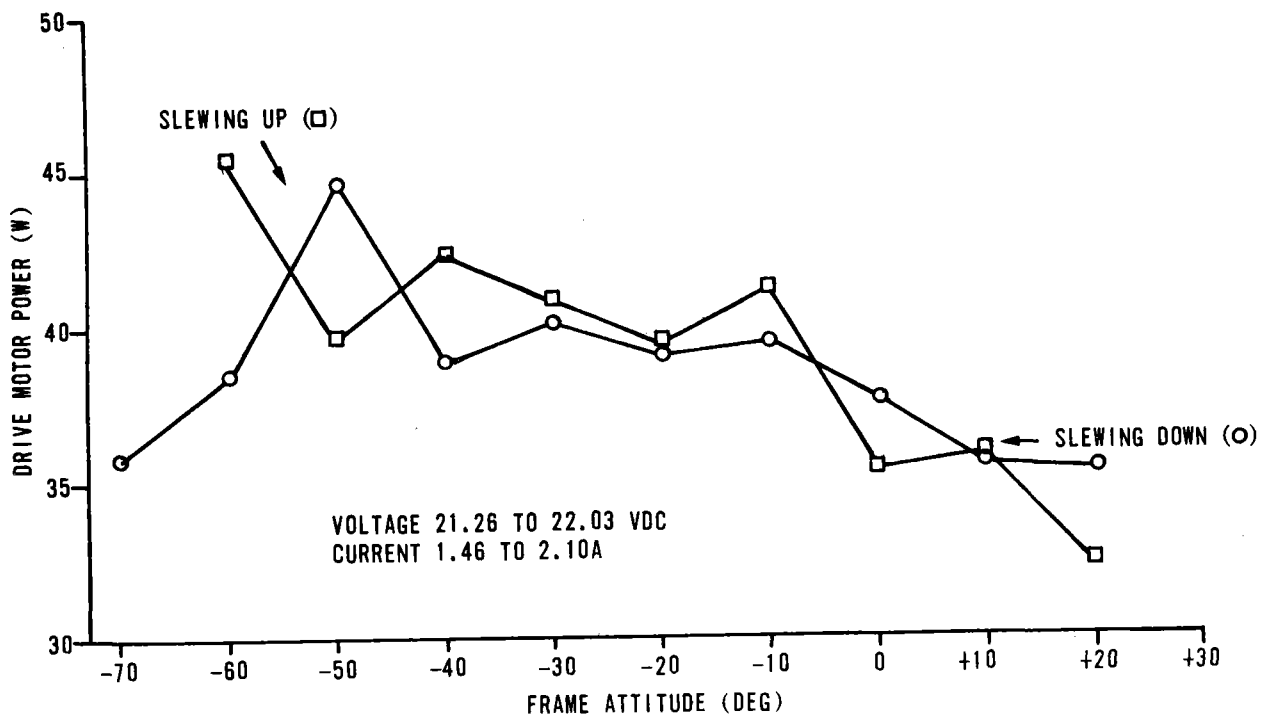
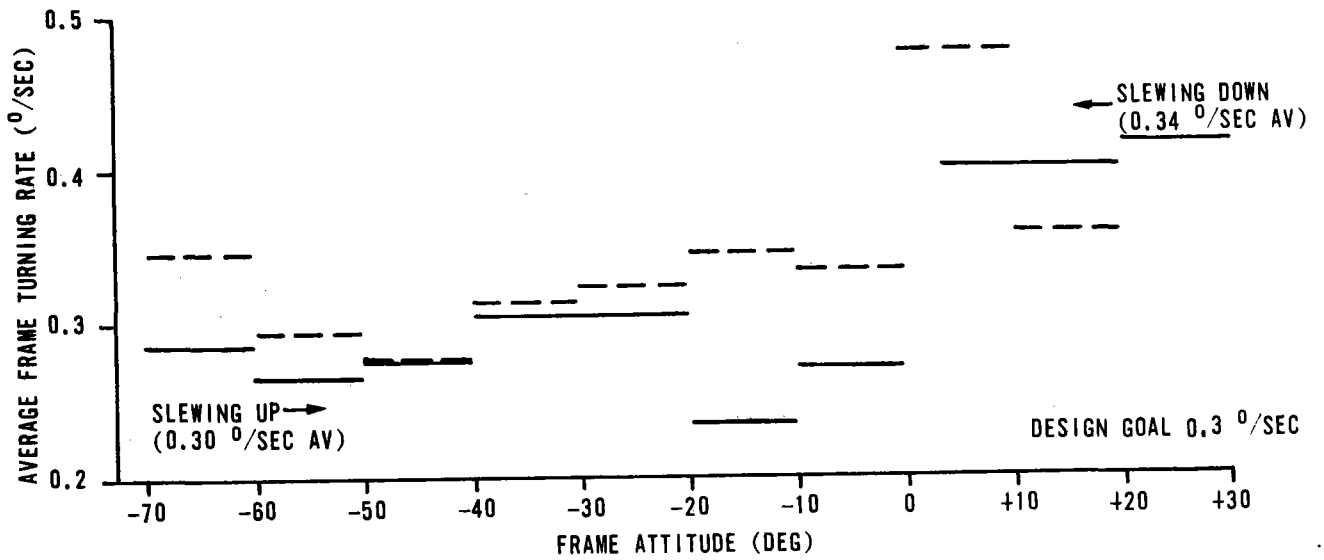


Figure 7-59. Engineering Model Heliostat
Rear Frame Drive Motor
(Data Taken Following Actuator Overhaul)

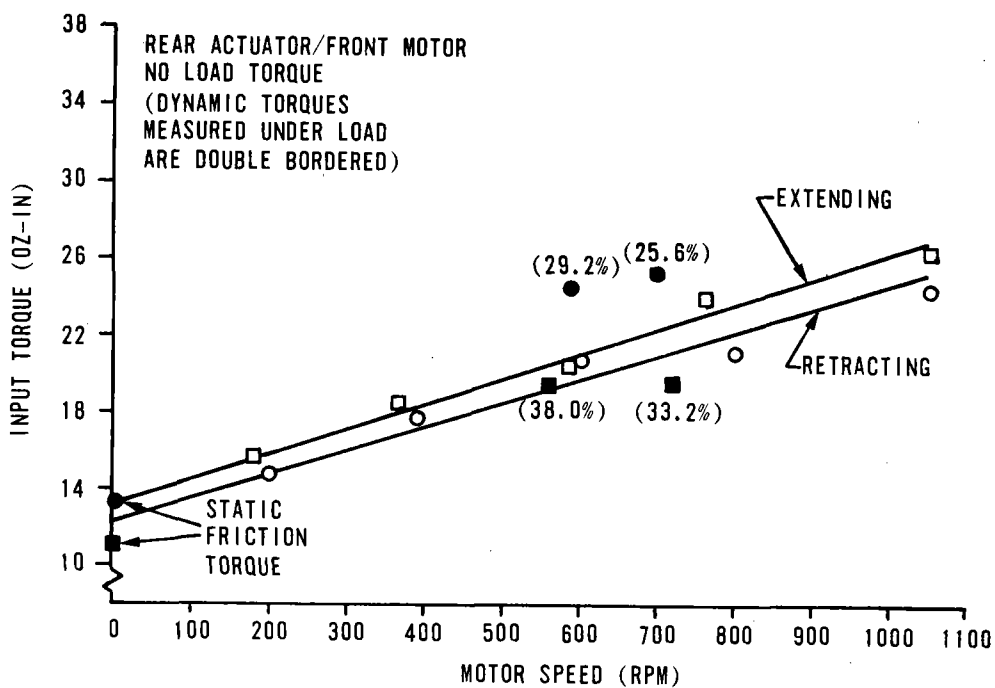
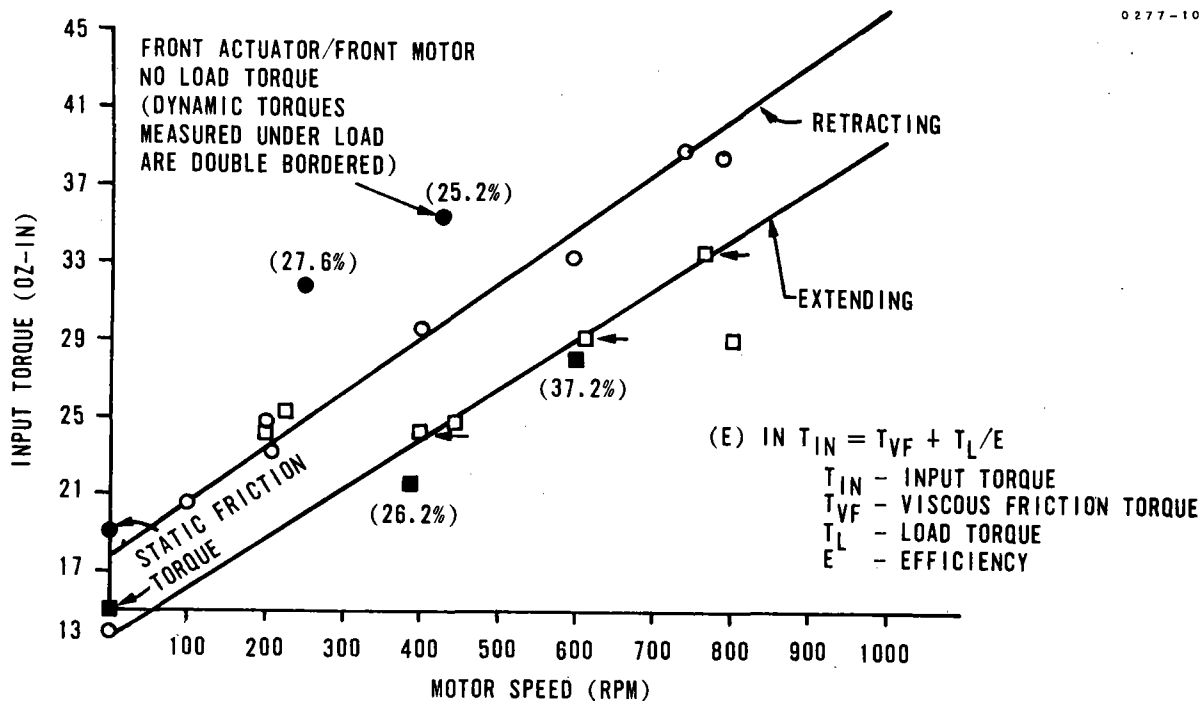


Figure 7-60. Engineering Model Heliostat Ball Screw Linear Actuators

The improved machine screw actuators were initially placed on the North experimental model heliostat (with the new 200 inch-ounce motors). Tables 7-8A and 7-8B show the tabulated power, torque obtained from the 200 inch-ounce motor characterization, and slew times for total outer gimbal travel. Notice that even with the larger 200 inch-ounce PMDC motors, the gimbal rate was only 0.22 to 0.25 degree/second average. This data can be compared to Tables 7-9A and 7-9B where the redesigned ball screw actuators replaced the machine screw actuators. Otherwise the North heliostat site was identical. On the average, the internally specified gimbal rate was met ($\approx \geq 0.3$ degree/second) and the power was reduced by a factor of 1/2 to 1/2.6. This is all because the input torque requirements were cut in half-- the difference being the actuators. At the lower ($-\theta$) angles, the slew rate falls to 0.28 degree/second. Figures 7-61A and 7-61B plot typical outer axis slew rates versus gimbal angle. The mirrors in stow position produce the worse case imbalance that must be driven at the large negative gimbal angles.

The current profile of the machine screw shown in Figure 7-62B shows the typical high current pulled during travel from $\theta = +30$ degrees (fully extended at heliostat) down to $\theta = -70$ degrees (retracted). Also notice the binding and then relaxing of the actuator when compared to the smoother power drain from a Ball Screw actuator under the identical heliostat travel with identical 200 inch-ounce Inland motor, Figure 7-62A.

Ball Screw Actuator Scale Factors

One tracking error source of an initially unexpected large magnitude results from the linear scale factor differences found between actuator screws. This is an easily calibratable and is compensated for as explained on Page 7-147. The screw lead (pitch) per vendor data, was 0.474 inch. At a gear ratio between the motor and actuator gear, the nominal scale factor should be 0.01185 inch per motor revolution.

By recording revolutions from the heliostat electronics (output from the encoders) with electronic counters and measuring traveled distances, scale factors of 0.011837 inch to 0.011770 inch were obtained. This represents a total lead variation of 0.0027 inch from actuator to actuator. Some of this variation may have resulted from end-to-end system and measurement induced changes, but the net result is the important parameter. Scale factor can be determined by a simple calibration after heliostat assembly. If two actuators are made from one screw cut in half so that they will be evenly matched, the actuator-to-actuator compatibility tolerance specification can be reduced slightly thereby reducing manufacturing costs at the expense of an additional on-site calibration requirement (although this may be necessary anyway due to end-to-end system differences).

Table 7-8A. North Site, 28 October 1976
 200 In-Oz Motor, SN No. 3 Using Machine Screw Actuator No. 1

+30 DEG → -70 DEG (CCW - MOTOR SHAFT) (EAST END)

<u>Angle</u>	<u>I</u>	<u>VD</u>	<u>Power (watt)</u>	<u>Torque (in-oz)</u>	<u>ΔT</u>
+30	2.60	21.2	55.1	96.0	0
+25	2.60	21.2	55.1	96.0	
+15	2.43	21.3	51.8	91.5	52
0	2.52	21.0	53.0	93.0	56
-15	2.35	21.3	50.1	88.5	68
-30	2.36	21.5	50.7	89.0	68
-45	2.31	21.5	49.7	87.5	68
-60	2.40	21.5	51.6	91.0	73
-70	2.48	21.2	52.6	93.0	40
Avg +30 → 0 =			53.75		Σ = 425 sec
Avg 0 → -70 =			51.28		= 0.24 deg/sec

-70 DEG → +30 DEG (CW - MOTOR SHAFT)

<u>Angle</u>	<u>I</u>	<u>VD</u>	<u>Power (watt)</u>	<u>Torque (in-oz)</u>	<u>ΔT</u>
-70	2.55	21.3	54.3	98.5	0
-60	2.20	21.6	47.5	88.0	40
-45	2.25	21.7	48.8	90.0	76
-30	2.47	21.3	52.6	96.0	70
-15	2.48	21.3	52.8	97.0	73
0	2.63	21.0	55.2	100.0	72
+15	2.55	21.2	54.1	98.5	69
+25	2.53	21.3	53.9	98.0	--
+30	2.40	21.4	51.4	94.0	55
Avg -70 → 0 =			51.87		Σ = 455 sec
Avg 0 → +30 =			53.65		= 0.22 deg/sec

Table 7-8B. North Site, 28 October 1976
200 In-Oz Motor, SN No. 4 Using Machine Screw Actuator No. 2

+30 DEG → -70 DEG (CCW - MOTOR SHAFT) (WEST END)

<u>Angle</u>	<u>I</u>	<u>VD</u>	<u>Power (watt)</u>	<u>Torque (in-oz)</u>	<u>ΔT</u>
+30	2.82	21.2	59.8	108.5	0
+25	2.48	21.5	53.3	99.0	
+15	2.46	21.5	52.9	98.0	49
0	2.52	21.3	53.7	99.5	52
-15	2.46	21.5	52.9	98.0	66
-30	2.40	21.5	51.6	96.0	62
-45	2.38	21.5	51.2	95.0	65
-60	2.52	21.4	53.9	100.0	66
-70	2.60	21.3	55.4	102.0	43
Avg +30 → 0 =			54.92		Σ = 403 sec
Avg 0 → -70 =			53.12		= 0.25 deg/sec

-70 DEG → +30 DEG (CW - MOTOR SHAFT)

<u>Angle</u>	<u>I</u>	<u>VD</u>	<u>Power (watt)</u>	<u>Torque (in-oz)</u>	<u>ΔT</u>
-70	2.90	21.1	61.2	109.0	0
-60	2.26	21.8	49.3	90.0	43
-45	2.30	21.6	49.7	91.0	63
-30	2.65	21.1	55.9	101.0	68
-15	2.60	21.3	55.4	100.0	68
0	2.95	20.8	61.4	109.0	70
+15	2.83	21.0	59.4	106.0	68
+25	2.80	21.0	58.8	105.0	
+30	2.85	21.0	59.8	107.0	55
Avg -70 → 0 =			55.48		Σ = 435 sec
Avg 0 → +30 =			59.85		= 0.23 deg/sec

* Includes static friction.

Table 7-9A. North Site, 3 November 1976
200 In-Oz Motor SN No. 3 Using Ball Screw Actuator

+25 DEG → -70 DEG (CCW - MOTOR SHAFT) (EAST END)

<u>Angle</u>	<u>I</u>	<u>V_D</u>	<u>Power (watt)</u>	<u>Torque (in-oz)</u>	<u>ΔT</u>
*+25	1.18	23.2	27.4	52.0	0
+15	1.04	23.2	24.1	47.0	26.0
0	1.01	23.1	23.3	45.5	36.9
-15	1.00	23.1	23.1	45.0	44.6
-30	1.01	23.0	23.2	45.0	50.4
-45	1.01	23.0	23.2	45.0	52.4
-60	1.07	22.9	24.5	47.5	48.5
-70	1.27	22.6	28.7	53.5	31.0
Avg +25 → 0 =			24.93		Σ = 289.8 sec
Avg 0 → -70 =			24.33		= 0.33 deg/sec

-70 DEG → +25 DEG (CW - MOTOR SHAFT)

<u>Angle</u>	<u>I</u>	<u>V_D</u>	<u>Power (Watt)</u>	<u>Torque (in-oz)</u>	<u>ΔT</u>
*-70	1.23	23.0	28.3	58.0	0
-60	1.30	22.8	29.6	60.0	31.4
-45	1.10	23.0	25.3	53.0	52.4
-30	1.07	23.0	24.6	52.0	52.8
-15	1.03	23.1	23.8	50.5	50.4
0	1.10	23.0	25.3	53.0	42.7
+15	1.10	23.0	25.3	53.0	41.1
+25	1.13	23.0	26.0	54.0	23.3
Avg -70 → 0 =			26.15		Σ = 294.1 sec
Avg 0 → +25 =			25.53		= 0.32 deg/sec

* Includes static friction.

Table 7-9B. North Site, 3 November 1976
200 In-Oz Motor SN No. 4 Using Ball Screw Actuator 241847

+25 DEG → -70 DEG (CCW MOTOR SHAFT) (WEST END)

Angle	<u>I</u>	<u>V_D</u>	Power (watt)	Torque (in-oz)	<u>ΔT</u>
*+25	0.93	23.4	21.8	46.0	0
+15	0.93	23.2	21.6	45.8	25.0
0	0.93	23.1	21.5	45.7	39.0
-15	0.90	23.1	20.8	44.7	43.7
-30	0.93	23.1	21.5	45.7	51.9
-45	1.00	23.0	23.0	48.0	51.9
-60	1.15	22.8	26.2	52.5	50.7
-70	1.23	22.8	28.0	55.2	23.0
Avg +25 → 0 =			21.63		Σ = 285.2 sec
Avg 0 → -70 =			23.50		= 0.33 deg/sec

-70 DEG → +25 DEG (CW - MOTOR SHAFT)

Angle	<u>I</u>	<u>V_D</u>	Power (watt)	Torque (in-oz)	<u>ΔT</u>
*-70	1.67	22.3	37.2	71.0	0
-60	1.10	22.8	25.1	52.0	36.0
-45	0.95	23.0	21.8	47.0	54.0
-30	0.95	23.0	21.8	47.0	52.8
-15	0.94	23.0	21.6	46.5	48.8
0	1.00	23.0	23.0	48.5	44.0
+15	1.00	23.0	23.0	48.5	44.0
+25	1.01	23.0	23.2	48.7	24.0
Avg -70 → 0 =			25.08		Σ = 303.6 sec
Avg 0 → +25 =			23.07		= 0.31 deg/sec

* Includes static friction.

0277-0976

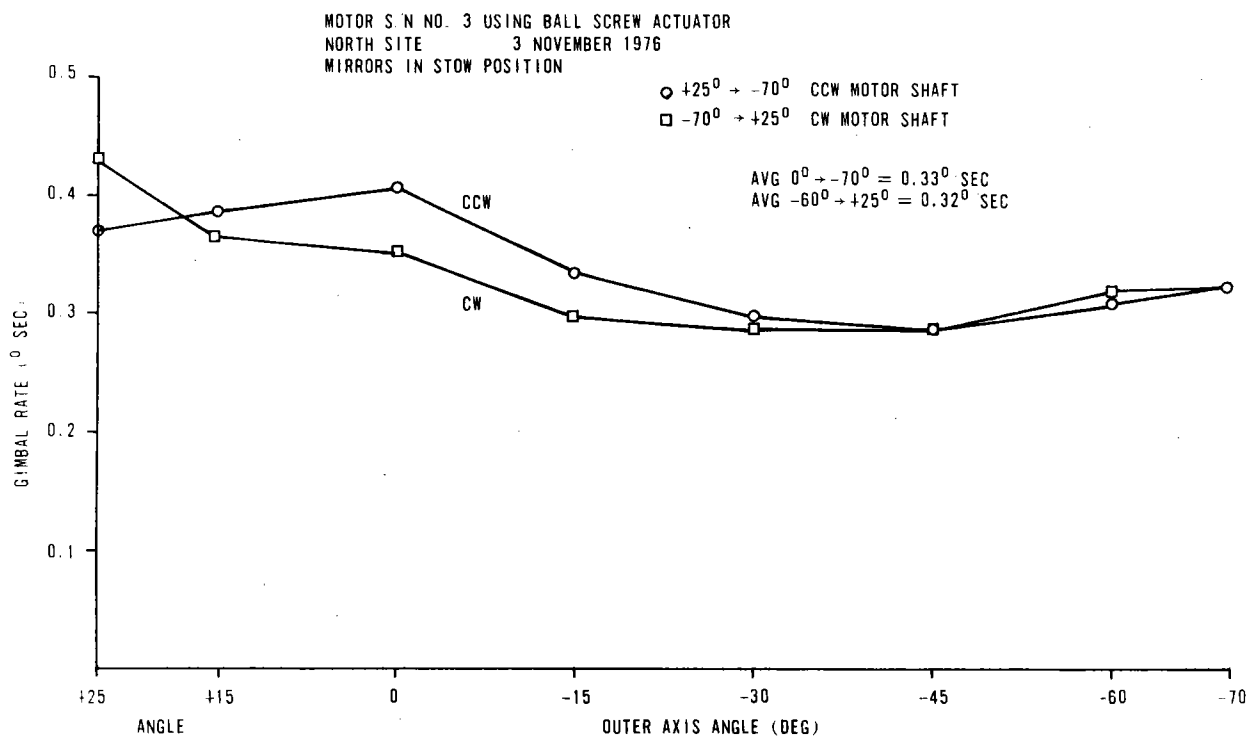


Figure 7-61A. Outer Axis Slew Rate

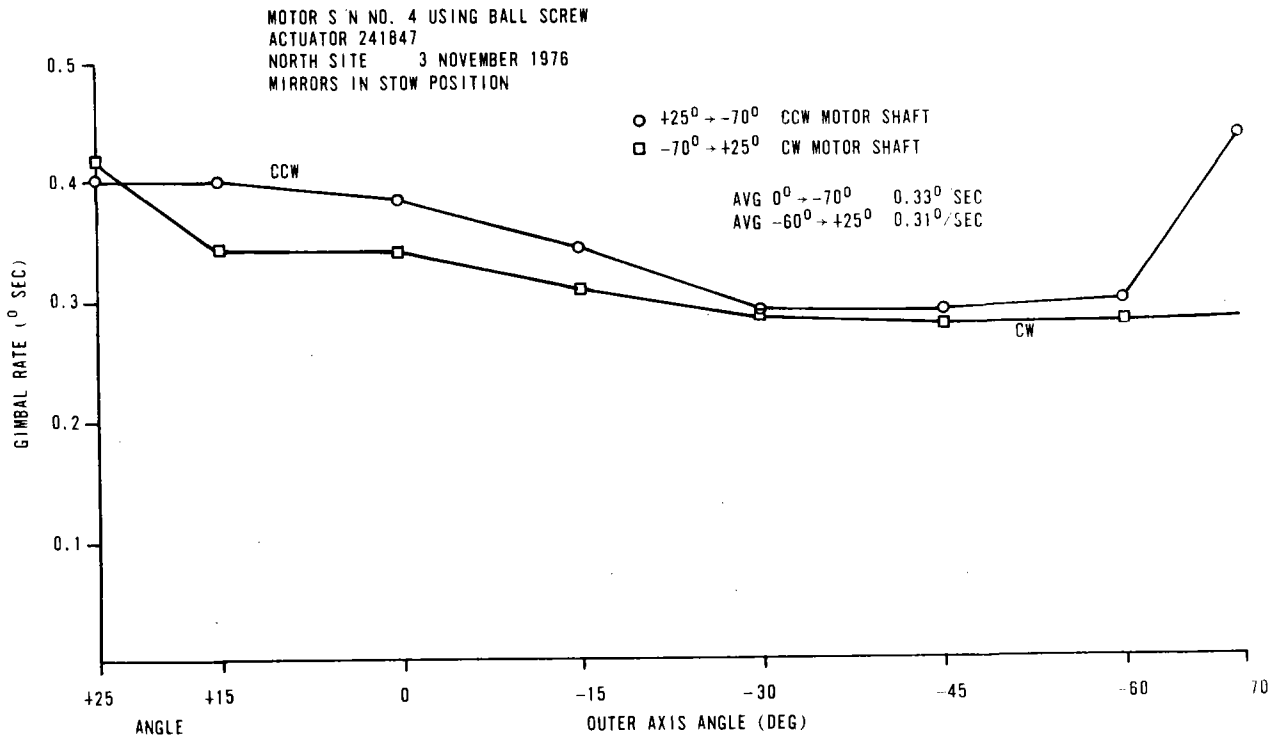
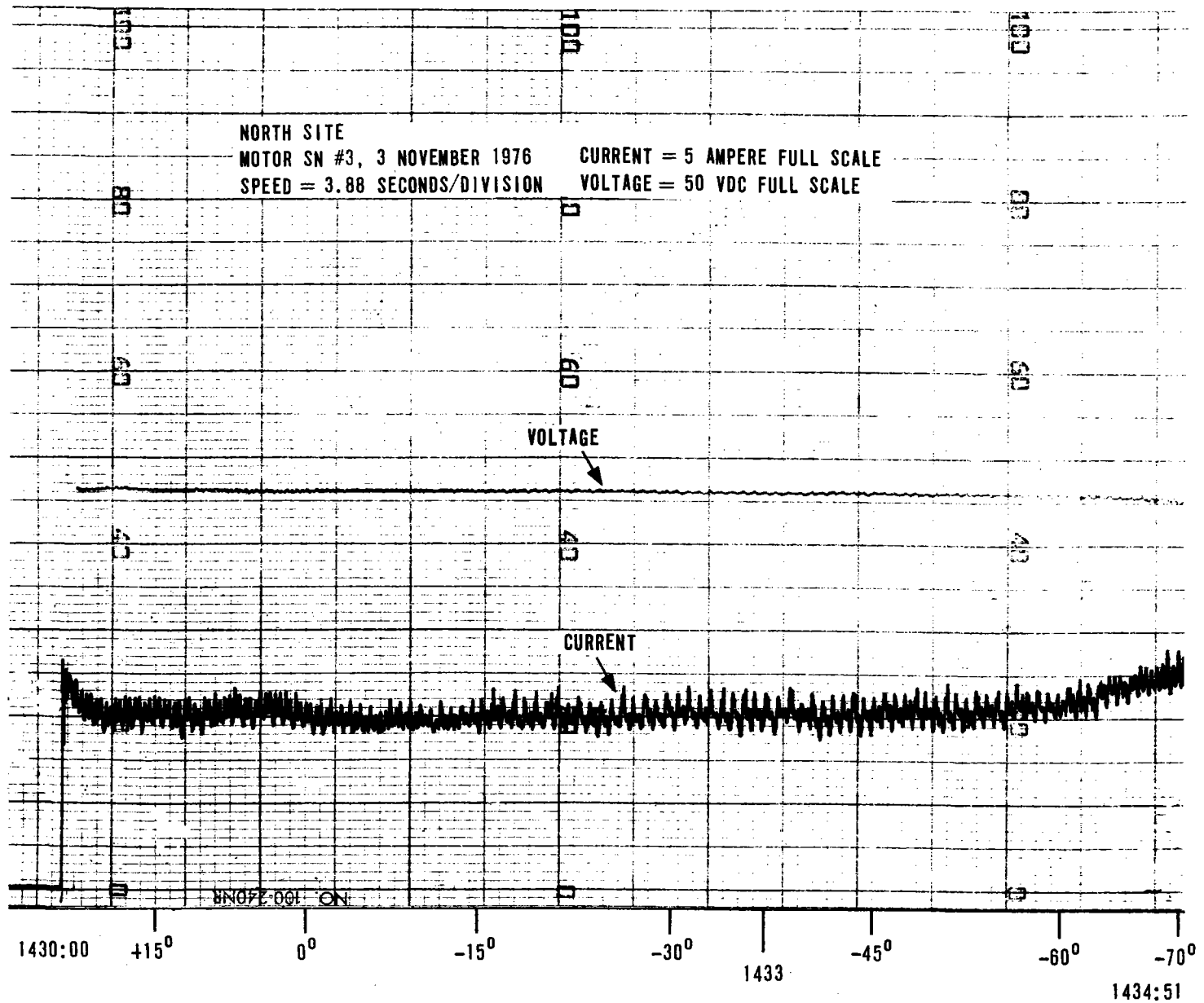


Figure 7-61B. Outer Axis Slew Rate



7-95

Figure 7-62A. Ball Screw Linear Actuator Power Response During OA Slew (+25° to -70°)

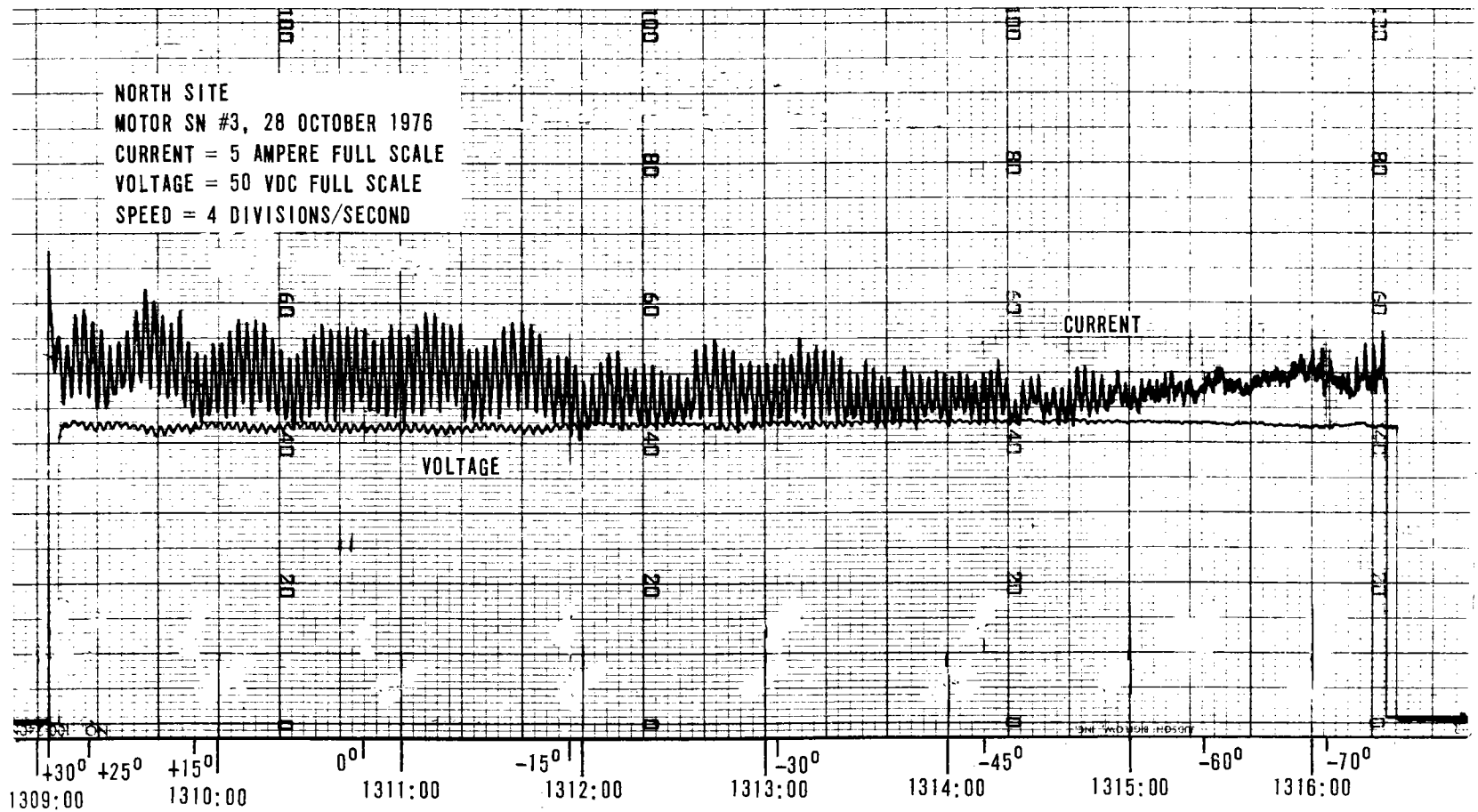


Figure 7-62B. Machine Screw Linear Actuator Power Response During OA Slew (+30° to -70°)

Outer Frame Lash

Under simulated loadings with one actuator disconnected from the frame, the total play, or lash, exhibited within the remaining actuator was only 0.00165 inch or 0.060 mr. This compares favorably with the error budgeted backlash of 0.180 mr about the outer axis.

Outer Frame Assembly and Balance

The assembly sequence (described on Page 6-1) involves mounting the frame on top of the two posts. A 1.9355 inch diameter shaft is welded to the cross member I-beam near each end of the frame. (See Figure 7-63) which pivots within the two 1-15/16 pillow blocks bolted to the top of each post. The first time the Engineering model outer frame was gimballed manually to -75 degrees, one outboard pillow block cracked across its entire foot (Figure 7-64). It was found that the welded shaft had a small offset run-out of 0.028 inch from the outer axis center line. The bearing casting will not withstand large tension loads. Subsequent corrections were made to further frame deliveries to insure the welded rod has no more run out than 0.010 inch.

Figure 7-65 shows the mass imbalance of the Engineering model heliostat at different mirror module positions for a full OA gimbal travel. The actuator was disconnected. After a 24-pound weight (added 1650 inch-pounds) was welded to the outer frame as indicated, the imbalance decreased for most orientations as shown in Figure 7-65. Note that after balance weights were added, the heliostat is still sensitive to gimbal angle. This is because the tie rods were 10 pounds heavier each than planned, thus causing the CG to rise when the mirrors are stowed. Corrections were made for the experimental models.

With the torque capability of the 200 inch-ounce motors for the experimental model, there was no need to fine tune the balance. However, for comparison purposes, the North site was balanced with 40 pound weight and the other two were not balanced. The larger weight required for the experimental models is due to the fact that the initial mass properties analysis did not include the wiring conduit attached to the frames which was not incorporated into the engineering model frame.

During tests, no noticeable difference in performance was detected between the "balanced" and unbalanced heliostats.

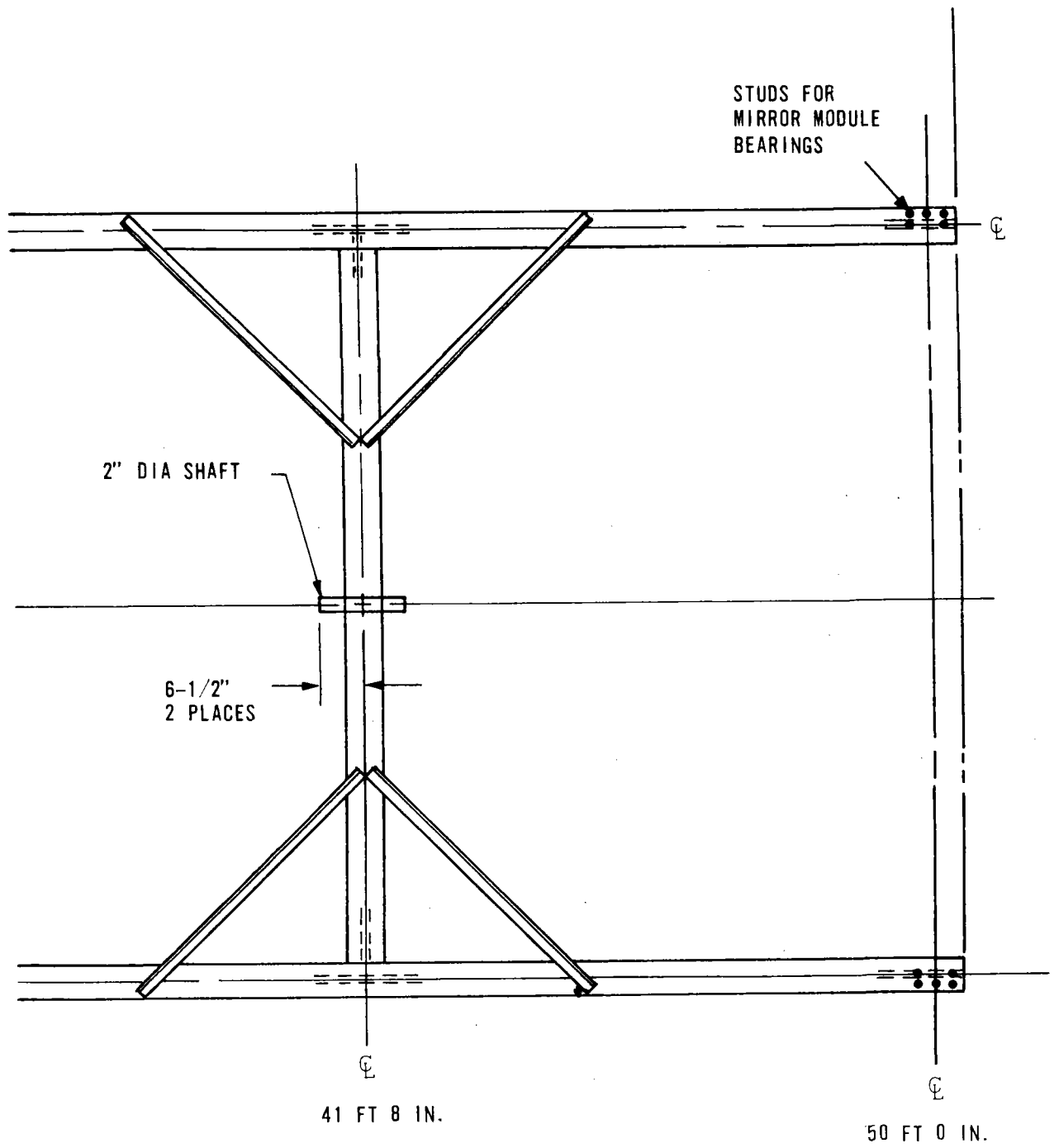
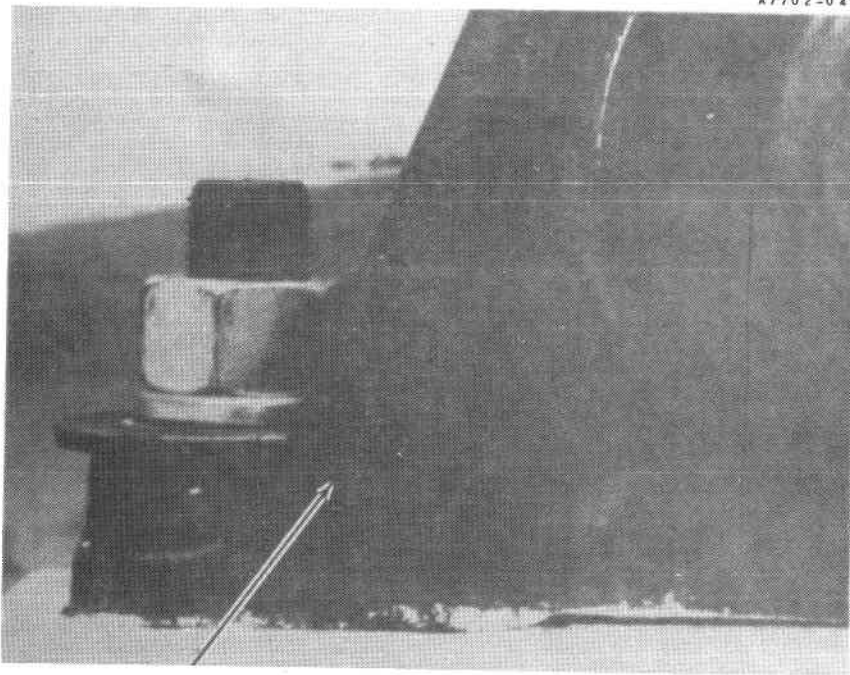


Figure 7-63. Outer Frame Mounting Shaft



**BREAK DUE TO
SHAFT RUNOUT**

Figure 7-64. Cracked Frame Pivot Pilot Block
Engineering Model Heliostat

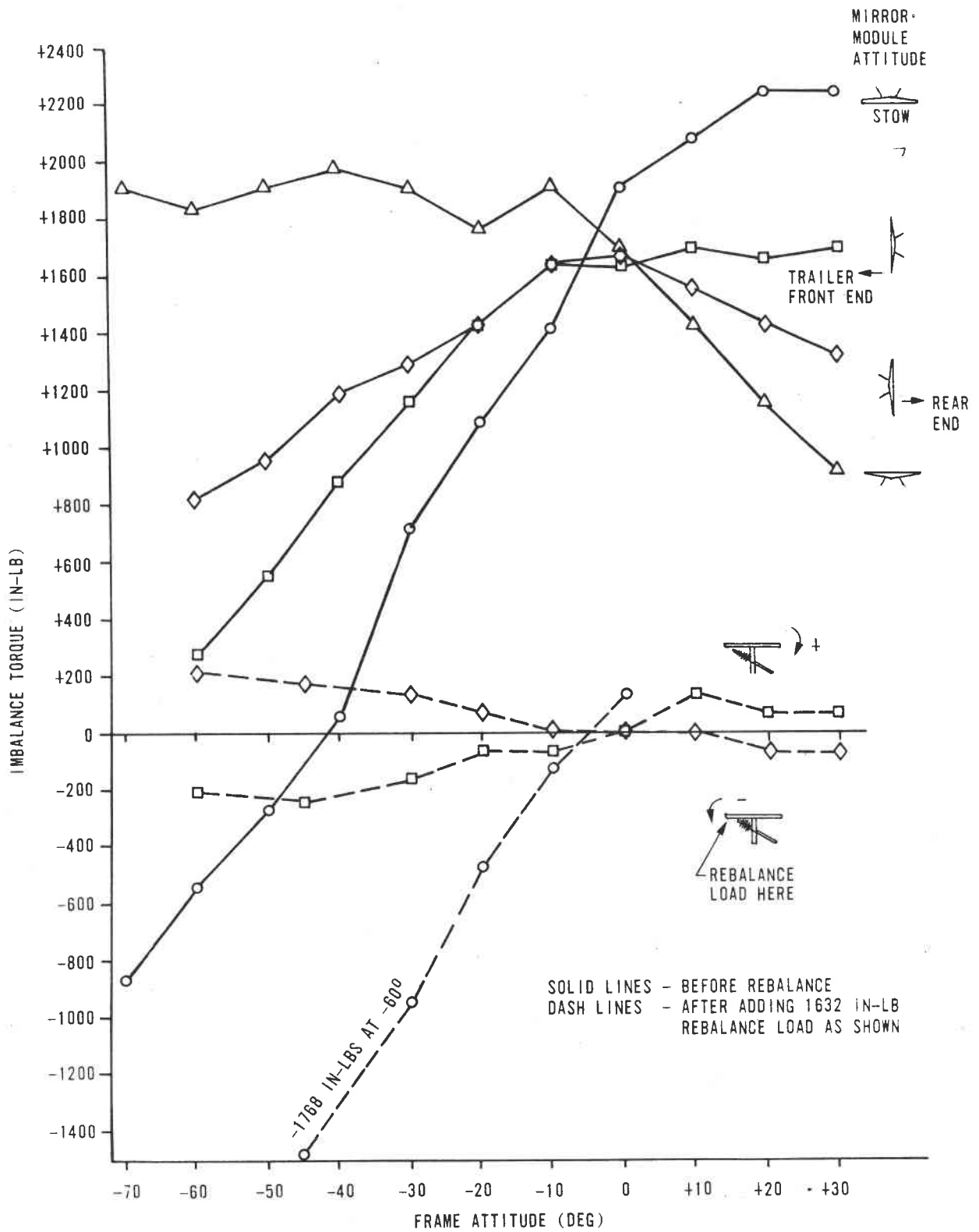


Figure 7-65. Engineering Model Heliostat Imbalance About Frame Axle (Linear Actuators Not Connected)

Inner Drive

Page 7-21 explains the inner drive operation including the tie rod/crank arm ganging of the four mirror modules. The inner drive backlash, spring rate (deflections due to torsional loads), and turning rates were evaluated. Total bending of inner modules and play under loads and during tracking are potentially the single largest contributor to tracking errors. For all heliostats, the 100 in-oz Inland PMDC motors were used.

Inner Drive Lash and Torsion Characteristics

The lash and total spring rate for the Spiroid inner drive gear box used on the Engineering Model was determined by measuring optically the rotation between the driver mirror module pillow block and the mirror module axle. Lead weights were incremented (5 pounds - 130 pounds) and loaded at the edge of the mirror module to create CW and CCW torques. Figure 7-66 plots the axial deflection for loads up to 7800 in-lb torque on the driver mirror module. The lash is the dominant influence upon rotation up to about ± 900 in-lb torque. The lash was approximately ± 1.4 arc-minute (± 0.41 mr) at which time the spring rate of the gear box and mirror module axle is the dominant effect on module movement.

The actual backlash of the Engineering Model is on the same order of magnitude as the error budget estimated value of ± 0.54 mr under static loads. Wind variations causing mirror module movement caused an estimated ± 10 arc-second inaccuracy at the low torque measurement (lash region).

During powered operation of the Engineering Model heliostat, the mirrors would oscillate during rotation. This problem was caused by excessive play (9 mr at the output pinion gear) in the gear box bearings. After Spiroid properly axially preloaded the bearings the induced oscillations disappeared.

Subsequent analysis has shown that the absolute stress limitation of the spur gear and gear box is 40,000 in-lb torque at the teeth of the 16-inch spur gear. Tooth deformation can occur at a lesser stress.

As a result of the engineering model experience, Spiroid designed a modified gear box as follows:

1. Pivot axis moved to lie in a plane tangent to the spur gear pitch diameter. This eliminates rocking moments due to tangential tooth forces.
2. Pivot hole diameter and tolerance reduced to control backlash.
3. Added 8-32 tapped hole to secure pivot pin.
4. Bearings preloaded axially to control backlash to 0.12 mr at the mirror.

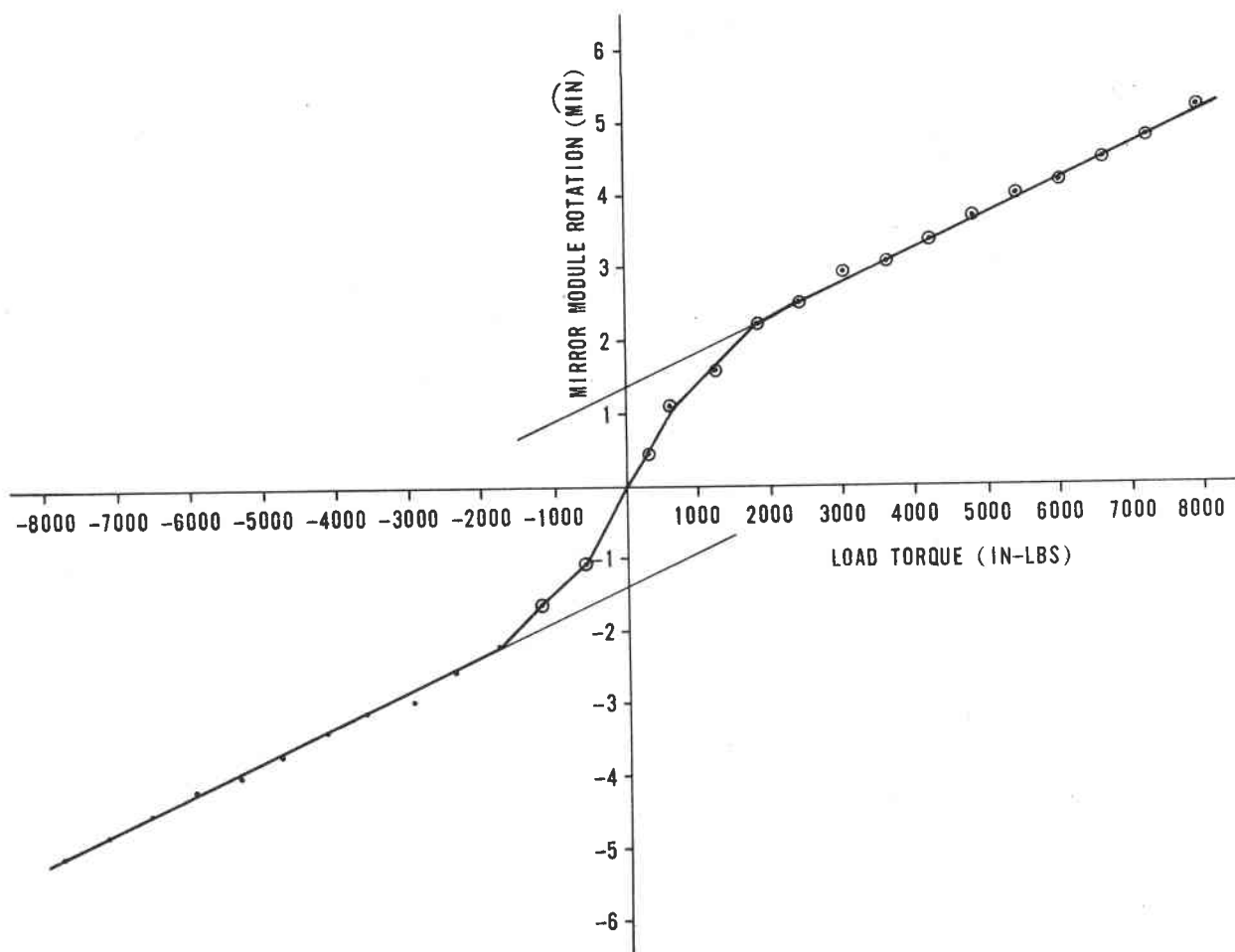


Figure 7-66. Engineering Model Heliostat
Gear Driven MM

5. Added locking element to stop gap screw.
6. Added drain hole below pinion for moisture escape.
7. Added an external extension on the intermediate shaft for an initialization encoder.
8. Reduced width of opening in pivot yoke area from two inches to 0.62 inches to mate with new pivot block and spherical bearing.
9. Pinion/motor shaft one piece construction to insure clamping preload will be maintained on the motor armature.

Revised Experimental Model Gear Box No. 2 on the South heliostat exhibited excessive lash. With the other three mirror modules decoupled an extensive evaluation was made 1 November - 3 November 1976 to determine the contributions of lash and torsion movement. Figure 7-67 shows part of the test set up to obtain the following contributions due to incremented moments:

- Total Mirror Module movement - electronic level on mirror skin.
- Spur gear torsion or rotation.
- Gear box pinion vertical displacement.
- Mirror Module shaft horizontal displacement.
- Mirror Module shaft vertical displacement.
- Spring axis vertical movement.

Calibrated dial indicators were used to detect movement with respect to the housing built into the I-beam frame. Clockwise and counter-clockwise loads of 15, 25, 35, 50, 80, 100 and 130 pounds were placed at the ± 58 inch edge from Mirror Module axis.

Backlash - Two methods were used simultaneously to determine angular displacement. A precision electronic level was mounted on the back surface of the mirror module (mirrors face down). At the 50 arc-sec/div scale with interpolation the accuracy of measurement is estimated at 10 arc-seconds. The second method was a dial indicator contacting the spur gear teeth.

Total lash as measured by the electronic level was:

$$410-10 = 400 \text{ arc-seconds}$$

or

$$430-35 = 395 \text{ arc-seconds.}$$

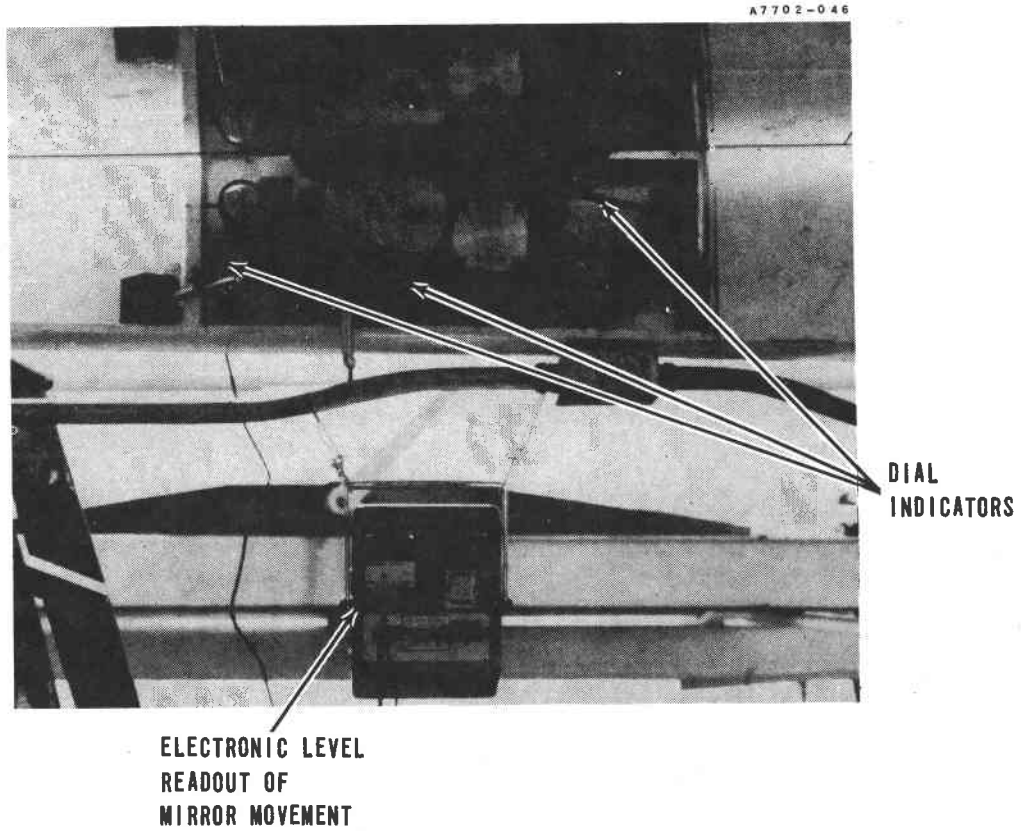


Figure 7-67. Experimental Model Inner Drive Gear Box
Lash/Spring Rate Test Set-Up

The total lash measured by the dial indicator was:

$$0.0135/8 = 0.001687 \text{ radians} = 348 \text{ arc-sec}$$

or

$$0.0130/8 = 0.001625 \text{ radians} = 335 \text{ arc-sec.}$$

where the gear radius = 8 inches.

The discrepancy between the two appears to be due to slippage between the spur gear and aluminum mirror module stub shaft. The -15(58) in-lb data point shifts from -35 seconds to +15 seconds or 50 seconds; this probably explains the discrepancy.

To obtain the backlash value for the gearbox itself we have to subtract out the other effects as shown in Table 7-10. Since the dial indicator was mounted on the side of the spur gear, the vertical movement of the mirror shaft must be subtracted out. Gear box lash = $\frac{0.01325 - 0.002}{8} = 0.0014$ radians.

The downward motion of the gear box at the spur pinion axis was 0.0005. The lash contribution was $\frac{0.0005(\tan 20^\circ)}{8} = 0.000022$ radians. This is ignored in Table 7-10.

Spring Rate - A review of Figure 7-68 and data taken previously on the engineering model inner drive shows that total spring rates in the linear regions are nearly identical. The difference is in the shape and magnitude of the backlash region.

Table 7-11 shows the breakdown of spring rate components. The data shows a spring rate for the gear box of $6670/0.000293 = 22.8 \times 10^6$ in-lbs/rad. The 0.001 radian total displacement is taken from the fitted curve in Figure 7-68. The gear box contribution (≈ 0.29 mr) was consistently obtained by subtracting out the other known contributions such that the total displacement was maintained.

Since all dial indicator readings were taken with respect to steel frame near the spur gear cutout, it was confirmed that relative movement between the top and bottom flanges was less than 0.001 inch.

Additional tests were run with the inner mirror module at orientations other than horizontal. The total lash did not vary from angle to angle by more than 41 seconds (0.2 mr) over the 360 degree range of mirror module rotation. All lash measurements were made with ± 900 in-lb torsion.

The resultant angular deflection of 0.29 mr at 6670 in-lbs torque gives a spring rate of 23×10^6 in-lbs/radian.

The total lash of 1.2 mr was confirmed by Spiroid upon return of the gear box assembly and corrected by shimming out the axial play. After the fix, a tangential load of ± 400 in-lbs resulted in a total lash of

Table 7-10. Backlash Components at ±870 In-Lbs.

MM Bearing Vertical	$\frac{(0.0023 - 0.003)0.364}{8}$	= 0.000091 radians
MM Bearing Horizontal	$\frac{(0.0894 - 0.0888)}{8}$	= 0.000074 radians
Point Horizontal	$\frac{(0.002 - 0.001)}{8}$	= 0.000125 radians
Gear Box		= 0.001400 radians
<hr/>		<hr/>
TOTAL	350 arc-seconds	0.001690

Table 7-11. Spring Rate Contributions

Item	Positive Moment (6670 in-lb)	Negative Moment (6670 in-lb)
Pivot	$\frac{+0.0012 - (-0.0010)}{8} = 0.000275$ Rad	$\frac{0.0031}{8} = 0.000388$
MM Shaft Horiz	$\frac{0.0924 - 0.0894}{8} = 0.000375$	$\frac{0.0887 - 0.0875}{8} = 0.000150$
MM Shaft Vert	$\frac{(0.0029 - 0.0023)0.364}{9} = 0.000027$	$\frac{(0.00275 - 0)0.364}{8} = 0.000125$
Gear Box Pinion Vert	$\frac{(0.0012 - 0.0005)0.364}{8} = 0.000032$	$\frac{(0.0010 - 0.0001)0.364}{8} =$
	Sum 709	$\frac{0.000041}{704}$
Gear Box	= 0.000291	= 0.000296
<hr/>	<hr/>	<hr/>
Total	0.001000	0.001000

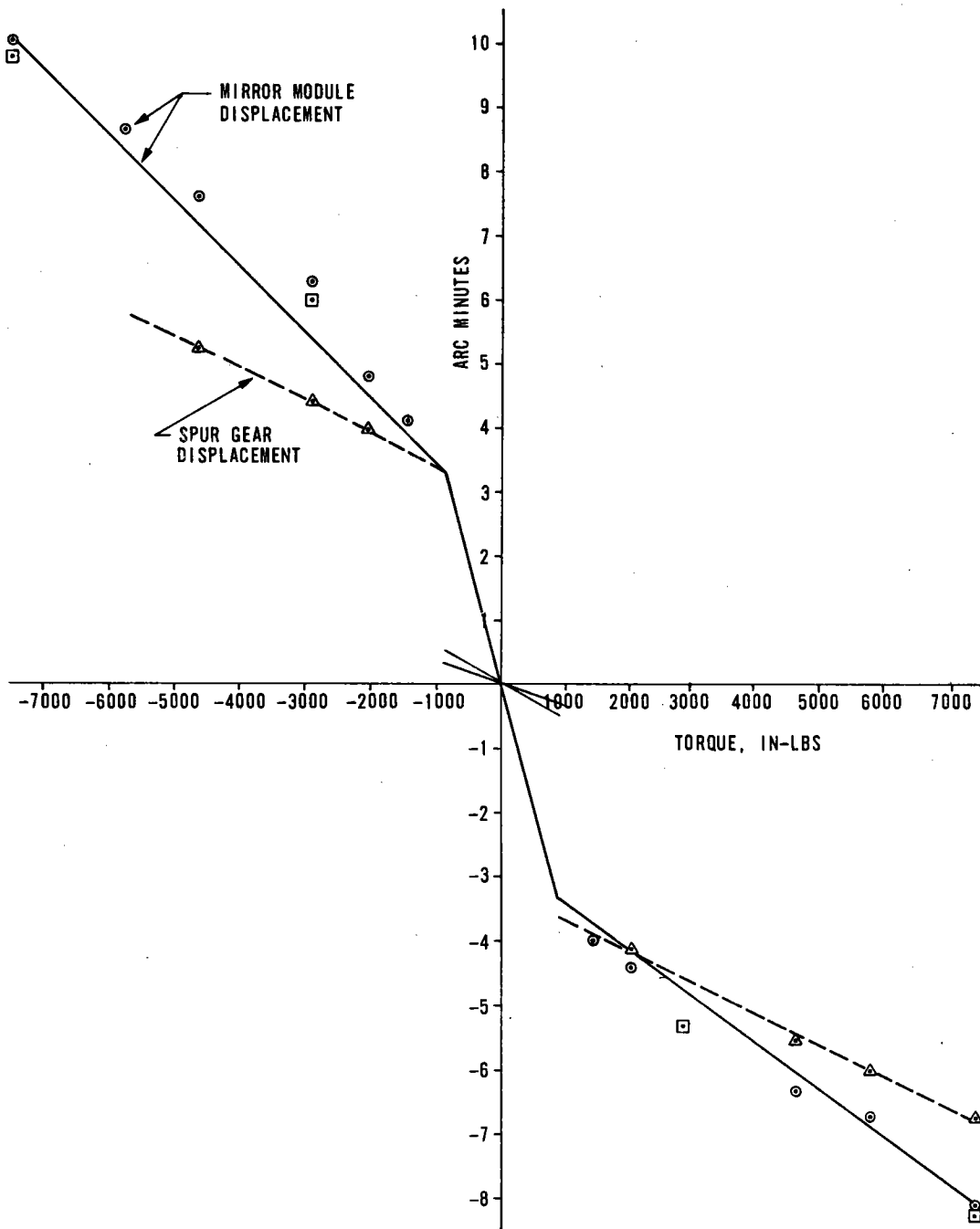


Figure 7-68. Mirror Module Rotation Versus Moment Loads

0.0025 to 0.003 inches (0.31 to 0.375 mr). This is compared to 0.54 mr per the error budget and 0.3 mr specification to Spiroid.

Similar measurements were made on the North site and East site without decoupling the other mirror modules. The North site exhibited a worst case lash build up of 1.1 mr at ± 870 in-lb torque. The East heliostat had a worse case lash of 0.85 mr. Both were correctable to under 0.6 mr with rework. Using ± 900 in-lb does start to work into a small portion of the spring rate, but under ambient wind conditions, the larger torque is needed to remove oscillations and obtain steady readings under wind gusting.

Inner Drive Power and Slew Rate Performance

The Inner Drive Slew rate requirement is ≥ 0.3 degree/second. Figure 7-69 shows that for the Engineering model the gimbals rate under manual power slew exceeds the requirement by a factor of 2 on the average. Power requirements went as high as 35 watts when the worse case torque is required due to the mass imbalance of the mirror modules.

Measurements taken on the experimental model heliostats with the outer frame at 0 degree and at -65 degrees, show average gimbal rates from 0.57 deg/sec to 0.60 deg/sec with the maximum peak power never exceeding 24.5 watts. The average power for a full 360 degree slew is less than 12 watts. The maximum power requirements come from wind loadings (15-20 mph) with the mirror modules at worse case angle of attacks. Under this configuration, the inner axis gimbal rate drops to 0.45 deg/sec. Figures 7-69A and 7-69B show typical results (from East site) graphically.

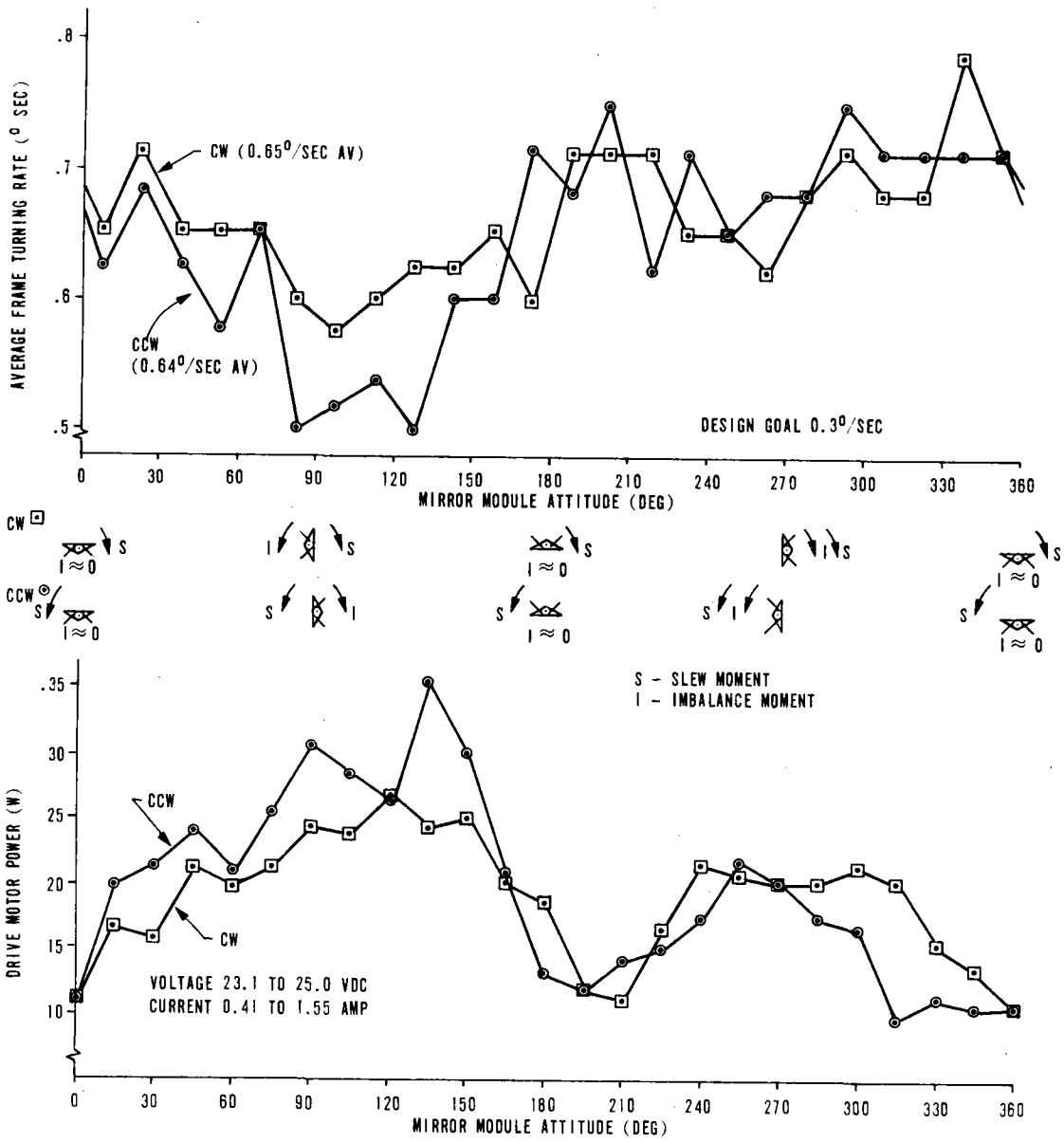


Figure 7-69. Engineering Model Heliostat Mirror Module Drive Motor (Data Taken Following Reducer Overhaul)

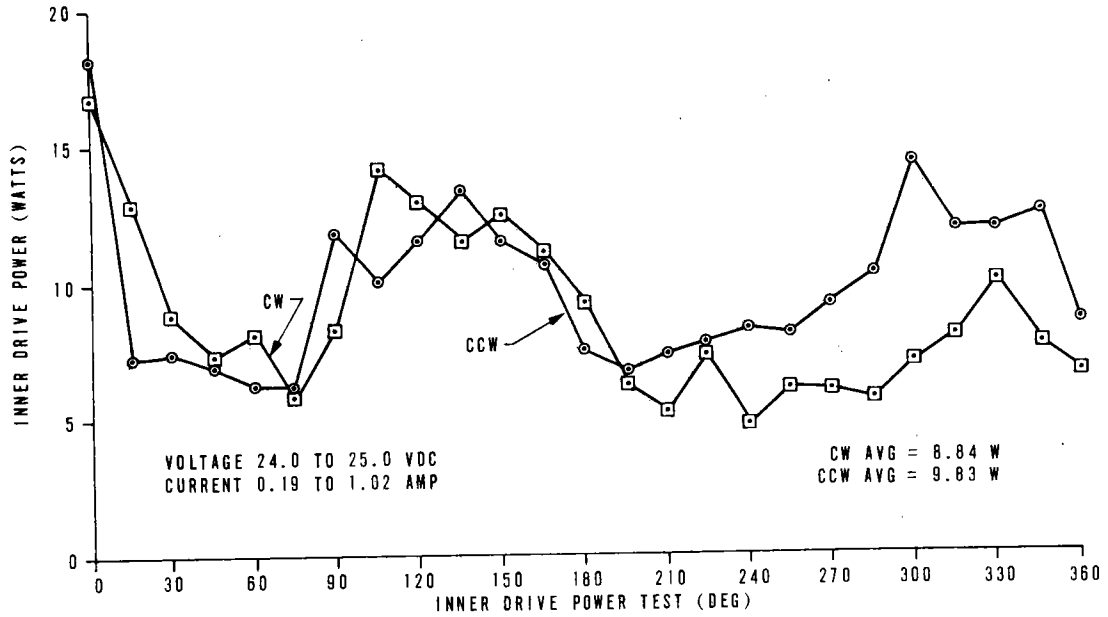
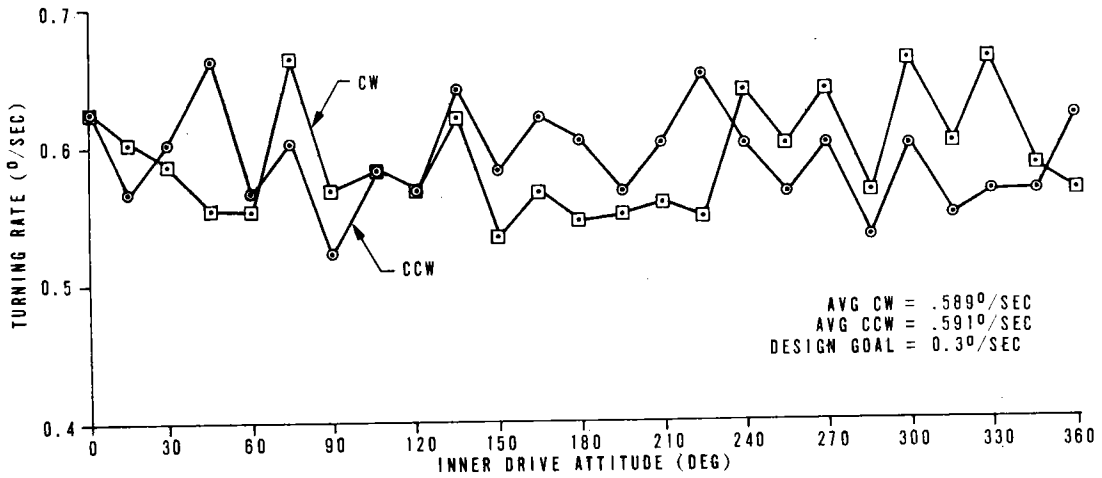


Figure 7-69A. Experimental Model Inner Drive Results
 (Outer Axis Orientation - 0°)

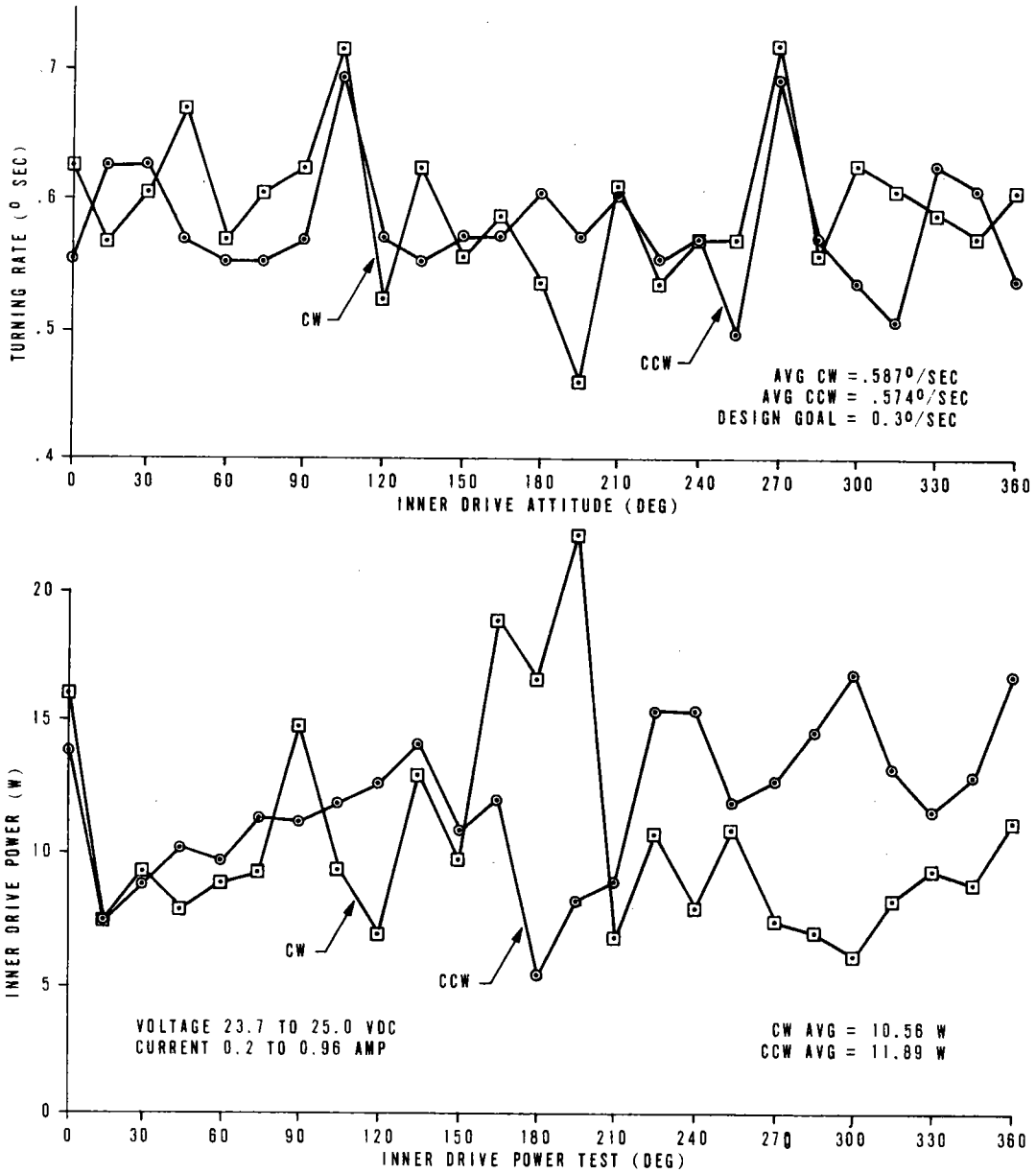


Figure 7-69B. Experimental Model Inner Drive Results
 (Outer Axis Orientation = -65°)

Electronics Performance

A block diagram of the electronics operation is shown in Figure 7-1 and with more detail in Figures 3-27 through 3-39. The in-house designed and built open loop heliostat and test equipment electronics performed excellently after iterative design changes from the Engineering Model experiences were incorporated into the Experimental Models.

Heliostat Electronics

Underground telephone grade shielded twisted pair cabling branches underground in PVC conduit from Building E-2 to each heliostat site. AC power is brought to each site from the nearest building and has ground fault isolation incorporated. The heliostat electronics are housed in a commercially purchased weather-sealed box.

Round trip cable resistance from each site is:

North: 11 Ω

East: 24 Ω

South: 29 Ω

On the engineering model, the original electronics build was responsible for what were initially unexplained glitches in heliostat operation. The inner or outer axis would suddenly gimbal through 3 degrees - 4 degrees of slew and then stop while in open loop track mode. On occasion, the inner axis would start to rotate while in the "stow" mode. On three occasions, one outer axis actuator would torque while the other remained stationary due to erroneous signals. Initialization electronics were never included in the engineering model heliostat electronics. Initially, adequate grounding was not provided for indirect lightning strike protection.

The following design changes were made prior to build of the experimental model electronics:

1. Lightning protection was incorporated. In addition to running cabling from the frame to 24 foot grounding rods, gas discharge tubes were put on all communication lines. They short voltages of 90 volts dc or greater. Series resistor and shunt zener diodes are also used, offering protection down to 5.1 volts dc thereby protecting all components.
2. A few nonused gate inputs were not left open thereby making the components subject to noise. Tying all open input lines to pull up resistors in the experimental model reduced the spurious slewing of the heliostat.
3. The optical pairs within the motor encoder housing were taken often becoming unaligned. This caused both constant slew of the inner and outer drives of the turning of one actuator and

not the other since no revolution-complete feedback was sent to the electronics. Cutting larger holes and stiffening the optical pair mounting supports helped solve the alignment problem.

4. A synchronization circuit between the two actuators was added to insure that under no circumstances would one actuator motor get further ahead or behind than two motor revolutions before power is removed from the nonlagging actuator motor.
5. Optical pair performance was being degraded by shavings from the encoder disk covering the optical windows. A thinner, non-painted disk was mounted to the motor shaft with greater precision to prevent binding and rubbing against the plastic housing of the optical pairs.

After build of the Experimental Model one additional systems' problem was discovered which seemed to eliminate all observed unexplained abnormalities in heliostat performance. After several days of high humidity, mostly cloudiness and some rain, the outer actuators would not stay in sync and one would drive to stall causing the motor to heat. The problem was found to be moisture collecting in the connectors leading to the motors. If wet, the 5 volts would leak into the 40K output impedance of the optical pairs confusing the incremental encoders. With motors on, the 24 volts dc made the leakage problem worse. The problems disappeared when the connectors were dried with a blower. Temporarily the connectors were wrapped and sealed. For pilot plant applications, the simple (and cheaper) solution will be to eliminate intermediate connectors and hard wire the motors to the electronics.

The commercial 12-volt dc car batteries (Sears "Die Hard") and chargers used for all heliostats exhibited no problems or degradation during their use. They were in a nonweather sealed wooden box outdoors at all times; the Engineering Model since mid May 1976. The batteries operated a heliostat without recharging after two months of inactivity. Under normal operation, the charger was connected to 120 volts dc only once every five to nine days of daily heliostat operation.

Only commercial grade components were used throughout the entire design. Even so, there was only one electrical component (LM 111D chip) failure during the entire test program involving the one engineering model and three experimental model heliostats. This failure history, of course, does not include the design changes as discussed previously or damage done to the engineering model heliostat electronics due to lightning (see Page 3-38). Based upon these preliminary findings, the reliability of the electronics design is expected to be very high-- especially when higher quality, screened parts are used for pilot and commercial plant operations.

Test Equipment Electronics

The performance of the special purpose test equipment built in-house was also excellent. The multiplexer linking the calibration array to

the RS232C interface box remained on the roof of Building E-2 in a nonweather sealed metal box for eleven months. For seven months the power was never turned off. During this time, only one 16 channel multiplexer component, interfacing one set of 16 photocells, failed and had to be replaced. The RS232C interface box never failed.

Again, due to the lightning strike of 10 August, and probable near lightning induced voltage surges at a later time, on 27 August 1976 four zener diodes and two Dips were replaced due to damage.

Five of the PVC tubes and caps sealed with RTV leaked water and the photocell electronics failed to a hard '0' output. Also, all the phototransistor cases rusted on the outer edge where exposed to the weather. For pilot plant applications, the photocell and the associated amplifiers must be sealed in a more uniform and consistent manner.

The biggest cause for complete test stoppage or lack of data acquisition was, next to inclement weather, commercial test support equipment failures. These are listed below:

1. Tape Decks - Through mid October, two older Kennedy tape drives were used. From start of Engineering Model testing until this time, eight to ten track stoppages occurred because of a hang-up at the DDP516 tape drive interface.

The original tape drives were replaced with newer Honeywell Model 10C Magnetic Tape Drives. Initially, there were two failures consisting of (a) marginal timing and (b) tape misalignment. The marginal timing problem was due to the crystal oscillator coming up to an off-sync frequency at turn-on. After main power to the tape drives was left on continuously, there have been no failures for 1-1/2 months of operation.

2. ASR-35 - There were two failures: (a) mechanical vibration loosened the drive mechanism, and (b) interface timing which was repaired.
3. DDP516 Honeywell Computer - There were two problems: (a) drifting 6 volts dc power supply, and (b) one program board had to be replaced. These repairs were over a nine month interval.
4. Bad Tape - During operation, two new commercial 2400 foot seven track magnetic tapes caused stoppages due to inability to be written on without parity errors.
5. Climatronics F-470 Weather Station - In addition to the twisted shielded pair cabling run to each heliostat site, an identical cable was run in the same conduit such that the weather station channels could be directly connected into the multiplexer at Building E-2.

- a. Transformer overheated in the receiver circuitry. Three week vendor turnaround resulted.

- b. Two temperature translator boards became inoperative. These channels were not used.
 - c. Wind anemometer failed once due to a mechanical displacement of the internal LED.
 - d. One of the nine transmitter channels failed early in the test program and was never repaired.
 - e. Calibration drifts of each of the translator boards resulted in uncertainty of the scaling associated with the digital representation to the central computer. Drifts and discrete changes were due to temperature effects and movement of the 40 to 50 manually adjusted resistor pots throughout the system.
6. The Epply Global Radiometer, Model 8-48 - There was one failure due to moisture leakage. Drying the dessicant solved this problem.

Power Frequency Variation

Local experience with Florida Power Corporation shows that the commercial power line frequency is allowed to drift ± 0.02 Hz over the period of one day. This error could result in a time base error of $0.02 \text{ Hz}/60 \text{ Hz} \times 3600 \text{ sec/hr} = 1.2$ second per hour if the GMT is based on an internal computer clock after time initialization at the beginning of a day as in our case. If this drift were to continue for 8 hours, a 9.6 second time error could result-- thereby inducing a 0.04 degree tracking error in sun location (144 arc-second error).

ELECTRONIC BREADBOARD TEST DATA

A breadboard of the Heliostat Servo Output Amplifier was built to check operation. Measured data on static threshold, signal swing, switching time margins, and output rise and fall time are presented. Signal swing and switching data were taken with a bipolar square wave as an input and with the amplifier driving a 15 ohm resistive load. Short term operating tests to full saturation into a 4 ohm load (± 5 amperes) were run with no apparent difficulty. No output ringing or tendency toward oscillation was noted. All tests were run at room temperature. The data shows that the amplifier will perform its expected function.

Heliostat Servo Output Amplifier Breadboard Test Data

Measured Point	Signal Swing (Volts) or Time (ms)	
	Inverting Side	Non-Inverting Side
Op Amp Output, Non Sat Output	+5.5V to -13.5V	+5.25V to -13.5V
Op Amp Output, Sat Output	+13.5V to -13.5V	+13.5V to -13.5V
Darlington Driver Base, Non Sat Output	+1.3V to -8V	+1.3V to -8V
Darlington Driver Base, Sat Output	+1.3V to -8V	+1.3V to -8V
Darlington Output Base, Non Sat Output	+0.7V to -0.4V	+0.7V to -0.4V
Darlington Output Base, Sat Output	+0.8V to -0.4V	+0.8V to -0.4V
Base 2N2222A, Non Sat Output	+5.25V to -1.2V	+5.25V to -1.2V
Base 2N2222A, Sat Output	+6.0V to -1.2V	+6.0V to -1.2V
Collector 2N2222A, Non Sat Output	+24V to 22.5V	24V to 22.5V
Collector 2N2222A, Sat Output	5.5V to 24V	5.5V to 24V
Base, PNP	24V to $24V - V_{BE}$	24V to $24V - V_{BE}$
Collector, PNP	0 to 24V	0 to 24V
Emitter, Linear Output	-0.3V to 24V	-0.3V to 24V
Op Amp Slew Rate, Pos. Going Signal	19V in 6 ms	19V in 6.7 ms
Op Amp Slew Rate, Neg. Going Signal	19V in 5.3 ms	19V in 7 ms

SWITCHING TIME MARGINS, BASE COLLECTOR DARLINGTON DRIVER TRANSISTOR

$V_{BC}=0$ Neg. Going, $V_{CE}=0$ Pos. Going, Non Sat. Output	4 ms	5 ms
$V_{BC}=0$ Neg. Going, $V_{CE}=0$ Pos. Going, Sat. Output	1.0 ms	3 ms
$V_{BC}=0$ Pos. Going, $V_{CE}=0$ Neg. Going, Going to 0, Non Sat Output	5 ms	4.2 ms
$V_{BC}=0$ Pos. Going, $V_{CE}=0$ Neg. Going, Going to 0, Sat. Output	2.5 ms	1.0 ms

SWITCHING TIME MARGINS, BASE COLLECTOR DARLINGTON OUTPUT TRANSISTOR

$V_{BC}=0$ Neg. Going, $V_{CE}=0$ Pos. Going, Non Sat. Output	4.4 ms	5.5 ms
$V_{BC}=0$ Neg. Going, $V_{CE}=0$ Pos. Going, Sat Output	1.0 ms	3 ms
$V_{BC}=0$ Pos. Going, $V_{CE}=0$ Pos. Going, Going to 0, Non Sat Output	5 ms	4.5 ms
$V_{BC}=0$ Pos. Going, $V_{CE}=0$ Pos. Going, Going to 0, Sat Output	3.5 ms	2.5 ms
Output Square Wave Risetime Non Sat Output		0.05 ms
Output Square Wave Risetime Sat Output		0.1 ms
Output Square Wave Falltime Non Sat Output		0.05 ms
Output Square Wave Falltime Sat Output		0.1 ms

Output Square Wave Time Threshold Non Sat Output	7 ms one side 6 ms other side,
Output Square Wave Time Threshold Sat Output	3.5 ms one side 2.5 ms other side

Static Threshold: ± 30 mv

SYSTEM LEVEL TESTING

Foundation and Post Stability

The heliostat frame is mounted within bearings atop two steel posts 10.16M (33 feet 4 inches) apart, 2.29M (90 inches) above foundation height (see Figure 3-12). The posts are bolted to reinforced steel supports which are an integral part of each of the two 1.73M x 1.07M x 0.305M thick (5 feet 8 inches x 3 feet six inches x one foot) reinforced concrete foundations. Two support beams are welded in place to provide additional structural rigidity to the support posts. The concrete foundations were poured into unprepared (non-hardened) ground sites

Movement During Gimbal Travel

The outer axis was gimballed from 0 degree (horizontal) to -70 degrees (Figure 7-70). Foundation movement and post movement was recorded with precision electronic levels (0.2 arc-sec resolution) during gimbal movements with the mirror modules at three different orientations. The movements that were obtained as typical for the East heliostat site are shown in Table 7-12.

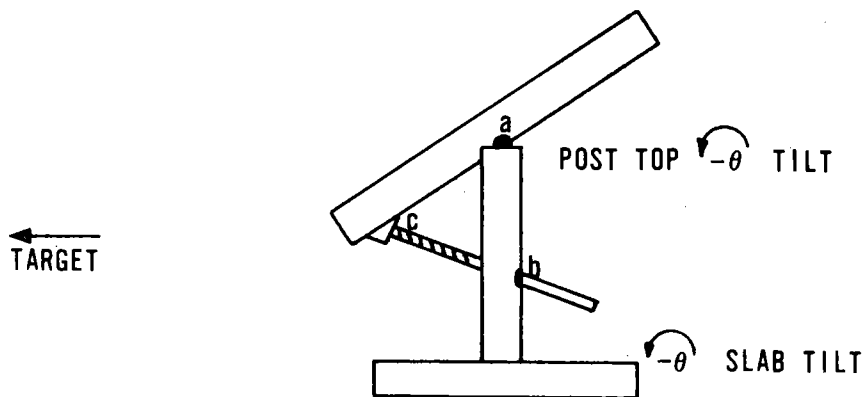


Figure 7-70. Foundation Movement Orientation

At 0 degree outer axis angle, gravity effects cause the frame to sag, drawing the top of the posts in towards each other. As the frame rotates toward the -75 degree position, the frame will elongate slightly due to reduced interaction g loading and mirror module loading on the outside beam. This effect is noted by the third entry above where the top of the posts are forced outwards (-53 arc-seconds) as the frame travels down to -70 degrees.

Similar data was taken for other sites with the largest post and foundation rotations occurring per Table 7-12.

Table 7-12. Post and Foundation Movement During Gimbal Travel
Of 0 Degree to -70 Degrees

	Inner Axis		
	180 Degrees (Stow)	90 Degrees	0 Degree (Mirror Up)
Maximum rotation of top of post about the Outer Axis (arc-seconds)	0 → -140	0 → -130	0 → -127
Maximum rotation of foundation (arc- seconds)	0 → -3.3	0 → -3.5	0 → -2.2
Tilt of top of post parallel to OA (arc- seconds)	0 → -53		

Rotations of the post top about the outer axis do not directly induce errors because the rotational angle remains constant with respect to the three legs of the triangle a-b-c of Figure 7-70. But the rotation projection down to pivot point b will induce a rotation at worst case angles (-70 degrees) of 140 arc-seconds x 47/90 or 73 arc-seconds (0.35 mr). The slab rotation induces directly another 0.02 mr error in vertical track. The combined effect is less than the resolution (≈ 80 seconds) of one incremental heliostat command.

During system level tracking, no attempt has yet been made to compensate for this error. Because of its being roughly linear (Figure 7-71), this minor error correction could be analytically added to the outer axis calculations for all heliostats based on actual outer axis position.

Long Term Foundation Stability

The foundations were poured in early July 1976 and allowed to cure. The first experimental heliostat was not completed until 25 October, 1976. Precision bubble levels (≈ 1 arc-second per division resolution) were permanently mounted on one slab (South side) starting 9 November 1976. The thermometer and levels were covered with a white box-cover to eliminate direct insolation effects on the instruments. True long term data is relatively uncertain because of the short time span involved. However, some insight has been obtained.

Parallel to the outer axis, temperature effects seem to cause the greatest rotation. This rotation has no impact upon tracking accuracy because of the self-aligning nature of the bearings. The steel frame I-beam has a temperature expansion coefficient of 9×10^{-6} inch/inch/ $^{\circ}$ F. Across the 33 foot length (bearing to bearing) and across an average slab temperature decrease of 22° C during early November to 10° C (early

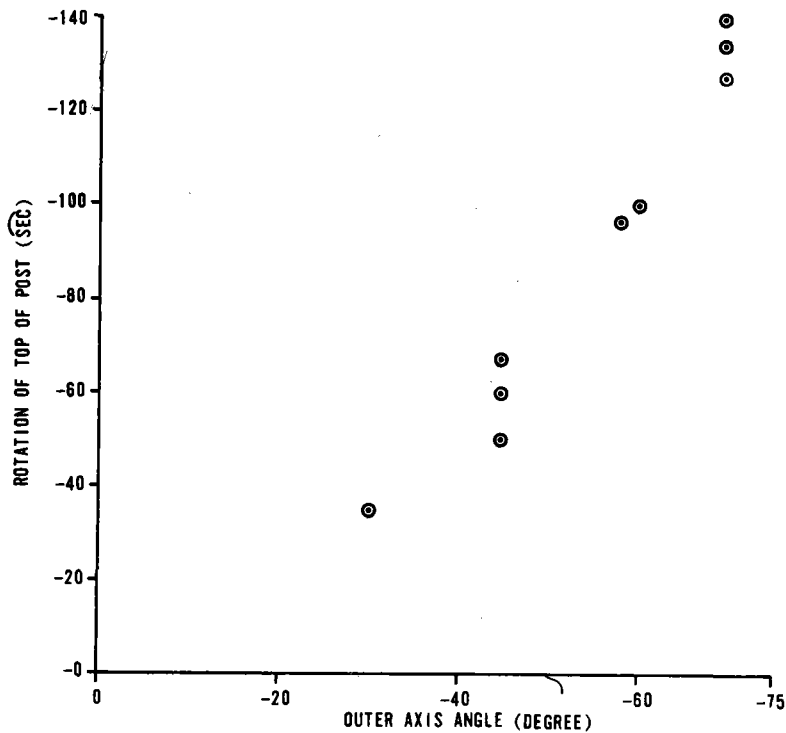


Figure 7-71. Top of Post Rotation Due to Outer Axis Frame Position

January 1977), 0.0385 inch contraction per post top would occur. Across the 90-inch post height this is 88 arc-second deflection. The slab rotation has been recorded at 11.5 seconds indicating that the bearing/shift slippage and post bending accounts for the remaining 76.5 arc-second change. This foundation and post rotation will induce no tracking errors.

Perpendicular to the OA (the 5 foot 8 inch slab dimension) total rotation shifting of only 23 arc-seconds has been observed. The direction varies from week to week, based on daily readings, under a combination of influences including wind direction changes, temperature changes, usage of the heliostat, and long term settling. It should be remembered that the ground preparation included no deep packing. The final long term shift cannot be determined yet, but this rotation (primarily a vertical pointing error source) will be removed by the periodic (≈ 1 week) calibration under normal operation by forcing an artificial change to primary and secondary target heights.

System Level Tracking

The operational program used always controls four heliostats, each in a different mode of operation or orientation if desired. Appendix and SRE System Description (Page 7-1) describe the six possible modes of heliostat operation. However, in the open loop configuration, often only one or two heliostats were actually in the "automatic" mode, i.e., responding to commands issued by the computer. In the subsequent paragraphs each heliostat will be discussed separately, even though data presented may show composite, nonapplicable information for other heliostats.

The daily tracking time of the heliostats was severely limited because of the short target height (15.5M). This was especially true for the experimental models which were operational only in late fall (November, December). Since the outer axis can gimbal to -75 degrees, tracking could not be accomplished after 2030 hours GMT (1530 Eastern Standard Time) due to low Sun elevation angle. North sites were limited in early morning for the same reason.

To correct for atmospheric refraction, a buffered algorithm was generated which was nonsingular for any elevation angle and gave good correlation with standard correction tables (<0.03 mr) for elevation angles greater than 10 degrees.

$$\text{Refraction} = \frac{57.9 \times \cos Z}{[\sin Z + 0.00019] \left[\frac{1 - 0.003}{(\sin Z)^2 + 0.000302} \right]}$$

where Z = elevation angle.

Table 7-13 tabulates the Sun angle from vertical and compares 10°C standard atmospheric refraction to the refraction algorithm used.

Engineering Model Heliostat

The engineering model was tested primarily from three different sites:

- North of target 140M (460 feet), Azimuth to target = 180 degrees
- North of target 189M (621 feet), Azimuth to target = 176 degrees
- South of target 329M (1080 feet), Azimuth to target = 337 degrees

Since the primary purpose of the engineering model was to evaluate hardware performance, the sites were never formally surveyed. Distances and angles were measured and calculated from other bench marks. When the trailer was hauled into position, the outer axis orthogonality to the radial vector was never precisely measured. Also, the initialization hardware was never incorporated, so this was done manually each day. After a few calibration attempts, good pseudo-target information was obtained such that the engineering model would track well.

Table 7-13. Comparison of Buffered Refraction Correction Algorithm

<u>Sun Angle From Vertical</u>	<u>Refraction From Table (Arc-Seconds)</u>	<u>Final Refraction Correction Used (Arc-Seconds)</u>
1.000	1.000	1.010
2.000	2.000	2.021
3.000	3.000	3.033
4.000	4.000	4.047
5.000	5.100	5.063
6.000	6.100	6.083
7.000	7.100	7.106
8.000	8.100	8.133
9.000	9.200	9.166
10.000	10.200	10.204
11.000	11.300	11.249
12.000	12.300	12.301
13.000	13.400	13.360
14.000	14.400	14.429
15.000	15.500	15.506
16.000	16.600	16.594
17.000	17.700	17.692
18.000	18.800	18.803
19.000	19.900	19.926
20.000	21.100	21.062
21.000	22.200	22.214
22.000	23.300	23.380
23.000	24.600	24.563
24.000	25.800	25.764
25.000	27.000	26.984
26.000	28.300	38.232
27.000	29.500	29.484
28.000	30.800	30.767
29.000	32.100	32.075
30.000	33.400	33.403
31.000	34.800	34.763
32.000	36.200	36.157
33.000	37.600	37.576
34.000	39.000	39.028
35.000	40.500	40.514
36.000	42.100	42.033
37.000	43.600	43.600
38.000	45.200	45.204
39.000	46.900	46.852
40.000	48.600	48.547
41.000	50.300	50.292
42.000	52.100	52.092
43.000	54.000	53.948
44.000	55.900	55.866
45.000	57.900	57.850
46.000	59.900	59.904

Table 7-13. Comparison of Buffered Refraction Correction Algorithm
(Continued)

<u>Sun Angle From Vertical</u>	<u>Refraction From Table (Arc-Seconds)</u>	<u>Final Refraction Correction Used (Arc-Seconds)</u>
47.000	62.000	62.033
48.000	64.000	64.243
49.000	66.500	66.541
50.000	68.900	68.932
51.000	71.400	71.425
52.000	74.000	74.027
53.000	76.700	76.748
54.000	79.500	79.598
55.000	82.500	82.587
56.000	85.600	85.729
57.000	88.900	89.037
58.000	92.400	92.527
59.000	96.100	96.217
60.000	100.000	100.127
61.000	104.100	104.280
62.000	108.500	108.702
63.000	113.200	113.422
64.000	118.200	118.476
65.000	123.500	123.903
66.000	129.300	129.749
67.000	135.600	136.070
68.000	142.300	142.929
69.000	149.700	150.403
70.000	157.800	158.583
71.000	166.600	167.581
72.000	176.300	177.530
73.000	187.200	188.597
74.000	199.200	200.988
75.000	212.800	214.964
76.000	229.200	230.858
77.000	245.700	249.103
78.000	265.900	270.273
79.000	289.500	295.140
80.000	317.300	324.776
81.000	350.600	360.699
82.000	391.100	405.141
83.000	441.300	461.500
84.000	505.100	535.185
85.000	588.400	635.271
86.000	700.200	777.813
87.000	857.600	992.191
88.000	1089.700	1323.560
89.000	1452.000	1658.497
90.000	2095.500	2006.272

A typical day of completely open loop tracking (Mode 2) is shown in the off-line data reduction printout of Figures 7-72A through 7-72L. Data is collected on-line once per minute. Figure 7-72A is annotated to show the location of certain interesting data pertaining to the engineering model heliostat designated in the third position and in Mode 2. Only the two Parsons mirrors were aligned to the target to remove the scatter from the foam filled modules. Two parts of the data acquisition system were inoperative during this period of time. The weather channels were inoperative; a transformer in the receiver had burned out. Also, one 16 channel multiplexer was hung on the previous channel output. This is apparent from the skewed repetition of the 9th column and first two elements of the 10th column.

The data was recorded 21 September 1976 (Julian Day 265) which was one day prior to Solar Equinox. The wind did not exceed 4.5 m/s and peak solar insolation was 771 watts/m². It rained lightly between 1535 and 1544 and then again later in the afternoon. Page 7-61 discusses briefly water accumulation on the mirrored surfaces during and after this rain. Notice that tracking continued through the rain and cloudy interval. At 1619, the recording tape drive generated a false end of tape signal to the computer, and all tracking stopped.

During the interval shown, the vertical movement of the image was about 0.75 foot (1.2 mr) and horizontal about ±1.2 feet (1.9 mr). This caliber of open loop tracking is typical for the engineering model and is considered to be excellent when considering its hardware and alignment limitations. After initial alignment parameters were determined through a series of calibration tracks (Mode 1, close loop), the engineering model can track open loop within 2.1 mr horizontally and 2.5 mr vertically as worse case limits during a complete day (e.g., 0930 to 1700 hours). Sometimes the yoke-and-collar assembly used to connect the actuators to the heliostat frame would bind causing vertical separation and horizontal shifts of the mirror module images. From this experience, a single pivot was designed for the experimental models and will also be used for the pilot plant heliostat.

Many photographs with 400 ASA B&W and 160 ASA EKACHROME slide film were taken during engineering model operation. Figure 7-10 was taken at 1658 hours 27 September 1976. This spot can be compared to the off-line calibration array printout at the same time, Figure 7-73. It was determined that the calibration array data was as accurate a "description" of the redirected image and track data as was required to obtain collector subsystem performance data. Normal photographic processes added no additional information. In subsequent operations, including experimental model testing, pictures were taken only of hardware, test set ups, etc., and were not used for image evaluation purposes.

South Site Experimental Model Heliostat

The South site was operational for test 25 October 1976. Site constants, except for heliostat unique scale factors, were from precise survey measurements. The line of sight distance to the 51.9 foot

DAYS RADGYR PRESS	HOURS PAX2MOM TEMP1	MINS SAX2MOM TAMB	DELVER PAXANG TEMP3	DELHOR GDF TDELTA	WINDSPD ANGSVN PYNOR	WINDDIR RADGLOBAL	CALMAX	BACKAVG	EM HELIOSTAT AS THIRD HELIOSTAT IN MODE 2							
DAY	HOURL	MINUTE	SECOND	5 OUTER AXIS ANGLE	5 INNER GIMBAL	5	1000.00	1000.00	621.00	1000.00	TGT ELEVATION	TGT ELEVATION	DISTANCE	DISTANCE	HORIZ DISTANCE OF CENTROID OF IMAGE FROM CENTER OF ARRAY	
265.00	13.00	10.00	0.00	55.00	55.00	55.00	50.90	55.00	55.00	55.00	55.00	55.00	55.00	55.00		
1000.00	1000.00	300.00	1000.00	0.00	176.00	176.00	0.00	0.00	0.00	0.00	0.00	0.00	0.00	0.00		
55.00	50.00	55.00	0.00	32.78	180.00	180.00	52.46	52.46	52.46	52.46	52.46	52.46	13.78	13.78		
176.00	0.00	180.00	180.00	-69.35	0.00	0.05	0.05	0.05	0.05	0.05	0.05	0.05	0.05	0.05		
52.46	0.00	0.00	0.00	1.00	1.00	1.00	-0.99	1.00	1.00	1.00	1.00	1.00	0.05	0.05		
0.00	0.00	0.07	0.00	0.00	0.00	0.07	0.00	0.00	0.00	0.00	0.00	0.00	1.00	1.00		
0.05	0.16	0.05	0.00	23.24	23.27	0.01	0.28	0.28	0.28	0.28	0.28	0.28	1.00	1.00		
-0.98	1.00	102.48	23.24	SUN AZ	SUN ELEV	SUN ELEV CORRECTED FOR REFRACTION	TGT ELEVATION	TGT ELEVATION	HORIZ DISTANCE OF CENTROID OF IMAGE FROM CENTER OF ARRAY	HORIZ DISTANCE OF CENTROID OF IMAGE FROM CENTER OF ARRAY	TGT ELEVATION	TGT ELEVATION	DISTANCE	DISTANCE		
PHOTOCELL INTENSITY ACROSS 16' x 14' ARRAY. PHOTOCELLS ARE ACTUALLY ON 1' GRID VERTICAL AND HORIZONTAL INTERVALS																
2	2	2	2	2	1	2	2	3	20	21	4	5	2	2	2	2
2	1	2	1	2	2	2	2	3	20	21	4	5	2	2	2	2
1	2	2	2	2	3	8	11	20	13	10	7	4	0	2	1	
2	2	1	2	2	7	13	20	20	26	19	13	6	0	2	2	
2	1	2	3	4	11	15	31	20	37	30	18	10	4	1	2	
2	2	2	3	6	14	31	42	21	47	37	24	13	5	2	1	
2	2	3	3	9	21	35	47	21	56	20	24	14	4	2	2	
2	2	2	2	0	21	32	47	21	51	40	15	11	4	2	2	
2	2	2	4	0	17	28	39	20	41	29	17	9	3	2	2	
2	1	2	2	7	12	22	29	21	28	21	15	5	2	2	1	
2	2	1	2	3	8	13	13	21	16	13	8	3	2	2	2	
1	2	0	2	2	0	6	7	21	8	6	3	1	2	1	2	
2	2	2	2	1	0	2	1	21	2	2	2	2	1	2	2	
0	2	2	2	2	2	2	2	21	2	2	2	2	2	2	2	
0	0	0	0	0	0	0	0	0	0	0	0	0	0	0	0	
265.0	13.00	10.00	0.2849	0.6858	0.0000	0.0000	0.0000	2.196	0.0000	0.0000	0.0000	0.0000	0.0000	0.0000	WEATHER CHANNELS (NOT OPERATING)	
4.028	7.176	9.051	0.151	0.8821	50.00											
914.0	15.00	-34.00	13.00	-11.00	0.0000	0.0000	0.0000									

Figure 7-72A. Engineering Model Open Loop Tracking Results

DAYS RADGYR PRESS	HOURS PAX2MOM TEMP1	MINS SAX2MOM TAMB	DELVER PAXANG TEMP3	DELHOR GOF TDELTA	WINDSPD ANGSVN PYNOR	WINDDIR RADGLOBAL	CALMAX	BACKAVG
265.00	13.00	30.00	0.00	5 5	2 5	1000.00	1000.00	621.00 1000.00
1000.00	1000.00	300.00	1000.00	55.00	55.00	50.90	55.00	55.00
55.00	50.00	55.00	0.00	0.00	176.00	0.00	0.00	0.00
176.00	0.00	180.00	180.00	30.41	180.00	52.46	52.46	14.83
52.46	0.00	0.00	-67.25	0.00	0.05	0.05	0.08	0.05
0.00	0.00	0.07	0.00	1.00	1.00	-0.99	1.00	0.05
0.05	0.16	0.05	0.00	0.00	0.07	0.00	1.00	1.00
-0.98	1.00	105.32	27.51	27.54	0.01	-0.29	1.51	1.00

MOSTLY CLOUDY

1	1	1	1	1	1	1	1	4	4	1	1	1	1	1	1
1	1	1	1	1	1	1	1	4	4	1	2	1	1	1	1
1	1	1	1	1	1	1	1	4	2	2	3	2	0	1	1
1	1	0	1	1	1	1	2	4	4	4	4	3	0	2	1
1	0	1	1	1	2	1	3	4	5	6	5	5	3	1	2
1	1	1	1	1	1	3	4	4	7	8	7	6	4	3	1
1	1	1	1	1	2	3	5	4	9	5	8	7	5	3	2
1	1	1	1	0	2	4	5	4	10	11	7	8	5	3	2
1	1	1	1	0	2	4	5	4	10	10	9	7	5	3	2
1	1	1	1	1	2	4	5	4	9	9	8	4	4	3	1
1	1	1	1	0	2	3	3	4	7	7	5	5	3	2	1
1	1	0	1	1	0	2	3	4	5	5	4	3	2	1	1
1	1	1	1	1	0	2	1	4	2	2	3	2	1	1	1
0	1	1	1	1	1	1	1	4	2	2	1	1	1	1	1
0	0	0	0	0	0	0	0	0	0	0	0	0	0	0	0

FAIN IMAGE
APPARENT
(≈ 1/2 SUN
PEAK FROM
2 MIRROR
MODULES)

7-125

265.0	13.00	30.00	-2.2883	1.509	0.0000	0.2000	0.4314	0.0000
4.787	10.00	12.12	-70.59	0.8415	51.02			
914.0	15.00	-34.00	13.00	-11.00	0.0000	0.0000		

Figure 7-72B. Engineering Model Open Loop Tracking Results

DAYS RADGYR PRESS	HOURS PAX2MOM TEMP1	MINS SAX2MOM TAMB	DELVER PAXANG TEMP3	DELHOR GOF TDELTA	WINDSPD ANGSVN PYNOR	WINDDIR RADGLOBAL	CALMAX	BACKAVG								
265.00	13.00	45.00	0.00	5	5	2	5	1000.00	1000.00	621.00	1000.00					
1000.00	1000.00	300.00	1000.00	55.00	55.00	176.00	50.90	55.00	55.00	55.00	55.00					
55.00	50.00	55.00	0.00	0.00	176.00	0.00	0.00	0.00	0.00	0.00	0.00					
176.00	0.00	180.00	180.00	28.59	180.00	52.46	52.46	52.46	52.46	15.57	15.57					
52.46	0.00	0.00	-65.84	0.00	0.05	0.05	0.05	0.05	0.05	0.05	0.05					
0.00	0.00	0.07	0.00	1.00	1.00	-0.99	1.00	1.00	1.00	0.05	0.05					
0.05	0.16	0.05	0.00	0.00	0.07	0.00	1.00	1.00	1.00	1.00	1.00					
-0.98	1.00	107.59	30.68	30.70	0.01	1.09	1.11	1.11	1.11	1.11	1.11					
2	2	2	2	2	1	2	3	22	24	7	6	4	2	2	2	2
2	1	2	1	2	2	3	5	23	24	17	14	8	5	2	2	2
1	2	2	2	2	4	9	17	23	32	30	25	15	0	3	1	1
2	2	1	2	2	6	15	31	24	50	44	34	19	2	4	2	2
2	1	2	3	3	10	15	42	24	66	57	43	25	11	2	2	2
2	2	2	3	4	12	29	51	24	69	62	45	23	10	4	2	2
2	2	2	3	6	15	31	47	24	63	26	32	17	9	3	2	2
2	2	2	2	0	15	26	37	24	49	40	17	13	5	2	2	2
2	2	2	2	0	11	18	29	24	34	25	14	7	4	3	2	2
2	1	2	1	4	6	11	15	24	17	12	6	2	2	2	2	1
2	2	1	2	1	4	5	5	24	5	4	2	3	2	2	2	2
1	2	0	2	2	0	3	3	24	3	2	2	1	2	1	2	2
2	2	2	2	1	0	2	1	24	2	2	2	2	1	2	2	2
0	2	2	2	2	2	2	2	24	2	2	2	1	2	2	2	2
0	0	0	0	0	0	0	0	0	0	0	0	0	0	0	0	0
265.0	13.00	45.00	1.000	1.100	0.0000	0.0000	0.0000	2.700	0.0000							
3.965	6.533	9.191	23.55	0.8695	51.69											
914.0	15.00	-34.00	13.00	-11.00	0.0000	0.0000										

7-126

Figure 7-72C. Engineering Model Open Loop Tracking Results

DAYS RADGYR PRESS	HOURS PAX2MOM TEMP1	MINS SAX2MOM TAMB	DELVER PAXANG TEMP3	DELHOR GOF TDELTA	WINDSPD ANGSVN PVNOR	WINDDIR RADGLOBAL	CALMAX	BACKAVG							
265.00	14.00	0.00	0.00	5	5	2	5	1000.00	1000.00	621.00	1000.00				
1000.00	1000.00	300.00	1000.00	55.00	55.00	50.90	55.00	55.00	55.00	55.00	55.00	55.00	55.00	55.00	55.00
55.00	50.00	55.00	0.00	0.00	176.00	0.00	0.00	0.00	0.00	0.00	0.00	0.00	0.00	0.00	0.00
176.00	0.00	100.00	100.00	26.72	100.00	52.46	52.46	52.46	52.46	16.26	16.26	16.26	16.26	16.26	16.26
52.46	0.00	0.00	-64.56	0.00	0.05	0.05	0.05	0.05	0.05	0.05	0.05	0.05	0.05	0.05	0.05
0.00	0.00	0.07	0.00	1.00	1.00	-0.99	1.00	1.00	1.00	1.00	1.00	1.00	1.00	1.00	1.00
0.05	0.16	0.05	0.00	0.00	0.07	0.00	1.00	1.00	1.00	1.00	1.00	1.00	1.00	1.00	1.00
-0.98	1.00	110.02	33.81	33.83	0.01	0.71	0.30	0.30	0.30	0.30	0.30	0.30	0.30	0.30	0.30
2	2	2	2	2	1	2	3	31	31	3	3	2	1	2	2
3	2	2	2	2	3	3	5	31	31	11	8	4	2	2	2
1	2	2	2	3	5	14	25	31	29	21	15	9	0	2	1
3	2	1	3	4	14	29	45	31	50	36	22	11	0	2	3
2	1	2	4	10	24	33	65	31	69	52	31	15	4	1	2
2	3	3	5	15	31	63	85	31	82	60	34	15	4	3	2
3	2	3	7	19	47	72	89	31	80	28	24	13	4	2	3
2	2	3	8	0	44	61	75	31	63	43	14	9	3	2	2
2	2	3	9	0	31	46	57	31	46	26	13	5	3	2	2
2	2	3	5	12	19	31	35	31	24	13	5	2	2	3	2
3	2	2	4	5	11	15	12	31	7	4	2	3	3	2	2
2	2	0	3	3	0	5	4	31	3	3	2	2	2	2	2
2	2	2	2	2	0	3	1	31	2	2	3	2	1	2	2
0	2	2	2	2	2	2	2	31	2	2	2	2	2	2	2
0	0	0	0	0	0	0	0	0	0	0	0	0	0	0	0
265.0	14.00	0.0000	0.7147	0.2984	0.0000	0.0000	0.0000	0.0000	3.490	0.0000	0.0000	0.0000	0.0000	0.0000	0.0000
3.831	6.183	8.494	20.56	0.8911	52.34	0.0000	0.0000	0.0000	0.0000	0.0000	0.0000	0.0000	0.0000	0.0000	0.0000
914.0	15.00	-34.00	13.00	-11.00	0.0000	0.0000	0.0000	0.0000	0.0000	0.0000	0.0000	0.0000	0.0000	0.0000	0.0000

7-127

Figure 7-72D. Engineering Model Open Loop Tracking Results

DAYS RADGYR PRESS	HOURS PAX2MOM TEMP1	MINS SAX2MOM TAMB	DELVER PAXANG TEMP3	DELHOR GOF TDELTA	WINDSPD ANGSVN PYNGR	WINDDIR RADGLOBAL	CALMAX	BACKAVG							
265.00	14.00	15.00	0.00	5 5	2 5	1000.00	1000.00	621.00	1000.00						
1000.00	1000.00	300.00	1000.00	55.00	55.00	50.90	55.00	55.00	55.00						
55.00	50.00	55.00	0.00	0.00	176.00	0.00	0.00	0.00	0.00						
176.00	0.00	180.00	180.00	24.80	180.00	52.46	52.46	16.88	16.88						
52.46	0.00	0.00	-63.40	0.00	0.05	0.05	0.00	0.00	0.05						
0.00	0.00	0.07	0.00	1.00	1.00	-0.99	1.00	0.05	0.05						
0.05	0.16	0.05	0.00	0.00	0.07	0.00	1.00	1.00	1.00						
-0.98	1.00	112.63	36.88	36.90	0.01	0.68	-0.03								
2	2	2	2	2	1	2	3	29	30	3	3	2	1	2	2
2	2	2	2	2	3	4	5	30	30	8	6	2	2	2	2
1	2	2	2	4	9	17	26	30	26	17	12	6	0	2	1
2	2	1	4	7	19	33	47	30	45	31	17	8	0	2	2
2	1	3	7	15	31	38	68	30	63	43	23	11	3	1	2
2	3	3	10	21	42	71	88	30	73	49	26	11	3	2	2
3	2	4	13	29	58	79	92	30	73	22	19	9	3	2	2
2	2	5	13	0	52	67	77	30	58	33	11	7	2	2	2
2	2	5	12	3	37	48	58	0	40	21	11	4	3	3	2
2	2	4	8	15	24	33	34	30	20	11	5	2	2	2	2
3	2	2	5	7	12	15	11	30	7	4	2	2	2	2	2
2	2	0	3	3	0	5	4	30	3	2	2	2	2	2	2
2	2	2	2	2	0	2	1	30	2	2	2	2	1	2	2
0	2	2	2	2	2	2	2	30	2	2	2	2	2	2	2
0	0	0	0	0	0	0	0	0	0	0	0	0	0	0	0
265.0	14.00	15.00	0.6825	-0.3263E-01	0.0000	0.0000	3.688	0.0000	0.0000						
3.815	6.251	8.300	20.64	0.8960	52.95	0.0000									
914.0	15.00	-34.00	13.00	-11.00	0.0000	0.0000									

7-128

Figure 7-72E. Engineering Model Open Loop Tracking Results

DAYS RADGYR PRESS	HOURS PAX2MOM TEMP1	MINS SAX2MOM TAMB	DELVER PAXANG TEMP3	DELHOR GOF TDELTA	WINDSPD ANGSVN PYNOR	WINDDIR RADGLOBAL	CALMAX	BACKAVG							
265.00	14.00	30.00	0.00	5 5	2 5	1000.00	1000.00	621.00							
1000.00	1000.00	300.00	1000.00	55.00	55.00	50.90	55.00	55.00							
55.00	50.00	55.00	0.00	0.00	176.00	0.00	0.00	0.00							
176.00	0.00	180.00	180.00	22.84	180.00	52.46	52.46	17.48							
52.46	0.00	0.00	-62.33	0.00	0.05	0.05	0.00	0.05							
0.00	0.00	0.07	0.00	1.00	1.00	-0.99	1.00	0.05							
0.05	0.16	0.05	0.00	0.00	0.07	0.00	1.00	1.00							
-0.98	1.00	115.45	39.90	39.92	0.01	1.33	0.18	1.00							
2	2	2	3	2	1	2	5	36	37	11	9	5	2	2	2
2	2	2	2	3	5	12	17	37	37	23	16	9	4	2	2
2	2	2	2	6	15	31	48	37	51	37	27	14	0	2	1
3	3	1	4	11	30	52	74	37	78	58	35	15	0	2	2
2	1	3	7	18	44	53	99	37	96	66	38	15	4	1	2
2	3	3	11	26	50	85	106	37	93	61	31	13	4	2	2
3	2	4	13	28	56	77	93	37	73	22	18	9	3	2	3
2	2	4	11	0	44	57	65	37	51	28	8	4	2	2	2
2	2	3	9	0	27	37	43	37	26	12	4	2	3	1	2
2	2	3	5	10	14	18	18	37	7	3	3	2	2	2	2
3	2	2	3	3	6	6	4	37	3	3	2	2	2	2	2
2	2	0	3	2	0	3	3	37	3	2	2	2	2	2	2
2	2	2	2	2	0	2	1	37	2	2	2	2	1	2	2
0	2	2	2	2	2	2	2	37	2	2	2	2	2	2	2
0	0	0	0	0	0	0	0	0	0	0	0	0	0	0	0
265.0	14.00	30.00	1.332	0.1768	0.0000	0.0000	4.157	0.0000							
3.000	5.930	8.571	20.97	0.8738	53.04	0.0000	0.0000								
914.0	15.00	-34.00	13.00	-11.00	0.0000	0.0000									

7-129

Figure 7-72F. Engineering Model Open Loop Tracking Results

DAYS RADGYR PRESS	HOURS PAX2MOM TEMP1	MINS SAX2MOM TAMB	DELVER PAXANG TEMP3	DELHOR GOF TDELTA	WINDSPD ANGSVN PYNOM	WINDDIR RADGLOBAL	CALMAX	BACKAVG							
265.00	14.00	45.00	0.00	5	5	2	5	1000.00	1000.00	621.00	1000.00				
1000.00	1000.00	300.00	1000.00	55.00	55.00	50.90	55.00	55.00	55.00	55.00	55.00				
55.00	50.00	55.00	0.00	0.00	176.00	0.00	0.00	0.00	0.00	0.00	0.00				
176.00	0.00	180.00	180.00	20.86	180.00	52.46	52.46	52.46	18.00	18.00	18.00				
52.46	0.00	0.00	-61.40	0.00	0.05	0.05	0.08	0.08	0.05	0.05	0.05				
0.00	0.00	0.07	0.00	1.00	1.00	-0.99	1.00	1.00	0.05	0.05	0.05				
0.05	0.16	0.05	0.00	0.00	0.07	0.00	0.00	1.00	1.00	1.00	1.00				
-0.98	1.00	118.53	42.85	42.86	0.01	0.38	-0.50								
3	3	3	3	3	1	2	3	31	31	3	3	2	2	3	3
3	2	3	2	3	3	4	5	31	31	8	5	2	3	3	2
2	3	3	2	3	6	15	22	31	21	15	11	5	0	2	2
3	3	1	4	7	21	33	46	31	37	25	15	7	0	3	3
3	1	3	8	21	41	44	77	31	60	37	19	9	3	1	3
2	4	5	15	34	59	90	104	32	72	45	21	8	3	3	2
3	3	7	21	49	88	104	111	31	73	20	15	7	3	2	3
3	3	11	27	0	88	100	101	32	60	31	9	5	3	2	3
3	4	11	25	15	64	77	91	31	42	18	7	3	3	3	3
3	3	10	18	31	44	52	47	31	18	7	4	2	2	3	2
4	4	7	13	16	24	26	15	31	5	4	2	3	3	3	3
2	3	0	8	10	0	10	6	31	4	3	3	2	3	2	3
3	3	3	4	4	0	4	2	31	3	2	3	3	2	2	2
0	3	3	3	3	3	2	2	31	3	3	2	2	3	3	2
0	0	0	0	0	0	0	0	0	0	0	0	0	0	0	0
265.0	14.00	45.00	0.3756	-0.4974	0.0000	0.0000	4.353	0.0000	0.0000						
3.855	6.298	8.566	32.43	0.9014	54.10										
914.0	15.00	-34.00	13.00	-11.00	0.0000	0.0000									

7-130

Figure 7-72G. Engineering Model Open Loop Tracking Results

DAYS RADGYR PRESS	HOURS PAX2MOM TEMP1	MINS SAX2MOM TAMB	DELVER PAXANG TEMP3	DELHOR GOF TDELTA	WINDSPD ANGSVN PYNOR	WINDDIR RADGLOBAL	CALMAX	BACKAVG								
265.00	15.00	0.00	0.00	5	5	2	5	1000.00	1000.00	621.00	1000.00					
1000.00	1000.00	300.00	1000.00	55.00	55.00	176.00	50.90	55.00	55.00	55.00	55.00					
55.00	50.00	55.00	0.00	0.00	0.00	176.00	0.00	0.00	0.00	0.00	0.00					
176.00	0.00	180.00	180.00	18.85	180.00	52.46	52.46	52.46	52.46	18.49	18.49					
52.46	0.00	0.00	-60.53	0.00	0.05	0.05	0.05	0.05	0.05	0.05	0.05					
0.00	0.00	0.07	0.00	1.00	1.00	-0.99	1.00	1.00	1.00	0.05	0.05					
0.05	0.16	0.05	0.00	0.00	0.07	0.00	0.00	1.00	1.00	0.05	0.05					
-0.98	1.00	121.90	45.70	45.71	0.01	0.74	-0.71			1.00	1.00					
3	3	3	3	3	1	3	4	31	31	4	3	2	2	3	3	
3	2	3	2	3	4	7	10	31	31	11	7	2	3	3	2	
2	3	3	2	5	15	26	35	31	27	17	13	5	0	2	1	
3	3	1	6	16	37	53	65	31	47	28	15	5	0	3	3	
3	1	5	15	36	64	62	100	31	66	39	18	7	3	1	2	
2	4	9	25	53	79	107	116	32	72	40	18	5	3	3	2	
3	3	14	32	63	102	113	114	32	63	15	12	4	3	2	3	
3	4	16	33	0	89	98	93	32	47	21	6	3	3	2	3	
3	5	13	27	15	60	66	63	<L	25	10	4	2	3	3	3	
3	3	11	17	28	34	39	30	31	7	4	3	2	2	3	2	
4	3	6	11	13	17	14	7	31	4	3	2	3	3	3	3	
2	3	0	5	6	0	5	4	31	3	3	3	2	3	2	3	
2	3	2	3	2	0	3	2	32	3	2	3	3	2	2	2	
0	3	3	3	3	3	2	2	31	3	3	2	2	3	3	2	
0	0	0	0	0	0	0	0	0	0	0	0	0	0	0	0	
265.0	15.00	0.0000	0.7378	-0.7957	0.0000	0.0000	4.549	0.0000	0.0000							
3.809	6.367	8.142	31.08	0.9019	54.61											
914.0	15.00	-34.00	13.00	-11.00	0.0000	0.0000										

7-131

Figure 7-72H. Engineering Model Open Loop Tracking Results

DAYS RADGYR PRESS	HOURS PAX2MOM TEMP1	MINS SAX2MOM TAMB	DELVER PAXANG TEMP3	DELHOR GOF TDELTA	WINDSPD ANGSVN PYNOR	WINDDIR RADGLOBAL	CALMAX	BACKAVG								
265.00	15.00	15.00	0.00	5	5	2	5	1000.00	1000.00	621.00	1000.00					
1000.00	1000.00	300.00	1000.00	55.00	55.00	50.90	55.00	55.00	55.00	55.00	55.00	55.00	55.00	55.00	55.00	55.00
55.00	50.00	55.00	0.00	0.00	176.00	0.00	176.00	0.00	0.00	0.00	0.00	0.00	0.00	0.00	0.00	0.00
176.00	0.00	180.00	180.00	16.82	180.00	52.46	180.00	52.46	52.46	52.46	52.46	52.46	52.46	52.46	52.46	52.46
52.46	0.00	0.00	-59.78	0.00	0.05	0.05	0.05	0.05	0.05	0.05	0.05	0.05	0.05	0.05	0.05	0.05
0.00	0.00	0.07	0.00	1.00	1.00	-0.99	1.00	1.00	1.00	1.00	1.00	1.00	1.00	1.00	1.00	1.00
0.05	0.16	0.05	0.00	0.00	0.07	0.07	0.07	0.07	0.07	0.07	0.07	0.07	0.07	0.07	0.07	0.07
-0.98	1.00	125.64	48.45	48.46	0.01	0.57	0.57	0.57	0.57	0.57	0.57	0.57	0.57	0.57	0.57	0.57
4	4	4	4	4	2	3	4	29	30	4	4	3	2	4	4	4
4	3	3	3	4	4	5	7	30	30	9	6	3	4	4	4	3
2	4	4	3	5	12	21	29	30	23	15	11	5	0	3	2	2
4	4	1	7	15	31	44	55	30	40	24	15	5	0	4	4	4
4	1	5	16	32	56	53	88	30	60	35	17	7	4	2	3	3
3	5	10	26	48	72	98	108	31	67	40	18	6	4	4	4	2
4	4	15	33	61	96	108	109	31	63	16	13	5	4	3	4	4
3	5	17	33	0	88	96	92	31	48	24	7	4	4	3	4	4
4	6	15	28	15	60	67	64	30	30	13	5	3	4	4	4	4
4	4	11	17	29	35	40	32	31	11	5	4	2	3	4	3	3
4	4	7	12	14	18	15	8	31	5	4	3	4	4	4	4	4
3	4	0	7	7	0	7	5	30	4	4	4	3	4	3	4	4
3	4	3	4	3	0	4	2	31	4	3	4	4	2	3	3	3
0	4	4	4	4	4	3	3	31	4	4	3	3	3	4	3	3
0	0	0	0	0	0	0	0	0	0	0	0	0	0	0	0	0
265.0	15.00	15.00	0.5689	-0.6670	0.0000	0.0000	0.0000	0.0000	0.0000	4.275	0.0000	0.0000	0.0000	0.0000	0.0000	0.0000
3.995	7.309	8.653	38.55	0.8932	55.08	55.08	55.08	55.08	55.08	55.08	55.08	55.08	55.08	55.08	55.08	55.08
914.0	15.00	-34.00	13.00	-11.00	0.0000	0.0000	0.0000	0.0000	0.0000	0.0000	0.0000	0.0000	0.0000	0.0000	0.0000	0.0000

7-132

Figure 7-72I. Engineering Model Open Loop Tracking Results

DAYS PDDGYR PRESS	HOURS PAX2MOM TEMP1	MINS SAX2MOM TAMB	DELVER PAXANG TEMP3	DELHOR GOF TDELTA	WINDSPD ANGSVN PYNOR	WINDDIR RADGLOBAL	CALMAX	BACKAVG							
265.00	15.00	27.00	0.00	5	5	2	5	1000.00	1000.00	621.00	1000.00				
1000.00	1000.00	300.00	1000.00	55.00	55.00	55.00	50.90	55.00	55.00	55.00	55.00				
55.00	50.00	55.00	0.00	0.00	176.00	0.00	0.00	0.00	0.00	0.00	0.00				
176.00	0.00	180.00	180.00	15.20	180.00	52.46	52.46	52.46	19.23	19.23	19.23				
52.46	0.00	0.00	-59.22	0.00	0.05	0.05	0.08	0.08	0.05	0.05	0.05				
0.00	0.00	0.07	0.00	1.00	1.00	-0.99	1.00	1.00	0.05	0.05	0.05				
0.05	0.16	0.05	0.00	0.00	0.07	0.00	1.00	1.00	1.00	1.00	1.00				
-0.98	1.00	128.91	50.55	50.56	0.01	0.02	0.15	0.15	0.15	0.15	0.15				
2	2	2	2	1	1	1	2	2	2	2	2	2	1	2	2
2	1	1	1	2	2	1	1	2	2	1	2	1	2	2	1
1	2	2	1	1	2	2	1	2	2	2	2	2	0	1	1
2	2	1	1	1	1	1	1	2	1	1	2	1	0	2	2
2	1	1	2	1	2	1	2	2	2	2	2	2	2	1	1
1	2	2	2	1	1	2	2	2	2	1	1	2	2	2	1
2	1	2	2	1	2	2	1	2	2	1	1	2	1	1	2
1	2	2	1	0	2	1	2	2	2	1	2	1	2	1	2
1	2	2	2	0	2	1	1	2	2	1	2	1	2	2	2
2	1	2	1	1	1	2	1	2	2	1	2	1	1	2	1
2	2	1	2	1	1	2	1	2	2	2	1	2	2	2	2
1	2	0	2	1	0	2	2	2	2	2	2	1	2	1	2
1	2	1	2	1	0	2	1	2	2	1	2	2	1	2	2
0	2	2	2	2	1	1	1	2	2	2	1	1	2	2	2
0	0	0	0	0	0	0	0	0	0	0	0	0	0	0	0
265.0	15.00	27.00	0.2312E-01	0.1532	0.0000	0.0000	0.7843E-01	0.0000	0.0000	0.0000	0.0000				
6.134	16.30	21.32	-00.87	0.7081	55.43										
914.0	15.00	-34.00	13.00	-11.00	0.0000	0.0000									
0	0	0	0	0	0	0	0	0	0	0	0	0	0	0	0
265.0	15.00	28.00	0.1678E-01	0.1812	0.0000	0.0000	0.7843E-01	0.0000	0.0000	0.0000	0.0000				
6.177	15.85	22.30	-76.48	0.7181	55.46										
914.0	15.00	-34.00	13.00	-11.00	0.0000	0.0000									

CLOUDY

7-133

Figure 7-72J. Engineering Model Open Loop Tracking Results

DAYS RADGYR PRESS	HOURS PAX2MOM TEMP1	MINS SAX2MOM TAMB	DELVER PAXANG TEMP3	DELHOR GOF TDELTA	WINDSPD ANGSYN PYNOR	WINDDIR RADGLOBAL	CALMAX	BACKAVG	FIRST SUN AFTER RAIN								
265.00	15.00	58.00	0.00	5	5	2	5	1000.00	1000.00	621.00	1000.00						
1000.00	1000.00	300.00	1000.00	55.00	55.00	50.90	55.00	55.00	55.00	55.00	55.00	55.00	55.00	55.00	55.00	55.00	55.00
55.00	50.00	55.00	0.00	0.00	176.00	0.00	0.00	0.00	0.00	0.00	0.00	0.00	0.00	0.00	0.00	0.00	0.00
176.00	0.00	100.00	100.00	10.92	100.00	52.46	52.46	52.46	52.46	52.46	52.46	52.46	52.46	52.46	52.46	52.46	52.46
52.46	0.00	0.00	-58.04	0.00	0.05	0.05	0.08	0.08	0.08	0.08	0.08	0.08	0.08	0.08	0.08	0.08	0.08
0.00	0.00	0.07	0.00	1.00	1.00	-0.99	1.00	1.00	1.00	1.00	1.00	1.00	1.00	1.00	1.00	1.00	1.00
0.05	0.16	0.05	0.00	0.00	0.07	0.00	1.00	1.00	1.00	1.00	1.00	1.00	1.00	1.00	1.00	1.00	1.00
-0.98	1.00	138.84	55.48	55.49	0.01	0.24	-1.06	-1.06	-1.06	-1.06	-1.06	-1.06	-1.06	-1.06	-1.06	-1.06	-1.06
3	3	3	3	3	1	3	4	17	18	3	4	3	2	3	3	3	3
3	2	3	2	4	4	4	3	17	18	3	4	2	3	3	3	3	2
2	3	3	3	4	6	9	12	17	9	5	4	4	0	3	3	2	2
4	4	1	6	10	20	25	28	17	15	10	5	3	0	3	3	4	4
3	1	7	16	28	41	35	49	18	28	15	7	4	4	4	2	3	3
3	5	13	28	45	57	73	69	18	35	18	8	4	4	4	4	2	2
4	6	19	36	58	81	84	76	18	37	9	6	4	4	4	3	4	4
3	9	21	38	0	77	80	69	18	31	15	4	4	3	3	3	3	3
3	9	16	31	16	58	60	53	17	20	9	5	3	4	4	4	3	3
3	6	12	19	30	34	33	28	18	10	5	4	2	3	4	4	3	3
4	4	7	12	13	15	14	7	18	5	4	3	4	4	4	4	3	3
2	3	0	6	5	0	5	4	18	4	4	4	3	4	2	3	3	3
3	3	3	3	3	0	4	2	18	4	3	4	3	2	3	3	3	3
0	3	3	3	3	3	3	3	18	3	4	3	3	3	3	3	3	3
0	0	0	0	0	0	0	0	0	0	0	0	0	0	0	0	0	0
265.0	15.00	58.00	0.2425	-1.058	0.0000	0.0000	3.294	0.0000	0.0000	0.0000	0.0000	0.0000	0.0000	0.0000	0.0000	0.0000	0.0000
4.000	7.682	8.965	74.05	0.8963	56.19	0.0000	0.0000	0.0000	0.0000	0.0000	0.0000	0.0000	0.0000	0.0000	0.0000	0.0000	0.0000
914.0	15.00	-34.00	13.00	-11.00	0.0000	0.0000	0.0000	0.0000	0.0000	0.0000	0.0000	0.0000	0.0000	0.0000	0.0000	0.0000	0.0000

7-134

Figure 7-72K. Engineering Model Open Loop Tracking Results

DAYS RADGYR PRESS	HOURS PAX2MOM TEMP1	MINS SAX2MOM TAMB	DELVER PAXANG TEMP3	DELHOR 30F TDELTA	WINDSPD ANGSWY PVNOR	WINDDIR RADGLOBAL	CALMAX	BACKAVG								
265.00	16.00	15.00	0.00	5	5	2	5	1000.00	1000.00	621.00	1000.00					
1000.00	1000.00	300.00	1000.00	55.00	55.00	176.00	50.90	55.00	55.00	55.00	55.00					
55.00	50.00	55.00	0.00	0.00	176.00	0.00	0.00	0.00	0.00	0.00	0.00					
176.00	0.00	180.00	180.00	3.54	180.00	52.46	52.46	52.46	52.46	23.20	23.20					
52.46	0.00	0.00	-57.53	0.00	0.05	0.05	0.05	0.05	0.05	0.05	0.05					
0.00	0.00	0.07	0.00	1.00	1.00	-0.95	1.00	1.00	1.00	0.05	0.05					
0.05	0.16	0.05	0.00	0.00	0.07	0.00	1.00	1.00	1.00	1.00	1.00					
-0.98	1.00	145.32	57.78	57.79	0.01	-0.02	-1.23	-1.23	-1.23	1.00	1.00					
3	3	3	3	3	1	2	3	27	28	3	3	2	1	3	3	
3	2	3	2	3	3	3	2	28	28	3	3	2	3	3	2	
2	3	3	2	3	4	5	6	28	5	3	4	3	0	2	1	
3	3	1	7	11	20	24	28	28	15	8	4	2	0	3	3	
3	1	9	21	33	52	44	62	28	31	15	7	4	3	1	2	
3	6	18	38	63	81	100	96	28	51	24	11	3	3	3	2	
4	10	28	54	89	127	133	122	28	63	15	11	4	3	2	3	
3	14	31	62	0	133	136	122	28	61	31	8	3	3	2	3	
4	13	25	53	34	102	111	104	28	44	20	8	2	3	3	3	
3	9	17	34	56	65	69	63	28	24	13	5	2	2	3	2	
4	5	11	18	24	33	30	18	28	10	5	2	3	3	3	3	
2	3	0	7	8	0	9	6	28	4	3	3	2	3	2	3	
2	3	3	3	3	0	4	2	20	3	2	3	3	2	2	2	
0	3	3	3	3	3	2	3	28	3	3	2	2	3	3	2	
0	0	0	0	0	0	0	0	0	0	0	0	0	0	0	0	
265.0	16.00	15.00	-0.1866E-01	-1.231	0.0000	0.0000	5.333	0.0000	0.0000							
3.694	5.291	7.358	56.73	0.9205	56.52	0.0000										
914.0	15.00	-34.00	13.00	-11.00	0.0000	0.0000										

7-135

Figure 7-72L. Engineering Model Open Loop Tracking Results

DAYS RADGYR PRESS	HOURS PAX2MOM TEMP1	MINS SAX2MOM TAMB	DELVER PAXANG TEMP3	DELHOR GOF TDELTA	WINDSPD ANGSVN PYNOR	WINDDIR RADGLOBAL	CALMAX RATIO	CALSUMG ENERGY	BACKAVG					
272.00	16.00	58.00	0.00	5 5	2 5	1000.00	1000.00	621.00	1000.00					
1000.00	1000.00	621.00	1000.00	55.00	55.00	50.90	55.00	55.00						
55.00	48.00	55.00	0.00	0.00	176.00	0.00	0.00	0.00						
177.00	0.00	180.00	180.00	2.01	180.00	52.46	52.46	19.96						
52.46	0.00	0.00	-57.96	0.00	0.05	0.05	0.08	0.05						
0.00	0.00	0.07	0.00	1.00	1.00	-0.99	1.00	0.05						
0.05	0.08	0.05	0.00	0.00	0.05	0.00	1.00	1.00						
-1.00	1.00	167.55	59.23	59.24	0.01	-1.99	0.54							
1	1	1	1	0	0	1	41	42	1	1	1	1	1	1
1	1	1	0	1	1	0	0	42	42	1	1	0	1	1
0	1	1	0	1	1	1	1	42	2	1	1	1	0	0
1	1	0	1	0	1	1	1	42	1	1	1	0	0	1
1	1	1	1	2	5	5	9	42	7	3	1	1	1	1
0	1	1	2	8	15	23	29	42	23	13	4	1	1	1
1	1	1	7	17	31	41	52	42	43	15	15	4	1	1
0	1	2	13	0	47	66	82	42	68	56	22	13	4	1
1	1	2	17	9	54	82	111	42	94	70	44	21	10	2
1	1	3	15	32	56	88	116	42	109	84	57	20	14	3
1	1	2	12	23	52	73	69	42	114	82	55	33	18	4
0	1	0	7	16	40	62	74	42	90	71	49	31	17	3
0	1	1	2	7	24	39	49	42	58	38	38	23	13	2
0	1	1	1	3	10	19	28	42	36	31	23	15	6	1
0	0	0	0	0	0	0	0	0	0	0	0	0	0	0
272.0	16.00	58.00	-1.995	0.5354	0.4830	0.0000	4.549	4068.	0.0000					
3.771	5.418	8.804	-10.93	0.8178	58.42									
914.0	0.0000	-34.00	0.0000	0.0000	87.20	20.30	0.0000	0.0000						

7-136

Figure 7-73. Calibration Array Image (Compare with Figure 7-10)

array height is 314M (1031 feet). This distance is not directly applicable to the present pilot plant tower one-half south field configuration for heliostats south of the tower (which is presently about 150 meters). However, for commercial plant sizes, the south site distance is representative except for target height.

Figures 7-74 and 7-75 show open loop track performance on the second day of operation. All error measurements are in feet with respect to the calibration array center and were taken at 15-minute intervals from the ASR on-line output. Notice that at this first open loop attempt, the total horizontal track error was less than 2 mr and the vertical track error was 2.7 mr worse case over a full day's interval. All hardware was operational with the exception of initialization electronics.

The cause for vertical drift errors for the South site were determined to be the same as for each of the heliostats - outer actuator scale factor differences (see Page 7-97). The linear actuators had a theoretical effective linear gear ratio of 0.01185 inch/motor revolution (i.e., single DCU command). Measured values were 0.70 percent less than derived values. Therefore, the operational program's predicted value of total outer axis gimbale angle is greater than the actual angle after 2000 to 4000 pulses, and the Sun's redirected image drifts upward after solar noon. This vertical error source also obviously couples into the horizontal track.

Another error source, for which software compensates (see Pages 7-147 and 7-149) results from the fact that the center line of the outer axis pivot is 5.4197 degrees off perpendicular with the radial vector from target to heliostat.

After compensation for these errors, the South site remained within 1.3 mr total track accuracy. Test time on the South site was limited for the following reasons:

1. Initial success in accurate tracking.
2. Moving the calibration array East 10 November 1976.
3. Removing and reworking of the inner drive gearbox because of excessive lash
4. Using one of the South site actuators temporarily on the East site while returning the binding actuator to vendor for rework.

North Site Experimental Model

Starting 26 October 1976, except for a brief special purpose imagery test on 17 December the calibration array was never faced North while the North experimental model was operational. Most of the engineering model testing was from near adjacent Northern azimuth locations.

Therefore, the North experimental model was never put into the closed loop calibration mode.

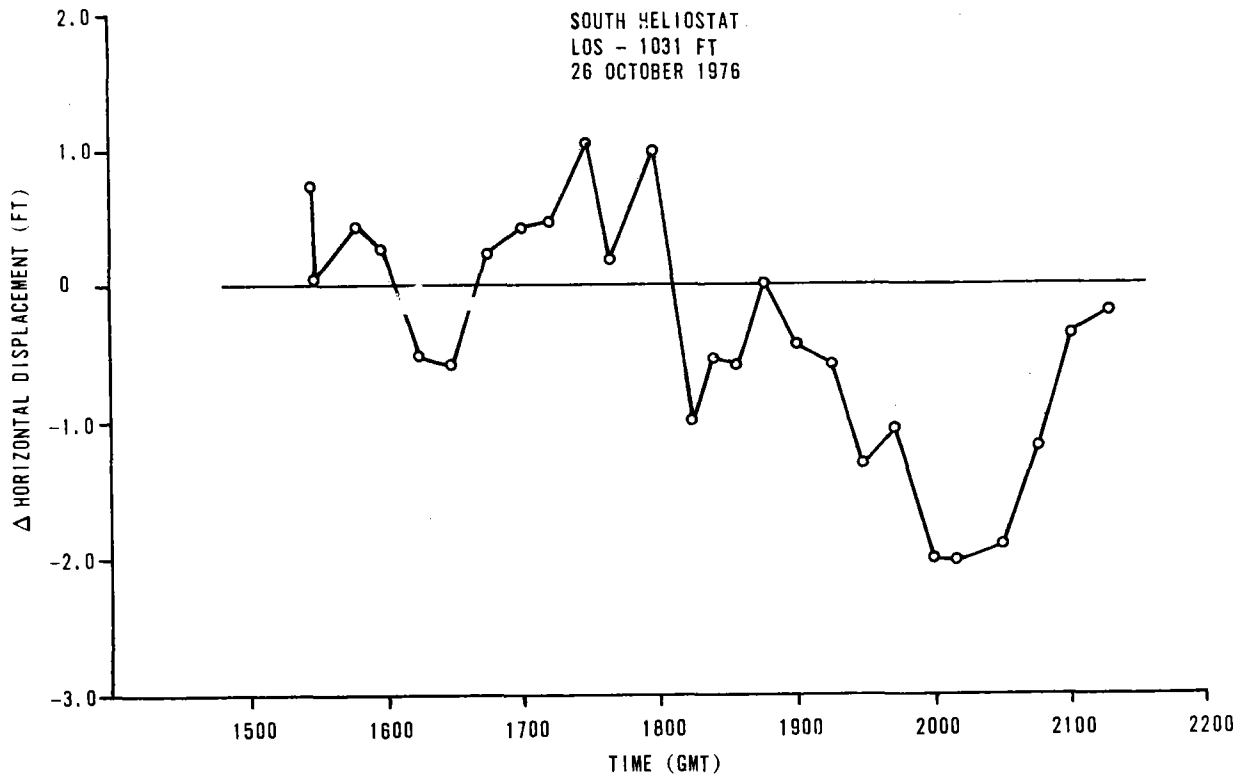


Figure 7-74. Image Horizontal Centroid Track,
South Site, Second Day of Operation

0277-092

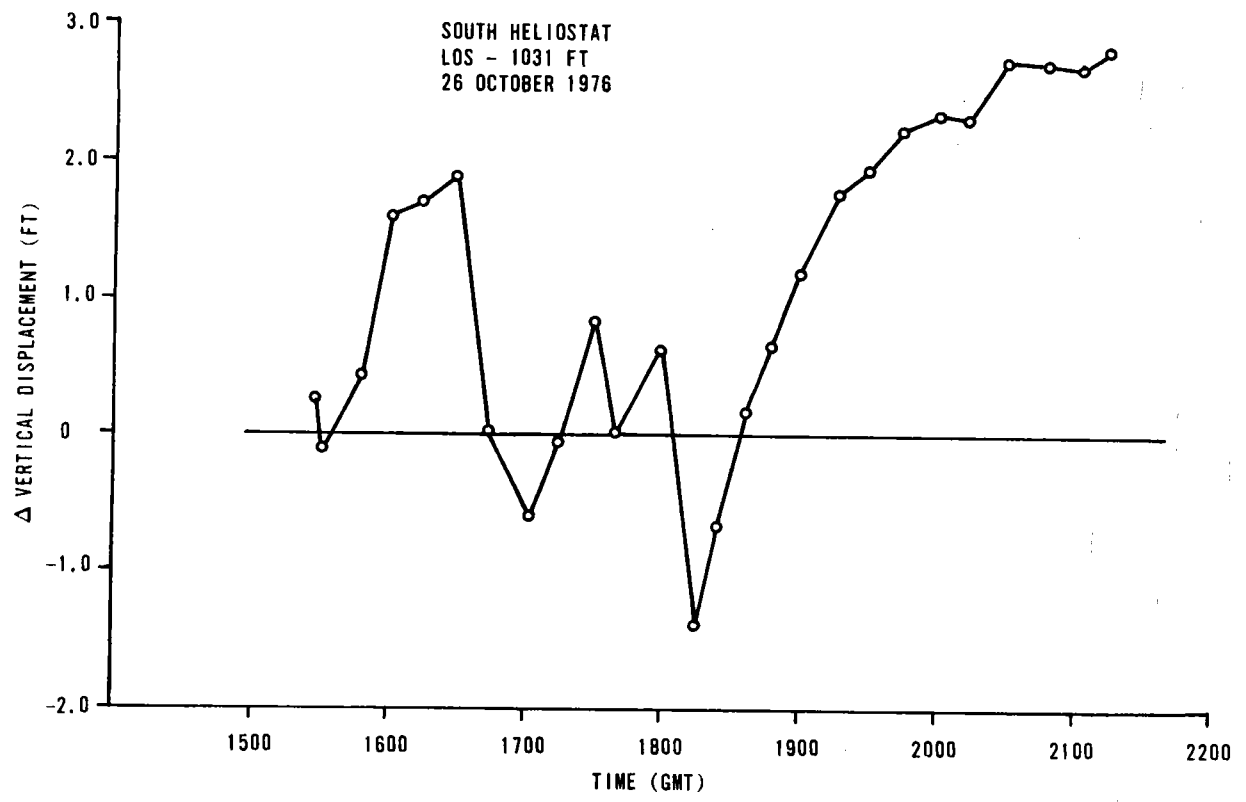


Figure 7-75. Image Vertical Centroid Track, South Site, Second Day of Operation

The target area was a spot only 36 feet in elevation (elevation angle = 4.27 degrees) at the center of the North side of Building E-2. Visual observation of the image, after determining the average outer axis scale factor 6 December 1976, (0.01811 inch/command) showed the day long (1500-1945) tracking error to be:

Horizontal +0.5 foot drift (1.05 mr)

Vertical \pm 1.3 feet variation (2.7 mr).

The majority of the drift occurs at the last 15 minutes of track when the outer axis is at -72 degrees to -74 degrees angle, which is the point when scaling errors have the largest degrading influence. For the pilot plant field layout, this outer axis tracking envelope will not be required during hours of useful solar insolation because of the taller tower. The most Northern heliostat site location will be at a line of sight angle of 18 degrees.

The outer axis was off-orthogonal to the radial target vector by -3.7461 degrees, for which software compensated. Considering the success from the Engineering Model and other sites and the limited time available with the only one calibration array, there was no attempt to further improve the tracking performance by necessary calibrations. Because of inclement weather and test equipment down time, the last recorded tracking from the North site was completed 9 December 1976.

East Site Experimental Model

The East site became operational 5 November 1976 but the first time weather and equipment permitted a full day of closed loop calibration was 23 November.

Azimuth to target = 268.117 degrees

Radial vector nonorthogonality to OA = +4.2101 degrees

Target height from OA height = 51.9 feet

Outer axis scale factor = 0.01180 inch/increment.

The technique used in calibrating a system via the closed loop mode of tracking is demonstrated by the following sequence:

1. Table 7-14 shows an approximate 15-minute interval of the computed pseudo target height and azimuth a few minutes after entering the calibration mode on 23 November. The pseudo target parameters are those that would have to exist if the Sun vector - mirror normal geometry were as determined by calculated gimbal angles based on commands (incremental counts) issued by the computer. Notice that the total height variation was greater than 25 feet, rapidly increasing as the Sun declined in elevation, which implies some sort of constant off-set having the greatest impact at the shorter actuator screw lengths. The

Table 7-14. 23 November 1976 Close Loop Track Data

<u>GMT</u>	<u>DCU OA Angle</u>	<u>Computed Target Height</u>	<u>Height Change</u>	<u>Computed Azimuth (Deg)</u>
1530		51.35		268.03
1600	-43.7	50.33	-1.02	268.17
1615	-45.42	49.79	-0.54	268.23
1630	-47.17	48.96	-0.83	268.40
1645	-48.94	48.58	-0.38	268.45
1700	-50.66	48.72	+0.14	268.49
1715	-52.39	49.48	+0.76	268.46
1730	-54.14	50.19	+0.71	268.39
1745	-55.86	50.54	+0.35	268.51
1800	-57.56	50.27	-0.27	268.60
1815	-59.27	51.28	+1.01	268.55
1831	-61.04	52.24	+0.96	268.57
1845	-62.62	53.51	+1.27	268.54
1900	-64.24	54.96	+1.45	268.60
1915	-65.87	56.65	+1.69	268.63
1930	-67.50	58.73	+2.18	268.66
1945	-69.05	61.63	+2.90	268.54
2000	-70.62	64.91	+3.28	268.53
2016	-72.20	69.51	+3.60	268.52
2030	-73.56	74.74	+5.23	268.60

reference screw length (set at 0 degree outer angle deflection, or initialization) being used by the program was the nominal 52.44 inches. The azimuth varied by 11 milliradians.

2. The actual actuator screw lengths were measured at initialization to be 51.687 inches. Using this value on 24 November, Table 7-15 reflects a great improvement. Less than five feet (6 mr) total drift resulted in required target height and a total azimuth variation of 2.7 mr.
3. The next available time that closed loop track could be entered by the East site was 7 December. No improvement resulted, leading to additional investigations. On 9 December it was found that there was a survey error in distance to the target. Previous survey data indicated 808 feet to the target when, in fact, the measured ground distance was 852 feet.
4. Using the corrected base parameter and a changed average reference length of 51.75 inches, a total error in vertical of 1.5 mr was obtained and 0.5 mr in azimuth tracking.

As with each of the sites, additional time is needed under an extended test effort to further evaluate all error sources for "fine tuning". With the limited testing so far, the combined tracking error is within the total error budget of 2 mr-- excluding possible worse case wind deflections.

Toe-In Strategy

One complication inherent in Honeywell's four separate facet tilt-tilt heliostat concept (which is not a factor in single facet concepts), is the relative adjustment between the mirror modules within one heliostat that must be made due to their linear displacement. See Figure 7-76 for a representation. For each site, the two outer mirror modules will be preset inward (α_o) at an angle different than the inner two mirror module toe-in angle (α_i) such that the four individual modules will create an overlapped image at the target.

At certain times of the day for any one fixed setting, image dispersion will occur-- particularly from East, West, and South field heliostats early in the morning and late in the evening. Honeywell's Energy Resources Center has the responsibility for establishing (from maximizing the total redirected energy on a yearly basis) the overall toe-in strategy for each heliostat in the field. Initially, they have found that a toe-in for all heliostats based on 21 March, solar noon delivers the best total energy flux over a yearly average basis. This is subject to change with additional investigation.

However, the Avionics Division test effort did support ERC by confirming that the theoretical toe-in angles generated by their Ray Trace Program were accurate. For our three experimental model sites, ERC's program determined the following toe-in angles.

Table 7-15. 24 November 1976 Close Loop Track Data

<u>GMT</u>	<u>DCU OA Angle</u>	<u>Computed Target Height</u>	<u>Height Change</u>	<u>Computed Azimuth (Deg)</u>
1645	-49.06	52.63		267.86
1700	-50.78	53.15	+0.52	267.86
1715	-52.54	52.38	-0.77	267.86
Sun peak elevation at 1720				
1730	-54.28	52.49	+0.11	267.85
1745	-56.01	52.16	-0.33	267.92
1800	-57.73	51.64	-0.52	267.94
1815	-59.46	51.82	+0.18	267.92
1830	-61.17	51.22	-0.60	267.94
1845	-62.89	51.09	-0.13	267.97
1900	-64.60	50.70	-0.39	267.96
1915	-66.28	50.56	-0.14	267.99
1930	-67.99	49.86	-0.70	267.96
1945	-69.67	49.59	-0.27	267.99
2000	-71.34	48.98	-0.61	268.02
2015	-73.05	48.26	-0.72	268.02
2030	-74.67	48.30	+0.04	268.00

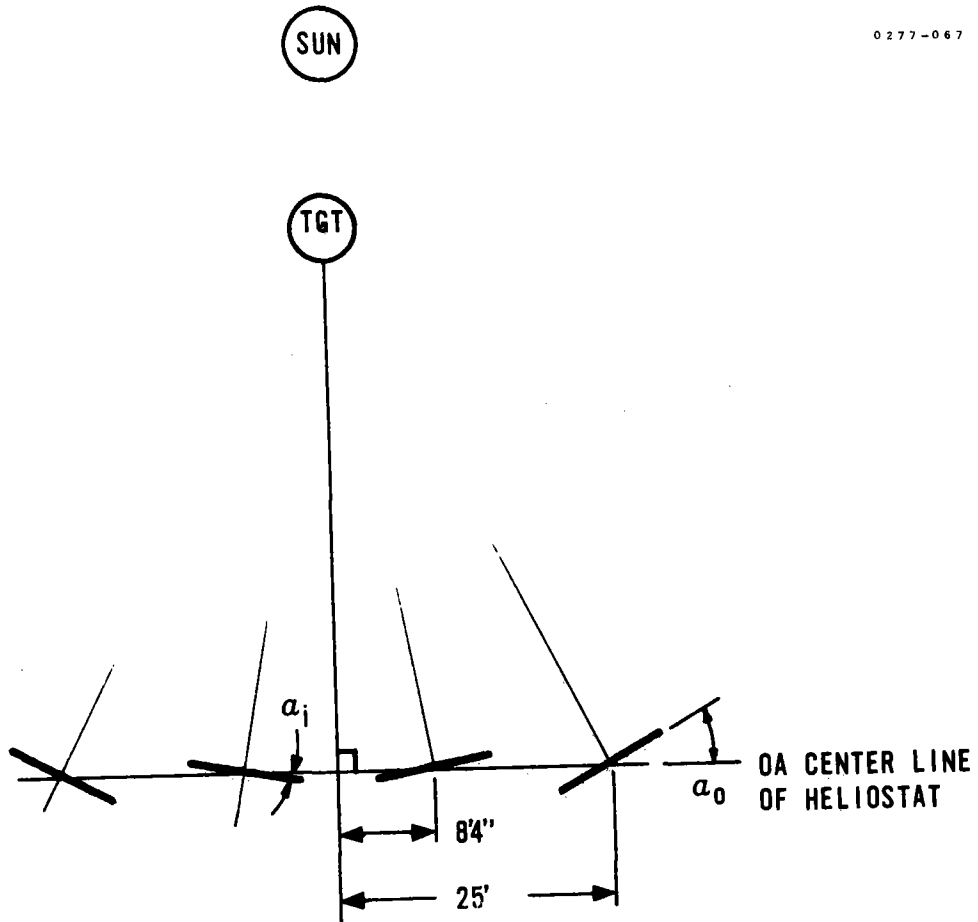


Figure 7-76. Mirror Module Toe-In Angle Representation

	<u>Outside MM</u>	<u>Inside MM</u>
North Site	±1.61 degrees	±0.54 degree
East Site	±1.11 degrees	±0.37 degree
South Site	±1.18 degrees	±0.39 degree

These angles compared within ±0.08 degree of the actual toe-in angles we found to give the best overall image on a daily time averaged basis.

The total width of scatter was also confirmed at other than the optimum time of day. For instance, per Ray Trace Program, 18 November 1976 at 1000 local time when toe-in was set for 1400 local solar time, the two outer facet centroids would be ±7.04 feet horizontal separation from the center of target. Our measurements on this day confirmed the validity of the program.

The output of the program, for pilot plant applications, will be a computerized listing of the pre-set angles for each heliostat in the field to be used when assembling the heliostats.

The range of outer mirror module toe-in angles is determined by minimum and maximum LOS distance to the target. Minimum range is 50M (165 feet) and maximum is 404.5M (1330 feet).

Using a target height of 131M (430 feet)

$$\alpha_0 \text{ max} = \tan^{-1} \frac{25'}{2\sqrt{165^2 + 430^2}} = 1.55 \text{ degrees}$$

$$\alpha_0 \text{ min} = \tan^{-1} \frac{25'}{2\sqrt{430^2 + 1330^2}} = 0.51 \text{ degrees}$$

Initialization

Obtaining a repeatable, known, initialization start point from which to begin slew to the target is absolutely essential for an open loop track system with a 2 mr total tracking accuracy requirement. An internal goal of ± 40 arc-sec (0.24 mr) accuracy and repeatability was established. No mechanical switch or physical locator could be found which would give the throw-switch precision needed. This led to designing the present detector scheme described in Paragraph A.4.3 and shown in Figure 3-24. One disk is mounted on the spur gear mirror module shaft of the inner axis and one assembly on each of the outer axis shafts. Two opposite pairs of photodetectors are mounted to the frame about each disk. The first initialization assembly was available for test on an experimental model 25 October 1976.

Initial testing showed that the inertia of the moving inner or outer axis would cause the frame or mirror modules to pass the detection point and then be forced to reenter the initialization zone from the opposite direction. Often, oscillation of the inner drive occurred, and sometimes the outer drive. Opening the angular difference (bandwidth) between $\pm \theta$ caused too great of a final uncertainty. To correct this problem, the heliostat electronics was modified to sense approaching the initialization zone and then to stop the open loop slew rate and issue one pulse at a time to "hic-up" the outer or inner gimbal slowly into the range where both photocells trigger the same phase. This scheme was successful; however, two other design deficiencies became apparent:

1. After about two weeks, the performance of the optical pairs became unreliable due to exposure to the environment. With the heavy nightly dew, high humidity and air pollutants, the optical pair windows became dirty and the LED light would not penetrate. Temporarily, a housing was built to help protect the assembly from direct dirty water contact. See Figure 3-24.
2. The optical pairs were each mounted on a metal bracket and then further secured with epoxy cement. Small adjustments caused the assembly to loosen, and the metal brackets tended to flex and bend causing slight relative physical location change between the two opposing optical pairs.

The net result of the above two problems was (a) a complete new re-design using the same basic detector concept, and (b) having to widen the dead zone by ± 300 arc-seconds temporarily.

The new design, which has not yet been built, will consist of photodetectors firmly mounted on plates which can be adjusted by turn screws external to the completely sealed environmental enclosure.

For test purposes, with the widened bandwidth, initialization was accomplished by always approaching from the same direction and performing two tests: (a) precisely measuring the repeatability of final stoppage of the inner or outer drives with attached precision levels (0.5 arc-second per division resolution), and (b) commanding Mode 2 (Open

Loop Track) after initialization was accomplished and observing how close the redirected image would stop to the same point on the calibration array.

When initialization was entered from a consistent direction, the average repeatability over 10 runs over two different sites was ± 35 arc-seconds. One reading was 55 arc-seconds different. The magnitude of the slew (total angle traveled before reaching the initialization stop point) had no effect on the accuracy of initialization detection.

As is mentioned in the calibration subsection, over a weekly period, the redirected image consistently fell within one foot of the same point when open loop track was commanded after initialization was reached. To obtain a common denominator and eliminate other possible tracking error sources, these tests were made approximately the same time of day (≈ 1530 GMT).

The SRE test effort has demonstrated the workability of this initialization design approach; however, additional effort is needed with the redesigned configuration to bracket conclusively its ultimate performance and long term performance characteristics.

Calibration of Heliostat Parameters

The collector subsystem SRE test program has shown that the calibration philosophy can be broken into two groupings: initial and periodic.

Initial Calibration

This phase is partly interwoven with the correct assembly sequence. The procedure is as follows:

1. The foundations are poured at surveyed sites.
2. After pouring and mounting the posts, the following precisely surveyed data must be obtained within 10 arc-seconds:
 - a. Azimuth of center between slabs to designated primary and secondary targets and distance to the base of the target.
 - b. Azimuth of center line between outer axis pillow blocks. This provides a reference angle to determine how far off normal the OA is to a radial vector from the heliostat to the target.
 - c. The height of the heliostat's primary target and secondary target must be determined with respect to the elevation along the heliostat outer axis.
3. After mounting the frame, the actuator's pivot points are set to a prescribed orientation via a special purpose tooling template. Frame level is determined by this tool also by extending the actuator 52.44 ± 0.010 inch such that all three pivot points are within known reference from each other at 0.0 degree horizontal position.
4. The mirrors are then mounted, leveled, and toed-in with special purpose tooling with the frame at 0 degree angle.
5. Each actuator scale factor is determined from actual gimbals travel to the nearest ± 0.000005 inch per motor revolution as averaged over a long slew using the heliostat electronics.
6. Concerning the latitude and longitude of the center of the field, since the pilot plant field is less than 520 meters across any length, one central plant geodetic coordinate applicable to the whole field will induce no error greater than 8.5 arc-seconds (0.04 mr). For a commercial plant, several different geodetic groupings may be advisable.

Each of the above parameters are stored as unique per heliostat and should not need to be redetermined. Some trade-offs still must be

made. For instance, for pilot plant operations, would it be better to relax tolerances on foundation-- post mount installation and then later perform a survey and have software compensate for the inherent errors at increased computation time, or should tight tolerances be maintained during site assembly?

Periodic Calibrations

A periodic calibration will be required to remove long term, trending errors such as foundation shifts, initialization mount shifts, electronic aging, consistent wind direction, longer term (week) thermally induced rotations, etc. Honeywell's concept is to command a slew over to a calibration array. The distance of the image from the center of the array is assumed to be an offset that has occurred since the last calibration time. An angular change in height adjustment and azimuth adjustment can be made to the primary target and secondary target based upon the offset distance determined from the calibration array.

Update data can be maintained for each heliostat, and if over a period of time a given heliostat is requiring an excessive correction factor, special investigations can be made or site recalibration performed.

The SRE experience so far shows that a periodic interval of one week or longer would be adequate. From the East, North sites, slew to target after correctly initializing resulted in the redirected beam stopping within one foot (measurable accuracy) of the same spot near the same time of day. These repetitions were carried out over weekly time spans.

After the redesigned initialization mechanization is incorporated, it is felt that this performance can be maintained over even a longer interval. However, only long term testing can absolutely confirm the actual maximum calibration interval required. It should be noted that this interval will be site dependent due to soil differences, seismic activity, average wind direction and magnitude, etc.

Operational Slew Rates

There are three slew rates that are of interest:

1. Target Track Rate. This rate is 1/2 the Sun's travel rate and requires no more than 5 to 7 incremental commands per minute. The only consideration here is the basic resolution which is nominally about 80 arc-seconds per inner or outer axis command.
2. Emergency Defocus. The requirement exists to travel 3 degrees in 12 seconds or 0.3 degree per second to point at a secondary target for system safing. As can be seen from Page 7-83, the outer axis alone under certain gimbals angles and heavy wind loads could possibly not provide 0.3 degree/second. However,

the inner axis rate is nominally 0.6 degree/second and is under 15 to 20 mph loads dropped to a low of 0.45 degree/second. Therefore, with a combination of inner and outer axis travel, a least rate of 0.5 degree/second is expected. From pilot or commercial plant systems considerations, there is no reason why the emergency defocus point for each heliostat cannot be selected to take advantage of a combined inner and outer gimbal rotation vector.

3. Stow Orientation. From any heliostat gimbal orientation, the requirement exists to be able to reach a safe, or stowed, orientation within 15 minutes. For the tilt-tilt heliostat stow position, the mirror surfaces are face down (180 degrees from initialization) and outer axis level is at 0 degree (same as initialization position).

Normally, a full 360 degree inner axis slew can be made in 10 minutes; therefore, a 180 degree maximum slew requirement can be met in about 5 minutes. If the worse case outer axis angle of -75 degrees is assumed along with a slower average rate of 0.25 degree/second, the 0 degree stow position can also be reached in 5 minutes.

There is some question as to the maximum time stowing would take under worse case wind loading. The heliostat was designed to meet all requirements at 13.5 M/S (30 mph), but as discussed on Page , no sustained testing under this condition has been done. With the new requirement of a 50 mph gust, the movement may temporarily halt, assuming no catastrophic failure, but will continue after the gust. Actual total moments induced under 30 and 50 mph winds are unclear with the complex heliostat design, turbulence, and field effects on the inner and outer drivers. Therefore, wind tunnel tests will be performed in the future.

From our test results to date, it has been determined that, with the spare time (10 minutes), from worse case orientations and the veering nature and gusting nature of winds, there is no reason to believe that the 15 minutes stow time cannot comfortably be met.

Control Software Update

The baseline software control program was presented during the Detail Design Review, 18 May 1976. Since that time, several block changes have been made as dictated during the SRE test program to obtain additional information and improve performance. Appendix E provides a listing of the latest program.

Most significant changes since DDR include the following:

- Correction of outer axis slew commands.
- Change of command issuance from once per second to once per 2 seconds.

- Reapportioning to subroutine blocks and common memory, elements of parameter storage to improve program operation dependability.
- Modification of refraction correction
- Incorporation of on-line magnetic tape drive mechanics capability (position, write end of file, etc.).
- Providing operator capability to change, from the ASR-35, individual heliostat drive scale factors and actuator pivot set points.
- Providing the capability to reinitialize GMT without starting program over.
- Incorporating the additional initialization mode (Mode 6).
- Calculating the ratio of pyroheliometer to photocell readings and calculating total redirected energy to calibration array.
- Giving operator the option to negate data dump to magnetic tape.
- Establishing a criteria based on total redirected energy to enter the calibration mode or not.
- Incorporating the capability to correct for the heliostat outer axis being nonperpendicular to the target radial vector.
- Masking the possibility of extraneous, nonused program interrupts occurring.
- Reducing round off error in accumulative gimbal angle calculations by using integer arithmetic based on number of commands issued.
- Providing, under operator control, the following on-line ASR printouts:
 - a. All weather channels and background sensor channels.
 - b. Actual target height and azimuth used when going to calibrate mode.
 - c. Angle cosine effect associated with each heliostat.
 - d. Energy redelivered to calibration array.
 - e. Full printout of the 224 calibration array elements without halting tracking program.

Other capabilities such as operator control of heliostat modes have not been changed. Assembly language is still incorporated in-line with the FORTRAN program where required.

For pilot plant applications, three major changes must be made to the heliostat control program:

1. Reduce all of the nonessential I/O and operator control functions. For the research experimental program, this function occupied most of the available DCU operational time.
2. Incorporate all control, safing, and plant performance monitoring functions. This report does not attempt to address suggested approaches to computer control and partitioning for optimum pilot plant or commercial plant operations.
3. Incorporate a larger number of heliostats in the control program.

Using the existing program, a limited number of time runs were made. Since the program is written mostly in a higher order language, FORTRAN, it is inefficient compared to coding the same functions in assembly or machine language. Also, the DDP 516 is relatively slow (0.96 μ s cycle time). Using an internal timer which records only the central processor time, times needed to perform one sun vector calculation, all calculations to have a heliostat track using each of the variable parameters discussed throughout the report, and to issue the separate commands were obtained. Within one second, approximately 360 heliostats could be serviced if nonindexed (subscripted) parameters were used and 350 heliostats if subscripted variables, per heliostat, were used.

This indicates that a penalty of 100 μ s per heliostat may be associated with indexing variables. In all data there is a quantization error of $\leq 1/60$ second.

This data is not strong evidence of total capacity of a pilot plant computational facility because of the higher order language used, machine peculiar capabilities, and slow basic processor time for the DDP 516. However, it does provide a lower limit as to the number of heliostats that one dedicated central processor can service, assuming the I/O bus has the interface capacity.

ENVIRONMENTAL TESTING

Environmental test data is relatively limited, partly due to inclement weather. There has been an abnormal amount of rain and cloudiness for this area and time of year. The Tampa, Florida, National Weather Station offered the following percentages, which should be approximately the same for this location since we are only 20 miles away.

<u>Month</u> (1976)	<u>Month Average</u> <u>% Cloudiness</u> (Daylight Hours)	<u>Days</u> <u>100%</u> <u>Cloudy</u>	<u>Days</u> <u>90%</u> <u>Cloudy</u>	<u>Days</u> <u>80%</u> <u>Cloudy</u>
October	60%	4	6	2
November	79%	12	4	5
December	70%	12	4	1

WindBackground Discussion

The initial intention of the Collector Subsystem SRE test program was to confirm proper operation under actual wind loading of 13.5 M/S (30 mph), but the desired combination of sunshine, operating instrumentation and strong winds during available man hours never completely materialized.

Wind loading is by far the largest cost driver regarding stiffness to operate (track with 2 mr accuracy) under 30 mph winds and strength to remain undamaged under survivability wind loads. Recently, the wind specifications have been altered to include surviving a 22.3 M/S (50 mph) wind gust under any operational gimbal orientation and surviving a 40 M/S (90 mph) wind at 10 degree angle of attack while the heliostat is in a stowed condition.

Stress loading on the inner drive spur gear, other drive components, and mirror module shafts, along with column and side loads on the linear actuator shafts due to wind loading, are of primary concern. The actual aerodynamic moments induced into the system are uncertain because of the low profile of our heliostat, the ground effects, turbulence and vortex shedding effects caused by the shadowing of one mirror module to the other and even one heliostat to the next within the field. To insure obtaining realistic aerodynamic moments and loads under the required envelope of wind/heliostat gimbal configurations, a proposal has been submitted for wind tunnel scale heliostat model and field model testing.

A comprehensive structural analysis report was prepared. It included static loading inputs for 30 mph winds and dynamic loading where the input frequencies (gusts) were tailored to the first four primary harmonic frequencies determined from the STARDYNE structural analysis program. It is of primary interest that four of the first nine natural

frequencies predicted by the program involved mirror module rotations (2.7, 4.6, 4.9, 6.2 cps). Under the analysis no yield stresses were reached.

Results to Date

With 25 to 30 mph gusting winds blowing end-on the East Heliostat, at a resultant mirror module angle of attack near theoretical worse case induced moments (flat plate theory ≈ 22 degree α), and the outer axis at -70 degrees, the redirected image oscillated about a steady track centroid to a peak excursion of 2.5 feet maximum (2.9 mr). However, the net average on RMS centroid position was much less.

Again with the OA ≈ -40 degrees, the IA at +45 degrees and end-on winds, and winds at 20 to 25 mph, the worse case excursions were ± 1 foot. The North site has never exhibited observed horizontal deflections of greater than ± 0.75 (1.6 mr). Vertical oscillation extremes of greater than ± 0.5 foot (0.6 mr) from the East site or ± 0.25 foot (0.51 mr) from the North site have never been observed under the same wind loading conditions.

Monitoring inboard mirror module oscillations, frequencies of 2 to 4 Hz have been observed at the outer tip of the modules. This order of magnitude compares favorably with the structural analysis output.

A special purpose program was developed to merely read and record on magnetic tape the 240 channels of array and weather data at a rate of once every two seconds. Using this approach, the heliostat is not tracking. The image can be placed manually at one edge of the calibration array, and due to the Sun's movement, the image will cross to the other edge. During post-analysis, the trend can be removed (i.e., movement due to sun movement) via a least squares fit and the residuals about the fit correlated with wind characteristics. Figure 7-77 shows such data during wind velocity variations of 8 to 11 M/S. Notice that the maximum extremes are approximately ± 1.1 feet.

The absolute magnitude of the gusts are greater than that which is obtained because of the 15-second time constant filtering action of the anemometer wind data channel. There is some smoothing of the centroid data also because the sample time to read all 240 channels is 0.4 second.

From a pilot plant systems approach, the wind load effect upon the receiver must be statistically treated (with respect to wind loads while operational) against:

- a. Actual thermal time constant of the receiver
- b. Duration of wind gust, or steady state wind
- c. Combined effect of all the heliostats and their corresponding beam redirection.

During the night of 12 August, the Engineering Model heliostat while stowed was exposed to severe winds; the magnitude is unknown. A

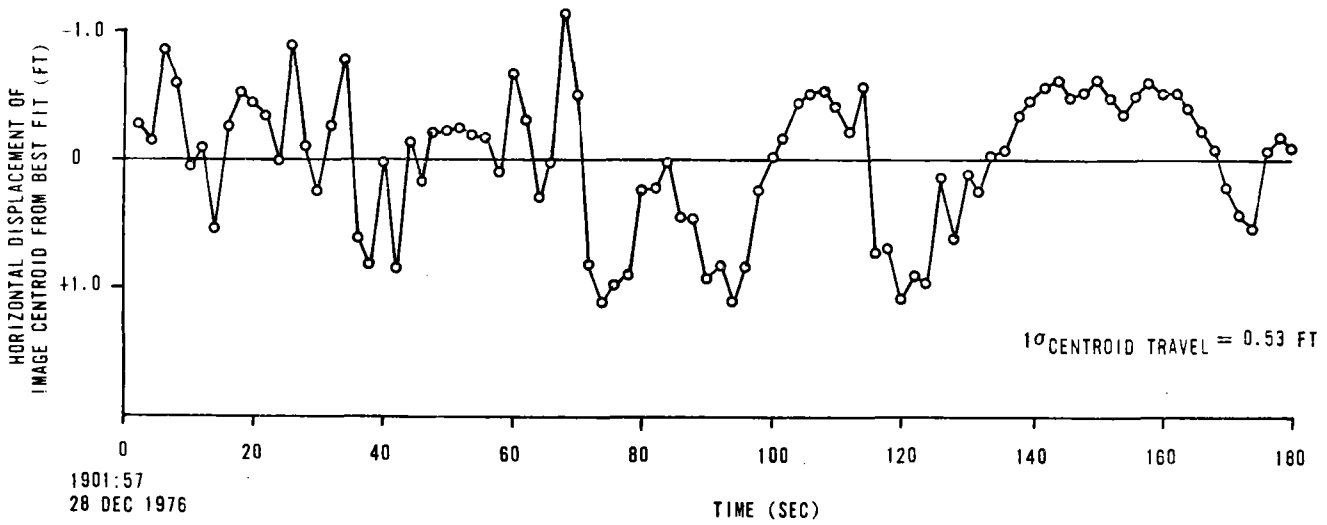
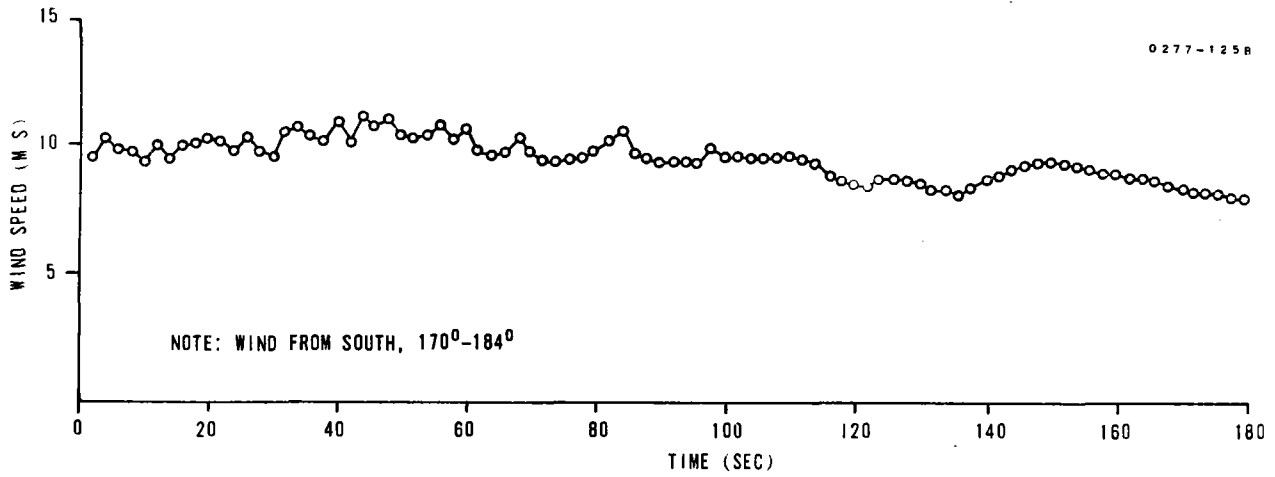


Figure 7-77. Image Centroid Variation Least Squares Fit East Site

tornado, or tornado fringe, passed through the area. Referring to the aerial photograph of Figure 7-2, the heliostat is approximately 160 feet from the present North site location to the North and West. At the North site (SE of the EM site) the wind tower blew over causing damage to the instrumentation. Although it was supported at the base with sandbags, a calculated wind of 42 mph or greater would have blown it over.

At point A (810 feet South of the EM) the metal side-roof flashing was torn from the SE corner of Plant 2.

At point B (1,100 feet West of the EM), a nine inch diameter tree was uprooted.

At point C (760 feet South of the EM), a camper trailer was literally shredded to pieces and street signs bent around their posts.

Atop Building E-2 (620 feet South of the EM), two of the calibration array support I-beams were twisted about 30 degrees.

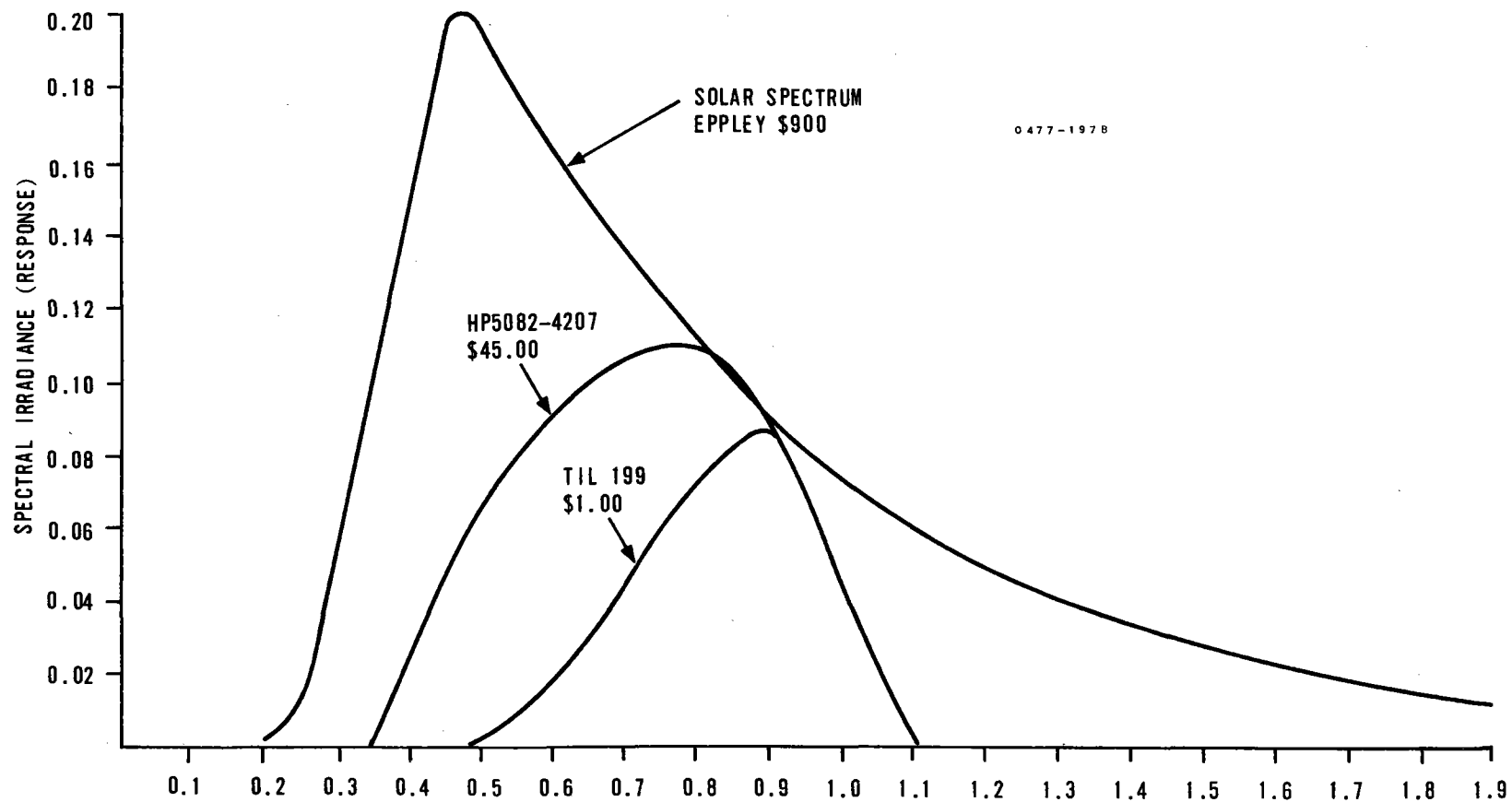
No damage was sustained by the Engineering Model.

Redirected Energy Measurement

Background

It is necessary to have an understanding of technical data relative to measurement techniques and calibration methods before discussing the energy balance between expected and measured values. Photocells mounted on the calibration array are used to measure the redirected energy. Three sensors that covered various portions of the solar spectrum were considered for use in the calibration array. A summary of the performance and cost of each is presented in Figure 7-78. It should be noted that cost of the unit with adequate bandwidth is prohibitive for large number use. The original 294 TIL 199 photocells were measured on a clear sunny day. Data from that measurement was presented at the March 1976 Quarterly Review (see Table 7-16). Measurements were made using an artificial incandescent light from a collimated source to further characterize these parts. Figure 7-79 shows the effects of off axis incident radiation as a function of normalized output voltage. Figure 7-80 shows the same data for output as a function of input angle using the sun as a light source on one sensor assembly.

Energy calculations made initially did not account for this very obvious departure from a cosine curve. This and other effects resulted in large differences between expected and measured energy levels. In subsequent tests, this factor was taken into account and results agree with expectations.



7-157

Figure 7-78. Sensor Bandwidth Versus Cost

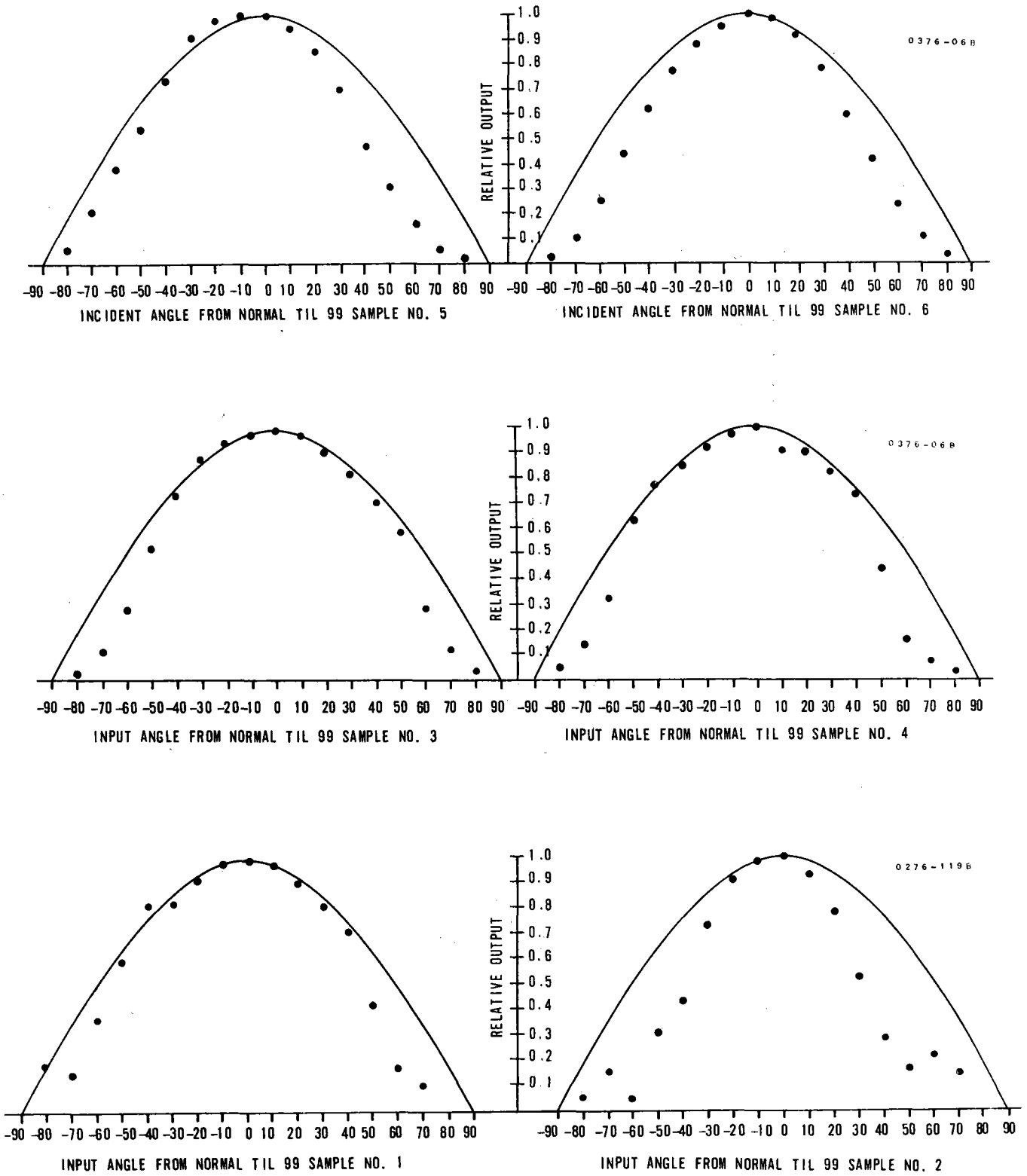


Figure 7-79. Photodetector Directional Sensitivity Measurements

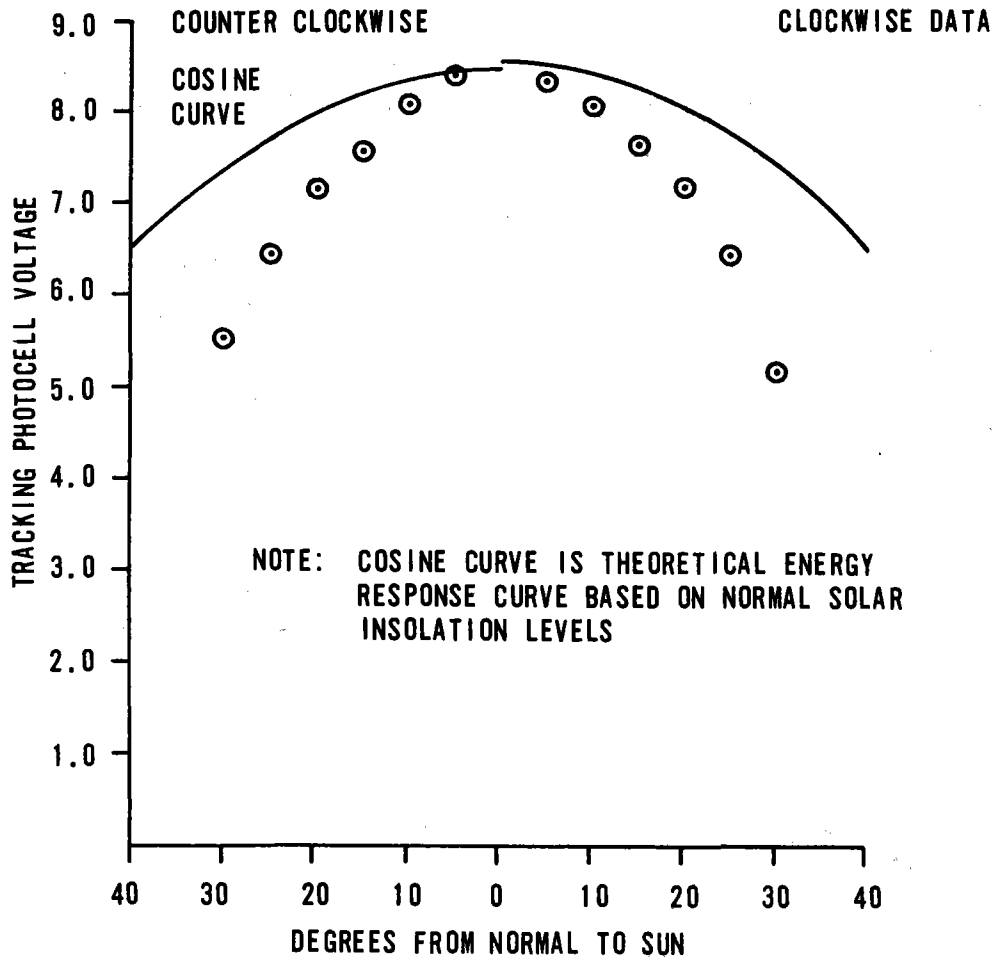


Figure 7-80. Photosensor Directional Sensitivity

Table 7-16. TIL99 Phototransistor Gain Calibration

Quantity - 294	
Light Source - Sun	
Date - 27 February 1976	
Reference Sample Data (10:30 AM to 12:15 PM)	
No. 1	±2.6 percent (Includes variation of insolation)
No. 2	±3.2 percent (Includes variation of insolation)
No. 3	±2.2 percent (Includes variation of insolation)
Calibration Accuracy - ±5 percent	

The performance of the calibration array itself is a factor in energy balance. Figure 7-81 is a sample printout showing several sensor/amplifier units with low output when the entire calibration array was facing the sun. These low outputs were caused by bad sensor amplifier assemblies. Repair of these eliminated the substantial low output error and has provided satisfactory performance.

Other improvements included: eliminating an extraneous strip chart recorder which was introducing small voltage errors, and improving accuracy of hardware scale factors used to convert energy measurements. This was confirmed by concurrent measurement between the array and the normal incidence pyrhelimeter.

An improved measurement and calibration was incorporated into the data collection scheme on 9 December 1976 to automatically calculate the redirected energy. Since the TIL99 photocells respond to only the 0.5 μ to 1.1 μ portion of the solar spectrum, energy absorption due to moisture, carbon dioxide, etc., will have a different and varying effect upon the energy as sensed by the photocell. The energy sensed by an instrument sensitive to the total solar spectrum in the wavelength of 0.28 μ to 2.8 μ may be used to continuously calibrate the data sensed by the other photocells. Silicon photocells sense 0.5 to 1.1 microns compared to 0.28 to 2.8 microns for the pyrhelimeter (see Figure 7-78). A patent application was made and submitted (File No. 1006987-US) on a calibration system that provides continuing correction of this parameter to yield accurate total energy data to be obtained using a large number of the less expensive photocells calibrated by a single Eppley tracking pyrhelimeter. Changes to the atmospheric moisture contents and the appearance of thin cirrus clouds create changes to the ratio of the tracking photocell output and tracking pyrhelimeter output (see Table 7-17). Figure 7-82 shows a photograph of the two tracking sensors. The field of view of each is 5.7 degrees. The readings of the calibration array photocells have this ratio applied for each minute of sampling. This output is then converted to absolute energy (watts) by multiplying by the output of the calibrated pyrhelimeter and the area of the calibration array (20.82M²) to obtain the total redirected energy. The on-line program was modified to perform this function and, optionally, print the result on the teletype.

DAYS/HOURS/MINS = 76./ 18./ 28. MAR 17, 1977

26	26	26	26	24	15	25	27	25	25	25	26	25	22	25	26
26	22	25	23	24	24	23	19	25	23	25	26	22	25	22	25
24	24	25	23	24	25	26	26	24	25	25	28	26	26	24	21
27	27	11	24	22	24	23	24	27	25	24	27	25	25	26	28
24	26	26	28	23	25	15	28	26	26	27	25	26	26	19	25
25	28	25	27	22	25	25	26	24	26	25	24	25	27	27	21
27	25	26	23	24	28	26	24	25	26	13	22	25	26	23	28
27	26	28	23	24	28	21	25	27	27	27	26	26	26	26	26
24	25	24	26	13	24	6	25	25	26	24	26	22	27	27	26
24	23	24	22	26	23	25	25	27	27	26	25	18	21	27	20
27	26	25	26	25	25	25	19	26	26	26	25	27	26	26	26
24	25	0	28	26	24	28	26	24	27	27	26	24	27	25	26
23	27	23	25	24	28	26	21	25	24	23	29	26	21	24	25
23	26	26	25	26	26	22	25	24	27	27	25	25	24	24	26

DELVER= -0.01 DELHOR= 0.05 CALSUM= 5500 NOMINAL 5600
 AZSUN= -156.014 RELSUN= 58.349

18.31. 1 5 0.0000 180.0000-155.971-1 58.3410 -0.00 0.08
 0 8079 55.0000 0.0000 3880
 RATIO= 7.7000, ENERGY=483972., COSSVM= 0.0000 0.0000 0.0000 0.0000
 0 0 0 0 0 0 0 2 0 0 0 0 0 0 0
 18.31. 1 5 0.000

0

Figure 7-81. One Sun (DNI) Flux (Before Repairs)

Table 7-17. Typical Time History of Photocell/
Pyrheliometer Comparison

17 December 1976

<u>Time (GMT)</u>	<u>Ratio of Pyroheliometer to Tracking Photocell</u>
1445	0.769
1500	0.774
1515	0.817
1530	0.835
1545	0.848
1600	0.858
1615	0.867
1630	0.868
1645	0.840
1700	0.828
1715	0.825
1725	Solar Noon
1730	0.822
1745	0.810
1800	0.805
1815	0.782
1830	0.792

DARKENED TUBE TO LIMIT
PHOTOCELL FIELD OF VIEW

A7701-035

EPPLEY
PYRHELIOMETER

TYPICAL CAL
ARRAY TYPE
PHOTOCELL

COMMUNICATION
CABLE TO FEED
DATA INTO CAL
ARRAY
MULTIPLEXER

EPPLEX
GLOBAL
RADIOMETER

EQUATORIAL
TRACKING
MOUNT

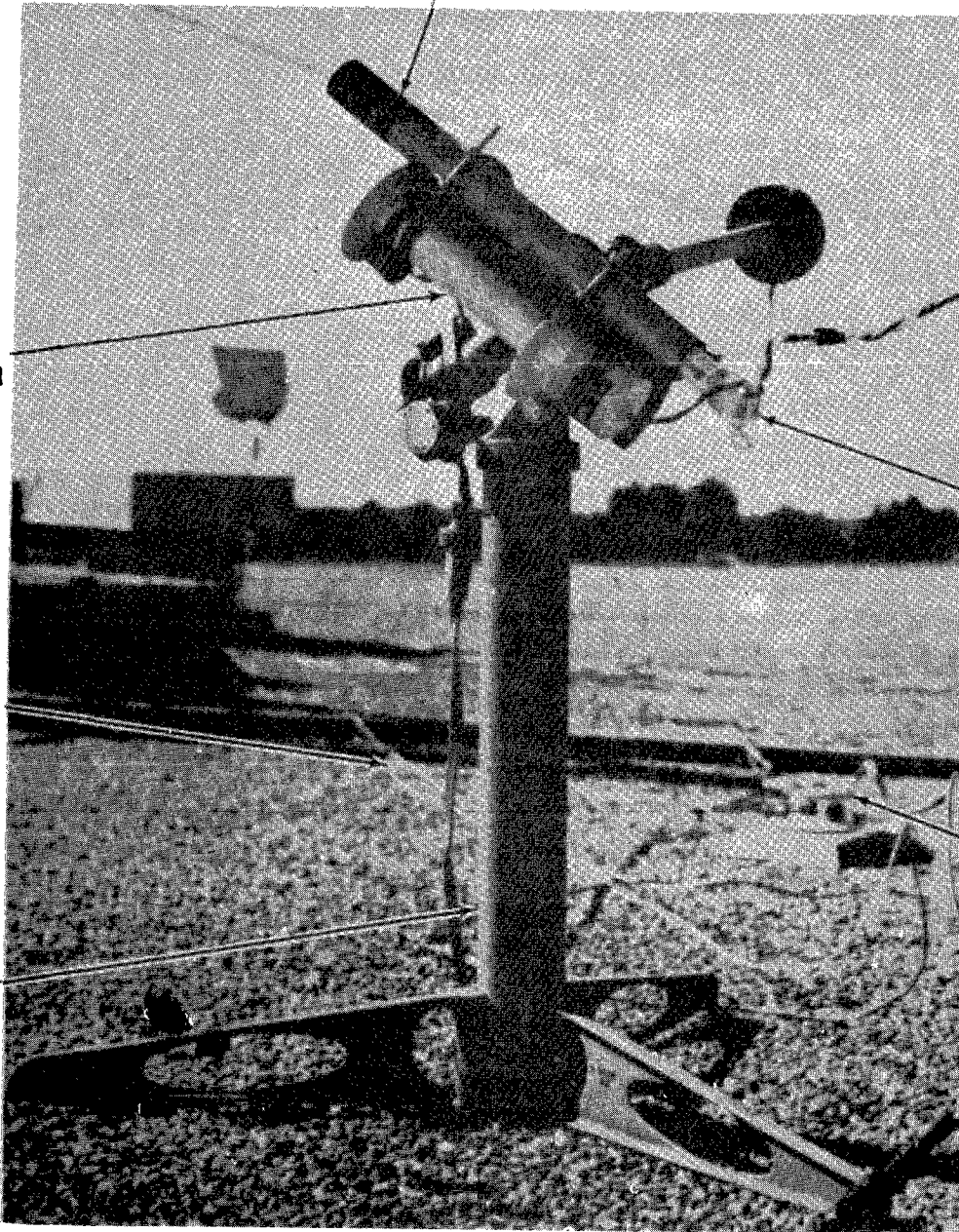


Figure 7-82. Tracking Pyrheliometer and Silicon Photocell

The following actions were taken and adjustments made since the December 17, 1976 results were documented.

1. The tracking photocell was changed and its output was accurately calibrated against the average array photocell output for the same insolation input-
2. Low output photocells were replaced.
3. The array was calibrated with respect to the pyrhelimeter by facing the array into the sun parallel to the pyrhelimeter line of sight.
4. It was determined that the off normal incident response of photocells does not follow a true cosine curve with respect to incident angle and this effect was accounted for in data reduction.
5. The pyrhelimeter multiplexer channel was recalibrated. The scale factor changed from $5.655 \text{ watt m}^{-2}/\text{bit}$ to $5.594 \text{ watt m}^{-2}/\text{bit}$ and the bias shifted from 87.2 watt m^{-2} to 59.7 watt m^{-2} .
6. A calibration test run was made by pointing the array at the sun after necessary electronics and array repairs were made. The data follows:
 - March 21, 1977 - 1816 hours
 - Insolation = $960.3 \text{ watt m}^{-2}$
 - Energy expected = 19071 watts
 - Energy determined 19077 watts (from calibration array)
7. The residual background readout from the array with no redirected insolation applied must be compensated for. Figure 7-83 shows a typical readout of a summation across the array equaling 200 bits. On a clear day with background suppression circuits operating, these residuals vary from 198 to 208. These small levels are subtracted from the redirected insolation value to assure that only redirected energy is measured and residual background is not included.

With these improvements, much better agreement was obtained between expected and measured energy levels. The net result is exceptionally good correlation between measured and expected energy levels of the order of 1 percent.

All energy calculations can easily be made on or off line by computer processing of the calibration array data. This can be done concurrent with centroid computation. The energy (on-axis to the calibration array) computation should be made using the following algorithm.

DAYS RADGYR PRESS	HOURS PAX2MOM TEMP1	MINS SAX2MOM TAMB	DELVER PAXANG TEMP3	DELHOR GOF TDELTA	WINDSPD ANGSVN PYNOR	WINDDIR RADGLOBAL	CALMAX RATIO	CALSUMG ENERGY	BACKAVG						
1	1	0	1	1	0	1	1	1	1	1	1	1	1	1	
1	1	1	1	1	1	1	1	1	1	1	1	1	1	1	
0	1	1	1	1	1	1	1	1	1	1	1	1	1	0	
1	1	0	1	0	1	1	1	1	1	1	1	1	1	1	
1	1	1	1	1	0	1	1	1	1	1	1	1	1	0	
1	1	1	1	1	1	1	1	1	1	1	1	1	1	0	
1	1	1	0	1	1	1	1	1	1	0	0	1	1	1	
1	1	1	0	1	1	0	0	1	1	1	1	1	1	1	
1	1	1	1	0	1	1	1	1	1	1	1	1	1	2	
1	1	1	0	1	1	1	1	1	1	1	1	1	1	0	
1	1	1	1	0	1	1	1	1	1	1	1	1	1	1	
1	1	1	1	1	0	1	1	1	1	1	1	1	1	1	
1	1	1	1	1	1	1	0	1	1	1	1	1	1	1	
0	1	1	1	1	1	1	1	1	1	1	1	1	1	1	
2	2	2	2	2	2	2	206	1	5	1	151	2	6	5	165
98.00	19.00	2.000	-0.1450	0.1050	0.6708	11.84	0.7843E-01	200.0	0.7843E-01						
6.111	16.16	21.19	-85.37	0.7150	27.44										
915.3	0.0000	-33.61	0.0000	0.0000	897.6	950.7	0.7850	-75.11							

7-165

Figure 7-83. Typical Level of Residual Calibration Array Readout with no Redirected Insolation

Energy (watts) =

$$\begin{aligned}
 & \text{Area of Array} \times \text{Scale Factor} \times \text{DNI} \\
 & \text{(in meters}^2\text{)} \quad \text{(No. units)} \quad \text{(watts/m}^2\text{)} \\
 & \times \frac{\text{Cal Array summation} - \text{residual background}}{224} \\
 & \quad \text{(No. units)} \\
 & \times \frac{1}{\text{Tracking Photocell Reading}} \\
 & \quad \text{(No. units)} \\
 & = 20.82\text{m}^2 \times 8.43 \times \text{DNI} \times \frac{(\text{Cal Sum} - \text{Residual})}{224} \\
 & \times \frac{1}{\text{Tracking Photocell}} = \text{Energy Indicated}
 \end{aligned}$$

One additional known correction must be made to the energy calculation from this algorithm, this being compensating for the angular difference between normal to the photocell and actual incident angle, i.e.:

$$\text{Energy Incident} = \frac{\text{Energy Indicated}}{\text{Cosine of beam incidence angle of array normal}}$$

If the angle is large, the additional corrections noted by Figures 7-79 and 7-80 must be made.

This angle (composite of both off-azimuth and off-vertical) for each heliostat will be accurately known from the site geometry and array orientation for any heliostat site in the pilot plant field. A reading to record the background residual can be obtained and used for the subsequent calculation before directing a heliostat to focus energy on the calibration array.

On March 29, a single mirror module (9.3 m^2) was tested at distances of 80.8m (265 feet) (line of sight) up to 323.5m (1061 feet). The digital sum for the calibration array for each site was used within the algorithm previously discussed.

Figures 7-84 through 7-88 show a bar chart for each site giving the reduction from the theoretical insolation input across 9.3m^2 due to

- Cosine effect across the mirror module
- 88 percent reflectivity
- Model atmospheric losses. The day was at 49 percent relative humidity.

Each chart also shows the energy computed from the calibration array and the percent difference. There was no shadowing or blocking effects. Table 7-18 presents the results.

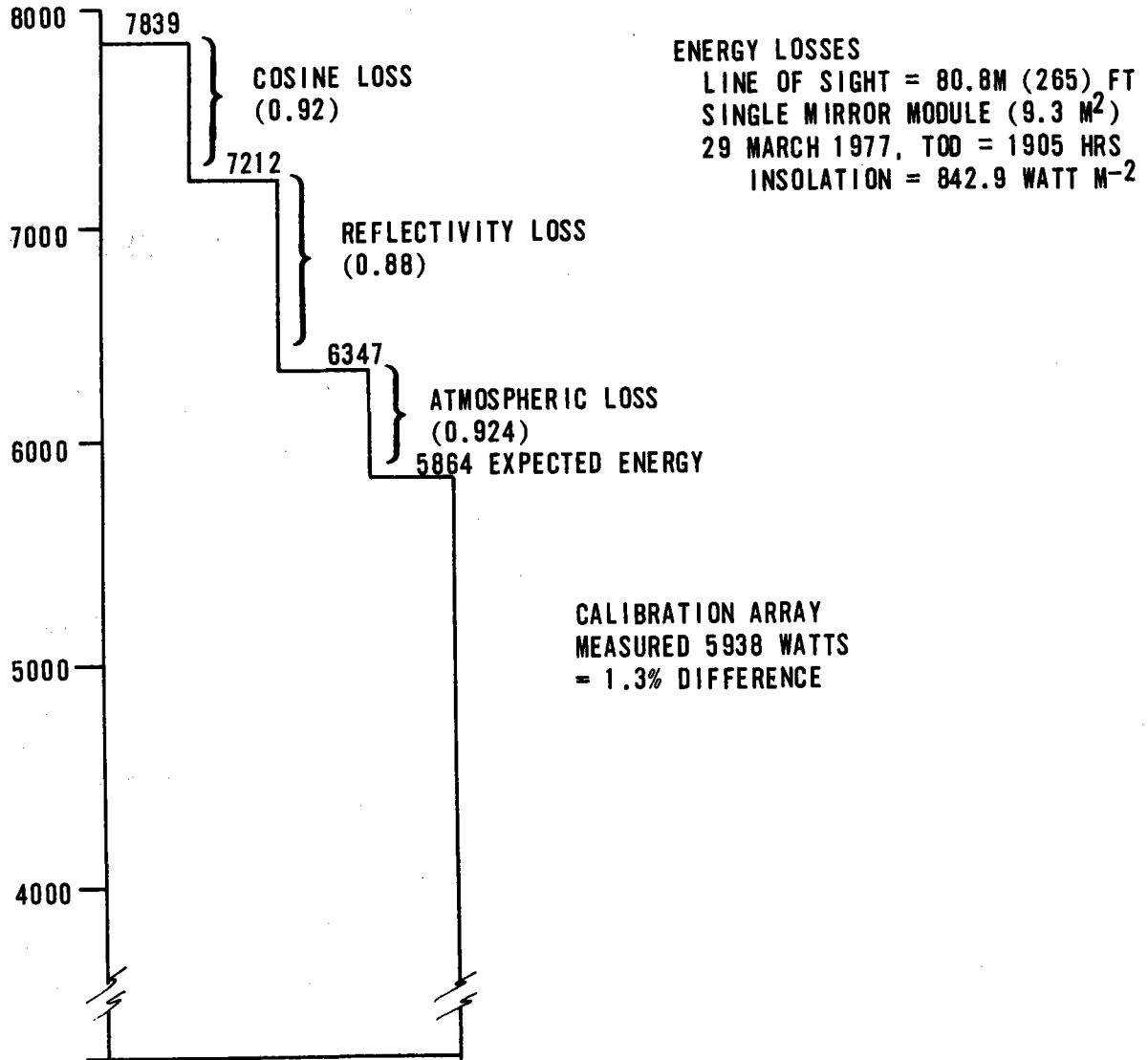


Figure 7-84. Energy Losses

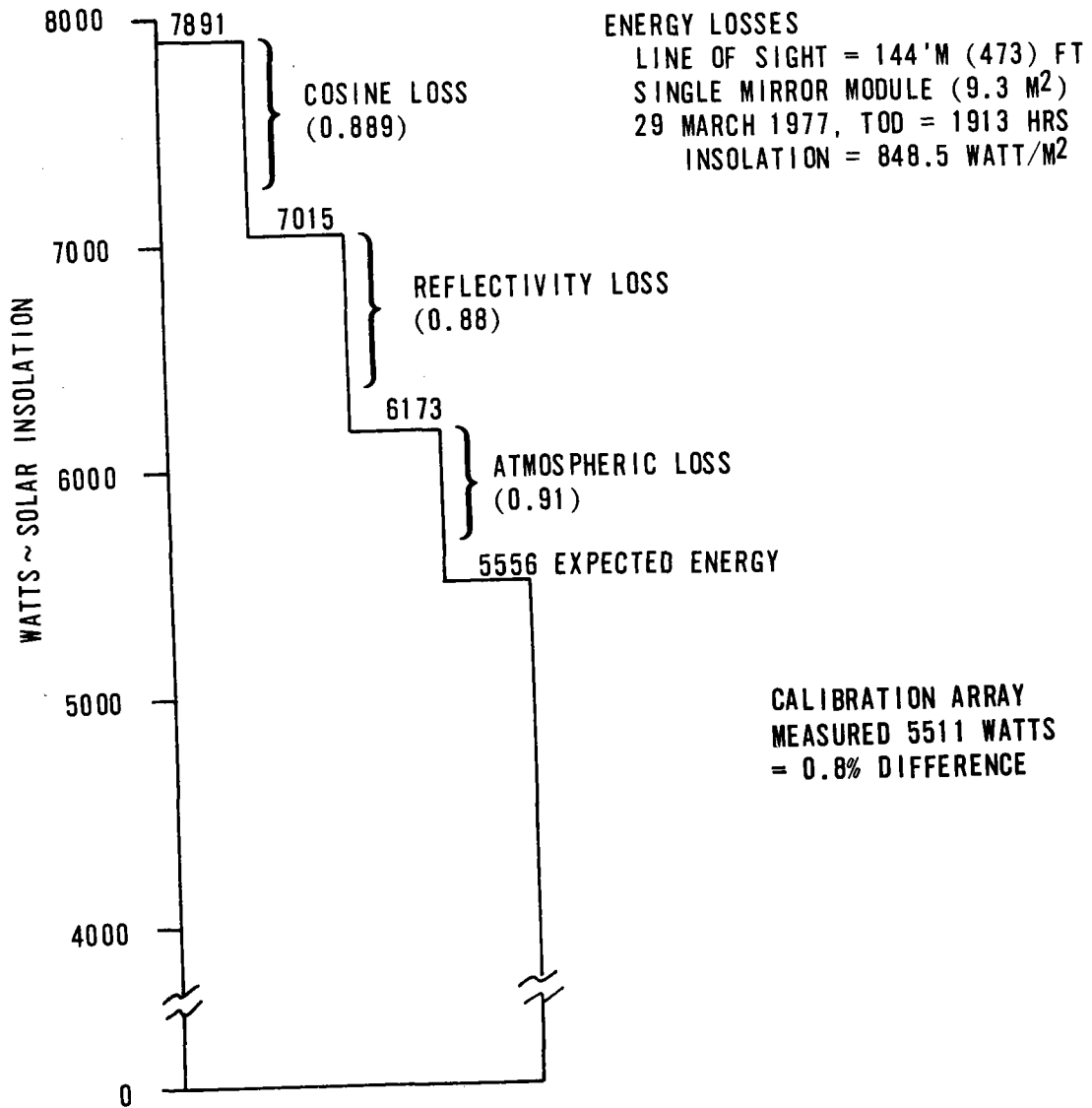


Figure 7-85. Energy Losses

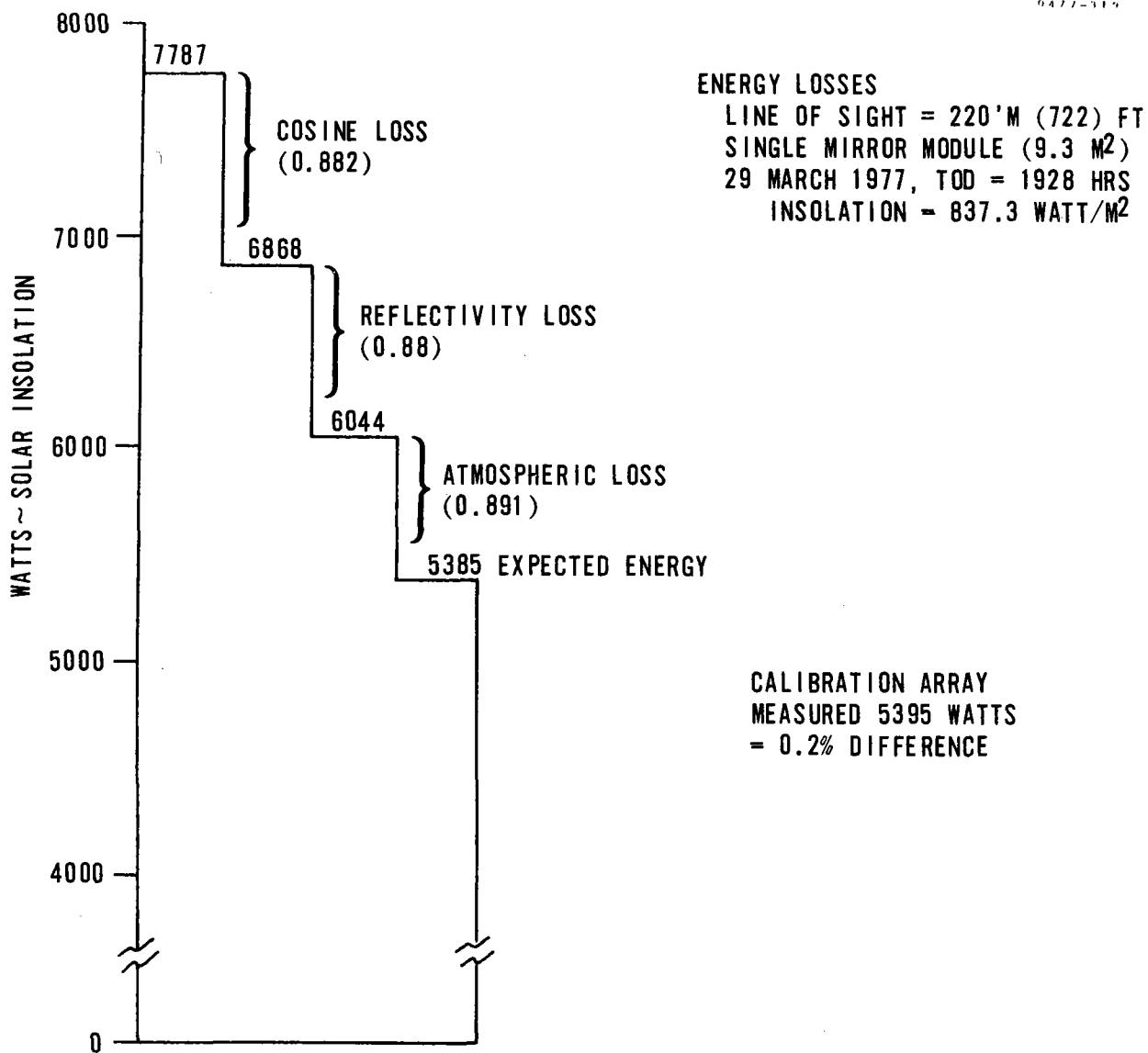


Figure 7-86. Energy Losses

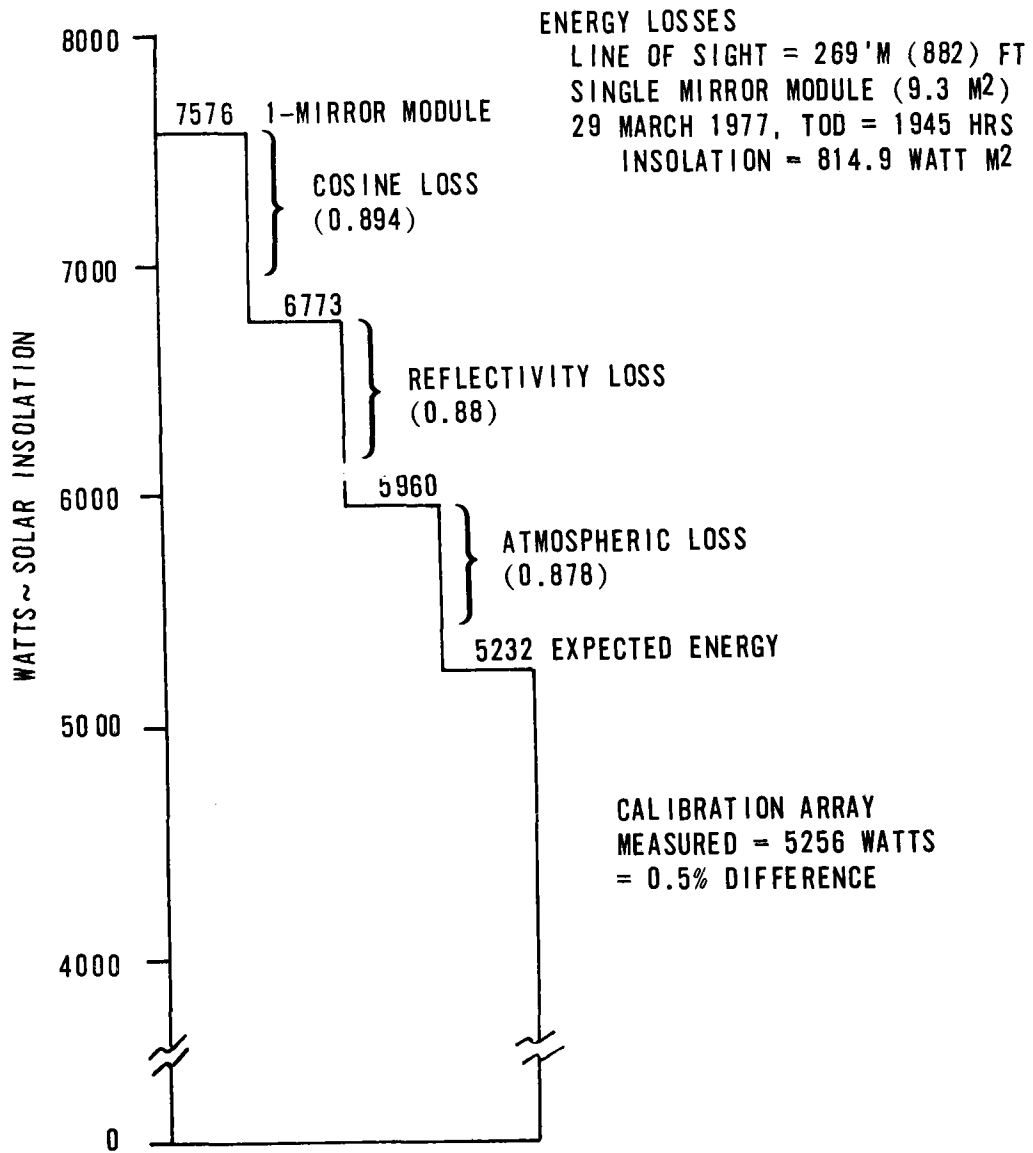


Figure 7-87. Energy Losses

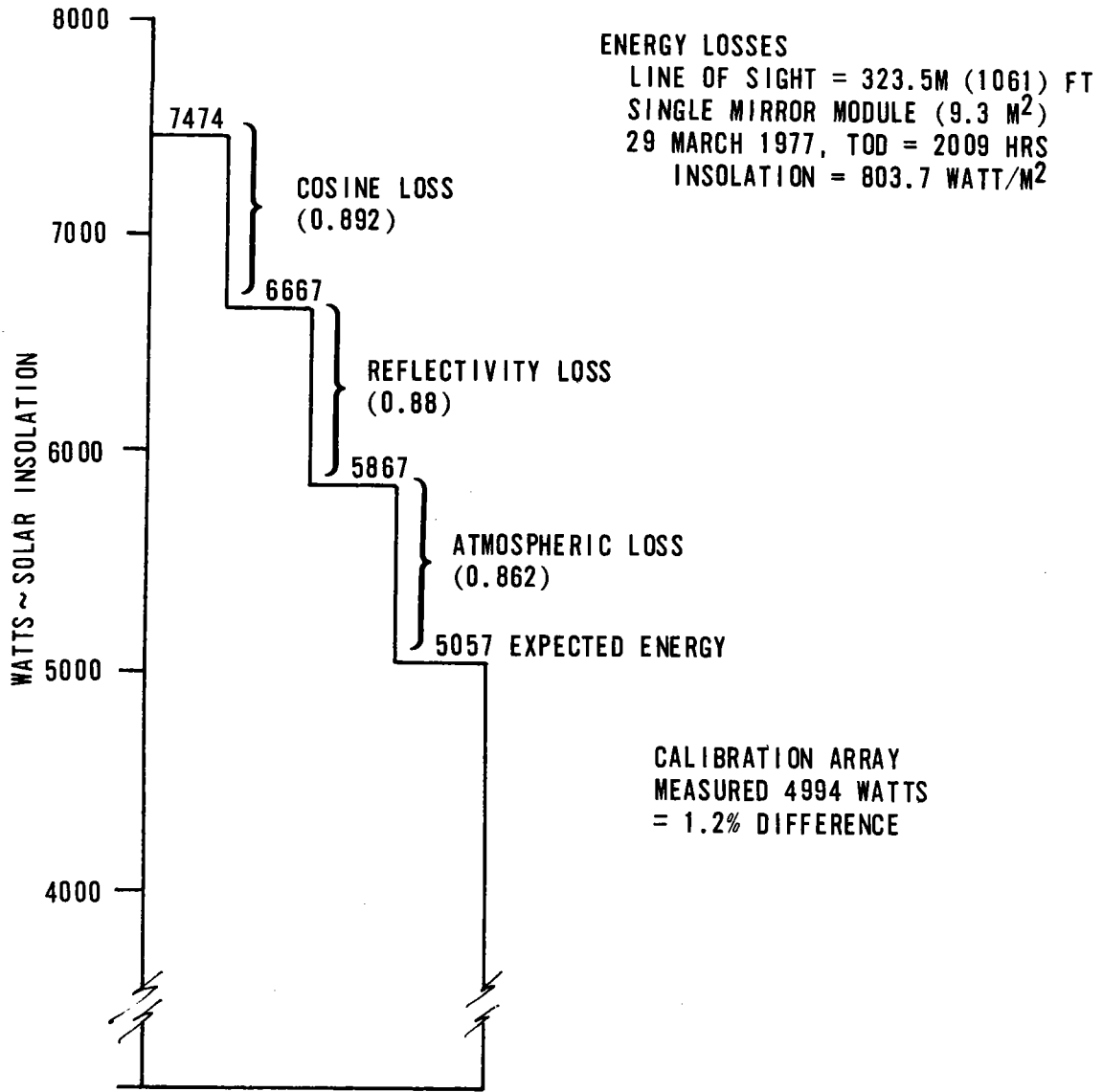


Figure 7-88. Energy Losses

Table 7-18. Energy Balance Comparison

<u>Ref Figure</u>	<u>Site (Meters)</u>	<u>Expected Energy (Watts)</u>	<u>Measured Energy Watts</u>	<u>Percent Diff + Is Greater</u>	<u>Remarks</u>
X1	80.8	5864	5938	+1.3	One Mirror Module
X2	144	5556	5551	-0.8	One Mirror Module
X3	220	5385	5395	+0.2	One Mirror Module
X4	269	5232	5256	+0.5	One Mirror Module
X5	323.5	5057	4994	-1.2	One Mirror Module
HH	148	22816	22716	-0.43	North Heliostat

On 7 April 1977, 1944 hours, the north site was directed onto the array with the results shown at the bottom of Table 7-18.

The energy losses due to atmospheric attenuation were assumed to follow ERC mathematical model of atmospheric attenuation effects of water vapor (55 percent RH), CO₂ and turbidity. (See Figure 7-89.)

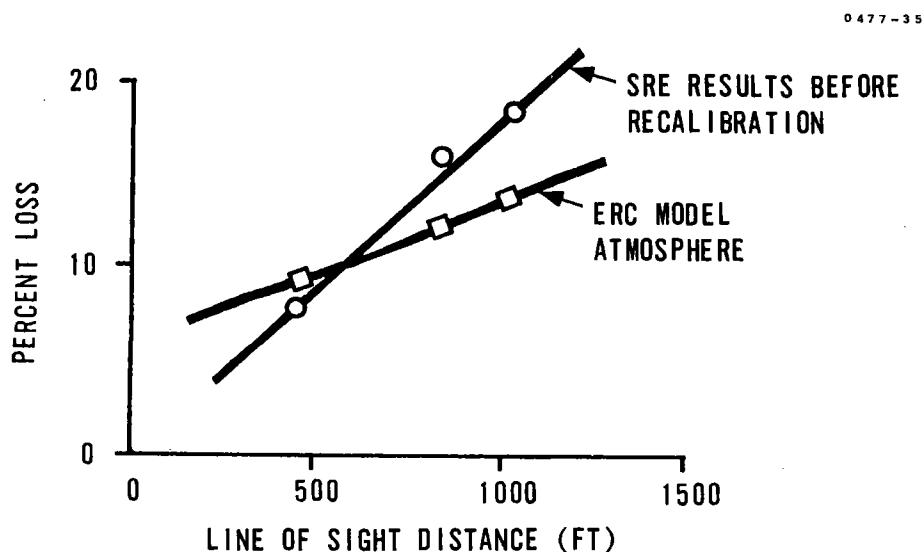
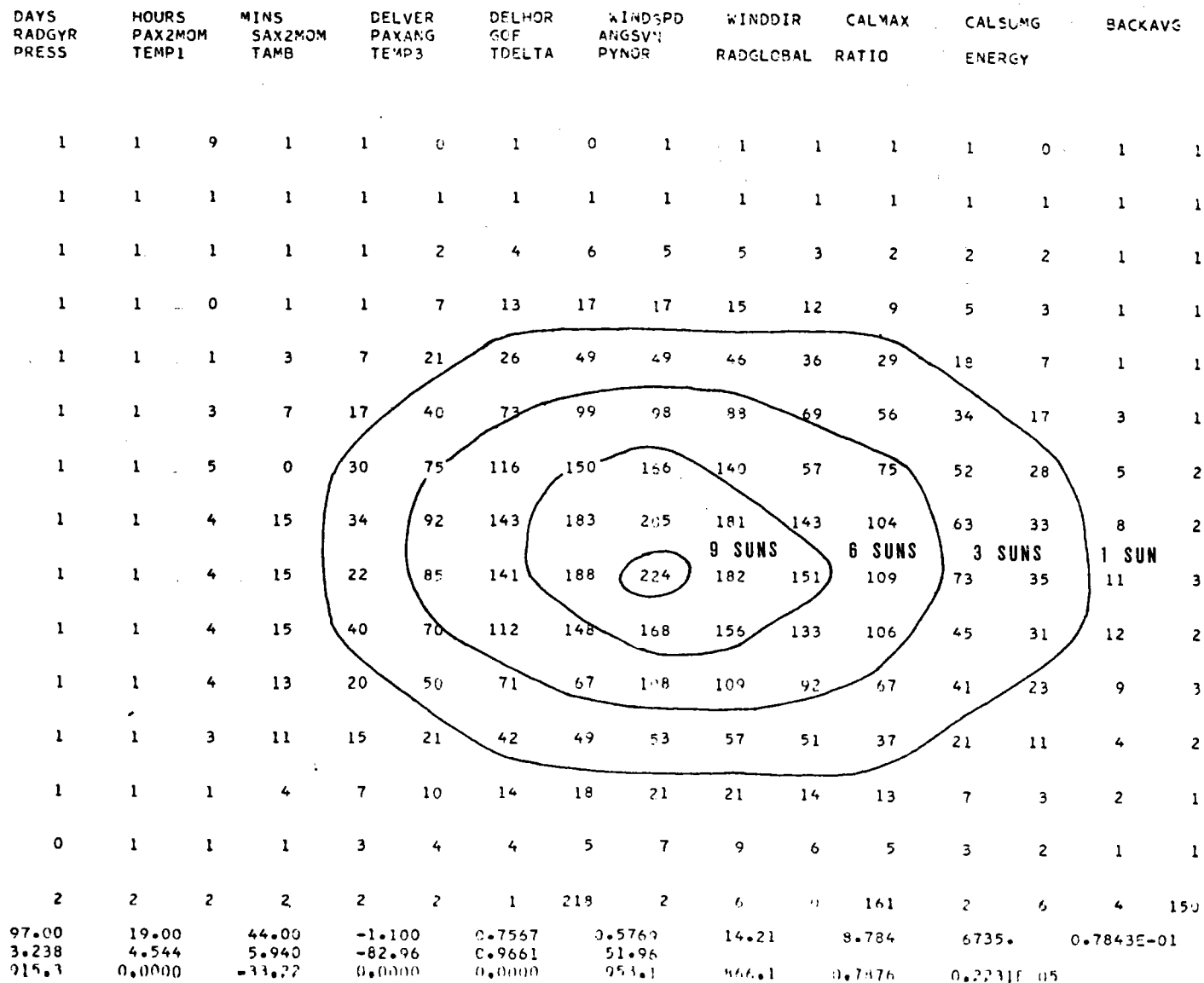


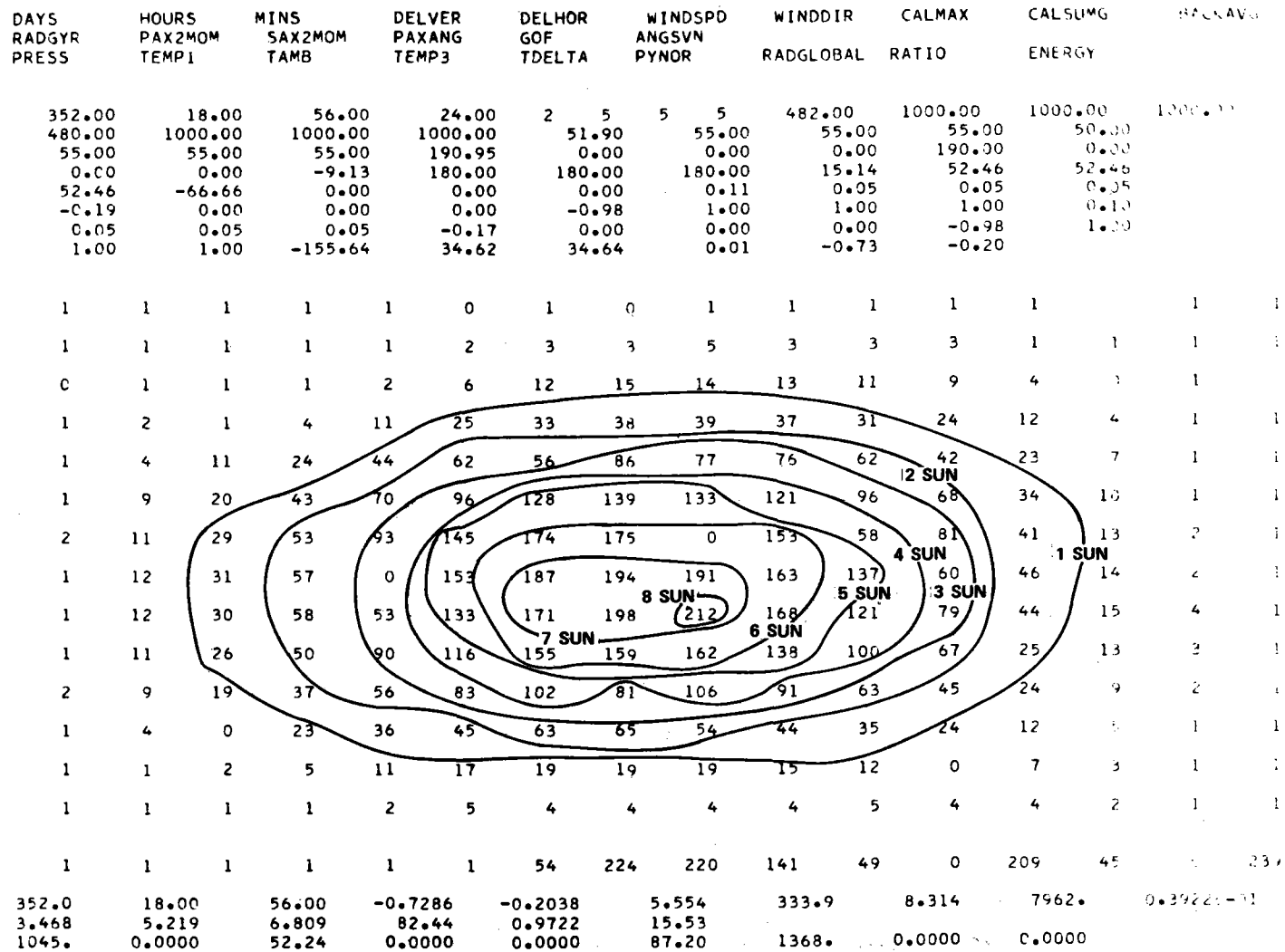
Figure 7-89. Percent Energy Losses Versus Line of Sight Distances for Humidity 55 Percent

The results to date, using the model atmospheric losses show excellent correlation between the calculated energy and the actual levels recorded by the calibration array. Most all readings to date are within 1 percent.



7-173

Figure 7-90. North Site - March 1977 Flux Map



7-174

Figure 7-91. Flux Map, North Site December 17, 1976

DAYS RADGYR PRESS	HOURS PAX2MOM TEMP1	MINS SAX2MOM TAMB	DELVER PAXANG TEMP3	DELHOR GOF TDELTA	WINDSPD ANGSVN PYNOR	WINDDIR RADGLOBAL	CALMAX RATIO	CALSUMG ENERGY	BACKAVG
352.00	19.00	10.00	0.00	2 5	5 5	482.00	1000.00	1000.00	1000.00
480.00	1000.00	1000.00	1000.00	51.90	55.00	55.00	55.00	50.30	
55.00	55.00	55.00	190.95	0.00	0.00	0.00	190.00	0.30	
0.00	0.00	-10.67	180.00	180.00	180.00	13.61	52.46	52.46	
52.46	-69.70	0.00	0.00	0.00	0.11	0.05	0.05	0.35	
-0.19	0.00	0.00	0.00	-0.98	1.00	1.00	1.00	0.10	
0.05	0.05	0.05	-0.17	0.00	0.00	0.00	-0.98	1.00	
1.00	1.00	-152.24	33.30	33.32	0.01	0.28	0.73		
1	1	1	1	0	0	1	0	1	1
1	0	1	0	1	3	4	4	5	4
0	1	1	1	2	7	12	15	12	13
1	1	0	1	5	12	17	22	25	25
1	1	1	3	9	17	18	35	37	37
1	1	1	4	9	21	33	45	48	47
1	1	2	6	11	26	37	46	0	53
1	1	1	2	0	24	37	47	53	50
1	1	1	2	4	17	29	43	47	44
1	0	1	1	6	13	21	28	31	31
1	1	1	1	1	7	12	11	15	15
1	1	0	1	1	1	5	6	5	6
1	1	1	1	1	1	1	1	1	1
1	1	1	1	1	1	1	1	1	1
1	1	1	1	1	1	1	1	1	1
1	1	1	1	1	1	14	225	194	147
352.0	19.00	10.00	0.2758	0.7334	1.798	348.1	2.078	2052.	0.3922E-01
3.517	5.993	6.375	-59.84	0.9630	15.67				
1029.	0.0000	42.05	0.0000	0.0000	87.20	1458.	0.0000	0.0000	

7-175

Figure 7-92. Flux Map - Single Mirror Module, North Site.

Insolation Recording

Side-by-side paper strip chart recordings of the tracking Eppley pyroheliometer and the Eppley global pyronometer mounted on a horizontal plane were made from 19 July 1976, until the end of December. Time resolution was one minute per chart division, so good discrimination can be made with regard to total versus direct insolation and the effect of cloud activity. Approximately 6 percent of the days are not available due to recorder failure.

All recorded data is available for use by interested parties. Qualitatively, the following lessons were learned:

- This area has a very high percentage of cloud coverage which would degrade the performance of a central solar power plant.
- On "clear" days the direct insolation normally reaches only 850 to 875 watts/M². This is due to a relatively high humidity factor. Peak intensities of 1015 watts have been obtained.
- With the occurrence of numerous white low clouds, but yet clear, direct insolation available, the total insolation level can exceed being 90 percent greater than the direct, even near solar noon.
- Cloud activity is exceptionally dynamic. Direct insolation can be reduced by 80 percent in less than 20 seconds by cloud edges. Pilot plant control strategies must include the handling of these thermal gradients induced by partial heliostat field cloud coverage.
- It would be highly desirable to obtain funding to digitally record this side-by-side insolation data along with a tracking photocell for more extensive off-line data processing and analysis.

Lightning

On 10 August, a lightning strike near the Engineering Model caused severe damage to the electronics. Approximately 75 percent of all 5 volt elements were destroyed due to high induced voltages. All three boards were reassembled with a complete complement of new logic elements. Subsequent to this occurrence, lightning protection was incorporated. Internal building circuit breakers within the Honeywell complex were thrown and one electronics board in the Delta 2000 monitoring system in Building 1 was damaged due to the strike on Honeywell grounds which was 250 feet due east of the heliostat. No subsequent damage has occurred since incorporating lightning protection on each of the heliostats.

Cold Weather Testing

We do not experience freezing weather often in Pinellas County. However, on one occasion (the morning of 20 January 1977) the ambient night temperature dipped to 28°F. At 0730 in the morning, the temperature was 33°F local and a mixture of thin ice and melting frost still covered exterior surfaces. There was negligible wind. Power measurements were made on the inner and outer drives of the North site under this condition. The North site had not been operated for 29 days.

The inner drive power ranged relatively smoothly from 14.9 watts to 15.5 watts. This can be compared to average powers of 12 watts on a warmer day of 65°F.

The outer drive power ranged from 41.9 watts to 55 watts for Motor No. 3 at steep negative angles (-70 degrees) which implies torque requirements of 74 to 96 in.-oz. During warm weather testing, the torque ranged from 45 to 54 in.-oz under the same gimbals activity. Obviously, this limited data only provides a clue as to the actual capability of proper operation at -30°C environment. The torque load on the drive systems will increase as temperature decreases due to stiffening of the lubricants and possible shrinking of bearing interfaces, tie-rod joints, etc., as these results indicate. A proposal has been submitted to perform controlled cold climate testing on the different drive systems.

ERROR BUDGET COMPARISON

Test results were obtained are compared to the analytical error budget proposed during the DDR and in Table 7-19. The wind deflection error source is the single overriding contributor, but the magnitude of 2.9 mr peak deflection is during gust peaking only.

Actual long term daily tracking accuracies of 1.5 mr vertical and 0.5 mr horizontal have been obtained as the outer limit averages from the East site. The North site performed even better considering the instrumented calibration array was never used to improve performance. Even under wind loadings, the redirected energy must be statistically averaged across a time interval because of the relatively long thermal time constant of the boiler compared to oscillations resulting from wind gusts. To date, wind data shows a standard deviation of ±0.5 to 0.7 mr about an average track trajectory. This type of number is more meaningful over a field of 1680 pilot plant heliostats than a single, worse case, short term (fraction of a second) excursion due to a wind gust or a worse case bending deflection attributed to one heliostat of 1.9 mr.

Table 7-19. Error Budget/Result Comparison

NOTE: Some Results are still Preliminary

- Tracking Error Requirements - 2 mr ERC/ERDA Requirements
Optical - 1 mr

<u>Item</u>	<u>Budgeted Error (3σ)</u>	<u>Test Results</u>	<u>Comments</u>
A. Independent Error Sources	(mr)	(mr)	
1. Foundation	0.031	0.14 Total (0.018 per Weekly Calibration)	Over two months. Temperature dependence included. Actually 0.018 mr assuming weekly calibration.
2. Mirror Not ⊥ to Frame	0.45 about M_1	Not Obtained	No impact to pointing accuracy. Taken out during visual toe-in check.
3. OA Alignment	0.16 about O_2/O_3	Large, due to initial site survey and layout errors	Compensated for by software angular computation.
4. Backlash	0.54 about I_2/M_2 0.18 about O_1/I_1	0.60 0.06	Included in total deflection.
5. Quantization	0.1 about $O_1/I_1/I_2/M_2$	0.20	One half of 80 arc-seconds.

Table 7-19. Error Budget/Result Comparison (Continued)

<u>Item</u>	<u>Budgeted Error (3σ)</u>	<u>Test Results</u>	<u>Comments</u>
A. Independent Error Sources (Cont'd)			
6. Gear Tooth-Tooth	0.54 about I_2/M_2 0.14 about O_1/I_1	Not Obtained	During test there was no indication of this error source. Partly included in backlash measurement taken at different gimbal rotations.
7. Computer Error	0.34 about O_1/I_1 I_2/M_2	0.34	Analytically derived only. Does not address commercial power frequency shifts.
8. Crank Arm Play	0.21 about I_2/M_2	Not Obtained	Result contained in wind load error. 30-100 arc-seconds taper lock slippage have occurred.
9. Mirror Normal Defocus	0.707 about $M_1/I_2/M_2$	0.10 mr	Sample only of most recent Parson's mirror module, 0.707 is derived from MM Spec.
10. Scaling for Outer Axis Drive	Not Defined Initially	6.41 mr about O_1/M_1 reduced to 0.1 mr	Software can reduce to 0.1 mr.
11. Initialization Repeatability	Not Defined Initially	0.24 mr about O_1/M_1 O_2/M_2	Based upon latest design.
TOTAL		RSS=0.51 about O_1/I_1 0.77 about O_2/I_2	

Table 7-19. Error Budget/Result Comparison (Continued)

<u>Item</u>	<u>Budgeted Error (3σ)</u>	<u>Test Results</u>	<u>Comments</u>
B. Deterministic Error Sources	(mr)	(mr)	
Temperature Effects:			
1. Crank Arm Differences	0.9 mr about I_2/M_2	0.4	Based on 10°C (Budget) Actual = 40°C
2. Frame Difference	0.28 about $I/3$	0.12	Worst Case (7°C) Noted during Thermal Test.
3. Support Posts	0.20 about O_1/I_1	0.26	3.8°C across post.
Sum of Temperature			Correct reflective painting of post and frame is important. Shadowing from mirror modules also helps.
I_2/M_2	0.90 mr	0.40	
O_1/I_1	0.20 mr	0.26	
Wind Effects:			NOTE - 30 mph winds only.
1. Servo Gain	0.24 mr about O_1/I_1	0.0	None due to non-reversing gears.
2. Mirror Module Deflection	0.124 mr about M_1/M_2	0.10	Due to static loading - change of mirror normal.
3. Total Deflection of MM	1.0 mr M_2/I_2	0.8	From torsion tests on MM. 0.8 mr is worst case.

Table 7-19. Error Budget/Result Comparison (Continued)

<u>Item</u>	<u>Budgeted Error (3σ)</u>	<u>Test Results</u>	<u>Comments</u>
B. Deterministic Error Sources (Continued)			
4. Total Deflection Due to Torsion, Lash, Crank Arm Bending, Spring Rate	1.54 mr M_2/I_2	1.9	Prior to rework of gear box = 3.6 mr. After rework 1.9 mr, tests performed at 7500 in-lb.
Sum of Wind Effects		2.9 mr	Total worst case <u>observed</u> during gusting winds. Therefore, maximum spring rate is included and is 2.9 mr present only during peak gust.
Gravity	0.25 about O_1/I_1	Not Obtained	Variation due to frame orientation on slab = 0.02 mr about O_1/I_1 .
TOTAL		RSS=2.94 mr About O_2/I_2 RSS=2.10 mr	Most due to wind loading at peak gust per observations. Due to static loading and temperature.

Appendix A
REFERENCE LOCATIONS OF DATA LISTS

Collector Subsystem - Design Characteristics

	<u>Pilot Plant*</u>	<u>Commercial Plant</u>	<u>SRE</u>
1. Field geometry and size	A-2	A-2	7-5
2. Field layout	A-2	A-2	
3. Field oversizing to allow for dirt on mirrors, reliability, etc.	A-6		
4. Beam pointing accuracy and error budget versus environmental effects	7-178	7-178	7-178
5. Heliostat beam quality and error budget versus environmental effects	6-22, 7-155	7-155	6-22, 7-155
6. Heliostat weight breakdown	A-13		A-13
7. Heliostat parts count	3-6, 3-32, A-13		3-32
8. Foundation and field wiring	3-64, A-13		
9. Identify nonstandard parts	6-37		
10. Identify single source parts	6-37		
11. Identify long lead items	6-37		
12. Identify parts having high infant mortality rates	6-26		

* Numbers refer to page numbers.

Appendix A
DESIGN CHARACTERISTICS

In accordance with a Sandia Letter by Al Skinrood on 11 February 1977.

Re: Central Receiver Solar Thermal System
Pilot Plant Preliminary Design Report
(PDR) Requirements

We are providing the following data. The numerical identifiers refer to a listing in PEL III Attachment B of 16 March 1977.

FIELD GEOMETRY AND SIZE

Reference to Figure A-1 and Table A-1 shows both pilot plant and commercial plant geometry and sizes.

Collector Field Geometry and Size

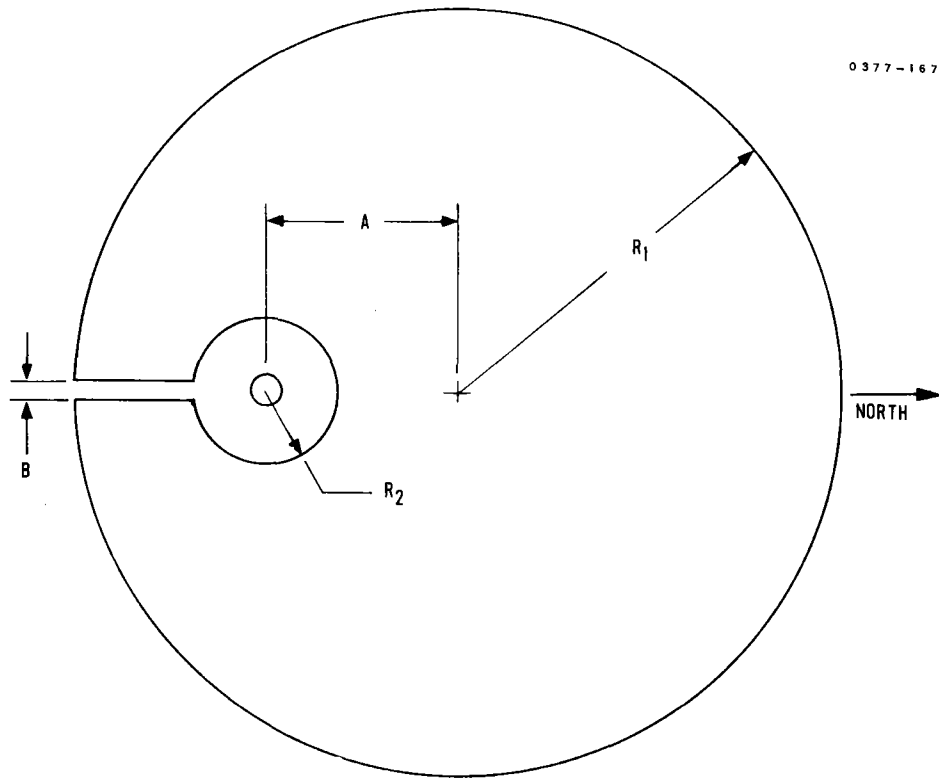
The pilot plant and commercial plant field layouts are similar in shape but dissimilar in proportion and quantity. As can easily be seen from the chart the four commercial fields are arranged in a matrix. Note from the table that the ratio of tower height to field outer radius for the pilot plant is $\frac{129.8}{274} = 0.474$ while the same ratio at commercial scale is $\frac{231.4}{475.5} = 0.487$ thus the proportions are slightly different though noticeable. Area of the pilot plant (including building grounds) is 235,858 square meters with 1600 heliostats or 147.4 square meters per heliostat. The commercial plant has 710,314 square meters with 5,055 heliostats or 141 square meters per heliostat. From these numbers it is easily seen that the commercial modules and pilot plants are related by a scale factor of about 1.74 in linear dimension and three in area.

FIELD LAYOUT

The Figures A-2 and A-3 show the layout of the heliostat field for the pilot and commercial plants, respectively.

Collector Field Layout

The figure shows approximate positions for all 1600 heliostats employed in the pilot plant collector subsystem. The commercial layout is similar but larger and has more heliostats. The small ovals show approximate dimensions and positions of heliostats to scale. Starting near the tower the rows are closely spaced and further out have greater separation. The heliostat locations are such that distances between heliostats are the same as spacing between adjacent mirror modules on a single heliostat frame. This produces within limits a uniform ring of mirror modules on each row. The figure is in error where it shows aisles through the field to the towers. They result from use of drafting aids. These aisles could allow channel effects of the wind which is undesirable.



PILOT PLANT AND MODULE DETAILS

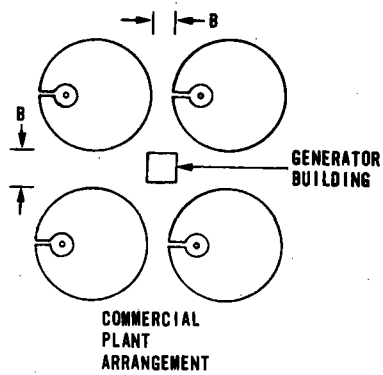
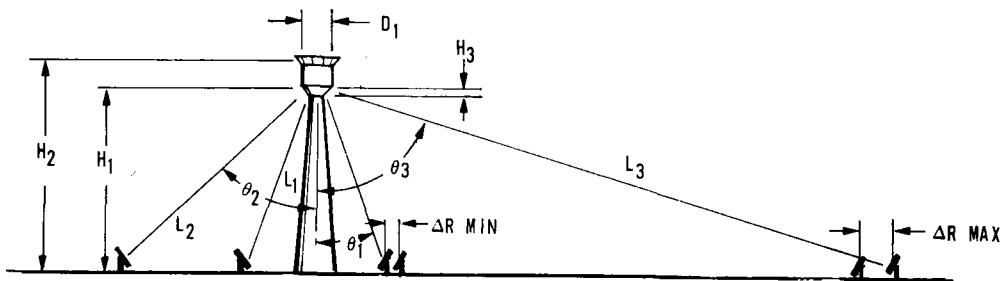


Figure A-1. Collector Field Layout

Table A-1. Solar Collector Subsystem

<u>Characteristic</u>	<u>Symbol</u>	<u>Ref Fig No.</u>	<u>Pilot Plant 10 mwe</u>	<u>Commercial-1</u>
Field				
1. Outer Field Radius (m)	R_1	1	274	475.5
2. Inner Field Radius (m)	R_2	1	50.3	89.9
3. Tower Offset (m)	A	1	137	237.7
4. Near Heliostat Angle (rad)	θ_1	1	0.24	0.38
5. Far South Heliostat Angle (rad)	θ_2	1	0.86	0.79
6. Far North Heliostat Angle (rad)	θ_3	1	1.21	1.26
7. Near Heliostat LOS Distance (m)	L_1	1	153.6	242.8
8. Far South Heliostat LOS Distance (m)	L_2	1	192.6	327.7
9. Far North Heliostat LOS Distance (m)	L_3	1	418	748.0
10. Min Radial Spacing (m)	ΔR Min	1	5.06	N/A*
11. Max Radial Spacing (m)	ΔR Max	1	11.03	N/A
12. Min Ground Cover Ratio	GC Min	1	0.173	N/A
13. Avg Ground Cover Ratio	GC Avg	1	0.29	0.29
14. Max Ground Cover Ratio	GC Max	1	0.437	N/A
15. Road Easement (m)	B	1	12.19	12.19
16. Number of Modules	N	1	1	4
17. Tower Height to Center of Aperture	H_1	1	129.8	231.4

* Not available

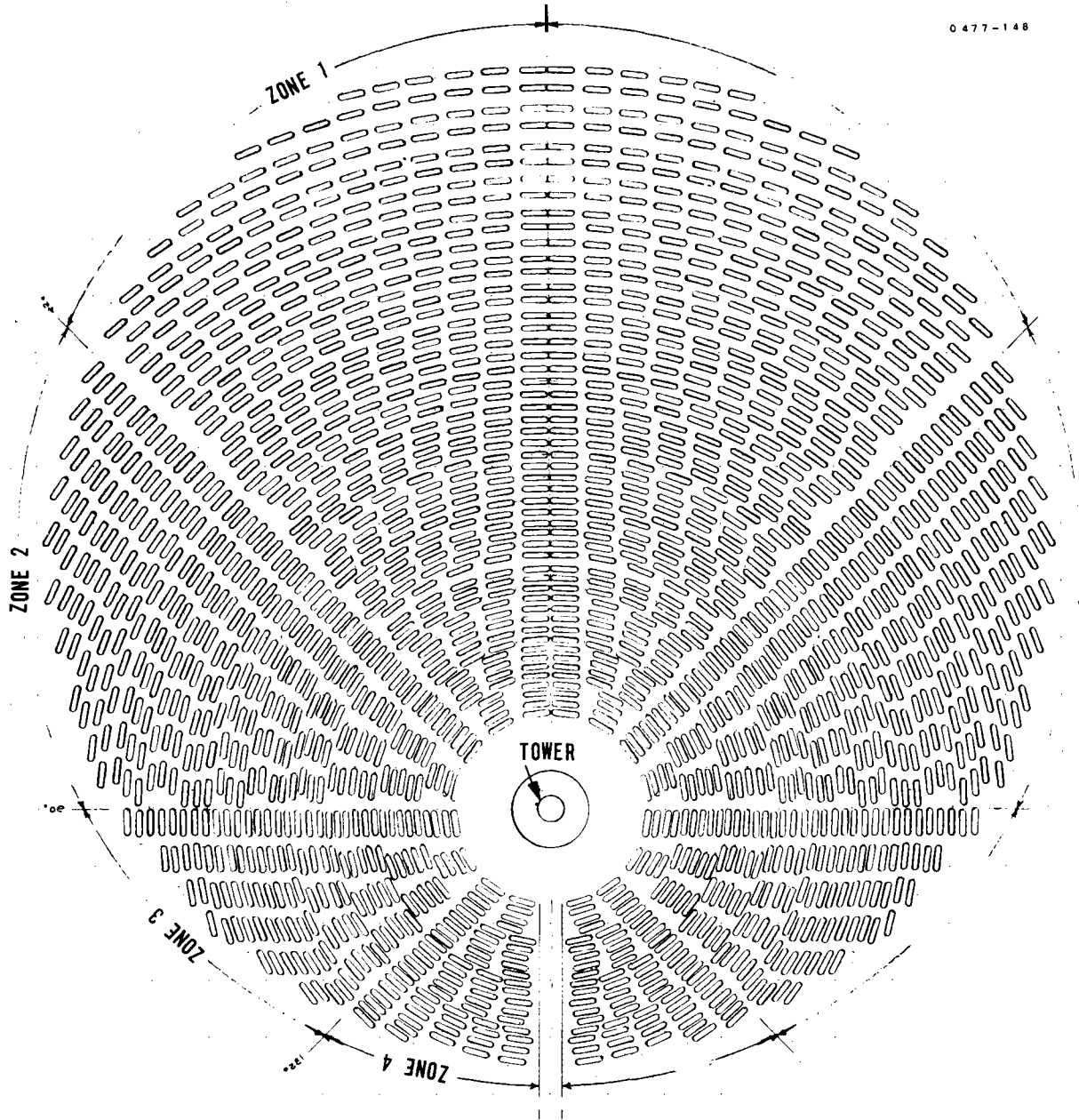
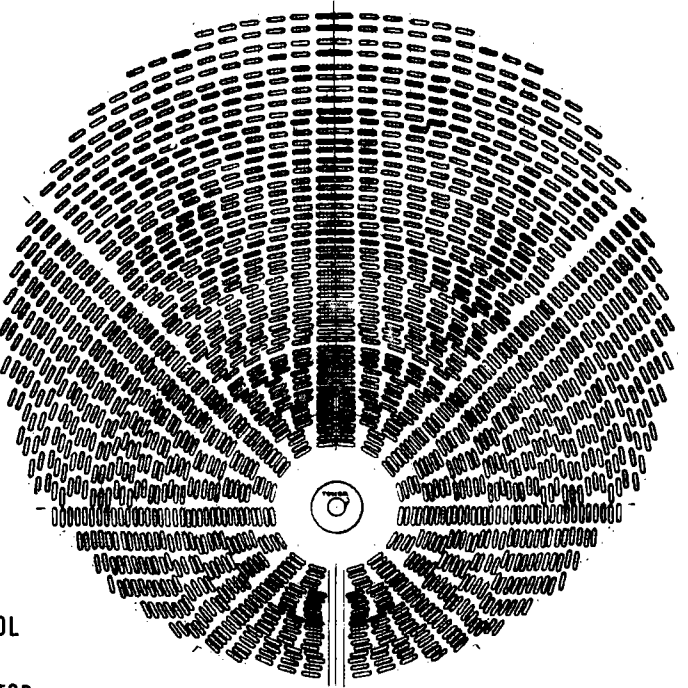
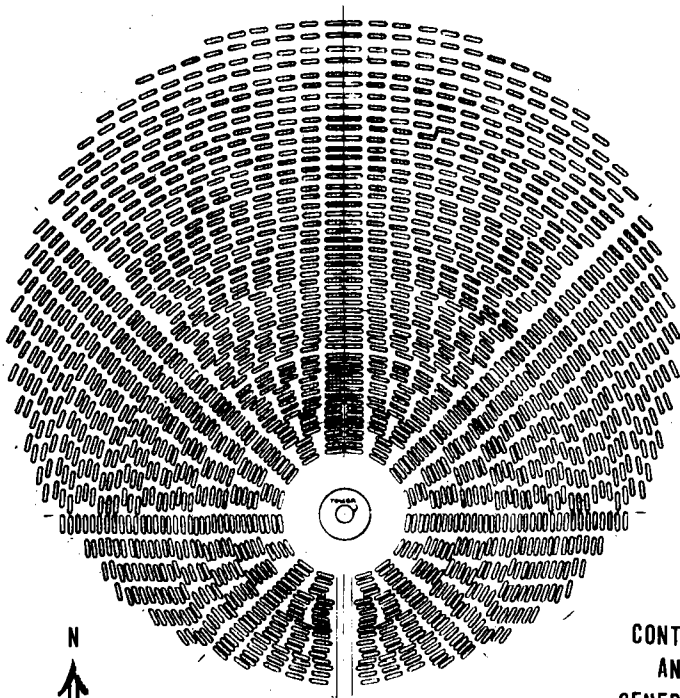


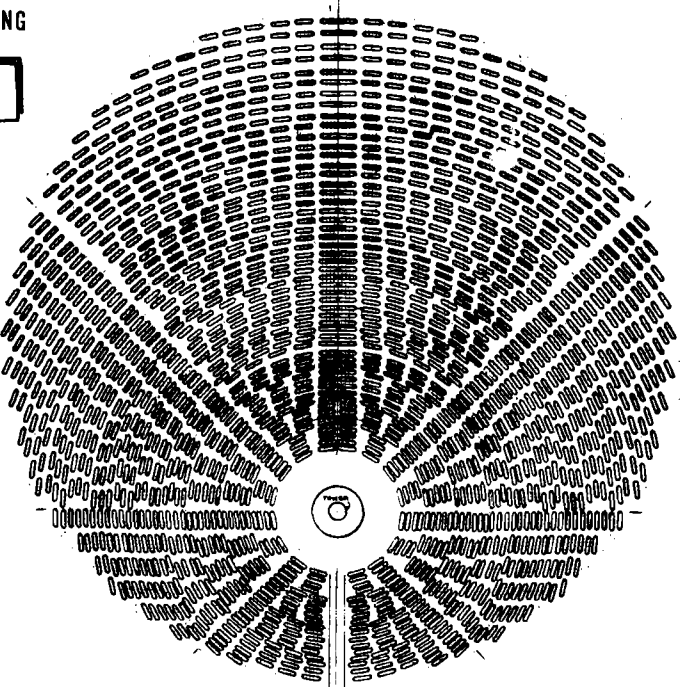
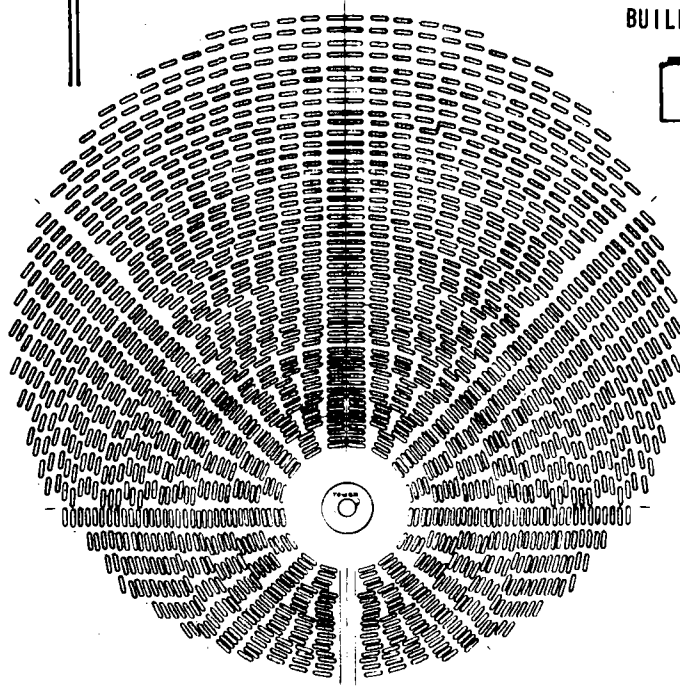
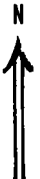
Figure A-2. Pilot Plant and Commercial Plant Module Collector Field

MODULE 1

MODULE 2



CONTROL
AND
GENERATOR
BUILDING



MODULE 4

MODULE 3

Figure A-3. Commercial Collector Fields

Commercial Plant Collector Fields Layout

The commercial plant collector fields are arranged in four modules of 5,055 heliostats each. Each field contains its own power, signal, and ground wiring. Steam lines connect to a common building which also controls the operation of all modules through a master control subsystem. The collector subsystem are spaced to allow access roads between each of the adjacent modules. In the base of each tower is the collector control equipment for that module. The modules are numbered clockwise starting in the northwest corner. The arrangement allows construction of four collector modules at once and thus decreases construction time and thereby costs.

FIELD OVERSIZING

The heliostat field is sized by Sandia direction for clean mirrors. The ray trace program then sizes the field assuming all heliostats are working. This results in a quantity of 1598 heliostats. As a convenience and to account for some failures which might not be repairable over night we have included two additional heliostats and refer to the quantity as 1600. If we were to increase the heliostat quantity we would recommend a 10 percent overbuy to account for dirty and failed units.

BEAM POINTING ACCURACY AND ERROR BUDGET VERSUS ENVIRONMENTAL EFFECTS

Figure A-4 shows the most predominant effects of environment versus tracking accuracy. The chart shows 0.53 foot (one sigma) centroid travel in a wind of 10 miles per hour blowing on the end of the heliostat (worst direction).

Temperature effects are minor. The total effects are shown in the attached Table A-2. The individual components are slightly different than budgeted but in total remain valid. A more detailed treatment may be found on Page 7-73. These errors are a small effect.

HELIOSTAT BEAM QUALITY

The heliostat beam quality is controlled by the machined-in contour of the mirror modules. This contour was measured and shown in Figure A-5. Loads were also applied as shown in Tables A-3 and A-4 with results that the optical contour or deflection was essentially unaffected (0.39 mr). Figure A-6 shows the calculated versus the measured flux density across the center of the beam from the north heliostat at the winter solstice. The major difference is a bias displacement of the peak.

HELIOSTAT WEIGHT BREAKDOWN

The pilot plant heliostat as now configured and previously described has a weight breakdown as shown in the same column as the SRE unit in Subsection 3.3. The expected producibility study will reduce the weight as shown as the estimate of Revised pilot commercial plant

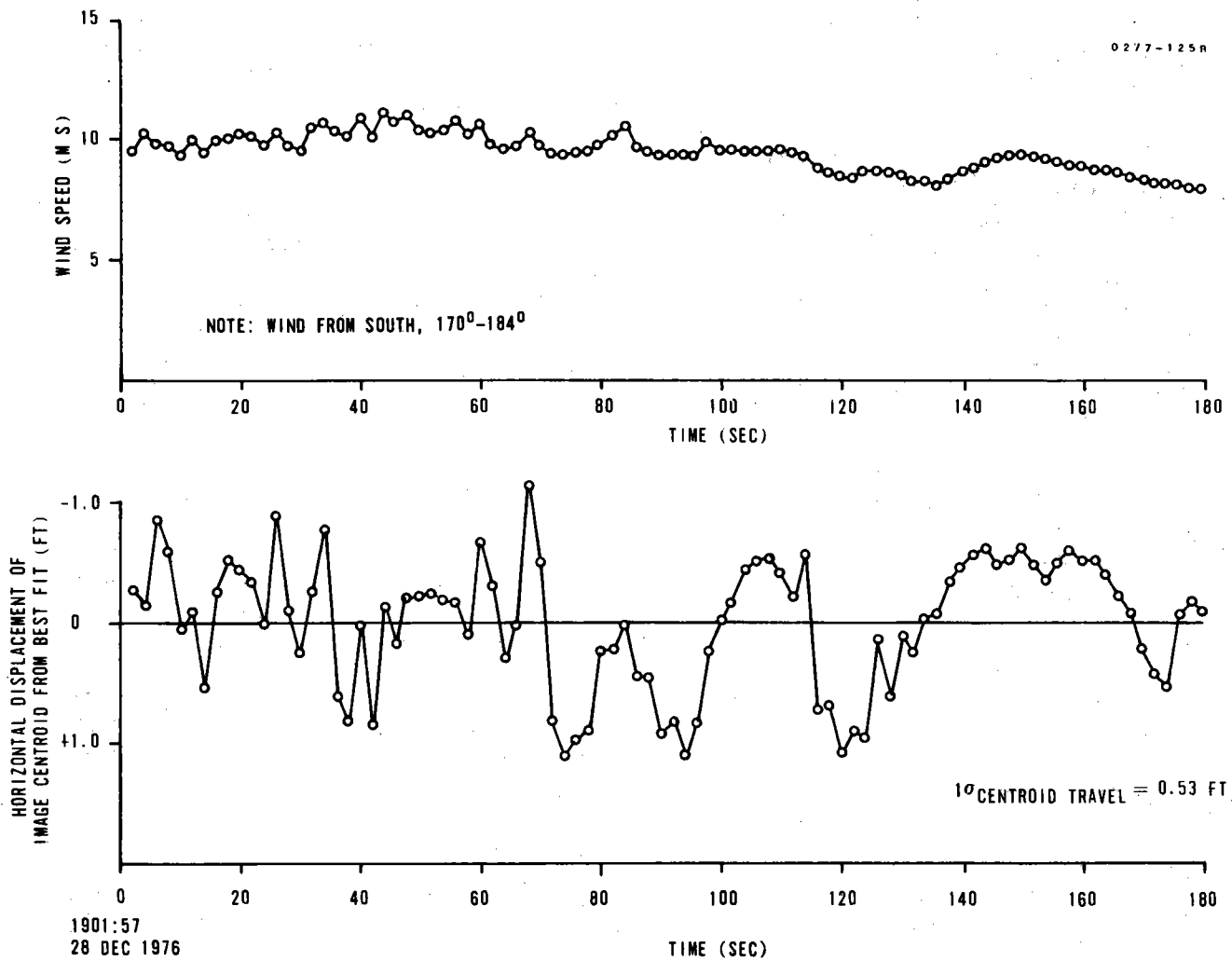


Figure A-4. Image Centroid Variation Least Squares Fit East Site

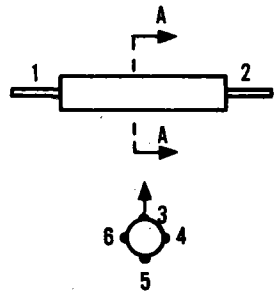
Table A-2. Thermal Gradient Data

0277-106B

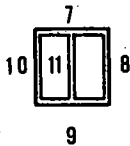
Sensor Time (EDT)	Tie Rod						Frame Box Sec					Frame at Cross Rail			Frame Center			Cross Rail			Post		Ambient	
	E	W	Center			T	N	B	S	I	T	N	B	T	N	B	T	W	B	N	S	EX	SH	
	1	2	3	4	5	6	7	8	9	10	11	12	13	14	15	16	17	18	19	20	21	22	23	24
1000	82	84	84	84	84	84	83	89	84	82	84	84	84	84	85	84	85	84	84	84	84	80	80	82
1030	83	84	84	84	83	83	85	88	84	83	84	85	86	85	86	87	85	85	85	84	84	83	84	83
1100	86	87	87	88	86	87	88	91	86	86	86	88	89	88	88	91	87	88	88	86	86	85	85	85
1130	90	90	90	91	89	88	91	97	88	88	89	91	92	91	91	94	91	90	90	90	88	86	84	85
1200	92	94	94	95	92	92	95	100	92	90	92	95	96	94	95	98	94	94	94	94	94	87	87	87
1215	93	95	93	95	92	92	97	103	93	93	92	96	98	96	97	100	96	95	94	94	94	88	92	89
1230	91	93	94	94	92	94	96	97	93	92	93	96	96	96	97	99	96	94	94	93	94	89	90	88
1300	97	98	98	99	96	97	100	106	97	94	97	100	102	100	100	104	100	98	98	98	98	92	93	90
1307	94	97	97	97	94	96	99	104	96	94	96	99	100	99	100	101	99	95	95	95	96	91	88	87
1318	92	92	92	93	91	92	96	99	93	91	93	96	97	96	96	97	96	94	93	93	94	90	88	86
1330	88	90	90	90	88	89	92	94	92	88	92	93	93	92	92	93	92	91	91	90	91	89	87	85
1335	89	90	91	91	89	90	92	95	91	88	91	93	93	92	93	93	93	91	90	90	91	88	87	87
1348	88	87	89	89	88	89	91	92	88	88	90	91	91	91	91	92	91	90	90	89	88	89	86	87
1400	94	94	95	96	93	93	94	100	89	89	93	94	95	94	94	97	93	91	91	91	88	89	86	88
1405	90	89	91	92	91	91	92	95	88	88	91	92	93	92	93	95	93	90	90	91	88	89	88	89
1430	92	93	92	95	92	92	96	103	90	91	96	95	96	95	96	98	95	92	93	93	89	89	87	88
1500	92	93	92	94	92	91	95	101	89	90	93	94	95	94	95	96	94	91	93	93	89	90	87	89
1530	92	93	92	94	92	92	94	99	90	90	92	95	95	94	95	96	94	92	94	93	90	91	88	90
1600	93	93	93	95	93	93	95	99	91	91	93	95	96	95	95	97	94	93	95	95	91	92	91	87

Partial Cloud Coverage

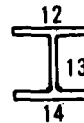
Partial Sun Sunny



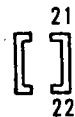
SECTION A-A



I-BEAM BOXED OFF WITH STIFFENER



OPEN I-BEAM



CROSS RAIL EXPOSED

NOTE: TEMPERATURES, °F

A-8

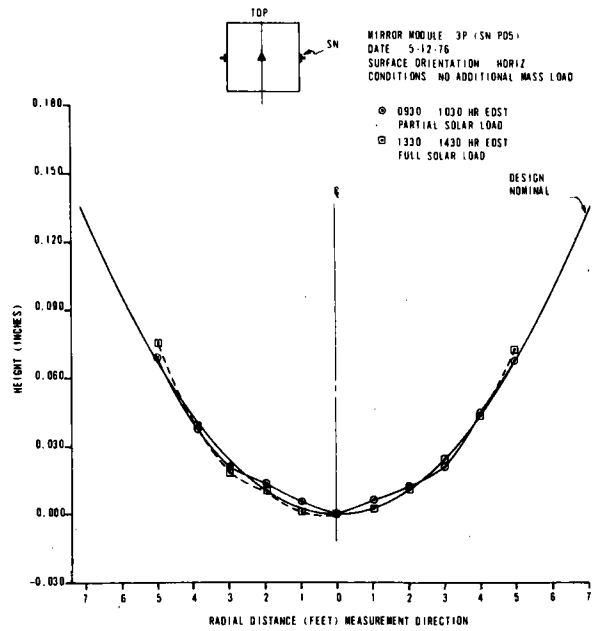
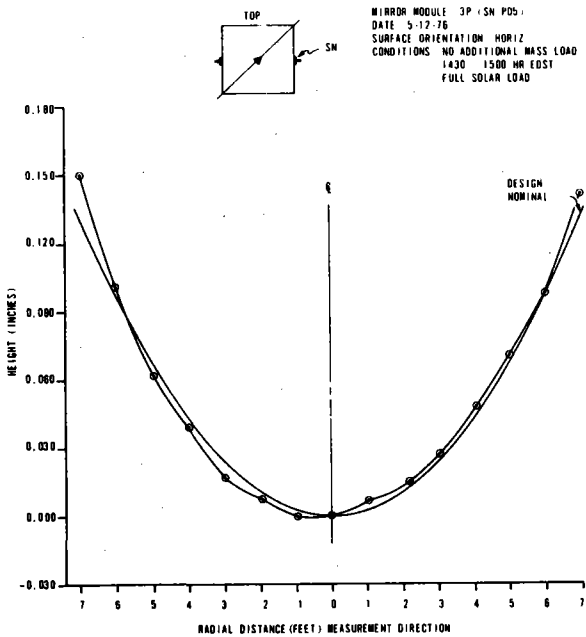
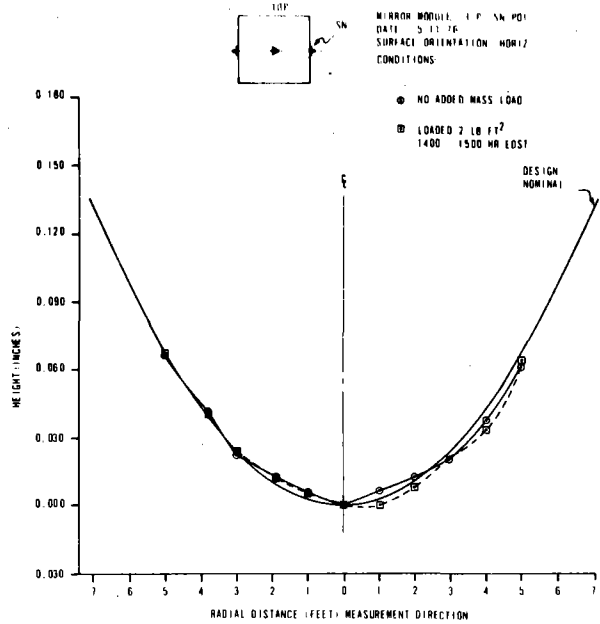
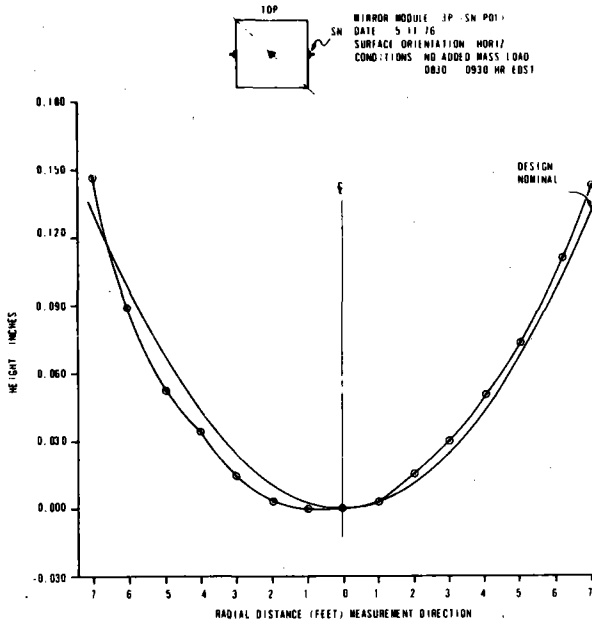


Figure A-5. Contour Data - Parson's Mirror Modules (Tapered Cross Section)

Table A-3. Mirror Module Static Stiffness Due to MM3P SN P01
Taper Locks Torqued to 150 Ft-Lbs

Δ Load (lbs) at 60 in Lever Arm	Deflection						
	E Arm	E Shaft	E Pad	Center	W Pad	W Shaft	W Arm
0 \rightarrow 20	0'0"+	+0'2"	+0'12"	+0'38"	+0'35"	+0'21"	+0'16"
20 \rightarrow 125	+1'10"	+2'7"	+2'52"	+2'59"	+2'34"	+2'4"	+1'0"
125 \rightarrow 20	-1'14"	-1'58"	-2'14"	-2'51"	-3'46"	-1'56"	+0'7"
					Bad Data Point		Bad Data Point
20 \rightarrow 0	-0'18"	-0'24"	-0'28"	-0'34"	+0'52"	-0'22"	-1'33"
0 \rightarrow \dots \rightarrow 0	-0'22"	-0'13"	+0'22"	+0'12"	+0'15"	+0'7"	-0'10"

Results: Optical axis deflected 0.39 MR at 7500 in-lbs.
(Design goal: 1 MR at 7500 in-lbs)

0277-054

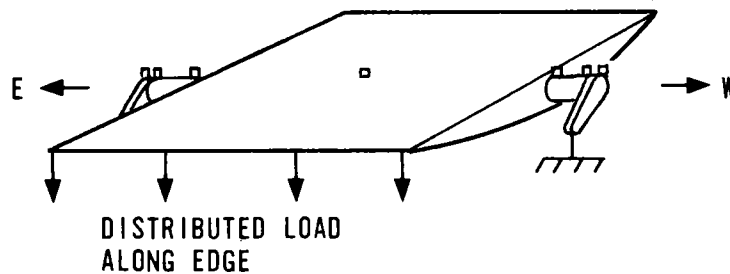
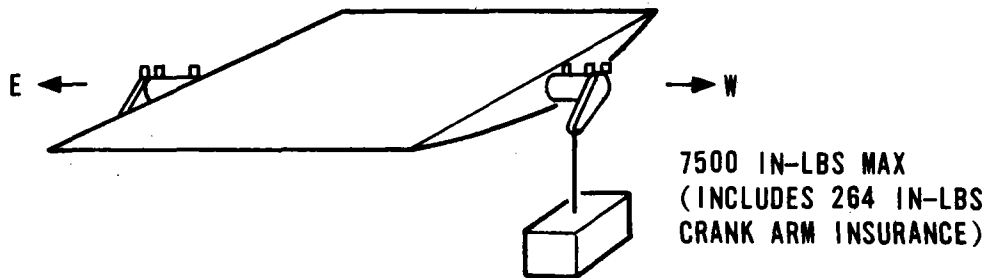


Table A-4. Mirror Module Static Stiffness MM3P SN P01
Taper Locks Torqued to 200 Ft-Lbs

Δ Load (lbs) at 24 in Lever	DEFLECTION					
	E Arm	E Shaft	E Pad	W Pad	W Shaft	W Arm
0 \rightarrow 30	+0'1"	+0'23"	+0'29"	+0'53"	+1'2"	+1'13"
30 \rightarrow 312	+4'10"	+7'6"	+7'46"	+10'3"	+11'15"	+13'25"
312 \rightarrow 30	-3'54"	-5'8"	-6'18"	-8'40"	-9'49"	-11'30"
30 \rightarrow 0	-0'18"	-0'27"	-0'34"	-0'48"	-0'59"	-1'7"
0 \rightarrow ... \rightarrow 0	-0'1"	+1'54"	+1'23"	+1'27"	+1'29"	+2'1"
30 \rightarrow ... \rightarrow 30	+0'18"	+1'58"	+1'28"	+1'22"	+1'26"	+1'55"

Results: Optical axis deflected 0.70 MR at 7500 in-lbs.
(Design goal: 1 MR max at 7500 in-lbs). E&W crank arms
slipped \approx 100 arc-sec and 30 sec, respectively. Investigation
showed taper locks did not bottom out.

0277 61



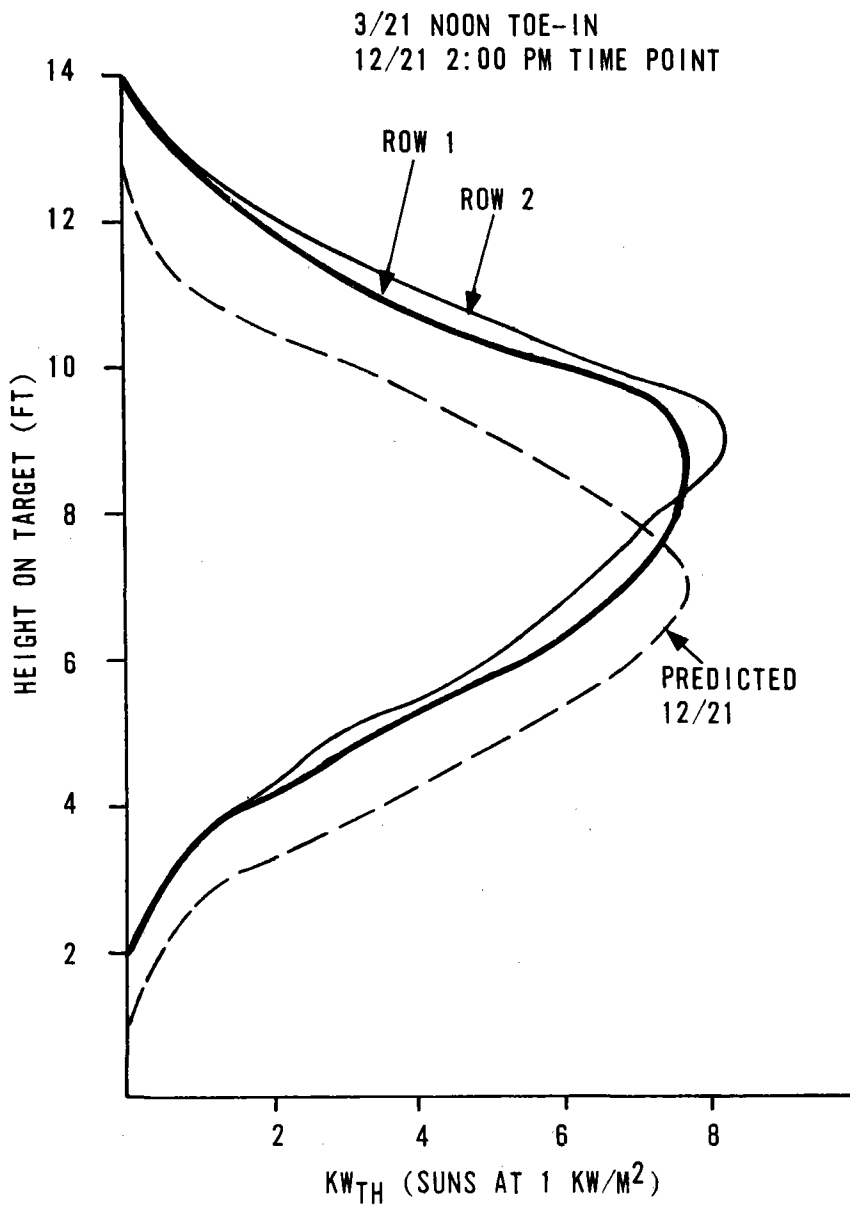


Figure A-6. Center Vertical Cross Section of Power on Target

weight Breakdown. Present and predicted weights are:

	<u>Pilot Present and SRE</u>	<u>Pilot Expected</u>
Gimbaled Weight	3,286 kg	2,207 kg
Total Weight Including Foundation	6,112 kg	5,019 kg

A detailed weight breakdown is as stated above shown on Page 3-33.

HELIOSTAT PARTS COUNT

A listing of heliostat parts was provided in reference 2 cost document. The breakdown of the parts is shown on Page 3-6 by major assembly. Of the 433 parts in a heliostat, 336 of them are in the electronics. This parts count will be about the same for the commercial and pilot plants.

FOUNDATION AND FIELD WIRING

Based upon calculations using site soil bearing pressures the pilot plant foundations will need to be about twice the area of the SRE foundations. Factors affecting this include (1) the shear modules of 300 psi for Barstow (Florida is higher), (2) the seismic load requirements (Florida has more), and (3) the heavy frame made for I-beams. Thus because of these factors the 3 foot by 5 foot foundation used in Florida for the SRE will be replaced by the 6 foot by 10 foot foundations being 1 foot deep.

Field wiring for power distribution signal distribution and field instrumentation are shown on Page 3-67 in some detail and are not repeated here for sake of brevity. The attached Figure A-7 was provided by Black and Veatch and shows more details of the power wiring in the field.

NONSTANDARD PARTS

The heliostat as configured by Honeywell does not use nonstandard parts as defined by "unique" or excessive machining tolerances or special materials such as toxic, fragile or frangible metals. Certain parts are custom made for the heliostat but an attempt was made to minimize these parts.

Any part with a Honeywell part number such as 34027499 is a custom part for the heliostat, thus in that specific part (tie rod assembly) standard tubing is mashed flat on each end and a plate with a nut on it is welded to the tube. While each element or part is standard or commercially available the exact configuration for the heliostat is custom or nonstandard.

Page 6-37 contains more data on long lead and sole source parts. Table A-5 lists some more significant parts which are nonstandard parts per the above.

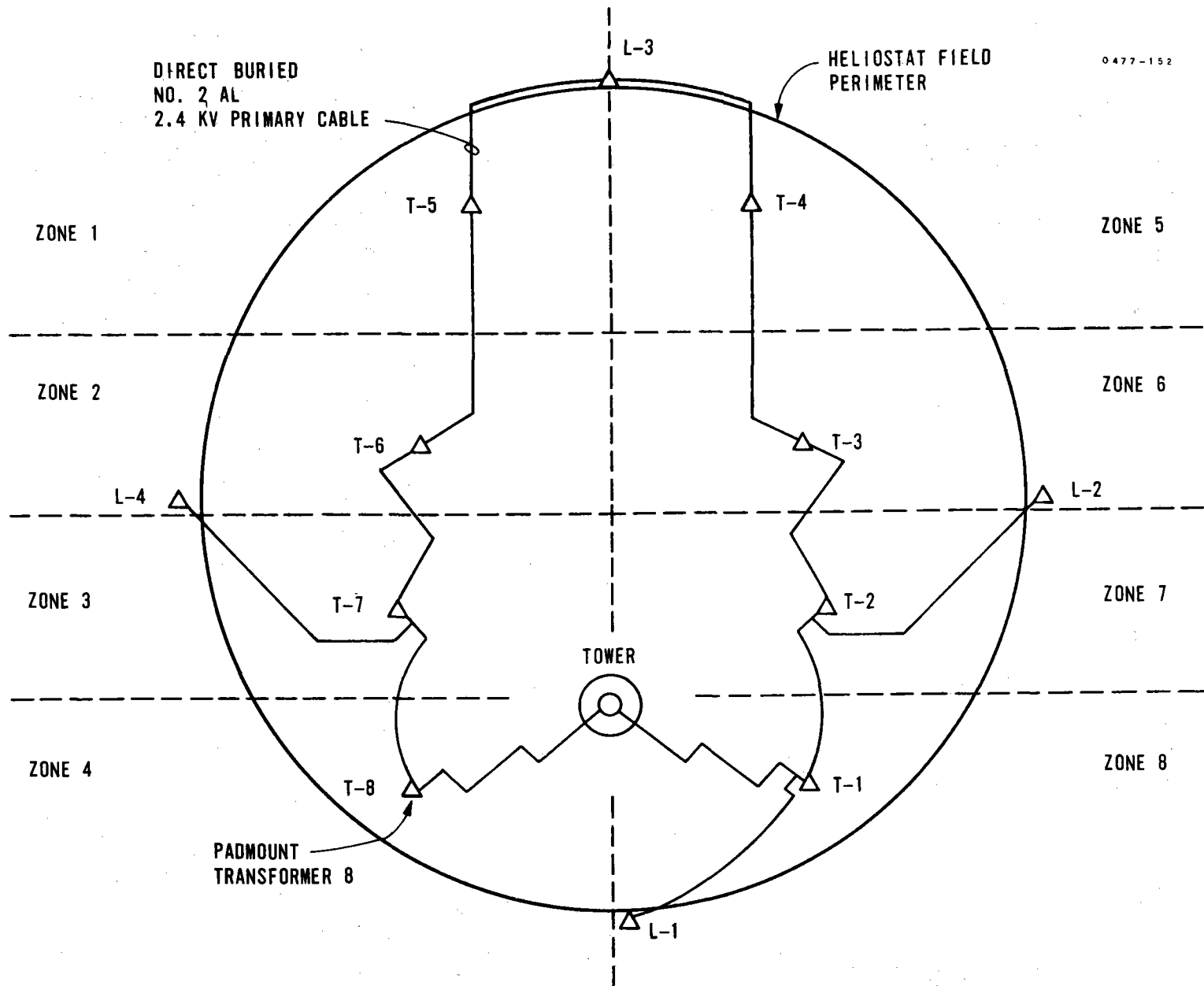


Figure A-7. Heliostat Field Primary Distribution System
Equipment Layout

Table A-5. Nonstandard and Sole Sources Parts

Nonstandard		Sole Source	
Part No.	Description	Part No.	Description
34027499	Tie Rod Assy	RR-3/4	Pillow Block
34027498	Actuator Bracket Assy	RAK-1 15/16	Pillow Block
34026597	Pivot Block	MHP-23	Spring, Preload
34026595	Mirror Module	D51-10245-02	Reductor
34026496	Frame Assembly	34026575	Mirror Module
34026613	Spur Gear	T1811	Inland Motor
34026615	Bearing Support Assy		
34026616	Bearing Retainer		
34026579	Crank Arm		
34026600	Taper Lock		
34027495	Support and Post Assy		
01-504-0120-4	Ball Screw Assy		
D51-10245-02	Reductor		

SOLE SOURCE PARTS

Specifically where a vendor part number is used (for example, RR-3/4) technically that exact part (a 3/4 inch pillow block bearing) is available from only one vendor but that vendor's competitors provide similar hardware under a different part number. To be complete and responsive we have listed several of these parts as sole source though we fully realize additional sources can be developed.

The mirror module is now a sole source but additional sources can be developed to meet program requirements. It is also listed on Page 6-37 as a long lead part as there are 1600 x 4 or 6400 units needed. With 10 to 12 months to full production this can be a pacing term.

Based upon the data in Table A-6 and our experience during the SRE procurement of pilot plant quantities will not constitute a problem and multiple sources generally are not deemed necessary. For the commercial scale plants and larger, then multiple sources are advised. The mirror modules constitute a special case because of the quantity. The pilot plant requires 6400 mirror modules in a years time; that requires over 533 per month. Based upon these numbers it may be worthwhile to develop an additional source for these parts. Also this approach would lay the foundation for a market with several vendors.

Table A-6. Sole Source Parts

	<u>Present Vendor</u>	<u>Potential Vendors</u>
Mirror Modules	Parsons	Brunswick* (1) Heath Tecna* Maney Aircraft* Hexcel Wirecomb*
Gear Box Reducer	Spiroid	Western Gear* Compudrive* U.S.M.*
Ball Screw Actuator	Limitorque	Duff-Norton Templeton-Kenley* (1) Saginaw Simmons Precision
Motor	Inland	Honeywell-Microswitch
Bearings	FAFNIR	McGill* Timkin SKF Torrington Morse

* Contact and coordination during SRE.
(1) Purchased hardware during SRE.

LONG LEAD PARTS

In general no long lead parts exist on the heliostat. Prudence dictates that planning for manufacturing, shipping and storing large quantities be performed well in advance of needed delivery. Consequently we plan to place certain critical vendors under contract as soon as possible to assure support during detail design and manufacturing planning phases.

Some parts are noted as "long lead" (LL) parts on Page 6-37 but the lead times are shown as 10 to 20 weeks. Note the mirror module vendor indicates 10 to 12 months before full production of approximately 500 per month.

INFANT MORTALITY PARTS

Honeywell has specified screened parts and does not expect to require a burn-in on parts or assemblies. Parts requirements are more fully treated on Page 6-26.

Appendix B
OPERATING CHARACTERISTICS

	<u>Pilot Plant</u>	<u>Commercial Plant</u>	<u>SRE</u>
1. Power required for track, slew, and emergency shutdown	3-64		7-115
2. Heliostat operating modes	3-35	3-35	7-9
3. Control system details and characteristics	3-71		7-1
4. Operation and survival versus environmental conditions	4-56, 7-155		7-155, 7-176
5. Heliostat focusing and alignment procedure	6-1, 6-12		6-12
6. Maintenance required	5-34		
7. Mirror cleaning method	6-22		

Appendix C
DESIGN DISCUSSION

	<u>Pilot Plant</u>	<u>Commercial Plant</u>	<u>SRE</u>
1. Define mirror requirements	3-19	3-19	3-19
2. Discuss mirror assembly details	3-21	3-21	3-21
3. Provide data on degradation rates of mirrors, seals, paint motors, drains, etc.	6-25		6-25
4. Discuss method for safe control of reflected light	6-31	6-31	
5. Discuss fail-safe features	6-32		
6. Discuss availability	5-34		

Appendix D
 HELIOSTAT POWER CONSUMPTION ANALYSIS
 Part 1. Continuous Power Analysis

The following estimates assume the use of low power Schottky T²L.

	<u>+5V</u> ma	<u>+15V</u> ma	<u>-15V</u> ma	<u>+24V</u> ma
1. Communications Interface, 1 per system				
(est) 1.1 Line Receiver	10	0	0	0
1.2 UART	20	0	20	0
Total Per subsystem, system	<u>30</u>	<u>0</u>	<u>20</u>	<u>0</u>
2. Osc and Clock Generator, 1 per system				
(est) 2.1 Flip-Flops (8)	32	0	0	0
2.2 Assorted Gate Chips (3)	11	0	0	0
Total per subsystem, system	<u>43</u>	<u>0</u>	<u>0</u>	<u>0</u>
3. Counter Control, Up/Down Counter, 2 per system				
(est) 3.1 4 bit up/down counters (2)	30	0	0	0
3.2 Assorted Chips (10)	36	0	0	0
Total per subsystem	<u>66</u>	<u>0</u>	<u>0</u>	<u>0</u>
Total per system	132	0	0	0
4. D/A Converters, 2 per system				
4.1 Burr Brown DAC-80 (1)	20	25	25	0
Total per subsystem	<u>20</u>	<u>25</u>	<u>25</u>	<u>0</u>
Total per system	40	50	50	0
5. Scaling and Threshold Amp, 2 per system				
5.1 Op Amps (3)	0	5.25	5.25	0
5.2 Bias Resistors	0	0.15	0.15	0
Total per subsystem	<u>0</u>	<u>5.4</u>	<u>5.4</u>	<u>0</u>
Total per system	0	10.8	10.8	0
6. Power Amp, 3 per system				
6.1 "OFF" Condition				
6.1.1 Leakage, Power Transistors (4)	0	0	0	8
6.1.2 Op Amps (2)	0	3.5	3.5	0
Total per subsystem	<u>0</u>	<u>3.5</u>	<u>3.5</u>	<u>8</u>
Total per system	0	10.5	10.5	24

	<u>+5V</u> ma	<u>+15V</u> ma	<u>-15V</u> ma	<u>+24V</u> ma
6.2 "ON" Condition				
6.2.1 R _B Output Switch (1)	0	0	0	10
6.2.2 R _B Output Switch driver (1)	0	4	0	0
6.2.3 R _B Output Linear Output Trans (1)	0	0	0	16
6.2.4 Quasi Linear Driver IC (1)	0	0	0	4.6
6.2.5 Op Amps (2)	0	3.5	3.5	0
6.2.6 Leakage Power Trans (2)	0	0	0	4
Total per subsystem	<u>0</u>	<u>7.5</u>	<u>3.5</u>	<u>34.6</u>
Total per system	0	22.5	10.5	103.8
7. Encoder, 3 per system				
7.1 Optical Pair Bias (2)	0	10	0	0
7.2 Assorted gates and Inv chips (4)	7.4	0	0	0
7.3 One Shots (6)	66	0	0	0
7.4 Op Amps (2)	<u>0</u>	<u>10.2</u>	<u>8.2</u>	<u>0</u>
Total per subsystem	73.4	20.2	8.2	0
Total per system	220.2	60.6	24.6	0
8. Initialization, 3 per system				
8.1 Op Amps (4)	10	13.7	12	0
8.2 Bias + Load	0	1	0	0
8.3 Logic Elements (2)	7	0	0	0
8.4 Bias for Opto Pairs (3)	<u>0</u>	<u>10</u>	<u>0</u>	<u>0</u>
Total per subsystem	17	24.7	12	0
Total per system	51	74.1	36	0
9. Two Motor Synchronizer, 1 per system				
9.1 Assort Logic (11)	40	0	0	0
9.2 4 Bit Counter	15	0	0	0
9.3 Relays (2)	0	0	0	100
9.4 Op Amp (1) + Bias Res	<u>15</u>	<u>5</u>	<u>4</u>	<u>0</u>
Totals per subsystem, system	70	5	4	100
Full System Current Totals	586	211.0	155.9	124
Full System Watt Totals	2.93	3.165	2.338	2.976

The +5 and ±15 volt power drains total 8.43 watts. For an assumed inverter conversion efficiency of 50%, power from the battery is $8.43/0.5 + 2.976 = 19.8$ watts.

Part 2. Transient Power Analysis

Conditions: Inner Axis 1 step command, T1806H Motor, $V_M = 11$ volts, $T_L = 119$ ft lbs,
 $N = 16000$, $E = 0.2$, $T_{FG} = 0.07$ ft lb, Final Speed = 0.123 deg/sec

Time ms	$1 - e^{-\frac{t}{13.3 \text{ ms}}}$	Gimbal Speed deg/sec	Avg Speed deg/sec	Gimbal Travel arc-sec	Accum Travel arc-sec	I_M amps	W_M watts	Cons Motor Power watt sec	Accum Motor Power watt sec
0	0	0	0	0	0	0	0	0	0
5	0.31	0.038	0.019	0.34	0.34	1.98	21.8	0.109	0.109
10	0.53	0.065	0.051	0.93	1.27	1.68	18.5	0.092	0.201
15	0.68	0.084	0.075	1.34	2.61	1.46	16.1	0.080	0.281
20	0.78	0.096	0.090	1.62	4.23	1.32	14.6	0.073	0.354
25	0.85	0.105	0.100	1.81	6.04	1.23	13.5	0.068	0.422
30	0.89	0.110	0.107	1.93	7.97	1.17	12.8	0.064	0.486
35	0.93	0.115	0.112	2.02	10.0	1.09	12.0	0.060	0.546
40	0.95	0.117	0.116	2.09	12.09	1.08	11.9	0.060	0.605
45	0.97	0.120	0.118	2.13	14.22	1.06	11.7	0.059	0.663
50	0.98	0.121	0.121	2.12	16.4	1.04	11.4	0.057	0.720
196	1.0	0.123	0.123	64.6	81	1.02	11.2	1.634	2.354

D-3

Power at battery level = $\left(\frac{24}{11}\right)(2.354) = 5.136$ watt sec

Conditions: Inner Axis 15 step command, T1806H Motor, $V_M = 22$ volts, $T_L = 119$ ft lbs,
 $N = 16000$, $E = 0.2$, $T_{FG} = 0.07$ ft lbs, Final Speed = 0.356 deg/sec

Time ms	$1 - e^{-\frac{t}{13.3 \text{ ms}}}$	Gimbal Speed deg/sec	Avg Speed deg/sec	Gimbal Travel arc-sec	Accum Travel arc-sec	I_M amps	W_M watts	Cons Motor Power watt sec	Accum Motor Power watt sec
0	0	0	0	0	0	0	0	0	0
5	0.31	0.110	0.055	0.99	0.99	3.81	83.7	0.418	0.418
10	0.53	0.189	0.150	2.69	3.68	2.92	64.4	0.322	0.739
15	0.68	0.242	0.215	3.88	7.56	2.32	51.1	0.256	0.995
20	0.78	0.278	0.260	4.68	12.24	1.91	42.0	0.209	0.785
25	0.85	0.303	0.290	5.23	17.46	1.63	35.8	0.179	0.964
30	0.89	0.317	0.311	5.58	23.04	1.44	31.8	0.159	1.123
35	0.93	0.331	0.324	5.84	28.87	1.31	28.9	0.144	1.267
40	0.95	0.339	0.335	6.03	34.90	1.21	26.7	0.133	1.400
45	0.97	0.346	0.342	6.16	41.06	1.15	25.3	0.126	1.526
50	0.98	0.349	0.347	6.26	47.30	1.10	24.2	0.121	1.647
911	1.0	0.356	0.356	1167.7	1215	1.02	22.4	20.409	22.056

D-4

$$\text{Power at battery level} = \left(\frac{24}{22}\right)(22.056) = 24.061 \text{ watt sec}$$

Conditions: Outer Axis 1 step command, T1804B Motor, $V_M = 22$ volts, $T_L = 258$ ft-lbs,
 $N = 16000$, $E = 0.25$, $T_{FG} = 0.26$ ft lbs, Final Speed = 0.2 deg/sec

Time ms	$1 - e^{-\frac{t}{7.4 \text{ ms}}}$	Gimbal Speed deg/sec	Avg Speed deg/sec	Gimbal Travel arc-sec	Accum Travel arc-sec	I_M amps	W_M watts	Cons Motor Power watt sec	Accum Motor Power watt sec
0	0	0	0	0	0	0	0	0	0
2.5	0.29	0.057	0.028	0.25	0.25	6.09	108.5	0.271	0.271
5.0	0.49	0.098	0.077	0.69	0.72	5.01	89.2	0.233	0.494
7.5	0.64	0.127	0.122	1.01	1.73	4.24	75.5	0.188	0.682
10	0.74	0.148	0.137	1.23	2.96	3.69	65.7	0.164	0.846
12.5	0.81	0.162	0.155	1.39	4.35	3.29	58.6	0.146	0.992
15.0	0.87	0.174	0.168	1.51	5.86	3.00	53.4	0.134	1.125
17.5	0.91	0.182	0.178	1.60	7.47	2.78	49.5	0.124	1.249
20.0	0.93	0.186	0.184	1.66	9.12	2.65	47.2	0.118	1.367
22.5	0.95	0.190	0.188	1.69	10.82	2.56	45.6	0.114	1.481
25	0.97	0.194	0.192	1.73	12.54	2.47	44.0	0.110	1.591
27.5	0.98	0.196	0.195	1.75	14.30	2.41	42.8	0.107	1.698
30	0.98	0.196	0.195	1.75	16.05	2.41	42.8	0.107	1.804
120	1.0	0.2	0.2	65	81	2.30	40.1	3.620	5.424

D-5

Power for 2 motors at battery level = $2 \left(\frac{24}{22} \right) (5.424) = 11.83$ watt sec

Conditions: Outer Axis 15 step command, T1804B Motor, $V_M = 22$ volts, $T_L = 258$ ft lbs,
 $N = 16000$, $E = 0.25$, $T_{FG} = 0.26$ ft lbs, Final Speed = 0.2 deg/sec.

For the outer axis $V_M = V_{Max} = 22$ volts for either 1 or 15 step commands which means that start-up will be identical for either command. The 15 step analysis will therefore simply pick up at 120 ms where the 1 step analysis left off.

<u>Time</u> <u>ms</u>	$1 - e^{-\frac{t}{7.4 \text{ ms}}}$	<u>Gimbal</u> <u>Speed</u> <u>deg/sec</u>	<u>Avg</u> <u>Speed</u> <u>deg/sec</u>	<u>Gimbal</u> <u>Travel</u> <u>arc-sec</u>	<u>Accum</u> <u>Travel</u> <u>arc-sec</u>	<u>I_M</u> <u>amps</u>	<u>W_M</u> <u>watts</u>	<u>Cons Motor</u> <u>Power</u> <u>watt sec</u>	<u>Accum Motor</u> <u>Power</u> <u>watt sec</u>
120	1.0	0.2	0.2	---	81	2.30	40.1	3.620	5.424
1575	1.0	0.2	0.2	1134	1215	2.30	40.1	63.157	68.58

D-6

Power for 2 such motors at battery level = $2 \left(\frac{24}{22} \right) (68.58) = 149.63$ watt sec

Summary

<u>Gimbal, Condition</u>	<u>Power Watt Sec/Step</u>	<u>Power Watt Sec/Deg</u>	<u>Power Watt Hrs/Deg</u>	<u>Travel Deg/Day</u>	<u>Total Power Watt Hrs/Day</u>
Inner, Track, 1 Step Commands	5.136	228.27	0.06341	90	5.707
Inner, Slew, 15 Step Commands	24.061	71.29	0.01980	450	8.911
Outer, Track, 1 Step Commands	11.83	525.78	0.14605	90	13.144
Outer, Slew, 15 Step Commands	149.63	443.35	0.12315	180	22.167
			TOTAL		49.93 watt hrs/day

Appendix E
PROGRAM LISTING
HELIOSTAT CONTROL PROGRAM

```

1 C HELIOSTAT CONTROL SOFTWARE 4/29/76-JRS, CONTINUING REVISIONS GLB,JGP
2 C
3 C**** DOES TAPE MECHANICS AND CALLS HELIO OR FORTRAN VERSION OF CALRAY
4   7 IDUM = 0
5 C**** INHIBIT INTERRUPTS
6 A   INH
7 A   OCP, '0220
9 C**** DISABLE EXTENDED ADDRESSING
9 A   DXS
10 A  JMP, **1
11 C**** ELIMINATE POSSIBILITY OF EXTRAENEUS INTERRUPTS
12 A   CRA
13 A   SMK, '0020
14 A   SMK, '0120
15 A   SMK, '0220
16 A   SMK, '0320
17   WRITE(1,111)
18   READ(1,444) IANS
19   IF(IANS.EQ.1HH) GO TO 4
20   IF(IANS.EQ.1HC) GO TO 5
21   WRITE(1,222)
22   READ(1,555) NEOF
23   IF(NEOF) 1,2,3
24 C
25   1 REWIND 6
26   GO TO 7
27 C
28   2 ENDFILE 6
29   GO TO 7
30 C
31   3 REWIND 6
32   DO 10 I=1,NEOF
33 A   CALL,C#FF
34 A   DEC,2
35   10 CONTINUE
36   GO TO 7
37 C
38   4 CALL HELIO
39   GO TO 7
40   5 CALL CALRAY
41   GO TO 7
42 C
43   888 STOP
44   111 FORMAT(///, ' HELIO, CALRAY, OR TAPE MECH. * (H/C/T) ')
45   222 FORMAT(/, ' TO REWIND ONLY          TYPE -1'
46   +         /, ' TO WRITE AN EOF          TYPE 0'
47   +         /, ' TO SKIP N EOFS          TYPE +N, ' )
48   444 FORMAT(A1)
49   555 FORMAT(I5)
50   END

```

0 FORTRAN ERRORS

\$FN-24-32 41204082-614 A

```
51     SUBROUTINE CALRAY
52 CC***  FORTRAN CALRAY ROUTINE
53     COMMON /CALIB/ ICRAY, ICAL(14,16), INEAT(16)
54     COMMON/WRITE6/DAYS, HOURS, AMINS, SECS, M(4), B(8), H(8), A(8), GINNER(4),
55     +GOUTER(4), GOUT(4), AZSUN, ELSUN, RELSUN, REFRAC, DELVER, DELHOR
56     COMMON/FLAG/ IFLAG, IENBHS, ICALF, ISKIP, ISUNY
57 C
58 C  SETUP INTERRUPTS (REAL TIME AND CAL ARRAY)
59     CALL INIDAP
60     REFRAC=.0149
61     DELHOR=0.
62     DELVER=0.
63 C  ENTER START GMT
64     WRITE(1,111)
65     READ(1,222) DAYS, HOURS, AMINS
66 C  SET CONTROL FLAGS TO DISABLE HELIOSTAT TRACKING
67     ISKIP = 0
68     IENBHS = -1
69     SECS = 59.
70 C  SITE INITIALIZATION
71     CALL SINIT
72 C  RESET INTERRUPT AND RUN REAL TIME CLOCK
73 A     OCP, '0020
74 C  GET CALRAY SNAPSHOT FIRST SEC. OF EACH AVAILABLE MINUTE
75     11 IF( SECS. NE. 0. ) GO TO 22
76     CALL SNPSHT
77     CALL SSWTCH(1,J)
78     IF(J.EQ.1) GO TO 33
79     22 GO TO 11
80     33 RETURN
81     111 FORMAT(30H ENTER GMT DAYS, HOURS, MINS )
82     222 FORMAT(5G10.0)
83     END
```

0 FORTRAN ERRORS

\$FN-24-32 41204082-614 A

```

84     SUBROUTINE SNPSHT
85 C*** CALRAY SNAPSHOT ROUTINE
86     COMMON/CALIB/ ICRAV, ICAL(14,16), IW(16)
87     COMMON/WRITES/DAYS, HOURS, AMINS, SECS, M(4), B(8), H(8), A(8), GINNER(4),
88     +GOUTER(4), GOUT(4), AZSUN, ELSUN, RELSUN, REFRAC, DELVER, DELHOR
89     COMMON/FLAG/ IFLAG, IENBHS, ICALF, ISKIP, ISUNY
90     INTEGER IC(224), ICALS(14,16), ICS(224)
91     EQUIVALENCE (ICALS(1,1), ICS(1)), (ICAL(1,1), IC(1))
92 C
93 C STORE ICAL DATA IN BUFFER
94     DVER = DELVER
95     DHOR = DELHOR
96     ICLSUM = ISUNY
97     DO 224 I=1,224
98     ICS(I) = IC(I)
99     224 CONTINUE
100 C
101 C ENABLE ASR IN OUTPUT MODE AND WRITE OUT CALRAY MATRIX
102 A     OCP, 104
103     WRITE(1,100) DAYS, HOURS, AMINS
104     WRITE(1,111)
105     DO 14 I=1,14
106     WRITE(1,222) (ICALS(I,J), J=1,16)
107     14 CONTINUE
108     WRITE(1,333) DVER, DHOR, ICLSUM, AZSUN, RELSUN
109     RETURN
110     100 FORMAT(// ' DAYS/HOURS/MINS = ', F6.0, 1H/, F6.0, 1H/, F6.0)
111     111 FORMAT(//)
112     222 FORMAT(2H  ,16I4, //)
113     333 FORMAT(// ' DELVER=', F7.2, ' DELHOR=', F7.2, ' CALSUM=', I6,
114     +// ' AZSUN=', F10.3, ' RELSUN=', F10.3, //)
115     END

```

0 FORTRAN ERRORS

#FN-24-32 41204082-614 A

```

116 SUBROUTINE SINIT
117 C**** SITE INITIALIZATION ROUTINE
118 COMMON /WRITE6/ DAYS, IDUM(94)
119 COMMON/MISC/ANMEAN, AMDOT, RLAT, SLAT, CLAT, SINCL, CINCL, OMEG, SINW, COSW
120 C NAUTICAL ALMANAC CONSTANTS. UPDATE ANNUALLY EACH JANUARY 1.
121 REAL JULDAT, LATI, LONG
122 DATA YEAR/76., JULDAT/2442777.5/, GHAA/6.5867/
123 C LOCAL GEODETIC COORDINATES
124 DATA LATI/27.8941/, LONG/82.7253/
125 DATA DTORAD/1.745329E-2/, RTODEG/57.29578/
126 C
127 11 D=JULDAT-2415020.
128 T=D/36525.
129 ARGPGE=281.2208+4.70684E-5*D+4.53E-4*T**2
130 TEMP= 9856003*(D-YEAR*360.)-5.183904*YEAR
131 ANMEAN=(TEMP+358.4758-5.686E-3-1.5E-4*T**2)*DTORAD
132 ANMEAN=356.27515*DTORAD
133 ECLPIN=(23.45229-1.30125E-2*T)*DTORAD
134 AMDOT=1.720279E-2
135 RLAT=LATI*DTORAD
136 SLAT=SIN(RLAT)
137 CLAT=COS(RLAT)
138 SINCL=SIN(ECLPIN)
139 CINCL=COS(ECLPIN)
140 OMEG= GHAA*15. +LONG*2.7379E-3-LONG
141 C
142 C DAY DEPENDENT PORTION
143 22 W=(ARGPGE+4.70684E-5*(DAYS+.71))*DTORAD
144 SINW=SIN(W)
145 COSW=COS(W)
146 RETURN
147 END

```

```

0 FORTRAN ERRORS
$FN-24-32 41204082-614 A

```

```

148       SUBROUTINE HELIO
149 C
150 C UP, EAST, NORTH HELIOSTAT CENTERED COORDINATE FRAME.
151 C BASE DISTANCE MEASURED HORIZONTALLY IN FEET FROM THE MIRROR SURFACE
152 C TO A POINT (C) AT THE SAME LEVEL BELOW THE TARGET.
153 C HEIGHT MEASURED VERTICALLY IN FEET FROM POINT (C) TO THE TGT CENTROID
154 C AZIMUTH MEASURED CLOCKWISE FROM TRUE NORTH IN DEGREES TO THE
155 C BASELINE AIMED AT THE TARGET FROM THE HELIOSTAT.
156 C HELIOSTAT OUTER AXIS NON-RIGHT TRIANGLE FIXED LEGS ARE 34 IN. AND
157 C 43.32436 IN. RESULTING IN A REFERENCE SCREW LENGTH OF 52.464 IN.
158 C THE REFERENCE ANGLE IN RADS IS 1.4754 = 84.537 DEG.
159 C THE NOMINAL VALUES OF RFSCRL, ALEG, BLEG, MAY BE CHANGED BY ASR INPUT
160 C THE CAL ARRAY IS 14,16 (ROWS, COLUMNS) AND IS INPUT BY COLUMNS.
161 C
162       COMMON /CALIB/ ICRAY, ICAL(14,16), IWERT(16)
163       COMMON/WRITE6/DAYS, HOURS, AMINS, SECS, M(4), B(8), H(8), A(8), GINNER(4),
164 +GOUTER(4), GOUT(4), AZSUN, ELSUN, RELSUN, REFRAC, DELVER, DELHOR
165       COMMON/DCOS/DC1(4), DC2(4), DC3(4), SDC1(4), SDC2(4), SDC3(4)
166       COMMON/MISC/ANMEAN, AMDOT, RLAT, SLAT, CLAT, SINCL, OMEG, SINW, COSW
167       COMMON/AZIM/ASIN(4), ACOS(4), SASIN(4), SACOS(4)
168       COMMON/FLAG/ IFLAG, IENBHS, ICALF, ISKIP, ISUNY
169       COMMON/SCALE/ SFO(4), SFI(4)
170       COMMON/DELTA/ DEL(4), SDEL(4), CDEL(4)
171       COMMON/COMND/ KC(4), NPO(4), NPI(4)
172       COMMON/REFER/ RFSCRL(4), RF2AB(4), RFA2B2(4), RFANGR(4)
173       COMMON/XTRAS/ COSSVN(4)
174       INTEGER ICALR(240)
175       EQUIVALENCE (ICALR(1), ICAL(1,1))
176       REAL ALEG(4), BLEG(4), GRI(4)
177 C DEFAULT VALUES OF BASE HEIGHT AND AZIMUTH
178       DATA B, H, A/8*1000., 8*55., 8*0. /
179       DATA ALEG/4*34. /, BLEG/4*43.32436/, RFSCRL/4*52.464/
180 C OUTER AXIS SINGLE PULSE SCALE FACTOR(SFO), INNER AXIS GEAR RATIO(GRI)
181       DATA SFO/4* .01185/
182       DATA GRI/4*16158. /
183       DATA DEL/4*0. /
184       DATA DTORAD/1.745329E-2/, RTODEG/57.29578/
185 C
186 C INPUT HELIOSTAT PARAMETERS UNDER SENSE SWITCH CONTROL
187       DO 20 I=1,4
188         M(I)=5
189         CALL SSWTCH(I,J)
190         IF (J .EQ. 2) GO TO 20
191         WRITE(1,10) I
192         READ(1,15)      B(I), H(I), A(I), B(I+4), H(I+4), A(I+4), DEL(I)
193         WRITE(1,16)
194         READ(1,15) XGRI, XSFO, XSCRL, XALEG, XBLEG
195         IF(XGRI.GT.15000. .AND. XGRI.LT.17000. ) GRI(I) = XGRI
196         IF(XSFO.GT.0.01 .AND. XSFO.LT.0.02) SFO(I) = XSFO
197         IF(XSCRL.GT.50. .AND. XSCRL.LT.60) RFS RL(I) = XSCRL
198         IF(XALEG.GT.30. .AND. XALEG.LT.50. ) ALEG(I) = XALEG
199         IF(XBLEG.GT.30. .AND. XBLEG.LT.50. ) BLEG(I) = XBLEG
200 C
201       10 FORMAT(/' ENTER BASE, HGHT, AZ, BASE, HGHT, AZ, DEL OF HS',I1/)
202       15 FORMAT( 7G10.0)
203       16 FORMAT(/' ENTER GRI, SFO, RFSCRL, ALEG, BLEG' /)

```



```

204 20 CONTINUE
205 C
206 C CALCULATE DERIVED HELIOSTAT PARAMETERS
207 DO 30 I=1,4
208     ELEV=ATAN2(H(I),B(I))
209     ASIN(I)=SIN(A(I)*DTORAD)
210     ACOS(I)=COS(A(I)*DTORAD)
211     CDEL(I) = COS(DEL(I)*DTORAD)
212     SDEL(I) = SIN(DEL(I)*DTORAD)
213     DC1(I)=SIN(ELEV)
214     DC2(I)=COS(ELEV)*ASIN(I)
215     DC3(I)=COS(ELEV)*ACOS(I)
216     ELEV=ATAN2(H(I+4),B(I+4))
217     SASIN(I)=SIN(A(I+4)*DTORAD)
218     SACOS(I)=COS(A(I+4)*DTORAD)
219     SDC1(I)=SIN(ELEV)
220     SDC2(I)=COS(ELEV)*SASIN(I)
221     SDC3(I)=COS(ELEV)*SACOS(I)
222     RF2AB(I) = 2. *ALEG(I)*BLEG(I)
223     RFA2B2(I) = ALEG(I)**2 + BLEG(I)**2
224     COSANG = (RFA2B2(I) - RFSCRL(I)**2)/RF2AB(I)
225     SINANG = SQRT(1. - COSANG**2)
226     RFANGR(I) = ATAN2(SINANG, COSANG)
227     SFI(I) = 360. /GRI(I)
228 30 CONTINUE
229 C
230 C FALL THRU OR BRANCH HERE FOR RESET OF GMT
231 33 CONTINUE
232 A   INH
233 C INITIALIZE FLAGS ETC.
234     IFLAG=0
235     MESSGE=0
236     ICALF=0
237     IDFLG = +1
238     INFLG = -1
239     INFLG = +1
240     ISKIP = +1
241     ISUNY = 0
242     DELVER=0.
243     DELHOR=0.
244     REFRAC=.0149
245     SECS=59.
246 C CALL DAP ROUTINE TO SET UP CHANNELS AND INTERRUPTS
247     CALL INIDAP
248     WRITE(1,35)
249     READ(1,40) DAYS,HOURS,AMINS
250     35 FORMAT(30H ENTER GMT DAYS, HOURS, MINS )
251     40 FORMAT(5G10.0)
252 C SITE INITIALIZATION FOR SUN POSITION CALCULATION IN PRIORITY BLOCK
253     CALL SINIT
254 C RESET INTERRUPT REQUEST AND RUN CLOCK
255 A     COP, /0020
256 C KEEP HELIOSTATS DISABLED UNTIL THRU PRIORITY BLOCK ONCE
257     99 IENBHS = 0
258     IF(IFLAG.EQ.0) GO TO 99
259     IENBHS=1

```

```

260 C
261 C***** BEGIN NON-PRIORITY BLOCK
262 100 IF (IFLAG .EQ. 0) GO TO 200
263 IFLAG=0
264 IF (IDFLG .LT. 0) GO TO 130
265 WRITE(6) DAYS, HOURS, AMINS, SECS, M, B, H, A, GINNER, GOUTER, GOUT, DC1, DC2,
266 +DC3, SDC1, SDC2, SDC3, AZSUN, ELSUN, RELSUN, REFRAC, DELVER, DELHOR,
267 +ICAL, IWEAT
268 130 CONTINUE
269 ICALSM = ISUNY
270 C ENABLE ASR 35 IN OUTPUT MODE
271 A OCP, 124
272 DO 150 IP=1, 4
273 CALL SSWTCH(IP, IX)
274 IF (IX .EQ. 2) GO TO 150
275 WRITE(1, 180) HOURS, AMINS, IP, M(IP), GOUT(IP), GINNER(IP), AZSUN,
276 +RELSUN, DELVER, DELHOR
277 IF (INFLG .GT. 0 .OR. M(IP) .EQ. 1) WRITE(1, 181) NPO(IP), NPI(IP),
278 + H(IP), A(IP), ICALSM
279 150 CONTINUE
280 IF (IWFLG .LT. 0) GO TO 190
281 PYRO = ICALR(236) + 15.4
282 PHOTOCL = ICALR(232)
283 RATIO = 0.
284 IF (PHOTOCL .GT. 0.) RATIO = PYRO/PHOTOCL
285 ENERGY = 20.82*(5.655*PYRO + 87.2)*RATIO*ICALSM/224.
286 WRITE(1, 183) RATIO, ENERGY, COSSVN
287 WRITE(1, 182) IWEAT
288 180 FORMAT(1H, 2F3. 0, 2I3, 4F9. 4, 2F8. 2)
289 181 FORMAT(1H, 14X, I6, 2X, I6, 2F11. 4, 2X, I6)
290 182 FORMAT(1H, 16I4)
291 183 FORMAT(' RATIO=', F7. 4, ', ENERGY=', F7. 0, ', COSSVN=', 4F7. 4)
292 190 CONTINUE
293 C SKIP IF ASR NOT BUSY
294 A SKS, 104
295 GO TO 190
296 195 CONTINUE
297 A OCP, 4
298 C
299 200 IF (MESSAGE .EQ. 0) GO TO 210
300 MESSAGE=0
301 WRITE(1, 205) IHS, M(IHS), HOURS, AMINS
302 205 FORMAT(4H HS, I1, 6H MODE, I1, 6H TIME, 3F3. 0)
303 207 CONTINUE
304 A SKS, 104
305 GO TO 207
306 208 CONTINUE
307 C ENABLE ASR 35 IN INPUT MODE
308 A OCP, 4
309 210 CONTINUE
310 A INA, 1004
311 GO TO 100
312 213 CONTINUE
313 ICAR=
314 C IF ICAR IS A T GO INPUT NEW TIME
315 IF (ICAR .EQ. :324) GO TO 33

```

```
316 C IF ICAR IS A D CHANGE IDFLG,WRITE DATA TO TAPE WHEN IDFLG .EQ. 1
317   IF(ICAR .EQ. :304) IDFLG = -IDFLG
318 C IF INFLG .EQ. 1 WRITE NET NUMBER OF PULSES TO ASR
319   IF(ICAR .EQ. :316) INFLG = -INFLG
320 C IF IWFLG IS ONE WEATHER DATA IS WRITTEN TO ASR
321   IF(ICAR .EQ. :327) IWFLG = -IWFLG
322 C IF THE INPUT CHARACTER IS AN H MODE WILL BE UPDATED
323   IF (ICAR .EQ. :310) GO TO 214
324 C IF R RETURNS TO MAIN ROUTINE TO DO TAPE MECHANICS
325   IF(ICAR .EQ. :322) RETURN
326 C IF S GET CALRAY SNAPSHOT
327   IF(ICAR .EQ. :323) CALL SNPSHT
328   GO TO 100
329   214 READ(1,215) IHS,MODE
330   215 FORMAT(2I1)
331   IF(IHS.LT.1.OR.IHS.GT.4.OR.MODE.LT.1.OR.MODE.GT.6) GO TO 100
332   M(IHS) = MODE
333   MESSAGE=1
334   GO TO 100
335 C
336 C DUMMY CALL TO INSURE PROR GETS LOADED
337   777 CALL PROR
338   END
```

0 FORTRAN ERRORS

*FN-24-32 41204082-614 A

```

339      SUBROUTINE PROR
340 C   PRIORITY INTERRUPT BLOCK CALLED BY REAL TIME INT. SERVICE ROUTINE
341 C   SENDS COMMANDS ONCE EVERY TWO SECONDS
342      COMMON /CALIB/ ICRAY, ICAL(14,16), IWERT(16)
343      REAL MINS
344      COMMON/WRIT6/DAYS, HOURS, MINS, SECS, M(4), B(8), H(8), A(8), GINNER(4),
345 +GOLTER(4), GOUT(4), AZSUN, ELSUN, RELSUN, REFRAC, DELVER, DELHOR
346      COMMON/DCOS/DC1(4), DC2(4), DC3(4), SDC1(4), SDC2(4), SDC3(4)
347      COMMON/MISC/ANMEAN, AMDOT, RLAT, SLAT, CLAT, SINCL, CINCL, OMEG, SINW, COSW
348      COMMON/AZIM/ASIN(4), ACOS(4), SASIN(4), SACOS(4)
349      COMMON/FLAG/ IFLAG, IENBHS, ICALF, ISKIP, ISUNY
350      COMMON/SCALE/ SFO(4), SFI(4)
351      COMMON/DELTA/ DEL(4), SDEL(4), CDEL(4)
352      COMMON/COMND/ KC(4), NPO(4), NPI(4)
353      COMMON/REFER/ RFSCRL(4), RF2AB(4), RFA2B2(4), RFANGR(4)
354      COMMON/XTRAS/ COSSVN(4)
355      REAL WT(16), NORTH
356      DATA DTORAD/1.745329E-2/, RTODEG/57.29578/
357      DATA WT/-7.5, -6.5, -5.5, -4.5, -3.5, -2.5, -1.5, -.5, .5, 1.5, 2.5, 3.5, 4.5,
358 + 5.5, 6.5, 7.5/
359
360 C   UPDATE GREENWICH MEAN TIME
361     250 SECS=SECS+1.
362         ISKIP = -ISKIP
363         TIME=HOURS+MINS/60. +SECS/3600.
364         IF (SECS .LT. 60.) GO TO 320
365         SECS=0.
366         MINS=MINS+1.
367 C   A REG. IS LOADED WITH DATA READY SIGNAL AND SENT ONCE PER MIN
368     =:377
369     302 CONTINUE
370 A   01A, '0115
371     GO TO 302
372     304 CONTINUE
373         ICALF=1
374         IFLAG=1
375         IF (MINS .LT. 60.) GO TO 305
376         MINS=0.
377         HOURS=HOURS+1.0
378         IF (HOURS .LT. 24.) GO TO 305
379         HOURS=0.
380         DAYS=DAYS+1.
381
382 C   COMPUTE SUNS ORBITAL POSITION
383     305 AM=ANMEAN+AMDOT*(DAYS+TIME/24.)
384         AE = 0.
385         DO 310 I=1,3
386     310 AE=AM+.01672*SIN(AE)
387         TEMP1=COS(AE)
388         TEMP2=1. -.01672*TEMP1
389         COSV=(TEMP1-.01672)/TEMP2
390         SINW=(.99986*SIN(AE))/TEMP2
391         EQUAT=COSV*COSW-SINW*SINW
392         TEMP=COSV*SINW+SINW*COSW
393         EASTI=TEMP*CINCL
394         POLAR=TEMP*SINCL

```

```

395 C COMPUTE EARTH FIXED POINTING VECTOR TO SUN
396 320 OMEGA=(OMEG+15.*(DAYS*6.57098E-2+TIME))*DTORAD
397 SINO=SIN(OMEGA)
398 COSO=COS(OMEGA)
399 TEMP=COSO*EQUAT+SINO*EASTI
400 UP=CLAT*TEMP+SLAT*POLAR
401 EAST=COSO*EASTI-SINO*EQUAT
402 NORTH=CLAT*POLAR-SLAT*TEMP
403 TEMP=SQRT(EAST**2+NORTH**2)
404 AZSUN=RTODEG*ATAN2(EAST, NORTH)
405 ELSUN=RTODEG*ATAN2(UP, TEMP)
406 C REFRACTION CORRECTION BUFFERED FOR VERY LOW AND ZERO ELEVATIONS
407 REFCOR = REFRAC*TEMP/(ABS(UP)+1.9E-4)*(1-.0003/(UP*UP+.000302))
408 RELSUN = ELSUN + REFCOR
409 DCS1=SIN(RELSUN*DTORAD)
410 TEMP=COS(RELSUN*DTORAD)
411 DCS2=TEMP*SIN(AZSUN*DTORAD)
412 DCS3=TEMP*COS(AZSUN*DTORAD)
413 C
414 IF(IENBHS.LT.0) GO TO 645
415 IF(SKIP.GT.0.OR.IENBHS.EQ.0) RETURN
416 C COMPUTE RESULTANT UNNORMALIZED HELIOSTAT POINTING VECTOR
417 DO 600 I=1,4
418 IK=M(I)
419 GO TO (430,440,450,460,470,480), IK
420 C CLOSED LOOP TRACK OF PRIMARY TGT, MODE 1
421 430 IF(ICALSM.LT.600) GO TO 440
422 H(I) = H(I) - DELVER
423 ELEV=ATAN2(H(I),B(I))
424 C P(I) = A(I) + ATAN2(DELHOR,B(I))*RTODEG ***EXACT, APPROX USED
425 A(I) = A(I) + DELHOR/B(I)*RTODEG
426 TEMP=A(I)*DTORAD
427 ASIN(I)=SIN(TEMP)
428 ACOS(I)=COS(TEMP)
429 DC1(I)=SIN(ELEV)
430 TEMP=COS(ELEV)
431 DC2(I)=TEMP*ASIN(I)
432 DC3(I)=TEMP*ACOS(I)
433 C INTENTIONAL FALL THRU AT THIS POINT
434 C OPEN LOOP TRACK OF PRIMARY TGT, MODE 2
435 440 V1=DCS1+DC1(I)
436 V2=DCS2+DC2(I)
437 V3=DCS3+DC3(I)
438 AS = ASIN(I)*CDEL(I) + ACOS(I)*SDEL(I)
439 AC = ACOS(I)*CDEL(I) - ASIN(I)*SDEL(I)
440 GO TO 490
441 C OPEN LOOP TRACK OF SECONDARY TGT, MODE 3
442 450 V1=DCS1+SDC1(I)
443 V2=DCS2+SDC2(I)
444 V3=DCS3+SDC3(I)
445 AS = SASIN(I)*CDEL(I) + SACOS(I)*SDEL(I)
446 AC = SACOS(I)*CDEL(I) - SASIN(I)*SDEL(I)
447 GO TO 490
448 C POINT AT SECONDARY TGT, MODE 4
449 460 V1=SDC1(I)
450 V2=SDC2(I)

```

```

451      V3=SDC3(I)
452      AS = SASIN(I)*CDEL(I) + SPCOS(I)*SDEL(I)
453      AC = SACOS(I)*CDEL(I) - SASIN(I)*SDEL(I)
454      GO TO 490
455 C HOME, MODE 5
456 470 KC(I) = 1
457      GOUTER(I) = RFSCLR(I)
458      NPO(I) = 0
459      GOUT(I)=0.
460      GINNER(I)=180.
461      NPI(I) = 180./SFI(I) + 0.5
462      COSSVN(I) = 0.
463      GO TO 600
464 C INITIALIZATION, MODE 6
465 480 KC(I) = 128
466      GOUTER(I) = RFSCLR(I)
467      GOUT(I) = 0.
468      NPO(I) = 0
469      GINNER(I) = 0.
470      NPI(I) = 0
471      COSSVN(I) = 0.
472      GO TO 600
473 C ROTATE 180 - AZ- DEL RELATIVE TO UP-EAST-NORTH COORDINATES
474 490 R1 = V1
475      R2 = -V2*AC + V3*AS
476      R3 = -V2*AS - V3*AC
477 C COMPUTE GIMBAL ANGLES
478 C THETA IS NEGATIVE WHEN NORMAL POINTS TOWARDS TARGET (R3.LT.0)
479      THETA = ATAN2(R3,R1)
480      PHI = ATAN2(R2,SQRT(R1*R1 + R3*R3))*RTODEG
481 C COMPUTE SCREW LENGTH
482      SCREW = SQRT(RFA2B2(I) - RF2AB(I)*COS(RFANGR(I) + THETA))
483 C CALC. COS OF ANGLE BETWEEN SUN VECTOR AND MIRROR NORMAL
484      COSSVN(I) = (V1*DCS1 +V2*DCS2 +V3*DCS3)/SQRT(V1*V1+V2*V2+V3*V3)
485 C FORMAT OUTER AXIS COMMAND. POSITIVE COMMANDS LENGTHEN SCREW
486 C AND ROTATE OUTER AXIS AWAY FROM THE TARGET.
487      ITEMP=(GOUTER(I)-SCREW)/SFO(I)
488      KC(I)=0
489      IF (ITEMP) 510,555,520
490 510 ISIGN = 1
491      ITEMP=-ITEMP
492      KC(I)=KC(I)+16
493      GO TO 530
494 520 ISIGN = -1
495 530 IF(ITEMP.GE.15) GO TO 540
496      KC(I)=KC(I)+32
497      NPO(I) = NPO(I) + ISIGN
498      GO TO 550
499 540 KC(I)=KC(I)+64
500      NPO(I) = NPO(I) + 15*ISIGN
501 550 GOUTER(I) = RFSCLR(I) + SFO(I)*FLOAT(NPO(I))
502      COSANG = (RFA2B2(I) - GOUTER(I)**2)/RF2AB(I)
503      SINANG = SQRT(1. - COSANG*COSANG)
504      GOUT(I) = (ATAN2(SINANG,COSANG) - RFANGR(I))*RTODEG
505 C FORMAT INNER AXIS COMMAND. POSITIVE COMMANDS CAUSE A POSITIVE
506 C ROTATION ABOUT AN AXIS DIRECTED RADIALLY OUTWARD FROM THE TARGET.

```

```

507 555 ITEMP=(PHI-GINNER(I))/SFI(I)
508 KC(I)=KC(I)+2
509 IF(ITEMP) 560, 600, 570
510 560 KC(I)=KC(I)-2
511 ISIGN = - 1
512 ITEMP=-ITEMP
513 GO TO 580
514 570 ISIGN = 1
515 580 IF(ITEMP .GE. 15) GO TO 590
516 KC(I)=KC(I)+4
517 NPI(I) = NPI(I) + ISIGN
518 GO TO 595
519 590 KC(I)=KC(I)+8
520 NPI(I) = NPI(I) + 15*ISIGN
521 595 GINNER(I) = SFI(I)*FLOAT(NPI(I))
522 600 CONTINUE
523 C
524 C ISSUE HELIOSTAT COMMANDS
525 610 CONTINUE
526 =KC(1)
527 A OTA, '0105
528 GO TO 610
529 620 CONTINUE
530 =KC(2)
531 A OTA, '0106
532 GO TO 620
533 630 CONTINUE
534 =KC(3)
535 A OTA, '0130
536 GO TO 630
537 640 CONTINUE
538 =KC(4)
539 A OTA, '0131
540 GO TO 640
541 C
542 C COMPUTE CAL ARRAY CENTROID
543 645 CONTINUE
544 IF (ICALF .EQ. 0) GO TO 730
545 C HANGS TIL CAL ARRAY IS FILLED (240 CHANNELS)
546 C OCTAL CONSTANT 27420 CONSISTANT WITH SETC OF 30000 IN INIDAP
547 650 IF (ICRAY .NE. :27420) GO TO 645
548 ICALF=0
549 CALSUM = 0.
550 WTSUM = 0.
551 DELVER=0.
552 DELHOR=0.
553 DO 700 I=1,14
554 ISUM = 0
555 DO 705 J=1,16
556 705 ISUM = ISUM + ICAL(I,J)
557 CALSUM = CALSUM + ISUM
558 710 WTSUM = WTSUM + ISUM*WT(I+1)
559 ICALSM = CALSUM
560 ISUNY = CALSUM
561 IF (CALSUM .EQ. 0.) RETURN
562 DELVER = -WTSUM/CALSUM

```

```
563 C
564     WTSUM = 0.
565     DO 720 J=1,16
566         ISUM = 0
567         DO 715 I=1,14
568             715 ISUM = ISUM + ICAL(I,J)
569             720 WTSUM = WTSUM + ISUM*WT(J)
570         DELHOR = WTSUM/CALSUM
571         RETURN
572     730 ICALSM = -CALSUM
573     800 CONTINUE
574 C
575 C COMPUTE WEATHER DATA AND REFRACTION CORRECTION
576     RETURN
577     END
```

0 FORTRAN ERRORS
SFN-24-32 41204082-614 A

COMMON BLOCK	LENGTH		ADDRESS
	OCTAL	DECIMAL	
CALIB	000361	241	027417
WRITE6	000140	96	027257
FLAG	000005	5	027252
MISC	000024	20	027226
DCOS	000060	48	027146
AZIM	000040	32	027106
SCALE	000020	16	027066
DELTA	000030	24	027036
COMND	000014	12	027022
REFER	000040	32	026762
XTRAS	000010	8	026752

COMMON LOW 026752
COMMON HIGH 030000

Appendix F
MATERIALS ENGINEERING LABORATORY
TEST REPORT
ON
MATERIALS AND PROCESS DESIGN
FOR
MIRROR MODULE ADHESIVE

Date 11 August 1976

TEST REPORT

MATERIALS ENGINEERING

Page 1 of 11

Subject:

Several epoxy and silicone adhesives were tested and evaluated for high reliability, long service life bonding of Heliostat solar reflective mirrors to structural substrates.

Purpose:

To determine the detail materials and processes design and fabrication requirements for an adhesive system suitable for bonding glass mirrors to a variety of materials used for structural supports. The subsequent structure must withstand service in outdoor environments for 20 to 30 years. Requirements include:

- . Structural Supports, Finish Selection;
- . Mirror Surface Design Considerations:
 - Thermal Expansion Joints,
 - Protective Edge Coatings,
 - Mirror Edge Flaws,
 - Mirror Enamel and Adhesive Compatibility and
 - Mirror Size Effects;
- . Adhesive Material Selection and
- . Adhesive Application Processing Detail.

Conclusions:

Based upon a literature search and followed by an adhesives testing and evaluation program, the following conclusions were reached:

1. Structural Supports:

Materials must be treated with one or more of the appropriate corrosion-resistant finishes:

- . Chromate films,
- . Anodizing,
- . Passivation,
- . Phosphate Conversions or
- . Electroplatings.

These types of finishes provide a suitable adhesive bonding surface for meeting the 20 to 30 year service requirements.

2. Reflective Mirror Surfaces:

The following precautions need to be observed when adhesive bonding glass mirrors:

(a) Thermal Expansion Joints:

To prevent transmitting excessive buckling stresses to both the adhesive bond and the mirrors, provide sufficient thermal expansion dimensional spacing (gapping) so that mirrors never meet.

(b) Protective Edge Coatings:

Common experience indicates that mirrors exposed to outdoor environments require protection of the silver's exposed edge to prevent physical loss of adhesion and chemical corrosive damage to the silver.

Conclusions (continued):2. Reflective Mirror Surfaces (continued):(b) Protective Edge Coatings (continued):

(A number of small mirrors: 1 inch X 1 inch failed to show silver degradation when subjected to laboratory sustained humidity exposures of 140°F, 98% relative humidity for 30 days.)

(c) Mirror Edge Flaws:

To minimize microcracks mirrors must be fabricated to provide a "clean cut" edge. In addition mirror edges must be protected ("guards") from accidental physical damage. Invariably microcracks in the mirror's edge will result in crack propagation; often cracking across the entire face of the mirror.

(d) Mirror Enamel and Adhesive Compatibility:

Adhesives must be free from lacquer thinner solvents and sulfur impurities (such as found in rubber cements) to prevent damage to the mirror's proprietary protective enamel and to the mirror's silver reflective finish. Solvents are usually added to facilitate use of the adhesive by brush, roller, and spray application methods.

(e) Mirror Size Effects:

All silicone and epoxy adhesives (except Peterson Chemical Company's "INSULON 100 - POLY-EP") were acceptable for bonding relatively large glass mirrors to rigid (steel) substrates. See Table I.

3. Adhesive Material Selection:

Silicone adhesive materials will provide tensile butt strengths of 100 to 300 psi (See Table I) over a wide range of thermal exposures for the required 20 to 30 year functional outdoor service life.

Conclusions (continued):3. Adhesive Material Selection (continued):

While silicones are the preferred adhesive for long service life, the epoxy adhesives will also probably (i.e., available hard life data for epoxies is about 10 years) also meet the 20 to 30 service life. The two-part, catalyzed semi-flexible epoxy adhesives will provide tensile butt strengths of 500 psi minimum. The adhesive bonded mirror has a large factor of safety i.e., requirements for relatively mild thermal exposures, low tensile and shear strengths and environmentally protected adhesive bond lines.

4. Adhesive Processing Detail:

Both silicone and epoxy adhesive materials have the desired ease of mixing, sufficient pot-life, spreadability for brush, trowel or roller application, require little to no clamping pressure and cure at ambient, room temperature processing environments.

Discussion and Recommendations:1. Structural Supports:

Analysis: Adhesive bonded joints, exposed to the weather, commonly fail by environmental moisture penetrating into the adhesive's bond line. The moisture migrates along the metal's surface, undermining and displacing the adhesive at the bonding interface, causing subsequent, premature joint failure. To prevent this occurrence, the metal must receive a corrosion resistant finish, e.g. chromate, phosphate, passivation, anodize or electroplating.

Recommend: The various Departments of Defense have issued several excellent government design specifications such as MIL-F-7179, MIL-STD-171 and MIL-STD-1250. These specifications define many suitable surface finishes, acceptable as an adhesive bonding substrate.

2. Reflective (Mirror) Precautionary Design Considerations:

(a) Analysis/Recommendations: The "Conclusions" section provides sufficient insight for "Analysis and Recommendations" of the following areas:

- . Thermal Expansion Joints,
- . Mirror Edge Flaws and
- . Mirror Enamel and Adhesive Compatibility.

(b) Protective Edge Coatings:

Analysis/Recommendations: To prevent chemical, corrosive-degradation of the exposed silver edge from sulfurous compound atmospheres or loss of silver to glass adhesion from moisture penetration, recommendations include:

- . "Cut" the mirror to size; then apply the silver, copper and protective enamel coatings in a manner to cover the silver edge (Preferred Technique),

OR

- . Protect the bare, exposed silver edge with a 5-mil pressure sensitive Teflon tape, treated for adhesive bondability per MIL-T-23594, Type II. The tape should cover the silver edge, extending onto both the mirror's front and back surfaces.

Discussion and Recommendations (continued):2. Reflective (Mirror) Precautionary Design Considerations (con'd):(c) Mirror Edge Restriction:

Analysis: Any condition which prevents the mirror from expanding or contracting freely with rising and falling temperatures induces compressive ("buckling") or tensile stresses into the mirror. The mirror surface in tension will eventually micro-fracture, with subsequent cracks propagating across the face of the mirror.

RECOMMEND: Avoid massive adhesive fillets at the edges of the mirror and avoid snug-fitting, metal edge protectors ("guards").

(d) Brittle Adhesive; Large Mirror Size Effects:

Analysis: RIGID epoxy adhesives may lack sufficient elasticity for adhesive bonding of large (60 inches X 60 inches) mirror panels. Under these conditions, adhesive bonds exposed to fluctuating high and low outdoor temperatures, can fracture the adhesive, particularly at the extremities (edges). While this fracture does not jeopardize the structural integrity of the adhesive bond, the fracture will provide an undesirable capillary crack ("wick") to environmental moisture. Entrance of moisture, particularly with freezing temperatures, may cause eventual mirror fracture. The adhesive failure is commonly due to the following:

- . Mis-Matched Materials: (*) Different substrate materials, sometimes with widely different thermal coefficients of expansion and contraction, cause stress conditions exceeding the adhesive's joint strength.
- . Adhesive Brittleness: RIGID epoxy adhesives lack sufficient elasticity "to stretch"; to accommodate to the dynamic changing of joint dimensions encountered during thermal exposures. The semi-rigid and flexible epoxies, as well as all silicones, however, have adequate elasticity to meet Program service requirements.

(*) See Table I: Note 10.

Discussion and Recommendations (continued):

2. Reflective (Mirror) Precautionary Design Considerations (con'd):

(d) Brittle Adhesive; Large Mirror Size Effects (continued):

Recommend: With the exception of the Peterson Chemical Company's epoxy "INSULON 100 - POLY-EP"(*), all adhesives listed in Table I have sufficient flexibility for bonding the Heliostat mirror panels.

(*) This material is intended to be used as a coating; not as an adhesive. It was selected purposely to show the danger of using a solvent-thinned adhesive.

3. Adhesive Material Selection:

Analysis: The desirable adhesive material properties and a comparison of the preferred type of adhesives are provided in the following tabulation:

DESIRABLE ADHESIVE MATERIAL PROPERTIES	PREFERRED TYPE OF ADHESIVE : "X"	
	EPOXY	SILICONE
. Compatibility of Mirror's Protective Enamel with Adhesive		X
. Sufficient Pot-Life for Application and Installation	---About Equal Merit---	
. Low Viscosity for Application Ease (Brush, Spray, Roller or Trowel)		X
. Ambient Room Temperature Curing, Minimal Clamping	X	
. Toxicity		X
. Service Life Capability		X
. Available and Inexpensive	X	

Discussion and Recommendations (continued):3. Adhesive Material Selection (continued):

Initially three families of adhesives were proposed: epoxies, silicones and polyurethanes. (The commercial/industrial "mastics" and "contact cements" are unsatisfactory due to short service life expectancies with outdoor exposures. As mentioned previously, contact cements invariably contain lacquer solvents, detrimental to the mirror's enamel coating.) After an initial examination, the polyurethanes were dropped from consideration, since many polyurethanes have relatively high toxicity of the curing agents (isocyanates) and curing temperature requirements of 150°F, minimum (unfeasible for the Helio-stat hardware).

RECOMMEND: Silicone adhesives are the preferred choice since there are no environmental hard life data for epoxy adhesives beyond 10 years.

4. Adhesive Application Processing Detail:

Analysis: The silicone and epoxies must be two-part, resin-catalyzed systems. The formulations (metering out) must be accurate. Pot-lives are typically one hour at 75°F, not long, but sufficient to complete bonding.

The application method selected (e.g. brush, trowel, roller and spray) must result in a uniform adhesive bond line thickness (preferably 0.003 to 0.007 inch), to provide and facilitate mirror panel flatness. To best meet the desired thickness objective, adhesives need to be solvent thinned and applied by spray application. However, this IS NOT acceptable for epoxies since epoxies require lacquer solvents (which are damaging to the mirror's protective enamel). This IS acceptable for silicones since thinning can be accomplished with a rapid evaporating solvent, non-damaging to the mirror's enamel (e.g. "Freon TF"). Consequently, solvent thinned, spray applied silicone adhesives show a significant application advantage both in ease and precise bond line thickness control. Epoxies however, will require a trowel, brush or roller application usually in the "As-Mixed" (unthinned) condition. The following tabulation of adhesive viscosities (compared to common liquids; water and motor oils) gives an indication of the adhesive's application spreadability:

Discussion and Recommendations (continued):4. Adhesive Application Processing Detail (continued):

<u>MATERIAL</u>	<u>VISCOSITY (Centipoises)</u>
Water	1
Epoxy: "Poly-Ep"	50
Motor Oil, SAE 10	55
SAE 30	250
SAE 50	650
Epoxy: "EC 2216"	10,000
Silicone: "RTV 11"	40,000
Silicone: "RTV 93-076"	300,000

Silicones require a preliminary priming of all surfaces to be adhesive bonded. Epoxies do not require a primer. For the best adhesive bonding, the adhesives should be applied to both the mirror and the structural support.

Both silicone and epoxy adhesives need clamping pressures of a few pounds per square inch, sufficient to provide uniform mirror flatness and reduce bond line voids. Vacuum bag clamping techniques are quite acceptable. Localized clamping methods such as "C-Clamps" and "Dead-Weights" are unacceptable.

Epoxies cure fully in a few days at ambient room temperatures, while silicones require seven days for full strength properties. From a practical consideration, the adhesive bonded equipment can be "moved about" after 36 hours for epoxies and 96 hours for silicones. The adhesives continue to polymerize to complete full cure "in situ", within seven days.

Recommend: Both silicone and epoxy adhesives have suitable application properties. Silicones have an added advantage over epoxies, i.e. silicones can be spray applied to precise adhesive bond line thickness to achieve mirror lay-up flatness.

TABLE I

ADHESIVE SYSTEMS: BUTT TENSILE STRENGTHS⁽¹⁾ (PSI)

ADHESIVE SYSTEM (2)(5)(6)	TEST BAR, ADHESIVE BONDED ⁽³⁾⁽⁴⁾⁽¹⁰⁾		
	Left	Center	Right
. Epoxy: 2216 (No Beads)	(7) > 600	> 840	> 660
. Epoxy: 2216 (With Beads)	> 920	> 730	> 700
. Silicone: RTV 11 (No Beads)	328	212	325
. Silicone: RTV 11 (With Beads)	178	181	152
. Silicone: RTV 560 (No Beads)	123	137	215
. Silicone: RTV 560 (With Beads)	94	77	65
. Epoxy: Poly-Ep (No Beads)	(8) 66	44	31
. Epoxy: Poly-Ep (With Beads)	(9) ---	(9) ---	(9) ---
. Epox-Sil-Rub (No Beads)	> 545	> 723	556
. Epox-Sil-Rub (With Beads)	171	162	188

NOTES:

(1) Butt tensile testing was selected (instead of lap shear) to reduce the tendency of failure in the glass.

(2) Adhesive Materials Tested:(a) Epoxies:

- . 3M Co., "EC-2216, Unfilled, Amber"
St. Paul, Minnesota
- . Peterson Chemical Company
"Insulon 100 (Poly-Ep)"
Sheboygon, Wisconsin

(b) Epoxy-Silicone:

- Isochem Resins Company
"Epox-Sil-Rub 400/411/114"
Lincoln, R. I.

(c) Silicones^(*):

- . General Electric Company "RTV 11"
Waterford, New York
- . General Electric Company "RTV 56"
Waterford, New York
- . Dow Corning Corp., "RTV 93-076"
Midland, Michigan
(Not tested: Viscosity too high)

(*) G.E.'s Silicone Primer "SS4004" was used prior to adhesive application.

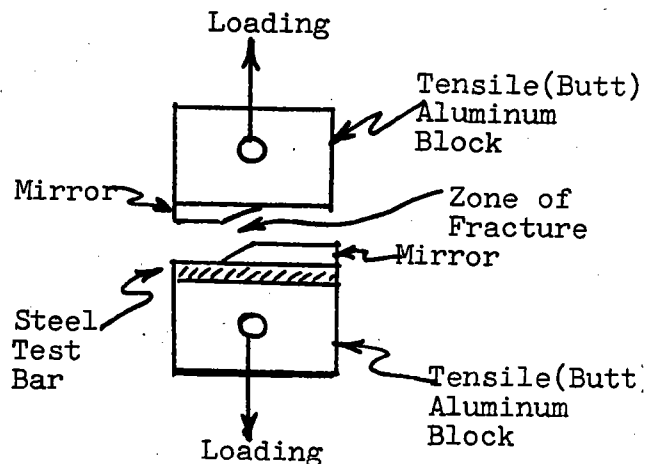
TABLE I
(continued)

Adhesive Systems: Butt Tensile Strengths (PSI)

NOTES:

- 3) Adhesive Bonded Test Bar:
Glass mirror, adhesive bonded to steel strips: 1" X 42" X 1/4"
- 4) Adhesive Test Coupons:
After thermal cycling tests:
0° to +140°F (2 hr. duration)
84 continuous cycles
(Temp. dwells @ 0°F = 15 min.)
(@ 140°F = 30 min.)
Coupons were cut from the left and right extremities, and also from the center of the test bar.
- 5) Glass Beads (.015 inch dia.):
Beads were added to the adhesive, to provide controlled .015" spacing of the bond line. With no beads, the bond line was approx. .003 inch.
- 6) Miscellaneous Butt Tensile Tests:
MPE's ETR No. 15992:
(a) Parsons: Mirror/Aluminum Honeycomb Structure:
Butt tensile strengths ranged from 242 to 538 psi (4 samples). The adhesive consisted of an epoxy: "EPON 828 Resin/DTA Hardener"
(b) Brunswick: Mirror/Steel Structure:
Butt tensile strengths ranged from 25 to 68 psi (4 samples). (The structure consisted of the mirrors bonded to a "Paint Grip Galvanized" steel with "Formica" type contact cement.)

- (7) Fracture of the Mirror:
The "greater than" sign (>) indicates failures occurred by cohesive fracturing of the glass mirror and adhesive failure of the mirror to the aluminum tensile block, typically as shown:



- (8) Mirror Enamel Coating/Adhesive Solvent Incompatibility:
This epoxy (coating) contains a lacquer solvent which softened the mirror enamel resulting in low adhesive test strength values.
- (9) Thermal Cycle Failure:
The use of .015 inch dia. glass beads, in conjunction with the large amount of solvent thinner used in this epoxy (coating) resulted in large voids in the adhesive bond line; causing low adhesive bond strengths and premature failure during thermal cycle testing.
- (10) "Bimetallic" Stress Configuration:
Note (3) configuration provides "worse case" stress loading to adhesive and mirror.